BEILSTEIN JOURNAL OF NANOTECHNOLOGY

Self-assembly at solid surfaces

Edited by Sidney R. Cohen and Jacob Sagiv

Imprint

Beilstein Journal of Nanotechnology
www.bjnano.org
ISSN 2190-4286
Email: journals-support@beilstein-institut.de

The *Beilstein Journal of Nanotechnology* is published by the Beilstein-Institut zur Förderung der Chemischen Wissenschaften.

Beilstein-Institut zur Förderung der
Chemischen Wissenschaften
Trakehner Straße 7–9
60487 Frankfurt am Main
Germany
www.beilstein-institut.de

Beilstein Journal
of Nanotechnology

Self-assembly at solid surfaces

Sidney R. Cohen*[1] and Jacob Sagiv*[2]

Editorial

Address:
[1]Department of Chemical Research Support, The Weizmann Institute of Science, P.O.B. 26, Rehovot 76100, Israel and [2]Department of Materials and Interfaces, The Weizmann Institute of Science, Rehovot 76100, Israel

Email:
Sidney R. Cohen* - sidney.cohen@bjnano.org; Jacob Sagiv* - jacob.sagiv@weizmann.ac.il

* Corresponding author

Beilstein J. Nanotechnol. **2011,** *2,* 824–825.
doi:10.3762/bjnano.2.91

Received: 06 December 2011
Accepted: 12 December 2011
Published: 20 December 2011

This article is part of the Thematic Series "Self-assembly at solid surfaces".

Editor-in-Chief: T. Schimmel

The spontaneous formation of highly ordered amphiphilic monolayers on solid surfaces by adsorption from organic solutions at the liquid–solid interface was first reported in the seminal work of W. A. Zisman and co-workers in the mid-20th century [1]. In that work, attention was focused on the remarkable wetting properties of such monolayers, which were not only hydrophobic, but also oleophobic, i.e., they are not wetted by many organic oils, including the solutions from which they were obtained. Several directions of basic study and applications were then pursued employing these *oleophobic monolayers*: Confinement of molecules of interest for surface examination, prevention of spreading of liquids, friction and wear reduction, and surface passivation and protection.

Whereas the early study of such monolayers indeed attracted considerable attention over the years, perhaps their greatest impact was yet to come, in new directions of research that could not have been foreseen at the time. These avenues exploit the ability to finely tune a wide variety of surface properties, for many diverse potential applications, through the combination of molecular self-assembly, chemical design, and postassembly surface manipulation by various chemical and physical techniques. The term *self-assembling monolayer* was thus coined with reference to the planned layer-by-layer assembly of organized films thicker than a single monolayer [2]. These directions, which gained momentum in the 1980s and continue strongly today, are forging new avenues of development. With the advent of relatively recent technologies for small-scale patterning, interest in self-assembled films has seen a surge of activity throughout a wide range of areas ranging from biointerfaces to data storage and devices.

This Thematic Series presents a small, but significant sampling of these exciting areas of research. Thus, the functionality of self-assembled films or of structures derived from them is demonstrated, including mechanical, electrical, and catalytic properties. Unique nanoscale structures are prepared employing lithographic processes and the templating capabilities of the films. Finally, the different characterization techniques employed in these studies point to the unique challenges involved in surface analysis at the nanoscale, and reveal the fascinating properties of the various films and structures.

We hope that this Thematic Series will serve as an inspiration for those wanting to learn about and become involved in the field, and will help expand the horizons of those already engaged in its active research. We would like to thank the Beilstein-Institut for the opportunity to present this Thematic Series, and of course the contributors for their efforts and ingenuity in furthering the research and development of self-assembly at solid surfaces into ever-expanding new areas of scientific activity.

Sidney R. Cohen and Jacob Sagiv

Rehovot, December 2011

References

1. Bigelow, W. C.; Pickett, D. L.; Zisman, W. A. *J. Colloid Sci.* **1946,** *1,* 513–538. doi:10.1016/0095-8522(46)90059-1
2. *New Sci.* **1983,** *98,* 20.

License and Terms

The definitive version of this article is the electronic one which can be found at:
doi:10.3762/bjnano.2.91

Beilstein Journal
of Nanotechnology

Mechanical characterization of carbon nanomembranes from self-assembled monolayers

Xianghui Zhang*, André Beyer and Armin Gölzhäuser

Full Research Paper

Open Access

Address:
Department of Physics, Physics of Supramolecular Systems and Surfaces, Bielefeld University, 33615 Bielefeld, Germany

Email:
Xianghui Zhang* - zhang@physik.uni-bielefeld.de

* Corresponding author

Keywords:
bulge test; carbon nanomembrane; mechanical characterization; self-assembled monolayers; two-dimensional materials

Beilstein J. Nanotechnol. **2011,** *2,* 826–833.
doi:10.3762/bjnano.2.92

Received: 02 September 2011
Accepted: 17 November 2011
Published: 20 December 2011

This article is part of the Thematic Series "Self-assembly at solid surfaces".

Guest Editors: S. R. Cohen and J. Sagiv

Abstract

This paper reports on the mechanical characterization of carbon nanomembranes (CNMs) with a thickness of 1 nm that are fabricated by electron-induced crosslinking of aromatic self-assembled monolayers (SAMs). A novel type of in situ bulge test employing an atomic force microscope (AFM) is utilized to investigate their mechanical properties. A series of biphenyl-based molecules with different types of terminal and/or anchor groups were used to prepare the CNMs, such as 4'-[(3-trimethoxysilyl)propoxy]-[1,1'-biphenyl]-4-carbonitrile (CBPS), 1,1'-biphenyl-4-thiol (BPT) and 4-nitro-1,1'-biphenyl-4-thiol (NBPT). The elastic properties, viscoelastic behaviors and ultimate tensile strength of these biphenyl-based CNMs are investigated and discussed.

Introduction

Ultrathin freestanding nanomembranes have recently attracted much attention as promising materials in nanotechnology [1,2]. They can be made with molecular or atomic thickness and macroscopic size, constituting two-dimensional (2-D) objects of fundamental interest as well as being suitable for applications. To this end, the mechanical stability is crucial for the fabrication of miniature yet highly sensitive nanodevices from freestanding nanomembranes. A variety of approaches to fabricate nanomembranes has been tested: Spin-assisted layer-by-layer (LBL) assembly [3,4]; spin-coating of organic–inorganic hybrid films with an interpenetrating network (IPN) structure [5,6]; cross-linking of ligand-stabilized nanoparticle assemblies at the fluid interfaces [7,8]. Freestanding nanomembranes with thicknesses from 20 to 70 nm were achieved by these approaches.

Eck et al. reported the fabrication of carbon nanomembranes (CNMs) with a thickness of 1 nm by electron-induced crosslinking of aromatic self-assembled monolayers (SAMs) [9]. Freestanding CNMs were fabricated after the dissolution of the substrate on which the SAMs were formed. A subsequent transfer with the aid of a polymeric transfer medium allowed the placement of CNMs onto arbitrary materials [10,11]. CNMs have been utilized as supporting material in transmission electron microscopy (TEM), which thus allows higher-contrast imaging of nanosized objects [11].

The mechanical properties of ultrathin nanomembranes are of particular interest as they will determine their applicability as filters, sensors or actuators. For some of the above-mentioned nanomembranes, elastic properties and tensile strength have been investigated by bulge tests [3-5]. Bulge testing is widely used to characterize the mechanical properties of freestanding films. The technique involves the clamping of a freestanding membrane over an orifice and the application of an overpressure to one side. The Young's modulus and the prestress are then calculated from the obtained pressure–deflection relationship. The deflection is usually monitored with an optical microscope, either by viewing the membrane from the side [12] or by using a laser interferometer [13]. Both methods have a resolution in the range of hundreds of nanometers. Atomic force microscopy (AFM) has also been used for indentation studies on soft [14] as well as stiff [15] membranes. In addition, it was recently reported that the curvature of a bulged membrane was determined by AFM, while its deflection was measured with a laser sensor [16]. An optical detection of CNMs is not feasible due to their thickness of only 1 nm. However, it is straightforward to perform a complete bulge test with an AFM deflection measurement and thus to improve the resolution such that bulge testing becomes practicable for the investigation of ultrathin CNMs [10].

Here we report the mechanical characterization of one-nanometer-thick freestanding CNMs by means of bulge testing in an AFM. The AFM is used to measure the deflection of the membrane center, either by scanning a bulged membrane (the line-scanning method), or by approaching the center of the membrane and measuring the corresponding deflection (the central-point method). These techniques can be used to determine Young's modulus and the prestress. They also allow us to investigate the viscoelastic behavior and thus generate insights into the mechanics of CNMs.

Results and Discussion

Figure 1a shows a schematic diagram of bulge test in an atomic force microscope. Loading of the membrane is achieved by applying a nitrogen gas pressure to the membrane. The pressure difference between the top and the bottom of the membrane is read by a pressure sensor, and the resulting deflec-

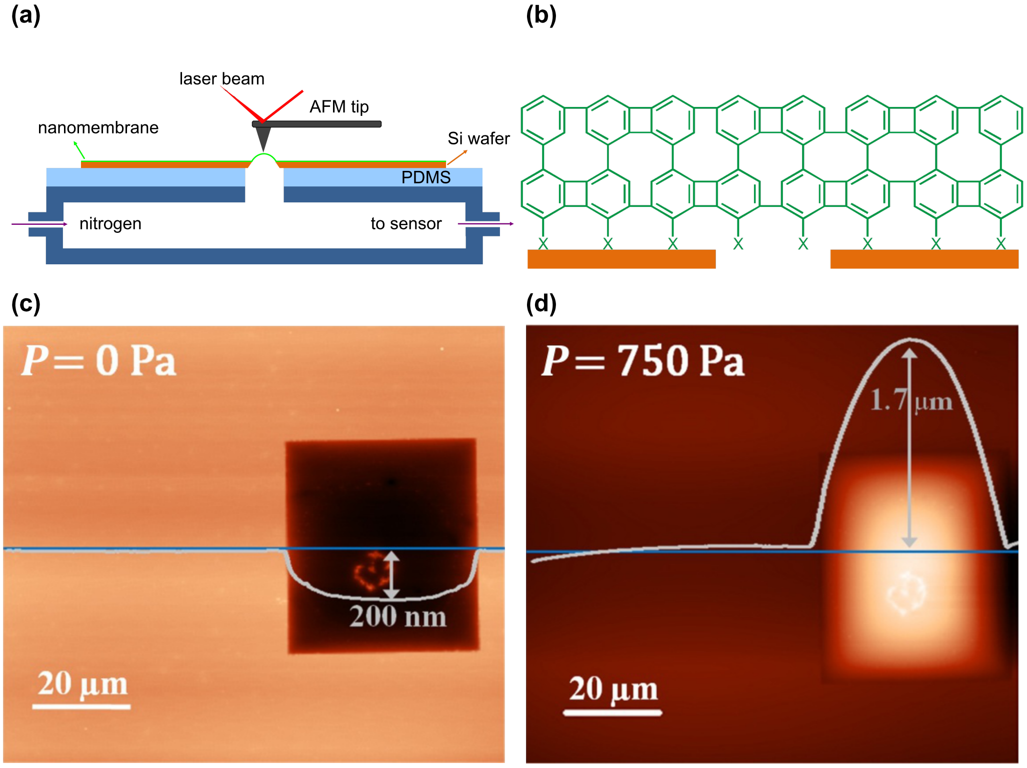

Figure 1: (a) Schematic diagram of a bulge test in AFM; (b) Schematic of a biphenylthiol CNM on a window-structured Si substrate, which is suspended over an orifice; (c) AFM image of a nonpressurized CNM in contact mode and the line profile with a downward deformation of 200 nm; (d) AFM image of the same membrane with an applied pressure of 750 Pa and a line profile with an upward deflection of 1.7 µm.

tion at the center of the membrane is recorded by an AFM tip. Figure 1b shows the scheme of a CNM that is suspended over an orifice. The high mechanical stability of CNMs allows both tapping and contact-mode scanning. Figure 1c shows a topographic contact-mode AFM image of a nonpressurized CNM, which was prepared on a rectangular opening in a silicon substrate by using the procedure described previously [9]. The CNM was formed from a self-assembled monolayer of 4'-[(3-trimethoxysilyl)propoxy]-[1,1'-biphenyl]-4-carbonitrile (CBPS) on silicon nitride membranes, which was cross-linked with a dose of 60 mC·cm^{-2} electrons. A downward step height of ~200 nm was observed due to the point load of the tip. This step height increases with the force applied by the tip. Figure 1d shows the same membrane with an applied pressure of ~750 Pa. An upward deflection of 1.7 µm was measured at the center of the membrane. Comparable images were retrieved from biphenylthiol CNMs, which were prepared by transferring the cross-linked SAMs onto window-structured silicon samples [10]. Note that the interfacial adhesion between the CNM and the substrate is mainly due to van-der-Waals contributions. Especially in the case of biphenylthiol CNMs, chemical bonds between the CNM and silicon are unlikely, as intermolecular disulfide bonds form immediately after the cleavage of the thiol-CNM from its original gold substrate. Because flexible CNMs may even conform to surfaces with a nanoscale roughness, the adhesion energy is enhanced due to an increased contact area. Apparently, this adhesion enhancement is sufficiently high to avoid delamination of CNMs from the silicon during gas-pressure loading, as shown by AFM images, e.g., Figure 1c,d.

The deflection of a membrane at the center is accessible from topographic AFM images such as in Figure 1c,d. However, this method of data retrieval is very time-consuming. In an earlier report [10] we restricted ourselves to recording line scans at the center of a membrane instead of recording full images for each applied pressure. A further development is presented in this work: The central-point method. In this method the AFM tip is brought into contact with the membrane at a preset force, only at the central point of the membrane. The main advantage of this method in comparison to scanning full lines is not in the saving of time but in the substantially reduced probability of membrane rupture events during data acquisition.

The measured deflection at the central point of a bulged membrane h_m is determined from the change of the AFM height signal due to pressurization of the membrane, as schematically shown in Figure 2a. Note that the position of the silicon frame changes when the applied pressure is varied. Therefore the AFM height signal is always measured with respect to the silicon frame. For this purpose, the AFM tip was used to probe the silicon frame near the membrane for each applied pressure. To demonstrate the feasibility of this “central-point method”, Figure 2b shows a comparison of the line-scanning method and the central-point method. It can clearly be seen that both deflection measurements are in very good agreement.

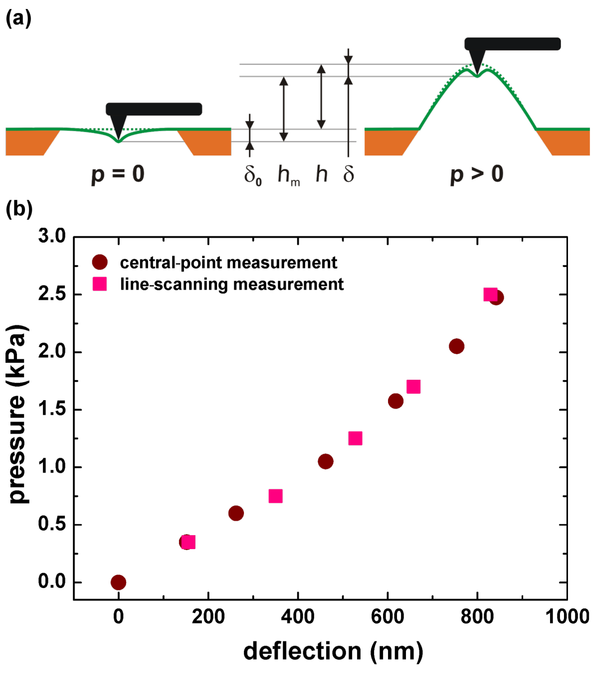

Figure 2: (a) Schematic of the central-point method in the bulge test; (b) Comparison of the line-scanning and the central-point method in the bulge test.

In the central-point method, the measurements are performed with a certain tip force, which is kept constant during the recording of a pressure–deflection curve. This force corresponds to an indentation depth δ_0, which appears as a step height in topographic AFM images of nonpressurized membranes. The indentation depth δ of pressurized membranes was evaluated in order to correct the measured deflection, as described previously [10]. In this system, the tension of the CNM is assumed to be the main contribution balancing the AFM tip force. The force contributed by the bending stiffness and the adhesion between the tip and the membrane was neglected. For a pressurized membrane, the indentation depth δ decreases with increasing pressure. The change of the indentation depth Δδ is given by [10]

$$\begin{aligned}\Delta\delta = \delta - \delta_0 &= \delta_0 \frac{\sigma_0}{\sigma_0 + \sigma} - \delta_0 \\ &= \delta_0 \frac{\sigma_0}{\sigma_0 + \frac{2}{3}\frac{E}{(1-\nu)}\frac{h^3}{a^2}} - \delta_0 \qquad (1)\end{aligned}$$

where δ_0 is the step height in topographic AFM images of the nonpressurized membrane, E is the Young's modulus, σ_0 is the residual stress, ν is the Poisson's ratio and $2a$ is the length of the short edge of the membrane. The corrected deflection h is then given by

$$h = h_\mathrm{m} + \Delta\delta \qquad (2)$$

Note that $\Delta\delta$ is negative, i.e., the corrected deflection is always smaller than the measured value h_m. This correction scheme typically results in an increase in the Young's modulus and a decrease in the residual stress by approximately 5%.

Elasticity

In a bulge test, the elastic response is derived from the relationship between the loading pressure p and the resulting deflection at the center of the membrane h. Three successive loading and unloading test cycles were applied to a CNM with a maximum strain of ~0.66%, as shown in Figure 3a. For such deformations the membrane displays elastic behavior with a very small hysteresis of less than 5%. The relationship between pressure and deflection was derived by Vlassak and Nix [17], and an analytical formula for square and rectangular membranes is given by

$$p = \mathrm{c}_1 \frac{\sigma_0 t}{a^2} h + \mathrm{c}_2 \frac{Et}{a^4(1-\nu)} h^3 \qquad (3)$$

where the applied pressure p is a function of the corrected deflection at the center of the membrane h. The membrane sizes were measured in a scanning electron microscope (SEM). The constants c_1 and c_2 were taken from the literature [17]. The Young's modulus E and the residual stress σ_0 are accessible by fitting the above equation to the measured data.

Three different biphenyl molecules were used to fabricate CNMs. SAMs of 4'-[(3-trimethoxysilyl)propoxy]-[1,1'-biphenyl]-4-carbonitrile (CBPS) were formed on silicon nitride, SAMs of 4'-nitro-1,1'-biphenyl-4-thiol (NBPT) and 1,1'-biphenyl-4-thiol (BPT) on gold surfaces. The thickness of the respective SAMs was determined by X-ray photoelectron spectroscopy (XPS) to be ~1.6 nm for CBPS SAMs, which was larger than that of NBPT SAMs (~1.2 nm) and BPT SAMs (~0.9 nm) [9,18,19]. As cross-linking occurs between the phenyl rings, a comparable thickness is expected for the corresponding CNMs. The CNM can be modeled as a composite layer with ~1 nm thick part containing cross-linked biphenyl rings and other parts containing merely hydrocarbon chains with no contribution to the elasticity. Therefore the mechanical properties of all CNMs were evaluated by taking the same thickness of 1 nm. Figure 3b shows the evolution of the CNM elasticity during the cross-linking process, i.e., a plot of Young's modulus of CNMs as a function of electron doses. Below 20 mC·cm^{-2}, only a few intact membranes are built, indicating that the number of cross-links in aromatic SAMs is too small to allow a reliable formation of freely suspended CNMs. For electron doses between 30 mC·cm^{-2} and 50 mC·cm^{-2}, more cross-links are formed and the mechanical stiffness is consequently enhanced, which facilitates the formation of freestanding CNMs. With further exposure, the Young's moduli remained constant, even when the membrane was exposed to much higher doses, up to 80 mC·cm^{-2} (cf. Figure 3b). This behavior is in accordance with an earlier study on the thermal stability of CNMs, which indicated almost complete cross-linking at an electron dose of ~45 mC·cm^{-2} [20]. Fully cross-linked BPT and NBPT CNMs that were made on a gold substrate had a Young's

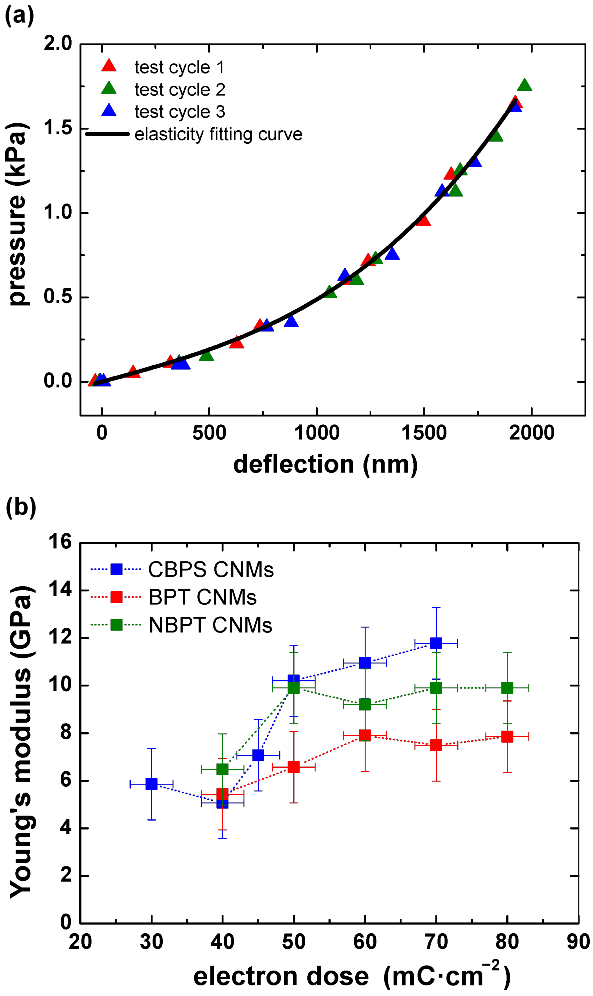

Figure 3: (a) Pressure–deflection relationship of an NBPT CNM with three successive loading and unloading cycles, and the corresponding elasticity fitting curve; (b) Young's modulus for CBPS, NBPT and BPT CNMs as a function of electron irradiation doses.

Table 1: Residual stress and strain of CNMs with different electron doses.

electron dose	30 mC·cm^{-2}	40 mC·cm^{-2}	50 mC·cm^{-2}	60 mC·cm^{-2}	70 mC·cm^{-2}	80 mC·cm^{-2}
BPT CNMs	–	75 MPa (1.6%)	75 MPa (1.2%)	95 MPa (1.2%)	46 MPa (0.64%)	51 MPa (0.67%)
NBPT CNMs	–	59 MPa (0.91%)	87 MPa (0.87%)	124 MPa (1.35%)	72 MPa (0.73%)	108 MPa (1.1%)
CBPS CNMs	71 MPa (1.2%)	57 MPa (1.1%)	53 MPa (0.5%)	44 MPa (0.4%)	57 MPa (0.5%)	–

modulus of 6–8 GPa and 8–10 GPa, respectively. CBPS CNMs that were formed from a SAM on silicon nitride showed a similar elastic behavior with a Young's modulus of 10–12 GPa. Note that CBPS SAMs are distinct from BPT and NBPT SAMs not only in the substrate, but also in the head group. Furthermore, CBPS CNMs were fabricated by direct dissolution of a 30 nm thick silicon nitride membrane without a transfer process. Conversely, for the fabrication of BPT and NBPT CNMs, it is necessary to transfer the CNM from a flat gold surface onto a silicon window. It was reported earlier that the degradation of alkanethiolate SAMs due to electrons is strongly dependent on the electrical conductivity of the substrate [21]; however, we observed the same dose dependence for both types of biphenyl-based CNMs, indicating that the conductivity of the substrate is less important. From the above, we can conclude that the elastic properties of the CNMs are mainly determined by the cross-linked aromatic units, and are independent of the type of substrate, head group or the transfer process.

Residual stresses of the CNMs were tensile in nature and varied from 40 to 120 MPa, and the residual strains varied from 0.4 to 1.6%. There was no obvious dependence on the electron dose, cf. Table 1. For CNMs, the stress is likely to be introduced during the cross-linking, as new covalent bonds are created. Obviously, the strain release is precluded due to the adhesion of the CNMs to the substrate or the polymeric transfer medium.

Viscoelasticity

Macroscopic viscoelasticity and local viscoelastic properties of soft materials have been intensively studied, for example in polymer networks or in nuclei of biological cells [22,23]. Gaining new insights into the viscoelastic behavior of one-nanometer-thick membranes requires a method with sufficient sensitivity as to determine the time-dependent deformation under a constant load. With the bulge-test setup we can perform quantitative measurements at room temperature. Figure 4a shows stress–strain curves from loading–unloading measurement cycles, with successively increasing maximum strain values of ~0.65%, ~1.2% and ~1.7%. The hysteresis loop becomes more and more pronounced with the increase in the maximum tensile strain of each cycle. Hysteresis is one major characteristic of viscoelasticity and is associated with the energy that is dissipated as heat in the loading cycles. The specific damping capacity is thus calculated based on the ratio of energy dissipated to energy stored, and the corresponding values are ~3.1%, ~9.8% and ~17.6%, respectively.

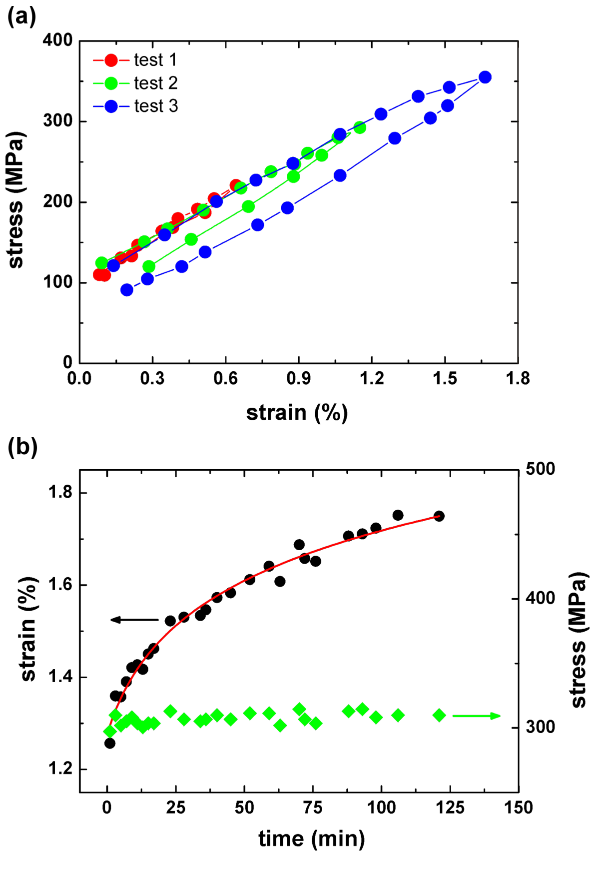

Figure 4: (a) Stress–strain relationship of three loading–unloading measurements on a NBPT CNM with different maximum strains at ~0.65%, ~1.2% and ~1.7%; (b) Strain exhibits a nonlinear increase at a stress of 304 ± 15 MPa, indicating a tensile-creep behavior.

When a CNM was loaded at a lower stress (~163 MPa), the deflection remained constant over time. However, when it was loaded at a higher stress (304 ± 15 MPa) the deformation exhibited a nonlinear increase, and thus this indicates tensile creep, as shown in Figure 4b. Note that delamination of CNMs would lead to a steplike increased deflection, but here we observed a continuous increase, indicating a strong adhesion between the CNM and the silicon. The applied strain at which creep deformation starts for CNMs is in the range of 0.8–1.2%. Strain rates as low as 10^{-8} s^{-1} can be measured with the employed AFM setup. At the beginning of loading, a linear relationship between strain and time was observed, as shown in the inset of Figure 5a. Initial creep rates were thus derived from the slopes of linear curve fits, and they increased with increasing tensile strain. As plotted in Figure 5a, initial creep rates are in the range of 10^{-6} s^{-1}. This is in contrast to some polymers whose creep rate can span several orders of magnitude under different stress levels [24]. CNMs possess rather stable initial creep rates, indicating higher resistance against the creep deformation.

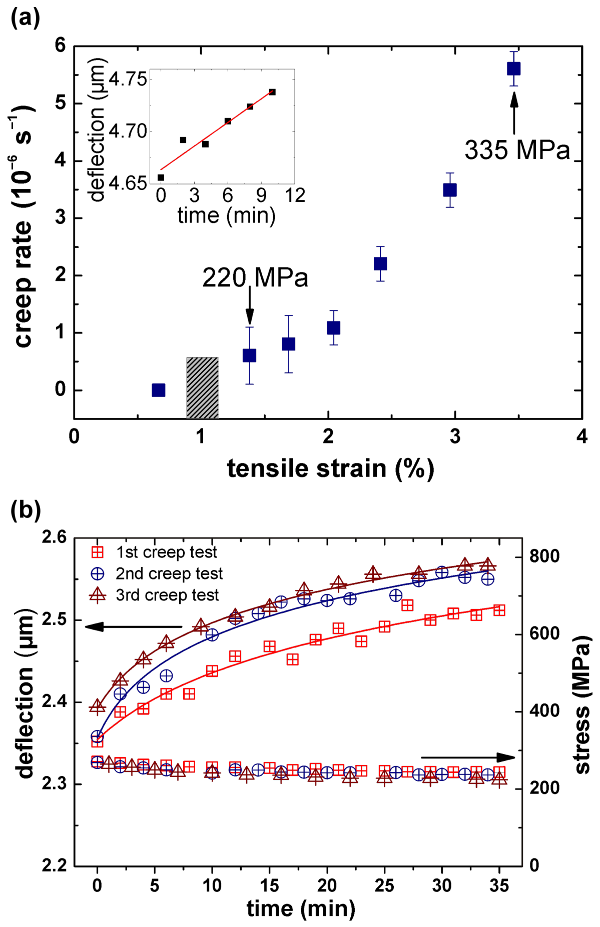

Figure 5: (a) Creep rate as a function of tensile strain; creep deformation can be only observed above a certain strain, e.g., ~1%. Inset: The deformation at the beginning of creep has a linear characteristic. (b) Three creep deformations were recorded at room temperature, the second test was performed 200 min after the first unloading, and the third test was performed 160 min after the second unloading.

In order to understand its reversibility, we also employed several creep tests on a CNM and examined its recovery from previous creep deformations. Three creep tests with the same initial stress of 260 MPa were presented in Figure 5b, with the second and third creep tests carried out 200 and 160 min after the previous test, respectively. The measurements show an almost complete recovery after each test cycle. The creep behavior is a manifestation of molecular rearrangements in CNMs around defects and molecular domains, caused by stress-dependent thermal activation, and which partially recover in the absence of an external load.

Ultimate tensile strength

Finally, we determined the ultimate tensile strength of CNMs by means of bulge tests. Rupture occurs usually at very high pressures and the corresponding deflection cannot be directly measured. The deflection is thus calculated from Equation 3. The ultimate tensile stress σ_u of rectangular membranes is presented as follows [13,17]:

$$\sigma_u{}^3 = \frac{Ep_u^2 a^2}{t^2(1-\nu)} \times \frac{c_2}{c_1^3} \qquad (4)$$

where p_u is the ultimate pressure at which the membrane ruptures. All other quantities are the same as in Equation 3. To minimize the deviation caused by different geometries of CNMs, we only selected circular membranes for the rupture tests. Equation 4 is valid for circular membranes as well [25] but with a constant value for the ratio $c_2/c_1{}^3 = 1/24$. Figure 6 shows the statistical histogram of tensile strength of nine NBPT CNMs and 12 BPT CNMs. The tensile strength of NBPT CNMs ranges from 440–720 MPa with a peak located at ~567 MPa. The tensile strength of BPT CNMs has a wider distribution, with a dominating peak at ~475 MPa. These results show that NBPT CNMs possess a higher mechanical stability than BPT CNMs do, which may be caused by a higher molecular packing density in NBPT CNMs. Compared to other nanomembranes, such as IPN nanocomposite with organic–inorganic networks, which exhibit a tensile strength of 105 MPa [5], the ultimate tensile strength of CNMs is 5–6 times higher.

Conclusion

Freestanding CNMs with 1 nm thickness were prepared from cross-linked biphenyl-based self-assembled monolayers. We employed bulge testing in order to obtain the mechanical properties of these CNMs. The preparation of fully cross-linked CNMs requires an electron dose of at least 50 mC·cm^{-2}. Viscoelastic behavior in CNMs was investigated quantitatively and the results show that CNMs exhibit a high resistance against creep deformation. It was demonstrated that CNMs display a remarkable ultimate tensile strength. The molecular thickness as well as the outstanding performance in the mechan-

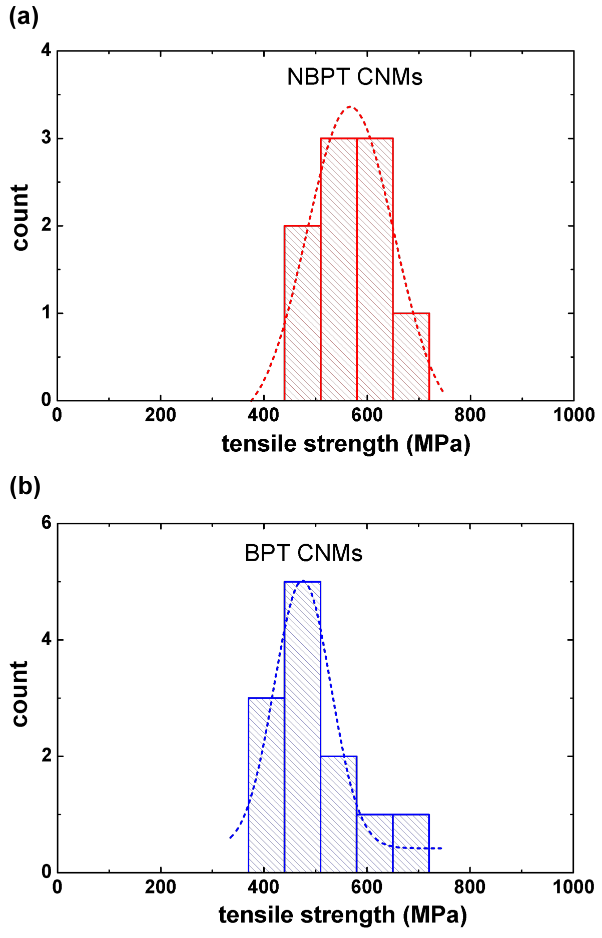

Figure 6: (a) Histogram of ultimate tensile strength of circular NBPT CNMs, with a peak at ~567 MPa (Gaussian peak fitting); (b) Histogram of ultimate tensile strength of circular BPT CNMs, with a peak at ~475 MPa.

ical stability enables CNMs to work in a variety of applications, e.g., as ultrathin support films in electron microscopy, as filter membranes or as highly sensitive and mechanically stable miniature transducers.

Experimental

To prepare 4'-[(3-trimethoxysilyl)propoxy]-[1,1'-biphenyl]-4-carbonitrile (CBPS) SAMs, we used 30 nm thick silicon nitride membranes on window-structured silicon substrates (Silson Ltd., UK). The membranes were cleaned with Piranha solution (H_2SO_4/H_2O_2 in volume ratio of 3:1) for 20 min to remove organic residues. Afterwards the membranes were immersed into a ~10 mL solution of dry and degassed toluene with 10 mmol CBPS molecules for 120 h in a sealed flask under nitrogen atmosphere. For the preparation of 1,1'-biphenyl-4-thiol (BPT) self-assembled monolayers (SAMs) and 4'-nitro-1,1'-biphenyl-4-thiol (NBPT) SAMs, we use a 300 nm polycrystalline Au layer with (111) crystal planes epitaxially grown on a mica substrate (Georg Albert Physical Vapor Deposition). The substrate was cleaned with a UV/ozone cleaner (UVOH 150 LAB FHR), rinsed with ethanol and then blown dry under a nitrogen stream. Afterwards the substrates were immersed into a ~10 mmol solution of dry and degassed dimethylformamide (DMF) with 10 mmol BPT or NBPT molecules for 72 h in a sealed flask under nitrogen atmosphere.

Cross-linking was achieved in high vacuum ($<5 \times 10^{-8}$ mbar) with an electron flood gun at an electron energy of 100 eV and a current of 3 mA. Freestanding CBPS CNMs were obtained by dissolving the Si_3N_4 membranes on a window-structured silicon substrate (Silson Ltd., UK) in hydrofluoric acid (HF, ~48%). For BPT and NBPT CNMs, the samples were spin-coated with a layer of poly(methyl methacrylate) (PMMA) for stabilization and baked on a hotplate. The sample was immersed into HF (~48%) for 20 min to weaken the adhesion between the gold and the mica. The separation of the PMMA/CNM/Au layer from the mica was achieved by careful dipping of the sample into water. Subsequently, the Au layer was completely etched by a gold etchant (5 wt % I_2 and 10 wt % KI in water). Afterwards, the CNM/PMMA layer was transferred to a silicon substrate with window-structured openings (Silson Ltd., UK), which was followed by dissolution of the PMMA in acetone and drying with a critical-point dryer (Autosamdri-815B, Tousimis, USA) to yield clean and suspended CNMs.

The mechanical characterization was carried out by means of bulge testing in an AFM (NTEGRA, NT-MDT, Russia). The pressure cell was made from a hollow steel cylinder with two side openings for applying and measuring the gas pressure, and one circular opening at the topside, which was sealed by the membrane. In order to establish a gas-tight connection between the membrane and the pressure cell, a layer of polydimethylsiloxane (PDMS) with a thickness of 2 mm was prepared on top of the pressure cell. The deflection at the center of the membrane was recorded by scanning the membrane with AFM in the contact mode.

In the central-point method, the AFM tip was positioned on the membrane's center to detect the deflection of the membrane. The center was determined by measuring the position of the four edges by AFM. To this end, the tip was approached several times near an edge. The difference in the AFM height signal upon contacting the silicon frame or the freestanding CNM is easily distinguished. For each applied pressure, the AFM height signal at the center of the membrane as well as at three points on the silicon frame was measured. The measurements on the silicon were taken in order to correct any movement of the silicon frame, i.e., any change in the height position or tilt.

Acknowledgements

We thank the Volkswagenstiftung and the BMBF for financially supporting this project. This work greatly benefited from scientific exchange supported by the European Science Foundation through the COST action CM0601.

References

1. Cheng, W.; Campolongo, M. J.; Tan, S. J.; Luo, D. *Nano Today* **2009,** *4,* 482–493. doi:10.1016/j.nantod.2009.10.005
2. Sakamoto, J.; van Heijst, J.; Lukin, O.; Schlüter, A. D. *Angew. Chem., Int. Ed.* **2009,** *121,* 1048–1089. doi:10.1002/anie.200801863
3. Jiang, C.; Markutsya, S.; Pikus, Y.; Tsukruk, V. V. *Nat. Mater.* **2004,** *3,* 721–728. doi:10.1038/nmat1212
4. Jiang, C.; Markutsya, S.; Shulha, H.; Tsukruk, V. V. *Adv. Mater.* **2005,** *17,* 1669–1673. doi:10.1002/adma.200500016
5. Vendamme, R.; Onoue, S.-Y.; Nakao, A.; Kunitake, T. *Nat. Mater.* **2006,** *5,* 494–501. doi:10.1038/nmat1655
6. Watanabe, H.; Kunitake, T. *Adv. Mater.* **2007,** *19,* 909–912. doi:10.1002/adma.200601630
7. Lin, Y.; Skaff, H.; Böker, A.; Dinsmore, A. D.; Emrick, T.; Russell, T. P. *J. Am. Chem. Soc.* **2003,** *125,* 12690–12691. doi:10.1021/ja036919a
8. Lin, Y.; Böker, A.; Skaff, H.; Cookson, D.; Dinsmore, A. D.; Emrick, T.; Russell, T. P. *Langmuir* **2005,** *21,* 191–194. doi:10.1021/la048000q
9. Eck, W.; Küller, A.; Grunze, M.; Völkel, B.; Gölzhäuser, A. *Adv. Mater.* **2005,** *17,* 2583–2587. doi:10.1002/adma.200500900
10. Turchanin, A.; Beyer, A.; Nottbohm, C. T.; Zhang, X.; Stosch, R.; Sologubenko, A.; Mayer, J.; Hinze, P.; Weimann, T.; Gölzhäuser, A. *Adv. Mater.* **2009,** *21,* 1233–1237. doi:10.1002/adma.200803078
11. Nottbohm, C. T.; Beyer, A.; Sologubenko, A. S.; Ennen, I.; Hütten, A.; Rösner, H.; Eck, W.; Mayer, J.; Gölzhäuser, A. *Ultramicroscopy* **2008,** *108,* 885–892. doi:10.1016/j.ultramic.2008.02.008
12. Watanabe, H.; Ohzono, T.; Kunitake, T. *Macromolecules* **2007,** *40,* 1369–1371. doi:10.1021/ma062850q
13. Xiang, Y.; Chen, X.; Vlassak, J. J. *J. Mater. Res.* **2005,** *20,* 2360–2370. doi:10.1557/jmr.2005.0313
14. Martins, P.; Delobelle, P.; Malhaire, C.; Brida, S.; Barbier, D. *Eur. Phys. J.: Appl. Phys.* **2009,** *45,* No. 10501. doi:10.1051/epjap:2008187
15. Lee, C.; Wei, X.; Kysar, J. W.; Hone, J. *Science* **2008,** *321,* 385–388. doi:10.1126/science.1157996
16. Schweitzer, E. W.; Göken, M. *J. Mater. Res.* **2007,** *22,* 2902–2911. doi:10.1557/JMR.2007.0373
17. Vlassak, J. J.; Nix, W. D. *J. Mater. Res.* **1992,** *7,* 3242–3249. doi:10.1557/JMR.1992.3242
18. Schnietz, M.; Turchanin, A.; Nottbohm, C. T.; Beyer, A.; Solak, H. H.; Hinze, P.; Weimann, T.; Gölzhäuser, A. *Small* **2009,** *23,* 2651–2655. doi:10.1002/smll.200901283
19. Turchanin, A.; Käfer, D.; El-Desawy, M.; Wöll, C.; Witte, G.; Gölzhäuser, A. *Langmuir* **2009,** *25,* 7342–7352. doi:10.1021/la803538z
20. Turchanin, A.; El-Desawy, M.; Gölzhäuser, A. *Appl. Phys. Lett.* **2007,** *90,* No. 053102. doi:10.1063/1.2437091
21. Zhou, C.; Trionfi, A.; Hsu, J. W. P.; Walker, A. V. *J. Phys. Chem. C* **2010,** *114,* 9362–9369. doi:10.1021/jp911402u
22. Schnurr, B.; Gittes, F.; MacKintosh, F. C.; Schmidt, C. F. *Macromolecules* **1997,** *30,* 7781–7792. doi:10.1021/ma970555n
23. Pollard, T. D.; Goldberg, I.; Schwarz, W. H. *J. Biol. Chem.* **1992,** *267,* 20339–20345.
24. Yang, J.; Zhang, Z.; Friedrich, K.; Schlarb, A. K. *Macromol. Rapid Commun.* **2007,** *28,* 955–961. doi:10.1002/marc.200600866
25. Pickhardt, V. Y.; Smith, D. L. *J. Vac. Sci. Technol. (N. Y., NY, U. S.)* **1977,** *14,* 823–825. doi:10.1116/1.569276

License and Terms

Beilstein Journal
of Nanotechnology

Direct monitoring of opto-mechanical switching of self-assembled monolayer films containing the azobenzene group

Einat Tirosh[1], Enrico Benassi[2], Silvio Pipolo[2,3], Marcel Mayor[4,5], Michal Valášek[4], Veronica Frydman[6], Stefano Corni[*2] and Sidney R. Cohen[*6]

Full Research Paper

Address:
[1]Weizmann Institute of Science, Department of Materials and Interfaces, Rehovot Israel, [2]Center S3, CNR Institute of Nanoscience, Modena, Italy, [3]Department of Physics, University of Modena and Reggio Emilia, Modena, Italy, [4]Karlsruhe Institute of Technology, Institute of Nanotechnology, PO Box 3640, D-76021, Karlsruhe, Germany, [5]University of Basel, Department of Chemistry, St. Johannsring 19, CH-4056 Basel, Switzerland and [6]Weizmann Institute of Science, Department of Chemical Research Support, Rehovot Israel

Email:
Stefano Corni[*] - stefano.corni@nano.cnr.it; Sidney R. Cohen[*] - sidney.cohen@weizmann.ac.il

* Corresponding author

Keywords:
AFM; azobenzene; elastic modulus; molecular dynamics; nanomechanics; photoswitch; quantum mechanics computation; self-assembled monolayer

Beilstein J. Nanotechnol. **2011,** *2,* 834–844.
doi:10.3762/bjnano.2.93

Received: 23 June 2011
Accepted: 30 September 2011
Published: 20 December 2011

This article is part of the Thematic Series "Self-assembly at solid surfaces".

Associate Editor: A. Gölzhäuser

Abstract

The potential for manipulation and control inherent in molecule-based motors holds great scientific and technological promise. Molecules containing the azobenzene group have been heavily studied in this context. While the effects of the *cis–trans* isomerization of the azo group in such molecules have been examined macroscopically by a number of techniques, modulations of the elastic modulus upon isomerization in self-assembled films were not yet measured directly. Here, we examine the mechanical response upon optical switching of bis[(1,1'-biphenyl)-4-yl]diazene organized in a self-assembled film on Au islands, using atomic force microscopy. Analysis of higher harmonics by means of a torsional harmonic cantilever allowed real-time extraction of mechanical data. Quantitative analysis of elastic modulus maps obtained simultaneously with topographic images show that the modulus of the *cis*-form is approximately twice that of the *trans*-isomer. Quantum mechanical and molecular dynamics studies show good agreement with this experimental result, and indicate that the stiffer response in the *cis*-form comprises contributions both from the individual molecular bonds and from intermolecular interactions in the film. These results demonstrate the power and insights gained from cutting-edge AFM technologies, and advanced computational methods.

Introduction

Molecule-based motors have great appeal due to their addressability, small size, and the possibility to incorporate them into unique structures. Molecules containing the azobenzene functionality are good candidates for converting light into mechanical work through a facile *cis*↔*trans* isomerization that is controlled by UV and visible light. The forces involved in this transition have been characterized by a number of techniques. For instance, changes in the stiffness of azobenzene-containing films were monitored by nanoindentation [1], by quartz-crystal resonator [2], and by electromechanical spectroscopy [3]. The force exerted per molecule during extension from *cis* to *trans* was extracted from cargo-lifting experiments on a macroscopic Hg droplet [4]. The mechanical response monitored in these works and others like them essentially measures a bulk response, which is governed by several effects including the stiffness of the molecular bond itself, as well as steric effects, electronic coupling, and film structure. Single-molecule force microscopy was used to monitor the mechanical and structural changes in the *cis*↔*trans* transition of individual azo-containing polymer molecules [5,6]. These elegant measurements were simulated by molecular dynamics [7]. It was shown that the mechanical response arises only partly from the azo moiety, and includes contributions from other constituents of the polymer chain.

The ability of azo-containing molecules to self-assemble into monomolecular layers (self-assembled monolayers, SAMs) provides an additional nanometer-scale mechanical system, combining the advantages of single-molecule properties with the coherence and template capabilities of macroscopic structures. These films enable such applications as sensors, and molecular-level mechanical manipulators. As an example, macroscopic transport at the solid–liquid interface was driven by modifying the solid–liquid surface tension at a droplet front by using a molecular switch based on a SAM of rotaxane [8]. Central to the function of such systems are changes in the inter- and intramolecular forces accompanying the transitions. In particular, by virtue of packing into a self-assembled film, steric constraints on the *cis*↔*trans* conversion, which do not exist in the isolated molecule or bulk disordered films, could dominate the switching [9,10]. Strictly, this steric hindrance requires close packing, thus some slight disorder in the film could be an enabling condition for the isomerization [11]. Molecular packing also governs the excitonic coupling between chromophores, which can strongly influence the conversion efficiency [12]. A variety of methods to monitor the *cis*↔*trans* switching have been demonstrated for SAMs. These include mechanical testing, as mentioned above, as well as changes in the local surface potential [13,14], UV–vis spectroscopy [10], wettability [15], and direct molecular-resolution imaging by scanning tunneling microscopy [10]. These methods vary in their ability to resolve the pattern of switching. For instance molecularly resolved images identified concerted switching in a small monolayer domain. And whereas concerted switching in such small domains may provide a path to overcome steric constraints, the fine mechanics of the *cis*↔*trans* conversion in SAMs of azobenzene-containing molecules is still not well understood.

The elastic modulus is a fundamental property based on microscopic properties of the system. As such, it provides a good metric for the isomerization, and is amenable to theoretical computation. Here, we report results of an atomic force microscopy (AFM) and atomistic computational study of the change in local stiffness, as induced by the optical *cis*↔*trans* conversion in a SAM of 4'-{[(1,1'-biphenyl)-4-yl]diazenyl}-(1,1'-biphenyl)-4-thiol (thio-2-DA). The experimental variation in stiffness shows quantitative agreement with the calculated values.

Results and Discussion

Experimental measurements

Measurement of the mechanical properties of monolayer films represents a technological challenge. Nanoindentation is appropriate for direct determination of local stiffness since the measurement is direct and, to first order, model-independent: A local deformation is induced and detected while a calibrated force is applied. Converting the stiffness thus measured to elastic modulus does, however, require a suitable model for the interaction. In this work the Derjaguin–Müller–Toporov (DMT) model was applied, which is appropriate for organic monolayer systems [16]. Another consideration for nanoindentation measurements is the substrate effect. "Buckle's rule" maintains that in order to gain information on the film only, and not the substrate, the depth of penetration into the film must not exceed 10% of the total film thickness. However, this range can be significantly extended in the case of sharp AFM tips [17], and, for soft films on hard substrates, as much as half of the film thickness can be penetrated without experiencing appreciable substrate effects [18]. In any case, film deformation must be kept to a minimum and reliable referencing to the substrate must be made.

The method applied here is time-resolved tapping force imaging, in which force–deformation curves are reconstructed from the amplitudes of the higher harmonics of oscillation of the flexural mode of the cantilever, spring-coupled to the torsional mode [19]. The latter mode is excited by using a special probe with the tip positioned off of the long axis. Since the force curves are generated simultaneously with the topo-

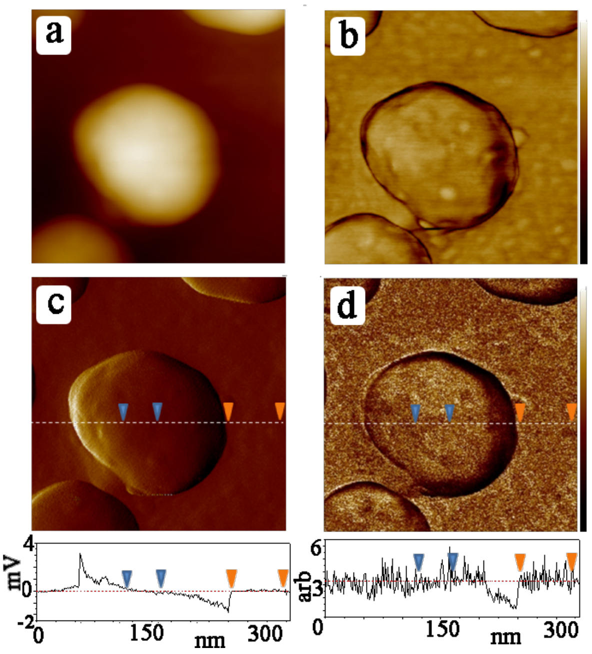

Figure 1: (a) Topography (color bar: 0–70 nm), (b) phase (color bar: 0–15 degrees), (c) error signal (scale indicated in profile), and (d) modulus (scale indicated in profile) of bare Au islands on glass. Cross sections are taken at the same scan line for the error and modulus signals and the triangles demark regions of zero error signal where the modulus measurement is valid (see text). Here, the modulus of the Au islands is the same as that of the glass substrate.

graphic scan, each pixel contains both topographic and mechanical information. Although in principle this method can give absolute modulus values, switching between samples can change probe alignment and hence calibration factors. For this reason, our samples contained an internal standard: The films were formed on Au islands with diameters of several tens of nanometers and a height of 50 nm on a glass substrate. The thio-2-DA molecules bind only to the gold, such that each scan line contains regions of hard surface (glass) and soft surface (SAM/Au). Figures 1–3 show how this concept is used to generate data. For each horizontal scan line, both the glass substrate and the gold island are sampled. For purposes of this measurement, Au and glass are considered equally stiff since the modulus signal saturates at about 5 GPa due to the limits of the cantilever spring constant and the signal sensitivities. The glass surface then serves as an in situ reference to which the film modulus can be compared. Scanning these samples before depositing the SAM gave no modulus contrast between glass and the Au islands, as seen in Figure 1.

Figure 2 shows a measurement in which the Au islands are coated with the SAMs. Images and cross sections show that the film has a significantly lower modulus than the substrate. The

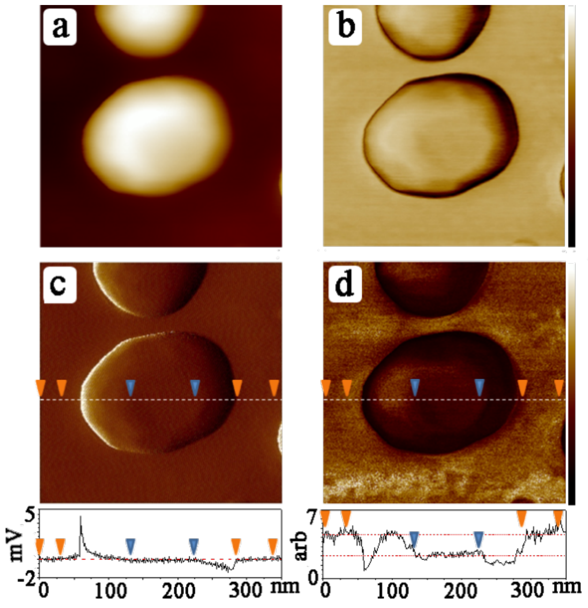

Figure 2: (a) Topography (color bar: 0–70 nm), (b) phase (color bar: 0–15 degrees), (c) error signal (scale indicated in profile), and (d) modulus signal (scale indicated in profile) of SAM-coated Au islands on glass. Data taken from as prepared samples (no irradiation), corresponding to the *trans* configuration.

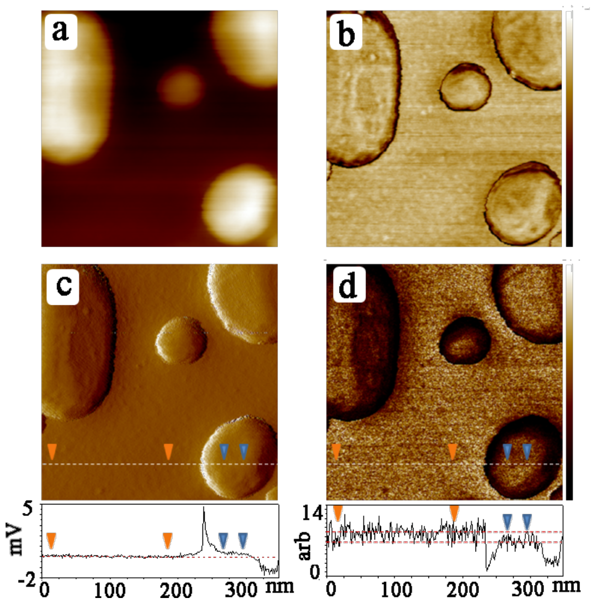

Figure 3: (a) Topography (color bar: 0–15 nm), (b) phase (color bar: 0–20 degrees), (c) error signal (scale indicated in profile), and (d) modulus signal (scale indicated in profile) of SAM-coated Au islands on glass after 120 min of irradiation at 365 nm (see text).

modulus is calculated simultaneously with the topography, from the experimentally derived force curves as fit to the DMT equation

$$E^* \cong \frac{3F}{\sqrt{R\delta^3}} \qquad (1)$$

where E^* is the reduced modulus, F the overall tip–surface force including adhesion, R the tip radius and δ the deformation [20]. In principle, individual force curves at specific pixel locations can be stored and analyzed to deduce the local stiffness, but by selecting and averaging entire areas corresponding to the regions of zero error signal as described above, much better statistics were obtained. The main constraint in this case is in the choice of areas of the image where the data can be taken to accurately represent stiffness. This requires monitoring of the corresponding error signal, shown in Figures 1–3. The error signal represents deviation of the modulated tip amplitude from that which is chosen as the feedback setpoint. When this is nonzero, the sample deformation can deviate strongly from the required controlled value. Furthermore, the error signal deviates from zero at the edges of the islands, where the contact area is ill-defined such that R in Equation 1 does not provide a good measure of the contact area (the model used here applies to a sphere indenting on a smooth half-plane). For this reason, the topography, error signal, and modulus images were compared to find the proper areas for signal acquisition on the plateau of the islands, with the additional check that the error signal should be less than 0.1% of the total oscillation amplitude. In Figures 1–3 this error value was less than 1 mV out of a 300–500 mV signal. Based on these considerations, the difference in the normalized stiffness of the thio-2-DA SAMs as function of light exposure was measured. Measurements were made on four different samples, with several different tips. Several tens of gold islands were included in the analysis, representing thousands of force–distance curves. The results are displayed in the histogram shown in Figure 4, and in Table 1. The results indicate that the modulus of the *cis*-isomer is approximately twice that of the energetically favored *trans*-isomer.

The illumination conditions were chosen by calibration based on UV–vis spectra of the samples both as solutions and in SAMs. The light sources as described in the methods section were used to illuminate the samples. The thermal back reaction (*cis*→*trans*) was previously verified as being slow in the SAM, with a half-life of 41 min [10]. As prepared, the sample is predominantly in the *trans*-state. By alternately irradiating first at 365 nm and then at 450 nm, the system could be switched between the two states, observed as a reversible transition in the measured stiffness as seen in Figure 4.

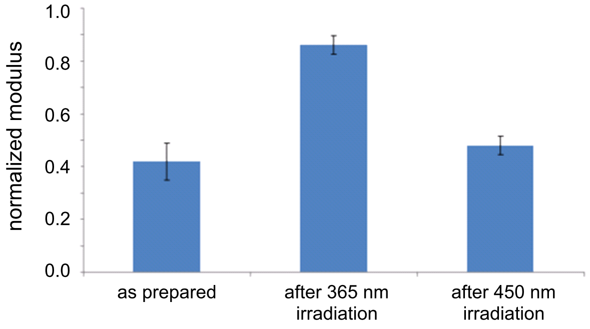

Figure 4: Histogram of the normalized modulus for different illumination conditions: As prepared, at 365 nm for *trans→cis* conversion and 450 nm for *cis→trans* conversion. The histograms represent collectively analyzed areas of over 80,000 nm^2, which is the equivalent of over 45,000 pixels of data. The E_{cis}/E_{trans} modulus ratio is 1.8 with a relative uncertainty of 20%.

Table 1: Mean values μ, standard deviation σ, relative error, and populations in the statistics for modulus values measured on the different samples.

sample	μ	σ	relative error 100·σ/μ	total area (nm^2)	total pixels
Au island	1.02	0.08	8	12760	6830
as prepared	0.42	0.14	33	32070	17160
365 nm	0.86	0.07	8	17830	9540
450 nm	0.048	0.07	15	24490	13100

Computational modeling

The investigation of the relative stiffness of the azobenzene SAM at the molecular level was also approached by computational modeling. The problem was modeled within two different schemes, one based on a quantum mechanical (QM) description of the single molecule, and the other on classical molecular dynamics (MD) simulations of the SAM. In the QM approach, the stiffness of the SAM is first related to a molecular quantity, the weighted molecular force constant <*k*>, through a simple model. Then, <*k*> is obtained by rigorous ab initio calculations (details in Experimental section). The molecular deformations (normal modes) that comprise the major contribution to <*k*> for [(1,1'-biphenyl)-4-yl] [4'-sulfanyl-(1,1'-biphenyl)-4-yl]diazene (2-DA) are shown in Figure 5 for both isomers. For the molecule in the *trans*-configuration, it corresponds to a stretching of the whole molecule along the principle axis. For the molecule in the *cis*-conformation, the dominant normal mode comprises the out-of-plane deformation of the phenyls. The QM model also predicts that the relative *cis*/*trans* stiffness decreases in the series of diphenyldiazene (1-DA) to bis[(1,1'-biphenyl)-4-yl]diazene (2-DA) to bis[(1,1':4',1''-terphenyl)-4-yl]diazene

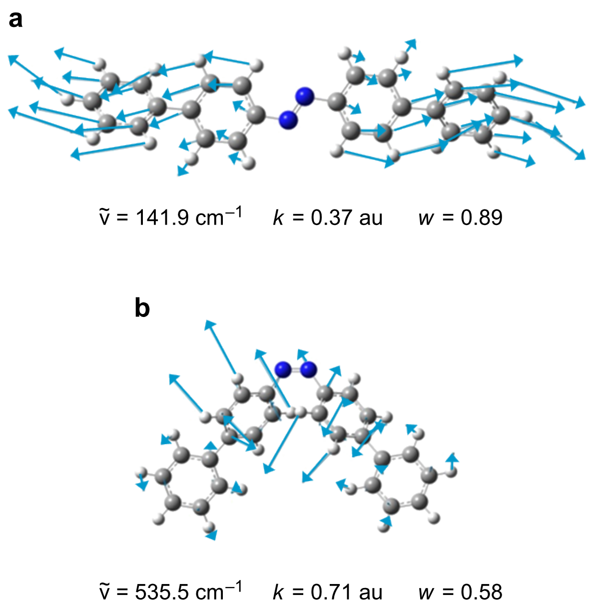

Figure 5: Displacement vectors for the normal mode that dominates the averaged force constant of (a) *trans*- and (b) *cis*-2-DA. The wavenumber (ṽ), the force constant (*k*, in atomic units, 1 au = 1.56·10^6 dyn/cm), and the weight (*w*) of each mode within <*k*> are also reported.

(3-DA), such that the calculated E_{cis}/E_{trans} ratios are 2.33, 1.79 and 1.64, respectively. Clearly, the *cis*-configuration is stiffer than the *trans* for all the compounds studied.

The MD model chosen to mimic the SAM is shown in Figure 6 and is fully described in the Methods section. It uses an atomistic (although empirical) description of the molecules and of their interactions in the SAM, and allows simulation of the compression of the SAM by a nanoindenter. It includes an annealed SAM surface fixed at the base by sulfur atoms, with no explicit inclusion of the gold substrate characteristics. The indenter is an incompressible Lennard–Jones sphere. Whereas the QM model is focused on the single-molecule properties, the MD simulation allows for steric interactions between neighboring molecules.

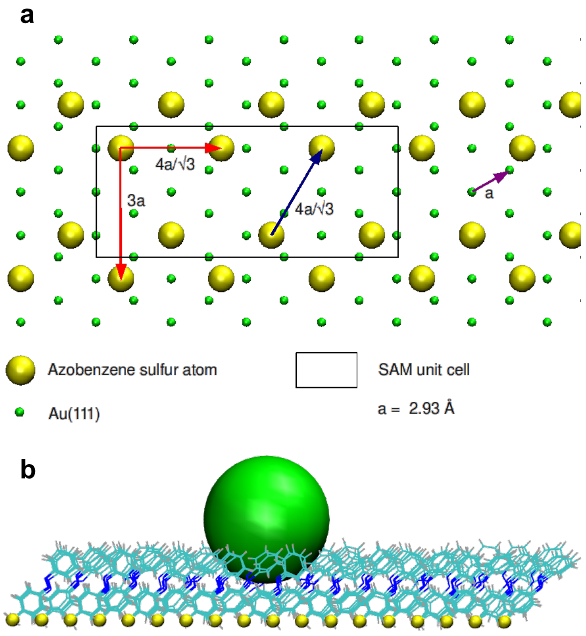

Figure 6: (a) Arrangement of the fixed sulfur atoms in the MD model of the SAM. The unit cell that has been periodically replicated to generate the starting conformation of the SAM is also shown as a black rectangle. It reproduces the periodicity of bright spots in the STM images of [3]. Only the Au atoms of the first surface layer are shown. (b) Snapshot from the MD simulation with the spherical probe (in green) upon the thio-1-DA SAM.

Table 2: Comparison of experimental and two different calculated values for the relative stiffness of the *cis*- and *trans*- configurations, E_{cis}/E_{trans}.

quantum mechanical^a	molecular dynamics^b	experimental
1.8	2.3 ± 0.2	1.8 ± 0.2

^{a}Calculated for the 2-DA SAM corresponding to the experiments. The value for 1-DA is 2.33. ^{b}Calculated for the thio-1-DA SAM. The uncertainty is the standard deviation from the calculations.

Comparison of experiment with computation

As shown in Table 2, the results of the two theoretical approaches are consistent with each other and agree reasonably well with the experimental data. We have also performed test simulations with a MD model that includes the Au surface (described in the Experimental section); the results confirm that the *cis*-isomer is stiffer than the *trans*-isomer also when the surface is included, with a relative stiffness larger than 1 and smaller than 2 for these preliminary calculations. In previous MD simulations of SAMs on gold, it was also found that neglecting the substrate did not qualitatively affect the results [21].

Previous work has generated some questions about the role of steric hindrance in the *cis*↔*trans* conversion within a monolayer film [9,10]. If the film is close-packed, there is some evidence that the conversion is restricted. The specific samples here restrict the domain size to a maximum corresponding to the area on top of the small gold islands, and probably to a much smaller area due to the lack of order induced by the relatively large number of molecules at boundary positions. The calculated values are confined to small systems due to considerations of computational power, but nevertheless may well serve as a good model for the small domains present in the experiment. We have no way to measure directly the efficiency of conversion for the island films. As a comparison, UV–vis spectroscopy performed on smooth, flat, semitransparent Au films, with RMS roughness of 0.7 nm showed only 30% conversion efficiency under similar illumination conditions. We propose that a lower degree of order in SAMs on Au island films allow higher conversion efficiency.

In addition to steric factors, electronic effects such as excitonic and plasmonic coupling have been cited as factors that hinder the switching process. The plasmon spectrum for the Au islands used here peaks at 730 nm, such that any quenching due to the 365 nm irradiation should be a minor effect [22].

The similarity of results from the MD (where intermolecular interactions play the dominant role) and QM (where only single-molecule stiffness is considered) models indicates that the individual molecular bonds and the intermolecular interactions contribute in the same sense to the relative *cis–trans* film stiffness. Therefore, it is likely that the higher stiffness of the *cis*-configuration revealed here for partially disordered molecules would hold also for a close-packed SAM of the same molecule, a situation where intra- and intermolecular effects are balanced differently. The QM model seems to be in better agreement with the experiments than the MD one is. This is almost certainly a coincidence, since both models include a number of simplifying approximations. However, based on this observation, one might deduce that for this case accurate modeling of the atomistic properties is more appropriate than inclusion of the overall complexity of the system concomitant with simplifying approximations, contrary to the situation in many cases.

Conclusion

Relative elastic moduli of the *cis*- and *trans*-isomers of an azobenzene monolayer have been measured and calculated. The modulus ratio of the *cis*- to *trans*-isomer is approximately 2. Results from both the QM-based model (which relates the SAM modulus to the resistance to deformation by individual molecules only) and the MD-based model (which includes intermolecular interactions) agree with this result. Therefore, the *cis*-isomer is stiffer than the *trans*, both as a single molecule and when part of a SAM. Analysis of the individual mode of deformation of the molecule showed that for *trans* there is a predominant normal mode to the stiffness, which corresponds to the molecular stretching/compression along the long axis, which distributes the stress over the entire molecule. For the *cis*-form, the dominant mode represents a deformation sensitive to the stiff steric interactions between the two arms of the azobenzene, and is mainly confined to this local functionality of the molecule (the inner phenyl rings) rather than being delocalized as for *trans*. This provides a microscopic rationale for the observation that the *cis* dominant mode has a force constant larger than the *trans* dominant mode, yielding an overall stiffer molecule.

Experimental

Experimental methods

Preparation of 4'-{[(1,1'-biphenyl)-4-yl]diazenyl}-(1,1'-biphenyl)-4-thiol (**2**, thio-2-DA)

Initial attempts to prepare monolayers directly from compound **1** as reported previously [23,24] were unsuccessful. Therefore, a reduction was carried out as indicated in Figure 7, and outlined below:

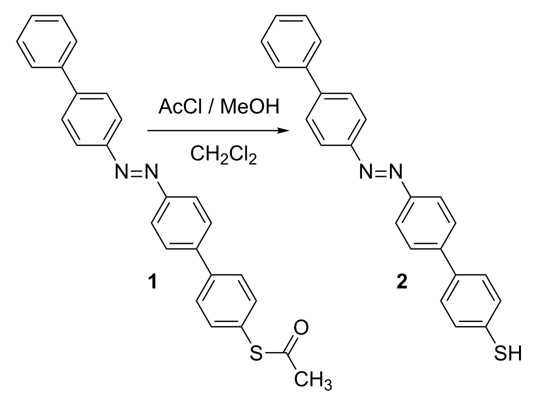

Figure 7: Compound **1** and compound **2** (2-DA-thiol), showing the deprotection reaction yielding the molecule used to form the SAM.

Compound **1** (10.1 mg, 0.025 mmol) was suspended in a mixture of deaerated dry CH_2Cl_2 (3 mL) and deaerated dry MeOH (2 mL) under nitrogen. The mixture was cooled in an ice–water bath and acetyl chloride (1.4 mL) was added dropwise by a syringe. After the addition was complete, the cooling bath was removed and the mixture was sealed and stirred at room temperature for 4 h. The solvents were then evaporated under reduced pressure affording the thiol **2**, thio-2-DA, which was used without further purification; ^{1}H NMR ($CDCl_3$) δ 3.5 (s, –S*H*), 7.4 (d, 3H), 7.5 (t, 2H), 7.6 (d, 2H), 7.7–7.8 (m, 6H), 8.0 (m, 4H); ESI–MS (*m*/*z*): $[M - 1]^+$ 365.09.

Monolayer preparation

Gold substrate preparation: AFM images of the different substrates are shown in Figure 8. Three types of gold substrates were used. For basic characterization of the monolayers (ellipsometry, AFM topography, XPS), a 150 nm gold film was prepared on Si by thermal evaporation. For UV–vis measurements, a 20 nm thick Au film was evaporated onto a quartz slide to allow sufficient transmission in the spectral region studied. For the nanomechanical measurements, Au islands on glass substrates were prepared.

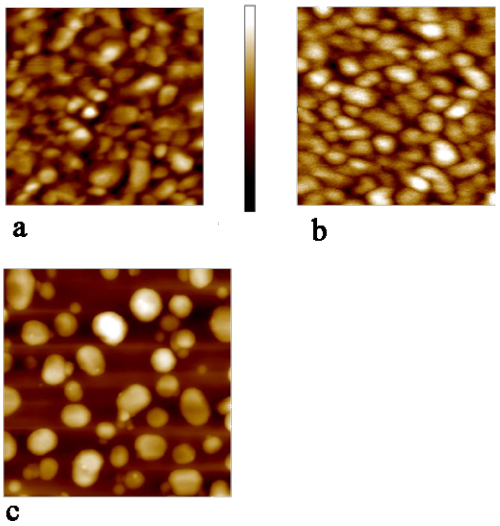

Figure 8: AFM images of (a) clean evaporated Au surface (500 × 500 nm^2 color bar 12 nm) and (b) surface coated with SAM (500 × 500 nm^2 color bar 12 nm); (c) Au islands on glass (1300 × 1300 nm^2 typical island height 50 nm).

Au island preparation: 15 nm of Au was evaporated at a deposition rate of 0.01 nm/s onto a clean glass slide. Au islands were developed upon annealing in air at 550 °C for 10 h [22]. The gold island sizes were in the range of 20–150 nm in diameter.

Au film preparation: Electron beam deposition from a Au target (99.99%) was performed with a deposition rate of 0.05 nm/s on top of 2 nm of Cr. The Cr serves as an adhesion layer between the gold and the substrate (Si/quartz). Prior to evaporation, the substrates were cleaned by piranha solution for 30 min, followed by copious rinsing with double distilled water (DDW) followed by sonication in ethanol and drying with nitrogen. Substrates for UV–vis analysis were prepared on quartz, with a Au thickness of 20 nm; substrates for other analyses were prepared on Si, with a Au thickness of 150 nm.

Preparation of monolayer films: All film preparation, as well as characterization and irradiation experiments were performed at room temperature, 23 ± 1 °C. Before adsorption, substrates were cleaned by a 20 min UV/ozone treatment followed by a 20 min immersion in ethanol. These cleaned Au substrates were immersed in a <0.1 mM solution of thio-2-DA (compound **2** in Figure 7) in degassed dimethylformamide (DMF) at room temperature for 24 h. After adsorption, the samples were rinsed with pure DMF and ethanol and blown dry with nitrogen. The monolayer quality was verified by ellipsometry, X-ray photoelectron spectroscopy, and AFM.

Ellipsometry

Ellipsometric measurements were carried out with a variable-angle spectroscopic ellipsometer WVASE32 (J.A. Woollam Co.) with a xenon source and a 1 mm spot at an angle of incidence $\varphi = 70°$. The film thickness was calculated by using a Cauchy model for the organic layer. The clean gold substrate was used as a reference. The thicknesses of the samples were in the range of 2.00–2.35 nm, which includes the expected value for the *trans*-SAMs.

X-ray photoelectron spectroscopy

XPS spectra were measured on an Axis-Ultra (Kratos, Manchester, UK) system. The characteristic N-peak was clearly seen. Attenuation of the Au signal indicated a film thickness of approximately 2.6 nm. The extent of the coverage was estimated to be close to 100%.

Irradiation parameters

The thio-2-DA molecules in solution were irradiated with UV light (wavelength $\lambda = 365$ nm; intensity $I = 25$ mW/cm^2) for up to 20 min. Irradiation of the molecules in solution gave quantitative conversion within 15 min of irradiation (Figure 9).

The azobenzene SAMs were irradiated with UV light ($\lambda = 365$ nm, $I = 25$ mW/cm^2) for 2 h and with visible light ($\lambda = 450$ nm, $I = 5$ mW/cm^2) for 1 h.

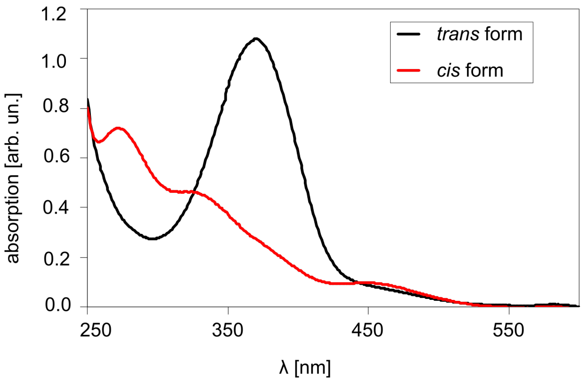

Figure 9: UV–vis spectra for thio-2-DA in chloroform solution after exposure to 365 nm light (*cis* form) and 450 nm light (*trans* form). Arbitrary units indicated in abscissa, since air was used with reference beam. See text for measurement conditions.

Scanning probe microscopy

AFM topographies were measured before and after SAM adsorption to check the monolayer quality. Tapping mode AFM measurements were carried out in air with a Multimode Nanoscope V AFM (Veeco, Woodbury, NY). Integrated Si tips (Olympus AC240, resonance frequency ca. 70 kHz) were used for these measurements. Images of the morphology of bare Au and the azobenzene on Au on Si samples are shown in Figure 8. Mechanical characterization was performed in the AFM by using HarmoniX^{TM} imaging (Bruker, Santa Barbara, CA USA). The HarmoniX AFM technique allows the acquisition of quantitative "images" of mechanical parameters (elastic modulus, adhesion, dissipation) simultaneously with and at the rate of acquisition of the tapping-mode image. This is done by analysis of higher harmonics in the oscillating cantilever signal in order to extract full force versus distance curves. A full description of the technique can be found in the literature [19,25]. Since the force curves and stiffness data are derived from the complex probe behavior and require instrumental stability after the necessary calibrations have been performed, the stiffness values reported here are comparisons between different regions, as sampled within a single scan line, which significantly reduces the uncertainty. Preliminary experiments showed no mechanical contrast within the films, except for some dispersed dots that likely represent a contamination on the gold. These dots had lower modulus and adhesion than the surrounding areas.

Computational methods

Quantum mechanical model

When an area A of the SAM is compressed by a force F (Figure 10), the SAM thickness changes by $\Delta l = l_0 - l$, where l_0 is the initial equilibrium thickness and l the compressed thickness. If the material is assumed to be homogeneous and isotropic, its Young's modulus E is given by

$$E = \frac{Fl_0}{A\Delta l} \ . \qquad (2)$$

We assume the molecules to behave as ideal (harmonic) springs, homogeneously distributed on the surface. The SAM is thus a collection of parallel springs aligned perpendicular to the surface, each with an elastic (force) constant k. Under this assumption:

$$F = Nk\Delta l \qquad (3)$$

where N is the number of molecules that occupy the area A (we assume that N is the same for *cis*- and *trans*-azo-SAMs). Therefore:

$$E = kl_0 / A_0 \qquad (4)$$

where $A_0 = A/N$ is the area of gold surface that one single molecule covers, and l_0 is obtained in our model as the projection of the molecular length d_0 (calculated as the largest interatomic distance between sulfur atom and an hydrogen atom) on the normal direction **n** with respect to the gold surface plus the S–Au bond length b_0 (Figure 10b). θ_0 is the tilt angle for *cis* and for *trans*; this angle was obtained after MD simulations.

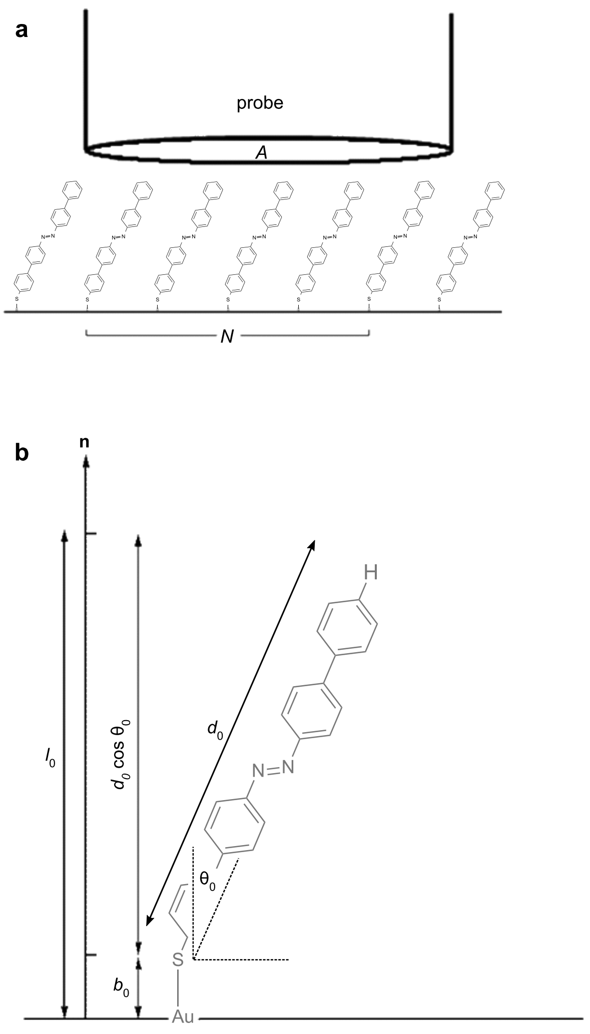

Figure 10: Sketch of the model used to derive SAM stiffness from QM results on the single molecule. (a) *A* is the probe area, *N* is the number of compressed molecules that occupy the area *A*; (b) schematic representation of the geometrical parameters of the QM model: d_0 is the molecule length, b_0 is the S–Au bond length, θ_0 is the tilt angle, and l_0 is the SAM thickness.

From a molecular point of view, the force constant k for a deformation perpendicular to the surface can be evaluated from vibrational spectra as a weighted sum over all the normal modes i. The weighting is needed to account for the different contributions along the normal direction **n** to the gold plane from the individual normal modes. In order to evaluate this, the force unit vector is decomposed into its Cartesian components u in the molecular coordinate reference system, and the weight w_{iu} is calculated as the product of the component of the normal mode i in the direction u with the u-th component of the force unit vector:

$$\langle k\rangle = \sum_i k_i \sum_u w_{iu} \quad (5)$$

Each k_i is related to the vibrational angular frequency ω_i and the reduced mass μ_I computed after the force matrix diagonalization:

$$k_i = \omega_i^2 \mu_i \quad (6)$$

These vibrational frequencies, reduced masses and normal modes were obtained by ab initio QM calculations. A full geometry optimization of the electronic ground state of 1-DA, 2-DA, and 3-DA, both *trans*- and *cis*-isomers, was obtained in the vacuum phase at the level of density functional theory (DFT) by using the Becke three-parameter Lee–Yang–Parr (B3LYP) exchange–correlation functional with cc-pVTZ basis set. The optimized geometries were then subject to vibration calculation in order to compute the vibrational properties and to investigate whether the convergence points were genuine energy minima. For all the calculations, the Gaussian 09 computational package was used [26].

In this framework, after QM computation, we obtained the relative structure factors $l_{0,cis}/l_{0,trans}$ = 1.061, 0.872, and 0.677 and the ratios between the average force constants $\langle k_{cis}\rangle/\langle k_{trans}\rangle$ = 2.196, 2.053, and 2.422, for 1-, 2-, and 3-DA respectively. From these values, the E_{cis}/E_{trans} values reported in the main text are recovered.

Finally, we also performed a test to evaluate the role of the Au–S–azobenzene bending angle in determining the stiffness ratio. In fact, in our QM model this bending is neglected. We therefore computed vibrational frequencies and normal modes for a thiolated azobenzene (thio-1-DA) molecule, where we gave to the H atom of the thiol group the atomic mass of gold. From such vibrational data we computed again the ratio $\langle k_{cis}\rangle/\langle k_{trans}\rangle$, finding a negligible (<1%) difference with respect to the data previously obtained. This is due to the upright orientation of the molecules in the SAM, which makes the bending unable to absorb the external compression.

Molecular dynamics approach

The problem of calculating the relative stiffness can also be treated through a classical molecular dynamics approach. An OPLS-type empirical force field [7] is combined with standard OPLS parameters [27] in order to describe the intra- and intermolecular interactions of the SAM. Point charges are derived from the electrostatic potential (RESP) calculated at a B3LYP/cc-pVTZ level of theory on the *trans*-thio-2-DA geometry. The structure of the SAM was built to reproduce the experimentally observed periodicity [10] (Figure 6) and the gold surface is described, in this first model, only implicitly by fixing the sulfur atom positions. Molecular dynamics (MD) simulations within the canonical ensemble at T = 300 K were run considering 126 thio-1-DA molecules in a 6.090 nm × 6.153 nm simulation supercell, with periodic boundary conditions applied. We apply periodic boundary conditions also in the direction perpendicular to the surface (the box size is 7.074 nm along this direction), allowing effective calculation of the electrostatic forces. The Nose–Hoover thermostat [28] was used (time constant for coupling of 0.1 ps). The time step for the simulations was 2 fs (bond lengths were constrained with the LINCS algorithm) [29]. The long-range electrostatic contribution was computed with the PME method with a direct-space cutoff of 1.2 nm. For van der Waals interactions, a switch cutoff of 1.0–1.1 nm was used.

In order to simulate the compression experiments, a computational protocol was set up: First a simulation was run with a spherical indenter positioned at a certain, fixed distance from the plane of the sulfur atoms (Figure 6b). The system was equilibrated for 2 ns, then, with the simulation still running, forces acting on the indenter were collected in the ensuing 8 ns. At the end of this simulation the distance between the indenter and the plane of the sulfur atoms was lowered, and a new (2 + 8) ns simulation was started. We considered 10 different indenter–surface distances. Therefore, a total of 100 ns of MD were run for each compression. This procedure was applied to both *trans* and *cis* thio-1-DA SAMs, and four independent compressions (consisting of 10 simulations each) were run for each isomer, for a total of (2 × 4 × 10 × 10) ns = 800 ns of MD simulations. The four independent compressions were started by four snapshots of equilibrated MD simulations (5 ns long) for the noncompressed *cis*- and *trans*-SAMs, chosen every 1 ns.

By block averaging [30] the forces collected for each simulation, we construct a force–distance plot (Figure 11). The error bars reported in Figure 11 represent the standard deviation from the mean, as estimated by the block-averaging technique for each simulation. They may be unrealistically small when the system remains trapped in metastable states. We minimized this problem by repeating the compressions four times, starting from four different initial conditions, and averaging the results. The ratio of the elastic moduli E_{cis}/E_{trans} is calculated considering a thickness ratio $l_{0,cis}/l_{0,trans}$ equal to 1.054 (estimated from simulations without the indenter). The indenter is a Lennard–Jones sphere with parameters set as: ε = 0.065 kJ/mol and σ = 1.425 nm. ε is chosen to give a negligible attraction with the SAM (it is one-tenth of the ε used in the GolP model [31] for Au atoms), and σ gives a van der Waals radius of

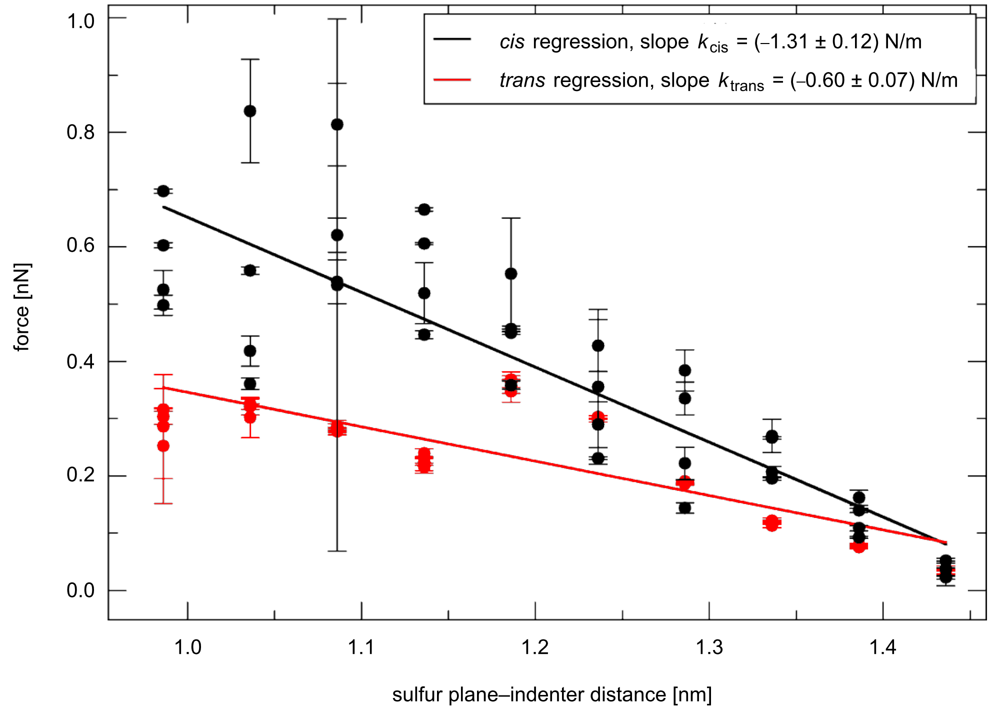

Figure 11: Computational compression procedure: Force acting on the indenter as a function of the distance between the indenter and the plane of the sulfur atoms. Each point refers to a step of the simulation sequence. Error bars are ±σ, where σ is the statistical deviation obtained for each simulation by statistical block average analysis.

0.8 nm for the indenter, which is compatible with our cell size. The van der Waals interactions between the indenter and the surface are neglected in this model. As the Au substrate is missing, the SAM–substrate van der Waals interactions are also neglected. Both of these interactions would affect the *cis* and the *trans* force–distance plots in the same way, so their effects on the E_{cis}/E_{trans} ratio should be small.

To check the possible role of the gold surface, including the SAM–substrate van der Waals interactions, we also performed test calculations with a second model, where the gold surface was explicitly considered by employing the GolP model [31]. Azobenzene was described with the same OPLS-type parameters mentioned above, with additional literature parameters for the gold–sulfur bond [32]. A computational protocol for the SAM compression similar to that described above was applied within this second model; the simulated system size and the procedural settings were the same as the previous protocol, except that two series of simulations were run for each isomer (instead of four), and the MD simulation for each distance was shorter (5 ns instead of 10 ns). Furthermore, the reference distance for penetration was calculated between the indenter centre and the plane of the surface gold atoms (as sulfur atoms are not fixed). As described in the main text, the results of these tests were qualitatively similar to those of the model that did not explicitly include the Au substrate. While these simulations are valuable as tests to approximately estimate the role of Au, in particular of the Au–SAM van der Waals interaction, further work is needed to properly assess the choices specific to these simulations, such as the Au–SAM force field, the arrangement of the SAM with respect to the Au lattice and the role of Au mobility. All simulations were carried out with the GROMACS package [33].

Acknowledgements

This work was supported by a Nanoscience E+ program of the ERA Net (Transnational project MaECENAS) and a “Nano-Grand” grant (CFN-WINI-RBNI). We gratefully acknowledge David Cahen and Yehiam Prior (WIS) and Maria Rampi (Ferrara) for their cooperation on this project. We thank Hagai Cohen and Tatyana Bendikov for making the XPS measurements, and Alexander B. Tesler and Stella Izhakov for help in preparation of the Au island films.

References

1. Moniruzzaman, M.; Zioupos, P.; Fernando, G. F. *Scr. Mater.* **2006,** *54,* 257–261. doi:10.1016/j.scriptamat.2005.09.025
2. Srikhirin, T.; Laschitsch, A.; Neher, D.; Johansmann, D. *Appl. Phys. Lett.* **2000,** *77,* 963–965. doi:10.1063/1.1288809

3. Mechau, N.; Neher, D.; Börger, V.; Menzel, H.; Urayama, K. *Appl. Phys. Lett.* **2002,** *81,* 4715–4717. doi:10.1063/1.1529081
4. Ferri, V.; Elbing, M.; Pace, G.; Dickey, M. D.; Zharnikov, M.; Samori, P.; Mayor, M.; Rampi, M. A. *Angew. Chem., Int. Ed.* **2008,** *47,* 3407–3409. doi:10.1002/anie.200705339
5. Hugel, T.; Holland, N. B.; Cattani, A.; Moroder, L.; Seitz, M.; Gaub, H. E. *Science* **2002,** *296,* 1103–1106. doi:10.1126/science.1069856
6. Holland, N. B.; Hugel, T.; Neuert, G.; Cattani-Scholz, A.; Renner, C.; Oesterhelt, D.; Moroder, L.; Seitz, M.; Gaub, H. E. *Macromolecules* **2003,** *36,* 2015–2023. doi:10.1021/ma021139s
7. Schäfer, L. V.; Müller, E. M.; Gaub, H. E.; Grubmüller, H. *Angew. Chem., Int. Ed.* **2007,** *46,* 2232–2237. doi:10.1002/anie.200604595
8. Berná, J.; Leigh, D. A.; Lubomska, M.; Mendoza, S. M.; Pérez, E. M.; Rudolf, P.; Teobaldi, G.; Zerbetto, F. *Nat. Mater.* **2005,** *4,* 704–710. doi:10.1038/nmat1455
9. Wang, Z.; Nygård, A. M.; Cook, M. J.; Russell, D. A. *Langmuir* **2004,** *20,* 5850–5857. doi:10.1021/la0498861
10. Pace, G.; Ferri, V.; Grave, C.; Elbing, M.; von Hänisch, C.; Zharnikov, M.; Mayor, M.; Rampi, M. A.; Samori, P. *Proc. Natl. Acad. Sci. U. S. A.* **2007,** *104,* 9937–9942. doi:10.1073/pnas.0703748104
11. Akiyama, H.; Tamada, K.; Nagasawa, J.; Abe, K.; Tamaki, T. *J. Phys. Chem. B* **2003,** *107,* 130–135. doi:10.1021/jp026103g
12. Gahl, C.; Schmidt, R.; Brete, D.; McNellis, E. R.; Freyer, W.; Carley, R.; Reuter, K.; Weinelt, M. *J. Am. Chem. Soc.* **2010,** *132,* 1831–1838. doi:10.1021/ja903636q
13. Muzikante, I.; Gerca, L.; Fonavs, E.; Rutkis, M.; Gustina, D.; Markava, E.; Stiller, B.; Brehmer, L.; Knochenhauer, G. *Mater. Sci. Eng., C* **2002,** *22,* 339–343. doi:10.1016/S0928-4931(02)00220-5
14. Nagahiro, T.; Akiyama, H.; Hara, M.; Tamada, K. *J. Electron Spectrosc. Relat. Phenom.* **2009,** *172,* 128–133. doi:10.1016/j.elspec.2009.02.009
15. Dietrich, P.; Michalik, F.; Schmidt, R.; Gahl, C.; Mao, G.; Breusing, M.; Raschke, M. B.; Priewisch, B.; Elsässer, T.; Mendelsohn, R.; Weinelt, M.; Rück-Braun, K. *Appl. Phys. A* **2008,** *93,* 285–292. doi:10.1007/s00339-008-4828-0
16. Burnham, N. A.; Dominquez, D. D.; Mowery, R. L.; Colton, R. J. *Phys. Rev. Lett.* **1990,** *64,* 1931–1934. doi:10.1103/PhysRevLett.64.1931
17. Clifford, C. A.; Seah, M. P. *Nanotechnology* **2006,** *17,* 5283–5292. doi:10.1088/0957-4484/17/21/001
18. Chen, X.; Vlassak, J. J. *J. Mater. Res.* **2001,** *16,* 2974–2982. doi:10.1557/JMR.2001.0408
19. Sahin, O.; Magonov, S.; Su, C.; Quate, C. F.; Solgaard, O. *Nat. Nanotechnol.* **2007,** *2,* 507–514. doi:10.1038/nnano.2007.226
20. Tabor, D. *J. Colloid Interface Sci.* **1977,** *58,* 2–13. doi:10.1016/0021-9797(77)90366-6
21. Gannon, G.; Larsson, J. A.; Greer, J. C.; Thompson, D. *Langmuir* **2009,** *25,* 242–247. doi:10.1021/la802548u
22. Karakouz, T.; Tesler, A. B.; Bendikov, T. A.; Vaskevich, A.; Rubinstein, I. *Adv. Mater.* **2008,** *20,* 3893–3899. doi:10.1002/adma.200703092
23. Shaporenko, A.; Elbing, M.; Blaszczyk, A.; von Hänisch, C.; Mayor, M.; Zharnikov, M. *J. Phys. Chem. B* **2006,** *110,* 4307–4317. doi:10.1021/jp056833z
24. Crivillers, N.; Orgiu, E.; Reinders, F.; Mayor, M.; Samori, P. *Adv. Mater.* **2011,** *23,* 1447–1452. doi:10.1002/adma.201003736
25. Sahin, O. *Rev. Sci. Instrum.* **2007,** *78,* 103707. doi:10.1063/1.2801009
26. *Gaussian 09,* Revision A.02; Gaussian, Inc.: Wallingford CT, 2009.
27. Jorgensen, W. L.; Maxwell, D. S.; Tirado-Rives, J. *J. Am. Chem. Soc.* **1996,** *118,* 11225–11236. doi:10.1021/ja9621760
28. Hoover, W. G. *Phys. Rev. A* **1985,** *31,* 1695–1697. doi:10.1103/PhysRevA.31.1695
29. Hess, B.; Bekker, H.; Berendsen, H. J. C.; Fraaije, J. G. E. M. *J. Comput. Chem.* **1997,** *18,* 1463–1472. doi:10.1002/(SICI)1096-987X(199709)18:12<1463::AID-JCC4>3.0.CO;2-H
30. Frenkel, D.; Smit, B. *Understanding Molecular Simulations,* 2nd ed.; Academic Press: New York, USA, 2001.
31. Iori, R.; Di Felice, R.; Molinari, E.; Corni, S. *J. Comput. Chem.* **2008,** *29,* 1465–1476. doi:10.1002/jcc.21165
32. Bizzarri, A. R.; Costantini, G.; Cannistraro, S. *Biophys. Chem.* **2003,** *106,* 111–123. doi:10.1016/S0301-4622(03)00156-X
33. Hess, B.; Kutzner, C.; van der Spoel, D.; Lindahl, E. *J. Chem. Theory Comput.* **2008,** *4,* 435–447. doi:10.1021/ct700301q

License and Terms

The definitive version of this article is the electronic one which can be found at:
doi:10.3762/bjnano.2.93

Beilstein Journal
of Nanotechnology

Self-assembled monolayers and titanium dioxide: From surface patterning to potential applications

Yaron Paz

Review

Address:
The Department of Chemical Engineering, The Russell-Berrie Institute of Nanotechnology and The Grand Water Research Institute, Technion, Haifa 32000, Israel

Email:
Yaron Paz - paz@tx.technion.ac.il

Keywords:
photocatalysis; remote degradation; self-assembled monolayers; titanium dioxide

Beilstein J. Nanotechnol. **2011,** *2,* 845–861.
doi:10.3762/bjnano.2.94

Received: 18 October 2011
Accepted: 06 December 2011
Published: 20 December 2011

This article is part of the Thematic Series "Self-assembly at solid surfaces".

Guest Editors: S. R. Cohen and J. Sagiv

Abstract

The ability to control the properties of self-assembled monolayers (SAMs) attached to solid surfaces and the rare photocatalytic properties of titanium dioxide provide a rationale for the study of systems comprising both. Such systems can be realized in the form of SAMs grown on TiO_2 or, in a complementary manner, as TiO_2 grown on SAMs. Accordingly, the current status of knowledge regarding SAMs on TiO_2 is described. Photocatalytic phenomena that are of specific relevance to SAMs, such as remote degradation, and cases where SAMs were used to study photocatalytic phenomena, are discussed as well. Mastering of micropatterning is a key issue en route to a successful assimilation of a variety of titanium dioxide based devices. Accordingly, particular attention is given to the description of a variety of methods and techniques aimed at utilizing the photocatalytic properties of titanium dioxide for patterning. Reports on a variety of applications are discussed. These examples, representing the areas of photovoltaics, microelectronics, microelectromechanics, photocatalysis, corrosion prevention and even biomedicine should be regarded as appetizers paving the way for further studies to be performed.

Introduction

Photocatalytic degradation of pollutants is attracting increasing attention. In this context, anatase-phase titanium dioxide is regarded as the photocatalyst of choice, due to its low cost, nontoxicity, and relatively high efficiency, which make it suitable not only for air and water decontamination [1,2] but also for self-cleaning applications [3]. The general scheme for the photocatalytic destruction of organics involves the excitation of this semiconductor by irradiation with suprabandgap photons and migration of the electron–hole pairs to the surface of the photocatalyst, where the holes are trapped by H_2O or OH^- adsorbed at the surface, thus forming hydroxyl radicals. In parallel, the electrons reduce adsorbed oxygen [4] to form superoxide radicals. The first step in the photocatalytic degradation of most organic compounds is an oxidative attack by the hydroxyl radicals, which eventually, following secondary reactions, gives stable molecules such as CO_2 and water [5,6].

Nevertheless, it was shown that some halo-organics [7,8] and highly toxic heavy-metal ions such as Cr(VI) [9,10] could be degraded reductively by photoinduced electrons. Langmuir–Hinshelwood type kinetics is often observed both in the liquid phase and in the gas phase, suggesting, albeit not proving [11,12] the need for adsorption as a prerequisite for photocatalysis.

Self-assembled monolayers (SAMs) being chemisorbed in an ordered manner on surfaces such as metals (Au, Ag), oxides (SiO_2, Al_2O_3, TiO_2) and semiconductors (Si, GaN, InP, InGaAs) provide a unique way to alter the properties of a surface at will. This ability may be manifested through a variety of phenomena, among which are wetting phenomena (hydrophobicity, hydrophilicity and oleophobicity), electronic phenomena (from affecting band bending and work function, to charge conduction), and, no less important, the ability to form tailored three-dimensional supramolecular arrays by attaching a specific molecule or a particle to an external functional group.

Being adsorbed on the surface of titanium dioxide or in its vicinity, organic self-assembled monolayers may affect the photocatalytic properties of titania as well as be affected by these properties. Likewise, the superhydrophilicity of TiO_2 known to be induced upon exposure to UV light [13] may affect the chemisorption process of SAMs. This gives rise to diverse phenomena, which can be utilized in many ways, from the study of fundamental issues in TiO_2 photocatalysis to the growth of supramolecular structures; from serving as a tool for patterning to suggesting means to obtain the selective photocatalytic degradation of highly toxic contaminants. This potential for synergism between self-assembled monolayers and photocatalytic titanium dioxide is the subject of the following review, whose aim is to bring the prospects and obstacles of this combination to the attention of the scientific community. It should be noted that for obvious reasons this manuscript does not cover devices where the titanium dioxide serves to accept photoinduced electrons from sensitizers that cannot be strictly considered as SAMs, i.e., most types of dye-sensitized solar cells (DSSCs).

Review

Self-assembled monolayers chemisorbed on TiO_2

Both TiO_2 and SiO_2 are oxides capable of forming surface hydroxyls, and therefore one could imagine that SAMs on titania may resemble SAMs on silica. This similarity is expected to be manifested primarily by the type of head groups that connect between the surface and the organic tails. Indeed, head groups such as chlorosilanes (R_nSiCl_{4-n} with $n = 1,2,3$), alkoxysilanes ($R_nSi(OR')_{4-n}$ with $n = 1,2,3$), carboxylic acids and isocyanates (–N=C=O) are common on both substrates. The fact that the Si–O bond length in silica (1.5–1.7 Å depending on the crystalline form) is similar to that of the Ti–O bond length in titania (1.9 Å) may suggest similar compactness. On the other hand, the difference between the electronegativity of Ti to that of Si, (1.54 and 1.90 by Pauling's scale, respectively) which affects the polarity of the M–O bond of the oxide, the point of zero charge of the oxide, and the number of OH sites on the surface are expected to influence the tendency of these two oxides to form SAMs and the structure and stability of the formed SAMs.

Chlorosilanes and alkoxysilanes SAMs are characterized by hydrolysis–condensation reactions leading to the formation of M–O–Si bonds where M is in this context is Si or Ti. The chemical anchoring of the alkylsilanes to TiO_2 is characterized by several changes in the FTIR spectrum, namely shifting of the 1091 cm^{-1} band found in neat TiO_2 (bending vibration of Ti–OH) to lower wavenumbers (ca. 1000 cm^{-1}) due to the formation of Ti–O-Si bonds, and the disappearance of the in-plane-bending vibration of surface O–H at 1402 cm^{-1} [14].

Generally speaking, a comprehensive comparison between SAMs on silica and SAMs on titanium dioxide is somehow problematic as the latter were by far less-extensively studied than the former. It is commonly claimed that silanes capable of cross linking (i.e., having at least three leaving groups) grow by an islandlike growth mechanism, whereas SAMs that are not capable of cross linking grow by a uniform growth mechanism [15]. While this is well-established for SAMs on Si, results for organosilanes SAMs on titanium dioxide are much more ambiguous. The lower electronegativity of titanium suggests that the condensation reaction is faster than on SiO_2, and as a consequence the grafting of octadecyl trichlorosilane (OTS) on TiO_2 is faster [16]. To some extent this is related to the known ability of $Ti(OR)_4$ to catalyze silanol condensation in TiO_2–SiO_2 sol–gel systems. Since island formation of OTS molecules requires lateral mobility, which may be hindered if the grafting is too strong, one may expect the OTS islands on TiO_2 to be smaller than on SiO_2.

There are several indications (most of them based on the FTIR signal of the C–H stretch envelope) that the amount of chemisorbed trichlorosilane molecules is higher in TiO_2 than in SiO_2, possibly due to the presence of surplus water [17] or, in the case of TiO_2 films consisting of sintered nanocrystalline TiO_2, due to a difference between the geometrical area and the true area [18]. Conversely, the density of a protein, immobilized on a substrate through an alkylsilane SAM having a terminal amine, was observed to be lower on a TiO_2 substrate than on a SiO_2 substrate [19]. Here, it was claimed by the authors that the more ionic character of the Ti–O bond may require higher energies to form Ti–OH groups, leading to lower density of surface hydroxyls unless an extended exposure to O_2 plasma in the presence of water vapor is performed.

The formation of OTS monolayers on titanium dioxide was studied in structures consisting of well-defined microdomains of TiO_2 and noble metals such as gold and platinum. It was found that monolayers chemisorbed in the presence of the metallic micro-islands were denser than monolayers chemisorbed on TiO_2 substrates that had no metallic islands. Results were explained in terms of charging effects [18]. That charging of the substrate may affect the chemisorption of organosiloxane monolayers can be deduced also from a comparison between SAMs on SiO_2, on mica and on mica coated with ultrathin layers of SiO_2. Here, it was found that the adsorption rate decreased with the width of the silica overlayer, and this result was explained by the increased shadowing of an electrostatic interaction between the negatively charged mica surface and the polar head group of the adsorbed molecules [20].

The effect of raising the temperature may be manifested in SAMs through disordering (formation of "kink" configurations), detachment of the molecules, or burning. FTIR studies of temperature effects on a variety of organosilane SAMs on TiO_2 found that all the organosilane SAMs exhibited good thermal and oxidative stability, with no mass loss below 200 °C [15], as is known also for organosilanes on silicon [21]. A different study on in-air pyrolization of thioacetate-terminated (trichlorosilyl) hexadecane on SiO_2 and TiO_2 did not reveal any substrate effect on the onset of burning and on the temperature dependence of the process [22].

Data on contact-angle comparisons between organosilanes on silica and on titania is quite scarce. In this respect, contact-angle measurements of CVD-made tetrafunctional cyclic siloxane monolayers (1,3,5,7-tetramethylcyclotetrasiloxane ($C_4H_{16}O_4Si_4$)) did not reveal much of a difference between SAMs on oxidized titanium versus SAMs on oxidized aluminum [23]. In both cases, the water contact angle was found to be 103° when the CVD process took place at 80 °C, and 163° when the process took place at 180 °C. The *n*-hexadecane contact angles were also the same for both substrates, i.e., 32° and 0° for monolayers grown at 80 °C and 180 °C, respectively. The fact that the contact angles on these very short SAMs (0.5 nm in thickness) revealed a lack of sensitivity to the type of substrate suggests (albeit not proves) that a similar situation may prevail also with SAMs having long alkyl chains, whose outer groups are located far from the substrate and in which multiple intermolecular van-der-Waals (VdW) interactions play a larger role.

The high solubility of polysiloxanes in CO_2 led researchers to study the silanization of titanium dioxide under supercritical conditions. It was found that despite a tendency to form a disordered, three-dimensional silanized structure [24], a monolayer with a very low degree of vertical polycondensation can be obtained at pressures above 10.0–12.5 MPa [25]. Such monolayers have a relatively lower grafting density with respect to chemisorption by conventional methods (2.8–3.0 molecules per nm^2 versus 4.3–4.8 molecules per nm^2).

It is worth mentioning that a study on organosilane monolayers formed on the surfaces of zirconia and titania (anatase and rutile), by a gas–phase process employing organosilicon hydrides, found that the effect of the underlying substrate on the adsorption of nitrogen on the SAMs was insignificant [26]. Here, the heat of adsorption of the nitrogen molecules was found to increase as the grafting density of the SAMs was decreased from 4.23 groups/nm^2 for $C_{18}H_{37}SiH_3$ to 2.75 groups/nm^2 for $H_3Si(CH_2)_8SiH_3$.

Unlike organosilane SAMs, whose tendency to form on TiO_2 and SiO_2 is quite similar, SAMs having phosphonic acid as their connecting head group are not formed on silicon dioxide but are formed easily from aqueous solutions on TiO_2, Al_2O_3, Ta_2O_5 and Nb_2O_5 [27].

FTIR measurements of self-assembled alkanephosphate monolayers revealed a clear shift in the symmetric and antisymmetric methylene stretching bands toward lower wavenumbers with increasing adsorption time, indicating a change from a disordered conformation to a well-ordered structure [28]. The observation of a disorder–order change for alkanephosphate SAMs on TiO_2 supported the validity of the uniform growth mechanism, i.e., strong chemisorption of single molecules that once chemisorbed are incapable of surface diffusion. The dichroic ratio of the methylene antisymmetric stretching band, defined as the intensity ratio of the band in the two polarizations (A_s/A_p), was found to increase with adsorption time and to level off at a ratio of 1.3, further supporting the uniform growth mechanism. The results of the dichroic ratio for the well-packed monolayer were analyzed under the assumption of uniaxial orientation, yielding a tilt angle of the alkyl chains of 21° relative to the surface normal. It should be noted that the uniform growth mechanism is considered to be typical for molecules that do not cross link (such as $Si(CH_3)_2$-Cl for example) [15], hence it may imply that this was the case also with the alkanephosphates.

The binding of self-assembled monolayers of ^{17}O-enriched phosphonic acids chemisorbed on titanium dioxide was studied by high-field NMR [29]. The presence of P–O–Ti, P=O, and

P–OH indicated that mono-, bi- and tridentate surface phophonate units can be present in these monolayers (Figure 1). The relative contribution of each form was found to vary according to the tail group, namely the relative contribution of P–O–Ti, P=O and P–OH was found to be different for $PhPO_3H_2/TiO_2$ and $C_{12}H_{25}PO_3H_2/TiO_2$. Unfortunately, the lack of uniqueness in the assignment of the relative contributions to the three forms of anchoring prevented calculation of the relative role of each type of anchoring. At any case, the chemical shift of the P–O–Ti sites was found to be consistent with bridging modes, negating the possibility of anchoring through chelating modes.

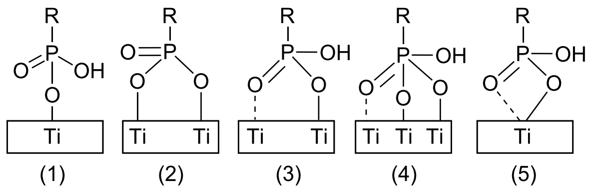

Figure 1: Schematic representation of binding modes between phosphonic acid SAMs and titanium dioxide (1) monodentate, (2) and (3) bridging bidentate, (4) bridging tridentate, (5) chelating bidentate (adapted from [29]).

A slightly different view of the binding between *n*-monoalkanephosphate SAMs and TiO_2 was presented by Chen et al. who claimed, based on XPS measurements, that this type of SAM can be bonded to the TiO_2 surface by way of both monodentate and bidentate coordination [30]. Accordingly, it was claimed that the monodentate and the bidentate of adjacent phosphate headgroups are linked by intermolecular hydrogen bonding.

An interesting phenomenon was found with SAMs connected to the TiO_2 surface through a carboxylic acid group. Here, doping TiO_2 nanoparticles with Co^{2+} at high concentrations (up to 23%), where the Co^{2+} replaces Ti^{4+} by substitution, was found to significantly improve the solubility and dispersibility of the nanocrystals in aprotic solvents, upon coating with thin films of oleic acid ($CH_3(CH_2)_7CH=CH(CH_2)_7COOH$) [31]. The aggregation on undoped particles was explained by the oleic acid forming a bilayer, with the carboxylic groups located at the solvent interface. In contrast, in doped particles, a monolayer exposing its hydrophobic functional groups to the aprotic solvents is formed, thus stabilizing the dispersion. This dependency in the formation of the thin layer on the doping was claimed to be related to the packing of the first layer. On doped nanoparticles the formed monolayer was denser than on undoped examples, thus preventing the interpenetration of hydrophobic chains that could have formed the bilayer structure.

Another functional headgroup used for the formation of SAMs on titanium dioxide is isocyanate ($CH_3(CH_2)_nN=C=O$), which forms a relatively weak carbamate linkage with the surface [32]. Here, water contact-angle hysteresis for the SAM-covered TiO_2 surfaces were found to be larger than that observed for the SAM-covered SiO_2 surface, suggesting that alkyl isocyanate SAMs on TiO_2 were more disordered and/or were less densely packed compared with alkyl isocyanate SAMs on SiO_2. Similar to other SAMs on many substrates, the longer the alkyl chains were, the more stable were the SAMs, by virtue of a larger number of VdW interactions.

TiO_2 grown on SAMs

There are quite a large number of manuscripts describing the growth of titanium dioxide on top of SAMs. The content of most of these publications is of little relevance to this mini-review, since in most cases the photocatalytic properties of the grown TiO_2 were not demonstrated. This lack of documented activity is at least partially related to the fact that in most cases the grown titanium dioxide was not in the photocatalytic anatase phase but rather it was amorphous. This amorphous phase can be transformed to anatase; however, it requires temperatures no less than 300 °C, which are expected to severely damage the underlying organic SAM.

Generally speaking, there are three main methods for growing titanium dioxide particles and films on SAMs: Liquid-phase deposition (LPD), atomic-layer deposition, and sol–gel. Within the context of growing TiO_2 on SAMs, the LPD method is probably the most popular. It employs a solution containing TiF_6^{2-} anions together with boric acid. The fluoride ligand serves to slow down the hydrolysis of the titanium fluoride complex (Equation 1), enabling the deposition of the formed titanium dioxide on the SAMs, whereas the borate ions act to scavenge the fluoride ions formed during hydrolysis according to Equation 2.

$$TiF_6^{2-} + 2H_2O \rightarrow TiO_2 + 4H^+ + 6F^- \qquad (1)$$

$$BO_3^{3-} + 4F^- + 6H^+ \rightarrow BF_4^- + 3H_2O \qquad (2)$$

As described below, the phase of the titanium dioxide obtained by this technique depends heavily on the substrate (namely the outer group of the SAM, the pH and the temperature).

Sulfonate ($-SO_3H$)-terminated SAMs can be used as substrates onto which nanoparticles and thin films of titanium dioxide can be deposited by an aqueous Ti(IV) route [33]. Here, the sulfonate group provides high local acidity and negative charge even at low pH, thus promoting the hydrolysis and surface attachment of solvated titanium-containing species. It is noteworthy that the fast growth rate on sulfonic-terminated SAMs was also found when the titanium dioxide was grown from a solution containing titanium sulfate and hydrogen peroxide [34]. Obtaining SAMs with sulfonate outer groups is not trivial. It is usually done either by reacting chemisorbed SAMs having a thioacetate terminal group [33] or by reacting terminating thiol groups with H_2O_2 in acetic acid [35,36].

By choosing sulfonate-terminated SAMs with long alkyl chains (or a sulfonate-capped polyelectrolyte multilayer) and by careful manipulation of the solution parameters, an anatase phase can be obtained with this method, without the need for high-temperature treatment. The same LPD conditions, but with a silicon substrate instead of a sulfonate-terminated SAM, yielded an amorphous film, demonstrating the importance of the substrate [37]. Low-temperature growth of anatase by LPD was also demonstrated with amine-terminated SAMs, taking advantage of the fact that at pH 2.8, the substrate was charged positively, whereas the TiO_2 precursor and the nucleated TiO_2 were charged negatively, as confirmed by ζ potential measurements [38]. At the time, this route was considered to be of large importance for photocatalysis, since (in the case of the aqueous route) it provided a way to form the photoactive anatase phase at temperatures lower than 100 °C, compared with 300–350 °C required in the sol–gel process, or with 170–240 °C required in the $TiCl_4$ process performed under vacuum [39]. Meanwhile, other low-temperature processes for producing anatase, such as the titanyl sulfate route [40], have been developed.

Apart from the sulfonate terminated SAMs and the amine-terminated SAMs, the LPD method was used also for the growth of titanium dioxide of unknown phase on SAMs (octadecyltrichlorosilane, phenyltrichlorosilane, vinyltrichlorosilane and *p*-tolyltrichlorosilane) that had been partially oxidized to yield –OH termination. The importance of this work was not in the growth itself, but rather in the fact that the underlying SAMs served as linkers to a polymeric substrate consisting of (aminopropyl)triethoxysilane grafted poly(ethylene terephthalate) [41].

The use of sol–gel methods, utilizing titanium alkoxides as TiO_2 precursors in an alcoholic medium is a well-known technique for forming TiO_2 (albeit not anatase) on solid substrates. The method was applied for the growth of titanium dioxide on $–CH_3$- [42,43], –OH- [44], and –COOH-terminated SAMs [45]. In the last work the authors compared a two-steps method, in which a $HS–(CH_2)_{10}–COOH$ monolayer was first adsorbed on gold and then exposed to an ethanolic TiO_2 colloid solution, and a one-step process in which an ethanolic colloid of TiO_2 nanocrystallites was prepared by the sol–gel method in the presence of the functionalized thiols prior to adsorption onto the gold surface. It was found that the one-step process yielded a lower coverage of the TiO_2 nanoparticles due to the formation of $HS–(CH_2)_{10}–COOH$ spacers connected to the titania nanoparticles. Similarly, Langmuir–Blodgett films of 1,12-dodecane dicarboxylic acid were used to connect a monolayer of TiO_2 spheres to silicon and glass substrates, upon performing a dehydration–condensation reaction between the carboxyl groups of the dicarboxylic acid and the surface hydroxyl groups on both the substrate and the ceramic spheres [46]. It was claimed that the flexibility of the alkyl chains in the LB film plays a role in improving the capturing of the spheres.

Atomic-layer deposition (ALD) is a gas–phase thin-film deposition method employing self-terminating surface reactions, leading to a linear correlation between the thickness of the layer and the number of deposition cycles. Mixed SAMs with different ratios of –OH- and $–CH_3$-terminated groups were used to control the surface energy and, as a result, to affect the growth of TiO_2 by ALD from titanium isopropoxide and water [47]. Here, two-dimensional growth was observed on SAM-coated substrates with high surface energy, whereas a three-dimensional growth mode was found on SAM-coated substrates with low surface energy. The high affinity between OH groups and the titania precursor was later utilized for the growth of patterned domains of titania on patterned OH-terminated alkanethiolate monolayers on gold [48].

SAMs as a means for studying photocatalysis

The fact that SAMs are adsorbed irreversibly (or almost irreversibly) on the surface of titanium dioxide makes them a valuable tool for studying fundamental phenomena in photocatalysis, as they provide a way to decouple adsorption and reaction. In this manner, SAMs were utilized to study the so-called "remote degradation" effect, namely the ability to photocatalytically decompose molecules that are located away from the TiO_2 surface. Here, a cross-linked SAM of OTS was chemisorbed on well-defined structures comprising alternating microstripes of titania and oxidized silicon of equal width. Upon exposure to UV light, complete mineralization of the OTS located on both types of substrates was observed, even in stripes as wide as 40 µm. The measured degradation kinetics on the TiO_2–Si micropatterned structures was fitted by a bi-exponential fit with two distinct apparent activation energies. Accordingly, it was suggested that oxidizing species leave the titanium dioxide domains to photocatalytically degrade molecules anchored on the remote silicon domains [49]. The remote degradation of OTS on the native oxide of silicon in a structure consisting of alternating stripes of silicon and titania was confirmed later by AFM measurements [16]. Here, XPS measurements showed that, upon complete degradation, the siloxane headgroups remain on the TiO_2 surface.

Unlike OTS located on silicon in the vicinity of TiO_2, monolayers of ODT ($CH_3(CH_2)_{17}SH$), attached to similar stripes made of gold or platinum located in the vicinity of TiO_2, were found to be quite resistant to remote degradation [50,51]. This stability was explained by the high cross section for the reaction between OH radicals and gold relative to that with silica, and was the basis for the development of photocatalysts having specificity, which utilized the "adsorb & shuttle" concept.

In a different study, octyltrichlorosilane (OCTS) SAMs chemisorbed on TiO_2 microelectrodes in an interdigitated TiO_2/Pt array were used to study the performance of an electrophotocatalytic cell as a function of applied bias [52]. The applied bias acted to push photogenerated holes to the external surface of the TiO_2 layer while pulling the photogenerated electrons to the platinum electrons, thus limiting the recombination rate. Indeed, the degradation rate constant was found to increase as the positive bias on the photocatalyst was raised up to 0.4–0.6 V. Unexpectedly, as the bias was increased above that level, not only did the degradation rate not increase, but in fact the oxidation rate of the SAM began to decrease.

The use of chemisorbed monolayers was crucial for understanding these results. If this phenomenon of counter-productive bias had been measured with a liquid-phase contaminant, one could have claimed that the observed decrease in the rate was due to a significant decrease in the adsorption rate of the target molecule. Here, the fact that the OCTS molecules were chemically and irreversibly attached to the TiO_2 electrodes suggested that there had to be another reason. Superoxide radicals, though by themselves ineffective agents for initiating the degradation, may play an important role in the secondary stages of many photocatalytic processes. Hence, a possible explanation could be a shortage of superoxide radicals, as these were formed at the reduction sites, namely at the platinum electrodes. Similar conclusions were drawn also from experiments in air upon studying a nonbiased system consisting of micrometer-size domains of TiO_2, onto which OTS was chemisorbed in close contact with micrometer-size domains made of gold and platinum [53]. The effect was found to depend on the size of the metallic domain, as well as on the humidity and on the type of metal. Overall, it can be concluded that the use of SAMs to study photocatalysis provided a unique tool to elucidate the role that superoxides may play in photocatalysis, a role that is quite often overlooked.

It is noteworthy that this discussion of the photocatalytic degradation of SAMs is based on the presumption of indirect oxidation, i.e., the transformation of the oxidative power of the photoinduced holes into oxygen-containing species, such as OH radicals. While this indirect oxidation is by all means the prevailing degradation mechanism in almost all organic species physisorbed on the surface of the photocatalyst, the situation can be different when the organic molecules are covalently bound to the surface. Indeed, the photocatalytic degradation of octadecyltrimethoxy silane (ODTMS) SAM on n-type GaN was attributed to a direct mechanism involving electron transfer from the HOMO level of the ODTMS to the valence band of the excited GaN [54]. As a consequence of this direct mechanism in gallium nitride, no remote degradation effects were observed on this photocatalyst. In contrast, the observation of remote degradation on TiO_2 indicates that indirect oxidation is the dominant mechanism on titanium dioxide. This conclusion is supported also by the fact that the rate of degradation of alkylphosphonic acid SAMs was found to correlate inversely with the ability of oxygen-containing species to reach the surface by penetrating in between the chains of the monolayer [55].

Surface patterning

Patterning of surfaces is one of the key issues in many applications involving SAMs. Generally speaking, patterning is manifested by the production of at least two types of surfaces having predesigned geometries that differ in at least one specific property. These properties can be chemical, electronic, optic, acoustic, etc. One of the most popular contrast mechanisms is the contrast between hydrophilic and hydrophobic surfaces, in particular since it can be utilized for selective deposition or growth of a large variety of materials.

The photocatalytic properties of titanium dioxide, enabling it to oxidize SAMs under the relatively weak intensity of UV light, together with the superhydrophilic nature of TiO_2 upon exposure to that light and its mechanical and optical characteristics make titanium dioxide a very interesting material for patterning. Indeed, scientific manuscripts on patterning of surfaces are the majority among those articles discussing both titanium dioxide and self-assembled monolayers.

In the context of SAMs, there are a large number of ways in which patterning can be manifested. Partial coverage of the substrate by SAMs, coverage of the surface with more than one type of SAM and selective deposition of materials on prepatterned SAMs, is only a partial list of examples; our discussion of the patterning techniques is organized accordingly, addressing namely the patterning of SAMs on TiO_2 and the patterning of TiO_2 on SAMs by selective growth.

Patterning of SAMs on TiO_2

Patterning of SAMs on TiO_2 can be obtained by both photocatalytic and nonphotocatalytic routes. Among the nonphotocatalytic methods is microcontact printing (Figure 2) [56], in which SAMs are transferred from stamps of a polymer (for example poly(dimethylsiloxane) (PDMS)) onto oxide substrates upon contact between the stamps and the substrate. Other so-called "soft-lithography" methods (replica molding, micro-transfer molding, micromolding in capillaries, and solvent-assisted micromolding) may work as well [57]. For example, colloidal lithography was used to create gold nanopits on a TiO_2 matrix, onto which methyl-terminated alkanethiol SAMs were chemisorbed [58].

While photochemical patterning of SAMs on a variety of substrates without the use of designated photoresists is possible under exposure to 185 nm light [59], it is limited to specific functional groups, under constrained environments. In contrast, SAMs located on titanium dioxide can be patterned quite easily by photocatalysis (Figure 3A). There is no need for a photoresist, and a standard patterning mask can be used, or otherwise one may imprint water-based ink patterns on the SAMs, which will prevent the photocatalytic degradation of the shadowed area [60]. Instead of exposure through a mask, one may "write" with a well-collimated beam of UV radiation, for example by using an UV laser, or by near-field optical microscope coupled to an UV laser [55].

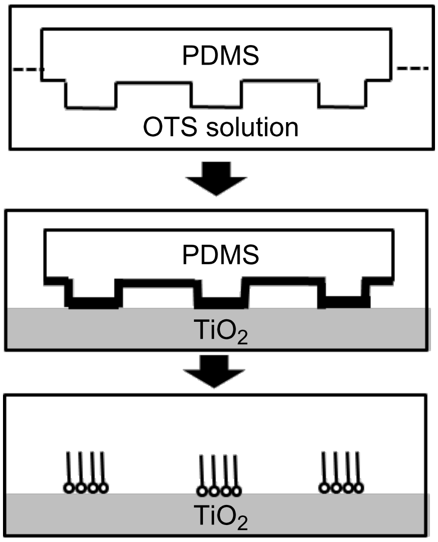

Figure 2: Patterning of SAMs on titanium dioxide by the microcontact printing method.

An interesting (but alas quite cumbersome) way to obtain patterned surfaces with hydrophilic–hydrophobic contrast is to form a prepatterned area comprising TiO_2 and another oxide by conventional lithography, and then to attach a hydrophobic SAM to the whole area. The hydrophobic–hydrophilic patterning is then obtained photocatalytically by exposure of the entire area to UV light, thus, degrading the SAM from the TiO_2 domains. This approach was demonstrated with CuO domains prepared by oxidation of Cu that had been deposited by electroless deposition on silver [61]. The silver was deposited on a titania film by photocatalytic reduction. Thus, in this case the photocatalytic properties of titanium dioxide were exploited twice, i.e., for the deposition of the silver domains and for the degradation of the SAMs chemisorbed on the photocatalyst

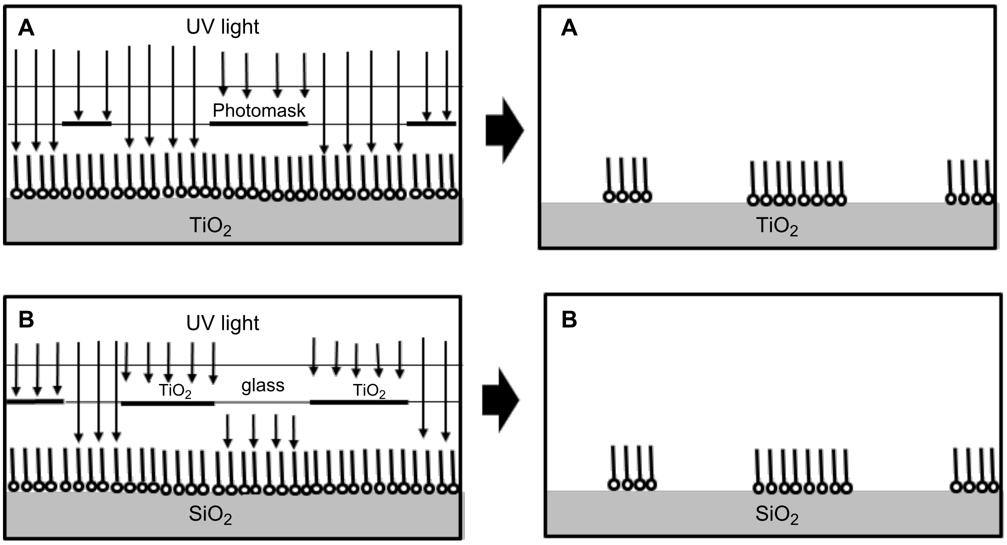

Figure 3: Photocatalytic patterning of SAMs. (A) SAMs on TiO_2 (B) SAMs on inert substrates.

domain. It is noteworthy that the hydrophobic spots were relatively large (0.5 mm in diameter), such that remote degradation effects were less acute for this system.

One of the problems associated with the formation of hydrophobic–hydrophilic contrast patterns comprising a hydrophobic SAM on TiO_2 and superhydrophilic titanium dioxide is the loss in contrast over time, which is due to eventual contamination of the TiO_2 surface upon adsorption of organic molecules from the air. Exposure to UV light may degrade these molecules, thus, restoring superhydrophilicity; however, it might also degrade the organic SAM and therefore cannot be used to solve the problem of contrast loss. A novel approach for the construction of a renewable superhydrophobic–superhydrophilic surface was presented by Nishimoto et al. [62]. The approach is based on through-mask photocatalytic patterning of hydrophobic SAM on TiO_2, followed by deposition of boehmite ($AlOOH\cdot nH_2O$) on the exposed TiO_2 domains. Then, a heat-treatment step converted the boehmite into Al_2O_3, while oxidizing the SAMs, forming a patterned TiO_2–boehmite surface. A hydrophobic SAM was then attached to both types of domains, which then went through a second step of exposure to UV light. At the end of the process a negative image of the first-step surface was obtained, consisting of superhydrophilic TiO_2 domains and superhydrophobic domains anchored to alumina. In that way, the restoration of hydrophilic contrast by exposure to UV was expected not to take its toll on the hydrophobic SAMs. With respect to remote degradation, the fact that the inert substrate here is alumina and not silica may assist to preserve the SAMs, as can be inferred from a comparison of the remote degradation effects of SAMs on silica to those of SAMs on alumina [51].

Remote degradation effects are not necessarily destructive when it comes to the patterning of SAMs. In fact, they can be utilized to pattern SAMs on inert surfaces (Figure 3B). The technique was demonstrated by Lee and Sung, who used a quartz mask containing patterned TiO_2 in order to pattern an octadecylsiloxane SAM on silicon [63]. Once patterned, ultra-thin layers of ZrO_2 were deposited by atomic-layer deposition on the exposed parts of the silicon substrate. The reported spatial resolution was striking: The nominal width of ZrO_2 lines and SAM-coated Si lines was approximately 0.5 μm. This relatively high resolution should be attributed to the intimate contact between the TiO_2 mask and the SAM-coated silicon as well as to the short exposure time, which minimized the blurring.

Another example of photocatalytic patterning of SAMs on inert substrates is the patterning of perfluorodecanethiol SAM on gold by a through-mask back exposure of thin films of titania located at a distance of 12.5 μm from the SAM-coated gold [64]. The quality of the patterned surface was examined by immobilizing a fluorescent dye on the oxidized regions of the patterned gold surface. The same method was used to pattern enzymes on a gold surface, by the attachment of fluorescein isothiocyanate labeled peroxidase (FITC-POD) onto the hydrophilic regions. Unfortunately, no details were given regarding the thickness of the TiO_2 layer and the wavelength. Such details could be of high importance for analyzing the significance of the data in this back-exposure configuration.

Photocatalytic lithography by remote degradation was also demonstrated by the formation of grayscale gradients in thiolated SAMs anchored to gold located as far as 60 μm from a TiO_2 thin film on quartz, back-irradiated through a mask [65]. The gaps in the thiolated SAM were then filled with 11-mercapto-1-undecanol or with 1*H*,1*H*,2*H*,2*H*-perfluorodecanethiol. The flux during irradiation was quite high (17 mW/cm^2). The apparent contradiction between this study and works that reported the high stability of SAMs on gold towards remote degradation [50] may be explained by the different position of the SAMs relative to the source of the oxidizing species and the high UV flux in the back-irradiation experiments.

An interesting, inexpensive way to use photocatalysis for the formation of patterns having hydrophobic–hydrophilic contrast was presented by Bai et al. [66]. Here, TiO_2 particles in solution were used to pattern an OTS monolayer on mica sheets, the size of the islands and concentration being affected by the UV flux impinging on the surface, as evidenced by AFM and wettability measurements.

The phenomenon of remote degradation raises a question regarding the fidelity of patterns obtained by through-mask exposure techniques. Indeed, exposure of OTS-coated TiO_2 to 254 nm light through a quartz mask covered with chromium stripes (40 μm in width and distance) caused a complete degradation of the alkyl chains, including those in the “dark” regions [67]. This does not necessarily contradict the reports on patterning presented above, since analysis of the kinetics revealed that the degradation rate in the exposed areas was 2–20 times faster than in the dark areas, and hence, obtaining a reasonable contrast is still possible. However, it definitively demonstrated that patterning can be very sensitive to overexposure, and that in terms of contrast, the best resolution that can be achieved with photocatalytic patterning is expected to be no better than a few microns. Moreover, if one accepts the notion that the dominant mechanism of remote degradation is photoinduced homolysis of photocatalytically formed hydrogen peroxide, then an important outcome is that structures that are patterned by exposure to 365 nm light may be sharper than structures patterned by 254 nm light. This conclusion, which seems contradictory to conventional wisdom, stems from the fact that the quantum efficiency of the generation of OH-radicals by photohomolysis of H_2O_2 with 365 nm photons is 110 times smaller than that with 254 nm photons [68].

Patterning of TiO_2 by selective growth on SAMs

Probably the most popular way by which SAMs have been used as a means to obtain patterned TiO_2 films is through site-selective deposition (SSD) of the oxide on prepatterned SAMs [69]. The concept here is to pattern SAMs on substrates, either by complete removal or by site-specific tailoring of the outer groups, thus forming areas with high tendency for titania growth, coexisting with domains onto which titania will not grow. It should be pointed out that the SSD technique is not limited to the deposition of titanium dioxide and was utilized for patterned growth of other oxides such as In_2O_3 [70], Ta_2O_5, SnO_2 and $SrTiO_3$ [69].

The most popular means for selective growth is direct site-selective deposition (Figure 4), based on patterning of SAMs on a substrate (either by exposure to 185 nm light or by conventional photolithography), followed by nucleation and growth of TiO_2 on areas that have been depleted of the SAMs. As an example, one may mention the patterning of OTS into methyl-terminated regions and silanol-terminated regions, onto which amorphous titanium dioxide formed from titanium dichloride diethoxide (TDD) was deposited either from the liquid phase (D-40) [71] or from the gas phase [72]. The latter was reported to yield higher quality films due to a lack of bulk nucleation. In a later study a comparison was made between three types of precursors, namely TDD, titanium tetrachloride (TC) and titanium tetraethoxide (TE), acting on deep UV-exposed OTS and PTCS (phenyltrichlorosilane) [73]. Quite surprisingly, it was found that the contrast in the patterns of the grown oxide depended on the type of precursor. While TC or TDD formed TiO_2 on the hydrophilic silanol groups but not on the hydrophobic methyl groups of OTS, TE induced TiO_2 growth on both types of substrates without any preference. Regardless of the precursor, the obtained TiO_2 films were amorphous. Conversion to anatase took place at 300 °C when TC was the precursor, whereas a temperature of 400 °C was required when TDD or TE were used as precursors. To improve the contrast in SSD growth on a patterned silanol–hydrophobic SAM surface one may use sonication, which has been demonstrated to remove loosely adhered TiO_2 particles from domains on which deposition was undesirable [74,75].

Exposure to deep UV through a photomask was also used for partial oxidation of SAMs of octadecyltrichlorosilane, phenyltrichlorosilane, vinyltrichlorosilane and *p*-tolyltrichlorosilane on an (aminopropyl)triethoxysilane grafted poly(ethylene terephthalate) surface. Subsequently, TiO_2 was grown selectively by LPD on the oxidized domains (Figure 5). It was found that SAMs containing aromatic rings were the most suitable for growing titania, producing strongly adhering films with distinct TiO_2 micropatterns [41]. To improve selectivity, a shielding reagent, reversibly adsorbed on the nonexposed domains of a *p*-tolyltrichlorosilane SAM, was added prior to the TiO_2 growth step [76]. This shielding reagent, dodecylbenzene sodium sulfonate, was chosen based on its tendency, in aqueous solutions, to attach only to hydrophobically-terminated SAMs, due to its amphiphilic nature. It is noteworthy that bubbling air to

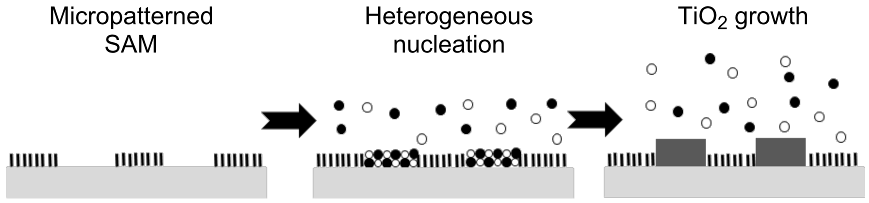

Figure 4: Patterning of SAM on a substrate followed by selective growth directly on the substrate.

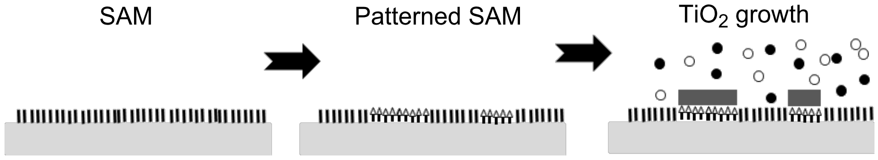

Figure 5: Partial oxidation of SAMs at predesigned locations followed by TiO_2 growth on the partially oxidized domains.

constantly replace the LPD solution close to the surface can be quite beneficial for forming crack-free TiO_2 films, as was demonstrated with patterned SAMs of heptadecafluoro-1,1,2,2-tetrahydrodecyltrichlorosilane (HFDTS) [77]. Another example of the approach portrayed in Figure 2B was the patterned oxidation of thioacetate-(–$SCOCH_3$) terminated SAMs to form patterned sulfonate-terminated domains onto which TiO_2 was grown [78].

A non-photoinduced means to pattern SAMs for selective deposition is microcontact printing (Figure 2). For example, microcontact printing of sulfonic acid terminated SAMs facilitated the growth of patterned TiO_2 from a solution containing titanium sulfate and hydrogen peroxide [34]. Another example is the transfer of OTS SAM onto silica followed by selective ALD growth of titanium dioxide on the noncoated areas [79]. Likewise, a technique called "edge-transfer lithography" was applied to form lines of titanium dioxide nanoparticles with nanometer-scale resolution [80]. Here, transfer of SAMs from the edges of micron-scale-patterned elastomeric stamps onto silica produced nanometer-scale patterned SAMs, with line widths as small as 60 nm. Such thin lines were obtained by a dewetting and blow-drying process, which trapped silane solution only in the recesses of the molded stamp. In a different work, OTS was deposited by microcontact printing onto both external sides of a nanoporous polycarbonate filter. As a consequence, the ALD growth of titanium dioxide was limited to the inner walls of the polycarbonate filter. In that way, the performance of 100–800 ALD cycles followed by the etching away of the polycarbonate template with chloroform yielded TiO_2 nanotubes, whose diameter could be predetermined according to the diameter of the pores in the PC filter [81].

Patterning of SAMs en route for selective deposition can be achieved by introducing a physical barrier for the deposition of SAMs, followed by TiO_2 growth once the barrier is removed. In that manner, coined "contact area lithography" (CAL), round nanoparticles were used to cover a silica surface, thus forming a close-packed structure with a hexagonal pattern of nanometer-sized contact dots (Figure 6). Then, OTS SAMs were deposited everywhere except for on the contact dots, facilitating the ALD growth of nanodisks of TiO_2 from a titanium tetraisopropoxide precursor [82].

It is noteworthy that the growth rate of anatase on top of SAMs (methyl-terminated or even amino-terminated) is significantly lower than that measured on top of amorphous TiO_2 underlayer. This was exploited for the growth of a patterned anatase layer on top of amorphous TiO_2 grown on patterned OH-terminated SAMs [83].

Although SAMs were used to obtain patterned TiO_2, mainly by directing the deposition of titania, it is possible to pattern TiO_2 by directing its etching instead of its growth (Figure 7). An interesting example is the patterning of an area made of TiO_2 nanotubes, formed by anodization of titanium in HF. Here, SAMs of 1*H*,1*H*,2*H*,2*H*-perfluorooctyl-triethoxysilane were chemisorbed on selected areas in the nanotube array and served to selectively protect the nanotubes upon immersion in HF [84].

Electron transfer in SAMs connected to TiO_2

Electron transfer through SAMs has been studied quite thoroughly for both organothiolated SAMs on metals and organosilanes on silicon. The appearance of dye-sensitized solar cells [85], based on (disordered) dye molecules attached to the

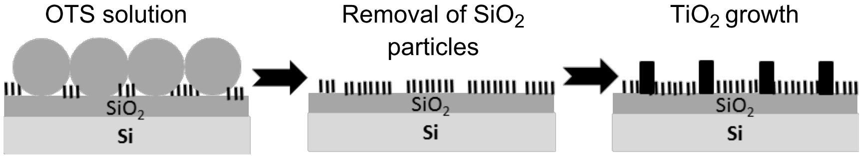

Figure 6: Patterned growth of TiO_2 by "contact area lithography" (CAL) (after [82]).

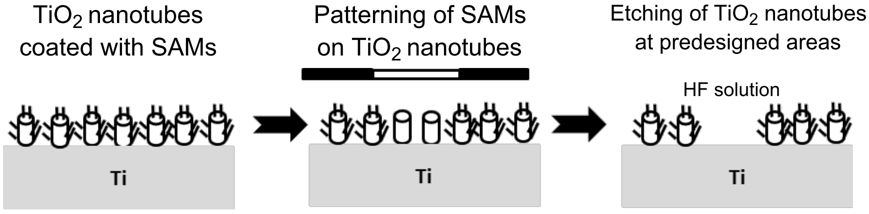

Figure 7: Patterning of a surface containing TiO_2 nanotubes by localized etching, by using patterned SAMs to protect selected areas (after [84]).

surface of nanoparticulate titanium dioxide, provoked interest also in the charge transport from SAMs to titanium dioxide. In many cases, as detailed below, the SAMs serve as mediators between the sensitizing molecules and the surface, and hence are required to exhibit good conductivity along the molecule, minimal contact resistance, and, no less important, a set of energy levels that can support vectorial charge transfer. Although many of the studies in this area are phenomenological they provide the necessary background required for the development of a variety of microelectronic devices such as solar cells, transistors and capacitors. It is noteworthy that in many publications discussing charge transport between SAMs and titanium dioxide, the characterization of the prepared films is somewhat partial; it is thus very rare to find manuscripts that provide data on the organization and orientation of the adsorbed molecules as well as on their surface concentration.

The finding that C_{60} may transfer electrons to titanium dioxide upon illumination with visible light [86] led to the study of a system in which the C_{60} is anchored to the titanium dioxide through a SAM mediator. The mediator comprised salicylic acid (attached to the TiO_2 surface through its carboxylate group) connected to a pyrrodine group of a modified C_{60} [87]. An agreement between the measured photocurrent action spectrum and the absorption spectrum of the modified fullerene served as an indication that the photoactive species was the modified fullerene. A photon-to-current conversion efficiency as high as 15% was measured, demonstrating the usefulness of using SAM mediators.

The same concept of using SAMs as mediators was demonstrated in a system comprising quantum dots and self-assembled-monolayer-coated titanium dioxide. Here, cadmium–sulfur–selenium (CdSSe) quantum dots were physically attached to hydrothermally synthesized anatase TiO_2 nanobelts, onto which SAMs of long chain carboxylic acids, exposing hydrophobic terminating groups, were chemisorbed [88]. An UV-induced compressive force between the nanoparticles and the TiO_2 nanobelts could be inferred based on Raman spectroscopy. To our understanding, this compressive force may compensate to some extent for the lack of chemical bonding between the quantum dots and the terminating groups of the monolayer, thus, enabling the high photocurrent response measured for this system.

Another study on charge transport between SAMs and TiO_2 was based on a mixed-monolayer configuration. Here, a self-assembled monolayer of a carotenoid (*trans*-8'-apo-β-caroten-8'-oic acid) was adsorbed on TiO_2. Long-chain molecules of pheophytin were immobilized in between the long-chain carotenoids by virtue of VdW forces. It was shown that excitation of the pheophytin molecules by 670 nm light was quenched reductively by electron transfer from the carotenoid [89]. It was suggested that the charged pheophytin recovers back to the parent molecule predominantly by injecting an electron into the TiO_2 conduction band, thus, facilitating the observation of a long-lived carotenoid radical cation. A claim was made that similar paths yielding long-lived charge separation situations may be relevant also in natural photosynthetic systems, and should be considered in the development of dye-sensitized solar cells.

In certain cases, feasibility studies with TiO_2-containing systems were later implemented in devices that are constructed on other substrates. As an example, a self-assembled monolayer of 5-cyano-2-(butyl-4-phosphonic acid)-3-butylthiophene (CNBTPA) was formed on TiO_2 by using its phosphonic acid group as a binding group. Once chemisorbed, the monolayer served to attach molecules of α,ω-dicyano substituted β,β'-dibutylquaterthiophene (DCNDBQT) molecules by forming a hydrogen bond between the cyano group of CNBTPA and a hydrogen on the thiophene ring of DCNDBQT, and by forming a hydrogen bond between the cyano group of DCNDBQT and a hydrogen on the thiophene ring of CNBTPA [90]. A quasi-perpendicular structure of the CNBTPA–DCNDBQT layer relative to the TiO_2 surface was inferred, suggesting optimal orbital overlap between neighboring thiophene rings. The same substituted oligothiophene was then used to form a nanoscopic organic field-effect transistor (OFET), albeit not on TiO_2 but on Si/SiO_2 substrate.

Applications

The study of the ways by which SAMs are attached to titanium dioxide (and, in a complementary manner, ways by which TiO_2 is grown on SAMs) as well as the study of fundamental phenomena and the developing of patterning techniques, have paved the way for the utilization of systems comprising SAMs and TiO_2 for a variety of applications. The following section discusses the main applications presented so far.

TiO_2-SAMs in electronic devices

The large dielectric constant k of TiO_2 ($25 < k < 30$) compared with that of silica ($k = 3.9$), as well as its refractory properties, suggest its use in MOSFET technology [91]. In that respect, it is interesting to mention that the dielectric constant of amorphous TiO_2 grown on patterned OTS from titanic acid (H_2TiO_3) [92] was estimated to be 63 at 100 kHz, significantly larger than the reported values of 22 measured for biomimetically deposited amorphous TiO_2 [93]. This was attributed to the existence of small crystallized particles. A significant drawback in the use of TiO_2 for microelectronic purposes is the relatively high leakage current (as high as 4.3×10^{-8} A cm^{-2} at 1 V and a thickness of

306 nm) and the linear decrease in the dielectric constant as a function of frequency (from *k* = 160 at 1 kHz to *k* = 23 at 1 mHz) [92]. These were explained by the presence of interface states and impurities such as OH^- and H_2O in the film. Still, well-behaved MOSFET transistors with a TiO_2 gate oxide were demonstrated already in 1997 [94], prior to the full development of patterning technologies. Likewise, a miniature capacitor, made of an oxide–SAM–TiO_2 sandwiched structure, was presented already in 1998 [95].

The possibility to deposit TiO_2 on top of sulfonate-terminated SAMs was utilized to form metal–oxide–metal (MOM) heterojunction nanowires by a "bottom-up" approach [96]. Here, Au–TiO_2–Au nanowires were prepared within nanoholes of anodic aluminum oxide templates. The preparation procedure included the deposition of gold by electroplating, chemisorption of 1,8-octanedithiol (HS–$(CH_2)_8$–SH), oxidation of the terminal thiol groups to form ω-sulfonate groups, deposition of polycrystalline anatase using $Ti(OPr)_4$ dissolved in a water–ethanol mixture, and capping of the TiO_2 with electroplated gold.

Self-assembled monolayers, with their ability to attach both to inorganic and organic materials may have a large potential in hybrid microelectronic systems containing titanium dioxide together with organic components. Along this line, the improvement of the performance of organic field-effect transistors (OFETs) by introducing SAMs was observed with OFETs comprising a titanium gate, dielectric layer of TiO_2 prepared by anodization, and a poly(triarylamine (PTAA)) layer (alternatively a pentacene layer) that served to form the source and the drain of the transistor [97]. Here, the addition of an OTS layer between the TiO_2 and the source–drain layer was found to increase the field-effect mobility (calculated in the saturation regime) by two orders of magnitude (with PTAA) or by a factor of 2 (with pentacene).

SAMs may assist in the preparation of hybrid electronic components not only by forming the connection between organic and inorganic layers but also by facilitating self-patterning. In that manner photopatternable SAMs of 1*H*,1*H*,2*H*,2*H*-perfluorododecyltrichlorosilane were used as a template for self-localization of conducting polymers en route to the formation of polymer-based transistors [98]. Here, the source and drain electrodes were formed by spin coating an aqueous solution of poly(3,4-ethylenedioxythiophene) (PEDOT) on TiO_2/SAM, resulting in dewetting and self-localization of the solution within the exposed domains. The substrates were then further coated with poly(3-hexylthiophene) (P3HT). Conformity of the structure was found to depend heavily on the humidity conditions during exposure, since too high a humidity resulted in remote degradation of nonirradiated areas, which could lead to an excess coverage of PEDOT. For the same reason (prevention of remote degradation) 365 nm light was found to give sharper patterns than 254 nm light.

The use of SAMs on oxidized silicon in order to reduce friction is well documented. In a similar manner, SAMs on titanium dioxide were utilized to simultaneously solve the problems of wear and stiction in microelectromechanical (MEMS) devices. Here, a thin (10 nm) layer of TiO_2 was coated by the ALD technique onto polysilicon substrates. A SAM of $CF_3(CF_2)_7(CH_2)_2SiCl_3$ (FDTS) was then chemisorbed on the titania layer [99]. Tribological measurements showed that the static-friction coefficient was dominated by the presence of FDTS as an external layer, as manifested by the fact that the coefficients of FDTS on TiO_2 and on SiO_2 were nine times lower than those of SiO_2 and three times lower than those of TiO_2. At the same time, wear tests showed that the lifetimes of moving parts were similar to those obtained with polysilicon-coated titanium dioxide, namely 1.5–3.0 times longer than those of noncoated polysilicon.

Solar cells

One of the most popular (if not *the* most popular) areas utilizing structures containing SAMs and titanium dioxide, is photovoltaics. In almost all designs these structures are characterized by the SAM serving as a mediator between the photosensitizer and the titanium dioxide acceptor. A variety of photosensitizers have been used: From the conventional ruthenium-based dyes to conductive polymers, C_{60} and inorganic quantum dots. Likewise, a variety of SAMs have been used, with various anchoring groups, including phosphonic acids, silanes, and carboxylic acids. Unfortunately, while the motivation for using SAMs as mediators ensuring vectorial charge transfer is clear, the results obtained so far are still insufficient in terms of cost and efficiency to justify commercial scale production. This does not necessarily mean that the approach of using SAMs as mediators is doomed to fail. On the contrary, analysis shows that this direction draws increasing attention.

Polyaniline (PANI), which has a bandgap of 2.8 eV, compared with 3.2 eV of TiO_2, was used as a sensitizer, absorbing visible light and transferring photoinduced charge to the titanium dioxide, by virtue of good matching between its LUMO level and the conduction band of TiO_2. PANI adheres to titanium dioxide by physical adsorption, and thus it was thought that a mediator that forms a strong interaction with both would improve charge transport. Indeed, silane-bearing aniline compound ($C_6H_5NHC_3H_6Si(OMe)_3$) was used to form solvent-free quasi-solid solar cells based on acid-doped polyaniline, but the efficiency was quite modest (0.12%) [100]. Another mediator between PANI and TiO_2 was aminopropylsilane, resulting in improved thermal stability of PANI and enhanced photocatalytic degradation rate of methyl orange molecules under sunlight, which was attributed to the sensitizing effect of PANI [14].

In a quest to replace expensive dyes in DSSCs, Senadeera et al. used grafted polypyrrole films covalently bonded to self-assembled monolayers of 3-(trimethoxysilyl)propyl methacrylate attached to mesoporous TiO_2 substrates [101]. Although the overall performance was poor, a comparative study showed that polypyrrole could be used more efficiently as a sensitizer for TiO_2 when covalently attached through the SAM than it could without the SAM.

The interface between TiO_2 and poly(3-hexylthiophene)/[6,6,]phenylC_{60} butyric acid methyl ester (P3HT/PCBM), in a based-inverted bulk-heterojunction (BHJ) solar cell, was modified by a series of carboxylic acid functionalized SAMs [102]. The presence of SAMs acted to reduce the contact resistance by passivating the surface trap sites at the TiO_2 surface, enhancing the electronic coupling between the TiO_2 and the organic layer, and also improved the growth mode and morphology of the upper organic layer. The largest enhancement was observed with a SAM of C_{60}-substituted benzoic acid. Here, the efficiency with the buried SAM layer was 3.8%, compared with 2.8% in the absence of a SAM interlayer.

In two similar systems, two SAMs attached to TiO_2 through phosphonic acid (2-oligothiophene phosphonic acid and ω-(2-thienyl)alkyl phosphonic acid) were used as interface modifiers on TiO_2 to increase compatibility with poly(3-hexylthiophene) (P3HT) [103]. The photoluminescence (PL)-quenching efficiency and the short-circuit current density of photovoltaic cells having this configuration were found to increase with the number of thiophene rings and as the alkyl–chain length decreased. Here, a drop in the LUMO level of the interface modifiers increased the photocurrent at the expense of the open-circuit voltage. It should be noted that the observation of correlation between structural parameters in the polymer and its photovoltaic performance is important as it may provide a strategy for stabilizing inorganic particles in the fabrication of high efficiency organic–inorganic photovoltaic devices.

The recent interest in utilizing quantum dots (QDs) for photovoltaics also has its influence on SAMs and titanium dioxide, as more and more cases in which SAMs are used as mediators between QDs and titanium dioxide are published. For example, a self-assembled monolayer of 3-mercaptopropyl-trimethoxysilane was preassembled onto a mesoporous TiO_2 film to be used as a surface-modified layer to induce the growth of CdSe quantum dots [104]. Here, it was claimed that the terminal thiol groups increased the nucleation and growth rate of CdSe QDs formed by the successive ionic layer adsorption and reaction (SILAR) process. The large uniformity of the CdSe films formed in that way inhibited charge recombination at the electrode–electrolyte interface, and as a consequence, higher efficiency in CdSe-sensitized DSSC solar cells was obtained. In a similar manner, SAMs of mercaptoacetic acid served as substrates for the growth of quantum dots of cadmium sulfide by the same SILAR method [105]. CdS QDs were also produced on SAMs attached to TiO_2 by a phosphonic acid headgroup [106]. The SILAR procedure here comprised successive cycles consisting of exposure to $CdSO_4$, rinsing in DI water, immersion in Na_2S and a second rinsing in DI water. The solar-cell performance was found to depend on the number of SILAR cycles (it was claimed that above six cycles, the CdS may aggregate or form recombination centers). The efficiency obtained with 3-aminopropyl phosphonic acid (APPA), 3-phosphonopropionic acid (PPA), and 1-butylphosphonic acid (BPA) (0.44%) was as much as three times higher than that measured in the absence of SAMs. Quite surprisingly, no tailgroup dependence was found, suggesting in this case that the CdS nanoparticles were not sitting at the surface of the SAMs, but were rather penetrating into the SAM network such that they resided close to the SAM/TiO_2 interface.

This part would not be complete without reference to another particular effect of SAMs in a totally different design. This is namely the use of SAMs anchored to titanium dioxide as a means to improve the stability and durability of dye molecules also anchored to TiO_2. This effect was well demonstrated in the coadsorbption of 1-decylphosphonic acid together with a heteroleptic ruthenium sensitizer that contained two long amphiphilic chains attached to its bipyridine rings (Z-907) [107]. Here, the presence of the SAMs was found to significantly reduce the drop in the open-circuit voltage (from 90 mV to 20 mV) measured following 1000 h of aging at 80 °C. This was achieved without any deleterious effect on the initial performance (approx. 7% efficiency). This enhanced stability was attributed to the ability of the SAM to exclude water molecules from the interface, probably by the formation of a hydrophobic barrier made from the long chained phosphonates interacting with the long amphiphilic chains of the dye.

Offset printing

Current offset printing technology is based on anodized aluminum plates patterned, by photosensitive means, into hydrophobic and hydrophilic regions to be wet selectively by oil-based ink and water, respectively. Color printing requires usually 3–4 plates that cannot be recovered. A new type of offset-printing plate that can be reused many times and with a resolution of up to 150 lines per inch was presented recently. This new offset technology is based on photocatalytic patterning of SAM-coated TiO_2 into superhydrophobic and superhydrophilic regions [108]. Here, the patterning of the SAMs chemisorbed on the TiO_2-coated plates was performed by using an ink-jet printer to deposit patterned ink, which served as a photomask shielding the SAMs during UV exposure [109].

Loading films or particles of nanoporous titanium dioxide with nanoparticles of silver (for example by photocatalytic deposition upon exposure to UV light) was shown to produce brownish-grey colored surfaces. Illumination of these surfaces by monochromatic visible light changes the color of the Ag–TiO_2 system to that of the incident light, due to reoxidation, causing the silver nanoparticles that had already absorbed at this specific wavelength to lose their ability to absorb more photons at this same wavelength. This phenomenon, termed “multicolor photochromism” [110] can, in principle, be utilized to form rewritable color papers and paints, or even optical memories. One of the problems preventing this application is the gradual bleaching of the color due to nonpreferential absorption upon exposure to white light. In this context, it was found that modification of the Ag–TiO_2 films with alkanethiol or fluoroalkanethiol SAMs may help to suppress bleaching, either by preventing the oxidative dissolution of silver or by blocking the electron transfer from silver to oxygen [111]. The mechanism for bleaching suppression is the same as that for coloring suppression, hence reactivation is needed. This reactivation could be obtained by photocatalytic decomposition of the ODT monolayers on the silver by exposure to UV light, and by relying on the remote degradation effect of TiO_2 as discussed above.

SAMs for selective photocatalysis

Heterogeneous photocatalysis, being based on oxidation by hydroxyl radicals, is known to hardly distinguish between different target molecules. Since some contaminants are more toxic than others, and since some contaminants are readily degradable by biological means while others are nonbiodegradable, there is an obvious need to develop selective photocatalysts that will address streams containing multiple contaminants in a manner that would handle preferentially those contaminants that are either highly toxic and/or nonbiodegradable [112].

A few years ago it was proposed that a structure comprising SAMs located in the vicinity of titanium dioxide domains could be used en route to achieve preferential degradation of toxic contaminants. The principle was to use SAMs on inert substrates as molecular recognition platforms able to selectively physisorb specific target molecules. Once physisorbed, the target molecules diffuse from the inert, adsorption sites to the photocatalytic domains, where they are photocatalytically degraded (Figure 8). The feasibility of this approach was first demonstrated by constructing metallic microdomains, onto which self-assembled monolayers of thiolated β-cyclodextrin were chemisorbed. The cavity of the β-cyclodextrin served as a molecular-recognition site for 2-methyl-1,4-naphthoquinone (2MNQ). The measured degradation rate ratio between 2MNQ and benzene was 8.1, compared with 0.8 in the absence of the molecular-recognition sites. As expected, the kinetics was found to depend on the average distance over which the adsorbed 2MNQ had to diffuse in order to get to the photocatalytic domains [113]. The same type of molecular recognition SAM (thiolated cyclodextrin) was found to enhance also the photocatalytic degradation of the dye-stuff Chicago Sky Blue 6, which is a long, symmetric molecule whose chemical structure fits the cyclodextrin cavity [51].

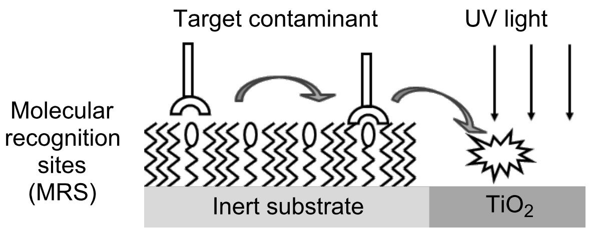

Figure 8: Specific photocatalytic degradation by the “adsorb and shuttle” approach (after [51]).

This so-called “adsorb and shuttle” approach was later implemented also by utilizing Cu^{2+} ions attached to SAMs of 1,1-mercaptoundecanate in order to physisorb diisopropyl methyl phosphonate (DIMP), a known simulant for the nerve gas sarin. Once physisorbed, the DIMP molecules diffused to the TiO_2 domains where they were photocatalytically degraded in a mechanism similar to that observed with TiO_2 alone, namely, via the formation of acetone as an intermediate product. An enhancement factor of 4–6 relative to bare TiO_2 was observed [114].

It is noteworthy that the phenomenon of remote degradation discussed above poses a severe limitation to the concept of selective photocatalysis, as the SAMs might be prone to eventual degradation upon exposure to UV light. Placing the molecular recognition sites on thin films of metals such as gold helps to overcome this problem, as it stabilizes the monolayers against remote degradation, nevertheless this solution might be insufficient in powders, where the size of the metallic domains is significantly smaller than the size in the works presented above.

Other applications

The ability to controllably tailor the properties of SAMs, in combination with the specific properties of titanium dioxide, which include photocatalytic activity and superhydrophilicity, provides a platform for a wide range of applications. Among these, one may highlight the UV-protected polymeric materials based on amorphous TiO_2 grown on sulfonated SAMs attached to polymeric sheets [115]. Another application is the use of hydrophobic SAMs (1*H*,1*H*,2*H*,2*H*-perflurooctyl-triethoxysilane) attached to TiO_2 on titanium to improve the blood compatibility of titanium-based biomedical devices and implants [116]. A different application is the prevention of pitting corrosion by the highly uniform films of TiO_2 grown on sulfonate-terminated SAMs [117].

Conclusion

The ability to control the properties of self-assembled monolayers (SAMs) attached to solid surfaces and the unusual photocatalytic properties of titanium dioxide provide a rationale for studying systems comprising of both. Such systems can be realized in the form of SAMs grown on TiO_2 or, in a complementary manner, as TiO_2 grown on SAMs.

This mini-review summarizes the current knowledge on SAMs attached to titanium dioxide while focusing on the resemblances and differences between SAMs on titania and SAMs on the more frequently studied substrate of silica. Among the differences one finds the use of sulfonic acid headgroups and the faster chemisorption of alkylsilane monolayers.

Mastering micropatterning is a key issue en route to the successful assimilation of a variety of titanium dioxide based devices. Accordingly, particular attention was given to describing a variety of methods and techniques aimed at exploiting the photocatalytic properties of titanium dioxide for patterning. Reports on a variety of applications were discussed. The examples portrayed above, representing the areas of photovoltaics, microelectronics, microelectromechanics, photocatalysis, corrosion prevention and even biomedicine should be regarded as appetizers, paving the way for further studies to be performed.

Acknowledgements

The assistance of I. Rozen in performing the literature search for this review is gratefully acknowledged. The author also thanks the Russell Berrie Institute of Nanotechnology and the Grand Water Research Institute for their support.

References

1. Blake, D. M. *Bibliography of Work on the Photocatalytic Removal of Hazardous Compounds from Water and Air;* National Renewable Energy Laboratory: Golden, Colorado, 1994.
2. Halman, M. M. *Photodegradation of water pollutants;* CRC Press: Boca Raton, 1996.
3. Paz, Y.; Luo, Z.; Rabenberg, L.; Heller, A. *J. Mater. Res.* **1995,** *10,* 2842–2848.
4. Gerischer, H.; Heller, A. *J. Phys. Chem.* **1991,** *95,* 5261–5267. doi:10.1021/j100166a063
5. Hoffmann, M. R.; Martin, S. T.; Choi, W.; Bahnemann, D. W. *Chem. Rev.* **1995,** *95,* 69–96. doi:10.1021/cr00033a004
6. Paz, Y. *Solid State Phenom.* **2010,** *162,* 135–162. doi:10.4028/www.scientific.net/SSP.162.135
7. Bahnemann, D. W.; Moeing, J.; Chapman, R. *J. Phys. Chem.* **1987,** *91,* 3782–3788. doi:10.1021/j100298a014
8. Cho, Y.; Choi, W.; Lee, C.-H.; Hyeon, T.; Lee, H.-I. *Environ. Sci. Technol.* **2001,** *35,* 966–970. doi:10.1021/es001245e
9. Shaham Waldmann, N.; Paz, Y. *J. Phys. Chem. C* **2010,** *114,* 18946–18952. doi:10.1021/jp105925g
10. Muñoz, J.; Domènech, X. *J. Appl. Electrochem.* **1990,** *20,* 518–521. doi:10.1007/BF01076066
11. Turchi, C. S.; Ollis, D. F. *J. Catal.* **1990,** *122,* 178–192. doi:10.1016/0021-9517(90)90269-P
12. Minero, C. *Catal. Today* **1999,** *54,* 205–216. doi:10.1016/S0920-5861(99)00183-2
13. Fujishima, A.; Rao, T. N.; Tryk, D. A. *J. Photochem. Photobiol., C: Photochem. Rev.* **2000,** *1,* 1–21. doi:10.1016/S1389-5567(00)00002-2
14. Li, J.; Zhu, L.; Wu, Y.; Harima, Y.; Zhang, A.; Tang, H. *Polymer* **2006,** *47,* 7361–7367. doi:10.1016/j.polymer.2006.08.059
15. Helmy, R.; Fadeev, A. Y. *Langmuir* **2002,** *18,* 8924–8928. doi:10.1021/la0262506
16. Lee, J. P.; Kim, H. K.; Park, C. R.; Park, G.; Kwak, H. T.; Koo, S. M.; Sung, M. M. *J. Phys. Chem. B* **2003,** *107,* 8997–9002. doi:10.1021/jp030077k
17. Mattigod, S. V.; Fryxell, G. E.; Alford, K.; Gilmore, T.; Parker, K.; Serne, J.; Engelhard, M. *Environ. Sci. Technol.* **2005,** *39,* 7306–7310. doi:10.1021/es048982l
18. Haick, H.; Sagatelian, Y.; Paz, Y. *Langmuir* **2003,** *19,* 2540–2544. doi:10.1021/la020452k
19. Kim, W.-J.; Kim, S.; Lee, B. S.; Kim, A.; Ah, C. S.; Huh, C.; Sung, G. Y.; Yun, W. S. *Langmuir* **2009,** *25,* 11692–11697. doi:10.1021/la901615e
20. Brunner, H.; Vallant, T.; Mayer, U.; Hoffmann, H.; Basnar, B.; Vallant, M.; Friedbacher, G. *Langmuir* **1999,** *15,* 1899–1901. doi:10.1021/la981426i
21. Cohen, S. R.; Naaman, R.; Sagiv, J. *J. Phys. Chem.* **1986,** *90,* 3054–3056. doi:10.1021/j100405a004
22. Shin, H.; Wang, Y.; Sampathkumaran, U.; De Guire, M. R.; Heuer, A. H.; Sukenik, C. N. *J. Mater. Res.* **1999,** *14,* 2116–2123. doi:10.1557/JMR.1999.0286
23. Hozumi, A.; Cheng, D. F.; Yagihashi, M. *J. Colloid Interface Sci.* **2011,** *353,* 582–587. doi:10.1016/j.jcis.2010.09.075
24. Loste, E.; Fraile, J.; Fanovich, M. A.; Woerlee, G. F.; Domingo, C. *Adv. Mater.* **2004,** *16,* 739–744. doi:10.1002/adma.200306214
25. García-González, C. A.; Saurina, J.; Ayllón, J. A.; Domingo, C. *J. Phys. Chem. C* **2009,** *113,* 13780–13786. doi:10.1021/jp9029985
26. Marcinko, S.; Helmy, R.; Fadeev, A. Y. *Langmuir* **2003,** *19,* 2752–2755. doi:10.1021/la026620q

27. Hofer, R.; Textor, M.; Spencer, N. D. *Langmuir* **2001,** *17,* 4014–4020. doi:10.1021/la001756e
28. Liu, H.-B.; Venkataraman, N. V.; Spencer, N. D.; Textor, M.; Xiao, S.-J. *ChemPhysChem* **2008,** *9,* 1979–1981. doi:10.1002/cphc.200800381
29. Brodard-Sevarac, F.; Guerrero, G.; Maquet, J.; Florian, P.; Gervais, C.; Mutin, P. H. *Chem. Mater.* **2008,** *20,* 5191–5196. doi:10.1021/cm8012683
30. Chen, Y.; Liu, W.; Ye, C.; Yu, L.; Qi, S. *Mater. Res. Bull.* **2001,** *36,* 2605–2612. doi:10.1016/S0025-5408(01)00731-0
31. Pan, D.; Xu, G.; Wan, J.; Shi, Z.; Han, M.; Wang, G. *Langmuir* **2006,** *22,* 5537–5540. doi:10.1021/la060401d
32. Hozumi, A.; Kim, B.; McCarthy, T. J. *Langmuir* **2009,** *25,* 2875–2880. doi:10.1021/la803564c
33. Shin, H.; Collins, R. J.; De-Guire, M. R.; Heuer, A. H.; Sukenik, C. N. *J. Mater. Res.* **1995,** *10,* 692–698.
34. Liang, S.; Chen, M.; Xue, Q. *Colloids Surf., A* **2008,** *324,* 137–142. doi:10.1016/j.colsurfa.2008.04.032
35. Xiao, Z.; Gu, J.; Huang, D.; Lu, Z.; Wei, Y. *Appl. Surf. Sci.* **1998,** *125,* 85–92. doi:10.1016/S0169-4332(97)00388-7
36. Xiao, Z.; Su, L.; Gu, N.; Lu, Z.; Wei, Y. *Thin Solid Films* **1998,** *333,* 25–28. doi:10.1016/S0040-6090(98)00760-3
37. Pizem, H.; Sukenik, C. N.; Sampathkumaran, U.; McIlwain, A. K.; De Guire, M. R. *Chem. Mater.* **2002,** *14,* 2476–2485. doi:10.1021/cm010776e
38. Masuda, Y.; Sugiyama, T.; Seo, W. S.; Koumoto, K. *Chem. Mater.* **2003,** *15,* 2469–2476. doi:10.1021/cm030255m
39. Desu, S. B. *Mater. Sci. Eng., B* **1992,** *13,* 299–303. doi:10.1016/0921-5107(92)90132-S
40. Yamabi, S.; Imai, H. *Thin Solid Films* **2003,** *434,* 86–93. doi:10.1016/S0040-6090(03)00539-X
41. Xiang, J.; Zhu, P.; Masuda, Y.; Koumoto, K. *Langmuir* **2004,** *20,* 3278–3283. doi:10.1021/la036088m
42. Lin, H.; Kozuka, H.; Yoko, T. *Mol. Cryst. Liq. Cryst.* **1999,** *337,* 217–220. doi:10.1080/10587259908023416
43. Lin, H.; Kozuka, H.; Yoko, T. *Thin Solid Films* **1998,** *315,* 111–117. doi:10.1016/S0040-6090(97)00759-1
44. Shin, H.; Collins, R. J.; De-Guire, M. R.; Heuer, A. H.; Sukenik, C. N. *J. Mater. Res.* **1995,** *10,* 699–703.
45. Rizza, R.; Fitzmaurice, D.; Hearne, S.; Hughes, G.; Spoto, G.; Ciliberto, E.; Kerp, H.; Schropp, R. *Chem. Mater.* **1997,** *9,* 2969–2982. doi:10.1021/cm970349u
46. Shimizu, Y.; Kawanabe, K.; Takao, Y.; Egashira, M. *J. Am. Ceram. Soc.* **2001,** *84,* 301–306. doi:10.1111/j.1151-2916.2001.tb00654.x
47. Lee, J. P.; Jang, Y. J.; Sung, M. M. *Adv. Funct. Mater.* **2003,** *13,* 873–876. doi:10.1002/adfm.200304445
48. Seo, E. K.; Lee, J. W.; Sung-Suh, H. M.; Sung, M. M. *Chem. Mater.* **2004,** *16,* 1878–1883. doi:10.1021/cm035140x
49. Haick, H.; Paz, Y. *J. Phys. Chem. B* **2001,** *105,* 3045–3051. doi:10.1021/jp0037807
50. Zemel, E.; Paz, Y. *J. Adv. Oxid. Technol.* **2002,** *5,* 27–32.
51. Ghosh-Mukerji, S.; Haick, H.; Paz, Y. *J. Photochem. Photobiol., A: Chem.* **2003,** *160,* 77–85. doi:10.1016/S1010-6030(03)00224-7
52. Shemer, G.; Paz, Y. *Int. J. Photoenergy* **2011,** No. 596710. doi:10.1155/2011/596710
53. Haick, H.; Paz, Y. *J. Phys. Chem. B* **2003,** *107,* 2319–2326. doi:10.1021/jp026940i
54. Howgate, J.; Schoell, S. J.; Hoeb, M.; Steins, W.; Baur, B.; Hertrich, S.; Nickel, B.; Sharp, I. D.; Stutzmann, M.; Eickhoff, M. *Adv. Mater.* **2010,** *22,* 2632–2636. doi:10.1002/adma.200903756
55. Tizazu, G.; Adawi, A. M.; Leggett, G. J.; Lidzey, D. G. *Langmuir* **2009,** *25,* 10746–10753. doi:10.1021/la901271c
56. Jeon, N. L.; Nuzzo, R. G.; Xia, Y.; Mrksich, M.; Whitesides, G. M. *Langmuir* **1995,** *11,* 3024–3026. doi:10.1021/la00008a029
57. Xia, Y.; Whitesides, G. M. *Angew. Chem., Int. Ed.* **1998,** *37,* 550–575. doi:10.1002/(SICI)1521-3773(19980316)37:5<550::AID-ANIE550>3.0.CO;2-G
58. Denis, F. A.; Hanarp, P.; Sutherland, D. S.; Dufrêne, Y. F. *Langmuir* **2004,** *20,* 9335–9339. doi:10.1021/la049188g
59. Ye, T.; Wynn, D.; Dudek, R.; Borguet, E. *Langmuir* **2001,** *17,* 4497–4500. doi:10.1021/la010697h
60. Nakata, K.; Nishimoto, S.; Yuda, Y.; Ochiai, T.; Murakami, T.; Fujishima, A. *Langmuir* **2010,** *26,* 11628–11630. doi:10.1021/la101947y
61. Nishimoto, S.; Kubo, A.; Zhang, X.; Liu, Z.; Taneichi, N.; Okui, T.; Murakami, T.; Komine, T.; Fujishima, A. *Appl. Surf. Sci.* **2008,** *254,* 5891–5894. doi:10.1016/j.apsusc.2008.03.153
62. Nishimoto, S.; Sekine, H.; Zhang, X.; Liu, Z.; Nakata, K.; Murakami, T.; Koide, Y.; Fujishima, A. *Langmuir* **2009,** *25,* 7226–7228. doi:10.1021/la9011372
63. Lee, J. P.; Sung, M. M. *J. Am. Chem. Soc.* **2004,** *126,* 28–29. doi:10.1021/ja038769+
64. Notsu, H.; Kubo, W.; Shitanda, I.; Tatsuma, T. *J. Mater. Chem.* **2005,** *15,* 1523–1527. doi:10.1039/b418884e
65. Blondiaux, N.; Zürcher, S.; Liley, M.; Spencer, N. D. *Langmuir* **2007,** *23,* 3489–3494. doi:10.1021/la063186+
66. Bai, Y.; Zhang, Y.; Li, W.; Zhou, X.; Wang, C.; Feng, X.; Zhang, L.; Lu, X. *Appl. Surf. Sci.* **2009,** *255,* 9296–9300. doi:10.1016/j.apsusc.2009.06.115
67. Haick, H.; Paz, Y. *ChemPhysChem* **2003,** *4,* 617–620. doi:10.1002/cphc.200200622
68. Kwon, B. G.; Kwon, J.-H. *J. Ind. Eng. Chem.* **2010,** *16,* 193–199. doi:10.1016/j.jiec.2009.10.007
69. Masuda, Y.; Gao, Y.; Zhu, P.; Shirahata, N.; Saito, N.; Koumoto, K. *J. Ceram. Soc. Jpn.* **2004,** *112,* S1495–S1505.
70. Masuda, Y.; Kondo, M.; Koumoto, K. *Cryst. Growth Des.* **2009,** *9,* 555–561. doi:10.1021/cg800856m
71. Masuda, Y.; Sugiyama, T.; Lin, H.; Seo, W. S.; Koumoto, K. *Thin Solid Films* **2001,** *382,* 153–157. doi:10.1016/S0040-6090(00)01761-2
72. Masuda, Y.; Seo, W. S.; Koumoto, K. *Langmuir* **2001,** *17,* 4876–4880. doi:10.1021/la0014609
73. Masuda, Y.; Jinbo, Y.; Yonezawa, T.; Koumoto, K. *Chem. Mater.* **2002,** *14,* 1236–1241. doi:10.1021/cm0107528
74. Koumoto, K.; Seo, S.; Sugiyama, T.; Seo, W. S.; Dressick, W. J. *Chem. Mater.* **1999,** *11,* 2305–2309. doi:10.1021/cm990223s
75. Masuda, Y.; Saito, N.; Hoffmann, R.; De Guire, M. R.; Koumoto, K. *Sci. Technol. Adv. Mater.* **2003,** *4,* 461–467. doi:10.1016/j.stam.2003.08.002
76. Xiang, J.; Masuda, Y.; Koumoto, K. *Adv. Mater.* **2004,** *16,* 1461–1464. doi:10.1002/adma.200400017
77. Masuda, Y.; Sugiyama, T.; Koumoto, K. *J. Mater. Chem.* **2002,** *12,* 2643–2647. doi:10.1039/b203786f
78. Collins, R. J.; Shin, H.; De Guire, M. R.; Heuer, A. H.; Sukenik, C. N. *Appl. Phys. Lett.* **1996,** *69,* 860–862. doi:10.1063/1.117916
79. Park, M. H.; Jang, Y. J.; Sung-Suh, H. M.; Sung, M. M. *Langmuir* **2004,** *20,* 2257–2260. doi:10.1021/la035760c

80. Cherniavskaya, O.; Adzic, A.; Knutson, C.; Gross, B. J.; Zang, L.; Liu, R.; Adams, D. M. *Langmuir* **2002,** *18,* 7029–7034. doi:10.1021/la0114575
81. Shin, H.; Jeong, D.-K.; Lee, J.; Sung, M. M.; Kim, J. *Adv. Mater.* **2004,** *16,* 1197–1200. doi:10.1002/adma.200306296
82. Bae, C.; Shin, H.; Moon, J.; Sung, M. M. *Chem. Mater.* **2006,** *18,* 1085–1088. doi:10.1021/cm052084m
83. Masuda, Y.; Seo, W.-S.; Koumoto, K. *Solid State Ionics* **2004,** *172,* 283–288. doi:10.1016/j.ssi.2004.02.068
84. Lai, Y.; Huang, J.; Gong, J.; Huang, Y.; Wang, C.; Chen, Z.; Lin, C. *J. Electrochem. Soc.* **2009,** *156,* D480–D484. doi:10.1149/1.3216032
85. O'Regan, B.; Grätzel, M. *Nature* **1991,** *353,* 737–740. doi:10.1038/353737a0
86. Kamat, P. V.; Gevaert, M.; Vinodgopal, K. *J. Phys. Chem. B* **1997,** *101,* 4422–4427. doi:10.1021/jp970047f
87. Shi, Z.; Li, Y.; Wang, S.; Guo, Z.; Du, C.; Xiao, S.; Sun, N.; Cao, Y.; Yao, J.; Zhu, D.; Gao, E.; Cai, S. *Chem. Phys. Lett.* **2001,** *336,* 19–23. doi:10.1016/S0009-2614(01)00071-9
88. Chong, S. V.; Suresh, N.; Xia, J.; Al-Salim, N.; Idriss, H. *J. Phys. Chem. C* **2007,** *111,* 10389–10393. doi:10.1021/jp072579u
89. Pan, J.; Xu, Y.; Sun, L.; Sundström, V.; Polívka, T. *J. Am. Chem. Soc.* **2004,** *126,* 3066–3067. doi:10.1021/ja031775l
90. Haubner, K.; Jaehne, E.; Adler, H.-J. P.; Koehler, D.; Loppacher, C.; Eng, L. M.; Grezner, J.; Herasimovich, A.; Scheinert, S. *Phys. Status Solidi A* **2008,** *205,* 430–439. doi:10.1002/pssa.200723407
91. Gilmer, D. C.; Colombo, D. G.; Taylor, C. J.; Roberts, J.; Haugstad, G.; Campbell, S. A.; Kim, H.-S.; Wilk, G. D.; Gribelyuk, M. A.; Gladfelter, W. L. *Chem. Vap. Deposition* **1998,** *4,* 9–11. doi:10.1002/(SICI)1521-3862(199801)04:01<9::AID-CVDE9>3.3.CO;2-V
92. Gao, Y.; Masuda, Y.; Koumoto, K. *Chem. Mater.* **2004,** *16,* 1062–1067. doi:10.1021/cm030543i
93. Koumoto, K.; Masuda, Y.; Wang, D. J. *Int. J. Soc. Mater. Eng. Resour.* **2002,** *10,* 49–52.
94. Campbell, S. A.; Gilmer, D. C.; Wang, X.-C.; Hsieh, M.-T.; Kim, H.-S.; Gladfelter, W. L.; Yan, J. *IEEE Trans. Electron Devices* **1997,** *44,* 104–109. doi:10.1109/16.554800
95. Shin, H.; De Guire, M. R.; Heuer, A. H. *J. Appl. Phys.* **1998,** *83,* 3311–3317. doi:10.1063/1.367132
96. Shyue, J.-J.; Padture, N. P. *Mater. Lett.* **2007,** *61,* 182–185. doi:10.1016/j.matlet.2006.04.100
97. Majewski, L. A.; Schroeder, R.; Grell, M. *Adv. Funct. Mater.* **2005,** *15,* 1017–1022. doi:10.1002/adfm.200400570
98. Avnon, E.; Paz, Y.; Tessler, N. *Appl. Phys. Lett.* **2009,** *94,* 013502. doi:10.1063/1.3064158
99. Ashurst, W. R.; Jang, Y. J.; Magagnin, L.; Carraro, C.; Sung, M. M.; Maboudian, R. Nanometer-thin titania films with SAM-level stiction and superior wear resistance for reliable MEMS performance. IEEE International Conference on Micro Electro Mechanical Systems, Maastricht, The Netherlands, Jan 25–29, 2004; pp 153–156. doi:10.1109/MEMS.2004.1290545
100. Senadeera, G. K. R.; Kitamura, T.; Wada, Y.; Yanagida, S. *J. Photochem. Photobiol., A: Chem.* **2004,** *164,* 61–66. doi:10.1016/j.jphotochem.2003.12.026
101. Senadeera, G. K. R.; Kitamura, T.; Wada, Y.; Yanagida, S. *J. Photochem. Photobiol., A: Chem.* **2006,** *184,* 234–239. doi:10.1016/j.jphotochem.2006.04.033
102. Hau, S. K.; Yip, H.-L.; Acton, O.; Baek, N. S.; Ma, H.; Jen, A. K.-Y. *J. Mater. Chem.* **2008,** *18,* 5113–5119. doi:10.1039/b808004f
103. Hsu, C.-W.; Wang, L.; Su, W.-F. *J. Colloid Interface Sci.* **2009,** *329,* 182–187. doi:10.1016/j.jcis.2008.10.008
104. Chong, L.-W.; Chien, H.-T.; Lee, Y.-L. *J. Power Sources* **2010,** *195,* 5109–5113. doi:10.1016/j.jpowsour.2010.01.044
105. Jin-nouchi, Y.; Naya, S.-i.; Tada, H. *J. Phys. Chem. C* **2010,** *114,* 16837–16842. doi:10.1021/jp1062226
106. Ardalan, P.; Brennan, T. P.; Lee, H.-B.-R.; Bakke, J. R.; Ding, I.-K.; McGehee, M. D.; Bent, S. F. *ACS Nano* **2011,** *5,* 1495–1504. doi:10.1021/nn103371v
107. Wang, P.; Zakeeruddin, S. M.; Humphry-Baker, R.; Moser, J. E.; Grätzel, M. *Adv. Mater.* **2003,** *15,* 2101–2104. doi:10.1002/adma.200306084
108. Nakata, K.; Nishimoto, S.; Kubo, A.; Tryk, D.; Ochiai, T.; Murakami, T.; Fujishima, A. *Chem.–Asian J.* **2009,** *4,* 984–988. doi:10.1002/asia.200900005
109. Nishimoto, S.; Kubo, A.; Nohara, K.; Zhang, X.; Taneichi, N.; Okui, T.; Liu, Z.; Nakata, K.; Sakai, H.; Murakami, T.; Abe, M.; Komine, T.; Fujishima, A. *Appl. Surf. Sci.* **2009,** *255,* 6221–6225. doi:10.1016/j.apsusc.2009.01.084
110. Naoi, K.; Ohko, Y.; Tatasuma, T. *J. Am. Chem. Soc.* **2004,** *126,* 3664–3668. doi:10.1021/ja039474z
111. Naoi, K.; Ohko, Y.; Tatasuma, T. *Chem. Commun.* **2005,** 1288–1290. doi:10.1039/b416139d
112. Paz, Y. *C. R. Chim.* **2006,** *9,* 774–787. doi:10.1016/j.crci.2005.03.032
113. Ghosh-Mukerji, S.; Haick, H.; Schvartzman, M.; Paz, Y. *J. Am. Chem. Soc.* **2001,** *123,* 10776–10777. doi:10.1021/ja0117635
114. Sagatelian, Y.; Sharabi, D.; Paz, Y. *J. Photochem. Photobiol., A: Chem.* **2005,** *174,* 253–260. doi:10.1016/j.jphotochem.2005.03.021
115. Baskaran, S.; Song, L.; Liu, J.; Chen, Y. L.; Graff, G. L. *J. Am. Ceram. Soc.* **1998,** *81,* 401–408. doi:10.1111/j.1151-2916.1998.tb02347.x
116. Yang, Y.; Lai, Y.; Zhang, Q.; Wu, K.; Zhang, L.; Lin, C.; Tang, P. *Colloids Surf., B* **2010,** *79,* 309–313. doi:10.1016/j.colsurfb.2010.04.013
117. Meth, S.; Savchenko, N.; Koltypin, M.; Starosvetsky, D.; Viva, F. A.; Groysman, A.; Sukenik, C. N. *Corros. Sci.* **2010,** *52,* 125–129. doi:10.1016/j.corsci.2009.08.052

License and Terms

The definitive version of this article is the electronic one which can be found at:
doi:10.3762/bjnano.2.94

Beilstein Journal
of Nanotechnology

X-ray spectroscopy characterization of self-assembled monolayers of nitrile-substituted oligo(phenylene ethynylene)s with variable chain length

Hicham Hamoudi[1], Ping Kao[2], Alexei Nefedov[3], David L. Allara[2] and Michael Zharnikov*[1,§]

Full Research Paper

Address:
[1]Angewandte Physikalische Chemie, Universität Heidelberg, D-69120 Heidelberg, Germany, [2]Departments of Chemistry and Material Science, Pennsylvania State University, University Park, PA16802, USA and [3]Institut für Funktionelle Grenzflächen, Karlsruher Institut für Technologie, D-76344 Eggenstein-Leopoldshafen, Germany

Email:
Michael Zharnikov* - Michael.Zharnikov@urz.uni-heidelberg.de

* Corresponding author
§ Phone: +49-6221-54 4921, Fax: +49-6221-54 6199

Keywords:
nitrile substitution; oligo(phenylene ethynylene); self-assembled monolayers; twist angle; X-ray absorption spectroscopy

Beilstein J. Nanotechnol. **2012,** *3,* 12–24.
doi:10.3762/bjnano.3.2

Received: 19 October 2011
Accepted: 13 December 2011
Published: 05 January 2012

This article is part of the Thematic Series "Self-assembly at solid surfaces".

Guest Editors: S. R. Cohen and J. Sagiv

Abstract

Self-assembled monolayers (SAMs) of nitrile-substituted oligo(phenylene ethynylene) thiols (NC-OPE*n*) with a variable chain length *n* (*n* ranging from one to three structural units) on Au(111) were studied by synchrotron-based high-resolution X-ray photoelectron spectroscopy and near-edge absorption fine-structure spectroscopy. The experimental data suggest that the NC-OPE*n* molecules form well-defined SAMs on Au(111), with all the molecules bound to the substrate through the gold–thiolate anchor and the nitrile tail groups located at the SAM–ambient interface. The packing density in these SAMs was found to be close to that of alkanethiolate monolayers on Au(111), independent of the chain length. Similar behavior was found for the molecular inclination, with an average tilt angle of ~33–36° for all the target systems. In contrast, the average twist of the OPE*n* backbone (planar conformation) was found to depend on the molecular length, being close to 45° for the films comprising the short OPE chains and ~53.5° for the long chains. Analysis of the data suggests that the attachment of the nitrile moiety, which served as a spectroscopic marker group, to the OPE*n* backbone did not significantly affect the molecular orientation in the SAMs.

Introduction

Current semiconductor microelectronics devices, although very efficient and compact, are being pushed to their physical limits in terms of further miniaturization with associated issues such as electrical leakage and heat dissipation, and hence this is driving consideration of entirely new types of platforms. One particular idea being actively investigated is molecular electronics, which involves the use of organic molecules as potential circuit elements or components, such as conductors, rectifiers, transistors, and logic gates [1,2]. An important structural element of all such device molecules is an electrically functional molecular unit, which in the simplest case is represented by a conducting oligomeric molecular chain, often termed a “molecular wire”. The charge transport properties of this chain are an essential factor affecting the performance of the entire molecular device. In this context, transport properties of several potential molecular wires, including alkyl, oligophenyl, and oligo(phenylene ethynylene) (OPE) chains have been studied by a variety of different techniques including, for example, conducting-probe mercury drops [3-5], break junctions [6-11], scanning-microscopy tips [12-18], in-wire junctions [9], and cross-nanowire junctions [19]. For most of these measurements the molecular wires were assembled on a conductive substrate, serving as the bottom electrode, by using self-assembled monolayer (SAM) methods. For this purpose, oligomeric chains were combined with a suitable anchor (head) group having a strong affinity to the selected substrate. The most frequently used group in this regard is thiol, which allows SAM-like assembly of the molecules on coinage metal and various semiconductor substrates, for example Au and GaAs, respectively. Another essential element of the experiments is the variation of the length of the molecular wire [3,4,12,14,18,20], which allows further insight into the mechanism of conductance, described as nonresonant superexchange tunneling in most cases [21], and gives the capability to determine essential characteristic parameters, most importantly the attenuation factor describing the trend of exponential tunnelling current versus molecular length. The interpretations of these types of results depend crucially on the actual physical and structural characteristics of the molecules in the SAMs, for example, packing density, molecular orientations, and molecular conformations; and yet in many cases these characteristics are neither precisely controlled nor measured, but simply assumed to be similar to those of other types of molecules and that they do not vary with different lengths of oligomers in the same series.

Considering the variety of electrically functional molecules of interest in molecular electronics, the class of molecules based on simple oligomers of phenylene–ethynylene units is of particular importance for several reasons. First, the OPE chain is one of the most effective conductors among the available molecular wires [22,23]. Second, the electrical properties of the OPE derivatives can be varied significantly by relatively minor chemical modifications [1,13,17,24,25]. In particular, a nonfunctionalized OPE-type molecule behaves as a molecular rectifier [23], whereas, when functionalized in specific ways with nitro, amino or fluoro groups, negative differential resistance can be observed [26-28]. Finally, the electrical properties of OPE-based molecules have been reported to be affected by the local environment, which makes the issue of molecular packing especially significant [9]. For these reasons OPE types of molecules are ideal for fundamental studies.

In this context, we present here the results of the detailed spectroscopic characterization of a series of nitrile-substituted thiolated OPEs assembled as SAMs on Au(111). A schematic drawing of the molecules in this study is presented in Figure 1 along with their acronyms; these molecules are nitrile-substituted thiophenol (NC-OPE1), nitrile-substituted tolanethiol (NC-OPE2), and nitrile-substituted 4-[4′-(phenylethynyl)phenylethynyl]benzenethiol (NC-OPE3). As seen in Figure 1, the length of the OPE chain was varied from one to three structural units, which is the typical length range of the transport experiments. The nitrile tail group served as a spectroscopic marker for X-ray measurements (see below), which allowed the use of electronic excitations to probe directly both the molecular tilt and twist [29,30]. In addition, this moiety can serve as a specific group that can be resonantly excited by X-rays to leave an excited electron on the CN group whose decay by charge transfer (CT) to the substrate can be followed to provide CT lifetimes through the molecular wires [31-33].

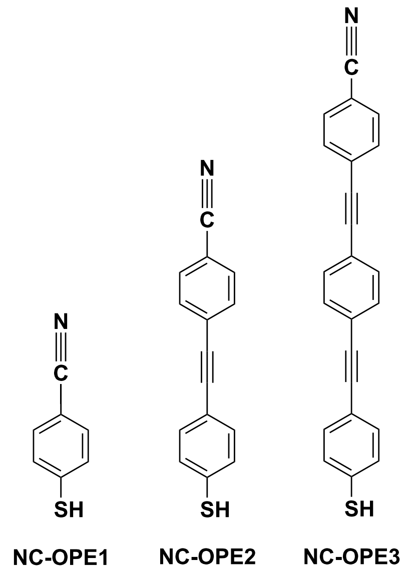

Figure 1: A schematic drawing of the target molecules along with their acronyms.

The SAM structures of the NC-OPE types of molecules have not been addressed previously (except for a resonance Auger spectroscopy study [33]), although some results on the structure and molecular packing in the SAMs of nonsubstituted OPE have been reported. In particular, based on STM data, Dhirani et al. reported that the degree of order in OPE SAMs on

Au(111) increases with chain length. The SAM of the simple molecule thiophenol (OPE1) exhibited no periodicity, that of tolanethiol (OPE2) showed a certain (although poor) degree of order, and that of 4-[4′-(phenylethynyl)phenylethynyl]benzenethiol (OPE3) displayed a highly ordered pattern, which was consistent with a 2√3×√3 structure [20]. These results were supported by further STM [34,35] and AFM [36] studies, which reported no ordered structure in OPE2/Au [34] and a high structural order in OPE3/Au [35,36]. However, in contrast to [20], a noncommensurate structure with a rectangular unit cell was observed for OPE3/Au in [35], while a basic √3×√3 arrangement was recorded in [36]. Whereas the reasons for the above discrepancies are not clear yet, the molecular packing densities in all three STM/AFM studies [20,35,36] were quite similar and close to those of alkanethiolate (AT) SAMs on Au(111). Furthermore, in addition to the STM/AFM characterization, molecular organization in OPE3/Au was probed by infrared-reflection spectroscopy (IRS) [36] and near-edge X-ray absorption fine-structure (NEXAFS) spectroscopy [37]. The average tilt angle of the OPE3 backbone was estimated at 33 ± 18° in [36] and 30 ± 5° in [37], while the twist angle of the backbone with respect to the tilt plane was estimated at 31 ± 6° in [36]. Finally, the preparation of well defined, nonsubstituted and F-, CH_3-, CF_3-, and OCH_3-substituted OPE SAMs on gold with variable length *n* of the OPE chain (*n* ranging from one to three structural units) was described in [38]. The authors, however, presented only results for the SAM-induced work-function tuning and did not provide any information about the SAM structure or packing density.

Results

High-resolution X-ray photoelectron spectroscopy

High-resolution X-ray photoelectron spectroscopy (HRXPS) provides information about the identity, character, integrity, chemical composition, and effective thickness of the target films. The S 2p, C 1s, and N 1s HRXPS spectra of the target SAMs acquired at photon energies of 350 eV and 580 eV are presented in Figure 2.

The S 2p HRXPS spectra of the target SAMs in Figure 2a are dominated by a characteristic S $2p_{3/2,1/2}$ doublet at a binding energy (BE) of 162.00–162.05 eV (S $2p_{3/2}$). This doublet can be clearly assigned to thiolate species bonded to the surface of gold [39-41]. The doublet is the only feature in the spectra of NC-OPE2/Au and NC-OPE3/Au suggesting that all the molecules in these films are bound to the substrate in the SAM fashion, i.e., through the thiolate–gold anchor. In the case of NC-OPE1/Au, this doublet is accompanied by an additional doublet at ~163.5 eV (S $2p_{3/2}$). This additional feature is associated with a small amount of the physisorbed molecules that are presumably caught in the hydrocarbon matrix or at the SAM-ambient interface, or both. It is quite difficult, or probably even impossible, to get rid of these species in the case of

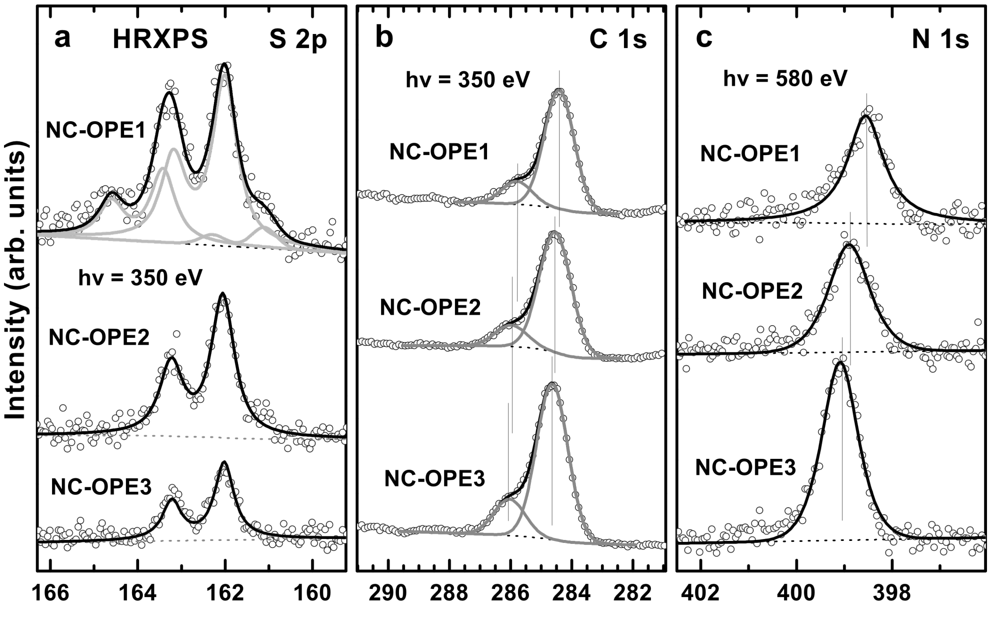

Figure 2: S 2p (a), C 1s (b), and N 1s (c) HRXPS spectra of the target SAMs acquired at photon energies of 350 eV (S 2p and C 1s) and 580 eV (N 1s). Some spectra are decomposed into the individual contributions related to the different species; see text for details. Vertical solid lines mark the positions of the individual emissions in (b) and (c).

phenylthiolate SAMs on Au [42,43]. The intensity of the thiolate-related doublet in the NC-OPE*n* SAMs decreases with increasing chain length, manifesting a stronger attenuation of the S 2p photoelectrons by the thicker NC-OPE2 and NC-OPE3 films. This is in accordance with the molecular composition and the SAM architecture.

The C 1s HRXPS spectra of NC-OPE1/Au, NC-OPE2/Au and NC-OPE3/Au in Figure 2b are dominated by an intense emission at BEs of 284.4, 284.55, and 284.65 eV, respectively, accompanied by a weaker shoulder at a BE ~1.35 eV higher. The intense emission is related to the OPE backbone, while the high BE shoulder can be assigned to the nitrile carbon. The spectra are mostly representative of the topmost part of the SAMs because of the strong attenuation of the C 1s photoelectrons at the given kinetic energy [41]. In view of this fact, the upward BE shift with the increasing chain length, of both the major emission and the shoulder, is related to a weaker screening of the photoemission hole upon its larger separation from the substrate. This behaviour is distinctly different from the behaviour of the S 2p spectra, in which the position of the thiolate-related doublet is independent of the backbone length. This is understandable, because the location of the thiolate moiety with respect to the substrate does not change with the variation of the backbone length.

The N 1s HXPRS spectra of NC-OPE1/Au, NC-OPE2/Au and NC-OPE3/Au in Figure 2c exhibit a single N 1s emission at BEs of 398.55, 398.85, and 399.10 eV, respectively. This emission is associated with the nitrile groups [30], which are exclusively located at the SAM–ambient interface. The observed BE increase at increasing length of the OPE backbone is similar to that of the C 1s emission and is explained by the same difference in the final state screening. Note that the widths of both of the main emission peaks in the C 1s spectra and in the N 1s spectra decrease with increasing length of the molecular backbone. Most likely, this behaviour reflects a progressive improvement in the orientational and conformational order in the SAMs [41].

Apart from the above qualitative analysis of the HRXPS spectra, we estimated the packing density and effective thickness of the target films on the basis of the HRXPS data. The packing density was estimated by a comparison of the $S2p_{thiolate}$/Au4f intensity ratios of the target films with those for the reference dodecanethiol (DDT) and hexadecanethiol (HDT) systems (a similar approach was successfully used in [44] and [45]). This ratio is a direct measure of the molecular packing density. As compared to the S 2p signal itself, this ratio does not suffer from the problems related to the absolute intensity comparison and to the difference in attenuation of this signal in different films. Due to the quite close binding energies of the Au 4f and S 2p emissions, both signals are attenuated similarly, although not absolutely equally, as far as the primary excitation is performed at high photon energy. The S2p/Au4f intensity ratios for all three target films were found to be quite close to one another (equal within the experimental error) and similar to those for the reference DDT and HDT monolayers. At least for NC-OPE3/Au this agrees with the STM and AFM results, which, as mentioned in the Introduction, suggest that the molecular packing densities in the OPE3 SAMs on Au are close to those of alkanethiol (AT) monolayers [20,35,36].

As for the effective thickness of the target films, this parameter was evaluated on the basis of the C1s/Au4f intensity ratio [46], by assuming a standard expression for the attenuation of the photoemission signal [47], and by using the attenuation lengths reported in [48]. The spectrometer-specific coefficient was calculated on the basis of the analogous procedure performed for the reference DDT and HDT films, the thickness of which is well known [49,50]. By using this approach, the effective thickness of NC-OPE1/Au, NC-OPE2/Au and NC-OPE3/Au was estimated at 13.3, 15.2, and 22.5 Å, respectively. These values can be compared to the corresponding molecular lengths of 7.3, 14.2, and 21.0 Å, which, after the addition of the S–Au spacing (~2.4 Å [51,52]), give the theoretical thickness of the target films for the case of the vertically standing molecules, viz. 9.7, 16.6, and 23.4 Å, respectively. These values suggest a small inclination of the molecules in the target SAMs, which, in view of a limited accuracy of the thickness evaluation procedure, can only be considered as a tentative statement, whereas the exact molecular orientation can be estimated by the NEXAFS spectroscopy (see the following section). Note, however, that whereas the theoretical thicknesses of the NC-OPE2 and NC-OPE3 films are lower than the values derived from the experiment, the opposite is true for the NC-OPE1 SAMs. This suggests, in accordance with the S 2p spectrum for these SAMs (Figure 2), the presence of a certain amount of the physisorbed molecules at the SAM-ambient interface in the case of NC-OPE1/Au.

NEXAFS spectroscopy

NEXAFS spectroscopy samples the electronic structure of unoccupied molecular orbitals and provides information about the integrity and chemical identity of the adsorbed film. In many cases, NEXAFS spectroscopy allows a better distinction between different chemical species and functional groups as compared to HRXPS and, in this regard, is a complementary technique. The chemical information is best represented by a spectrum acquired at the so-called magic angle of X-ray incidence (55°); this spectrum is not affected by any effects related to molecular orientation and is only representative of the chemical identity of investigated samples [53]. Furthermore, by using the angular dependence of the transition-matrix elements for resonant excitations [53], the average orientation of the film constituents can be derived from the NEXAFS experiment. A fingerprint of such an orientation is the linear dichroism (see Experimental section), which, among other means, can be efficiently monitored by plotting the difference between the NEXAFS spectra acquired at normal (90°) and grazing (20°) angles of X-ray incidence.

The C K-edge NEXAFS spectra of the NC-OPE*n* SAMs acquired at an X-ray incidence angle of 55° are presented in Figure 3a, whereas the π^*-resonance photon-energy range of these spectra is shown in detail in Figure 4, along with the spectra of the two reference systems, viz. SAMs of nitrile-substituted biphenylthiol (NC-BPT) [30] and 1,1′;4′,1″-terphenyl-4-thiol (TPT) [42,43] on Au. The spectra of the target films are dominated by a strong peak, consisting of at least three absorption resonances at 284.9–285.0 eV (**1**), 285.40–285.45 eV (**2**), and 286.0 eV (**3**); see Figure 4. The resonances **1** and **3** can be assigned with certainty to the π_1^* orbital of the aromatic rings and to the $\pi^*(C\equiv C)$ orbital [53], respectively, and this is additionally supported by the intensity increase of the latter resonance with the increasing chain length. The resonance **2** is presumably comprised of several different contributions, including a conjugation between the π^* orbital of the rings and C≡C groups [53]. There are also contributions from the phenyl rings themselves, as seen in the spectrum of TPT/Au in which a tentative decomposition of the asymmetric resonance is performed (note that the asymmetry is related to the vibrational structure of the resonance) [53].

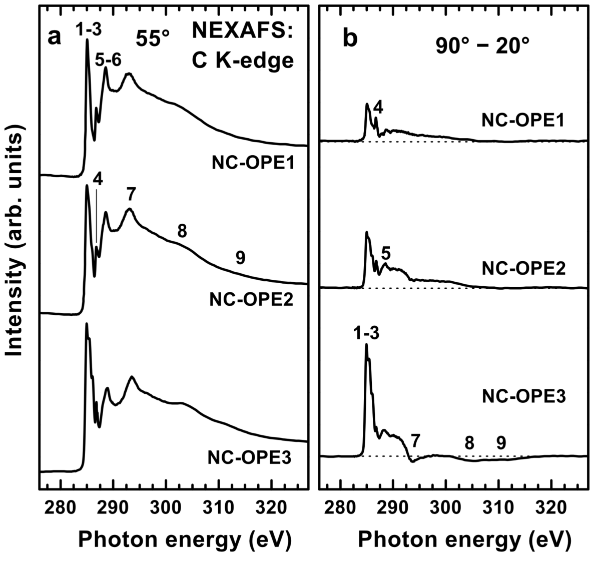

Figure 3: (a) C K-edge NEXAFS spectra of the NC-OPE*n* SAMs acquired at an X-ray incidence angle of 55°. (b) Difference between the C K-edge spectra acquired at X-ray incidence angles of 90° and 20°. The zero level of the difference spectra is shown by dotted lines. The most prominent absorption resonances are marked by numbers; see text for details.

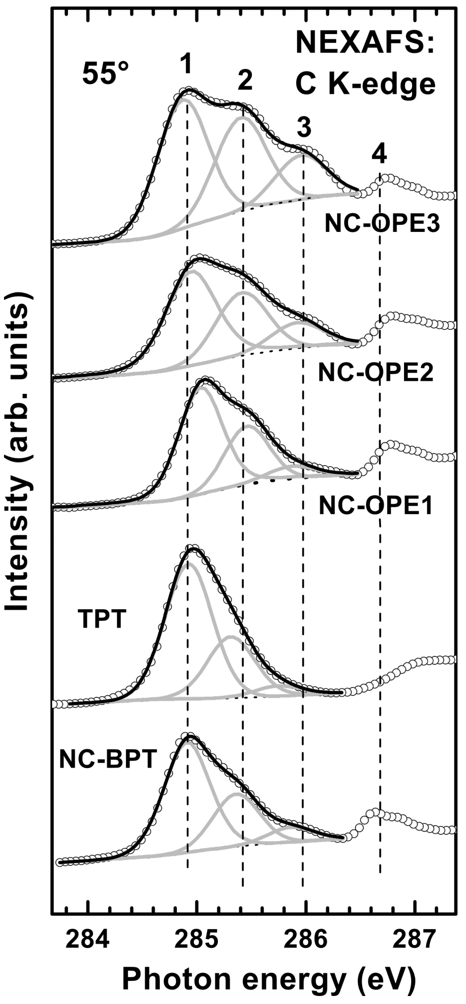

Figure 4: π^*-resonance photon-energy range of the C K-edge NEXAFS spectra of the target SAMs and two reference films, NC-BPT/Au and TPT/Au. The spectra are decomposed into the individual contributions, which are marked by numbers; see text for details.

In addition to the joint resonance **1**–**3**, a comparatively sharp resonance at 286.75 eV (**4**) is observed in the spectra of all the NC-OPE*n* films. This resonance can be, with certainty, associated with the nitrile group since it has exactly the same energy as the characteristic π^* resonance of nitrile in the films of nitrile-substituted alkanethiolates [31,32,54] and oligophenyls [30,33]. In particular, this resonance is clearly seen in the spectrum of NC-BPT, as shown in Figure 4. At the same time, this resonance is not observed in the spectra of nonsubstituted OPEs [37] and oligophenyls [42,55], including the spectrum of TPT/Au shown in Figure 4.

Along with the above-mentioned features, there are several further resonances at 288.1 eV (**5**), 288.7 eV (**6**), 293.6 eV (**7**), ~304.6 eV (**8**), and ~311.0 eV (**9**); these resonances are marked by numbers in Figure 3. The respective molecular orbitals have either π* character (**5** and **6**) or σ* character (**7**–**9**) [42,53,54,56].

The N K-edge NEXAFS spectra of the NC-OPE*n* SAMs acquired at an X-ray incidence angle of 55° are presented in Figure 5a. A dominant feature in these spectra is a characteristic double resonance at ~398.80 eV (**1**) and ~399.75 eV (**2**); it is accompanied by several weaker features, including a π*-character resonance at ~401.5 eV and several σ*-character resonances at higher photon energy. These spectra resemble that of benzonitrile [57,58] and are also typical of SAMs containing this moiety [29,30,33,59]. The appearance of the dominant double resonance is caused by the conjugation between the π* orbitals of the nitrile group and those of the adjacent phenyl ring. Due to such a conjugation, the degeneracy of the π* orbitals of the nitrile group is lifted, and they split into two states with different energies. One of the resulting orbitals (lower photon energy; π_1* or **1**) is oriented perpendicular to the ring plane; the another one (higher photon energy; π_3* or **2**) is parallel to this plane [33,57,58]. Due to the delocalization of the π_1* orbital over the entire benzonitrile moiety, the intensity of the π_1* resonance is lower as compared to the π_3* resonance (the orbital is almost exclusively localized on the nitrile group) [30,33]. Note that the π* resonance of the nitrile group splits not only at the N but also at the C K-edge (see Figures S3 and S4 in Supporting Information File 1). However, since there is only one carbon atom in the nitrile group, the respective split resonance has a relatively low intensity in the C K-edge spectra. As a result, only π_3*(CN) is clearly visible (resonance **4** in Figure 4; see [30]), whereas the even weaker π_1*(CN) resonance overlaps with the resonance **3** (Figure 4) and is practically imperceptible.

Along with the above results, the NEXAFS data provide information on the orientation of the molecular constituents in the target films. Both C and N K-edge spectra of the target SAMs exhibit significant linear dichroism as follows from the differences between the spectra acquired at normal and gracing (20°) incidence of the primary X-ray beam shown in Figure 3b and Figure 5b. The difference peaks related to the π* resonances are distinctly positive, which, in view of the orientation of the transition dipole moments (TDMs) associated with these resonances (perpendicular to the molecular backbone), suggests an upright orientation of the target molecules in the SAMs. A schematic drawing of this orientation is shown in Figure 6, through the example of NC-OPE3, which presumably takes a planar conformation in the densely packed SAM (see below).

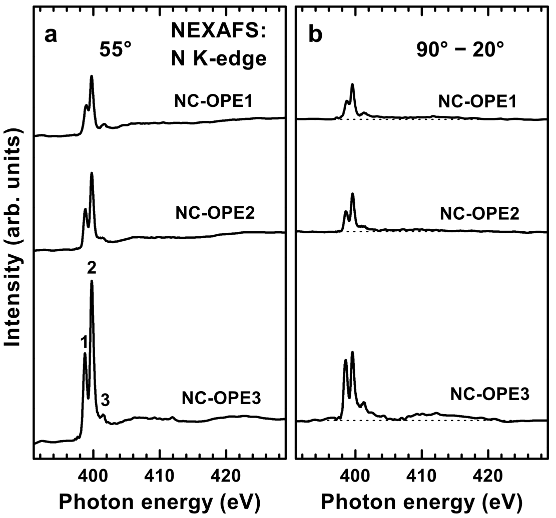

Figure 5: (a) N K-edge NEXAFS spectra of the NC-OPE*n* SAMs acquired at an X-ray incidence angle of 55°. (b) Difference between the N K-edge spectra acquired at X-ray incidence angles of 90° and 20°. The zero level of the difference spectra is shown by dotted lines. The most prominent absorption resonances are marked by numbers; see text for details.

The π* orbitals of the phenyl rings (π_{ph}*) are perpendicular to the molecular plane; the respective TDM_{ph}, which is perpendicular to the molecular plane as well, is shown as a blue arrow. π_1* (blue) and π_3* (red) orbitals of the nitrile group are perpendicular and parallel to the molecular plane, respectively. The molecular orientation is described by the tilt (β) and twist (γ) angles of the molecular backbone. The molecular tilt occurs within the z–y plane. The twist is defined in terms of γ = 0 when TDM_{ph} lies in the plane spanned by the z- and the molecular axes (i.e., in the z–y plane).

For the nonsubstituted aromatic and OPE SAMs, β and γ cannot be strictly evaluated on the basis of the NEXAFS data. These data only provide information on the average orientation of the TDM_{ph}, given by the tilt angle α (Figure 6), whereas the value of β can only be calculated as far as a reasonable assumption about the molecular twist can be made [60,61], e.g., on the basis of the molecular orientation in the respective bulk materials. This situation changes, however, in the case of the nitrile substitution due to the presence of the π_1* and π_3* orbitals of the nitrile group, which are perpendicular to each other and one of which is aligned with the π_1* orbitals of the phenyl rings. In this case, both β and γ can be directly derived from the NEXAFS data at the N K-edge from a system of nonlinear equations

$$\cos(\alpha_1) = \sin(\beta)\cos(\gamma) \tag{1}$$

$$\cos(\alpha_3) = \sin(\beta)\cos(\pi/2-\gamma), \tag{2}$$

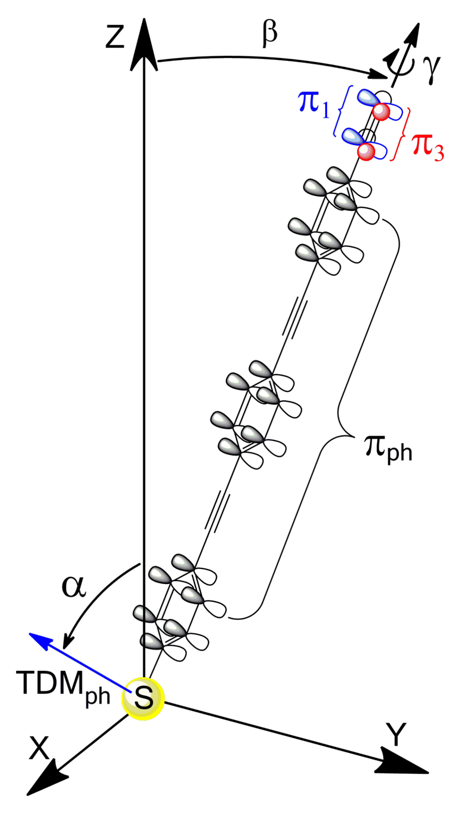

Figure 6: Orientation of the NC-OPE*n* molecules in the respective SAMs (by the example of NC-OPE3; a planar conformation is assumed). The orientation of the molecular backbone is given by the tilt angle β (tilt within the z–y plane) and twist angle γ. The π* orbitals of the phenyl rings (π_{ph}*), constituting the backbone, are perpendicular to the ring plane, with the orientation of TDM_{ph} (blue arrow) given by the tilt angle α. π_1* (blue) and π_3* (red) orbitals of the nitrile group are perpendicular and parallel to the plane of the adjacent phenyl ring, respectively.

where α_1 and α_3 are the average tilt angles of the π_1* and π_3* orbitals of the nitrile group, respectively [29]. These angles can be derived from the evaluation of the entire set of the N K-edge NEXAFS spectra taken at different angles of X-ray incidence, θ, according to the standard equation for the intensity of a vector-type orbital [53]

$$I(\alpha,\theta) = A\{P\times(1/3)[1 + (1/2)(3\cos^2\theta-1)(3\cos^2\alpha-1)] + (1-P)(1/2)\sin^2\alpha\}, \tag{3}$$

where I(α,θ) is the intensity of either the π_1* or π_3* resonance, *A* is a constant, and *P* is the polarization factor of the synchrotron light. The resulting values of α_1 and α_3 are given in Table 1. By using these values, the average twist angle of the OPE backbone in the NC-OPE SAMs can be directly calculated from equation

$$\tan(\gamma) = \cos(\alpha_3)/\cos(\alpha_1) \tag{4}$$

obtained from the division of Equation 2 by Equation 1. Equal values of α_1 and α_3, as are found for NC-OPE1/Au and NC-OPE2/Au, mean thus that γ is close to 45°. A higher value of α_1 as compared to α_3, as is the case for NC-OPE3/Au, means that γ is larger than 45°. The derived values of γ presented in Table 1 are in accordance with these qualitative considerations. Furthermore, using either Equation 1 or Equation 2, the average tilt angle of the OPE backbone in the NC-OPE*n* SAMs can be calculated, and the respective values are given in Table 1; they are close to each other for all target SAMs, independent of the chain length. Note that this result is somewhat in contrast to the C K-edge spectra in Figure 3, which exhibit an increasing linear dichroism with increasing length of the molecular chain in NC-OPE*n*/Au. This dichroism can be presumably associated with the improved orientational order on going from NC-OPE1/Au to NC-OPE2/Au and further to NC-OPE3/Au.

Table 1: Derived average tilt angles for the π_1*and π_3* orbitals of the nitrile group (from Equation 3) as well as twist and tilt angles for the OPE backbone in the NC-OPE*n* SAMs on Au(111). The absolute accuracy of the angle values is ±3°, which are the standard error bars in the case of NEXAFS spectroscopy. The relative accuracy is noticeably higher.

Film	NC-OPE1	NC-OPE2	NC-OPE3
α_1	67.4°	65.5°	70.2.°
α_3	67.4°	65.1°	62.9°
γ	44.9°	45.3°	53.3°
β	33.0°	36.3°	34.5°

Note that we assumed a planar conformation of the OPE backbone for NC-OPE2/Au and NC-OPE3/Au within the analysis of the molecular orientation. We expect this conformation for the densely packed NC-OPE*n* monolayers (see next section), similar to the SAMs with oligophenyl backbone, for which the individual rings are twisted differently (torsion) in the molecular state but adapt to a planar conformation in the monolayer state [62]. According to our estimates, the barrier for adapting to a planar conformation is much lower in the case of OPE as compared to that of oligophenyl, as far as no side functionalization of the individual rings along the OPE backbone is performed.

Calculation of the NEXAFS spectra

We calculated the NEXAFS spectra of the OPE3 (Supporting Information File 1) and NC-OPE3 molecules in two different conformations, viz. in the planar conformation, with all three phenyl rings located in the same plane, and in a twisted conformation, with the central ring rotated by 90° with respect to the two other rings about the molecule axis. Note that the latter conformation may occur in the gaseous phase while the former is expected to be preferred for the densely packed molecular assembles, such as bulk samples and SAMs.

Calculated C and N K-edge NEXAFS spectra of NC-OPE3 in the planar and twisted conformations are presented in Figure 7 and Figure 8, respectively, along with the corresponding experimental spectrum of NC-OPE3/Au taken at an X-ray incidence angle of 55°. The theoretical C K-edge spectra represent sums over the separately calculated partial spectra of the 17 different carbon atoms in the NC-OPE3 molecule, which allows identification of the contribution of each of the different functional groups to the individual resonances. The three major functional groups are the phenyl rings, the C≡C group, and the nitrile moiety. Whereas the exact decomposition of the theoretical spectra can be found in Supporting Information File 1, we assigned the most prominent absorption resonances in Figure 7 in accordance with the functional groups that provide the major contribution to these resonances. Taking into account these assignments and comparing the theoretical and experimental data, we can conclude that the theoretical spectrum for the planar conformation of NC-OPE3 reproduces the experimental spectrum of NC-OPE3/Au much better than does the calculated curve for the twisted conformation of NC-OPE3. In addition, this comparison supports our assignment of the most prominent absorption resonances: **1** as related to the phenyl rings; **3** to the C≡C groups; **2** to the conjugation of the above two moieties; and **4** to the nitrile group. Interestingly, the molecular orbitals associated with the resonance **2** are mostly located on the phenyl rings.

The theoretical N K-edge spectra of NC-OPE3 in Figure 8 reproduce perfectly the experimental result, both from the viewpoint of the resonant pattern and of the relative intensity of the most prominent π_1* and π_3* features. However, similar to the C K-edge data, the theoretical spectrum for the planar conformation of NC-OPE3, which exhibits much lower relative intensity of the resonance **3**, reproduces the experimental spectrum of NC-OPE3/Au much better than does the calculated

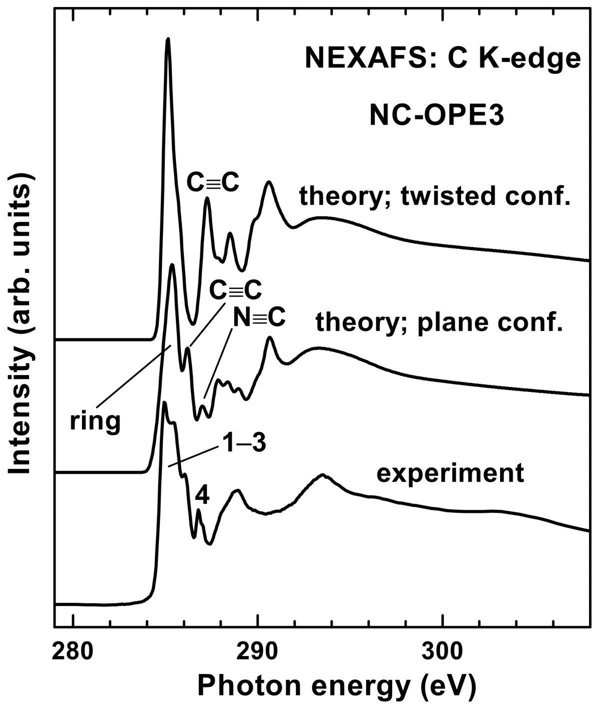

Figure 7: Calculated C K-edge NEXAFS spectra of NC-OPE3 in the planar and twisted conformations, along with the experimental spectrum of NC-OPE3/Au taken at an X-ray incidence angle of 55°. The theoretical spectra were shifted by ca. 1.3 eV to lower photon energies in order to align the most intense π* resonances in the theoretical and experimental spectra. The most prominent absorption resonances in the experimental spectrum are marked by numbers. The most prominent absorption resonances in the theoretical spectrum are marked by the functional groups that are associated with these resonances.

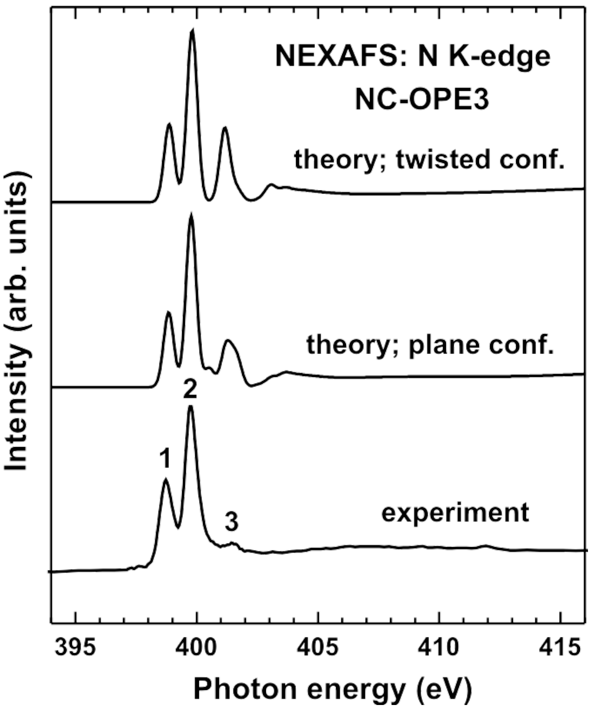

Figure 8: Calculated N K-edge NEXAFS spectra of NC-OPE3 in the planar and twisted conformations, along with the experimental spectrum of NC-OPE3/Au taken at an X-ray incidence angle of 55°. The theoretical spectra were shifted by ca. 2.3 eV to lower photon energies in order to align the most intense π* resonances in the theoretical and experimental spectra. The most prominent absorption resonances in the experimental spectrum are marked by numbers.

curve for the twisted conformation of NC-OPE3. This supports our above conclusion about the planar molecular conformation of NC-OPE3/Au in the respective SAMs. Note that the same conformation can also be expected for NC-OPE2/Au.

Discussion

Both HRXPS and NEXAFS data suggest consistently that the NC-OPE*n* SAMs on Au(111) are well-defined and contamination-free, apart from a minor portion of physisorbed molecules in NC-OPE1/Au, with the SAM molecules bound to the substrate through the gold–thiolate anchor and the nitrile tail groups exclusively located at the SAM–ambient interface. The HRXPS data show that independent of the chain length, all of the SAMs have similar packing densities, which, in accordance with the literature data [20,35,36], are quite close to those of AT SAMs on Au(111). Such packing density likely means that a herring-bone type of motif exists, which is the typical configuration for both bulk aromatic materials (see, e.g., [63]) and their respective monolayers [62,64,65].

Similar to the SAMs with a nonsubstituted OPE backbone [42,43], orientational order in NC-OPE*n* films depends on the length of the molecular chain, improving with increasing chain length according to the C K-edge NEXAFS data. At the same time, molecular inclination of the SAM constituents in the NC-OPE*n* SAMs is almost independent of the chain length, with an average tilt angle of ~33–36°. Interestingly, the twist angle of the OPE backbone, which exhibits a fully planar conformation for the SAMs (all three rings in the same plane), is identical for the NC-OPE1 and NC-OPE2 SAMs at 45°, similar to the case of the nonsubstituted oligophenyl backbone (34.5–41.2° [29]), whereas it is higher for the NC-OPE3 SAM at 53.5°. According to a previous detailed IRS analysis, OPE3 SAMs with no terminal group exhibit an average molecular tilt of 33 ± 18° from the surface normal [36], which correlates well with our value of 34.5° for NC-OPE3/Au. Further, the average twist angle in the OPE3 films was found to be 31 ± 6° [36], which, when converted to match our definition of twist angle, is equivalent to 59° and hence is very close to our value of 53.3° for NC-OPE3/Au [66]. From this comparison it is clear that substitution of the OPE3 backbone by the nitrile group does not affect the molecular orientation significantly. This is in contrast to the aliphatic NC-terminated SAMs in which the introduction of the nitrile tail group results in a significant disturbance of the molecular orientation and orientational order [54]. This disturbance can be understood in terms of the strong electrostatic interactions between the nitrile groups, bearing a large dipole moment of 3.9 D [67], which will provide electrostatic stresses when neighbouring dipoles have unfavourable alignments. In the case of the flexible aliphatic backbone, the stresses can be relieved in part by inducing strains, primarily through the appearance of *gauche* defects at the terminal $–CH_2–$ units of the alkyl chain. Such conformational changes, however, are not possible in the case of rigid oligophenyl or OPE backbone, which leads to a certain persistence of the molecular lattice even in the case of the strongly interacting tail groups.

It is interesting to compare the NC-OPE*n* monolayers with the respective systems without the triple bonds. The closest systems are the NC-BPT SAMs [29,30] and the monolayers of 4″-(mercaptomethyl)terphenyl-4-yl-carbonitrile, $NC–(C_6H_4)_3–(CH_2)–SH$ (NC-TP1) [29] (regrettably, there are no published data for the closest system, $NC–(C_6H_4)_3–SH$, abbreviated as NC-TPT). The NC-BPT SAMs on Au(111) are characterized by an average tilt angle of ~39° and a twist angle of 40.8° [29]. These values are quite close to the analogous values for NC-OPE2 SAMs (36.3° and 45.3°, respectively). The molecular tilt in the latter system is slightly smaller, presumably due to a longer molecular backbone, whereas the twist is higher. Analogously, the NC-TP1 SAMs on Au(111) are characterized by an average tilt angle of ~34.0° and a twist angle of 47.1°. Once more, these values are quite close to the analogous values for the NC-OPE3 SAMs (34.5° and 53.3°, respectively). Considering that the introduction of the methylene linker results in a lesser molecular inclination in the terphenyl-based SAMs [68], we could assume that the molecular tilt in the NC-OPE3 SAMs is smaller than that in the NC-TPT monolayers; this is once more a clear effect of the molecular backbone length. The twist angle for the NC-OPE3 SAMs is higher than that for the NC-TP1 monolayers and presumably even higher than that for the NC-TP0 film (on the basis of the values for the biphenyl-based SAMs [29]). In summary, the introduction of the –C≡C– groups into the oligophenyl backbone results in an expected slight decrease of molecular inclination (chain-length effect) and a noticeable increase of molecular twist. The latter can be of importance for understanding of the exact molecular arrangement in the OPE SAMs.

Conclusion

We presented here the results of the spectroscopic characterization for a series of nitrile-substituted thiolated OPEs assembled in the SAM fashion on Au(111). This characterization included the synchrotron-based complementary techniques of HRXPS and angle-resolved NEXAFS spectroscopy at both C and N K-edges, which were additionally supported by quantum-mechanical calculations of the NEXAFS spectra. The length of the OPE chain in the SAMs was varied from one to three structural units to test the effect of the chain length on the integrity, packing density, and molecular orientation of the SAMs. The nitrile tail group serves as a distinct spectroscopic marker for X-ray absorption measurements, which allowed us to probe directly both the molecular tilt and twist.

The experimental data suggest that the NC-OPE*n* molecules form well-defined and contamination-free SAMs on Au(111). Apart from a minor proportion of physisorbed molecules in NC-OPE1/Au, all molecules in these SAMs are bound to the substrate over the gold-thiolate anchor, whereas the nitrile tail groups are exclusively located at the SAM–ambient interface. Independent of the chain length, all the SAMs have similar packing densities, which are quite close to those of AT SAMs on Au(111). Whereas the orientational order in NC-OPE*n* films depends on the length of the molecular chain, improving with increasing chain length, the molecular inclination of the SAM constituents is almost independent of the chain length, with an average tilt angle of ~33–36°. At the same time, the twist of the OPE*n* backbone was found to depend on the molecular length, being close to 45° for NC-OPE1/Au and NC-OPE2/Au, but ~53.5° for NC-OPE3/Au. Comparison of the molecular orientation in the NC-OPE3/Au system with the literature data for the analogous nonsubstituted film suggests that the attachment of nitrile to the OPE3 backbone does not significantly affect the molecular orientation in the SAMs. This was explained by the rigidity of the OPE3 backbone and stability of the densely packed molecular lattice, which consists of OPE3 moieties in planar conformation arranged, presumably, in a herring-bone fashion.

The results of this study provide important data that are relevant to the use of these types of "molecular wires" for applications in molecular-electronics devices, particularly with regard to studies of the dynamics of charge-transport behaviour.

Experimental

The NC-OPE*n* compounds were synthesized according to previous protocols [69]. The purity of all the compounds was checked by NMR. The gold substrates were prepared by thermal evaporation of 100–200 nm of gold (99.99% purity) onto polished single crystal silicon (100) wafers (Silicon Sense) primed with either a 5 nm titanium or a 5 nm chromium adhesion layer. The evaporated films were polycrystalline, with a predominant (111) texture [40,70] and grain sizes of 20–50 nm. To prepare the SAMs, these substrates were immersed into a 1 mmol solution of the NC-OPE*n* compounds in toluene or in methylene chloride for 24 h at room temperature, with identical results in either solvent. Afterwards, the SAM samples were carefully rinsed by immersion in the solvent and further rinsing with absolute ethanol. Finally, they were blown dry with argon or nitrogen gas.

In addition to the OPE SAMs of interest, several reference SAMs were prepared on Au(111) substrates using standard procedures. The reference SAMs included those formed from DDT [50], HDT [71], TPT [42,43], and NC-BPT [30].

The SAMs were characterized by several complementary spectroscopic techniques, viz., high-resolution X-ray photoelectron spectroscopy (HRXPS), angle-resolved near-edge X-ray absorption fine-structure (NEXAFS) spectroscopy and infrared reflection spectroscopy (IRS). The HRXPS and NEXAFS spectroscopy experiments were conducted at the bending magnet beamline D1011 (plane-grating monochromator) of the synchrotron storage ring MAX II at MAX-Lab in Lund, Sweden. We used an experimental station equipped with a SCIENTA SES200 electron-energy analyzer and a partial-electron-yield (PEY) detector. The experiments were carried out under UHV conditions at a base pressure $<1.5 \times 10^{-10}$ mbar. We took care to avoid any noticeable damage induced by X-rays [72-75], minimizing the spectra acquisition time and performing control measurements on reference samples.

The HRXPS spectra were collected in normal emission geometry. Photon energy (PE) was varied; it was set at 350 eV for the S 2p region, at 350 and 580 eV for the C 1s range, and at 580 eV for the N 1s and O 1s regions. The BE scale of every spectrum was individually calibrated with reference to the Au $4f_{7/2}$ emission line of the substrate at 83.95 eV [76]. For this purpose, Au 4f spectra were acquired for each sample and at each PE change. The energy resolution was better than 100 meV, which is noticeably smaller than the full widths at half maximum (fwhm) of the photoemission peaks of the S 2p, C 1s, and N 1s spectra.

HRXPS spectra were fitted by symmetric Voigt functions and either a Shirley-type or linear background. To fit the S $2p_{3/2,1/2}$ doublets we used a pair of such peaks with the same fwhm, a branching ratio of 2 ($2p_{3/2}/2p_{1/2}$), and spin-orbit splittings (verified by fit) of ~1.18 eV ($2p_{3/2}/2p_{1/2}$) [77]. The fits were carried out self-consistently: The same peak parameters were used for identical spectral regions. The accuracy of the resulting BE/fwhm values is 0.02–0.03 eV.

The NEXAFS spectra were acquired at the carbon and nitrogen K-edges. We used the partial-electron-yield acquisition mode with retarding voltages of −150 and −300 V for the C and N K-edges, respectively. Primary X-ray beam was linearly polarized with a polarization factor of ~95%. The energy resolution was less than 100 meV. To monitor the orientational order of the target molecules within the films, the incidence angle of the X-ray beam was varied from 90° (**E**-vector in the surface plane) to 20° (**E**-vector nearly normal to the surface) in steps of 10–20°. This approach is based on the strong dependence of the cross-section of the resonant photoexcitation process on the orientation of the electric field vector of the linearly polarized light with respect to the molecular orbital of interest [53]. This effect is usually described as linear dichroism in X-ray absorption [53]. The accuracy of the incidence-angle adjustment was ±0.5°.

The raw spectra were normalized to the incident photon flux by division by a spectrum of a freshly sputtered, clean gold sample and were reduced to the standard form [53]. The energy scale was calibrated to the most intense π^* resonance of highly oriented pyrolytic graphite at 285.38 eV [78] in combination with the well-known $\Delta(h\nu) \propto (h\nu)^{3/2}$ behaviour of plane grating monochromators [79]. The resultant energy positions are expected to be accurate and reproducible within ±0.05 eV.

In order to provide a reliable basis for the assignment of the features in the experimental NEXAFS spectra and to get information about the molecular conformation in the target SAMs, a series of calculations with the quantum-chemistry program package StoBe (**Sto**ckholm-**Be**rlin) [80] were carried out for the OPE3 and NC-OPE3 molecules. Note that StoBe is used to evaluate and analyze the electronic structure as well as spectroscopic and other properties of molecules and atom clusters. The approach is based on self-consistent solutions of the Kohn-Sham equations employing linear combinations of Gaussian type orbitals. The theory and numerical details of the realization can be found in [80-83]. As a further verification of the integrity of the SAMs, infrared spectra were obtained. In all cases the SAMs had the expected spectra based on reference spectra of the pure thiol molecules used for self-assembly.

Supporting Information

Supporting Information features the calculated C and N K-edge spectra of OPE3 and NC-OPE3 in the planar and twisted conformation, decomposed into the partial spectra related to the individual building blocks of the target molecules.

Supporting Information File 1

Calculated X-ray absorption spectra.
[http://www.beilstein-journals.org/bjnano/content/supplementary/2190-4286-3-2-S1.pdf]

Acknowledgements

MZ and HH thank M. Grunze for the support of this work and the MAX-lab staff, including A. Preobrajenski in particular, for assistance during the experiments. This work was supported by DFG (ZH 63/14-1), the European Community's Seventh Framework Programme (FP7/2007-2013) under grant agreement No. 226716 and, in part, by the NSF-funded PSU Center for Nanoscale Science (MRSEC DMR-0080019).

References

1. Tour, J. M. *Molecular electronics;* World Scientific: Singapore, 2003.
2. Troisi, A.; Ratner, M. A. *Nano Lett.* **2004,** *4,* 591–595. doi:10.1021/nl0352088
3. Rampi, M. A.; Schueller, O. J. A.; Whitesides, G. M. *Appl. Phys. Lett.* **1998,** *72,* 1781–1783. doi:10.1063/1.121183
4. Weiss, E. A.; Chiechi, R. C.; Kaufman, G. K.; Kriebel, J. K.; Li, Z.; Duati, M.; Rampi, M. A.; Whitesides, G. M. *J. Am. Chem. Soc.* **2007,** *129,* 4336–4349. doi:10.1021/ja0677261
5. Seitz, O.; Vilan, A.; Cohen, H.; Hwang, J.; Haeming, M.; Schoell, A.; Umbach, E.; Kahn, A.; Cahen, D. *Adv. Funct. Mater.* **2008,** *18,* 2102–2113. doi:10.1002/adfm.200800208
6. Park, H.; Park, J.; Lim, A. K. L.; Anderson, E. H.; Alivisatos, A. P.; McEuen, P. L. *Nature* **2000,** *407,* 57–60. doi:10.1038/35024031
7. Park, J.; Pasupathy, A. N.; Goldsmith, J. I.; Chang, C.; Yaish, Y.; Petta, J. R.; Rinkoski, M.; Sethna, J. P.; Abruña, H. D.; McEuen, P. L.; Ralph, D. C. *Nature* **2002,** *417,* 722–725. doi:10.1038/nature00791
8. Selzer, Y.; Cabassi, M. A.; Mayer, T. S.; Allara, D. L. *J. Am. Chem. Soc.* **2004,** *126,* 4052–4053. doi:10.1021/ja039015y
9. Selzer, Y.; Cai, L.; Cabassi, M. A.; Yao, Y.; Tour, J. M.; Mayer, T. S.; Allara, D. L. *Nano Lett.* **2005,** *5,* 61–65. doi:10.1021/nl048372j
10. Xu, B.; Xiao, X.; Yang, X.; Zang, L.; Tao, N. *J. Am. Chem. Soc.* **2005,** *127,* 2386–2387. doi:10.1021/ja042385h
11. Mishchenko, A.; Vonlanthen, D.; Meded, V.; Bürkle, M.; Li, C.; Pobelov, I. V.; Bagrets, A.; Vilajas, J. K.; Pauly, F.; Evers, F.; Mayor, M.; Wandlowski, T. *Nano Lett.* **2010,** *10,* 156–163. doi:10.1021/nl903084b
12. Wold, D. J.; Haag, R.; Rampi, M. A.; Frisbie, C. D. *J. Phys. Chem. B* **2002,** *106,* 2813–2816. doi:10.1021/jp013476t
13. Fan, F.-R. F.; Yao, Y.; Cai, L.; Cheng, L.; Tour, J. M.; Bard, A. J. *J. Am. Chem. Soc.* **2004,** *126,* 4035–4042. doi:10.1021/ja0359815
14. Engelkes, V. B.; Beebe, J. M.; Frisbie, C. D. *J. Am. Chem. Soc.* **2004,** *126,* 14287–14296. doi:10.1021/ja046274u
15. Tivanski, A. V.; He, Y.; Borguet, E.; Liu, H.; Walker, G. C.; Waldeck, D. H. *J. Phys. Chem. B* **2005,** *109,* 5398–5402. doi:10.1021/jp050022d
16. Akkerman, H. B.; Blom, P. W. M.; de Leeuw, D. M.; de Boer, B. *Nature* **2006,** *441,* 69–72. doi:10.1038/nature04699
17. Moore, A. M.; Dameron, A. A.; Mantooth, B. A.; Smith, R. K.; Fuchs, D. J.; Ciszek, J. W.; Maya, F.; Yao, Y.; Tour, J. M.; Weiss, P. S. *J. Am. Chem. Soc.* **2006,** *128,* 1959–1967. doi:10.1021/ja055761m
18. Kim, B.-S.; Beebe, J. M.; Jun, Y.; Zhu, X.-Y.; Frisbie, C. D. *J. Am. Chem. Soc.* **2006,** *128,* 4970–4971. doi:10.1021/ja0607990
19. Yoon, H. P.; Maitani, M. M.; Cabarcos, O. M.; Cai, L.; Mayer, T. S.; Allara, D. L. *Nano Lett.* **2010,** *10,* 2897–2902. doi:10.1021/nl100982q
20. Dhirani, Al-A.; Zehner, R. W.; Hsung, R. P.; Guyot-Sionnest, P.; Sita, L. R. *J. Am. Chem. Soc.* **1996,** *118,* 3319–3320. doi:10.1021/ja953782i
21. Adams, D. M.; Brus, L.; Chidsey, C. E. D.; Creager, S.; Creutz, C.; Kagan, C. R.; Kamat, P. V.; Lieberman, M.; Lindsay, S.; Marcus, R. A.; Metzger, R. M.; Michel-Beyerle, M. E.; Miller, J. R.; Newton, M. D.; Rolison, D. R.; Sankey, O.; Schanze, K. S.; Yardley, J.; Zhu, X. *J. Phys. Chem. B* **2003,** *107,* 6668–6697. doi:10.1021/jp0268462
22. Bumm, L. A.; Arnold, J. J.; Cygan, M. T.; Dunbar, T. D.; Burgin, T. P.; Jones, L., II; Allara, D. L.; Tour, J. M.; Weiss, P. S. *Science* **1996,** *271,* 1705–1707.
23. Dhirani, A.; Lin, P.-H.; Guyot-Sionnest, P.; Zehner, R. W.; Sita, L. R. *J. Chem. Phys.* **1997,** *106,* 5249–5253. doi:10.1063/1.473523
24. Tour, J. M. *Acc. Chem. Res.* **2000,** *33,* 791–804. doi:10.1021/ar0000612

25. Lewis, P. A.; Inman, C. E.; Maya, F.; Tour, J. M.; Hutchison, J. E.; Weiss, P. S. *J. Am. Chem. Soc.* **2005,** *127,* 17421–17426. doi:10.1021/ja055787d
26. Chen, J.; Reed, M. A.; Rawlett, A. M.; Tour, J. M. *Science* **1999,** *286,* 1550–1552. doi:10.1126/science.286.5444.1550
27. Chen, J.; Wang, W.; Reed, M. A.; Rawlett, A. M.; Price, D. W.; Tour, J. M. *Appl. Phys. Lett.* **2000,** *77,* 1224–1226. doi:10.1063/1.1289650
28. Rawlett, A. M.; Hopson, T. J.; Nagahara, L. A.; Tsui, R. K.; Ramachandran, G. K.; Lindsay, S. M. *Appl. Phys. Lett.* **2002,** *81,* 3043–3045. doi:10.1063/1.1512815
29. Ballav, N.; Schüpbach, B.; Dethloff, O.; Feulner, P.; Terfort, A.; Zharnikov, M. *J. Am. Chem. Soc.* **2007,** *129,* 15416–15417. doi:10.1021/ja0751882
30. Ballav, N.; Schüpbach, B.; Neppl, S.; Feulner, P.; Terfort, A.; Zharnikov, M. *J. Phys. Chem. C* **2010,** *114,* 12719–12727. doi:10.1021/jp1045386
31. Neppl, S.; Bauer, U.; Menzel, D.; Feulner, P.; Shaporenko, A.; Zharnikov, M.; Kao, P.; Allara, D. L. *Chem. Phys. Lett.* **2007,** *447,* 227–231. doi:10.1016/j.cplett.2007.09.013
32. Kao, P.; Neppl, S.; Feulner, P.; Allara, D. L.; Zharnikov, M. *J. Phys. Chem. C* **2010,** *114,* 13766–13773. doi:10.1021/jp1042816
33. Hamoudi, H.; Neppl, S.; Kao, P.; Schüpbach, B.; Feulner, P.; Terfort, A.; Allara, D. L.; Zharnikov, M. *Phys. Rev. Lett.* **2011,** *107,* 027801. doi:10.1103/PhysRevLett.107.027801
34. Jeong, Y.; Lee, C.; Ito, E.; Hara, M.; Noh, J. *Jpn. J. Appl. Phys., Part 1* **2006,** *45,* 5906–5910.
35. Yang, G. H.; Qian, Y. L.; Engtrakul, C.; Sita, L. R.; Liu, G. *J. Phys. Chem. B* **2000,** *104,* 9059–9062. doi:10.1021/jp001611g
36. Stapleton, J. J.; Harder, P.; Daniel, T. A.; Reinard, M. D.; Yao, Y.; Price, D. W.; Tour, J. M.; Allara, D. L. *Langmuir* **2003,** *19,* 8245–8255. doi:10.1021/la035172z
37. Nilsson, D.; Watcharinyanon, S.; Eng, M.; Li, L.; Moons, E.; Johansson, L. S. O.; Zharnikov, M.; Shaporenko, A.; Albinsson, B.; Mårtensson, J. *Langmuir* **2007,** *23,* 6170–6181. doi:10.1021/la0636964
38. Zehner, R. W.; Parsons, B. F.; Hsung, R. P.; Sita, L. R. *Langmuir* **1999,** *15,* 1121–1127. doi:10.1021/la981114f
39. Laibinis, P. E.; Whitesides, G. M.; Allara, D. L.; Tao, Y.-T.; Parikh, A. N.; Nuzzo, R. G. *J. Am. Chem. Soc.* **1991,** *113,* 7152–7167. doi:10.1021/ja00019a011
40. Heister, K.; Zharnikov, M.; Grunze, M.; Johansson, L. S. O. *J. Phys. Chem. B* **2001,** *105,* 4058–4061. doi:10.1021/jp010127q
41. Zharnikov, M. *J. Electron Spectrosc. Relat. Phenom.* **2010,** *178–179,* 380–393. doi:10.1016/j.elspec.2009.05.008
42. Frey, S.; Stadler, V.; Heister, K.; Eck, W.; Zharnikov, M.; Grunze, M.; Zeysing, B.; Terfort, A. *Langmuir* **2001,** *17,* 2408–2415. doi:10.1021/la001540c
43. Shaporenko, A.; Terfort, A.; Grunze, M.; Zharnikov, M. *J. Electron Spectrosc. Relat. Phenom.* **2006,** *151,* 45–51. doi:10.1016/j.elspec.2005.10.008
44. Chesneau, F.; Schüpbach, B.; Szelągowska-Kunstman, K.; Ballav, N.; Cyganik, P.; Terfort, A.; Zharnikov, M. *Phys. Chem. Chem. Phys.* **2010,** *12,* 12123–12127. doi:10.1039/c0cp00317d
45. Dauselt, J.; Zhao, J.; Kind, M.; Binder, R.; Bashir, A.; Terfort, A.; Zharnikov, M. *J. Phys. Chem. C* **2011,** *115,* 2841–2854. doi:10.1021/jp1118647
46. Thome, J.; Himmelhaus, M.; Zharnikov, M.; Grunze, M. *Langmuir* **1998,** *14,* 7435–7449. doi:10.1021/la9808317
47. Ratner, B.; Castner, D. In *Surface Analysis – The principal techniques;* Vickerman, J. C., Ed.; Wiley: Chichester, 1997.
48. Lamont, C. L. A.; Wilkes, J. *Langmuir* **1999,** *15,* 2037–2042. doi:10.1021/la981168p
49. Zharnikov, M.; Frey, S.; Heister, K.; Grunze, M. *Langmuir* **2000,** *16,* 2697–2705. doi:10.1021/la991034r
50. Chesneau, F.; Zhao, J.; Shen, C.; Buck, M.; Zharnikov, M. *J. Phys. Chem. C* **2010,** *114,* 7112–7119. doi:10.1021/jp100522n
51. Kondoh, H.; Iwasaki, M.; Shimada, T.; Amemiya, K.; Yokoyama, T.; Ohta, T.; Shimomura, M.; Kono, S. *Phys. Rev. Lett.* **2003,** *90,* 066102. doi:10.1103/PhysRevLett.90.066102
52. Roper, M. G.; Skegg, M. P.; Fisher, C. J.; Lee, J. J.; Dhanak, V. R.; Woodruff, D. P.; Jones, R. G. *Chem. Phys. Lett.* **2004,** *389,* 87–91. doi:10.1016/j.cplett.2004.02.109
53. Stöhr, J. In *NEXAFS Spectroscopy;* Ertl, G.; Lüth, H.; Mills, D. L., Eds.; Springer Series in Surface Science, Vol. 25; Springer-Verlag: Berlin, 1992.
54. Frey, S.; Shaporenko, A.; Zharnikov, M.; Harder, P.; Allara, D. L. *J. Phys. Chem. B* **2003,** *107,* 7716–7725. doi:10.1021/jp0221690
55. Ballav, N.; Zharnikov, M. *J. Phys. Chem. C* **2008,** *112,* 15037–15044. doi:10.1021/jp8047357
56. Horsley, J. A.; Stöhr, J.; Hitchcock, A. P.; Newbury, D. C.; Johnson, A. L.; Sette, F. *J. Chem. Phys.* **1985,** *83,* 6099–6107. doi:10.1063/1.449601
57. Carniato, S.; Ilakovac, V.; Gallet, J.-J.; Kukk, E.; Luo, Y. *Phys. Rev. A* **2005,** *71,* 022511. doi:10.1103/PhysRevA.71.022511
58. Rangan, S.; Gallet, J.-J.; Bournel, F.; Kubsky, S.; Le Guen, K.; Dufour, G.; Rochet, F.; Sirotti, F.; Carniato, S.; Ilakovac, V. *Phys. Rev. B* **2005,** *71,* 165318. doi:10.1103/PhysRevB.71.165318
59. Hallmann, L.; Bashir, A.; Strunskus, T.; Adelung, R.; Staemmler, V.; Wöll, C.; Tuczek, F. *Langmuir* **2008,** *24,* 5726–5733. doi:10.1021/la702836r
60. Rong, H.-T.; Frey, S.; Yang, Y.-J.; Zharnikov, M.; Buck, M.; Wühn, M.; Wöll, C.; Helmchen, G. *Langmuir* **2001,** *17,* 1582–1593. doi:10.1021/la0014050
61. Zharnikov, M.; Grunze, M. *J. Phys.: Condens. Matter* **2001,** *13,* 11333–11365. doi:10.1088/0953-8984/13/49/314
62. Shaporenko, A.; Elbing, M.; Błaszczyk, A.; von Hänisch, C.; Mayor, M.; Zharnikov, M. *J. Phys. Chem. B* **2006,** *110,* 4307–4317. doi:10.1021/jp056833z
63. Trotter, J. *Acta Crystallogr.* **1961,** *14,* 1135–1140. doi:10.1107/S0365110X6100334X
64. Bashir, A.; Käfer, D.; Müller, J.; Wöll, C.; Terfort, A.; Witte, G. *Angew. Chem., Int. Ed.* **2008,** *47,* 5250–5252. doi:10.1002/anie.200800883
65. Track, A. M.; Rissner, F.; Heimel, G.; Romaner, L.; Käfer, D.; Bashir, A.; Rangger, G. M.; Hofmann, O. T.; Bučko, T.; Witte, G.; Zojer, E. *J. Phys. Chem. C* **2010,** *114,* 2677–2684. doi:10.1021/jp9102756
66. In our case, TDM_{ph} lies in the plane spanned by the z- and the molecular axes at $\gamma = 0$ (see Figure 6). In contrast, according to the definition of [36], the molecular plane lies in the plane spanned by the z- and the molecular axes at $\gamma = 0$. Considering that TDM_{ph} is perpendicular to the molecular plane, a twist angle of 31° for OPE3/Au transforms to 59° in our definition.
67. Hautman, J.; Bareman, J. P.; Mar, W.; Klein, M. L. *J. Chem. Soc., Faraday Trans.* **1991,** *87,* 2031–2037. doi:10.1039/ft9918702031
68. Shaporenko, A.; Brunnbauer, M.; Terfort, A.; Grunze, M.; Zharnikov, M. *J. Phys. Chem. B* **2004,** *108,* 14462–14469. doi:10.1021/jp0400521

69. Tour, J. M.; Rawlett, A.; Kozaki, M.; Yao, Y.; Jagessar, R. C.; Dirk, S. M.; Price, D. W.; Reed, M. A.; Zhou, C.-W.; Chen, J.; Wang, W.; Campbell, I. *Chem.–Eur. J.* **2001,** *7,* 5118–5134. doi:10.1002/1521-3765(20011203)7:23<5118::AID-CHEM5118>3.0.CO;2-1
70. Köhn, F. Diploma Thesis, Universität Heidelberg, Germany, 1998.
71. Heister, K.; Johansson, L. S. O.; Grunze, M.; Zharnikov, M. *Surf. Sci.* **2003,** *529,* 36–46. doi:10.1016/S0039-6028(03)00299-1
72. Wirde, M.; Gelius, U.; Dunbar, T.; Allara, D. L. *Nucl. Instrum. Methods Phys. Res., Sect. B* **1997,** *131,* 245–251. doi:10.1016/S0168-583X(97)00140-7
73. Jäger, B.; Schürmann, H.; Müller, H. U.; Himmel, H.-J.; Neumann, M.; Grunze, M.; Wöll, C. *Z. Phys. Chem.* **1997,** *202,* 263–272. doi:10.1524/zpch.1997.202.Part_1_2.263
74. Heister, K.; Zharnikov, M.; Grunze, M.; Johansson, L. S. O.; Ulman, A. *Langmuir* **2001,** *17,* 8–11. doi:10.1021/la001101d
75. Zharnikov, M.; Grunze, M. *J. Vac. Sci. Technol., B: Microelectron. Nanometer Struct.--Process., Meas., Phenom.* **2002,** *20,* 1793–1807. doi:10.1116/1.1514665
76. Surface chemical analysis – X-ray photoelectron spectrometers – Calibration of the energy scales. ISO 15472:2001, 2006.
77. Moulder, J. F.; Stickle, W. E.; Sobol, P. E.; Bomben, K. D. In *Handbook of X-ray Photoelectron Spectroscopy;* Chastian, J., Ed.; Perkin-Elmer Corp: Eden Prairie, MN, 1992.
78. Batson, P. E. *Phys. Rev. B* **1993,** *48,* 2608–2610. doi:10.1103/PhysRevB.48.2608
79. Domke, M.; Mandel, T.; Puschmann, A.; Xue, C.; Shirley, D. A.; Kaindl, G.; Petersen, H.; Kuske, P. *Rev. Sci. Instrum.* **1992,** *63,* 80–89. doi:10.1063/1.1142615
80. StoBe-deMon, Version 3.1, 2011; Fritz-Haber-Institut der Max-Planck-Gesellschaft, Berlin, Stockholm University, Stockholm, 2011.
81. Kohn, W.; Sham, L. J. *Phys. Rev.* **1965,** *140,* A1133–A1138. doi:10.1103/PhysRev.140.A1133
82. Salahub, D. R.; Castro, M. E.; Proynov, E. I. In *Relativistic and electron correlation effects in molecules and solids;* Malli, G. L., Ed.; NATO ASI Series (Physics), Vol. B318; Plenum Press: New York, 1994; p 411.
83. Salahub, D. R.; Castro, M. E.; Fournier, R.; Calaminici, P.; Godbout, N.; Goursot, A.; Jamorski, C.; Kobayashi, H.; Martinez, A.; Papai, I.; Proynov, E.; Russo, N.; Sirois, S.; Ushio, J.; Vela, A. In *Theoretical and Computational Approaches to Interface Phenomena;* Sellers, H.; Gotlab, J. T., Eds.; Plenum Press: New York, 1995; p 187.

License and Terms

Beilstein Journal
of Nanotechnology

Octadecyltrichlorosilane (OTS)-coated ionic liquid drops: Micro-reactors for homogenous catalytic reactions at designated interfaces

Xiaoning Zhang and Yuguang Cai*

Letter

Address:
Department of Chemistry, University of Kentucky, 505 Rose Street, Lexington, KY 40506, USA

Email:
Yuguang Cai* - ycai3@uky.edu

* Corresponding author

Keywords:
AFM; catalyst encapsulation; chemical pattern; ionic liquid; OTS

Beilstein J. Nanotechnol. **2012,** *3,* 33–39.
doi:10.3762/bjnano.3.4

Received: 01 September 2011
Accepted: 19 December 2011
Published: 12 January 2012

This article is part of the Thematic Series "Self-assembly at solid surfaces".

Guest Editors: S. R. Cohen and J. Sagiv

Abstract

An ionic liquid (IL), 1-butyl-3-methylimidazolium chloride ([Bmim]Cl) can assemble on prefabricated carboxylic acid–terminated chemical patterns on octadecyltrichlorosilane (OTS) film. The chemical pattern controls the position, shape and size of the IL on the surface. After the IL assembly – by incubating IL drops assembled on sample surface in an OTS silane vapor – an OTS layer was coated on the IL drop surface which encapsulated the IL drop. The OTS-coated capsule can exist stably under aqueous solution. The OTS coating protected the IL drops from being instantaneously dissolved by other solutions. We found that a homogenous catalyst ($FeCl_3$) dissolved in [Bmim]Cl can be assembled together on the chemical patterns and subsequently encapsulated together with [Bmim]Cl by OTS coating. The pinhole defects within the vapor-coated silane layer provide space for the catalyst inside the capsule and reactants outside the capsule to meet and react. When the OTS-coated capsule containing a $FeCl_3$/IL mixture was soaked under H_2O_2 solution, the Fe^{3+} ions catalyzed the decomposition reaction of hydrogen peroxide at the vapor-coated OTS-water interface. Since the shape and position of the interface is defined by the underneath chemical pattern, our findings show that the OTS-coated IL drops assembled on chemical patterns can be used as novel micro-reactors. This allows homogenous catalytic reactions to occur at the designated interfaces.

Introduction

Ionic liquids (ILs) have promising applications as environmentally friendly solvents [1,2]. Ionic liquids are low temperature melting salts with very low vapor pressure. Thanks to their low vapor pressure, ILs are ideal extraction solvents or reaction media because simple evaporation methods can be used to separate solutes from ILs [3]. In addition, ILs can be custom-made with targeted functions. Because of these advantages, ILs have been engineered as extraction solvents, reaction media and drug delivery materials [4,5]. In most IL applications – such as extraction, lubrication, IL super capacitors – the core function of the IL occurs at the ionic liquid–solid interfaces.

ILs are different from conventional molecular liquids because no individual molecule exists in the liquid. Moreover, ILs are not diluted electrolyte solutions either. Hence, no existing theory and model can precisely describe the behavior of ILs, especially at the IL interfaces. Therefore, studies of the IL interfacial properties are necessary for further developments of IL-based applications. Furthermore, new applications – such as IL reactor, IL-circuit, and surface pattern visualization – require the precise control over the position of the IL drop on surface [6-8].

In this letter, we report studies of the chemical pattern-directed assembly of IL on surface. We found that the chemical patterns can control the shape, size and position of the IL on surface. Furthermore, IL drops on surface can be coated with a layer of silane film, forming an IL capsule. We discovered that the homogenous catalyst $FeCl_3$ could be encapsulated together with IL. The pinhole defects on the OTS coating layer provided spaces for the catalyst inside the capsule and reactants outside the capsule to react. Hence, the coated IL drops enable the interfacial chemical reactions.

Results and Discussion

Chemical pattern-directed assembly of IL on surface

The carboxylic acid-terminated chemical patterns (partially degraded octadecyltrichlorosilane, OTSpd) were fabricated on the self-assembled monolayer of octadecyltrichlorosilane (OTS) film using the scanning probe deep oxidation lithography method [9]. The OTSpd pattern is a high energy, lyophilic surface whereas the OTS background is a methyl-terminated, low energy, lyophobic surface. Based on the wetting-driven assembly approach [10], liquid can be assembled on the chemical patterns due to the contrast in surface energy [11,12]. Figure 1a shows a representative OTSpd disc array. Figure 1b shows the same region after a liquid [Bmim]Cl drop rolled over the OTSpd discs. By comparing Figure 1a with Figure 1b, we found that the IL micro-drops were selectively deposited on the high-surface energy OTSpd chemical patterns. Figure 1c is the optical image of the IL drop arrays assembled on OTSpd patterns. The background is the OTS film. Each dark spot in Figure 1c is an IL drop assembled on the OTSpd disc. The regions shown in Figure 1a and 1b are highlighted within the red box in Figure 1c.

Figure 1c reveals that the amounts of IL assembled on each OTSpd disc are similar but not identical. Some discs appear darker than the rest, indicating that more IL was assembled on that OTSpd disc. Correspondingly, in the atomic force microscopy (AFM) topography image (Figure 1b), the height of IL drops varies between 250–800 nm. The AFM image reveals more details about the shape of the IL droplet assembled on the OTSpd discs. A representative high-resolution AFM image of the IL drop is shown in Supporting Information File 1, Figure S1. The AFM topography image shows that the IL is not a hemispherical drop that covers the whole OTSpd disc. Instead, the IL adopts a Mexican hat shape – a partial drop sitting on top of a precursor layer. In the OTSpd disc center is the partial drop, which only covers the central part of the OTSpd disc and is typically 250–800 nm high. The central drop is surrounded by a rim, which extends out and covers the remaining part of the OTSpd disc. The rim is thickest at the foot of the central drop and gradually becomes thinner as it extends out. The Mexican hat shape indicates that the IL drop co-exists with an IL

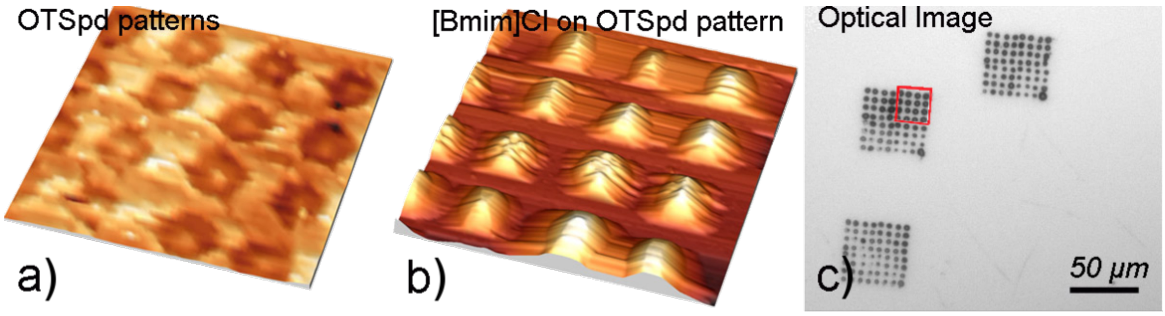

Figure 1: [Bmim]Cl assembles on the OTSpd pattern. a) OTSpd discs fabricated by scanning probe deep oxidation lithography on OTS film. Topography image. The center-to-center distance between two neighboring discs is ~7 µm. b) The same area after [Bmim]Cl was coated on the sample. [Bmim]Cl selectively assembled on the lyophilic OTSpd discs. Topography image. c) Optical image of [Bmim]Cl assembled on the OTSpd patterns. The light background is the OTS film. The red box is the zone shown in a) and b). In this optical image, each IL drop assembled on an OTSpd disc appears as a dark dot.

precursor layer (the "rim"). The observed Mexican hat shape for an IL drop is not a surprise. Since first discovered by Hardy in 1919 [13], the existence of the precursor layer of a drop on a solid surface has been extensively studied. In fact, the Mexican hat shape has been confirmed as the real shape for most liquid drops on solid surfaces, provided that the drop can be resolved with a sufficient resolution [14].

[Bmim]Cl is miscible with water. When the sample shown in Figure 1c was immersed in water, all IL micro-droplets on the patterned area disappeared instantaneously, indicating that the IL micro-droplets were dissolved in water.

Silane-coated IL capsules

Silane molecules react with water to form silanols, which subsequently cross-link with each other using the Si–O–Si covalent bonds and form a polymer network [15,16]. Such a silane network is mechanically stable and chemically inert. When silane molecules react with hydrophilic surfaces, a self-assembled silane layer is formed on the surface. The cross-linked silane film can be formed on the IL drop surface as well because water adsorbed there. In our experiment, we incubated IL drop arrays in OTS vapor. We found that an OTS layer covered the IL drop surface, forming a capsule that encapsulated the IL inside (Figure 2). The capsule had the same Mexican hat shape of the IL assembled on the OTSpd disc. The hemispherical cap shaped drop is in the center on the OTSpd disc and co-exists with the surrounding precursor layer (the rim of the Mexican hat), which covers the remaining OTSpd disc. The height cross-sectional profile along the cyan line in the AC mode topography image (Figure 2a) is plotted in Figure 2d (black line), which reveals that the drop in Figure 2a is 300 nm in height. Figure 2b is an optical image of the OTS-coated [Bmim]Cl drop array. The image was acquired under water after 1 h of incubation. Under the optical microscope, interfaces separating the drop and the water can be clearly observed. In contrast, in the control experiment for those IL drops assembled on OTSpd disc without OTS coating after water was applied to the patterned area, the un-coated IL drop was instantaneously miscible with water, and thereby disappeared.

Because the coated-drops still existed after incubation, we conclude that the coating was a complete layer which can separate [Bmim]Cl inside the capsule and the water outside the

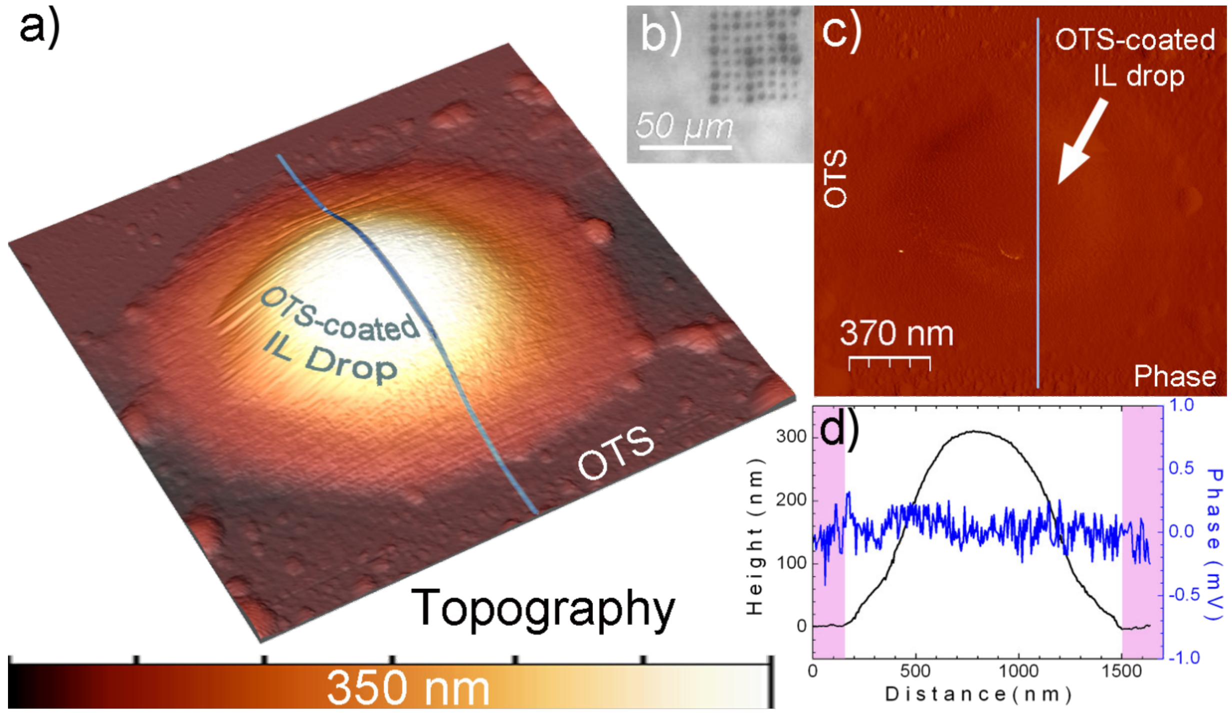

Figure 2: a) A representative OTS-coated [Bmim]Cl drop on the OTSpd pattern. AC mode topography image. b) Optical image of OTS-coated [Bmim]Cl drops on the OTSpd disc array. The imaged was acquired under water. c) The phase image corresponding to the topography image in a). d) The topography (black line) and phase (blue line) channel cross-sectional profiles corresponding to the cyan lines shown in a) and c). The topography cross-section profile reveals that the drop height is 300 nm. The phase cross-section profile indicates that the phase signal of the OTS regions (pink zones in d) and the phase signal of the OTS-coated drop surface are the same because their difference in phase signal is smaller than the noise level.

capsule. In the phase image (Figure 2c) corresponding to the topography image shown in Figure 2a, the phase signals over the drop and the OTS background are the same. This can be further quantitatively illustrated by the phase cross-sectional profile along the cyan line in Figure 2c which is plotted as the blue line in Figure 2d. In the plot, the phase signal difference between the drop surface (central white region in Figure 2d) and the OTS film (pink regions in Figure 2d) is smaller than the noise level. Thus, we conclude that OTS and the drop surface have the same phase signal. The phase signal acquired during the same scanning line and under the same instrumental set-ups represents the surface identity. Since the OTS background is methyl-terminated, we conclude that the vapor treated [Bmim]Cl drop is also covered with a layer of methyl-terminated OTS silane.

During the AC mode imaging, we also varied the tapping amplitude set point in order to examine how the encapsulated IL responds to different external tapping intensities. At a high amplitude set point (99.5% of the free oscillation amplitude), the tip tapped the OTS-coated drop gently. A smooth topography profile of the drop was acquired. In contrast, at a low set point (95% of the free oscillation amplitude), the tip tapped the OTS-coated drop hard, with a high force. Phase signal oscillations were observed when the tip scanned over the drop, as shown in the Supporting Information File 1, Figure S1. The oscillation at a low set point indicates that the drop was disturbed when the tip tapped it hard which caused the IL inside to oscillate. Hence, the IL inside the capsule was still fluidic. In comparison, under the same low set point, the AFM scan lines over the OTS film background did not show any oscillation because the OTS film was in solid phase. Hence, this control reveals that the oscillation we observed over the drop is the true physical oscillation of the IL inside the drop rather than the electronic oscillation originated from the AFM feedback loop. Therefore, from this experiment we conclude that the coated silane layer only formed at the surface of the IL drop.

Reaction of the OTS-coated IL capsules

Pinholes widely exist in the silane film that was prepared without stabilization [17]. When the “unstablized” OTS film was imaged using a MikroMasch ultra-sharp AFM tip (~1 nm in tip diameter), no pinholes could be resolved. On the other hand, when the unstablized OTS film is incubated in 11-mercaptoundecyltrimethoxysilane toluene solution, the 11-mercaptoundecyltrimethoxysilane molecules can fill the pinholes in the OTS film, leaving the terminal –SH groups on top. The –SH group can subsequently bond to gold nanoparticles and immobilize them on the surface. Hence, we infer that the size of the pinhole would be around 0.5–1 nm. These pinholes provide spaces for reactions and encounters between the materials encapsulated inside the drop and reactants in the external solvent.

Figure 3 shows OTS-coated [Bmim]Cl drop arrays. The IL inside drops contained 30% (w/w) of $FeCl_3$. The sample was incubated under 30% H_2O_2 solution at 25 °C. $FeCl_3$ is a homogenous catalyst for the decomposition reaction of H_2O_2 [18]. When $FeCl_3$ was added in H_2O_2 solution, the H_2O_2 decomposed and oxygen bubbles were generated in the solution as the decomposition product. In our experimental set-up, the $FeCl_3$ was dissolved in IL solution, which was encapsulated by the OTS coating and existed as the immobilized capsules arrays on the designated places on the sample surface. We applied one drop (30 μL) 30% H_2O_2 solution onto the surface to cover the OTS-coated $FeCl_3$/IL arrays. The Fe^{3+} inside the IL was slowly released from the pinholes on the OTS film. The released Fe^{3+} catalyzed the decomposition reaction of H_2O_2, which generated O_2 bubbles. The reaction was monitored by the optical microscope in real time. As Figure 3 shows, after immersion, oxygen

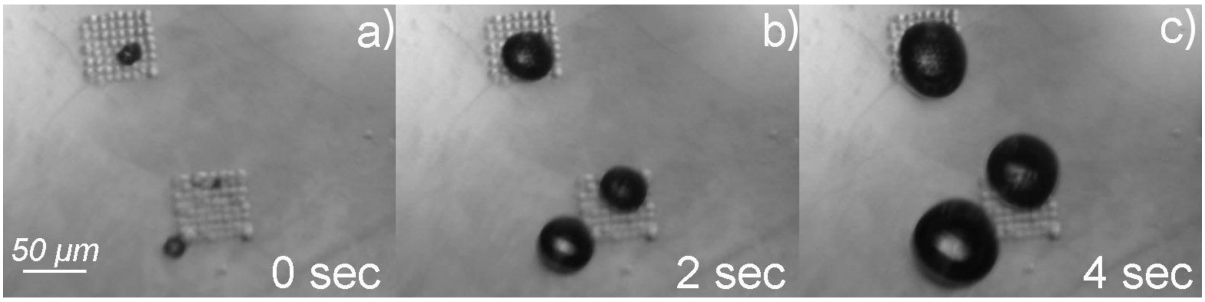

Figure 3: H_2O_2 decomposition reaction catalyzed by $FeCl_3$. The process was recorded by the optical microscope under 30% H_2O_2 solution. The $FeCl_3$ [Bmim]Cl solution assembled on two 8 × 8 OTSpd disc arrays. The IL drops were protected by a layer of OTS film coating. a), b), c): The same region with two OTS-coated IL arrays were immersed under 30% H_2O_2 solution and recorded at 0, 2, and 4 seconds, respectively. The observed oxygen bubbles (black spots) grew with time, indicating that the H_2O_2 decomposition reaction was proceeding.

bubbles were observed on the patterned area immediately (within 0.5 s after the H_2O_2 drop was applied onto the sample). Under the optical microscope, the smallest bubble that can be resolved is around 600 nm in size, which is at the resolution limit of our microscope. At the beginning, these small bubbles randomly appeared at the surface of the IL capsules. However, nearby oxygen bubbles fused together to form large bubbles. The size of the bubbles increased with time. Upon further growth, the fused bubbles took off from the surface and the patterned area became clean. Then, new bubbles appeared at the interfaces of the OTS-coated IL drops. These new bubbles may not always originate from exactly the same spot in the array as the previous bubbles did. However, the bubbles always started from the OTS-coated IL drops in the arrays. The overall decomposition reaction lasted for ~12 h, until all H_2O_2 was consumed. During the reaction, all oxygen bubbles generated from the decomposition were observed to originate from the surface of the IL capsules. This fact suggests that the majority of Fe^{3+} ions did not diffuse into the solution.

The potential leaking of IL into solution was assessed through the following experiment: As the first step, we fabricated one 8 × 8 OTSpd disc array on a 1 × 1 cm^2 OTS sample. In total, we fabricated three such samples (sample A, sample B and sample C). Within the array, each OTSpd disc has a diameter (*D*) of 3.5 μm. For sample A, we coated the array with IL solution and then coated a layer of OTS silane to encapsulate it. Then, each capsule's volume can be obtained through the flooding analysis using the AFM topography image. On average, the volume for each capsule was about 8 μm^3. Then, we put one drop (10 μL) of deionized water over the 8 × 8 OTS-coated IL capsule array for 2 h. Next, we transferred the drop to sample B and let this drop cover on the 8 × 8 OTSpd disc array on sample B. This drop evaporated in air within 30 min. If the IL leaked out from the capsule during the previous 2 h long incubation over sample A, the dissolved IL would be transferred to sample B. Since the IL would not evaporate with the water, IL would be deposited on sample B. Furthermore, because this IL ([Bmim]Cl) does not wet the OTS film, as demonstrated in Figure 1c, the deposited IL would be selectively concentrated on the high-energy 8 × 8 OTSpd disc array on sample B. Therefore, we can use AFM to characterize the 8 × 8 OTSpd disc array to reveal how much IL was deposited. Figure S2 in Supporting Information File 1 shows a representative image of one OTSpd disc after the drop evaporated over the OTSpd disc array. From the image (Figure S2), we computed that the volume of the IL deposition on this OTSpd disc was 0.044 μm^3. We used AFM to characterize all 64 OTSpd discs in the array and computed the IL deposition volume, which yielded an average IL deposition volume of 0.04 μm^3/disc. AFM scan also revealed that no IL was deposited on the OTS surface. In the control experiment, we put one drop (10 μL) of deionized water over the 8 × 8 OTSpd array for 2 h over sample C, which just had a clean 8 × 8 OTSpd array. After the drop evaporated in air, we characterized the 8 × 8 OTSpd array on sample C. No deposit was found, the OTSpd arrays did not change. Hence, we conclude that the material deposited on OTSpd disc on sample B is the leaked IL. After a 2 h long incubation, only 0.5% (v/v) IL inside OTS-coated capsule was slowly released to water. The OTS coating leads to the slow release of the IL.

The potential leaking of Fe^{3+} from the OTS-coated IL capsule was also studied. We put one drop (30 μL) 30% H_2O_2 solution onto the surface to cover the OTS-coated $FeCl_3$/IL arrays to initiate the reaction. After 1 h, while the reaction was still proceeding, we used a pipette to transfer the solution onto another clean OTS-coated wafer surface. At this stage, if a large amount of Fe^{3+} was released into the bulk solution phase, the Fe^{3+} would have been transferred onto the clean OTS-coated wafer surface as well. Then, we injected additional 30 μL 30% H_2O_2 solution into this drop. Since Fe^{3+} is the catalyst in the decomposition reaction, it will not be consumed. On the contrary, it would continue to catalyze the decomposition reaction. Nevertheless, we did not observe any oxygen bubbles generated within this drop. This fact suggests that the concentration of Fe^{3+} within this 60 μL drop was just too low. The Fe^{3+} concentration in the original 30 μL drop was just twice as high as that of in the 60 μL drop. Therefore, the Fe^{3+} concentration in the original 30 μL drop would be low as well. Our data show that the OTS coating on the IL drop surface effectively suppressed the diffusion of Fe^{3+} into the external solution.

In a separated control experiment, OTS-coated $FeCl_3$-free IL drops were incubated with H_2O_2 solution. No oxygen bubbles were generated, indicating that Fe^{3+} was responsible for the decomposition of H_2O_2. From these experimental results we conclude that the H_2O_2 decomposition reaction occurred at the IL–OTS–water interface. The reaction occurred either because the Fe^{3+} ions diffused out of or the H_2O_2 molecules diffused into the IL capsules through pinholes in the OTS film.

Conclusion

We found that lyophilic carboxylic acid-terminated OTSpd chemical pattern can direct the assembly of the IL on the OTS film surface. The chemical pattern can control the position, size and shape of the IL on the surface. The IL drops assembled on the chemical patterns can be coated with a protective layer of silane which encapsulates the IL and the solute within the IL. The coated IL drops can stably exist in other solvents that are miscible with the IL. Pinholes in the silane coating layer enable a slow material exchange between both sides of the protective silane layer.

Our experiments show that the $FeCl_3$ catalyst encapsulated within the IL drop can still catalyze the decomposition reaction of the hydrogen peroxide at the IL–OTS coating–water interface when the coated IL drops were immersed in hydrogen peroxide solution. Therefore, the coated IL drop may allow homogenous catalytic reactions to proceed in a heterogeneous fashion at the designated places. This capability provides conveniences for the subsequent product separation procedures.

Experimental

Instruments

The chemical pattern fabrication and characterization were conducted by the Agilent PicoPlus 2500 environmental AFM. The optical examination of the surface was conducted using a Nikon Eclipse 55c microscope.

Procedures

The silicon wafers (Nitrogen doped, resistivity 1–40 Ω·cm) were polished to an ultra-flat level (root mean square roughness <5 Å) and were then cut into 1 × 1 cm^2 pieces. The wafer samples were cleaned by piranha solution (1 part of 98% H_2SO_4 and 2 parts of 30% hydrogen peroxide) at 125 °C for 15 min. After rinsing the samples in deionized water and drying in an ultrapure nitrogen environment, the cleaned samples were immersed in a 5 mM OTS (octadecyltrichlorosilane, 97%, Gelest, Inc) toluene solution for 12 h at 20 °C in order to form an OTS film on the sample surface.

Next, the OTS-coated samples were rinsed in toluene and annealed in a sealed vial at 40 °C, 100% relative humidity (RH) for 12 h. Subsequently, the samples were incubated in a 5 mM OTS toluene solution again. The stabilization (*rinsing-annealing-OTS solution incubating*) process was repeated for three times in order to remove the pinholes inside the OTS film [17,19-21]. The final OTS film was an ultra-flat, pinhole-free, featureless film.

The OTSpd patterns were fabricated by the scanning probe deep oxidation lithography. In a 100% RH environment (at 25 °C), a Pt–Ti coated conducting AFM tip (CSC-17 Pt–Ti, from MikroMasch) was used to contact the OTS-coated sample. A 10 V voltage was applied to the silicon wafer, whereas the conducting AFM tip served as the ground. Due to the bias voltage, OTS under the tip was oxidized and degraded into carboxylic acid-terminated OTSpd pattern. Several 8 × 8 OTSpd disc arrays were fabricated on the OTS film. The size of the array was 50 × 50 μm^2.

Coating IL on OTSpd patterns

[Bmim]Cl was purchased from Sigma-Aldrich. It has a melting point of 70 °C and an advancing contact angle of 88° on OTS film [22]. In a sealed vial, 10 g [Bmim]Cl powder was heated to 120 °C and then cooled to room temperature. After cooling, [Bmim]Cl in the vial existed as a viscous super-cooled liquid at 25 °C. A drop of [Bmim]Cl was placed on the patterned area on the OTS-coated sample. Then, we used a pipette to remove the IL drop from the sample surface. After contacting the patterned surface, the IL assembled on the OTSpd patterns as drops.

Samples with IL drops assembled were placed in a sealed vial with 33 µL OTS. The vial was incubated at 55 °C for 2 h. The OTS molecules from the vapor formed a layer at the IL drop surface.

Supporting Information

Supporting Information File 1

Supporting material.
Figure S1: The oscillation during the AC mode scanning of an OTS-coated IL drop.
Figure S2: Assessment of IL leaking from the OTS-coated capsule.
[http://www.beilstein-journals.org/bjnano/content/supplementary/2190-4286-3-4-S1.pdf]

Acknowledgements

This research is partially supported by the University of Kentucky Faculty Start-up fund. Xiaoning Zhang thanks the support from the Chinese Government Scholarship and the Kentucky Opportunity Fellowship.

References

1. Petkovic, M.; Seddon, K. R.; Rebelo, L. P. N.; Pereira, C. S. *Chem. Soc. Rev.* **2011,** *40,* 1383–1403. doi:10.1039/c004968a
2. Koel, M. *Crit. Rev. Anal. Chem.* **2005,** *35,* 177–192. doi:10.1080/10408340500304016
3. Barikbin, Z.; Rahman, M. T.; Parthiban, P.; Rane, A. S.; Jain, V.; Duraiswamy, S.; Lee, S. H. S.; Khan, S. A. *Lab Chip* **2010,** *10,* 2458–2463. doi:10.1039/c004853d
4. Dubois, P.; Marchand, G.; Fouillet, Y.; Berthier, J.; Douki, T.; Hassine, F.; Gmouh, S.; Vaultier, M. *Anal. Chem.* **2006,** *78,* 4909–4917. doi:10.1021/ac060481q
5. Viau, L.; Tourné-Péteilh, C.; Devoisselle, J.-M.; Vioux, A. *Chem. Commun.* **2010,** *46,* 228–230. doi:10.1039/b913879j
6. Perera-Núñez, J.; Méndez-Vilas, A.; Labajos-Broncano, L.; González-Martín, M. L. *Langmuir* **2010,** *26,* 17712–17719. doi:10.1021/la102799x
7. Hozumi, A.; Bien, P.; McCarthy, T. J. *J. Am. Chem. Soc.* **2010,** *132,* 5602–5603. doi:10.1021/ja102044x
8. Nanayakkara, Y. S.; Moon, H.; Armstrong, D. W. *ACS Appl. Mater. Interfaces* **2010,** *2,* 1785–1787. doi:10.1021/am100269d
9. Cai, Y. *Langmuir* **2009,** *25,* 5594–5601. doi:10.1021/la9004483

10. Chowdhury, D.; Maoz, R.; Sagiv, J. *Nano Lett.* **2007,** *7,* 1770–1778. doi:10.1021/nl070842x
11. Lu, L.; Cai, Y. *Langmuir* **2009,** *25,* 13914–13917. doi:10.1021/la9016917
12. Lu, L.; Zander, K. J.; Cai, Y. *Langmuir* **2010,** *26,* 5624–5631. doi:10.1021/la904387d
13. Hardy, W. B. *Philos. Mag.* **1919,** *38,* 49.
14. Radigan, W.; Ghiradella, H.; Frisch, H. L.; Schonhorn, H.; Kwei, T. K. *J. Colloid Interface Sci.* **1974,** *49,* 241–248. doi:10.1016/0021-9797(74)90357-9
15. Sagiv, J. *J. Am. Chem. Soc.* **1980,** *102,* 92–98. doi:10.1021/ja00521a016
16. Wasserman, S. R.; Whitesides, G. M.; Tidswell, I. M.; Ocko, B. M.; Pershan, P. S.; Axe, J. D. *J. Am. Chem. Soc.* **1989,** *111,* 5852–5861. doi:10.1021/ja00197a054
17. Zeira, A.; Chowdhury, D.; Hoeppener, S.; Liu, S.; Berson, J.; Cohen, S. R.; Maoz, R.; Sagiv, J. *Langmuir* **2009,** *25,* 13984–14001. doi:10.1021/la902107u
18. Kozlov, Y. N.; Nadezhdin, A. D.; Pourmal, A. P. *Int. J. Chem. Kinet.* **1974,** *6,* 383–394. doi:10.1002/kin.550060308
19. Maoz, R.; Frydman, E.; Cohen, S. R.; Sagiv, J. *Adv. Mater.* **2000,** *12,* 725–731. doi:10.1002/(SICI)1521-4095(200005)12:10<725::AID-ADMA725>3.0.CO;2-Z
20. Liu, S.; Maoz, R.; Schmid, G.; Sagiv, J. *Nano Lett.* **2002,** *2,* 1055–1060. doi:10.1021/nl025659c
21. Hoeppener, S.; Maoz, R.; Sagiv, J. *Nano Lett.* **2003,** *3,* 761–767. doi:10.1021/nl034176l
22. Carrera, G. V. S. M.; Frade, R. F. M.; Aires-de-Sousa, J.; Afonso, C. A. M.; Branco, L. C. *Tetrahedron* **2010,** *66,* 8785–8794. doi:10.1016/j.tet.2010.08.040

License and Terms

Beilstein Journal
of Nanotechnology

Direct-write polymer nanolithography in ultra-high vacuum

Woo-Kyung Lee[1], Minchul Yang[2], Arnaldo R. Laracuente[1], William P. King[3],
Lloyd J. Whitman[4] and Paul E. Sheehan[*1]

Letter

Open Access

Address:
[1]Chemistry Division, U.S. Naval Research Laboratory, Washington, DC 20375, USA, [2]US Patent and Trademark Office, Alexandria, VA 22314, USA, [3]Department of Mechanical Science and Engineering, University of Illinois Urbana-Champaign, Urbana, IL 61801, USA and [4]Center for Nanoscale Science and Technology, National Institute for Science and Technology, Gaithersburg, MD 20899, USA

Email:
Paul E. Sheehan[*] - paul.sheehan@nrl.navy.mil

* Corresponding author

Keywords:
additive lithography; polymer; scanning probe lithography; ultra high vacuum

Beilstein J. Nanotechnol. **2012,** *3,* 52–56.
doi:10.3762/bjnano.3.6

Received: 11 October 2011
Accepted: 16 December 2011
Published: 19 January 2012

This article is part of the Thematic Series "Self-assembly at solid surfaces".

Guest Editors: S. R. Cohen and J. Sagiv

Abstract

Polymer nanostructures were directly written onto substrates in ultra-high vacuum. The polymer ink was coated onto atomic force microscope (AFM) probes that could be heated to control the ink viscosity. Then, the ink-coated probes were placed into an ultra-high vacuum (UHV) AFM and used to write polymer nanostructures on surfaces, including surfaces cleaned in UHV. Controlling the writing speed of the tip enabled the control over the number of monolayers of the polymer ink deposited on the surface from a single to tens of monolayers, with higher writing speeds generating thinner polymer nanostructures. Deposition onto silicon oxide-terminated substrates led to polymer chains standing upright on the surface, whereas deposition onto vacuum reconstructed silicon yielded polymer chains aligned along the surface.

Introduction

The deposition of materials in vacuum is the foundational technology for creating modern electronic circuits; a vacuum being essential both to preserve the cleanliness of the substrate and the deposited materials and to minimize the creation of defects [1]. Consequently, most deposition techniques from thermal evaporation to atomic layer deposition require a high level of vacuum, preferably ultra-high vacuum (UHV), to be used effectively. While the suite of established vacuum deposition technologies is vast and capable of highly precise deposition, there are relatively few methods to perform additive lithography in a single deposition step. Additive lithography deposits only the material that is needed for the intended device in the correct position.

This is in contrast to the standard practice where an entire film is generated, the great majority of this film is then removed. In addition to the benefit of reduced material cost, additive techniques have further benefits, including the ability to create softer, heterogeneous structures – such as polymers – that would be contaminated or destroyed by the multiple requisite coating and removal steps associated with conventional "lift-off" lithography. To date, additive lithographies such as inkjet [2], dip-pen nanolithography (DPN) [3] and micro-contact printing [4] have been limited to deposition under ambient pressures, and therefore cannot achieve the benefits of the controlled environment under vacuum.

One type of additive lithography is scanning probe lithography (SPL) where sharp probes either guide the deposition of material to a substrate or modify previously deposited films [5,6]. In the case of DPN, the AFM probe can be used to write a wide range of molecular inks with resolutions down to 15 nm [3,7,8]. However, in conventional DPN writing depends on the intrinsic fluidity of the ink molecules or on the creation of ink fluidity using solvents [9]. Unfortunately, inks and solvents that have sufficient intrinsic fluidity for DPN evaporate quickly in vacuum. This paper reports that thermal dip-pen nanolithography (tDPN) [10] can deposit polymer nanostructures from a heated AFM tip in a high vacuum environment (Figure 1b). In tDPN, the probe temperature may be varied precisely within microseconds over a temperature range of 1000 °C. The probe temperature controls the viscosity of the coated ink allowing independent control over the overall deposition rate and the ability to turn off and on deposition (Figure 1a). Many different materials (e. g., metals [11], nanoparticles [12], and SAM molecules [10]) have been deposited using this technique. Thermal DPN closely mirrors the capabilities of conventional DPN but with greater control over the ink flow [5]. Critically, the heat from the probes enables the deposition of high melting point inks such as polymers that also have low volatility and so may be deposited under a vacuum.

Results and Discussion

Our initial approach for depositing organic inks was to attempt DPN with octadecanethiol (ODT), a classic ink for DPN that reproducibly transfers to the substrate. However, it was found that the ink on the DPN tip would invariably evaporate in the load lock chamber (~10^{-7} Torr) leaving insufficient coverage for observable deposition. Evaporation is readily observed visually since the ink leaves a haze on the tip that is absent after placing in a load lock chamber. This anecdotal observation was more rigorously examined by creating a sample that mimicked the DPN tip surface chemistry: A silicon oxide on a silicon chip that was coated by holding it over ODT in a scintillation vial heated to 65 °C, for 30 min. This procedure produced an ODT film that was 20 nm thick (measured by ellipsometry). After placing the chip briefly under vacuum in a load lock chamber (~10^{-7} Torr), no ODT film was detectable. Additional attempts with less volatile inks – such as eicosanethiol – yielded similar results, leading us to conclude that typical inks used in conventional DPN cannot be used for DPN under vacuum.

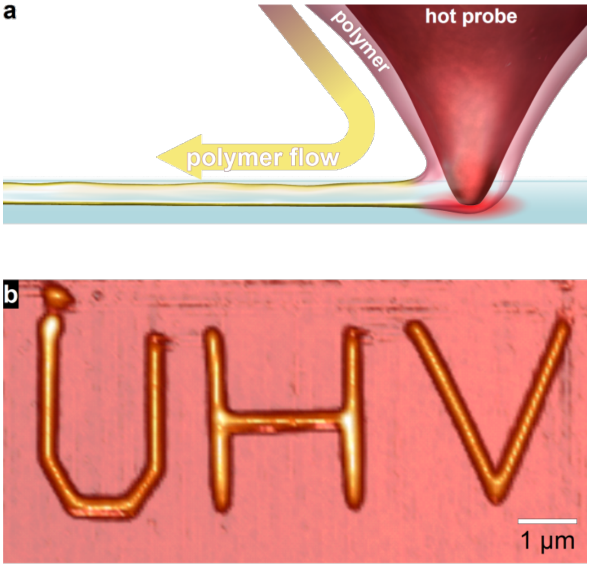

Figure 1: (a) Schematic of the tDPN process which uses a heated scanning probe microscope tip to deposit polymer from a moving tip. (b) Leaving the tip in contact, deposition is started and stopped by turning the heat on and off as shown by writing "UHV". The poly(3-dodecylthiophene) (PDDT) was written on SiO_2 (non-UHV prepared) in UHV (~10^{-10} Torr). The height of each polymer line was 20 nm (= 8 ML) while the polymer width was 150 nm (fwhm).

While alkanethiols could not be deposited, we found that heated probes would retain and deposit polymer in UHV. For this work, we chose the polymer to be poly(3-dodecylthiophene) (PDDT), a conducting polymer that has found widespread usage in organic electronics (Figure 1b) [13]. PDDT is also interesting because it becomes highly ordered, forming self-assembled layers on a silicon surface [14], when it is properly annealed. This ordering increases its ability to conduct current after electron beam exposure [15].

The probe temperature was controlled by applying current through the probe heater [16]. One of the advantages of UHV tDPN is the lower melting point of inks under UHV. Because the molar volume of PDDT is lower in solid form than in liquid form, thermodynamics indicate that its melting point should drop as the surrounding pressure is lowered. Thus, while PDDT routinely deposits at its melting point of 120 °C in air, we observed that the writing temperature of PDDT could be decreased down to ~100 °C in UHV. As a result, the temperature window between melting and thermal decomposition of PDDT (175 °C in air) widens, thereby enabling greater control of line widths and thicknesses deposited in UHV. The lower deposition temperature also reduces the risk of thermal damage when applied to pre-fabricated devices.

While heating the probe to the vacuum melting temperature of the PDDT, the tip was rasterized across the “as is” native oxide Si substrate at different speeds. We found that monolayer-by-monolayer control of the film thickness, as previously established under nitrogen, is also possible under UHV. Figure 2 shows two polymer nanowire lines written at different speeds. Assuming a thickness of 2.6 nm for each PDDT monolayer as previously determined by XRD [14], the polymer deposited by the probe moving at 20 µm/s was only a single monolayer thick, with the structure written at 8 µm/s being four monolayers thick. The widths of the deposited polymer structures were 280 nm at 20 µm/s and 303 nm at 8 µm/s, with the width principally determined by the relatively blunt silicon tip. Note that recent advances – where the tips remain sharp due to a coating of wear-resistant diamond – readily show line thicknesses of 40 nm [17]. The line width and heights were measured as a function of the probe speed (Figure 3). The heights of the deposited polymer structures roughly decrease as the inverse square root of the scan speed. The widths of the deposited structures decrease monotonically with the scan speed but do not show a clear power law relationship. When patterning under ambient conditions, dimensional control may be achieved by varying the tip temperature; however, the tip temperature was fixed in UHV to limit the number of experimental parameters.

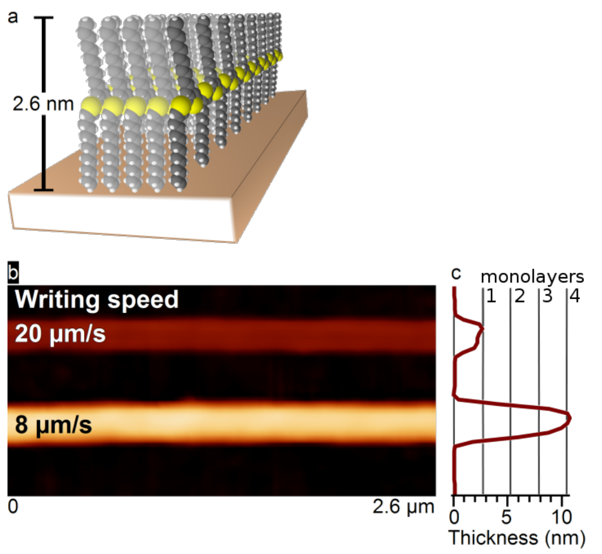

Figure 2: Orientations of UHV deposited polymer. (a) PDDT typically organizes in such way that the polymer is oriented normal to the surface with a monolayer height of 2.6 nm. (b) Deposition of polymer at different speeds on a non-UHV prepared substrate showing the upright orientation in (a). By varying the tip speed, the scanning probe will deposit polymer at different thicknesses. At the relatively high speed of 20 µm/s, only a single monolayer is deposited as shown by the line average to the right of the image. Lower speeds deposit thicker polymer lines as shown by line averages in (c).

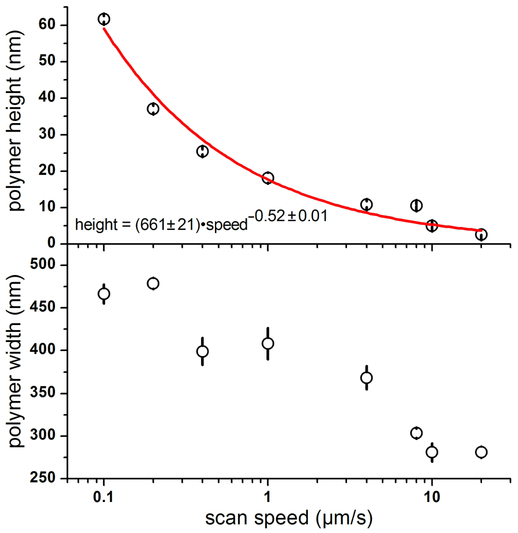

Figure 3: The polymer deposit heights and widths of PDDT deposited onto Si substrate (non-UHV prepared) as a function of scanning speed. Both the height and width decrease monotonically with tip speed.

Polymer nanostructures were also written on atomically clean and flat Si(001)-2×1 (Figure 4) where monoatomic steps are clearly visible. Interestingly, we found that surface chemistry of the silicon substrate had a major effect on the apparent structure of the deposited polymer as determined by the monolayer film thickness. On the native oxide surface, PDDT self-assembles in such way that the side chains are perpendicular to the surface (Figure 2a), as typically observed for PDDT deposited on non-UHV prepared surfaces under ambient conditions [18]. The upright orientation is due to the hydrophobic alkyl side chains minimizing their exposure to the hydrophilic oxide substrate. In contrast, PDDT written on Si(001)-2×1 has a film thickness of ~0.4 nm, corresponding to polymer side-chains oriented parallel to the surface, as illustrated in Figure 4a. Note that the thickness of our films lies intermediate to values reported previously for PDDT on other substrates. Scifo et al. used STM to measure the thickness in UHV of a PDDT film drop cast on highly oriented pyrolytic graphite (HOPG) and reported a film thickness of 0.24 ± 0.04 nm [19]. In contrast, Terada et al. [20] reported poly(3-hexylthiophene) (P3HT) on H-terminated Si(100) in UHV to be 0.5 nm thick. Our measured value is closer to the 0.4 nm intermolecular spacing measured for thick films of PDDT [14]. In the prior STM measurements, the measured thickness is a convolution of the topographic height and electronic properties of the polymer film, complicating the comparison. However, the polymer's lying flat strongly suggests that alkyl side chains must interact more favorably with the silicon surface than with the oxide surface and so has a significant impact on the observed molecular film thickness.

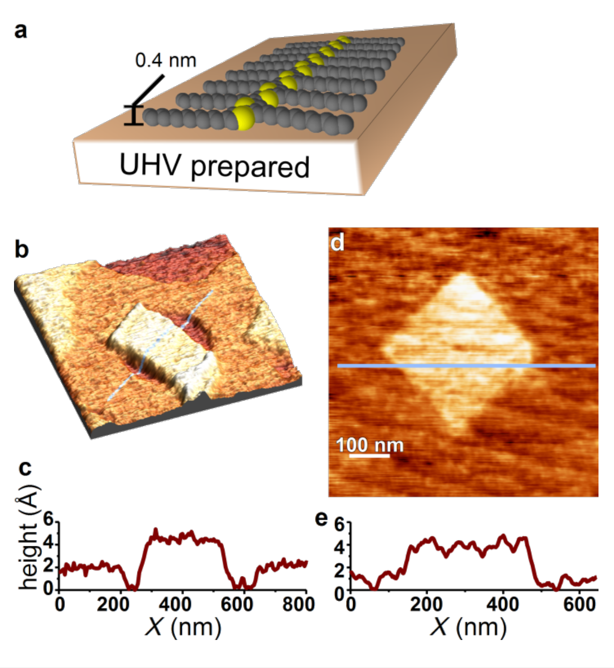

Figure 4: (a) Deposition onto the UHV prepared Si substrate in UHV shows the polymer lying on its side. (b) Polymer deposited across a Si step edge an atom thick. (c) The cross section [pale blue line in (b)] shows that the polymer thickness is 0.4 nm, indicating that the polymer molecules are lying flat. (d) A second image of polymer deposited on a UHV-prepared clean silicon surface with diagonal monatomic steps that go from the upper left to the lower right. (e) Cross section from (d) that again gives a polymer thickness of 0.4 nm.

Conclusion

In conclusion, we have developed a method for direct, additive deposition of polymer in UHV using thermal dip-pen nanolithography. The molecular structure of the written PDDT monolayer nanostructure films depends on the chemistry of the silicon surface. Oxide termination leads to polymer side chains aligning perpendicular to the substrate, whereas silicon termination leads to the polymer lying flat. The thickness of the deposited polymer is a function of the speed of the scanning probe and may be controlled monolayer-by-monolayer. This new UHV-compatible direct-write technique should be of value both for nanoscale lithography of polymer structures and for the study of molecularly-ordered polymer nanostructures. This result would also open a new method of studying polymer-semiconductor surface interaction at a molecular level which is useful to develop polymer-based electronics compatible with inorganic semiconductor technology.

Experimental

The silicon wafer substrates were prepared using one of two protocols. In both protocols, substrates for depositing PDDT were scribed from Sb-doped Si(001) wafers (0.01 to 0.02 Ω·cm) oriented to within 0.1° of (001). The substrates were then sonicated in $CHCl_3$, dried with a stream of N_2, and transferred into the UHV chamber (base pressure ~5×10^{-11} Torr). In the first protocol, the substrate was used as-is to take advantage of the ~2 nm thick native oxide. In the second cleaning protocol, samples were prepared to leave an atomically pristine, 2×1-reconstucted Si(001) surface. In this protocol, the substrates were initially degassed in UHV overnight at 500 °C and resistively heated for 30 s at 1230 °C, cooled down for at least 5 min, and then briefly heated again to 1230 °C for 5 s, while maintaining a pressure below 1×10^{-9} Torr. Depending on the sample holder history, several heating-cycles were necessary before the pressure could be maintained below 1×10^{-9} Torr.

Poly(3-dodecylthiophene) (PDDT) was purchased from Sigma-Aldrich (M_w ~ 60,000) and used without any further purification. To pattern PDDT via tDPN in UHV, the heatable cantilever was first mounted on a UHV tip holder. Next, a solution of 0.1% by volume of PDDT in chloroform was loaded onto the cantilever and tip by using a 3 mm diameter loop of copper wire containing the solution in the meniscus. Using a micromanipulator, the tip was immersed into the droplet, dried on a hot plate at 60 °C and then loaded into the UHV chamber.

References

1. Wolf, S.; Tauber, R. *Silicon Processing for the VLSI Era;* Lattice Press: Sunset Beach, CA, 1986; Vol. 1 Process Technology, p 660.
2. de Gans, B.-J.; Duineveld, P. C.; Schubert, U. S. *Adv. Mater.* **2004,** *16,* 203–213. doi:10.1002/adma.200300385
3. Ginger, D. S.; Zhang, H.; Mirkin, C. A. *Angew. Chem., Int. Ed.* **2004,** *43,* 30–45. doi:10.1002/anie.200300608
4. Ruiz, S. A.; Chen, C. S. *Soft Matter* **2007,** *3,* 168–177. doi:10.1039/b613349e
5. Lee, W.-K.; Sheehan, P. E. *Scanning* **2008,** *30,* 172–183. doi:10.1002/sca.20084
6. Tseng, A. A.; Notargiacomo, A.; Chen, T. P. *J. Vac. Sci. Technol., B: Microelectron. Nanometer Struct.–Process., Meas., Phenom.* **2005,** *23,* 877–894. doi:10.1116/1.1926293
7. Piner, R. D.; Zhu, J.; Xu, F.; Hong, S.; Mirkin, C. A. *Science* **1999,** *283,* 661–663. doi:10.1126/science.283.5402.661
8. Jaschke, M.; Butt, H.-J. *Langmuir* **1995,** *11,* 1061–1064. doi:10.1021/la00004a004
9. Sheehan, P. E.; Whitman, L. J. *Phys. Rev. Lett.* **2002,** *88,* 156104. doi:10.1103/PhysRevLett.88.156104
10. Sheehan, P. E.; Whitman, L. J.; King, W. P.; Nelson, B. A. *Appl. Phys. Lett.* **2004,** *85,* 1589–1591. doi:10.1063/1.1785860
11. Nelson, B. A.; King, W. P.; Laracuente, A. R.; Sheehan, P. E.; Whitman, L. J. *Appl. Phys. Lett.* **2006,** *88,* 033104. doi:10.1063/1.2164394

12. Lee, W. K.; Dai, Z.; King, W. P.; Sheehan, P. E. *Nano Lett.* **2010,** *10,* 129–133. doi:10.1021/nl9030456
13. Roncali, J. *Chem. Rev.* **1992,** *92,* 711–738. doi:10.1021/cr00012a009
14. Prosa, T. J.; Winokur, M. J.; Moulton, J.; Smith, P.; Heeger, A. J. *Macromolecules* **1992,** *25,* 4364–4372. doi:10.1021/ma00043a019
15. Laracuente, A. R.; Yang, M.; Lee, W. K.; Senapati, L.; Baldwin, J. W.; Sheehan, P. E.; King, W. P.; Erwin, S. C.; Whitman, L. J. *J. Appl. Phys.* **2010,** *107,* 103723. doi:10.1063/1.3428963
16. Lee, J.; Beechem, T.; Wright, T. L.; Nelson, B. A.; Graham, S.; King, W. P. *J. Microelectromech. Syst.* **2006,** *15,* 1644–1655. doi:10.1109/JMEMS.2006.886020
17. Fletcher, P. C.; Felts, J. R.; Dai, Z.; Jacobs, T. D.; Zeng, H.; Lee, W.; Sheehan, P. E.; Carlisle, J. A.; Carpick, R. W.; King, W. P. *ACS Nano* **2010,** *4,* 3338–3344. doi:10.1021/nn100203d
18. Yang, M.; Sheehan, P. E.; King, W. P.; Whitman, L. J. *J. Am. Chem. Soc.* **2006,** *128,* 6774–6775. doi:10.1021/ja0612807
19. Scifo, L.; Dubois, M.; Brun, M.; Rannou, P.; Latil, S.; Rubio, A.; Grévin, B. *Nano Lett.* **2006,** *6,* 1711–1718. doi:10.1021/nl061018w
20. Terada, Y.; Miki, K.; Fujimori, M.; Heike, S.; Suwa, Y.; Hashizume, T. *J. Appl. Phys.* **2005,** *97,* 124302. doi:10.1063/1.1928326

License and Terms

Beilstein Journal
of Nanotechnology

Substrate-mediated effects in photothermal patterning of alkanethiol self-assembled monolayers with microfocused continuous-wave lasers

Anja Schröter[1,2], Mark Kalus[1,2] and Nils Hartmann*[1,2]

Full Research Paper

Open Access

Address:
[1]Fakultät für Chemie, Universität Duisburg-Essen, 45117 Essen,
Germany and [2]Center for Nanointegration Duisburg-Essen (CENIDE),
Universität Duisburg-Essen, 47048 Duisburg, Germany

Email:
Nils Hartmann* - nils.hartmann@uni-due.de

* Corresponding author

Keywords:
femtosecond lasers; nonlinear laser processing; self-assembled
monolayers; subwavelength patterning; ultrathin resists

Beilstein J. Nanotechnol. **2012,** *3,* 65–74.
doi:10.3762/bjnano.3.8

Received: 24 October 2011
Accepted: 03 January 2012
Published: 26 January 2012

This article is part of the Thematic Series "Self-assembly at solid
surfaces".

Guest Editors: S. R. Cohen and J. Sagiv

Abstract

In recent years, self-assembled monolayers (SAMs) have been demonstrated to provide promising new approaches to nonlinear laser processing. Most notably, because of their ultrathin nature, indirect excitation mechanisms can be exploited in order to fabricate subwavelength structures. In photothermal processing, for example, microfocused lasers are used to locally heat the substrate surface and initiate desorption or decomposition of the coating. Because of the strongly temperature-dependent desorption kinetics, the overall process is highly nonlinear in the applied laser power. For this reason, subwavelength patterning is feasible employing ordinary continuous-wave lasers. The lateral resolution, generally, depends on both the type of the organic monolayer and the nature of the substrate. In previous studies we reported on photothermal patterning of distinct types of SAMs on Si supports. In this contribution, a systematic study on the impact of the substrate is presented. Alkanethiol SAMs on Au-coated glass and silicon substrates were patterned by using a microfocused laser beam at a wavelength of 532 nm. Temperature calculations and thermokinetic simulations were carried out in order to clarify the processes that determine the performance of the patterning technique. Because of the strongly temperature-dependent thermal conductivity of Si, surface-temperature profiles on Au/Si substrates are very narrow ensuring a particularly high lateral resolution. At a 1/e spot diameter of 2 µm, fabrication of subwavelength structures with diameters of 300–400 nm is feasible. Rapid heat dissipation, though, requires high laser powers. In contrast, patterning of SAMs on Au/glass substrates is strongly affected by the largely distinct heat conduction within the Au film and in the glass support. This results in broad surface temperature profiles. Hence, minimum structure sizes are larger when compared with respective values on Au/Si substrates. The required laser powers, though, are more than one order of magnitude lower. Also, the laser power needed for patterning decreases with decreasing Au layer thickness. These results demonstrate the impact of the substrate on the overall patterning process and provide new perspectives in photothermal laser patterning of ultrathin organic coatings.

Introduction

In the past decades, self-assembled monolayers (SAMs) have developed into a particularly versatile means to tailor the surface properties of technologically important materials, such as gold, silicon and glass [1-3]. Because of the self-limiting growth mechanism, well-defined coating with a layer of monomolecular thickness is ensured [4]. Varying the chemical structure of the precursor molecules, in turn, allows one to alter the chemical reactivity and resistance of these coatings [5]. These characteristics of SAMs have been widely exploited in numerous micro- and nanofabrication schemes [1-3]. A prominent example, addressed here, considers the application of SAMs as ultrathin resists. Patterning techniques, such as scanning-probe techniques, e-beam lithography, micro-contact printing and photolithography have been employed along this path [6-9]. Furthermore, laser processing of SAMs has attracted significant attention [9-12]. Generally, laser techniques provide a variety of powerful features and hence are the preferred choice in many technical and medical applications [13]. Prominent examples include optical data storage, photo-mask fabrication and manufacturing of medical implants [14]. Owing to the optical diffraction limit, laser nanofabrication encounters significant challenges. Typically, minimum structure sizes are not much smaller than the wavelength of the laser source [13]. A means to extend the lateral resolution of laser patterning techniques into the subwavelength range is to take advantage of nonlinear effects, such as photothermal and multiphoton absorption processes [11-17]. In photothermal processing, laser light is used in order to locally heat the substrate surface and initiate chemical reactions [12]. Commonly, photothermal patterning of SAMs is carried out by sequential processing with microfocused lasers [11,18-25]. In addition, some contributions also demonstrated parallel processing through the use of microlens arrays and interference patterns [26,27]. These contributions emphasize the prospects of photothermal laser routines in micro- and nanopatterning of different types of SAMs and other ultrathin organic coatings [11,18-28]. Because of the photothermal process, the performance of such laser techniques depends on both the peculiar chemical structure of the SAM, notably the surface linkage, and the optical and thermal properties of the substrate [11,13]. In this contribution we focus on substrate-mediated effects in photothermal laser patterning of alkanethiol SAMs on Au-coated Si and glass substrates. Patterning experiments are combined with temperature calculations and thermokinetic simulations. Although photothermal patterning of alkanethiol SAMs on distinct substrates has been investigated previously [11,21-24,27], a systematic study on the influence of the substrate on the performance of the patterning technique is still missing. The results reported here demonstrate a strong dependence of the patterning process on the support material, i.e., on its thermal conductivity. Comparative experiments with Au-coated glass substrates also show a strong impact of the Au layer thickness.

Results and Discussion

General approach

The general experimental approach is illustrated in Figure 1. Alkanethiol SAMs were prepared by immersion of Au-coated glass and silicon substrates into a millimolar solution of hexadecanethiol (HDT). Photothermal processing was carried out by using a microfocused laser beam at $\lambda = 532$ nm and $d_{1/e} = 2$ µm. The experimental setup allows the variation of the laser power P and the laser pulse length τ. In a patterning experiment the sample was moved in the focal plane of the laser. This provides a convenient means to test distinct laser parameters in adjacent surface areas. At sufficiently high laser powers and/or sufficiently long pulse lengths, thermal desorption of the thiol molecules is initiated [11]. Subsequently, the Au layer in these laser-depleted surface areas was removed by means of wet-chemical

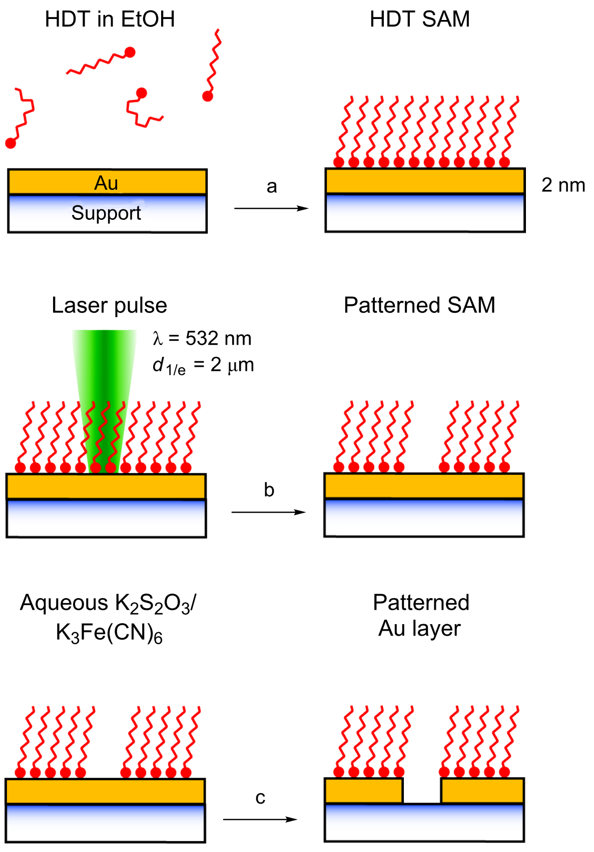

Figure 1: Schematic diagram of the process flow: (a) SAM formation upon immersion in an ethanolic solution of HDT; (b) photothermal laser processing of the HDT SAM at $\lambda = 532$ nm; and (c) pattern transfer into the Au film upon etching in an aqueous solution of $K_2S_2O_3$ and $K_3Fe(CN)_6$. Adapted from [11].

etching [11,29]. For this purpose, the patterned substrates were immersed into an aqueous solution of $K_2S_2O_3$ and $K_3Fe(CN)_6$. The HDT SAM acts as an ultrathin resist and inhibits etching in the coated surface areas. The immersion time was adjusted in order to completely dissolve the Au film in the laser-depleted surface areas and to minimize widening of the structures owing to the isotropic etching process.

Characterization of substrates and monolayers

As substrates, Au-coated glass plates with Au layer thicknesses of 10 nm, 30 nm, 50 nm and 100 nm were used. In addition, experiments with Au-coated silicon substrates with a 30 nm Au layer were carried out. UV–vis spectra of Au-coated glass supports are displayed in Figure 2 [30,31]. Evaporated Au films with a thickness of 10 nm or below often exhibit a discontinuous structure and show a plasmon resonance in the UV–vis spectrum, that is, a pronounced minimum in the spectral transmission between 500 and 600 nm. This plasmon resonance is not observed here, suggesting that all substrates exhibit a continuous Au layer. Atomic force microscopy (AFM) revealed a surface roughness of a few nanometers. Note that Au/glass substrates with 100 nm thick Au layers and Au/Si substrates are opaque and, hence, do not allow for characterization by means of UV–vis spectroscopy. In addition, the transmittance T and reflectance R at a wavelength of 532 nm and normal incidence was determined. The respective data are summarized in Table 1. Taking into account the transmittance and reflectance data allows one to calculate the absorbance A and the effective absorption coefficient α_{Au} of the films from [12]:

$$A = 1 - R - T \quad (1)$$

and

$$\alpha_{Au} = \frac{1}{h} \ln\left(\frac{1-R}{T}\right) \quad (2)$$

It is worth noting that substrates with thin Au layers exhibit the highest absorbance; the optical data for glass substrates with 100 nm thick Au layers, in turn, correspond to the bulk values of Au [32]. For comparison, the 1/e penetration depth of bulk Au at a wavelength of 532 nm is about 18 nm only [32].

HDT coated substrates are characterized by contact-angle measurements and infrared reflection–absorption spectroscopy (IRRAS). Static water contact angles are about 109°. IR measurements show no difference for all samples considered here. A typical spectrum is shown in Figure 3, and peak assignments are given in Table 2. Based on the peak positions of the antisymmetric methylene stretching vibrations, these data indicate densely packed monolayers [33].

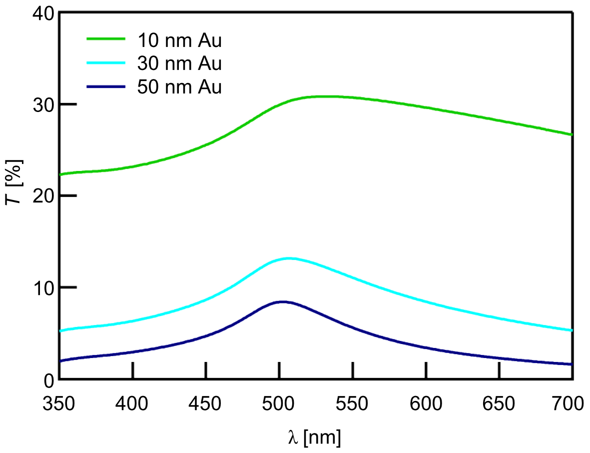

Figure 2: UV–vis spectra of Au/glass substrates with Au layer thicknesses of 10 nm, 30 nm and 50 nm.

Table 1: Optical properties of Au-coated substrates at λ = 532 nm.

Support	h_{Au} [nm]	R	T	A	α_{Au} [cm^{-1}]
Glass	10	0.34	0.31	0.35	$7.56 \cdot 10^5$
Glass	30	0.61	0.12	0.27	$3.90 \cdot 10^5$
Glass	50	0.68	0.07	0.25	$3.08 \cdot 10^5$
Glass	100	0.75	0.00	0.25	$5.69 \cdot 10^{6,a}$
Si	30	0.71	0.00	0.29	—[b]

[a]Given value refers to the bulk value for Au [32].
[b]Indeterminable because of the opacity of the Si support.

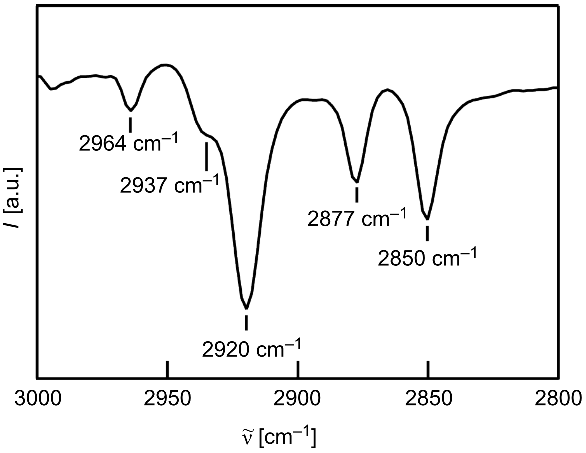

Figure 3: IRRAS-spectra of an HDT-coated Au/glass substrate exposing a 50 nm Au layer.

Table 2: Assignment of IR peaks.[a]

Peak	Position [cm^{-1}]
$\nu_{as}(CH_3)_{ip}$	2964
$\nu_s(CH_3)_{FR}$	2937
$\nu_{as}(CH_2)$	2920
$\nu_s(CH_3)_{FR}$	2877
$\nu_s(CH_2)$	2850

[a] ν_s and ν_{as} refer to the symmetric and antisymmetric stretching vibrations; ip refers to in-plane vibrations; FR indicates vibrations which are split because of Fermi resonance interactions with lower-frequency vibrations [33].

Photothermal laser patterning

After the etching process, patterned samples were characterized by optical microscopy. Typical micrographs of patterns on a glass support are shown in Figure 4. Each micrograph displays a pattern that has been fabricated at a given laser power and with distinct laser pulse lengths between 50 µs and 10 ms. In order to check the reproducibility, the patterning was carried out under identical conditions along three rows. For precise characterization of the structures, atomic force microscopy (AFM) was used. Figure 5 displays a topographic AFM image and a height profile of structures with diameters of 0.9 µm and 1.7 µm. The depth of these structures is equivalent to the thickness of the Au layer of 30 nm. Diameters are measured at the half depth. Because of the isotropic etching process, these values are expected to be slightly larger than the diameter of the depleted areas after laser processing. Considering a 30 nm thick film, for example, the widening at the half depth amounts to about ±15 nm. For all structure sizes reported here this is <<10% of the total width. Hence, this effect is considered to be negligible and is not taken into account. Note also, that the measurements are not corrected for the tip size. Hence, the measured diameters, indeed, are somewhat smaller than the actual width of the structures. This to some extent compensates for the widening of the structures during etching.

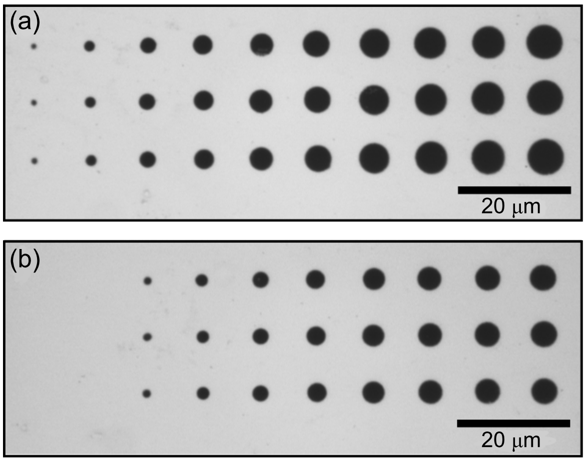

Figure 4: Optical micrograph of a laser-fabricated dot pattern. HDT-SAMs on a Au/glass substrate exposing a 30 nm thick Au layer are processed with single laser pulses with distinct τ between 50 µs (left) and 10 ms (right) and (a) P = 24.3 mW, (b) P = 20.3 mW. After laser processing, the pattern is transferred to the Au layer by wet-chemical etching.

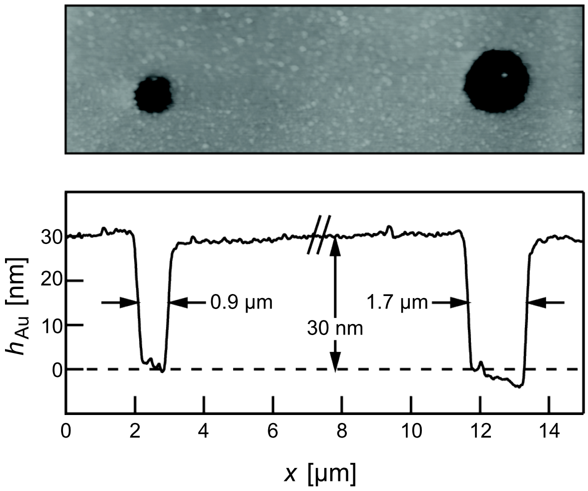

Figure 5: AFM data from patterning experiments with HDT-SAMs on Au/glass substrates exposing a 30 nm thick Au layer. The structures were fabricated by using single laser pulses at P = 24.3 mW and with distinct τ of 50 µs (left) and 100 µs (right). Pattern transfer to the Au layer was carried out by wet-chemical etching. Diameters refer to values at half-depth.

Figure 6 displays the dependence of the structure diameter d on the laser parameters. In order to ensure comparability, only data from structures exhibiting a depth that is equivalent to the respective Au layer thickness are considered. Complete etching of the laser-depleted areas on patterned substrates with a 100 nm thick Au layer turned out to be difficult. Hence, no data for such samples are shown. All diagrams display the typical dependence of the structure diameter on the laser power and laser pulse length, as observed in a previous study focusing on photothermal patterning of HDT-SAMs on Au/Si substrates [11]. It is noteworthy, though, that processing of HDT-SAMs on Au/glass substrates can be carried out at much lower laser powers. Photothermal patterning of alkanethiols on Au/glass substrates at low laser powers has been reported previously [21,24]. Due to the different experimental parameters, however, a quantitative comparison of these data is not feasible. The data presented here demonstrate that, under otherwise identical conditions, the laser powers needed for patterning of HDT-

SAMs on glass supports are reduced by more than one order of magnitude when compared with those values needed for patterning of HDT-SAMs on Si supports. Moreover, when comparing the data on the Au-coated glass substrates, a strong dependence of the patterning results on the Au layer thickness is evident. The average laser power required for fabrication of identical structures decreases from 28 mW to 9 mW when the Au layer thickness is reduced from 50 nm to 10 nm. Patterning of HDT-SAMs on Au/glass supports with Au layer thicknesses of 10 nm can be carried out at laser powers below 8 mW, a value comparable with the emitted power of a laser pointer. This opens up an opportunity for truly cost-effective laser processing of thiol-based SAMs. In addition, parallel processing, e.g., by using micromirror displays [34], appears feasible.

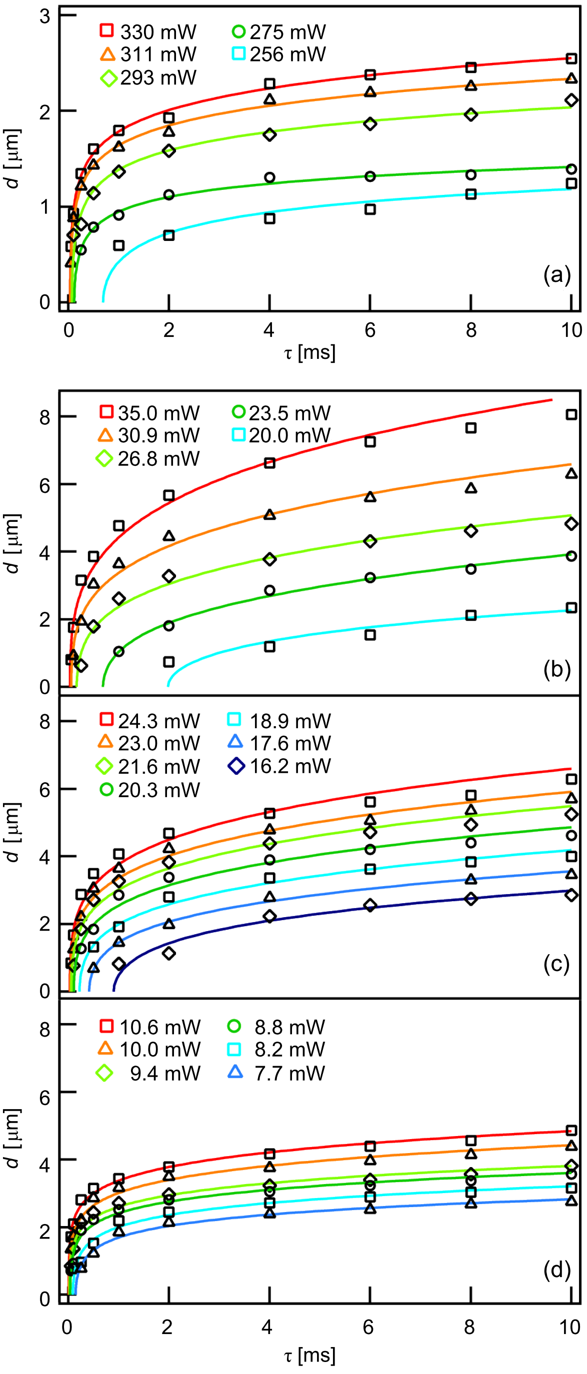

Figure 6: Dependence of the structure diameter *d* on the incident laser power *P* and the pulse length τ of HDT-SAMs on (a) Au/Si substrates with a 30 nm Au layer, (b) Au/glass substrates with a 50 nm Au layer, (c) Au/glass substrates with a 30 nm Au layer and (d) Au/glass substrates with a 10 nm Au layer. The lines are guides for the eyes only.

The choice of the support material, of course, also affects the lateral resolution of the laser technique. Processing of HDT-SAMs on Au/Si substrates can be carried out with a high lateral resolution. In particular, structure sizes are much smaller when compared with the data from equivalent patterning experiments with Au/glass substrates (Figure 6). Minimum structure sizes on Si supports are between 300 and 400 nm. This is somewhat larger when compared with those values in the range of 200–300 nm that were obtained with a very similar laser setup [11]. Structure sizes on Au/glass substrates, in turn, decrease with decreasing Au layer thickness. However, irrespective of the Au layer thickness, the smallest structures on glass supports exhibit a width between 600 and 700 nm, which is to say that no correlation between the achievable minimum structure size and the Au layer thickness is evident. For comparison, in a previous study focusing on photothermal patterning of alkanethiol SAMs on Au/glass substrates, by using high-aperture immersion optics, minimum structure sizes in the range of 400–500 nm were reported [24].

Temperature calculations

All patterning experiments described here were carried out with HDT-coated substrates. Hence, the distinct experimental observations are attributed to the peculiar optical and thermal properties of the Au-coated supports. This, of course, affects the temperature rise on the substrate surface and, hence, is well expected to influence the overall patterning process. Commonly, in photothermal processing with microfocused lasers the local temperature rise is calculated by considering the underlying heat-conduction equation [12]. Constant surface temperatures are rapidly established. Hence, for pulse lengths in the micro- or millisecond range, stationary temperature profiles $T(r)$ are considered, where r corresponds to the radial position relative to the center of the laser spot [11]. The following paragraphs detail how the surface temperature profiles are calculated for Au/Si and Au/glass substrates. A description of all parameters and constants, as introduced in the following, is given in Table 3.

Table 3: Parameters and constants used in temperature calculations and thermokinetic simulations.

Description	Symbol	Value
Laser spot diameter at 1/e	$d_{1/e}$	2 µm
Incident laser power	P	see Figure 7
Laser pulse length	τ	see Figure 7
Sample reflectance	R	see Table 1
Thermal conductivity of Au[a]	κ_{Au}	$3.15\ W \cdot cm^{-1} \cdot K^{-1}$
Thermal conductivity of glass[a]	κ_{glass}	$1.2 \cdot 10^{-2}\ W \cdot cm^{-1} \cdot K^{-1}$
Thermal conductivity of Si at T_0[a]	κ_{Si}	$1.48\ W \cdot cm^{-1} \cdot K^{-1}$
Basic sample temperature	T_0	300 K
Fit parameter for Si[a]	T_k	96 K
Absorption coefficient of Au[b]	α_{Au}	see Table 1
Au layer thickness	h_{Au}	see Table 1
Activation energy[b,c]	E_A	$145\ kJ \cdot mol^{-1}$
Frequency factor[b,c]	ν	$1.1 \cdot 10^{18}\ s^{-1}$
Ideal gas constant	R_G	$8.314\ J \cdot K^{-1} \cdot mol^{-1}$

[a] [12]. We note that the thermal conductivity of thin Au films is generally lower when compared with the bulk value for Au. The exact value depends on the film thickness and on the specific film structure, which, in turn, varies depending on the detailed preparation procedure. Hence, widely varying thermal conductivities are discussed in the literature [35]. For simplicity, the bulk value is considered here. Very similar results are obtained with lower thermal conductivities.
[b] Given parameters refer to effective parameters.
[c] [11].

In the case of Au/Si substrates, laser absorption largely takes place in the thin Au layer, whereas heat conduction is dominated by the underlying Si support. This allows the calculation of the respective surface-temperature profiles on the basis of an analytical solution of the underlying heat-conduction equation considering surface absorption [11,12]:

$$T(r) = T_k + (T_0 - T_k)\exp\left(\frac{\Delta T(r)}{T_0 - T_k}\right) \tag{3}$$

with

$$\Delta T(r) = T_{\max} I_0\left(\left(\frac{\sqrt{2}r}{d_{1/e}}\right)^2\right)\exp\left(-\left(\frac{\sqrt{2}r}{d_{1/e}}\right)^2\right) \tag{4}$$

and

$$T_{\max} = \frac{P(1-R)}{\sqrt{\pi}\kappa_{Si} d_{1/e}} \tag{5}$$

Note, I_0, here and in the following, denotes the modified Bessel function of order zero. Moreover, Equation 3 takes into account the temperature-dependent thermal conductivity of Si.

In the case of Au/glass substrates laser absorption is strictly limited to the thin Au layer. Hence, again surface absorption applies. In contrast to Si, however, glass exhibits a very low thermal conductivity. For this reason, heat conduction is strongly affected by the Au layer. An approach reported by Calder and Sue allows one to take this into account and numerically calculate respective surface temperature profiles [36]. Considering a Gaussian beam and the dimensionless parameters $r^* = 2r/d_{1/e}$, $\kappa^* = \kappa_{Au}/\kappa_{glass}$, $\alpha_{Au}^* = \alpha_{Au} d_{1/e}/2$, and $h^* = 2h_{Au}/d_{1/e}$, the surface temperature profiles $T(r)$ are given by [12,35]:

$$T(r) = T_0 + F\int_0^\infty I(\xi)\left[\begin{Bmatrix}\kappa^* C(\xi) + S(\xi) \\ +\left(K(\xi) - \kappa^*\right)\exp\left(-\alpha_{Au}^* h_{Au}^*\right)\end{Bmatrix} \times \left(C(\xi) + \kappa^* S(\xi)\right)^{-1} - K(\xi)\right] d\xi \tag{6}$$

with

$$F = \frac{2P(1-R)\alpha_{Au}^{*2}}{\pi d_{1/e}\kappa_{Au}} \tag{7}$$

$$I(\xi) = \frac{I_0(\xi r^*)}{2\alpha_{Au}^{*2} - \xi^2}\exp\left(-\frac{\xi^2}{4}\right) \tag{8}$$

$$C(\xi) = \cosh\left(\xi h_{\mathrm{Au}}^{*}\right) \qquad (9)$$

$$S(\xi) = \sinh\left(\xi h_{\mathrm{Au}}^{*}\right) \qquad (10)$$

and

$$K(\xi) = \frac{\xi}{\alpha_{\mathrm{Au}}^{*}} \qquad (11)$$

Despite certain approximations, calculations on the basis of Equations 3–5 and Equations 6–11 provide reasonable estimates of the surface-temperature profiles on the distinct substrates considered here [11,12,36]. This offers insights into the processes that determine the performance of the patterning technique.

To illustrate the impact of the distinct substrate structure on the local temperature rise, surface-temperature profiles exhibiting the same peak temperature of 600 K are shown in Figure 7. Two general effects are evident from these data. Firstly, the laser power required in order to establish a certain peak temperature on Au/glass substrates is much lower than that needed for Au/Si substrates. Moreover, on glass supports, the required laser power strongly decreases with decreasing Au layer thickness. Secondly, the width of the temperature profile is much broader on glass supports and increases with increasing Au layer thickness.

Generally, in photothermal laser processing the peak temperature T_{max} is proportional to the absorbed laser power P_{Abs} and inversely proportional to the thermal conductivity of the substrate κ, that is $T_{\mathrm{max}} \propto P_{\mathrm{Abs}}/\kappa$ [12]. As evident from Table 1, the absorbances of the substrates all are of comparable magnitude. The thermal conductivities of the supports, in turn, strongly vary (Table 3). In particular, depending on the specific temperature, the thermal conductivity of Si is one to two orders of magnitude larger than the thermal conductivity of glass [12]. Hence, the strong difference in the laser power required in order to reach a certain peak temperature rise is attributed to the largely distinct heat dissipation in the supports, Si versus glass.

Au, of course, exhibits a very high thermal conductivity. Thus, with increasing Au layer thickness thermal conduction in Au/glass substrates is more and more affected by heat dissipation within the Au film and the laser power required in order to establish a certain peak temperature increases.

The distinct thermal properties of the substrates also determine the width of the temperature profiles. The width of the temperature profiles on Au/Si substrates is determined by the Si support. Because of the temperature-dependent thermal conductivity of Si this results in a particularly narrow surface-temperature profile. Au/glass substrates, in turn, exhibit a strong difference in lateral and vertical heat conduction. Lateral heat conduction within the Au film is much faster than vertical heat conduction into the bulk of the support. For this reason, surface temperature profiles on Au/glass substrates are much broader when compared to those on Au/Si substrates. Also, with increasing Au layer thickness, in the range of 10 to 100 nm, lateral heat conduction increases. Hence, the width of the temperature profiles broadens.

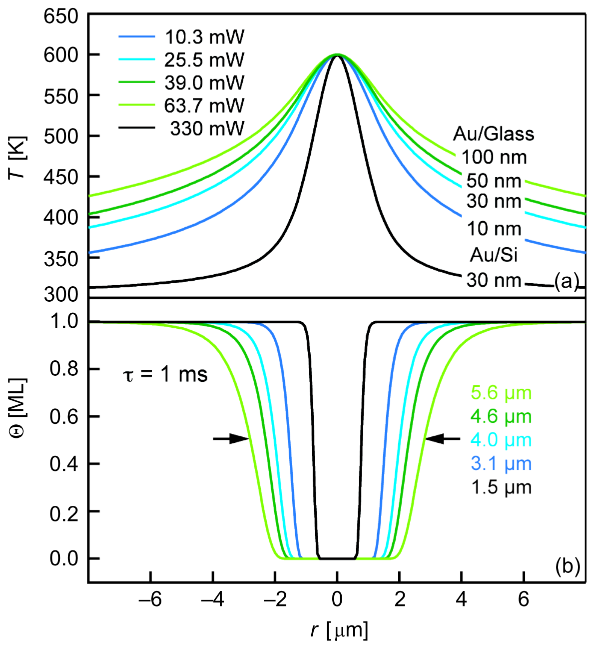

Figure 7: (a) Calculated stationary temperature profiles on different types of Au-coated substrates used for the patterning experiments. Laser powers *P* were adjusted in order to reach the same peak temperature of 600 K. Values are given in the diagram. (b) Corresponding surface coverage profiles at a laser pulse length of τ = 1 ms.

Thermokinetic simulations

Thermokinetic simulations are helpful to illustrate the impact of the surface temperature profiles $T(r)$ on the diameter of the laser-fabricated structures. For this purpose, surface-coverage profiles $\theta(r)$ are calculated assuming first-order kinetics. A description of all parameters and constants, as introduced in the following, is given in Table 3. Due to rapid heating and cooling rates, the reaction time in photothermal laser processing essentially corresponds to the laser pulse length τ. Further details are discussed in a previous study [11]. Following this approach, surface coverage profiles $\theta(r)$ are calculated from

$$\theta(r) = \exp(-k(r)\tau) \quad (12)$$

with $k(r)$ denoting the radially varying reaction rate constant:

$$k(r) = \nu \exp\left(-E_A / R_G T(r)\right) \quad (13)$$

Considering Equation 12 and Equation 13, the local reaction kinetics depends on the irradiation time τ and the rate constant $k(r)$, which itself depends on the temperature. At a constant irradiation time, a certain temperature is required in order to induce substantial desorption of thiol molecules [21,22,37]. Following Equations 3–11 this necessitates a critical laser power density. Processing at short irradiation times demands high power densities, which may lead to complications, such as surface melting and substrate ablation. Hence, the procedure has to be carefully optimized in order to ensure selective processing of the SAM [11,24].

Calculated surface-coverage profiles at a typical laser pulse length of τ = 1 ms are displayed in Figure 7. Clearly, an increase in the diameter of the laser-depleted surface areas can be seen when comparing Au/Si to Au/glass substrates exposing Au layers of the same thickness. Also, for Au/glass substrates the diameters of the structures increase with increasing thickness of the Au layer. This is in agreement with the experimental data shown in Figure 6. Note that the structure diameter at short laser pulse lengths is ultimately determined by the width at the very top of the temperature profiles [11]. As evident from Figure 7a, this width is of comparable size for all Au/glass substrates considered here. For this reason, minimum structures on Au/glass supports are of comparable size irrespective of the Au layer thickness.

Conclusion

Photothermal laser processing has developed into a valuable technique for the fabrication of micro- and nanostructured SAMs. The results presented here emphasize the impact of the substrate on the performance of this technique. In particular, the results of photothermal processing of thiol-based SAMs on Au/Si and Au/glass substrates, with Au layer thicknesses in the range of 10–50 nm, are compared. Minimum structure sizes are significantly smaller on Au/Si substrates. It is, however, worth noting that the processing of Au/glass substrates can be carried out at very low laser powers. In addition, the required laser power for patterning on Au/glass substrates strongly decreases with decreasing Au layer thickness. This opens up new perspectives in low-cost laser processing of thiol-based SAMs. Also parallel laser processing, e.g., by using micromirror displays, appears to be feasible.

Experimental

Au-coated Si and glass supports from commercial suppliers were used as substrates (Albert PVD, Phasis). Si (100) wafers and borosilicate glass slides were chosen as the support materials. A thin Ti film, thickness ≤3 nm, served as an adhesion layer. For the experiments, the substrates were cut into pieces of about 10 × 10 mm^2 in size. For coating with alkanethiol SAMs, all substrates were cleaned with ethanol (p.a., VWR Prolabo) and piranha solution (5 min), a 3:1 mixture of 96% sulfuric acid (suprapur, Merck) and 30% hydrogen peroxide (p.a., AppliChem), rinsed in deionized water (18 MΩ·cm Millipore), dried in a stream of high purity argon (5.0, Air Liquide) and then immersed into a 1 mM solution of 1-hexadecanethiol (HDT, ≥95%, Fluka) in degassed ethanol in a glove box at room temperature for 18 h. Subsequently, the substrates were rinsed in ethanol and dried with argon. All subsequent experiments were carried out immediately after coating.

Photothermal patterning was carried out under ambient conditions using a continuous-wave laser setup [11]. Briefly, the beam of a diode-pumped solid state (DPSS) laser operated at λ = 532 nm was focused onto the sample by means of a standard microscope objective with a numerical aperture of 0.25 (10×, Olympus). The 1/e laser spot diameter $d_{1/e}$ obtained in this way was 2 µm. An acousto–optical modulator was used to chop the laser beam and adjust the laser power. The incident laser power P on the samples was measured on a commercial power meter with a thermal sensor (PM3Q Field Mate, Coherent).

After laser processing the patterns were transferred into the gold film by selective etching [29]. For this purpose, the patterned samples were immersed in a solution of 0.1 M $K_2S_2O_3$ (>98%, Fluka), 1.0 M KOH (p.a., Merck), 0.01 M $K_3Fe(CN)_6$ (99%, Sigma Aldrich), and 0.001 M $K_4Fe(CN)_6$ (purum, 99%, Riedel de Haën) at room temperature. For each substrate type, the immersion time was adjusted in order to completely dissolve the Au film in the laser-depleted surface areas and to minimize widening of the structures due to the isotropic etching process. For this purpose, line patterns were fabricated on a given sample type. Subsequently the laser-patterned sample was stepwise dipped into the etching solution by employing a stepper motor stage. This allows one to test distinct immersion times on a single sample (Figure 8). After etching, the samples were rinsed in deionized water and blown dry with argon.

For the characterization of bare and HDT-coated substrates, UV–vis spectroscopy, laser reflectance and transmittance measurements, contact angle measurements and infrared reflection–absorption spectroscopy (IRRAS) were used. UV–vis spectra were measured with a Perkin Elmer UV–vis spectrometer (Lambda 950). Laser reflectance and transmittance

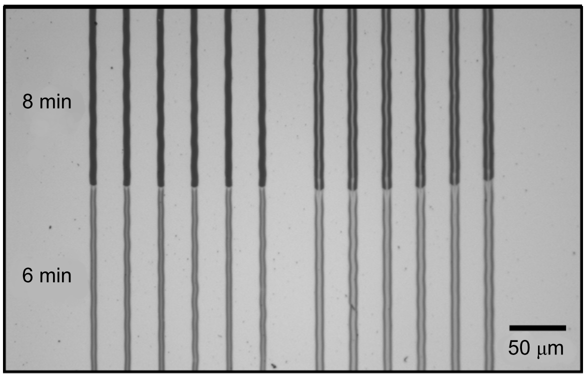

Figure 8: Optical micrograph of a laser-patterned HDT SAM on a Au/glass substrate exposing a 10 nm thick Au layer after wet-chemical etching. The micrograph displays surface areas that have been dipped into the etchant for 6 min (bottom) or 8 min (top).

measurements were carried out at λ = 532 nm by using the DPSS laser of the patterning setup and a power meter with a thermal sensor (cf. above). Static water contact angles were measured with an OEG SURFTENS universal goniometer. Infrared spectra were collected with a Bruker spectrometer (Vertex 70) equipped with a variable-angle reflection accessory (A513). A polarizer was placed in front of the sample in order to measure spectra with p-polarized light. The angle of the incident light was set to 85° with respect to the surface normal. The spectra were taken at a resolution of 4 cm^{-1} by using 1024 scans and were referenced to a clean gold sample without any further data manipulation.

For characterization of patterned samples, optical microscopy (BX41TS, Olympus) and AFM (Autoprobe CP from Veeco) were used. AFM images were recorded in contact mode with standard cantilevers. Width measurements were not corrected for tip-size effects and refer to values measured at half depth.

Acknowledgements

Financial support by the European Union, and the Ministry of Innovation, Science and Research of the State of North Rhine-Westphalia in Germany (NanoEnergieTechnikZentrum, NETZ, Objective 2 Programme: European Regional Development Fund, ERDF), the BASF Coatings AG and the Deutsche Forschungsgemeinschaft (DFG, Grant HA-2769/3-1, Grant HA-2769/5-1, SPP 1327) is gratefully acknowledged. The authors thank S. Franzka and D. Diesing for helpful discussions. N.H. also gratefully thanks Eckart Hasselbrink for his continuing support.

References

1. Love, J. C.; Estroff, L. A.; Kriebel, J. K.; Nuzzo, R. G.; Whitesides, G. M. *Chem. Rev.* **2005,** *105,* 1103. doi:10.1021/cr0300789
2. Onclin, S.; Ravoo, B. J.; Reinhoudt, D. N. *Angew. Chem., Int. Ed.* **2005,** *44,* 6282. doi:10.1002/anie.200500633
3. Buriak, J. M. *Chem. Rev.* **2002,** *102,* 1271. doi:10.1021/cr000064s
4. Schreiber, F. *Prog. Surf. Sci.* **2000,** *65,* 151. doi:10.1016/S0079-6816(00)00024-1
5. Sullivan, T. P.; Huck, W. T. S. *Eur. J. Org. Chem.* **2003,** 17. doi:10.1002/1099-0690(200301)2003:1<17::AID-EJOC17>3.0.CO;2-H
6. Wouters, D.; Hoeppener, S.; Schubert, U. S. *Angew. Chem., Int. Ed.* **2009,** *48,* 1732. doi:10.1002/anie.200801013
7. Zharnikov, M.; Grunze, M. *J. Vac. Sci. Technol., B: Microelectron. Nanometer Struct.–Process., Meas., Phenom.* **2002,** *20,* 1793. doi:10.1116/1.1514665
8. Xia, Y.; Whitesides, G. M. *Angew. Chem., Int. Ed.* **1998,** *37,* 550. doi:10.1002/(SICI)1521-3773(19980316)37:5<550::AID-ANIE550>3.0.CO;2-G
9. Smith, R. K.; Lewis, P. A.; Weiss, P. S. *Prog. Surf. Sci.* **2004,** *75,* 1. doi:10.1016/j.progsurf.2003.12.001
10. Leggett, G. J. *Chem. Soc. Rev.* **2006,** *35,* 1150. doi:10.1039/b606706a
11. Mathieu, M.; Hartmann, N. *New J. Phys.* **2010,** *12,* 125017. doi:10.1088/1367-2630/12/12/125017
12. Hartmann, N. Sub-wavelength patterning of organic monolayers via nonlinear processing with femtosecond laser pulses. In *Laser Pulses, Coherence and Ultrashort Pulse Laser Emission;* Duarte, F. J., Ed.; InTech, 2010. ISBN: 978-953-307-242-5, open access: http://intechopen.com.
13. Bäuerle, D. *Laser Processing and Chemistry;* Springer: Berlin, 2011.
14. Bäuerle, D. *Grundlagen und Anwendungen in Photonik, Technik, Medizin und Kunst;* Wiley-VCH: Berlin, 2008.
15. Ali, M.; Wagner, T.; Shakoor, M.; Molian, P. A. J. *Laser Appl.* **2008,** *20,* 169. doi:10.2351/1.2955556
16. Chong, T. C.; Hong, M. H.; Shi, L. P. *Laser Photon. Rev.* **2010,** *4,* 123. doi:10.1002/lpor.200810057
17. Koch, J.; Korte, F.; Fallnich, C.; Ostendorf, A.; Chichkov, B. N. *Opt. Eng.* **2005,** *44,* 051103. doi:10.1117/1.1904053
18. Balgar, T.; Franzka, S.; Hartmann, N. *Appl. Phys. A* **2006,** *82,* 689. doi:10.1007/s00339-005-3439-2
19. Dahlhaus, D.; Franzka, S.; Hasselbrink, E.; Hartmann, N. *Nano Lett.* **2006,** *6,* 2358. doi:10.1021/nl061608u
20. Klingebiel, B.; Scheres, L.; Franzka, S.; Zuilhof, H.; Hartmann, N. *Langmuir* **2010,** *26,* 6826. doi:10.1021/la903926z
21. Shadnam, M. R.; Kirkwood, S. E.; Fedosejevs, R.; Amirfazli, A. *Langmuir* **2004,** *20,* 2667. doi:10.1021/la0354584
22. Shadnam, M. R.; Kirkwood, S. E.; Fedosejevs, R.; Amirfazli, A. *J. Phys. Chem. B* **2005,** *109,* 11996. doi:10.1021/jp0500642
23. Rhinow, D.; Hampp, N. A. *Adv. Mater.* **2007,** *19,* 1967. doi:10.1002/adma.200602387
24. Iversen, L.; Younes-Metzler, O.; Martinez, K. L.; Stamou, D. *Langmuir* **2009,** *25,* 12819. doi:10.1021/la901872g
25. Klingebiel, B.; Schröter, A.; Franzka, S.; Hartmann, N. *ChemPhysChem* **2009,** *10,* 2000. doi:10.1002/cphc.200900278
26. Zhang, F.; Pei, L.; Bennion, E.; Jiang, G.; Connley, D.; Yang, L.; Lee, M. V.; Davis, R. C.; Smetkowski, V. S.; Strossman, G.; Linford, M. R.; Asplund, M. C. *Langmuir* **2006,** *22,* 10863. doi:10.1021/la060562h
27. Geldhauser, T.; Leiderer, P.; Boneberg, J.; Walheim, S.; Schimmel, T. *Langmuir* **2008,** *24,* 13155. doi:10.1021/la801812j
28. Mathieu, M.; Schunk, D.; Franzka, S.; Mayer, C.; Hasselbrink, E.; Hartmann, N. *Small* **2009,** *5,* 2099. doi:10.1002/smll.200801933
29. Xia, Y.; Zhao, X.-M.; Kim, E.; Whitesides, G. M. *Chem. Mater.* **1995,** *7,* 2332. doi:10.1021/cm00060a023

30. Siegel, J.; Lyutakov, O.; Rybka, V.; Kolská, Z.; Svorcik, V. *Nanoscale Res. Lett.* **2011,** *6,* 96. doi:10.1186/1556-276X-6-96
31. Doron-Mor, I.; Barkay, Z.; Filip-Granit, N.; Vaskevich, A.; Rubinstein, I. *Chem. Mater.* **2004,** *16,* 3476. doi:10.1021/cm049605a
32. Palik, E. D. *Handbook of Optical Constants of Solids;* Academic Press: Boston, 1985.
33. Nuzzo, R. G.; Dubois, L. H.; Allara, D. L. *J. Am. Chem. Soc.* **1990,** *112,* 558. doi:10.1021/ja00158a012
34. Pan, H.; Hwang, D. J.; Ko, S. H.; Clem, T. A.; Fréchet, M. J.; Bäuerle, D.; Grigoropoulos, C. P. *Small* **2010,** *6,* 1812. doi:10.1002/smll.201000345
35. Bourgoin, J.-P.; Allogho, G.-G.; Haché, A. *J. Appl. Phys.* **2010,** *108,* 073520. doi:10.1063/1.3490185
36. Calder, I. D.; Sue, R. *J. Appl. Phys.* **1982,** *53,* 7545. doi:10.1063/1.330123
37. Zhang, M. Y.; Shadnam, M. R.; Amirfazli, A. *Optics & Laser Technol.* **2011,** *43,* 1377. doi:10.1016/j.optlastec.2011.03.034

License and Terms

The definitive version of this article is the electronic one which can be found at:
doi:10.3762/bjnano.3.8

Beilstein Journal
of Nanotechnology

Surface functionalization of aluminosilicate nanotubes with organic molecules

Wei Ma[1], Weng On Yah[2], Hideyuki Otsuka[1,2,3] and Atsushi Takahara*[1,2,3,§]

Review

Address:
[1]Institute for Materials Chemistry and Engineering, Kyushu University, 744 Motooka, Nishi-ku, Fukuoka 819-0395, Japan, [2]Graduate School of Engineering, Kyushu University, 744 Motooka, Nishi-ku, Fukuoka 819-0395, Japan and [3]International Research Center for Molecular Systems, Kyushu University, 744 Motooka, Nishi-ku, Fukuoka 819-0395, Japan

Email:
Atsushi Takahara* - takahara@cstf.kyushu-u.ac.jp

* Corresponding author
§ Fax: +81-92-802-2518; Tel: +81-92-802-2517.

Keywords:
chemisorption; imogolite; inorganic nanotube; surface functionalization.

Beilstein J. Nanotechnol. **2012,** *3,* 82–100.
doi:10.3762/bjnano.3.10

Received: 31 October 2011
Accepted: 06 January 2012
Published: 02 February 2012

This article is part of the Thematic Series "Self-assembly at solid surfaces".

Guest Editors: S. R. Cohen and J. Sagiv

Abstract

The surface functionalization of inorganic nanostructures is an effective approach for enriching the potential applications of existing nanomaterials. Inorganic nanotubes attract great research interest due to their one-dimensional structure and reactive surfaces. In this review paper, recent developments in surface functionalization of an aluminosilicate nanotube, “imogolite”, are introduced. The functionalization processes are based on the robust affinity between phosphate groups of organic molecules and the aluminol (AlOH) surface of imogolite nanotubes. An aqueous modification process employing a water soluble ammonium salt of alkyl phosphate led to chemisorption of molecules on imogolite at the nanotube level. Polymer-chain-grafted imogolite nanotubes were prepared through surface-initiated polymerization. In addition, the assembly of conjugated molecules, 2-(5’’-hexyl-2,2’:5’,2’’-terthiophen-5-yl)ethylphosphonic acid (HT3P) and 2-(5’’-hexyl-2,2’:5’,2’’-terthiophen-5-yl)ethylphosphonic acid 1,1-dioxide (HT3OP), on the imogolite nanotube surface was achieved by introducing a phosphonic acid group to the corresponding molecules. The optical and photophysical properties of these conjugated-molecule-decorated imogolite nanotubes were characterized. Moreover, poly(3-hexylthiophene) (P3HT) chains were further hybridized with HT3P modified imogolite to form a nanofiber hybrid.

Review

Surface functionalization of metal or metal-oxide surfaces has received considerable attention in recent years [1-3]. It presents an easy, accurate and precise approach for the fabrication of functional surfaces with highly controlled chemical properties. Functionalized surfaces can be used in a number of applications, including passivation of metal surfaces, adhesion promotion, and adsorption of biomolecules to substrates for sensing [1,4]. Recently, the assembly of organic molecules on inorganic nanostructures instead of flat surfaces has been demonstrated to be an effective process for preparing various previously untested functional organic/inorganic nanohybrids. The organic parts generally provide functional groups for the nanohybrids, while the inorganic parts act as the scaffold for organic molecules and determine both the individual morphology and the texture of the obtained nanohybrids [5,6]. Among various nanostructures with different shapes, nanotubes attract special research interest, not only because of their high mechanical strength, but also because of their large aspect ratios and ability to form network structures. It is no doubt that nanotubes with reactive surfaces and a reliable supply are preferred for the application as scaffold of organic molecules. Carbon nanotubes (CNTs) play an important role in the nanotube family. However, the surface of CNTs is inert for most molecules. On the contrary, clay nanotubes present a reactive surface for numerous coupling agents and are emerging as useful structural units for many kinds of nanohybrid materials [7-11].

For the assembly of organic molecules on an inorganic surface, most work has been carried out with alkyl silanes adsorbed on silicon oxide or with thiols adsorbed on noble metals [1,12,13]. A different class of self-assembling agents, namely phosphonic and phosphoric acids, has gained more and more attention due to their ability to bind to a wide range of metal-oxide surfaces [14]. Organosilane and organophosphorus coupling molecules show remarkably different reactivities. Silicon derivatives are prone to nucleophilic substitution, and the main reactions involved in the assembly process are hydrolysis and condensation reactions. Heterocondensation between the organosilanols and the inorganic part leads to the formation of Si–O–M bonds, while homocondensation between two coupling molecules leads to the formation of Si–O–Si bonds. The presence of a trace amount of water appears to be necessary for the formation of complete monolayers [15,16]. However, homocondensation increases as the water content increases and there is a risk of formation of multilayers due to the uncontrolled polymerization of the multifunctional organosilanes [17,18]. Phosphorus derivatives are much less sensitive to nucleophilic substitution than silicon derivatives are, because phosphorus has a higher electrophilicity compared to silicon. Consequently, P–O–C bonds are quite stable against hydrolysis, and P–O–H groups are quite stable against homocondensation. Thus, during the surface-modification process, they should form only monolayers, independent of the water content. Moreover, organophosphoric acids can selectively assemble on the surfaces of metal oxides rather than on SiO_2 surfaces in an aqueous medium, due to the sensitivity of Si–O–P bonds to hydrolysis [19-21].

In this review paper, the chemisorption and assembly of several phosphonic-acid-containing organic compounds on imogolite nanotubes, based on the robust affinity between the phosphate groups and the nanotube surface, is reviewed.

Aluminosilicate nanotube

Structure of imogolite

Imogolite was discovered as early as 1962, and detail investigation using electron diffraction analysis by Cradwick et al. in 1972 confirmed its composition [$Al_2O_3·SiO_2·2H_2O$] [22]. The schematic representation of imogolite is shown in Figure 1. The gas adsorption data of N_2, CO_2, and CH_4 concluded that imogolite possesses an inner-pore diameter of 1 nm [23]. The wall structure of imogolite comprises a layer of gibbsite on the outer wall, and a layer of silicate on the inner wall [22]. The latest crystallographic study showed that the imogolite tubes pack in a monoclinic arrangement through hydrogen bonds that form

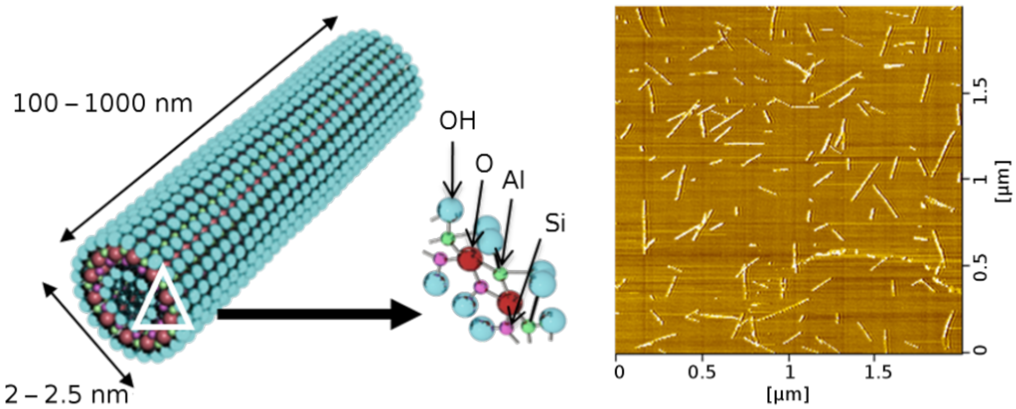

Figure 1: Schematic illustration of imogolite-nanotube structure (left). DFM image of imogolite (right).

between the tubes (Figure 2) [24]. The artificial method to prepare imogolite was proposed by Farmer et al. in 1977 using the mild chemistry of $Al(ClO_4)_3$ and $Si(OH)_4$ [25]. The formation mechanism of imogolite is not well understood, but an early study suggested that the evolution of the tubular morphology is started by the binding of isolated silicate groups to the gibbsite sheet, in which the tetravalent Si atoms pull the oxygen atoms of the gibbsite sheet into the curvature cylinder [26]. Attempts to tune the imogolite dimensions appear to be futile, as the tubular structure does not change significantly throughout the synthesis process and the formation of nanotubes occurs at an early stage [24]. Individually dispersing imogolite nanotubes on a transmission electron microscopy (TEM) carbon grid, by means of the droplet evaporation technique, has made semiquantitative analysis of imogolite dimensions possible [27]. Semiquantitative analysis on the TEM images supports the kinetic-growth mechanism, in which protoimogolites and short imogolites are observed in the initial stage of synthesis, and the average length of the nanotubes increases rapidly with reaction time [28].

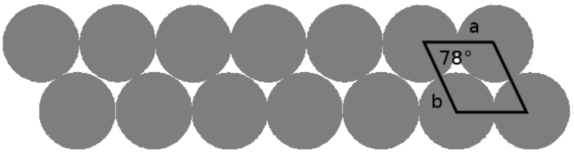

Figure 2: Monoclinic solid-state packing arrangement of the imogolite nanotubes.

Imogolite nanotubes through chemical synthesis and natural resource

The synthesis of imogolite was first reported by Farmer et al. in 1977 [25]. As a typical preparation method, a tetraethoxysilane solution mixed with aluminum chloride ($AlCl_3 \cdot 6H_2O$) aqueous solution is pH adjusted to 5.0 giving the resulting solution of 2.4 mM of Al and 1.4 mM of Si. The pH adjusted solution is heated under reflux at 369 K for 120 h and gelated by NaCl solution at room temperature. The suspended material is washed with deionized water, filtered, and redispersed again in a weak acidic solution. Finally the imogolite solution is freeze dried and the final product of imogolite, which appears as cottonlike solid, is recovered. It is also possible to synthesize aluminogermanate imogolite, in which the Si is substituted with Ge, from a solution containing aluminum chloride and tetraethyl orthogermanate. The Ge substituted imogolite was found to be similar in tubular morphology to the natural imogolite and the external diameter could be expanded up to 3.3 nm by increasing the Ge/(Ge + Si) ratio. The expansion is attributed to the longer O–O distance in GeO_4, which decreases the curvature of the gibbsite sheet [29,30].

In an alternative method imogolite can be derived from glassy volcanic ash soil, but it then usually contains organic and inorganic impurities. These impurities can be separated from imogolite by purification as described in the literature [31]. In the typical purification procedure, the imogolite mineral collected from Kitakami, Iwate, Japan is suspended in water by ultrasonication. Occluded organic contaminants are removed by treating the mineral with hot 1.8 M H_2O_2, followed by citrate-bicarbonate (CB) to extract inorganic impurities (iron and manganese oxide). The resulting gel is washed with cold 0.5 M Na_2CO_3 to remove citrate remnants, and redispersed in weak acidic solution. The final product, cottonlike imogolite, is obtained by freeze-drying of the solution. Figure 3 shows the step-by-step purification procedure to recover the imogolite from the raw mineral.

Surface functionalization of the imogolite-nanotube surface

Chemisorption of alkyl phosphate on imogolite nanotubes

As mentioned above, imogolite is a very useful inorganic nanotube. The adsorption and assembly of organic molecules on the imogolite surface is expected to produce interesting results. Imogolite may act as a one-dimensional scaffold for functional molecules. Moreover, the surface energy of imogolite nanotubes can be lowered by the organic layer, and this can greatly improve the dispersibility of imogolite in organic solvents, as well as in various polymer matrices and nanocomposites. The metal–oxygen–phosphorus (M–O–P) interaction plays an important role for surface functionalization of imogolite nanotubes. The strong affinity between octadecylphosphonic acid and the imogolite surface has been reported by our group [32]. More recently, we developed an approach for anchoring alkyl chains on an imogolite surface from aqueous solution [33]. The adsorption of molecules on the inorganic surface from aqueous solution is particularly necessary for imogolite, because imogolite nanotubes are dispersible only in water, due to their AlOH surface. For this purpose, a step toward the modification of imogolite nanotubes at the nanotube level with alkyl phosphate from an aqueous solution was achieved by converting the water-insoluble alkyl phosphate into the corresponding water-soluble ammonium salt. The detailed assembly procedure is shown in Figure 4. The ammonium salt of dodecylphosphate ($DDPO_4(NH_4)_2$) was precipitated from a 2-propanol solution of dodecylphosphoric acid ($DDPO_4H_2$) by the addition of ammonia. The outer surface of imogolite nanotubes is composed of aluminol groups, thus, it can be positively charged and dispersed under acidic conditions by electrostatic repulsion. It should be noted that surface modification of inorganic nanostructures in an aqueous solution is an environmentally friendly method.

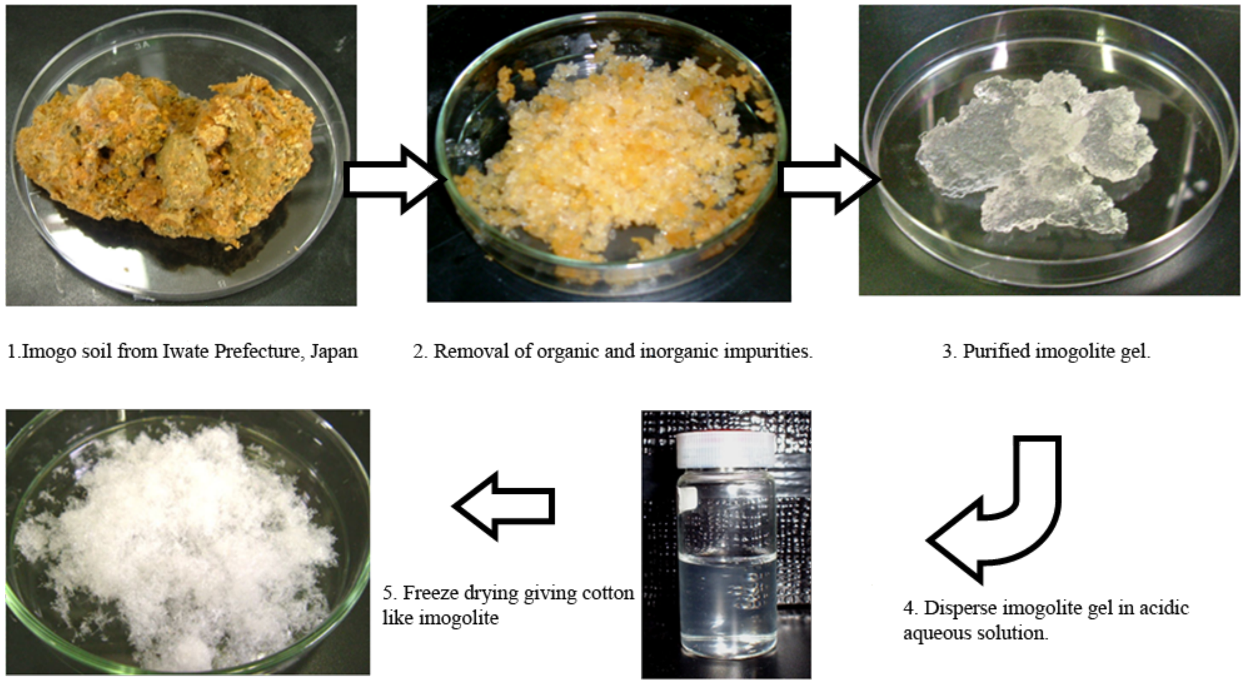

1.Imogo soil from Iwate Prefecture, Japan

2. Removal of organic and inorganic impurities.

3. Purified imogolite gel.

4. Disperse imogolite gel in acidic aqueous solution.

5. Freeze drying giving cotton like imogolite

Figure 3: Purification steps of imogolite from imogo soil.

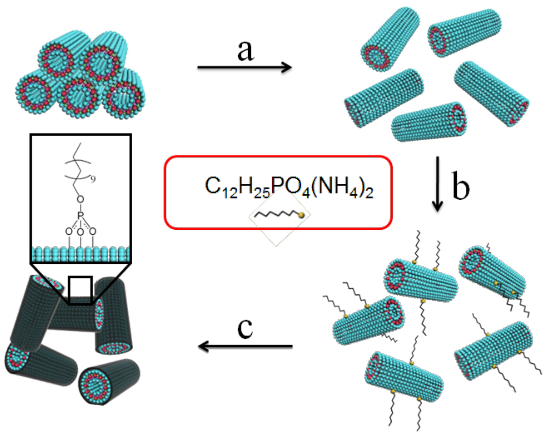

Figure 4: Schematic illustration of dodecylphosphate chemisorbing onto the surface of individually dispersed imogolite nanotubes: (a) Dispersion of freeze-dried imogolite powder into weak acidic water by electrostatic repulsion; (b) chemisorption of dodecylphosphate onto the outer surface of individually dispersed imogolite nanotubes; (c) purifying the product and solidifying it by freeze-drying. Reprinted with permission from W. Ma et al., *Chem. Lett.* **2011,** *40,* 159–161 [33]. © 2011, The Chemical Society of Japan.

Figure 5 shows the thermogravimetric profiles of the original imogolite, $DDPO_4$-imogolite, and $DDPO_4H_2$. The synthetic imogolite loses 30% of its total mass in two steps. The first step is from 300 to 420 K with a weight loss of 13.5%, and the second step is from 420 to 800 K with a weight loss of 16.5%. The first step is attributed to the loss of adsorbed water, while the second one corresponds to the dehydroxylation of imogolite. $DDPO_4$-imogolite has a similar weight-loss profile, although the second step also includes the decomposition of dodecylphosphate. The weight loss in the first step is 8.5%, while in the second step it is 33.5%. $DDPO_4H_2$ loses 70% of its initial mass at 800 K, indicating that phosphate groups are left over after the thermal decomposition. Thus, taking the weight loss of imogolite and dodecylphosphate into account, the imogolite content in $DDPO_4$-imogolite is calculated to be 65.6%. Moreover, dodecyl phosphate exhibits an improved thermal stability in $DDPO_4$-imogolite compared with the neat dodecylphosphoric acid. The onset decomposition temperature for $DDPO_4H_2$ is 420 K; while for the immobilized dodecyl phosphate the temperature increases to 520 K. This may be because, at the same temperature, the thermal motion of the anchored dodecylphosphate molecules is significantly restricted compared to the unanchored ones.

The interaction between imogolite and $DDPO_4$ is confirmed by IR measurements and X-ray photoelectron spectroscopy (XPS) [33]. The typical absorption bands of imogolite at 995, 935, and 560 cm^{-1} still exist, suggesting the retention of the Si–O–Al skeleton in imogolite nanotubes, while the absorption at 995 cm^{-1} is strengthened by the coexistent absorption of the phosphate groups. The absorption of P=O at 1239 cm^{-1} for $DDPO_4H_2$ and at 1201 cm^{-1} for $DDPO_4(NH_4)_2$ disappears from the spectrum of $DDPO_4$-imogolite, presumably due to the

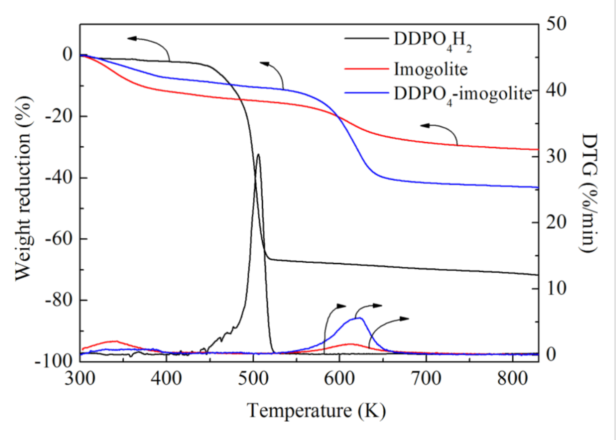

Figure 5: Thermogravimetric profiles of the original imogolite, DDPO$_4$H$_2$, and DDPO$_4$-imogolite in N$_2$ atmosphere at a heating rate of 10 K min^{-1}.

condensation between the phosphate groups and the aluminol groups. Figure 6 shows the high-resolution XPS spectra of Al$_{2p}$. For the original imogolite, the Al$_{2p}$ signal is found around 74.3 eV with a symmetric peak; while for DDPO$_4$-imogolite the Al$_{2p}$ peak becomes wide and asymmetric, and this can be fitted with two Gaussian curves corresponding to a contribution from peaks at 74.3 eV and 76.3 eV. The second component is ascribed to an increase in the positive charge on Al atoms due to the formation of Al–O–P bonds at the surface of imogolite, while the first indicates the unreacted Al–OH. Thus, it can be concluded that dodecylphosphate attaches to the surface of imogolite through covalent interaction.

In order to obtain further insight into the molecular aggregation state of the DDPO$_4$-imogolite, wide-angle X-ray diffraction (WAXD) measurements were carried out. Figure 7 shows WAXD profiles of the freeze-dried imogolite and DDPO$_4$-imogolite. Scattering vector q [nm^{-1}] is defined as q = (4π/λ)sinθ, where θ is the scattering angle. The d-spacing was calculated by d [nm] = 2π/q. The WAXD pattern of imogolite consists of a number of diffractions. The diffraction peaks at 2.25, 1.62, 0.93, and 0.67 nm for the freeze-dried imogolite can be assigned to the (100), (110), (001), and (211) planes of the quasi-monoclinic packing of the synthetic imogolite nanotubes [24]. For DDPO$_4$-imogolite, the broad diffraction around q = 13.8 nm^{-1} is probably due to the disordered grafted alkyl chains. The diffractions at 2.25 and 1.62 nm suggest the presence of imogolite bundles. On the other hand, however, the intensity of the diffractions at 2.25 and 1.62 nm significantly decreased compared with those of the pure imogolite, indicating the exfoliation of the imogolite bundles. Imogolite cylinders may interact through their Al–OH groups, and bundles of imogolite tubes still exist even in weak acidic water. When dodecylphosphate attaches to the surface of these bundles, a one-dimensional core–shell structure forms with imogolite bundles as the core. However, it is expected that only tightly packed bundles can be maintained during the modification process. The modification agent may easily enter the gaps within the loosely packed bundles and adsorb on the surface.

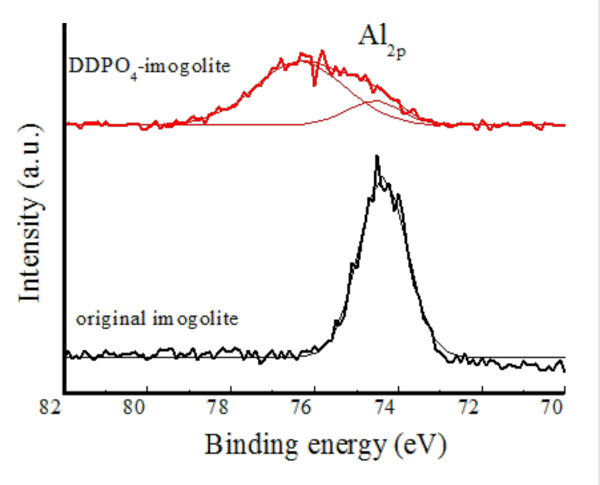

Figure 6: High-resolution XPS spectra for Al$_{2p}$ of the original imogolite and DDPO$_4$-imogolite. Adapted with permission from W. Ma et al., *Chem. Lett.* **2011,** *40,* 159–161 [33]. © 2011, The Chemical Society of Japan.

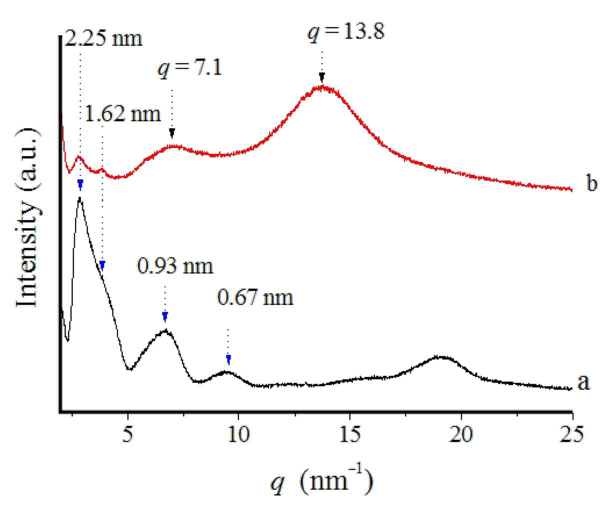

Figure 7: WAXD profiles of (a) original imogolite and (b) DDPO$_4$-imogolite. Adapted with permission from W. Ma et al., *Chem. Lett.* **2011,** *40,* 159–161 [33]. © 2011, The Chemical Society of Japan.

The individual tubular structure of the dodecylphosphate modified imogolite is directly confirmed by TEM observation. The sample for TEM observation was prepared by placing a drop of the DDPO$_4$-imogolite suspension (toluene as the solvent) on a carbon-coated copper grid and allowing it to dry in air. Figure 8 shows the TEM image of DDPO$_4$-imogolite, in which fiberlike structures with a diameter about 2 nm were observed. This diameter is similar to that of the individual imogolite nanotubes, indicating that these are individual tubes rather than bundles. To the best of our knowledge, this is the first observation of individual imogolite nanotubes with a hydrophobic external surface.

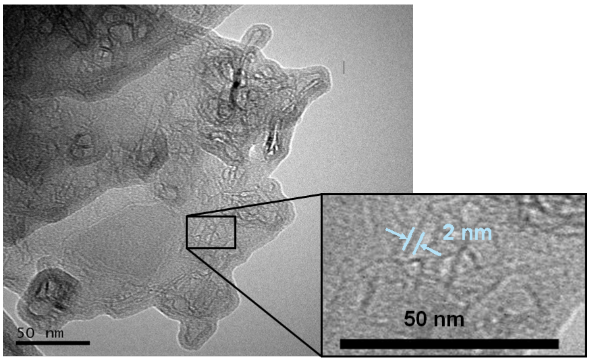

Figure 8: TEM image of $DDPO_4$-imogolite. Reprinted with permission from W. Ma et al., *Chem. Lett.* **2011,** *40,* 159–161 [33]. © 2011, The Chemical Society of Japan.

The wettability of this dodecylphosphate modified imogolite nanotube was evaluated by measurement of the water contact angle (CA) of the $DDPO_4$-imogolite film. $DDPO_4$-imogolite was dispersed in ethanol at a concentration of 2 mg mL^{-1}, and this dispersion was cast onto a silicon wafer by spin coating. For comparison, an aqueous imogolite solution was also cast onto a silicon wafer by the same procedure. The static contact angle was measured by dropping 1 μL water onto the corresponding surface. As shown in Figure 9, the static contact angle for the original imogolite cast surface was 22°. In contrast, for the $DDPO_4$-imogolite cast surface, the contact angle increased to 93°. This result indicates that the hydrophilicity of the external surface of imogolite is changed upon absorption of $DDPO_4$, which converts the hydrophilic surface of imogolite nanotubes to a hydrophobic one.

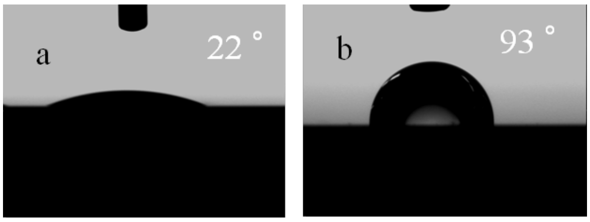

Figure 9: Static-contact-angle images of water droplets on a silicon wafer cast with (a) original imogolite and (b) $DDPO_4$-imogolite. Reprinted with permission from W. Ma et al., *Chem. Lett.* **2011,** *40,* 159–161 [33]. © 2011, The Chemical Society of Japan.

Poly(methyl methacrylate) grafted imogolite nanotubes

The above content demonstrated the chemisorption of alkyl phosphonic chains on imogolite surface at the nanotube level from an aqueous solution. However, such low-molecular-weight compounds are insufficient to prevent nanotube aggregation. As a better alternative, the grafting of polymer chains from the nanostructure surface has been developed as a powerful technique for homogeneously dispersing nanostructures [34-36]. Several strategies can be used to graft polymers from the inorganic surface, including “grafting to”, “grafting through” and “grafting from” approaches [37,38]. In many cases, “grafting from” is preferred, in which the polymer chains are in situ grown from the surface by means of surface-initiated polymerization, and the grafting density is higher compared to the “grafting to” and “grafting through” approaches. The “grafting from” process can be performed with various polymerization techniques, from anionic and cationic to free-radical polymerization [39]. Free-radical polymerization is preferable to ionic processes on economic grounds, because it is easier to perform and much less sensitive to the presence of water.

Recently, we reported the grafting of poly(methyl methacrylate) (PMMA) on the imogolite surface, in which surface-initiated radical polymerization, called “activators regenerated by electron transfer for atom transfer radical polymerization” (ARGET ATRP), was used [40]. ARGET ATRP is a newly developed controlled/living radical polymerization technique, and has been attracting more and more research interest due to its convenience, e.g., it can be carried out without strict deoxygenation and only needs ppm levels of catalyst [41,42]. Figure 10 presents the preparation procedure of a PMMA grafted imogolite nanotube.

To realize polymerization of MMA from the surface of imogolite nanotubes, a suitable surface-attachable ATRP initiator is needed. So far, various ATRP initiators that can be fixed on inorganic surfaces have been synthesized by several groups [43-47]. Among them, surface-attachable groups have almost exclusively been alkoxy- or chlorosilanes. However, organosilanes are not suitable for the modification of imogolite, because surface modification with organosilanes usually needs dry conditions in order to prevent unfavorable side reactions. Whereas with an AlOH functionalized external surface imogolite is a very hydrophilic material and can be dispersed only in acidic water by electrostatic repulsion [48]. Moreover, surface bonds between organosilane and the external surface of imogolite have been reported to be labile in a humid atmosphere [49]. On the other hand, organophosphorous compounds appear complementary to organosilanes, as they show an excellent affinity toward metal oxides [14,36,50]. In addition, they are

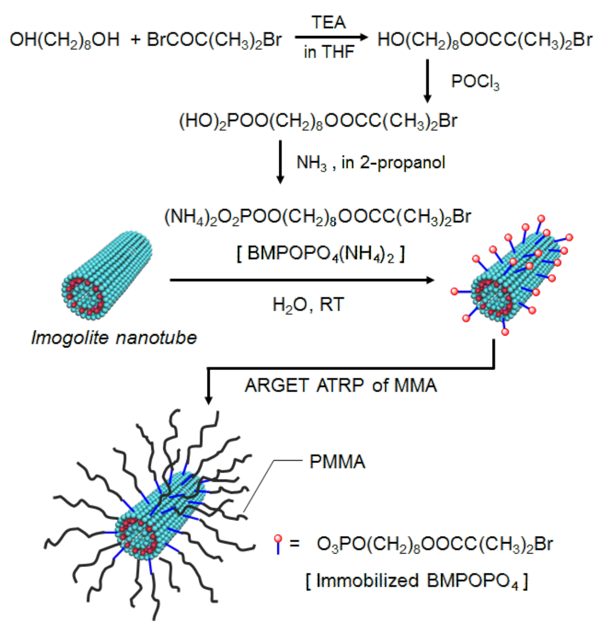

Figure 10: Schematic representation for the preparation of a PMMA grafted imogolite nanotubes. Reprinted with permission from W. Ma et al., *Chem. Commun.* **2011,** *47,* 5813–5815 [40]. © 2011, The Royal Society of Chemistry.

rather insensitive to nucleophilic substitution and prone to heterocondensation (M–O–P bond formation) as compared to homocondensation (P–O–P). Thus, surface modification with organophosphorous compounds has the advantage of being operable in a wide range of solvents from aprotic to protic, and even in water.

In line with the above discussion, we synthesized an initiator carrying a phosphoric acid group, 8-(2-bromo-2-methylpropanoyloxy) octyl phosphoric acid ($BMPOPO_4H_2$), which was further converted to a water-soluble ammonium salt [$BMPOPO_4(NH_4)_2$]. Figure 11 shows the chemical structure of this initiator molecule. To the best of our knowledge, the closest analogous molecules appear in two papers, in which 11-(2-bromoisobutyrate)-undecyl-1-phosphonic acid and its diethyl ester were synthesized [51,52]. However, these two molecules were both designed for application in organic solvents and are not soluble in water. The homogeneous modification of the imogolite surface can be achieved by using a water-soluble initiator carrying a surface-attachable group. In addition, the molecule we designed here seems capable of providing the modified imogolite with adequate hydrophobicity, as it contains a relatively long hydrophobic chain.

The ATRP initiator $BMPOPO_4$ was immobilized on the imogolite surface from an aqueous solution at room temperature. The pH is an important parameter in this modification reaction. A low pH value is favorable for the fine dispersion of imogolite in water. However, if the pH is too low, the phosphate group may cause the dissolution of metal oxides. It was reported that $PhPO(OH)_2$ can cause the release of aluminum cations from the alumina surface by cleavage of Al–O–Al bonds at pH 4 [54]. In this work, the acidity of the initial reaction mixture was controlled and set to be pH 5 in order to avoid a similar dissolution process of imogolite, whose external surface is similar to that of alumina. In our case, a pH 5 acetate buffer was employed. The adsorption of $BMPOPO_4$ onto the imogolite surface was confirmed by FT-IR measurements and XPS analysis. FT-IR spectra show that the Al–O–Si vibrations of imogolite at 992 and 930 cm^{-1} still exist after modification, indicating that this reaction does not destroy the structure of the imogolite nanotube [40]. The absorbance bands at 2932 cm^{-1} (C–H) and 1735 cm^{-1} (C=O) confirm the adsorption of the ATRP initiator onto the imogolite surface, while the absence of the N–H vibration band at 3130 cm^{-1} indicates that ammonium counter cations do not adsorb onto imogolite. XPS spectra (Figure 12) provide more information on the interaction between the imogolite surface and the ATRP initiator. In the wide-scan XPS spectra of $BMPOPO_4$-imogolite, the characteristic peaks of P_{2p}, P_{2s}, and Br_{3d} were found at around 134.5, 191.8, and 70.0 eV, respectively. In addition, no signal of nitrogen was found, further confirming that the ammonium counter cations do not adsorb onto imogolite. The high-resolution XPS spectra of Al_{2p} show that the peak position of Al_{2p} shifts from 74.85 to 74.09 eV (Figure 12, inset) after modification, which is ascribed to a decrease in the positive charge on Al atoms because of the adsorption of the negatively charged phosphate groups. Thus, the initiator is attached onto the imogolite surface possibly through electrostatic adsorption. In this case, the electron density of the surface aluminum atoms becomes higher compared with the unmodified imogolite, due to the influence of the negatively charged phosphate groups. In contrast, the formation of Al–O–P covalent bonds has been reported to cause an increase in the positive charge on Al atoms, as mentioned above. The difference in bonding manner between $DDPO_4$ and $BMPOPO_4$ on the imogolite surface may be due to the different hydrophobicity of these two molecules. The amount of adsorbed $BMPOPO_4$ was estimated to be 49 wt % by thermogravimetric analysis (TGA) [40].

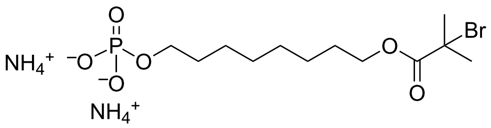

Figure 11: Chemical structure of $BMPOPO_4(NH_4)_2$. Reprinted with permission from W. Ma et al., *Polymer* **2011,** *52,* 5543–5550 [53]. © 2011, Elsevier B.V.

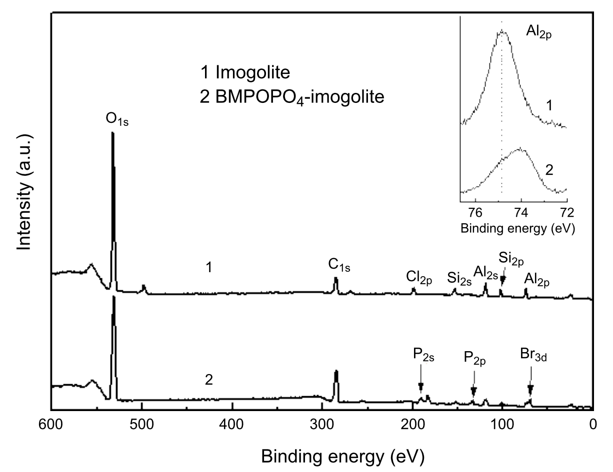

Figure 12: Wide-scan XPS spectra of the original imogolite and $BMPOPO_4$-imogolite (inset, high-resolution XPS spectra of Al_{2p}). Reprinted with permission from W. Ma et al., *Polymer* **2011,** *52,* 5543–5550 [53]. © 2011, Elsevier B.V.

The subsequent ARGET ATRP was carried out by using ascorbic acid (AA) as the reducing agent and anisole as the solvent. Ascorbic acid is insoluble in anisole, hence, the reduction of the Cu(II) complex takes place at the surface of solid ascorbic acid. The slow reaction rate of this heterogeneous redox process is beneficial for building up a necessary equilibrium between the activator (Cu(I) complex) and deactivator (Cu(II) complex). Polymeric products were isolated by precipitation from methanol. GPC data showed that grafted PMMA with molecular weights of M_n = 26600 and 32700, and corresponding molecular weight distributions of M_w/M_n = 1.22 and 1.33 were obtained after a polymerization time of 50 and 90 min, respectively. Hence, grafted PMMA with controllable molecular weight can be achieved by controlling the reaction time.

Bare imogolite cannot be dispersed in any organic solvent, but after modification with $BMPOPO_4$, the resulting modified imogolite can be dispersed in various solvents. Unfortunately, the dispersions are neither homogenous nor stable. However, when PMMA was grafted to the surface of imogolite nanotubes, PMMA-*g*-imogolite showed good dispersibility in organic solvents, such as THF, chloroform, and toluene. As shown in Figure 13d the homogenous dispersion of PMMA-*g*-imogolite in THF with a concentration of 10 mg mL^{-1} was stable for more than two months.

Morphology of PMMA grafted imogolite nanotubes was observed with scanning force microscopy (SFM) in a dynamic

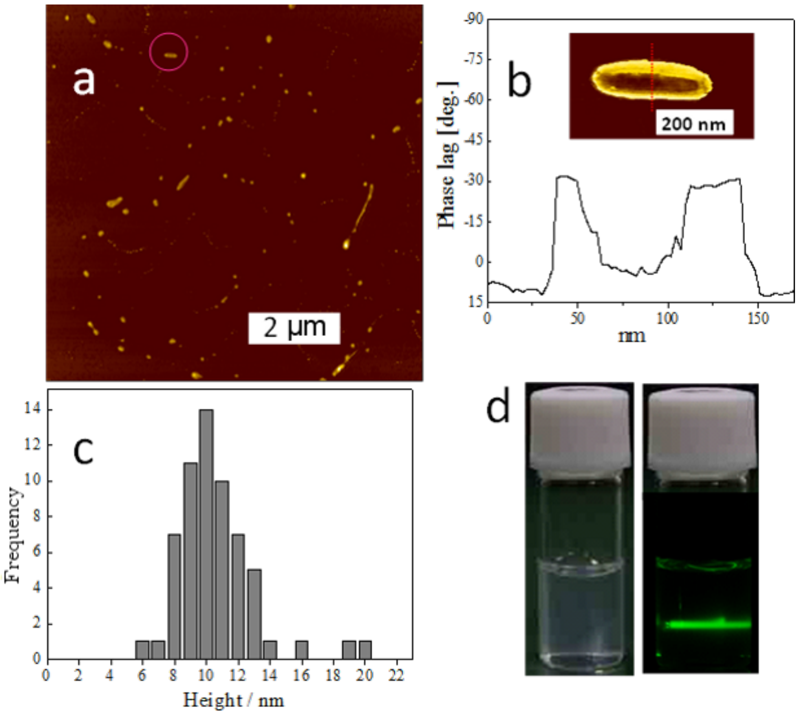

Figure 13: (a) A SFM height image of PMMA grafted imogolite (M_n = 32700, M_w/M_n = 1.33). (b) A phase image (insert) and cross-sectional analysis of a PMMA-*g*-imogolite marked with a circle in (a). (c) Height distribution of the above sample as estimated by SFM. (d) Photographs of the THF dispersion of the same sample with a concentration of 10 mg mL^{-1} (the one on the right shows scattering of a green light beam by the dispersion due to the Tyndall effect). Reprinted with permission from W. Ma et al., *Chem. Commun.* **2011,** *47,* 5813–5815 [40]. © 2011, The Royal Society of Chemistry.

force microscopy (DFM) mode employing a sharp diamondlike carbon (DLC) tip with a radius of curvature of 1 nm. Figure 13a shows a height image of one sample with M_n = 32700 and M_n/M_w = 1.33. Discrete nanostructures were randomly distributed on the mica surface and no aggregation was observed, indicating excellent dispersibility of PMMA grafted imogolite. The high-resolution phase image and the corresponding cross-sectional analysis in Figure 13b indicates that PMMA grafted imogolite renders a hard middle part and a soft edge. This further confirms the core–shell structure of PMMA-*g*-imogolite. Figure 13c shows the height distribution of the above PMMA-*g*-imogolite analyzed from 60 SFM images. The average height value was determined to be 10.6 ± 2.5 nm, although there are still some images having heights of more than 15 nm. If we consider the sample with the smallest height value (6 nm) as containing an individual imogolite nanotube at the core, the ones with larger height values are expected to have nanotube bundles as their rigid cores.

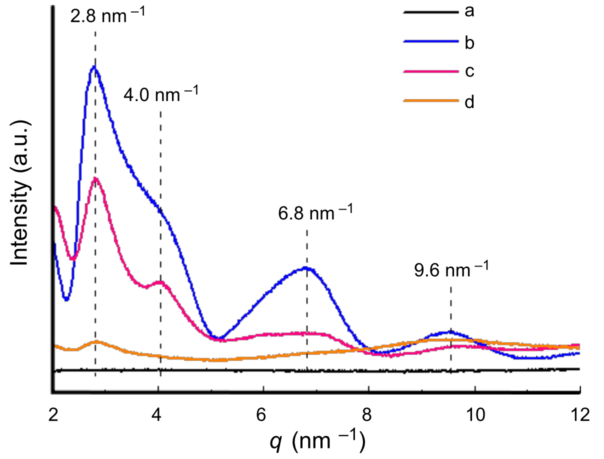

Figure 14: WAXD profiles of (a) quartz-glass capillary background, (b) bare imogolite, (c) BMPOPO$_4$-imogolite, and (d) PMMA-*g*-imogolite with M_n = 32700 and M_w/M_n = 1.33. Reprinted with permission from W. Ma et al., *Chem. Commun.* **2011,** *47,* 5813–5815 [40]. © 2011, The Royal Society of Chemistry.

Further evidence on the bundle structures was provided by wide-angle X-ray diffraction (WAXD) measurements. As shown in Figure 14, the diffraction peaks at q = 2.8, 4.0, 6.8, and 9.6 nm^{-1} can be assigned to the (100), (110), (001), and (211) planes of the parallel bundles of the imogolite nanotubes, respectively [24]. For BMPOPO$_4$ modified imogolite, these four diffraction peaks still exist, suggesting the presence of imogolite bundles. In addition, the peaks at around q = 2.8 and 4.0 nm^{-1} become sharper than those of the bare imogolite and, as a result, can easily be distinguished from the overlapped profile, indicating the higher regularity of the bundles compared to that of the bare imogolite. Hence, it is reasonable to conclude that during the modification process only highly ordered imogolite bundles can remain. In addition, the diffraction from (001) plane at ca. q = 6.8 nm^{-1} becomes much weaker and broader, suggesting that the bundle size significantly decreased along the (001) plane direction. The above results indicate that small-sized imogolite bundles with high regularity form the rigid core of BMPOPO$_4$-imogolite during the modification process. After surface-initiated polymerization of MMA, these small-sized imogolite bundles become the cores of PMMA-*g*-imogolite, and the diffraction of the (100) plane at around q = 2.8 nm^{-1} can still be observed. This result is consistent with the explanation for the SFM observation.

Terthiophene/imogolite hybrid

Grafting of functionalized molecules (porphyrins, phtalocyanines, viologens, rhodamine B, etc.) onto metal-oxide surfaces of SiO$_2$, TiO$_2$, ITO, WO$_3$, and ZrO$_2$ can induce the formation of well-defined nanoscopic photoactive molecular arrays of heterosupramolecular assemblies [55,56]. Imogolite lacks the intrinsic semiconductivity of the carbon nanotube, but it can be an interesting condensed phase for heterosupramolecular systems due to its high surface area for molecular component adsorption, abundance of empty surface sites for covalent binding of acidic anchoring groups, and high stability under ambient conditions. A more promising approach to render aluminosilicate nanotubes semiconducting is by functionalization with conjugated molecules, such as terthiophene with alkyl spacers consisting of –CH$_2$CH$_2$– and P=O(OH)$_2$ (Scheme 1). Thiophene oligomers have been extensively studied in recent years due to their excellent optic properties. It has been reported that thiophene oligomers exhibit high quantum yields of photoluminescence, both in solution as well as the solid state, and a broad range of fluorescence frequencies in the entire UV–visible and the near-IR spectrum, through molecular engineering [57-59].

For preparation of terthiophene/imogolite hybrid materials, imogolite solution was added dropwise to a THF solution of 2-(5’’-hexyl-2,2’:5’,2’’-terthiophen-5-yl)ethylphosphonic acid (HT3P) and stirred overnight at room temperature in the dark. The weight ratio of imogolite to HT3P was 1:1. HT3P/imogolite precipitate was obtained by centrifugation of the suspended solution and rinsing with fresh THF three times to remove weakly or nonchemisorbed HT3P. The precipitate was redispersed in deionized water before being freeze dried. Freeze drying of the precipitate resulted in a cottonlike yellow solid. The same preparation method was used for 2-(5’’-hexyl-2,2’:5’,2’’-terthiophen-5-yl)ethylphosphonic acid 1,1-dioxide (HT3OP) to produce the cottonlike pale brown solid of HT3OP/imogolite hybrid. As a control sample, no precipitate was observed for OH group derivatives (HT3OH and HT3OOH) (Figure 15).

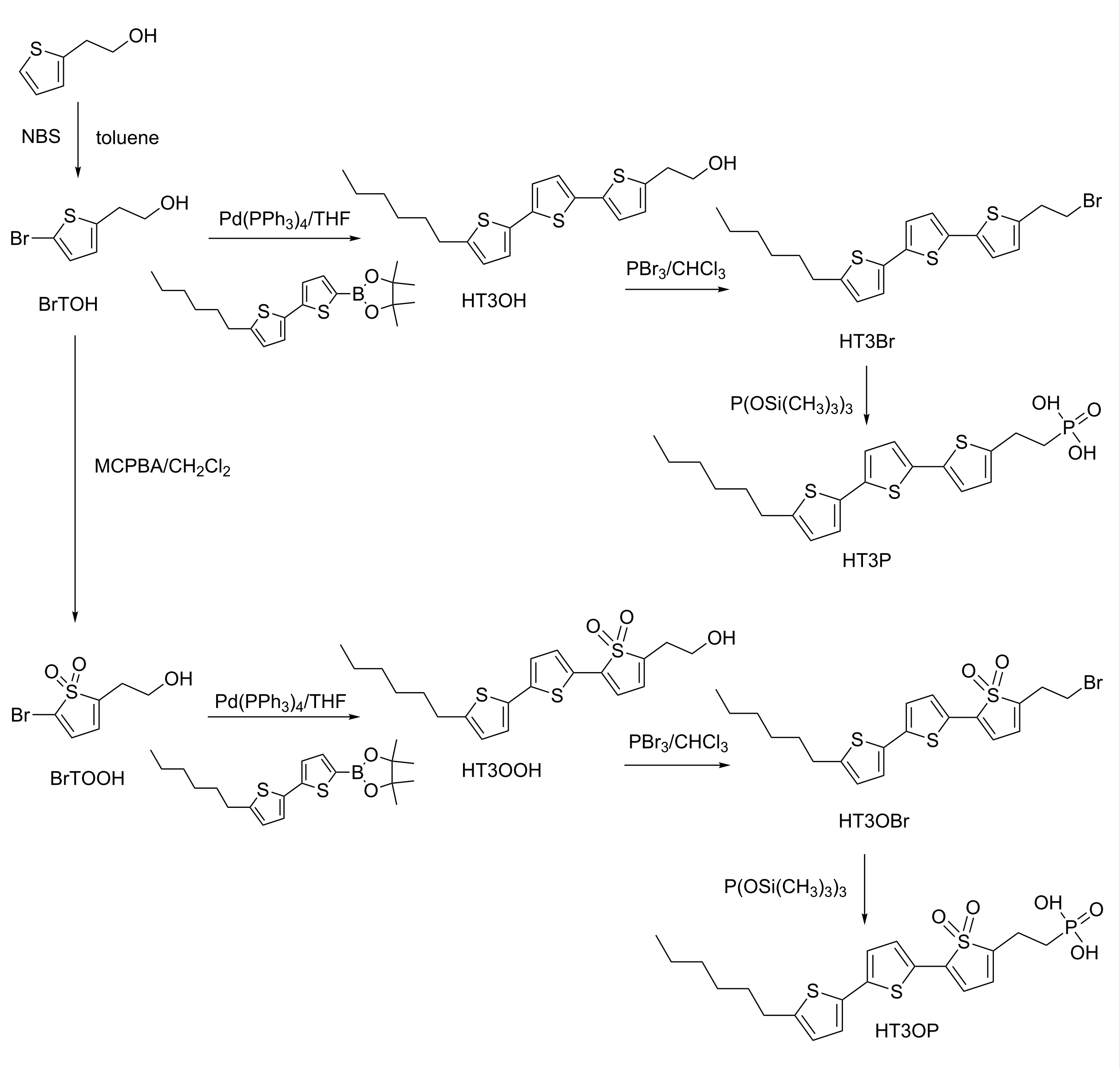

Scheme 1: Synthesis pathway for electron donating (HT3P) and accepting (HT3OP) terthiophene of phosphonic acid derivatives. Reprinted with permission from W. O. Yah et al., *Bull. Chem. Soc. Jpn.* **2011,** *84,* 893–902 [60]. © 2011, The Chemical Society of Japan.

In the FTIR spectrum of HT3P/imogolite hybrid in Figure 16a, the spectrum showed the characteristic absorptions corresponding to the CH_2 stretching vibration of HT3P at 2850–2950 cm^{-1}. The broadness of the peaks in the P–O region between 1200 and 900 cm^{-1} makes the result difficult to interpret, but the greatly diminished absorption at 2200–2500 cm^{-1} assigned to the OH stretching of the phosphonic acid groups indicates that the phosphonate headgroup strongly interacted with the imogolite surface [61]. In addition, the absence of the 1004 cm^{-1} band, which is assigned to P–O–H groups [62,63], was another indication that HT3P molecules were chemisorbed onto the surface of the imogolite nanofiber. The FTIR spectrum of HT3OP/imogolite hybrid as shown in Figure 16b gives a similar result with the disappearance of P–O–H at around 1011 cm^{-1} suggesting that HT3OP molecules also undergo chemisorptions when in contact with imogolite.

To investigate the optical properties of terthiophenes on the imogolite surface, a comparison of the UV–vis spectra of terthiophenes (HT3P and HT3OP)/imogolite hybrid between their solutions and solid-state counterparts was made (Figure 17). Blue-shifting was observed in the spectra of the solvent-cast film for both terthiophene hybrids to a different extent, and with a significantly broadened band. The spectral

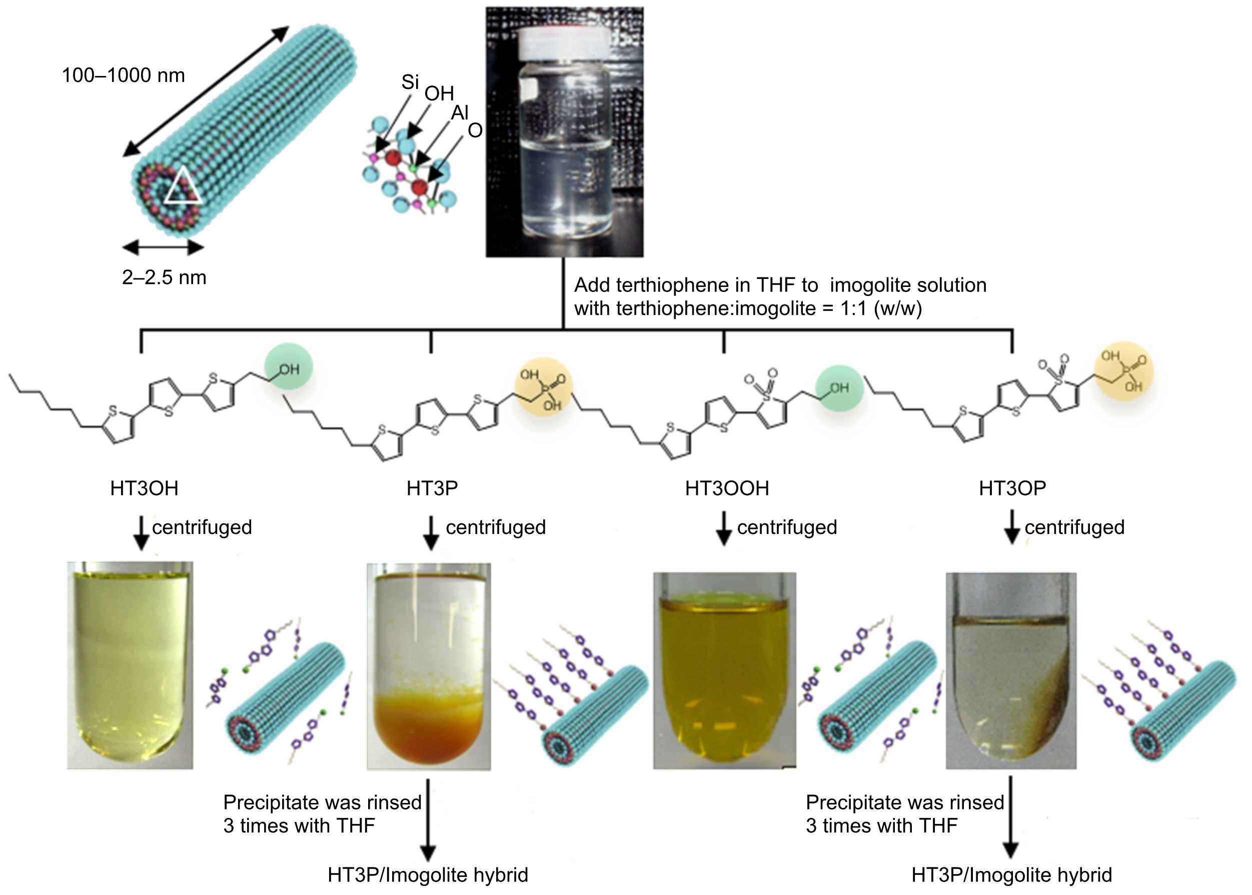

Figure 15: Schematic illustration of imogolite structure and the preparation of terthiophene/imogolite hybrid materials. Reprinted with permission from W. O. Yah et al., *Bull. Chem. Soc. Jpn.* **2011,** *84,* 893–902 [60]. © 2011, The Chemical Society of Japan.

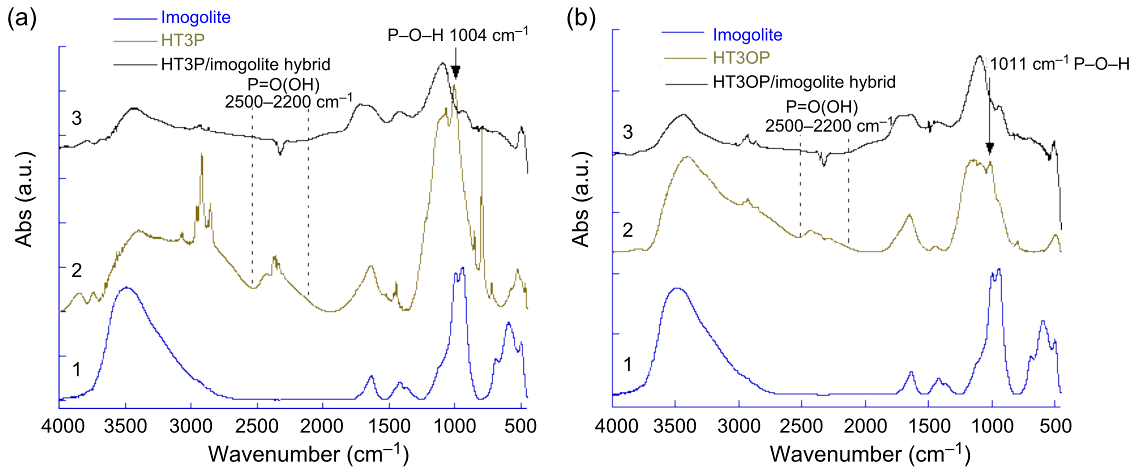

Figure 16: FTIR spectra (a) of HT3P/imogolite hybrid, HT3P, and imogolite, (b) of HT3OP/imogolite hybrid, HT3OP, and imogolite. Reprinted with permission from W. O. Yah et al., *Bull. Chem. Soc. Jpn.* **2011,** *84,* 893–902 [60]. © 2011, The Chemical Society of Japan.

changes upon solidification from solution arise from two factors: Planarity and intermolecular interaction [64-66]. Normally, red-shifting occurs in the solid state when the molecular backbone is more planar compared to the isolated state in solution, due an increase in conjugation length. Thus, the blue-shifting observed in the spectra of thiophene/imogolite films

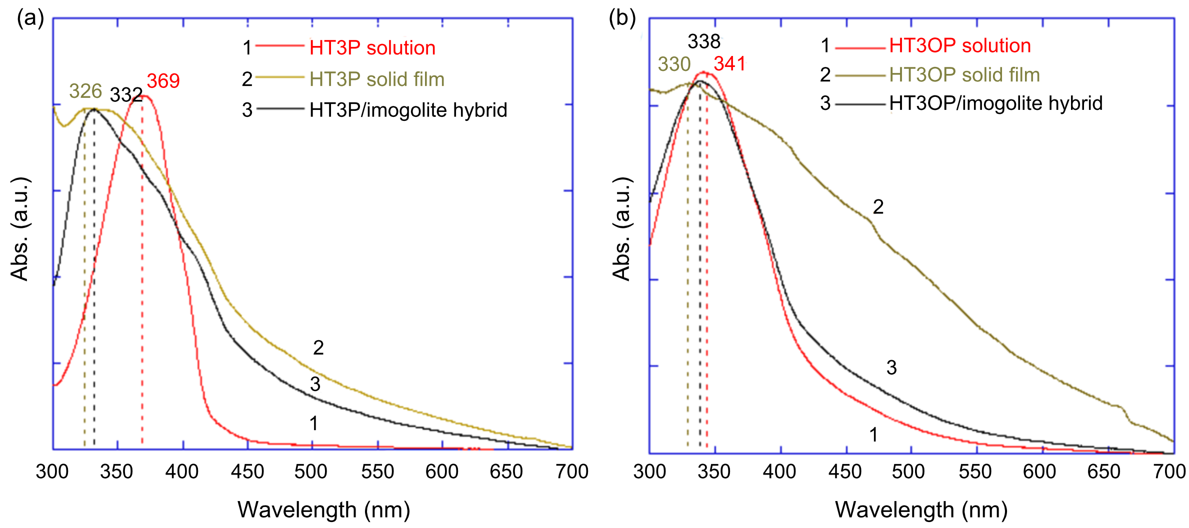

Figure 17: Normalized solid-state (cast film), imogolite hybrid and solution absorption spectra of (a) HT3P and (b) HT3OP. Reprinted with permission from W. O. Yah et al., *Bull. Chem. Soc. Jpn.* **2011,** *84,* 893–902 [60]. © 2011, The Chemical Society of Japan.

compared to solution indicates that additional an intermolecular interaction was present that plays a role in controlling the solid-state optical properties [65].

Fluorescence spectroscopy is a suitable analytical tool for monitoring the intermolecular interactions of terthiophene before and after chemisorption on imogolite. The absorption peak of the HT3P/imogolite hybrid at 322 nm, shifted from that of the HT3P in THF solution (λ_{max} 367 nm), provides additional proof for the formation of an H-type intermolecular interaction of terthiophene on the imogolite surface (Figure 18). The emission spectra also reveal the impact of intermolecular interaction in the hybrid with a peak at 515 nm that was red-shifted with respect to that of the HT3P solution (λ_{max} 445 nm) [67,68]. The formation of H-aggregates of HT3OP on the imogolite surface was also evidenced as the absorption peak shows blue-shifting relative to the HT3OP solution (λ_{max} 360 nm). The emission peak in the fluorescence spectrum of HT3OP/imogolite was red-shifted with respect to that of the HT3OP solution (λ_{max} 455 nm), suggesting the presence of an intermolecular interaction [67,68]. In the case of HT3OP/imogolite, however, the peaks are shifted to a lesser extent in the fluorescence spectrum

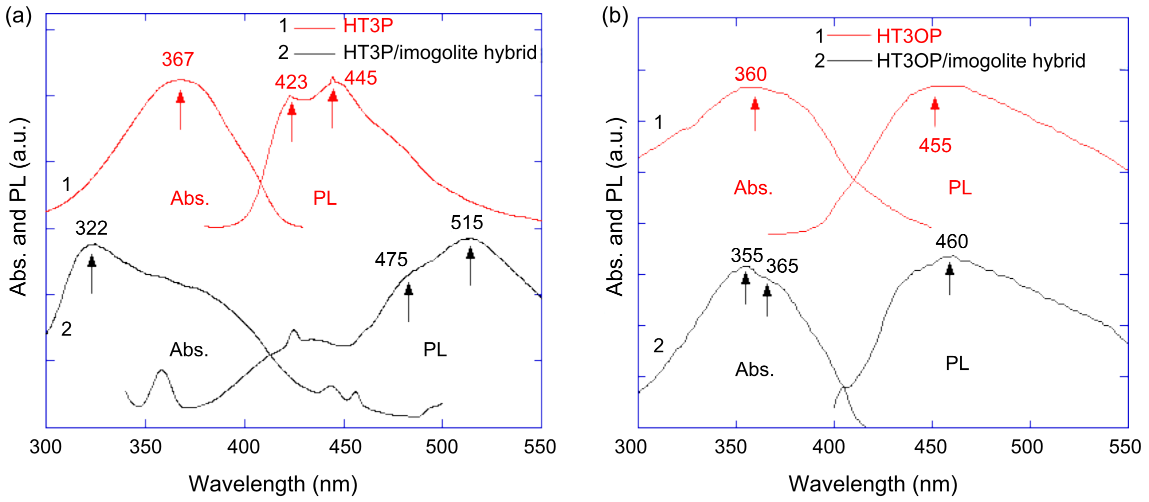

Figure 18: Fluorescence excitation/emission spectra of (a) HT3P, HT3P/imogolite hybrid and (b) HT3OP, HT3OP/imogolite hybrid. The emission wavelengths monitored for the excitation spectra and the excitation wavelengths used for the emission spectra were as follows: (a, 1) λ_{em} = 445 nm, λ_{ex} = 366 nm, (a, 2) λ_{em} = 326 nm, λ_{ex} = 519 nm. (b, 1) λ_{em} = 455 nm, λ_{ex} = 360 nm, (b, 2) λ_{em} = 460 nm, λ_{ex} = 460 nm. Reprinted with permission from W. O. Yah et al., *Bull. Chem. Soc. Jpn.* **2011,** *84,* 893–902 [60]. © 2011, The Chemical Society of Japan.

compared to those of the HT3P/imogolite hybrid, due to distortion of the HT3OP backbone by S=O groups, which decrease its planarity and π–π interaction causing weaker H-aggregates of HT3OP on the imogolite.

Imogolite has been thought of as an insulator since imogolites consist of wide-bandgap alumina and silica. In fact, due to its unique tubular structure and high aspect ratio, imogolite can be used as an electron-emitting material and water sensor in nanoelectronic devices. The conductivities of the pure imogolite and of the terthiophene/imogolite hybrids were investigated by *I–V* measurement. By coating the pure imogolite or terthiophene/imogolite onto a silicon wafer and connecting by silver paste at two ends, the conductivity was measured by means of a source meter. The *I–V* plots, of current on the order of milliamperes versus applied bias voltage in the range from −30 to 30 V, are shown in Figure 19.

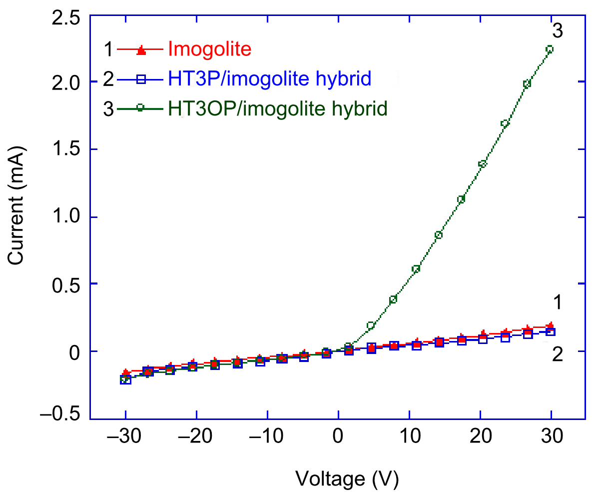

Figure 19: *I–V* curves of imogolite, HT3P/imogolite, and HT3OP/imogolite hybrid. Reprinted with permission from W. O. Yah et al., *Bull. Chem. Soc. Jpn.* **2011,** *84,* 893–902 [60]. © 2011, The Chemical Society of Japan.

The averaged electrical conductance calculated from the forward bias region of the pure imogolite *I–V* curve is 5.9 µS. It was speculated that the current flow was due to charge hopping on the hydrated imogolite surface. Oh et al. studied the *I–V* characteristics of imogolite and proposed that bound water molecules contribute to the surface conductivity [69,70]. The current flow observed was attributed to the ability of OH groups on the imogolite surface to lose or gain positive charge (a proton) from water molecules resulting in a net change of surface charge. The electrical conductance of HT3OP/imogolite was improved to 60.8 µS, which is one order of magnitude greater than that of pure imogolite. It was observed that HT3OP/imogolite shows non-ohmic characteristics in the *I–V* curve, which signifies a disordered packing of HT3OP on the imogolite surface, in which it behaves like a semiconductor or metal–semiconductor Schottky junction. The HT3OP can act as an electron acceptor when interacting with imogolite, in which the high electron affinity of S=O of HT3OP causes a withdrawal of negative charge from imogolite resulting in the effective motion of positive charges on the imogolite surface. The introduction of HT3OP onto the imogolite surface amplifies the p-type conductivity of imogolite, which resembles the phenomenon of chemical doping of carbon nanotubes with alkaline metals [71-74]. On the other hand, the electrical conductance of HT3P/imogolite calculated from the forward bias region is 4.5 µS, which is lower than that before HT3P doping. Here, HT3P acts like an electron donor when interacting with imogolite. The p-type conductivity of imogolite is reduced when the HT3P thiophene ring transfers negative charge to imogolite, which restricts the effective motion of positively charged species on the imogolite surface.

Poly(3-hexyl thiophene)/imogolite nanofiber hybrid

Polythiophenes are one of the well-known families of conductive polymers, and their physicochemical properties, such as their synthesis, electrical and mechanical properties, thermochromism, solvatochromism, and crystal structure [75-78], have been extensively studied. Their optical properties, conductivity, and field-effect mobility (FEM) strongly depend on chain conformation and the solid-state-packing mode. For example, well-aligned and highly ordered crystalline polythiophene films will lead to significant improvements in conductivity and FEM; whereas the FEM of the disordered polythiophene film was below the detection level [79,80]. Generally, solidification of polythiophene by rapid evaporation of the polymeric solution in good solvent can result in a weak crystalline solid without perceptible morphological structure [81,82]. On the other hand, the slow cooling from 70 °C to room temperature of a P3HT solution in a poor solvent, such as xylene or anisole, leads to the formation of a fibrous semicrystalline structure (Figure 20). Nanofiber formation is always accompanied by a color change from orange to dark red, which is referred to as thermochromism [83].

Recently, a chemiresistive sensor based on a nanofiber hybrid of carbon nanotube/poly(3-hexylthiophene)- and carbon nanotube/hexafluoroiso-propanol-substituted polythiophene systems was reported [84]. Using a simple solution fabrication process, by dispersing carbon nanotubes in a polythiophene solution followed by spin coating of the solution onto a glass substrate, a highly sensitive and selective chemiresistor was successfully developed. Due to the favorable H-binding of the fluoro-alkyl groups of polythiophene to the phosphate ester, the

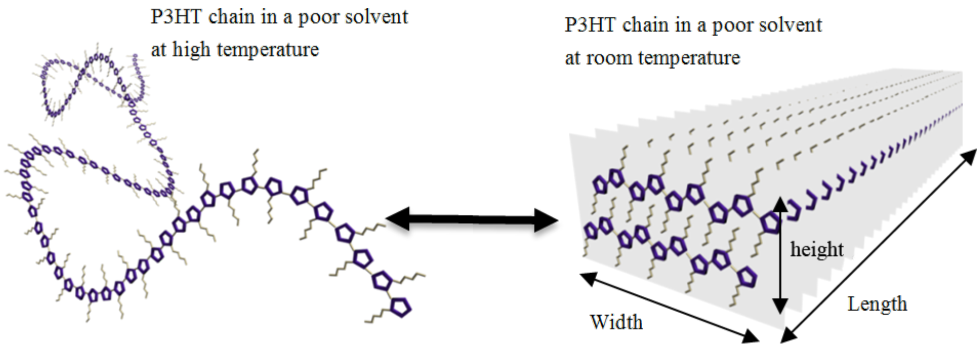

Figure 20: Schematic illustration of reversible formation of P3HT nanofiber.

nanofiber hybrid was reported to be able to detect several numbers of chemical warfare agents, such as dimethyl methylphosphonate (DMMP) and sarin gas [85]. Nevertheless, large-quantity synthesis of carbon nanotubes involves highly expensive and time-consuming preparation processes. Moreover, it is not practical for certain optical applications that use opaque carbon nanotubes, due to its conjugated π-system. Here, imogolite, the transparent hydrous aluminosilicate nanotube material, with its unique nanostructure was proposed as the inorganic nanotube to be hybridized with P3HT nanofibers. Reinforcement of P3HT nanofibers by imogolite is expected to impart additional mechanical and thermal stability to organic compounds, making the resulted hybrid material more durable under the outer environmental conditions. Therefore, it is crucial to develop a facile synthetic method capable of making uniform and template-free imogolite/P3HT nanofiber hybrids in bulk quantities. Such a synthetic method would be useful for tuning the properties of sensors and photovoltaic or light-emitting devices, which are dependent on well-defined low-dimensional structures. In order to improve compatibility with the P3HT nanofibers, hydrophilic Al–OH groups on the imogolite surface were modified with alkyl phosphonic acid substituted terthiophene (HT3P), as shown in Figure 21. The molecular aggregation states and molecular orientation of the P3HT chain on imogolite were investigated.

Figure 22 displays the evolution of the absorption spectra of the P3HT solution (a) and the P3HT/HT3P-imogolite nanofiber hybrid (b) cooled from 70 °C to 20 °C. Notably, both spectra exhibit a single peak with λ_{max} of 450 nm at 70 °C. The spectrum resembles that observed for the P3HT/chloroform system indicating that P3HT was completely dissolved in anisole at the higher temperature. When cooled to room temperature, the band intensity at λ_{max} = 450 nm decreases in both spectra but is compensated by the appearance of vibronic structure at longer wavelengths (500–650 nm). The isosbectic points observed at 489 nm and 525 nm indicate that P3HT and P3HT/HT3P-imogolite exhibit both isolated coil-like conformation and rodlike conformation in the solution [87]. The isosbectic point of P3HT/HT3P-imogolite is slightly shifted to a longer wavelength compared to P3HT and was ascribed to a larger amount of the P3HT/HT3P-imogolite aggregate. Upon hybridization, HT3P-imogolite greatly restricts the rotational motion of the P3HT backbone, such that it produces a much longer conjugation length than pure P3HT.

Dynamic force microscopy (DFM) has proved to be a powerful tool for the direct observation of the aggregation of polymeric nanofibers. By spin coating a dilute solution in anisole, a network of nanofibers more or less entirely covers the silicon substrate. The dimensions of the nanofiber were determined

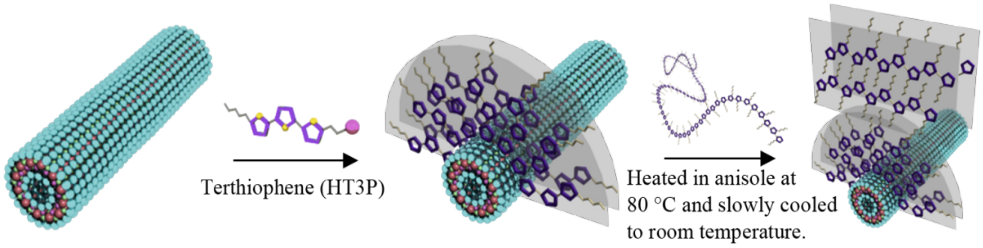

Figure 21: Fabrication and proposed molecular arrangement of P3HT/HT3P-imogolite nanofiber hybrid. Reprinted with permission from W. O. Yah et al., *J. Phys.: Conf. Ser.* **2011,** *272,* 012021 [86]. © IOP Publishing 2011.

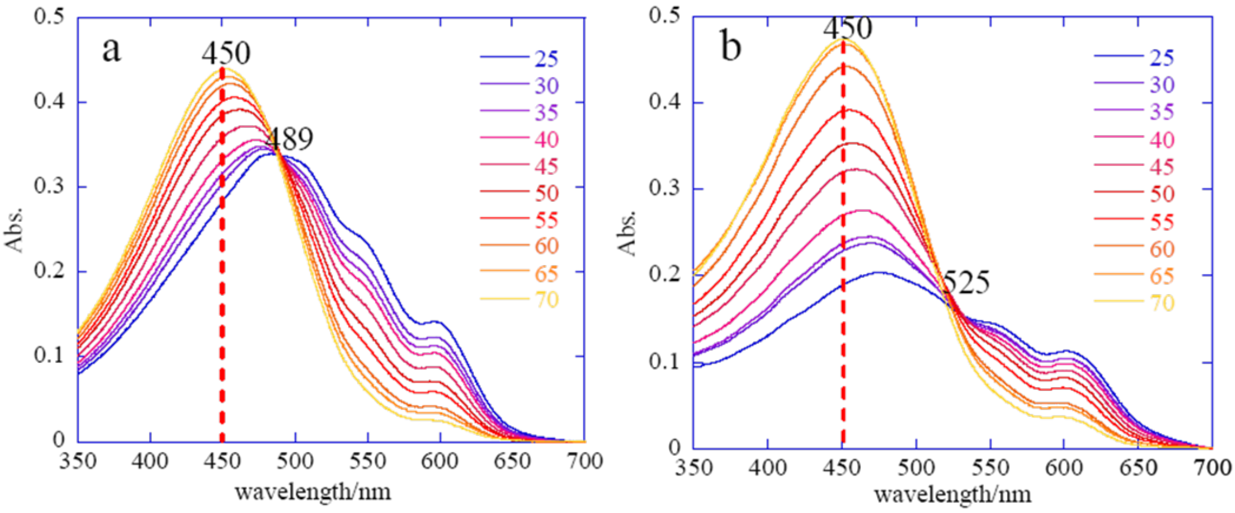

Figure 22: UV–vis absorption spectra of P3HT (a) and P3HT/HT3P-imogolite hybrid (b) in anisole (0.0005%) during cooling. Reprinted with permission from W. O. Yah et al., *J. Phys.: Conf. Ser.* **2011,** *272,* 012021 [86]. © IOP Publishing 2011.

from DFM images; as shown in Figure 23a, P3HT nanofibers have a width and a length on the order of ca. 15 nm and 1 μm, respectively. The thickness, as estimated from the height image of DFM, was on the order of ca. 5 nm. On the other hand, it was observed that the heights of the nanofiber hybrids were 2 to 3 times larger than that of the P3HT nanofiber, indicating the formation of the bundle of the imogolite nanofiber [22]. Judging from the DFM images, the nanofiber hybrid as shown in Figure 23b exhibited a swollen morphology compared to the pure P3HT nanofiber. It was speculated that the swollen morphology was caused by the intertwining effect of the P3HT nanofiber with the imogolite bundle.

Recent studies on P3HT by grazing-incidence X-ray diffraction revealed the crystallinity and nanostructure in the nanofiber. The structure of P3HT nanofibers is similar to crystalline microdomains in which the P3HT chains pack in lamellar sheets perpendicular to the nanofiber axis. The orientation of the P3HT crystalline phase on the imogolite surface was studied by grazing-incidence wide-angle X-ray diffraction (GIWAXD), as shown in Figure 24. The out-of-plane GIWAXD pattern revealed only those crystalline plane positions that are in a direction parallel to the x–y axis. Likewise, in the in-plane GIWAXD pattern, only crystalline planes aligned to the z-axis are revealed.

In the out-of-plane GIWAXD pattern, the peaks at $d = 4$ (100) and 7.8 nm (200) were attributed to the ordering of the P3HT hexyl side chains. In other words, the nanofiber height corresponds to the stacking of the hexyl side chains and was parallel to the z-axis of the unit cell. The intensity at (100) was dramatically reduced when the incidence angle, $\alpha_i = 0.08°$, was increased to 0.16°, suggesting that the semicrystalline P3HT mostly resides on the outermost region of the nanofiber hybrid. For the in-plane GIWAXD pattern, one noticeable diffraction peak associated with the (010) diffraction was observed. The diffraction peak corresponds to the π–π* stacking of the P3HT thiophene ring and was parallel to the y-axis, i.e., the nanofiber direction. Again, the (010) peak was diminished when the incidence angle, $\alpha_i = 0.08°$, was increased to 0.16°. These results indicate that P3HT chains reside on the outermost region of nanofiber hybrid along the imogolite axis.

Conclusion

This paper reviews the recent progress in the surface functionalization of imogolite nanotubes, which is based on the robust affinity between the phosphate group of the organic molecule and the aluminol (AlOH) surface of the imogolite nanotube. Surface modification of imogolite at the nanotube level is achieved from an aqueous solution by using a water-soluble ammonium salt of an alkyl phosphate. In addition, poly(methyl methacrylate) (PMMA) grafted imogolite nanotubes are prepared through a surface-initiated polymerization. PMMA grafted imogolite nanotubes can be homogenously dispersed in various organic solvents. A water-soluble surface-attachable ATRP initiator, $BMPOPO_4(NH_4)_2$, contributes to the successful polymer-grafting process. Furthermore, the assembly of conjugated molecules, HT3P and HT3OP, on the imogolite nanotube surface was described. UV–vis spectra indicate that both HT3P and HT3OP exhibit an H-aggregate formation on the imogolite surface. An increase in the conductivity of imogolite is detected when assembled with electron-withdrawing HT3OP molecules.

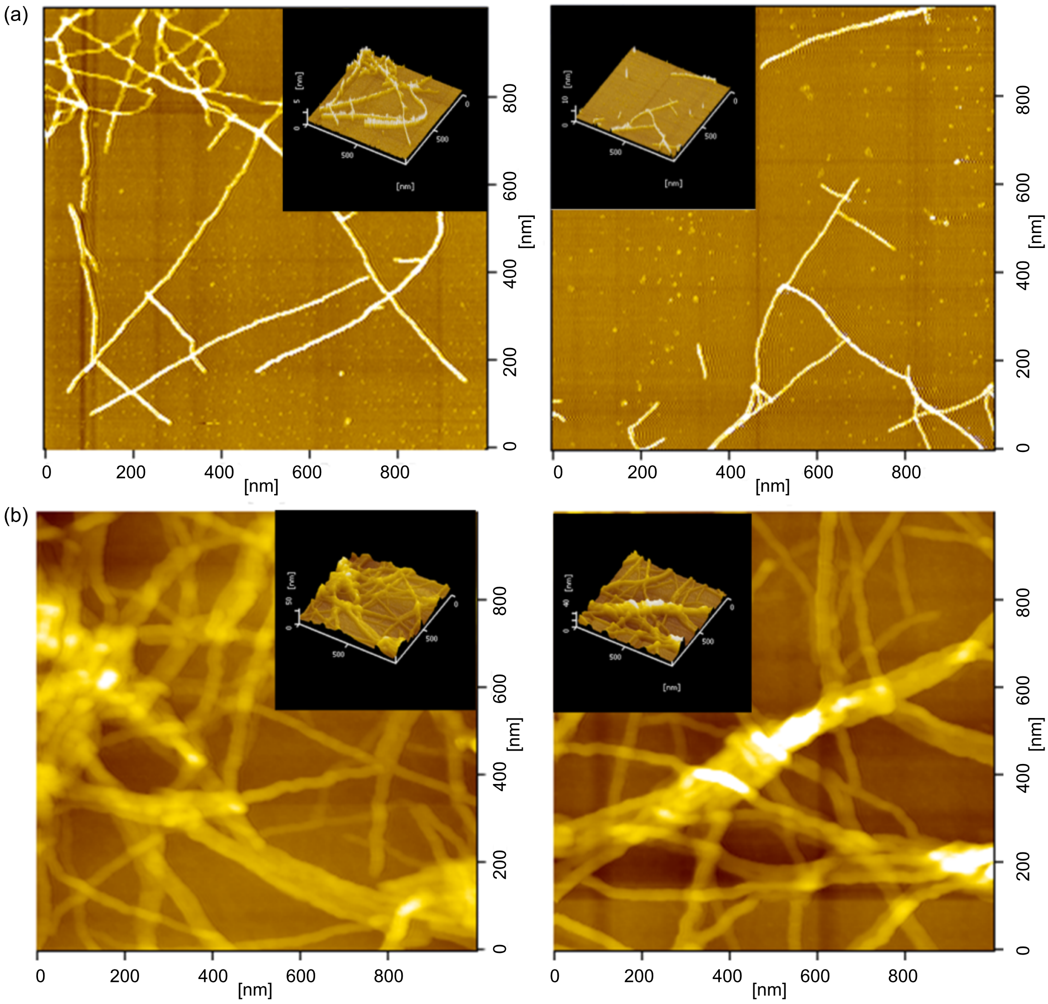

Figure 23: DFM images of (a) P3HT nanofiber and (b) P3HT/HT3P-imogolite nanofiber hybrid. Adapted with permission from W. O. Yah et al., *J. Phys.: Conf. Ser.* **2011,** *272,* 012021 [86]. © IOP Publishing 2011.

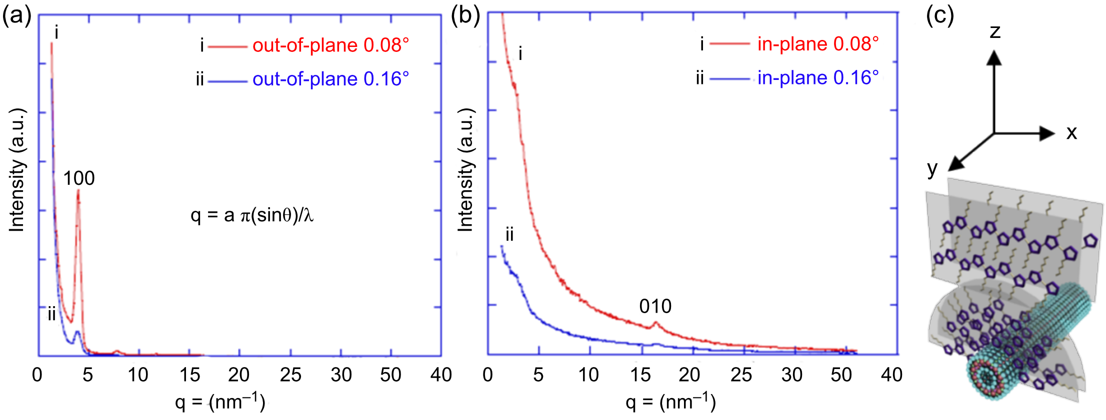

Figure 24: Out-of-plane (a) and in-plane (b) GIWAXD patterns of P3HT/HT3P-imogolite nanofiber hybrid. (c) Schematic illustration of the molecular arrangement of P3HT on imogolite. Reprinted with permission from W. O. Yah et al., *J. Phys.: Conf. Ser.* **2011,** *272,* 012021 [86]. © IOP Publishing 2011.

Further hybridization of HT3P assembled imogolite with P3HT, using a poor solvent, results in a P3HT/HT3P-imogolite nanofiber hybrid. UV–vis, DFM and GIWAXD studies showed that a P3HT nanofiber wrapping around the HT3P-imogolite nanotube causes the increase in diameter of the resultant nanofiber hybrid. It is believed that surface functionalization of the imogolite nanotube is an effective way to obtain nanomaterials with practical applicability.

Acknowledgments

The authors gratefully acknowledge the financial support of a Grant-in-Aid for Scientific Research (A) (No. 19205031) from the Japan Society for the Promotion of Science. The present work is also supported by a Grant-in-Aid for the Global COE Program, “Science for Future Molecular Systems” from the Ministry of Education, Culture, Science, Sports and Technology of Japan. The synchrotron radiation experiments were performed at BL02B2 in SPring-8 with the approval of the JASRI (Proposal No. 2010A1454).

References

1. Love, J. C.; Estroff, L. A.; Kriebel, J. K.; Nuzzo, R. G.; Whitesides, G. M. *Chem. Rev.* **2005,** *105,* 1103–1170. doi:10.1021/cr0300789
2. Ulman, A. *Chem. Rev.* **1996,** *96,* 1533–1554. doi:10.1021/cr9502357
3. Spori, D. M.; Venkataraman, N. V.; Tosatti, S. G. P.; Durmaz, F.; Spencer, N. D.; Zürcher, S. *Langmuir* **2007,** *23,* 8053–8060. doi:10.1021/la700474v
4. Van Alsten, J. G. *Langmuir* **1999,** *15,* 7605–7614. doi:10.1021/la981694g
5. Jennings, J. R.; Ghicov, A.; Peter, L. M.; Schmuki, P.; Walker, A. B. *J. Am. Chem. Soc.* **2008,** *130,* 13364–13372. doi:10.1021/ja804852z
6. Han, W. S.; Kang, Y.; Lee, S. J.; Lee, H.; Do, Y.; Lee, Y.-A.; Jung, J. H. *J. Phys. Chem. B* **2005,** *109,* 20661–20664. doi:10.1021/jp0547156
7. Veerabadran, N. G.; Mongayt, D.; Torchilin, V.; Price, R. R.; Lvov, Y. M. *Macromol. Rapid Commun.* **2009,** *30,* 99–103. doi:10.1002/marc.200800510
8. Abdullayev, E.; Lvov, Y. *J. Mater. Chem.* **2010,** *20,* 6681–6687. doi:10.1039/C0JM00810A
9. Yamamoto, K.; Otsuka, H.; Wada, S.-I.; Sohn, D.; Takahara, A. *Polymer* **2005,** *46,* 12386–12392. doi:10.1016/j.polymer.2005.10.108
10. Yamamoto, K.; Otsuka, H.; Wada, S.-I.; Sohn, D.; Takahara, A. *Soft Matter* **2005,** *1,* 372–377. doi:10.1039/B508669H
11. Yah, W. O.; Yamamoto, K.; Jiravanichanun, N.; Otsuka, H.; Takahara, A. *Materials* **2010,** *3,* 1709–1745. doi:10.3390/ma3031709
12. Sagiv, J. *J. Am. Chem. Soc.* **1980,** *102,* 92–98. doi:10.1021/ja00521a016
13. Bain, C. D.; Troughton, E. B.; Tao, Y. T.; Evall, J.; Whitesides, G. M.; Nuzzo, R. G. *J. Am. Chem. Soc.* **1989,** *111,* 321–335. doi:10.1021/ja00183a049
14. Mutin, P. H.; Guerrero, G.; Vioux, A. *J. Mater. Chem.* **2005,** *15,* 3761–3768. doi:10.1039/b505422b
15. Angst, D. L.; Simmons, G. W. *Langmuir* **1991,** *7,* 2236–2242. doi:10.1021/la00058a043
16. Le Grange, J. D.; Markham, J. L.; Kurkjian, C. R. *Langmuir* **1993,** *9,* 1749–1753. doi:10.1021/la00031a023
17. Fadeev, A. Y.; McCarthy, T. J. *Langmuir* **2000,** *16,* 7268–7274. doi:10.1021/la000471z
18. Trau, M.; Murray, B. S.; Grant, K.; Grieser, F. *J. Colloid Interface Sci.* **1992,** *148,* 182–189. doi:10.1016/0021-9797(92)90126-7
19. Michel, R.; Lussi, J. W.; Csucs, G.; Reviakine, I.; Danuser, G.; Ketterer, B.; Hubbell, J. A.; Textor, M.; Spencer, N. D. *Langmuir* **2002,** *18,* 3281–3287. doi:10.1021/la011715y
20. Michel, R.; Reviakine, I.; Sutherland, D.; Fokas, C.; Csucs, G.; Danuser, G.; Spencer, N. D.; Textor, M. *Langmuir* **2002,** *18,* 8580–8586. doi:10.1021/la0258244
21. Mutin, P. H.; Lafond, V.; Popa, A. F.; Granier, M.; Markey, L.; Dereux, A. *Chem. Mater.* **2004,** *16,* 5670–5675. doi:10.1021/cm035367s
22. Cradwick, P. D. G.; Farmer, V. C.; Russell, J. D.; Masson, C. R.; Wada, K.; Yoshinaga, N. *Nature (London), Phys. Sci.* **1972,** *240,* 187–189. http://www.nature.com/nature-physci/journal/v240/n104/abs/physci240187a0.html
23. Ackerman, W. C.; Smith, D. M.; Huling, J. C.; Kim, Y. W.; Bailey, J. K.; Brinker, C. J. *Langmuir* **1993,** *9,* 1051–1057. doi:10.1021/la00028a029
24. Mukherjee, S.; Bartlow, V. M.; Nair, S. *Chem. Mater.* **2005,** *17,* 4900–4909. doi:10.1021/cm0505852
25. Farmer, V. C.; Fraser, A. R.; Tait, J. M. *J. Chem. Soc., Chem. Commun.* **1977,** 462–463. doi:10.1039/c39770000462
26. Farmer, V. C.; Smith, B. F. L.; Tait, J. M. *Clay Miner.* **1979,** *14,* 103–107. doi:10.1180/claymin.1979.014.2.02
27. Yang, H.; Su, Z. *Chin. Sci. Bull.* **2007,** *52,* 2301–2303. doi:10.1007/s11434-007-0305-y
28. Yang, H.; Wang, C.; Su, Z. *Chem. Mater.* **2008,** *20,* 4484–4488. doi:10.1021/cm8001546
29. Levard, C.; Rose, J.; Masion, A.; Doelsch, E.; Borschneck, D.; Olivi, L.; Dominici, C.; Grauby, O.; Woicik, J. C.; Bottero, J.-Y. *J. Am. Chem. Soc.* **2008,** *130,* 5862–5863. doi:10.1021/ja801045a
30. Wada, S.-I.; Wada, K. *Clays Clay Miner.* **1982,** *30,* 123–128. doi:10.1346/ccmn.1982.0300206
31. Wada, S.; Kakuto, Y. *Soil Sci. Plant Nutr. (Abingdon, U. K.)* **1999,** *45,* 947–953.
32. Yamamoto, K.; Otsuka, H.; Wada, S.-I.; Takahara, A. *Chem. Lett.* **2001,** *30,* 1162–1163. doi:10.1246/cl.2001.1162
33. Ma, W.; Kim, J.; Otsuka, H.; Takahara, A. *Chem. Lett.* **2011,** *40,* 159–161. doi:10.1246/Cl.2011.159
34. Perruchot, C.; Khan, M. A.; Kamitsi, A.; Armes, S. P.; von Werne, T.; Patten, T. E. *Langmuir* **2001,** *17,* 4479–4481. doi:10.1021/la0102758
35. Vestal, C. R.; Zhang, Z. J. *J. Am. Chem. Soc.* **2002,** *124,* 14312–14313. doi:10.1021/ja0274709
36. Matsuno, R.; Yamamoto, K.; Otsuka, H.; Takahara, A. *Macromolecules* **2004,** *37,* 2203–2209. doi:10.1021/ma035523g
37. Wang, C.; Guo, Z.-X.; Fu, S.; Wu, W.; Zhu, D. *Prog. Polym. Sci.* **2004,** *29,* 1079–1141. doi:10.1016/j.progpolymsci.2004.08.001
38. Spitalsky, Z.; Tasis, D.; Papagelis, K.; Galiotis, C. *Prog. Polym. Sci.* **2010,** *35,* 357–401. doi:10.1016/j.progpolymsci.2009.09.003
39. Jagur-Grodzinski, J. *React. Funct. Polym.* **2001,** *49,* 1–54. doi:10.1016/S1381-5148(01)00059-1
40. Ma, W.; Otsuka, H.; Takahara, A. *Chem. Commun.* **2011,** *47,* 5813–5815. doi:10.1039/c1cc10661a
41. Jakubowski, W.; Min, K.; Matyjaszewski, K. *Macromolecules* **2006,** *39,* 39–45. doi:10.1021/ma0522716

42. Matyjaszewski, K.; Jakubowski, W.; Min, K.; Tang, W.; Huang, J.; Braunecker, W. A.; Tsarevsky, N. V. *Proc. Natl. Acad. Sci. U. S. A.* **2006,** *103,* 15309–15314. doi:10.1073/pnas.0602675103
43. Husseman, M.; Malmström, E. E.; McNamara, M.; Mate, M.; Mecerreyes, D.; Benoit, D. G.; Hedrick, J. L.; Mansky, P.; Huang, E.; Russell, T. P.; Hawker, C. J. *Macromolecules* **1999,** *32,* 1424–1431. doi:10.1021/ma981290v
44. Shah, R. R.; Merreceyes, D.; Husemann, M.; Rees, I.; Abbott, N. L.; Hawker, C. J.; Hedrick, J. L. *Macromolecules* **2000,** *33,* 597–605. doi:10.1021/ma991264c
45. Mori, H.; Böker, A.; Krausch, G.; Müller, A. H. E. *Macromolecules* **2001,** *34,* 6871–6882. doi:10.1021/ma0019048
46. von Werne, T.; Patten, T. E. *J. Am. Chem. Soc.* **2001,** *123,* 7497–7505. doi:10.1021/ja010235q
47. Pyun, J.; Jia, S.; Kowalewski, T.; Patterson, G. D.; Matyjaszewski, K. *Macromolecules* **2003,** *36,* 5094–5104. doi:10.1021/ma034188t
48. Farmer, V. C.; Adams, M. J.; Fraser, A. R.; Palmieri, F. *Clay Miner.* **1983,** *18,* 459–472. doi:10.1180/claymin.1983.018.4.11
49. Johnson, L. M.; Pinnavaia, T. J. *Langmuir* **1990,** *6,* 307–311. doi:10.1021/la00092a003
50. Matsuno, R.; Yamamoto, K.; Otsuka, H.; Takahara, A. *Chem. Mater.* **2003,** *15,* 3–5. doi:10.1021/cm020766t
51. Maliakal, A.; Katz, H.; Cotts, P. M.; Subramoney, S.; Mirau, P. *J. Am. Chem. Soc.* **2005,** *127,* 14655–14662. doi:10.1021/ja052035a
52. Minet, I.; Delhalle, J.; Hevesi, L.; Mekhalif, Z. *J. Colloid Interface Sci.* **2009,** *332,* 317–326. doi:10.1016/j.jcis.2008.12.066
53. Ma, W.; Otsuka, H.; Takahara, A. *Polymer* **2011,** *52,* 5543–5550. doi:10.1016/j.polymer.2011.09.054
54. Guerrero, G.; Mutin, P. H.; Vioux, A. *J. Mater. Chem.* **2001,** *11,* 3161–3165. doi:10.1039/b104411g
55. Marguerettaz, X.; O'Neill, R.; Fitzmaurice, D. *J. Am. Chem. Soc.* **1994,** *116,* 2629–2630. doi:10.1021/ja00085a057
56. Marguerettaz, X.; Fitzmaurice, D. *J. Am. Chem. Soc.* **1994,** *116,* 5017–5018. doi:10.1021/ja00090a069
57. Barbarella, G.; Pudova, O.; Arbizzani, C.; Mastragostino, M.; Bongini, A. *J. Org. Chem.* **1998,** *63,* 1742–1745. doi:10.1021/jo972108b
58. Barbarella, G.; Favaretto, L.; Sotgiu, G.; Zambianchi, M.; Antolini, L.; Pudova, O.; Bongini, A. *J. Org. Chem.* **1998,** *63,* 5497–5506. doi:10.1021/jo980507g
59. Barbarella, G.; Zambianchi, M.; Pudova, O.; Paladini, V.; Ventola, A.; Cipriani, F.; Gigli, G.; Cingolani, R.; Citro, G. *J. Am. Chem. Soc.* **2001,** *123,* 11600–11607. doi:10.1021/ja011209v
60. Yah, W. O.; Irie, A.; Jiravanichanun, N.; Otsuka, H.; Takahara, A. *Bull. Chem. Soc. Jpn.* **2011,** *84,* 893–902. doi:10.1246/bcsj.20110080
61. Gao, W.; Dickinson, L.; Grozinger, C.; Morin, F. G.; Reven, L. *Langmuir* **1996,** *12,* 6429–6435. doi:10.1021/la9607621
62. O'Brien, J. T.; Zeppenfeld, A. C.; Richmond, G. L.; Page, C. J. *Langmuir* **1994,** *10,* 4657–4663. doi:10.1021/la00024a044
63. Steiner, G.; Sablinskas, V.; Savchuk, O.; Bariseviciute, R.; Jähne, E.; Adler, H. J.; Salzer, R. *J. Mol. Struct.* **2003,** *661–662,* 429–435. doi:10.1016/j.molstruc.2003.08.031
64. Facchetti, A.; Yoon, M.-H.; Stern, C. L.; Hutchison, G. R.; Ratner, M. A.; Marks, T. J. *J. Am. Chem. Soc.* **2004,** *126,* 13480–13501. doi:10.1021/ja048988a
65. Zhang, X.; Johnson, J. P.; Kampf, J. W.; Matzger, A. J. *Chem. Mater.* **2006,** *18,* 3470–3476. doi:10.1021/cm0609348
66. Zhang, X.; Matzger, A. J. *J. Org. Chem.* **2003,** *68,* 9813–9815. doi:10.1021/jo035241e
67. Yassar, A.; Horowitz, G.; Valat, P.; Wintgens, V.; Hmyene, M.; Deloffre, F.; Srivastava, P.; Lang, P.; Garnier, F. *J. Phys. Chem.* **1995,** *99,* 9155–9159. doi:10.1021/j100022a031
68. DiCésare, N.; Belletête, M.; Garcia, E. R.; Leclerc, M.; Durocher, G. *J. Phys. Chem. A* **1999,** *103,* 3864–3875. doi:10.1021/jp9901085
69. Oh, J.; Chang, S.; Jang, J.; Roh, S.; Park, J.; Lee, J.; Sohn, D.; Yi, W.; Jung, Y.; Kim, S.-J. *J. Mater. Sci.: Mater. Electron.* **2007,** *18,* 893–897. doi:10.1007/s10854-007-9125-8
70. Park, J.; Lee, J.; Chang, S.; Park, T.; Han, B.; Han, J. W.; Yi, W. *Bull. Korean Chem. Soc.* **2008,** *29,* 1048–1050. doi:10.5012/bkcs.2008.29.5.1048
71. Lee, R. S.; Kim, H. J.; Fischer, J. E.; Thess, A.; Smalley, R. E. *Nature* **1997,** *388,* 255–257. doi:10.1038/40822
72. Mordkovich, V. Z.; Baxendale, M.; Yoshimura, S.; Chang, R. P. H. *Carbon* **1996,** *34,* 1301–1303. doi:10.1016/0008-6223(96)82802-8
73. Kong, J.; Zhou, C.; Yenilmez, E.; Dai, H. *Appl. Phys. Lett.* **2000,** *77,* 3977–3979. doi:10.1063/1.1331088
74. Kim, B. H.; Park, T. H.; Baek, S. J.; Lee, D. S.; Park, S. J.; Kim, J. S.; Park, Y. W. *J. Appl. Phys.* **2008,** *103,* 096103. doi:10.1063/1.2913170
75. Ito, M.; Tsuruno, A.; Osawa, S.; Tanaka, K. *Polymer* **1988,** *29,* 1161–1165. doi:10.1016/0032-3861(88)90039-0
76. Elsenbaumer, R. L.; Jen, K. Y.; Oboodi, R. *Synth. Met.* **1986,** *15,* 169–174. doi:10.1016/0379-6779(86)90020-2
77. Yoshino, K.; Nakajima, S.; Fujii, M.; Sugimoto, R. *Polym. Commun.* **1987,** *28,* 309–310.
78. Winokur, M. J.; Wamsley, P.; Moulton, J.; Smith, P.; Heeger, A. J. *Macromolecules* **1991,** *24,* 3812–3815. doi:10.1021/ma00013a011
79. Sirringhaus, H.; Tessler, N.; Friend, R. H. *Science* **1998,** *280,* 1741–1744. doi:10.1126/science.280.5370.1741
80. Sirringhaus, H.; Brown, P. J.; Friend, R. H.; Nielsen, M. M.; Bechgaard, K.; Langeveld-Voss, B. M. W.; Spiering, A. J. H.; Janssen, R. A. J.; Meijer, E. W.; Herwig, P.; de Leeuw, D. M. *Nature* **1999,** *401,* 685–688. doi:10.1038/44359
81. Prosa, T. J.; Winokur, M. J.; Moulton, J.; Smith, P.; Heeger, A. J. *Macromolecules* **1992,** *25,* 4364–4372. doi:10.1021/ma00043a019
82. McCullough, R. D.; Tristram-Nagle, S.; Williams, S. P.; Lowe, R. D.; Jayaraman, M. *J. Am. Chem. Soc.* **1993,** *115,* 4910–4911. doi:10.1021/ja00064a070
83. Inganäs, O.; Salaneck, W. R.; Österholm, J.-E.; Laakso, J. *Synth. Met.* **1988,** *22,* 395–406. doi:10.1016/0379-6779(88)90110-5
84. Wang, F.; Gu, H.; Swager, T. M. *J. Am. Chem. Soc.* **2008,** *130,* 5392–5393. doi:10.1021/Ja710795k
85. Snow, E. S.; Perkins, F. K.; Houser, E. J.; Badescu, S. C.; Reinecke, T. L. *Science* **2005,** *307,* 1942–1945. doi:10.1126/science.1109128
86. Yah, W. O.; Irie, A.; Otsuka, H.; Sasaki, S.; Yagi, N.; Sato, M.; Koganezawa, T.; Takahara, A. *J. Phys.: Conf. Ser.* **2011,** *272,* 012021. doi:10.1088/1742-6596/272/1/012021
87. Samitsu, S.; Shimomura, T.; Heike, S.; Hashizume, T.; Ito, K. *Macromolecules* **2008,** *41,* 8000–8010. doi:10.1021/Ma801128v

License and Terms

Beilstein Journal
of Nanotechnology

Electron-beam patterned self-assembled monolayers as templates for Cu electrodeposition and lift-off

Zhe She[1], Andrea DiFalco[2], Georg Hähner[1] and Manfred Buck*[1]

Full Research Paper

Address:
[1]EaStCHEM School of Chemistry, University of St. Andrews, KY16 9ST, U.K and [2]School of Physics and Astronomy, University of St. Andrews, KY16 9ST, U.K

Email:
Manfred Buck* - mb45@st-andrews.ac.uk

* Corresponding author

Keywords:
electrochemical nanotechnology; electrodeposition; lithography; metallic nanostructures; self-assembled monolayers; thiols

Beilstein J. Nanotechnol. **2012,** *3,* 101–113.
doi:10.3762/bjnano.3.11

Received: 13 November 2011
Accepted: 18 January 2012
Published: 06 February 2012

This article is part of the Thematic Series "Self-assembly at solid surfaces".

Guest Editors: S. R. Cohen and J. Sagiv

Abstract

Self-assembled monolayers (SAMs) of 4'-methylbiphenyl-4-thiol (MBP0) adsorbed on polycrystalline gold substrates served as templates to control electrochemical deposition of Cu structures from acidic solution, and enabled the subsequent lift-off of the metal structures by attachment to epoxy glue. By exploiting the negative-resist behaviour of MBP0, the SAM was patterned by means of electron-beam lithography. For high deposition contrast a two-step procedure was employed involving a nucleation phase around −0.7 V versus Cu^{2+}/Cu and a growth phase at around −0.35 V versus Cu^{2+}/Cu. Structures with features down to 100 nm were deposited and transferred with high fidelity. By using substrates with different surface morphologies, AFM measurements revealed that the roughness of the substrate is a crucial factor but not the only one determining the roughness of the copper surface that is exposed after lift-off.

Introduction

Covering the range from tens of micrometers down to nanometers, the scope of applications of metal structures in electronics [1,2], sensing [3-7], electrochemical analysis [8], optics and imaging [9-12] will vitally depend on the extent to which the feature size that is required for a particular application can be achieved by processes that enable an affordable high-throughput production. Commonly pursued routes to match resolution with simplicity are based on schemes involving templated deposition on a reusable master substrate followed by a transfer of the structure to the substrate of interest. A key point underlying these processes is to exploit differences in the interfacial forces between the deposited material and the different substrates [10,13-17]. Among the various deposition techniques [18], which also include evaporation [19,20], chemical vapour deposition (CVD) [21,22] and electroless deposition [22-24], electrodeposition [25-28] offers interesting perspectives, in particular at the nanoscale, due to the level of control over the deposition process. The electrochemical approach combines favourably with self-assembled monolayers (SAMs) as it enables the scheme illustrated in Figure 1a [15]. On the one hand, metal can be selectively deposited by using patterned SAMs, which act as template by defining electrochemically active and passive areas of an electrode [25,26,29-33]. On the other hand, the control of interfacial energies afforded by SAMs enables the lift-off and transfer of deposited metal structures. Since a number of techniques exist which cover the range from macroscopic to nanoscopic dimensions [30,34-38] the combination of patterned SAMs and electrochemistry offers a flexible approach for the generation of metal structures.

While structured SAMs exhibiting electrochemical contrast can be made from two different types of molecules that differ in their blocking properties [15], electron-induced modification of a single component SAM is an alternative that is particularly attractive for providing access to the nanoscale, since e-beam lithography as a high-resolution technique can be employed [26,30]. However, the effect is strongly dependent on the type of SAM [25,30,39,40]. Aliphatic SAMs degrade upon exposure to electrons (positive-resist behaviour), in contrast to aromatic SAMs in which the molecular structure of the SAM is essentially preserved [40] apart from the cross-linking of the aromatic moieties. The rather ill-defined electron-induced degradation of aliphatic SAMs makes it very difficult to control electrodeposition and adhesion of a deposit precisely, whereas an aromatic negative-resist SAM does not have this problem. Therefore, for the scheme outlined in Figure 1a, a negative-resist behaviour employing aromatic SAMs is preferred. As illustrated in Figure 1b the effect of electron irradiation is a cross-linking of the aromatic units, which results in the elimination of defects through which metal ions can penetrate the SAM and be reduced at the SAM–substrate interface. In contrast to a scheme that involves complexation of metal ions with the SAM [41-43] and in which the metal is deposited on top of the SAM, the mechanism explored in the present paper relies on defect-mediated deposition, i.e., the metal nucleation takes place at the SAM–substrate interface at sites of structural imperfections in the monolayer. Since the metal deposit grows in a mushroom-type fashion the contact area and, thus, adhesion between the deposited und substrate metal is greatly reduced. The poor adhesion between the metal deposit and the SAM makes the lift-off possible by simple breaking of the stem of the mushrooms [15,17]. Even though it is not the focus of the present paper, we note that if the patterned SAM layer does not deterio-

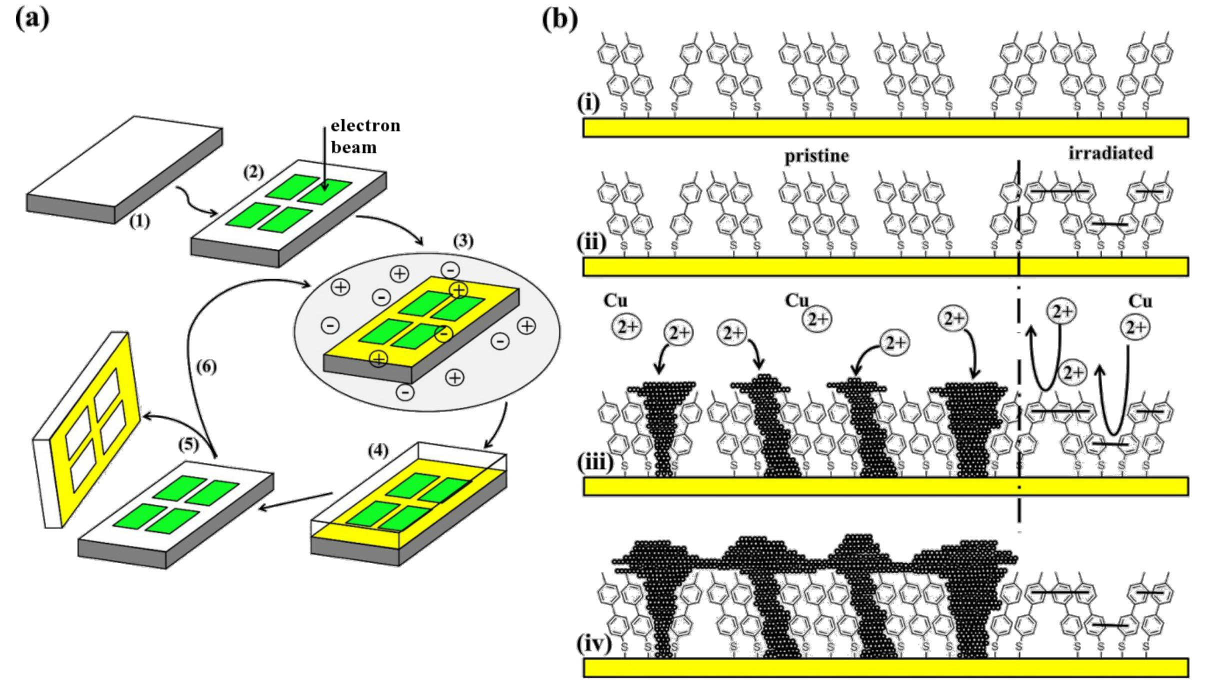

Figure 1: (a) Scheme of SAM controlled electrodeposition and lift-off of metal structures. Starting from a uniform SAM of MBP0 (1), patterning is accomplished by e-beam lithography (2). Acting as a negative resist, electrochemical metal deposition (3) selectively occurs only in the nonirradiated areas. The low surface energy of the CH_3 terminated SAM enables the transfer of the metal pattern to an insulating substrate (4,5) and reuse of the master pattern (6). (b) Illustration of patterning and deposition processes on the molecular scale. When a pristine aromatic SAM (i) is irradiated by an e-beam, cross-linking of molecules results in bridging of defects (right of ii). The resulting passivation confines the deposition to areas of the native SAM (iii). Metal nucleation starts at the bottom of the SAM and deposits grow in a mushroom-type fashion until they coalesce to form a film (iv).

rate during the lift-off process it may serve as a master that can be straightforwardly reused [15]. This is of particular advantage for small-scaled structures in which patterning becomes increasingly time-consuming and expensive.

The feasibility of this SAM based deposition and lift-off scheme has been demonstrated for different metals and alloys such as Cu or CoNiFe with uniform SAMs [17,19,20,44,45] and for micrometer-sized Cu structures with a binary SAM consisting of ω-(4'-methylbiphenyl-4-yl)methanethiol ($CH_3–C_6H_4–C_6H_4–CH_2–SH$, MBP1) as a nonblocking and hexadecane thiol ($CH_3(CH_2)_{15}SH$, MC16) as a blocking thiol [15]. The present paper is an investigation of a scheme for creating surface features with smaller dimensions by using e-beam patterning of a single-component SAM of ω-(4'-methylbiphenyl-4-yl)thiol ($CH_3–C_6H_4–C_6H_4–SH$, MBP0). While selective deposition based on e-beam-modified aromatic SAMs has been demonstrated before [25,26,33], with features down to about 50 nm [26], a transfer of the metal structures has not been reported. It is the focus of the present paper to study steps 1–5 of the deposition–lift-off process depicted in Figure 1a, by using an e-beam-patterned SAM, and to investigate the mutually dependent parameters that are crucial for determining key aspects such as the achievable feature size, the precision of the structure, and the fidelity of the lift-off process.

Results and Discussion

Guided by the scheme depicted in Figure 1, the presentation of the results is organised into two sections discussing electrodeposition and lift-off.

1. SAM templated metal deposition

General aspects

Analogous to unmodified uniform electrodes [46], we assume that the initial stages of the deposition process can be described by the simple case of a time-independent nucleation rate

$$J = Z_0 \Omega \cdot \exp\left[\frac{(n_c + \alpha) z e \eta}{kT}\right] \qquad (1)$$

where Z_0 [cm^{-2}] is the number density of sites on the substrate where nucleation can occur. Ω is a frequency factor, which, besides other quantities, depends on the concentration of metal ions according to $c^{1-\alpha}_{Me^{z+}}$ with α as the charge-transfer coefficient; n_c is the size of the critical nucleus, e the electron charge, and $\eta = (E^0 - E)$ is the overpotential (E^0 = standard potential). From Equation 1 it is seen that the nucleation rate increases exponentially with the overpotential. Another point is that a critical overpotential η_{crit} exists, below which the nucleation rate becomes very small. These two points together are very important as they are the key to high-resolution patterning. A double-pulse-polarisation scheme is applied in which an initial nucleation phase at an overpotential that is significantly larger than η_{crit} is followed by further growth at lower overpotentials, resulting in the achievement of high contrast between areas that differ in η_{crit}.

For the defect-mediated metal deposition on a SAM modified surface (see Figure 1b), nucleation can occur at different types of defects, as illustrated in Figure 2a and discussed in more detail in [47]. Imperfections such as domain boundaries, substrate steps, missing molecules or contaminations can all serve as nucleation sites. Since reduction of the metal ion is determined by tunnelling of the electron, discharge is much more likely to occur close to the Au substrate than at the outer surface of the SAM. Therefore, nucleation starts preferentially at defects through which the ions can penetrate the layer and, thus, approach the Au surface more closely. The probability that an ion penetrates is dependent on the detailed nature of the defects, and thus the rate at which ions are discharged and at which the critical nucleation size is reached can vary substantially for the different types and sizes of defects. Note that the defects are not necessarily static, i.e., potential-dependent changes or fluctuations in the SAM structure also have to be considered, which makes Z_0 a dynamic quantity. Another factor affecting the nucleation rate is specific to metals that bind more strongly to the thiol head group than the original substrate metal. In this case the metal deposited at defects can easily intercalate and diffuse at the SAM–substrate interface [48].

In the case of templated deposition by means of an e-beam patterned SAM, Z_0 becomes a function of the exposed topology. For aromatic SAMs, such as MBP0, which exhibit negative-resist behaviour, the density of nucleation sites Z_0 is determined by the extent of cross-linking of the molecules. While the exact relationship between the defect size in the SAM and the nucleation probability is not known, a nonlinear behaviour can be expected due to the exponential dependence of the electron transfer on the distance between the ion and the metal surface. Reducing the size of defects by cross-linking should strongly decrease the nucleation probability and, thus, result in a substantial reduction in the nucleation density. This is illustrated in Figure 2b in which a spatial profile in the irradiation dose by e-beam lithography generates an inverted profile in the nucleation rate. It is noted that the cross-linking in the SAM is primarily caused by low-energy electrons (<100 eV) [39,40], and, therefore, the spatial resolution is determined by the distribution of secondary electrons, e_s, rather than by the one of the high-energy electrons, e_p, of the primary beam. If a pulsed deposition is used, rather sharp boundaries in the deposition should be possible since two nonlinear effects are superim-

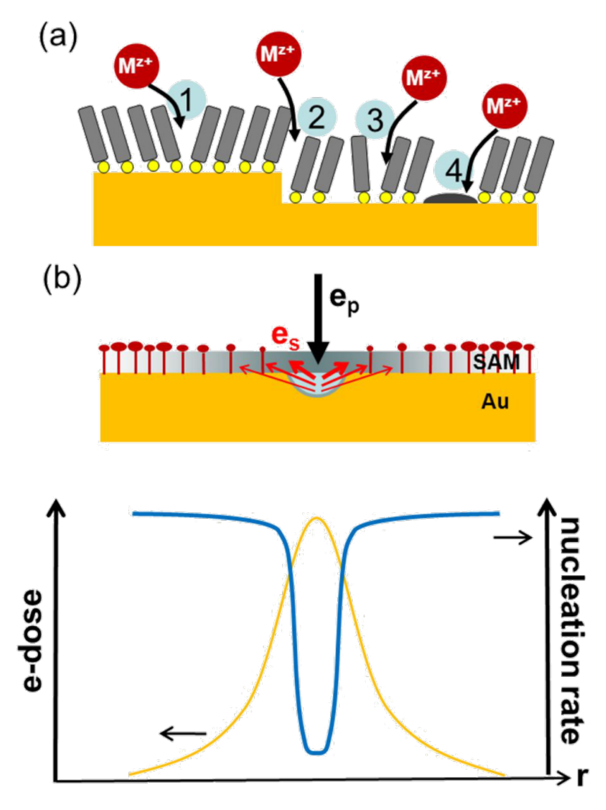

Figure 2: (a) Illustration of different types of defects in a SAM. Domain boundaries (1) and substrate steps (2) as intrinsic defects; missing molecules (3) and contaminations (4) as extrinsic defects. (b) Metal electrodeposition on a negative-resist SAM patterned by e-beam lithography. Top: A primary e-beam, e_p, generates a spatial profile of secondary electrons, e_s. The resulting gradient in the cross-linking of the SAM yields a gradient in the density of nucleation sites for the metal mushrooms. Bottom: Illustration of the inverse relationship between irradiation dose and nucleation rate.

posed, i.e., the one due to cross-linking and the one due to the overpotential according to Equation 1. The precision at which the contour of a metal deposit can be defined is ultimately dependent on two factors. The first one is the gradient in the nucleation rate; the second one is the density of nucleation sites. Although one seeks to maximise the latter, this is ultimately defined by the defect density in the native SAM, which is thus the limiting factor in the achievable resolution.

Experiments

Study of deposition parameters: Prior to metal deposition on e-beam-patterned MBP0-SAMs, the pristine, uniform monolayers were studied and their passivating properties compared with reference systems previously studied in the literature. As seen from Figure 3, the onset of Cu deposition is shifted to more cathodic potentials for the MBP0 coated electrode compared to the clean Au surface, similar to alkanethiol SAMs [29,30,49,50] and other biphenyl based thiols previously studied [15,25,26,33]. The shift of about −0.27 V to +0.3 V is, however, significantly smaller compared to a long chain alkanethiol such as octadecanethiol for which the shift amounts to about −0.6 V. We note at this point that both the sharpness of the onset of deposition and the value of the peak potential are significantly dependent on the quality of the SAM. An important parameter is the cleanliness of the substrate prior to SAM formation [48]. Contaminations result in pinholes in the SAM (defect 4 in Figure 2a) and as a consequence the cyclic voltammograms (CVs) show an earlier onset of deposition and an initially much more gradual increase than those shown in the CVs of Figure 3. When small structures are desired, the preferential nucleation at such extrinsic defects is unfavourable as they are only present at low density, and it is the nucleation density which ultimately limits the feature size. Another parameter is the preparation temperature, for which a higher temperature, in general, improves the crystallinity of the SAM, i.e., increases the domain size. As seen from Figure 3 this influence is rather small for MBP0 and does not, in fact, lie unambiguously outside the range of sample-to-sample variations, which is in agreement with the overall poor crystallinity of this type of SAM [51]. For this reason samples prepared either at room temperature or elevated temperature were used throughout the experiments.

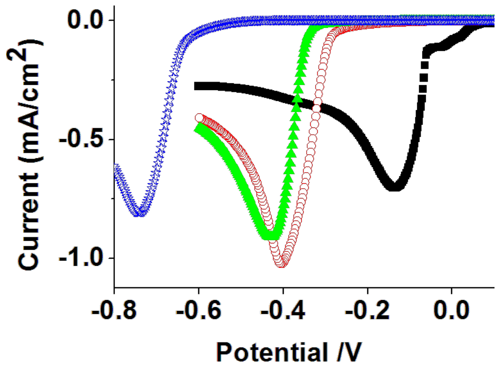

Figure 3: Linear-sweep voltammograms comparing the electrodeposition of Cu on clean (black squares) and SAM modified Au/Si electrodes, from a 50 mM $CuSO_4$/0.1 M H_2SO_4 electrolyte. SAMs were prepared by 24 h immersion of Au/Si substrates into solutions of octadecane thiol (blue stars) at room temperature and of MBP0 at room temperature (red circles) and 65 °C (green triangles).

The selective deposition on a patterned SAM depends on a number of parameters, some of which exert an opposite influence on the deposition. As outlined above, on the one hand, a more negative deposition potential increases the nucleation density and, thus, improves the contour definition of the Cu pattern and the achievable resolution. On the other hand, it reduces the deposition contrast between irradiated and nonirradiated areas since defects in the irradiated SAM are unlikely to be fully eliminated.

For this reason the deposition process was investigated by chronoamperometry. Figure 4a shows *I–t* curves of a uniform, pristine MBP0-SAM recorded at three different potentials.

All curves show the characteristic shape of a nucleation-and-growth process. In the initial stage, nucleation is inhibited since Cu reduction is limited by the SAM [45,52]. The current increases due to the formation of nuclei and mushroom structures at defects in the SAM (Figure 1b). At this point the electrode surface can be described by a statistical array of nanoelectrodes. Subsequently the current becomes transport-limited and, therefore, passes a maximum after a given time, which becomes shorter with higher cathodic potential. Diffusion-controlled growth is reflected by a decreasing current whose time dependence evolves into that of a flat electrode upon overlap of the diffusion fields of the mushrooms [53]. This is the region beyond 7 s where the curves adopt an identical shape. An optimisation of the conditions has to take into account three factors: The gradient of the cross-linking, the potential affecting the nucleation density, and the time.

Deposition on an e-beam-patterned MBP0-SAM under the condition of a constant potential is shown in Figure 4c. The SEM image showing Cu free lines about 400 nm wide clearly demonstrates the passivation of the SAM by e-beam-induced cross-linking, which either seals the defects in the SAM or reduces them to a size such that the overpotential required for bulk metal deposition is not reached anymore. It might be worth noting that the absence of bulk Cu deposition does not mean that Cu is not deposited at all. Ions can still penetrate and, analogous to underpotential deposition (UPD), be intercalated at the SAM–Au interface. If the rate of penetration is lower than the diffusion rate at the SAM–substrate interface, mushroom formation is suppressed [48]. While the SEM image demonstrates a clear passivation effect, the contour definition is poor and prohibitive for extension to smaller dimensions. In order to improve the contour definition the nucleation density has to be increased, and an obvious way to do this is to increase the overpotential. However, when going to a larger overpotential, one has to bear in mind that the deposition process is a trade-off between different factors. On the one hand, a more negative

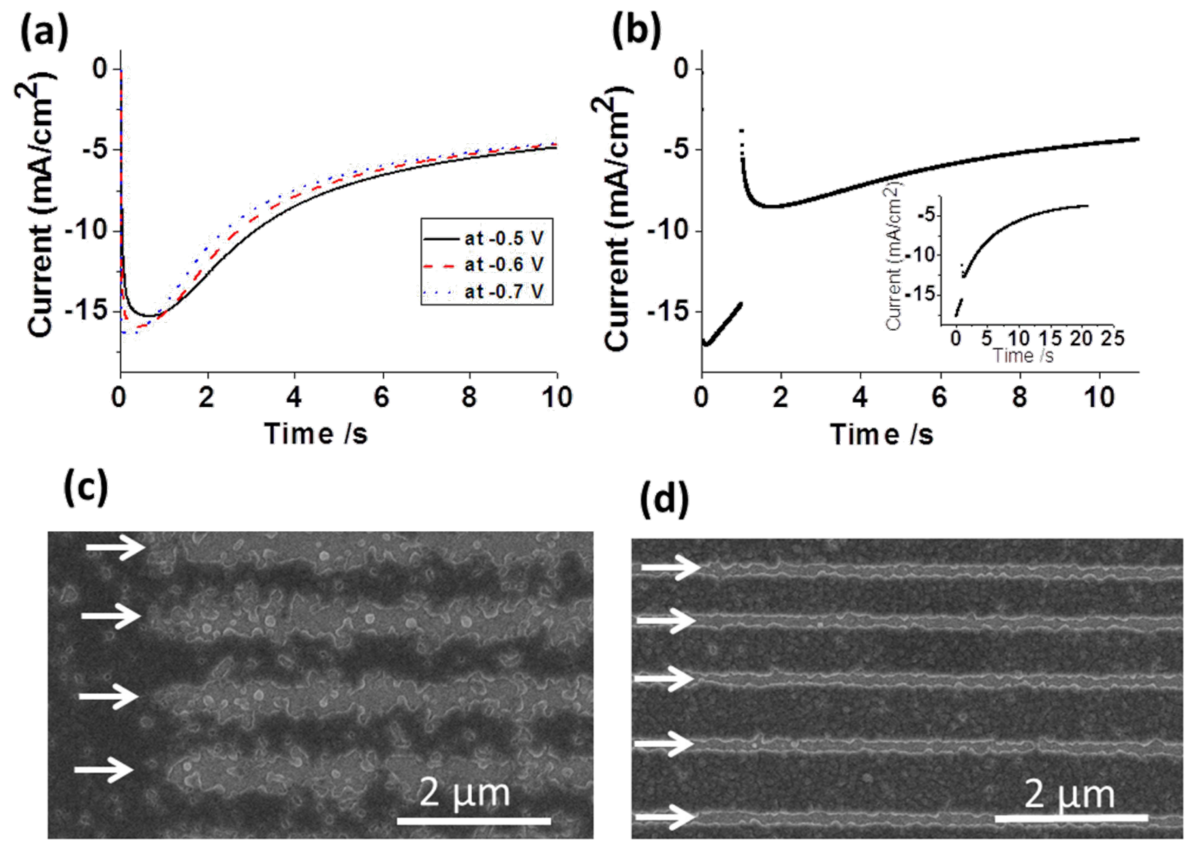

Figure 4: (a,b) Chronoamperograms of single potential (a) and double potential (b) deposition processes on a uniform MBP0-SAM on Au/Si. Potentials of *I–t* curves in (a) are −0.5 V (black line), −0.6 V (red dashed line) and −0.7 V (green dotted line) and in (b) −0.7 V for 1 s, −0.35 V for 10 s on MBP0/Au/Si. For comparison an *I–t* curve for a clean Au/Si substrate and identical deposition conditions is shown in the inset. (c,d) SEM images of Cu deposition on e-beam-patterned SAMs. Lines indicated by arrows were written with an electron dose of 800 mC/cm^2 in both cases. Deposition was carried out in (c) at −0.5 V for 15 s, and in (d) at −0.7 V for 1 s and at −0.35 V for 10 s.

potential increases the nucleation density but, on the other hand, will reduce the contrast between native and cross-linked MBP0 areas. Furthermore, with increasing density of mushrooms the lift-off will become more difficult. For these reasons we explored a two-step-deposition procedure as illustrated in Figure 4b. A short nucleation step at potentials more negative than for the one-step sample (Figure 4c) is followed by a growth phase at potentials even more positive than for the single-step procedure.

As evidenced by Figure 4d this results in significantly better pattern definition. Besides the improved contour definition it is obvious that the passivated lines are significantly narrower, despite the fact that identical irradiation conditions were used. The reason for this is the cross-linking profile. Even though the primary e-beam is well focused (~20 nm) the cross-linking is caused by the secondary electrons from the substrate, as illustrated in Figure 2b, thus resulting in line broadening and a gradient orthogonal to the line. With increasingly negative potentials the boundary moves towards the line centre, since nucleation is, as discussed above, a complex process that is nonlinearly dependent on the potential and on SAM defects.

The evolution of the deposition for the two-step process is shown in Figure 5, under the conditions depicted in the *I–t* diagram of Figure 4b. After 1 s at −0.7 V Cu deposits are observed, which range in size, from small isolated clusters to extended irregularly shaped islands, and demonstrate a significant statistical variation in the nucleation density. After 5 s of further growth at −0.35 V (Figure 5b) a continuous Cu layer is observed with, however, a significant number of holes varying in size, which close upon further deposition.

The statistical variation in the nucleation density evidenced in Figure 5 highlights the limiting factor for the precision of the deposition process, i.e., how sharply the contour between deposition and Cu free areas can be defined. At present the exact relationship between the threshold for nucleation of Cu mushrooms and the nature of the defect is not clear, but the rate at which Cu penetrates through to the Au electrode can be safely assumed to be a decisive factor. Similar to what has been observed for Cu-UPD on a SAM [48], the statistical distribution of rates is determined by the structural quality of the SAM. To improve the precision further one has to develop a process that is independent of the statistical defects in a SAM by, for example, producing a highly passivating SAM and then introduce defects afterwards in a controlled way.

Deposition on e-beam-patterned SAMs: As discussed above, the extent to which defects in the SAM are modified by electron-induced cross-linking is crucial for the spatial resolution. Therefore, besides the parameters for the electrochemical deposition the influence of the irradiation dose on the quality of the Cu structures was also studied. In a series of lines written by the electron beam, the dose was varied between 50 and 750 mC/cm^2. As seen from Figure 6a, there is a pronounced improvement in the definition of the lines for which Cu deposition was suppressed. It is noted that the doses needed to produce good contrast in our electrochemical experiment are substantially higher compared to those reported in the literature. For example, for Ni deposited from the gas phase about 45 mC/cm^2 was used [54]. In electrochemical deposition of Cu on C_6H_5–C_6H_4SH SAMs [26,33] and CH_3–C_6H_4–C_6H_4–$(CH_2)_{12}$–SH [25] a dose of maximal 80 mC/cm^2 was used. However, it is difficult to compare the conditions, both with regard to the patterning parameters and the deposition conditions. The yield of the low-energy secondary electrons causing the cross-linking may vary substantially as a primary beam with an energy of 30 keV was used in the present experiments compared to the few hundred eV to 3 keV in the other experiments. Furthermore, the potential in the two potential protocols where nucleation occurs was significantly more negative compared to potentials applied in the one-step-deposition process reported in the literature [26,33]. For the

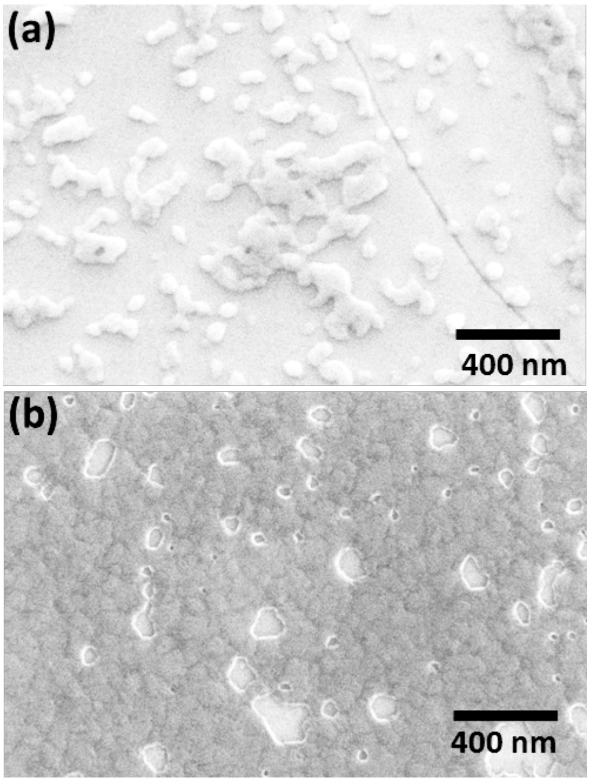

Figure 5: SEM images of Cu nucleation and growth on a MBP0-SAM on Au/Ag/Mica prepared at 65 °C for 24 h. (a) Cu nucleation sites and islands after deposition at −0.7 V for 1 s. (b) Cu layer after nucleation at −0.7 V for 1 s and growth at −0.35 V for 5 s.

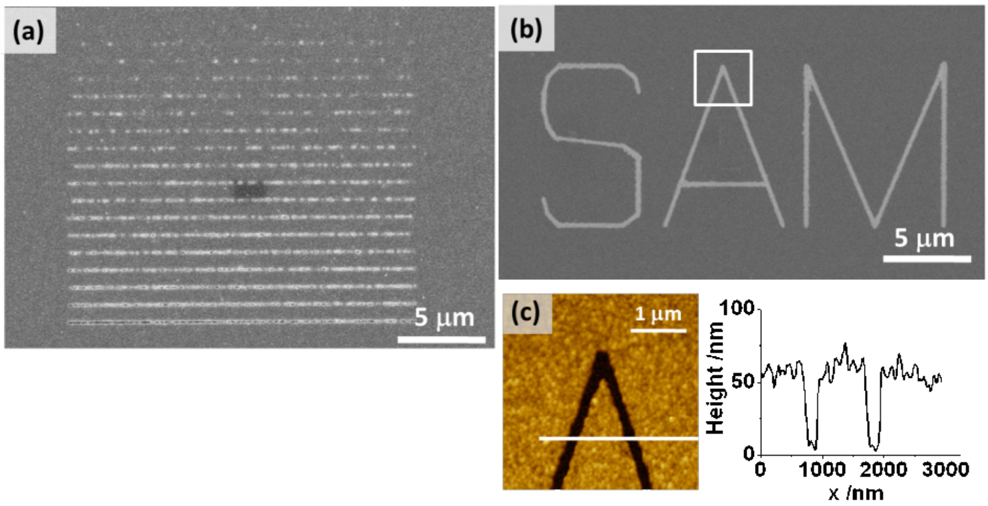

Figure 6: Electrochemical deposition of Cu on e-beam-patterned MBP0-SAM/Au/Si. (a) SEM image of a series of passivating lines written at different doses. The difference in the dose between lines is 25 mC/cm^2, with 750 mC/cm^2 as the highest dose for the bottom line. (b) SEM image of “SAM” written with an electron beam at a dose of 1000 mC/cm^2. (c) AFM image of the area marked by the square in (b) together with a height profile along the line. Deposition conditions: −0.7 V for 1 s, −0.25 V for 20 s (a); −0.7 V for 1 s, −0.35 V for 10 s (b).

high doses used in this work in combination with the two-step-deposition procedure, an excellent contrast is achieved as demonstrated by the pattern depicted in the SEM image of Figure 6b and the AFM image of Figure 6c showing grooves about 170 nm wide and 60 nm deep.

2. Lift-off of Cu structures

With regard to the transfer of the deposited pattern to an insulating substrate we were particularly interested in the following points: (i) The fidelity of the lift-off process; (ii) the morphology of the metal surface originally facing the SAM in comparison with the surface of the growing film exposed to the electrolyte; and (iii) the relationship between the roughness of the substrate and the Cu structure.

Figure 7, showing a copper structure as deposited and after lift-off, demonstrates that the pattern is transferred without distortion. All features of the trench seen on the original structure (Figure 7a) are precisely reproduced in the structure attached to the epoxy glue (Figure 7b), which, due to the lift-off, appears as a mirror image of the original structure. The fidelity with which the pattern is transferred demonstrates that the simple transfer process is suitable for the routine generation of high-resolution metal patterns on insulating substrates even for significantly smaller structures down to ~50 nm, which have been tried. However, even though the transfer process imposes no restrictions on the feature size, at this point we did not systematically pursue the fabrication of features smaller than those shown here, for reasons that are obvious from Figure 7. There are deviations from the straight boundary line separating the copper-free and deposition areas, by up to 20 nm. This is due to a statistical variation in the nucleation density, which is determined by the random defects present in the native SAM and already addressed above. Another point is an increase in the width of the line by about 20% when going from the structure as deposited (Figure 7a) to that after the lift-off (Figure 7b). We ascribe this to nonvertical growth of the trench walls due to transport-limited deposition, similar to subconformal Cu deposition in microelectronics [55,56].

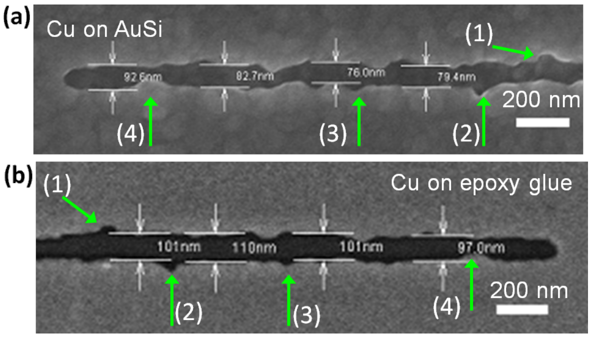

Figure 7: SEM images of a SAM templated copper deposit on the original MBP0 coated Au/Si substrate (a) and after transfer to epoxy glue (b). The passivating line of the cross-linked SAM was written by using an e-beam dose of 750 mC/cm^2 . Deposition parameters are −0.7 V for 1 s, −0.25 V for 20 s. The numbered green arrows mark the corresponding features in (a) and (b).

Besides the definition of the lateral dimensions, another point of interest is the surface topography. Reminding ourselves that the SAM and electrolyte-facing surfaces of the Cu deposition layer

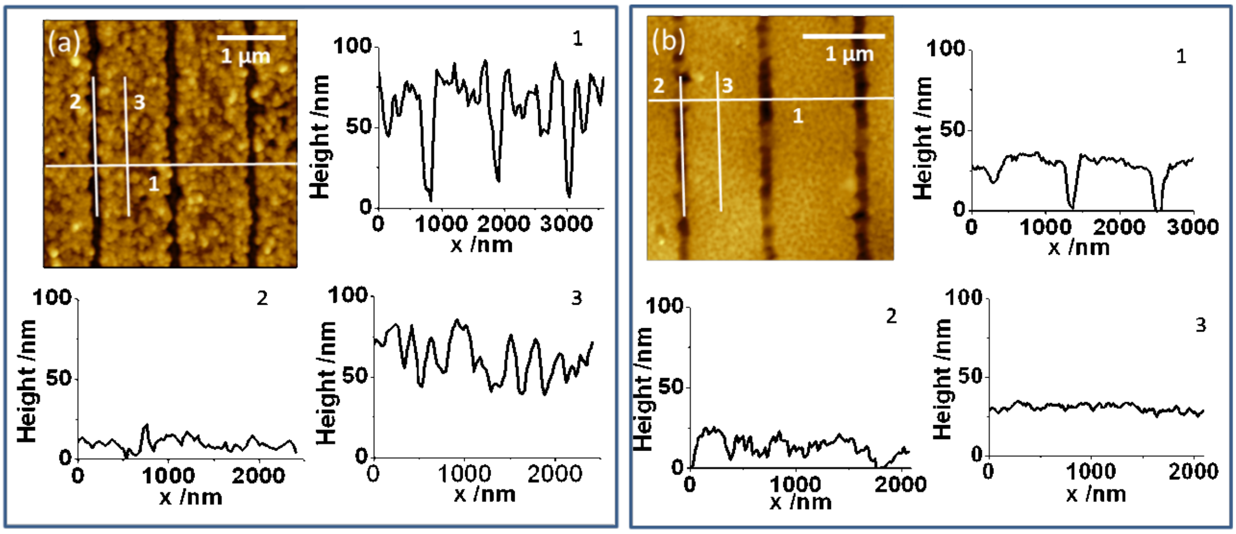

Figure 8: AFM topography images of Cu electrodeposited onto an e-beam-patterned MBP0-SAM on Au/Si (a) before and (b) after lift-off. The height profiles shown are taken along the numbered cross-sections. Lines of cross-linked MBP0 were written by using a dose of 1000 mC/cm^2. The parameters for Cu deposition were −0.7 V for 1 s, −0.35 V for 10 s.

become the exposed and buried ones, respectively, after transfer, a comparison of their topography is of interest with regard to potential applications in optics, for example, where the smoothness of films is important.

Figure 8 shows a compilation of AFM images comparing the structure as deposited on a MBP0 patterned Au/Si substrate with the one transferred to the epoxy glue. Parallel lines about 1 µm apart were written into the SAM by e-beam lithography. As inferred from the difference between the grooves, where the cross-linked MBP0-SAM inhibits deposition, and the areas of deposition, the two-step deposition involving a 10 s growth period yields a thickness of the Cu layer of about 70 nm (Figure 8a, curve 1).

Comparison of the height profiles inside and outside of the grooves (Figure 8a, curves 2 and 3) shows that the growing surface of the Cu deposition is significantly rougher than the original substrate. This is very different from the Cu surface facing the SAM which is depicted in Figure 8b. It is seen from the height profile (Figure 8b, curve 3) that this Cu surface has a corrugation comparable to that of the substrate (Figure 8a, curve 2). In contrast, the profile along the line is less-smooth compared to the corrugation in the original groove. Together with the line depth (Figure 8b, curve 1), which is significantly smaller than for the original grooves and ranges between 10–40 nm, this demonstrates that the filling of the grooves with epoxy glue is rather incomplete. Taking into account that the fairly viscous glue is applied under ambient conditions, we consider air trapped in the grooves to be the major reason. Unfortunately, further studies excluding air, in particular to see whether the glue in the lines can be made coplanar with the metal surface, were impossible, since we could not apply the epoxy glue under vacuum.

Similar results were observed with a wider trench structure. Figure 9 shows a comparison between the two Cu surfaces analogous to the line structure in Figure 8. Again, the deposition contrast is excellent with a complete suppression of deposition also for this extended cross-linked area. The thickness of the Cu deposit was approximately 70 nm as seen from the line profile in Figure 9a, i.e., the same as measured for the line structure (Figure 8) for which the deposition parameters were the same. The depth between the Cu surface and the copper-free area was 30 nm after lift-off, revealing an incomplete filling of the trench by the glue, which is again likely due to trapping of air. On comparison of the friction images of the Cu structure as deposited and after lift-off (Figures 9b and 9d), a very different friction contrast is seen between deposition and Cu free areas according to the mechanical properties of the materials. While in both cases the friction inside the trench is higher than on the Cu deposit, the difference between the two areas is more than 30 times larger between the rather soft epoxy glue and Cu, compared to SAM/Au and Cu.

Roughness measurements: Since, as evident from Figures 8 and 9, the Cu surface facing the SAM is substantially smoother than the opposite one with a roughness close to that of the substrate, the influence of the substrate quality was studied in more detail.

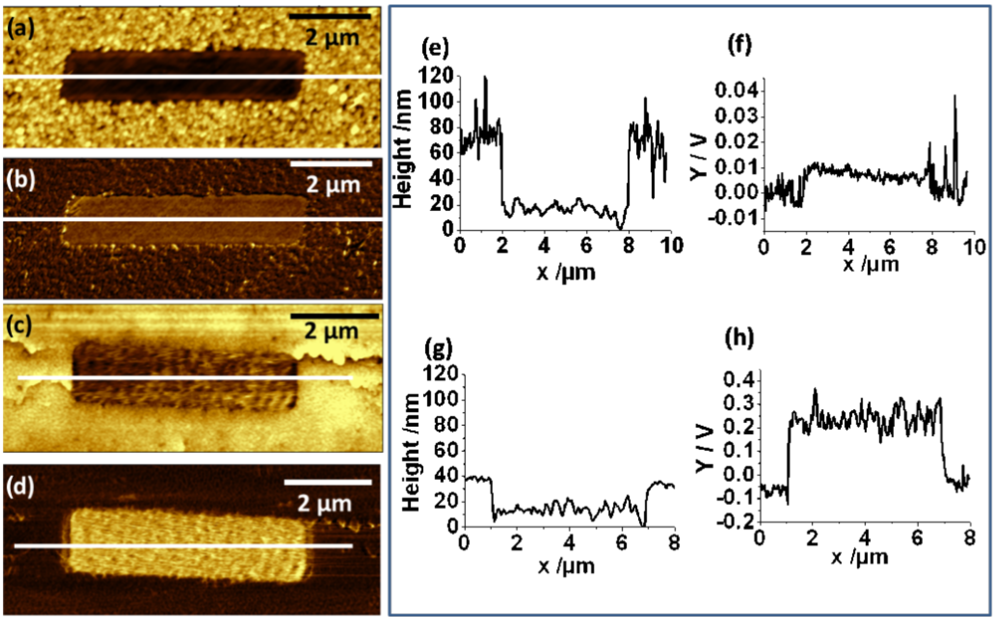

Figure 9: AFM images of Cu electrodeposition onto a MBP0/Au/Si sample demonstrating the quality of passivation of the cross-linked MBP0-SAM. Topography (a,c) and friction (b,d) images of the Cu structure as deposited (a,b) and after transfer to epoxy glue (c,d); (e) height and (f) friction profile along the line for Cu as deposited; (g,h) corresponding profile for the lifted-off structure. The 5 × 1 µm^2 rectangle of cross-linked MBP0-SAM was generated with an electron beam dose of 500 mC/cm^2. Conditions for the two-step electrodeposition were −0.7 V for 1s and −0.35 V for 10 s.

For this purpose substrates with different degrees of roughness were compared. Besides Au/Si whose morphology is determined by small crystallites of different orientations, Ag/mica and Au/Ag/mica substrates were used because Au and Ag can be grown epitaxially on mica [57,58], and this results in less corrugated films with a well-defined (111) orientation of the crystallites and much larger terraces. The reason for using Ag either as a substrate directly, or as interlayer, is that Au adheres poorly to mica. While the poor adhesion of Au has been taken advantage of for the generation of ultraflat Au substrates through the template-stripping method [59,60], it is a limiting factor for our scheme. Even though transfer using Au/mica can be achieved to some extent, the parameters must be so narrowly defined as to prohibit a reliable, routinely applicable process. By using silver this problem is significantly alleviated.

In a series of experiments Cu films were uniformly deposited on MBP0 modified substrates and subsequently transferred to epoxy glue, and the surfaces were then compared with the original substrate. Representative examples for Au/Si and Au/Ag/mica are shown in Figure 10a. The latter is also essentially identical to Ag/mica (not shown) as inferred from the histograms shown in Figure 10b and Table 1, which compiles the averaged root-mean-square (RMS) values and their variations expressed as the standard deviation σ. Figure 10b represents the results from 30 RMS measurements for each substrate and with values grouped into intervals of 0.1 nm.

From the histograms and the tabulated values one can infer that, on the one hand, the substrate substantially influences the roughness of the Cu surface but, on the other hand, is not the limiting factor. The improvement in the surface roughness of the Cu structure from 1.74 nm to 1.22 nm upon changing from Au/Si to the mica-based substrates is evidence for the former, whereas the increase in roughness of the lift-off Cu structure compared to the substrates reveals the latter and demonstrates that the deposition process is also crucial for the topography. This is not unexpected, as the roughness must be dependent on the morphology of the mushrooms, in particular at the point of coalescence. In this context we note that deposition on Au/Si under slightly different conditions such as −0.7 V for 1 s and −0.25 V for 20 s for nucleation and growth, respectively, can result in a slightly smoother surface of the deposit, hence indicating that the deposit does not exactly reproduce the contour of the SAM surface. While the roughening of the Cu structure by a factor of two compared to the mica substrate is substantial, its cause is not clear at present. The mushroom morphology, as the factor ultimately limiting the flatness, cannot account for it. Even though it is not clear where the stems of the mushroom break during the lift-off process, with a maximal height of about 1.5 nm and a density of less than 1 per 100 nm^2 the contribution to the roughness must be significantly smaller. There is scope for further improvement, as the optimisation of parameters, such as nucleation potential, time, growth potential, and the use of additives [45], was not systematically investigated.

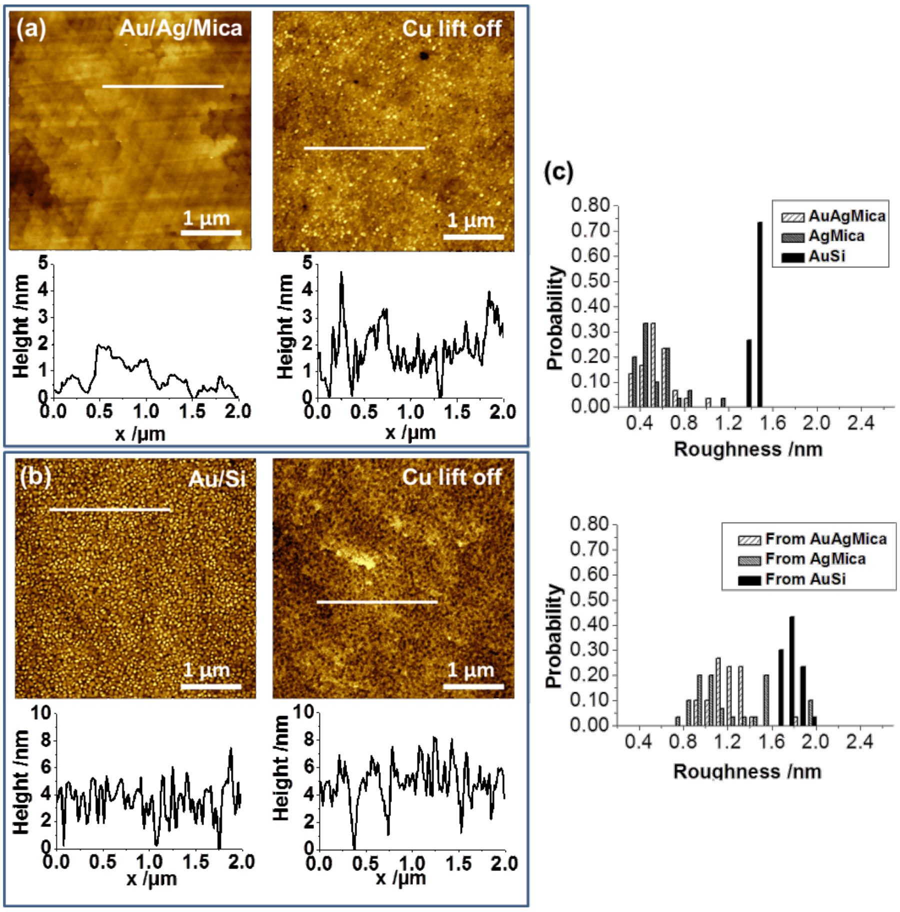

Figure 10: (a,b) AFM topography images and height profiles along the lines indicated, comparing the roughness of different substrates with the corresponding surface of the Cu film after lift-off; (a) Au/Ag/mica (b) Au/Si. Conditions for Cu deposition: −0.8 V for 2 s and −0.35 V. (c) Roughness histograms of substrates (top) and Cu surfaces after lift-off (bottom) from 30 measurements of areas 1 × 1 µm^2 in size for each surface.

Furthermore, the lift-off process has not been studied in detail and it is currently an open question as to what extent the forces that act during the curing of the epoxy and the lift-off process influence the roughness of the exposed metal surface.

Table 1: Statistical analysis of the roughness measurements for different substrates and corresponding Cu surfaces after lift-off. Root-mean-square (RMS) average determined from 30 measurements of areas 1 × 1 µm^2 in size. σ is the standard deviation of the RMS values.

substrate		RMS average [nm]	σ [nm]
Au/Si	substrate	1.42	0.03
	Cu lift-off	1.74	0.07
Au/Ag/Mica	substrate	0.57	0.15
	Cu lift-off	1.22	0.17
Ag/Mica	substrate	0.54	0.18
	Cu lift-off	1.22	0.35

Conclusion

The possibility to control both electrode activity and interfacial energies by means of a patterned SAM is exploited in a scheme to generate metal structures on an insulating substrate by a simple electrodeposition/lift-off scheme. An important point with regard to the realisation of small features is that the scheme relies on a trade-off between the nucleation density and the control of adhesion. Since the deposition is defect-mediated, an increase in the number of defects will necessarily result in higher adhesion. While this will become a resolution-limiting factor at one point, the currently realised structural features of down to around 50 nm are limited by the precision at which nucleation can be controlled. Rather than relying on statistical defects originating from the SAM preparation itself, the controlled introduction of defects ex post facto into a well passivating SAM should be the way forward towards significantly higher resolution. Considering the excellent blocking of metal deposition by the cross-linked MBP0-SAM, inducing defects by means of a focused ion beam seems like a promising strategy.

An advantage of the scheme is that the metal surface exposed after lift-off is very smooth and, thus, very similar to template-stripped uniform films but with the additional feature of small-scale patterns. Even though the substrate roughness plays a crucial role for the topography of the film, there are still contributions from additional factors that have yet to be elucidated. One obvious point is a further optimisation of the deposition parameters with regard to the mutual interplay between growth rate and morphology. So far the scheme has been demonstrated for Cu, and it will be of interest to extend this to other metals, such as Ag or Au, and to see how the different interactions between these metals and the SAM will affect the deposition process. Another aspect is to explore the repeatability of the process, i.e., the stability of the SAM patterns upon multiple cycling comprising all of the steps 2–6 as depicted in Figure 1a.

Experimental

Substrates, SAM preparation and patterning: Two types of gold substrates purchased from Georg Albert PVD, Germany were used: (i) 100 nm of Au evaporated onto a Si(100) wafer with a 5 nm titanium interlayer; (ii) 300 nm of Au on 300 nm of silver on mica slides. Both Ti and Ag served as adhesion promoters. Substrates were cut into 3–5 cm^2 pieces. SAMs were prepared by immersion of the substrate into a 100 µM solution of ω-(4'-methylbiphenyl-4-yl)thiol [51] ($CH_3–C_6H_4–C_6H_4–SH$, MBP0) in ethanol, either at room temperature or at 65 °C, for 24 h. Samples were then rinsed with ethanol and blown dry in a stream of nitrogen.

Patterning of the SAM was performed by e-beam lithography (RAITH Elphy Plus/LEO 1530 hybrid system) with a 30 kV beam, and exposures varied between 40 and 1000 mC/cm^2. Patterned SAMs were reimmersed in MBP0 solution at room temperature for 8 h.

Electrochemistry: Using an Eco Chemie AUTOLAB PGSTAT128N and NOVA 1.4 software, the electrochemical experiments were performed in a home-built cell with a standard three-electrode configuration. Cu wires served as both reference and counter electrodes. The area of the working electrode was 40 mm^2. Electrodeposition of Cu was carried out with a 50 mM $CuSO_4/H_2SO_4$ solution of about pH 1 (chemicals from Sigma-Aldrich, 99.999%). After electrochemical deposition the substrates were rinsed with deionised water and dried under a stream of nitrogen.

A two-potential deposition was employed for deposition of the Cu structures. Typical values for the two steps were in the ranges between −0.6 and −0.8 V for 1–2 s and between −0.25 and −0.35 V for 10–20 s, respectively.

Lift-off of electrodeposited Cu: Both uniform films and patterns were lifted off mechanically by applying epoxy glue (Araldite rapid set), which was cast by placing a Teflon plate with a hole of 6 mm diameter onto the substrate. Curing of the epoxy was performed at room temperature, typically overnight.

Characterization: Cu structures were characterised by scanning electron microscopy (Hitachi S4800) and atomic force microscopy (PicoPlus, Molecular Imaging). Using Veeco NPS10 nonconductive silicon nitride tips (spring constant 0.06 N/m) AFM images were recorded in contact mode by using forces between 7 and 13 nN and scan rates of 0.9 to 1.2 Hz. Images were analysed using either the Picoscan software (Molecular Imaging) or Gwyddion. For the roughness analysis of the AFM topography images (4 × 4 $µm^2$, 512 × 512 pixels) images were line-corrected by matching to the height median, and horizontal scars were removed. The root-mean-square values were measured by performing Gwyddion statistical analysis of areas 1 × 1 $µm^2$ in size from 4 × 4 $µm^2$ sized images (512 × 512 pixels).

Acknowledgements

This work was supported by EPSRC (SCH0-YEP061). ADF is supported by a Career Acceleration Fellowship from EPSRC (EP/I004602/1).

References

1. Choi, J.; Lee, K.; Janes, D. B. *Nano Lett.* **2004,** *4,* 1699–1703. doi:10.1021/nl049113x
2. Hu, J.; Yu, M.-F. *Science* **2010,** *329,* 313–316. doi:10.1126/science.1190496
3. Finklea, H. O. Electrochemistry of Organized Monolayers of Thiols and Related Molecules on Electrodes. In *Electroanalytical Chemistry: A Series of Advances;* Bard, A. J.; Rubinstein, I., Eds.; Marcel Dekker: New York, 1996; Vol. 19, pp 109–335.
4. Goldenberg, L. M.; Bryce, M. R.; Petty, M. C. *J. Mater. Chem.* **1999,** *9,* 1957–1974. doi:10.1039/a901825e
5. Gooding, J. J.; Lai, L. M. H.; Goon, I. Y. Nanostructured Electrodes with Unique Properties for Biological and Other Applications. In *Chemically Modified Electrodes;* Alkire, R. C.; Kolb, D. M.; Lipkowski, J.; Ross, P. N., Eds.; Advances in Electrochemical Science and Engineering, Vol. 11; Wiley-VCH: Weinheim, 2009; pp 1–56.
6. Penner, R. M. *MRS Bull.* **2010,** *35,* 771–777. doi:10.1557/mrs2010.506
7. Huang, S.; Chen, Y. *Nano Lett.* **2008,** *8,* 2829–2833. doi:10.1021/nl801429p
8. Salaün, P.; Planer-Friedrich, B.; van den Berg, C. M. G. *Anal. Chim. Acta* **2007,** *585,* 312–322. doi:10.1016/j.aca.2006.12.048
9. Barnes, W. L.; Dereux, A.; Ebbesen, T. W. *Nature* **2003,** *424,* 824–830. doi:10.1038/nature01937
10. Nagpal, P.; Lindquist, N. C.; Oh, S.-H.; Norris, D. J. *Science* **2009,** *325,* 594–597. doi:10.1126/science.1174655
11. Mühlschlegel, P.; Eisler, H.-J.; Martin, O. J. F.; Hecht, B.; Pohl, D. W. *Science* **2005,** *308,* 1607–1609. doi:10.1126/science.1111886

12. Yu, N.; Cubukcu, E.; Diehl, L.; Belkin, M. A.; Crozier, K. B.; Capasso, F.; Bour, D.; Corzine, S.; Höfler, G. *Appl. Phys. Lett.* **2007,** *91,* 173113. doi:10.1063/1.2801551
13. Zach, M. P.; Ng, K. H.; Penner, R. M. *Science* **2000,** *290,* 2120–2123. doi:10.1126/science.290.5499.2120
14. Loo, Y.-L.; Willett, R. L.; Baldwin, K. W.; Rogers, J. A. *Appl. Phys. Lett.* **2002,** *81,* 562–564. doi:10.1063/1.1493226
15. Thom, I.; Hähner, G.; Buck, M. *Appl. Phys. Lett.* **2005,** *87,* 024101. doi:10.1063/1.1991992
16. Schilardi, P. L.; Azzaroni, O.; Salvarezza, R. C. *Langmuir* **2001,** *17,* 2748–2752. doi:10.1021/la0016672
17. Schilardi, P. L.; Dip, P.; dos Santos Claro, P. C.; Benítez, G. A.; Fonticelli, M. H.; Azzaroni, O.; Salvarezza, R. C. *Chem.–Eur. J.* **2005,** *12,* 38–49. doi:10.1002/chem.200500203
18. Haick, H.; Cahen, D. *Prog. Surf. Sci.* **2008,** *83,* 217–261. doi:10.1016/j.progsurf.2008.04.002
19. Azzaroni, O.; Fonticelli, M.; Schilardi, P. L.; Benítez, G.; Caretti, I.; Albella, J. M.; Gago, R.; Vázquez, L.; Salvarezza, R. C. *Nanotechnology* **2004,** *15,* S197–S200. doi:10.1088/0957-4484/15/4/014
20. Azzaroni, O.; Fonticelli, M. H.; Benítez, G.; Schilardi, P. L.; Gago, R.; Caretti, I.; Vázquez, L.; Salvarezza, R. C. *Adv. Mater.* **2004,** *16,* 405–409. doi:10.1002/adma.200306190
21. Weckenmann, U.; Mittler, S.; Krämer, S.; Aliganga, A. K. A.; Fischer, R. A. *Chem. Mater.* **2004,** *16,* 621–628. doi:10.1021/cm031094p
22. Walker, A. V. *Langmuir* **2010,** *26,* 13778–13785. doi:10.1021/la903937u
23. Bhuvana, T.; Kulkarni, G. U. *Bull. Mater. Sci.* **2008,** *31,* 201–206. doi:10.1007/s12034-008-0036-y
24. Nottbohm, C. T.; Turchanin, A.; Gölzhäuser, A. *Z. Phys. Chem.* **2008,** *222,* 917–926. doi:10.1524/zpch.2008.6015
25. Felgenhauer, T.; Yan, C.; Geyer, W.; Rong, H.-T.; Gölzhäuser, A.; Buck, M. *Appl. Phys. Lett.* **2001,** *79,* 3323–3325. doi:10.1063/1.1415771
26. Völkel, B.; Kaltenpoth, G.; Handrea, M.; Sahre, M.; Nottbohm, C. T.; Küller, A.; Paul, A.; Kautek, W.; Eck, W.; Gölzhäuser, A. *Surf. Sci.* **2005,** *597,* 32–41. doi:10.1016/j.susc.2004.08.046
27. Xiang, C. X.; Kung, S.-C.; Taggart, D. K.; Yang, F.; Thompson, M. A.; Güell, A. G.; Yang, Y. A.; Penner, R. M. *ACS Nano* **2008,** *2,* 1939–1949. doi:10.1021/nn800394k
28. Zeira, A.; Berson, J.; Feldman, I.; Maoz, R.; Sagiv, J. *Langmuir* **2011,** *27,* 8562–8575. doi:10.1021/la2009946
29. Sondag-Huethorst, J. A. M.; Fokkink, L. G. J. *Langmuir* **1995,** *11,* 4823–4831. doi:10.1021/la00012a039
30. Sondag-Huethorst, J. A. M.; van Helleputte, H. R. J.; Fokkink, L. G. J. *Appl. Phys. Lett.* **1994,** *64,* 285–287. doi:10.1063/1.111182
31. O'Brien, B.; Stebe, K. J.; Searson, P. C. *J. Phys. Chem. C* **2007,** *111,* 8686–8691. doi:10.1021/jp072176u
32. Pesika, N. S.; Radisic, A.; Stebe, K. J.; Searson, P. C. *Nano Lett.* **2006,** *6,* 1023–1026. doi:10.1021/nl060368f
33. Kaltenpoth, G.; Völkel, B.; Nottbohm, C. T.; Gölzhäuser, A.; Buck, M. *J. Vac. Sci. Technol., B: Microelectron. Nanometer Struct.–Process., Meas., Phenom.* **2002,** *20,* 2734–2738. doi:10.1116/1.1523026
34. Love, J. C.; Estroff, L. A.; Kriebel, J. K.; Nuzzo, R. G.; Whitesides, G. M. *Chem. Rev.* **2005,** *105,* 1103–1170. doi:10.1021/cr0300789
35. Smith, R. K.; Lewis, P. A.; Weiss, P. S. *Prog. Surf. Sci.* **2004,** *75,* 1–68. doi:10.1016/j.progsurf.2003.12.001
36. Shen, C.; Buck, M. *Nanotechnology* **2009,** *20,* 245306. doi:10.1088/0957-4484/20/24/245306
37. Turchanin, A.; Schnietz, M.; El-Desawy, M.; Solak, H. H.; David, C.; Gölzhäuser, A. *Small* **2007,** *3,* 2114–2119. doi:10.1002/smll.200700516
38. Klauser, R.; Huang, M.-L.; Wang, S.-C.; Chen, C.-H.; Chuang, T. J.; Terfort, A.; Zharnikov, M. *Langmuir* **2004,** *20,* 2050–2053. doi:10.1021/la030398n
39. Geyer, W.; Stadler, V.; Eck, W.; Zharnikov, M.; Gölzhäuser, A.; Grunze, M. *Appl. Phys. Lett.* **1999,** *75,* 2401–2403. doi:10.1063/1.125027
40. Zharnikov, M.; Grunze, M. *J. Vac. Sci. Technol., B: Microelectron. Nanometer Struct.–Process., Meas., Phenom.* **2002,** *20,* 1793–1807. doi:10.1116/1.1514665
41. Baunach, T.; Ivanova, V.; Kolb, D. M.; Boyen, H.-G.; Ziemann, P.; Büttner, M.; Oelhafen, P. *Adv. Mater.* **2004,** *16,* 2024–2028. doi:10.1002/adma.200400409
42. Shekhah, O.; Busse, C.; Bashir, A.; Turcu, F.; Yin, X.; Cyganik, P.; Birkner, A.; Schuhmann, W.; Wöll, C. *Phys. Chem. Chem. Phys.* **2006,** *8,* 3375–3378. doi:10.1039/b606488d
43. Silien, C.; Lahaye, D.; Caffio, M.; Schaub, R.; Champness, N. R.; Buck, M. *Langmuir* **2011,** *27,* 2567–2574. doi:10.1021/la104561j
44. Azzaroni, O.; Schilardi, P. L.; Salvarezza, R. C. *Appl. Phys. Lett.* **2002,** *80,* 1061–1063. doi:10.1063/1.1448852
45. Azzaroni, O.; Schilardi, P. L.; Salvarezza, R. C. *Electrochim. Acta* **2003,** *48,* 3107–3114. doi:10.1016/S0013-4686(03)00388-8
46. Staikov, G., Ed. *Electrocrystallization in Nanotechnology;* Wiley-VCH: Weinheim, 2007. doi:10.1002/9783527610198
47. Buck, M. Structure, Electrochemistry and Applications of Self-Assembled Monolayers of Thiols. In *Chemically Modified Electrodes;* Alkire, R. C.; Kolb, D. M.; Lipkowski, J.; Ross, P. N., Eds.; Advances in Electrochemical Science and Engineering, Vol. 11; Wiley-VCH: Weinheim, 2009; pp 197–255.
48. Silien, C.; Buck, M. *J. Phys. Chem. C* **2008,** *112,* 3881–3890. doi:10.1021/jp710947r
49. Pattanaik, G.; Shao, W. B.; Swami, N.; Zangari, G. *Langmuir* **2009,** *25,* 5031–5038. doi:10.1021/la803907p
50. Langerock, S.; Ménard, H.; Rowntree, P.; Heerman, L. *Langmuir* **2005,** *21,* 5124–5133. doi:10.1021/la050078z
51. Azzam, W.; Fuxen, C.; Birkner, A.; Rong, H.-T.; Buck, M.; Wöll, C. *Langmuir* **2003,** *19,* 4958–4968. doi:10.1021/la020868y
52. Schilardi, P.; Méndez, S.; Salvarezza, R. C.; Arvia, A. J. *Langmuir* **1998,** *14,* 4308–4314. doi:10.1021/la971358k
53. Heinze, J. *Angew. Chem., Int. Ed.* **1993,** *32,* 1268–1288. doi:10.1002/anie.199312681
54. Tai, Y.; Shaporenko, A.; Grunze, M.; Zharnikov, M. *J. Phys. Chem. B* **2005,** *109,* 19411–19415. doi:10.1021/jp053340l
55. Andricacos, P. C.; Uzoh, C.; Dukovic, J. O.; Horkans, J.; Deligianni, H. *IBM J. Res. Dev.* **1998,** *42,* 567–574. doi:10.1147/rd.425.0567
56. Moffat, T. P.; Wheeler, D.; Edelstein, M. D.; Josell, D. *IBM J. Res. Dev.* **2005,** *49,* 19–36. doi:10.1147/rd.491.0019
57. Munoz, R. C.; Vidal, G.; Mulsow, M.; Lisoni, J. G.; Arenas, C.; Concha, A.; Mora, F.; Espejo, R.; Kremer, G.; Moraga, L.; Esparza, R.; Haberle, P. *Phys. Rev. B* **2000,** *62,* 4686–4697. doi:10.1103/PhysRevB.62.4686
58. Satterley, C. J.; Lovelock, K. R. J.; Thom, I.; Dhanak, V. R.; Buck, M.; Jones, R. G. *Surf. Sci.* **2006,** *600,* 4825–4828. doi:10.1016/j.susc.2006.07.062

59. Baserga, A.; Vigano, M.; Casari, C. S.; Turri, S.; Li Bassi, A.; Levi, M.; Bottani, C. E. *Langmuir* **2008,** *24,* 13212–13217. doi:10.1021/la801903u
60. Wagner, P.; Hegner, M.; Guentherodt, H.-J.; Semenza, G. *Langmuir* **1995,** *11,* 3867–3875. doi:10.1021/la00010a043

License and Terms

The definitive version of this article is the electronic one which can be found at:
doi:10.3762/bjnano.3.11

Beilstein Journal
of Nanotechnology

Self-assembly of octadecyltrichlorosilane: Surface structures formed using different protocols of particle lithography

ChaMarra K. Saner, Kathie L. Lusker, Zorabel M. LeJeune, Wilson K. Serem
and Jayne C. Garno*

Full Research Paper

Open Access

Address:
Chemistry Department, Louisiana State University, 232 Choppin Hall, Baton Rouge, LA 70803, USA. Telephone: +1 225 578 8942; Fax: +1 225 578 3458

Email:
Jayne C. Garno* - jgarno@lsu.edu

* Corresponding author

Keywords:
atomic force microscopy; nanopatterning; nanostructures; octadecyltrichlorosilane; particle lithography; self-assembled monolayer; self-assembly

Beilstein J. Nanotechnol. **2012,** *3,* 114–122.
doi:10.3762/bjnano.3.12

Received: 15 November 2011
Accepted: 25 January 2012
Published: 09 February 2012

This article is part of the Thematic Series "Self-assembly at solid surfaces".

Guest Editors: S. R. Cohen and J. Sagiv

Abstract

Particle lithography offers generic capabilities for the high-throughput fabrication of nanopatterns from organosilane self-assembled monolayers, which offers the opportunity to study surface-based chemical reactions at the molecular level. Nanopatterns of octadecyltrichlorosilane (OTS) were prepared on surfaces of Si(111) using designed protocols of particle lithography combined with either vapor deposition, immersion, or contact printing. Changing the physical approaches for applying molecules to masked surfaces produced OTS nanostructures with different shapes and heights. Ring nanostructures, nanodots and uncovered pores of OTS were prepared using three protocols, with OTS surface coverage ranging from 10% to 85%. Thickness measurements from AFM cursor profiles were used to evaluate the orientation and density of the OTS nanostructures. Differences in the thickness and morphology of the OTS nanostructures are disclosed based on atomic force microscopy (AFM) images. Images of OTS nanostructures prepared on Si(111) that were generated by the different approaches provide insight into the self-assembly mechanism of OTS, and particularly into the role of water and solvents in hydrolysis and silanation.

Introduction

Self-assembled monolayers (SAMs) of organosilanes have become important as surface resists and functional coatings for micro- and nanopatterning applications [1-9]. The surface self-assembly of organosilanes such as octadecyltrichlorosilane (OTS) is complicated, with multiple steps of hydrolysis, cross-linking and silanation [10-13]. To develop robust and reproducible lithography procedures with OTS, parameters, such as temperature, humidity, solvents, physical deposition conditions, and mask materials, can be systematically changed to enable nanoscale studies of surface assembly.

For methods of particle lithography, a surface mask of polystyrene latex or silica mesospheres is used to direct the deposition of organic thin films and nanomaterials. The surface density of nanostructures can be designed by selecting the diameter of mesospheres, for high-throughput patterning on the order of 10^9 nanostructures per square centimeter. Different approaches with particle lithography have been successful for producing periodic, 2D arrays of nanostructures of different materials and molecular films, including metals [14,15], nanoparticles [16-19], proteins [20-22], polymers [23-26] and SAMs [27-31]. A significant advantage of using organosilanes in comparison to thiolated SAMs is that silane films can be prepared on a wide range of substrates, such as glass [32], mica [33-35], quartz [36,37], indium tin oxide (ITO) [38], or silicon (Si) [11,32,39-42] or metal oxides such as gold [43,44]. This versatility of organosilanes in the preparation of nanostructures on different surfaces will be helpful for new applications and developments in the patterning of biomolecules or nanoparticles for optical measurements and biosensor surfaces.

The morphology of SAMs or nanostructures of OTS reflects a balance of the interactions that occur between the silane precursor and the silanol groups, interactions between the end groups, interactions between the alkyl chains of the silane molecules, and the nature of the substrates [45,46]. These intramolecular interactions, along with parameters such as temperature, solvent type and trace amounts of water, present a challenge for reproducible fabrication with organosilanes such as OTS [10,11,45-50]. Preparation methods affect the growth rate, surface coverage and orientation of OTS [51].

Molecular-level differences in the thickness and morphology of OTS nanostructures prepared by different lithography procedures can be investigated by performing atomic force microscopy (AFM) studies [52,53]. Particle lithography enables control of the deposition parameters for tailoring the surface coverage, surface geometries and pattern dimensions. Close-packed arrays of latex or silica mesoparticles were used as surface masks to direct the deposition of OTS on surfaces to form nanopatterns. Essentially, the physical state of the molecule was changed for the three protocols. Molecules were applied either in a vapor phase, as a liquid film, or under dilute-solvent conditions, to enable nanoscale studies of the surface organization and self-assembly of OTS.

Results and Discussion

A comparison of the geometries and thicknesses of the nanostructures produced by particle lithography was used to systematically investigate parameters for surface self-assembly of octadecyltrichlorosilane (OTS). Three methods of particle lithography for preparing organosilane nanostructures are compared, as shown in Figure 1. Each approach uses a different strategy for applying the organosilanes to the masked surface of Si(111), using either heated-vapor deposition, contact printing, or immersion in a silane solution. For comparison of the different particle lithography strategies, the samples were prepared using masks of polystyrene latex (200 nm diameter); the mesospheres have a size variation of 1–2%. Organosilanes attach to the surfaces by successive steps of hydrolysis and condensation, therefore nanoscopic amounts of water are needed to initiate the reaction. By controlling the drying parameters of the latex masks, different nanopattern geometries are produced [30,38].

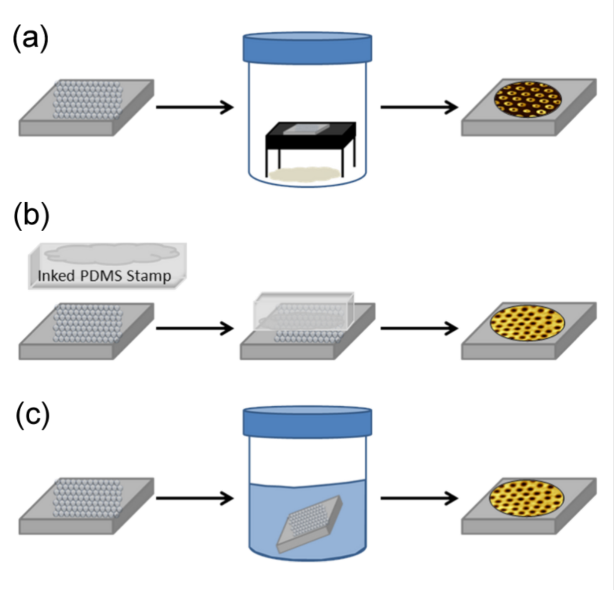

Figure 1: Strategies for preparing organosilane nanostructures by means of particle lithography. Basic steps are shown for (a) vapor deposition; (b) contact printing with PDMS; and (c) solution immersion of Si(111) surfaces coated with mesoparticle masks.

Nanostructures produced by particle lithography using vapor deposition of OTS

By combining particle lithography with vapor deposition of OTS, arrays of ring-shaped nanostructures were formed on Si(111), as shown in the contact-mode AFM images in Figure 2. A wide-area frame (8 × 8 μm^2) in Figure 2a and Figure 2b reveals the arrangement of hundreds of circular nanostructures, showing a few gaps corresponding to the uncovered substrate. There are 336 ring nanostructures within the 4 × 4 μm^2 frame of Figure 2c and Figure 2d. If the array were perfectly ordered and densely packed the frame would accommodate 360 nanostructures, indicating a defect density of ~7%. The dimensions and circular shapes of the nanostructures correspond to highly regular circles of consistent heights. Within the 1 × 1 μm^2 close-up view, 29 patterns are packed closely together (Figure 2e and Figure 2f). This scales to an overall surface density of 3 × 10^9 patterns/cm^2. The areas confined within the

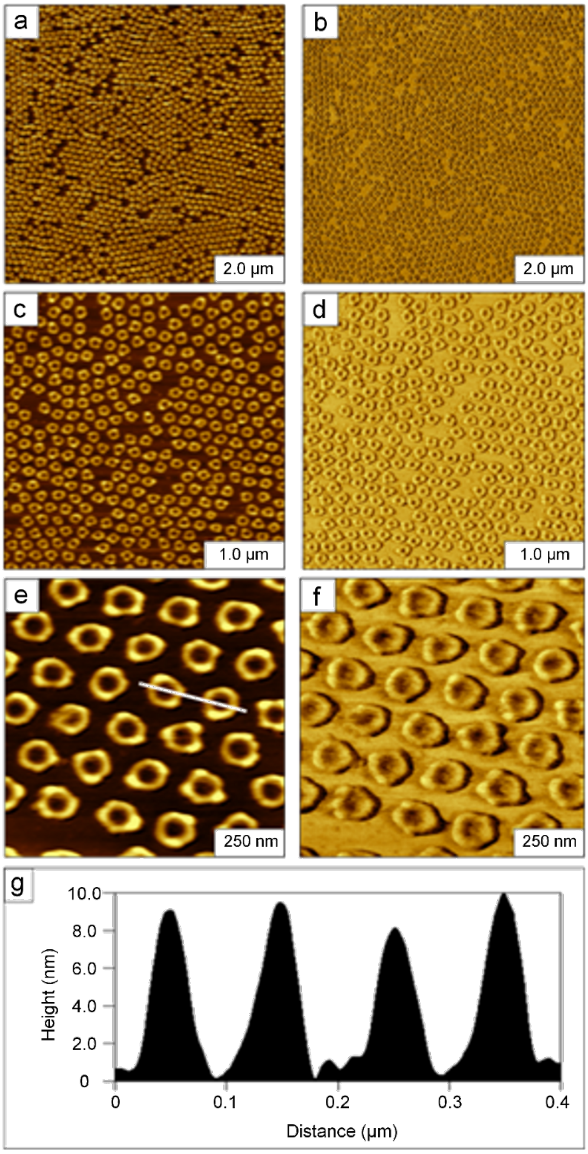

Figure 2: Combining particle lithography with vapor deposition of OTS produced ring-shaped nanostructures. (a) Contact-mode topograph, 8 × 8 µm^2; (b) simultaneously acquired lateral-force image. (c) Higher-magnification topograph (4 × 4 µm^2); (d) corresponding lateral-force image. (e) zoom-in topography view of 1 × 1 µm^2 area; and (f) lateral-force frame. (g) Height profile for the white line cross-section in (e).

centers of the rings appear to have the same contrast as the surrounding substrate for both the topography and lateral-force frames of Figure 2e and Figure 2f. Careful examination of zoom views from this experiment shows discontinuous surface coverage of small OTS islands with molecular heights of ~0.5 nm. The central areas of the rings were masked by the latex mesospheres, and meniscus-shaped areas of OTS were formed surrounding the base of the latex particles, generating the nanopatterns. The cursor line profile across two of the rings (Figure 2g) shows that the baseline within the rings is nearly the same height as the background areas of bare Si(111). The thickness of OTS monolayers has been reported to range from 2.26 to 2.76 nm under various conditions of sample preparation [1,42,54-56]. An “ideal” OTS monolayer of a dense, highly ordered film, in which all of the molecular tails are fully extended and oriented perpendicular to the substrate, would have a well-defined thickness of 2.6 ± 0.1 nm. The height of the rings is measured as 10 ± 2 nm, which corresponds to 3–4 layers of OTS (Figure 2). The center-to-center spacing between the ring structures is approximately 200 nm, which matches the diameter of the latex mask.

When the latex masks were dried, a water meniscus persisted at the base of each latex sphere on the surface, and this defined the reaction sites for hydrolysis and condensation of the organosilanes [54]. For the example in Figure 2, the interstitial areas between the OTS rings do not have consistent coverage, and OTS was shown to bind mainly in the areas pinned beneath the base of latex spheres. The cursor profile shows that the areas surrounding the rings and inside the rings are nearly the same height, where the height scale refers to the baseline of the uncoated substrate. The location of water residues on the surface defines the sites for OTS binding; for example, with the more hydrophilic substrate of mica (0001) attachment to the interstitial areas of the surface between spheres was observed for latex masks that were briefly dried [57]. If the masks formed on Si(111) are dried briefly, more water persists on the surface, thus OTS also binds to the interstitial areas between the rings (Figure 3). An example is shown of OTS nanopatterns with different heights outside and within the rings. The cursor profile across two of the ring patterns shows a height of 4 ± 1 nm between the rings, the rings measure 12 ± 2 nm in height, and the shallowest area inside the rings can be used as a reference baseline for the uncoated Si(111) substrate. Water residues persist across the surface; however, there is a higher zone of water trapped in the meniscus areas surrounding the spheres. Interestingly, we have observed that the height of the meniscus is greater for larger-diameter latex spheres, which correspondingly leads to scalable heights for organosilane-ring nanopatterns [54].

Particle lithography combined with contact printing with PDMS stamps

To produce monolayer nanostructures of OTS, particle lithography with contact printing and immersion were evaluated to optimize the deposition conditions for achieving a densely packed SAM. Images of a nanostructured film of OTS prepared by using particle lithography combined with contact printing are shown in Figure 4. A honeycomb arrangement of nanopores is shown in Figure 4a, with approximately 25 × 20 rows of dark holes within a film of OTS within the frame. The corres-

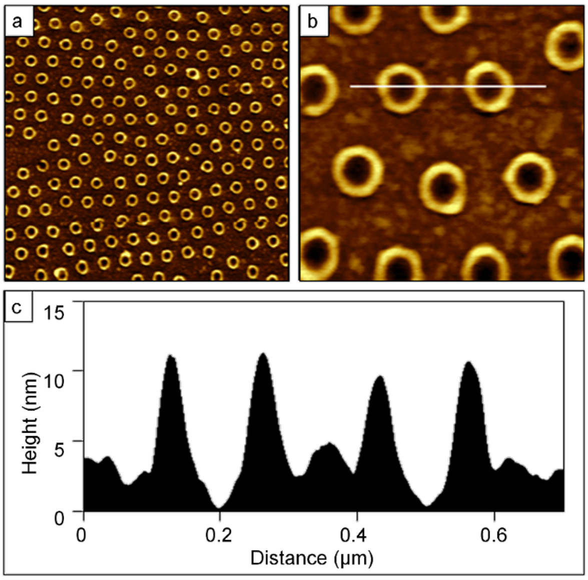

Figure 3: Particle lithography with vapor deposition of OTS produced multilayered ring nanostructures surrounded by an OTS monolayer. (a) Contact-mode topograph, 4 × 4 μm^2; (b) zoom-in view, 1 × 1 μm^2; (c) corresponding cursor profile for (b).

ponding lateral-force image of Figure 4b reveals the shapes of the holes as bright spots, corresponding to the bare areas of Si(111) where latex was displaced. At higher magnification, 438 nanopores are packed within the 4 × 4 μm^2 images of Figure 4c and Figure 4d, which scales to an approximate surface density of 2.7 × 10^9 nanostructures/cm^2. This value is comparable to the pattern density for Figure 2, because the latex diameter of the surface mask determines the packing density. The inset of Figure 4c is an FFT of the topograph, and represents a mathematical average of the 2D lattice of the hexagonal array. A further magnified view is presented in Figure 4e and Figure 4f showing ~27 nanopores. The lateral-force image confirms that the holes are uncovered Si(111), evidenced by the distinct change in chemical contrast between OTS and the nanopores. Referencing the uncovered areas of the substrate as a baseline, the height of the OTS film measures 0.6 ± 0.1 nm (Figure 4g), which indicates submonolayer surface coverage. Since the overall diameter of an alkyl chain is approximately 0.5 nm, the thickness value suggests a side-on arrangement of the molecules, with the backbone of the molecule oriented parallel to the substrate.

Multiple replicate samples were prepared using contact printing, for different size masks, showing that the heights were consistent with the example of Figure 4. For OTS transfer by contact printing, a solution of solvent and silane at a 40% (v/v) concentration was placed on the surface of a PDMS block and dried. This process most likely forms a thin cross-linked film of OTS that does not bind to the polymeric surface of PDMS. After the mask was placed in contact with the sample, the liquid film was transferred to the Si(111) substrate by liquid permeation through the latex mask.

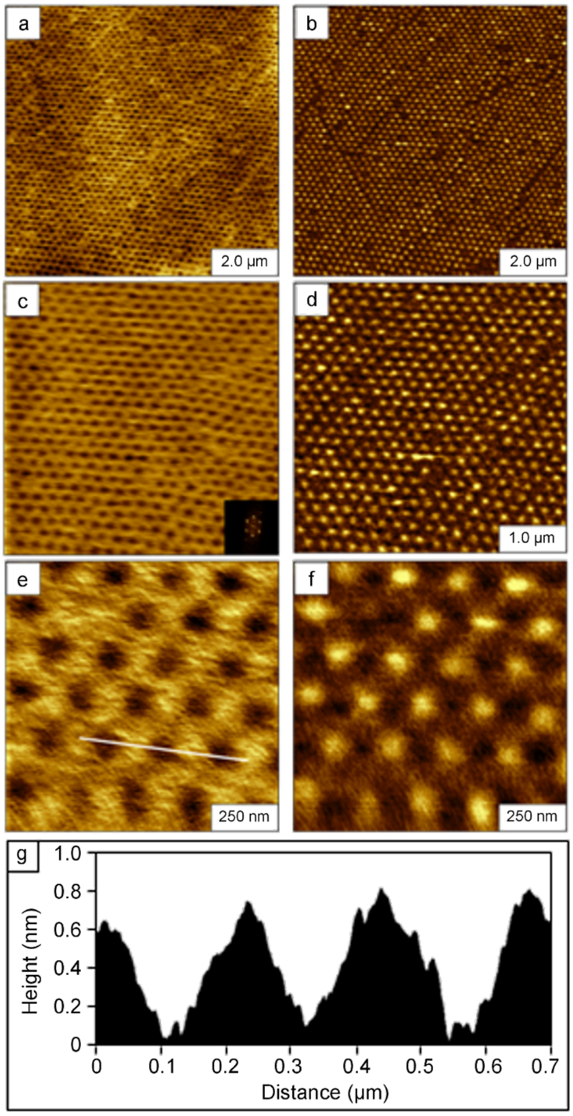

Figure 4: Nanopore structures of OTS were formed with particle lithography combined with contact printing. Contact-mode AFM images are shown for a sample prepared with 200 nm latex mesospheres on Si(111). (a) 8 × 8 μm^2 topograph and (b) corresponding lateral-force image. (c) Zoom-in topograph (4 × 4 μm^2) with FFT shown in the inset; (d) simultaneously acquired lateral-force frame. (e) Topography frame (1 × 1 μm^2) with (f) showing the corresponding lateral-force image. (g) Height profile for the white line in (e).

Particle lithography by immersion of latex-masked substrates in silane solutions

A completely different morphology other than rings or nanopores was observed for OTS nanostructures produced by the immersion of particle masks. Dot-shaped nanostructures were produced by using latex-particle lithography with immersion, as shown in Figure 5 with wide-area and zoom-in topography views. The long-range periodicity of the array of nanodots is shown with an FFT within the inset of Figure 5a. The surface density of the nanodots is approximately 3.3 × 10^9 nanostructures/cm^2, showing ~120 nanopatterns within the 2.5 × 2.5 µm^2 frame shown in Figure 5b. The heights of the nanodots measure 0.5 ± 0.3 nm.

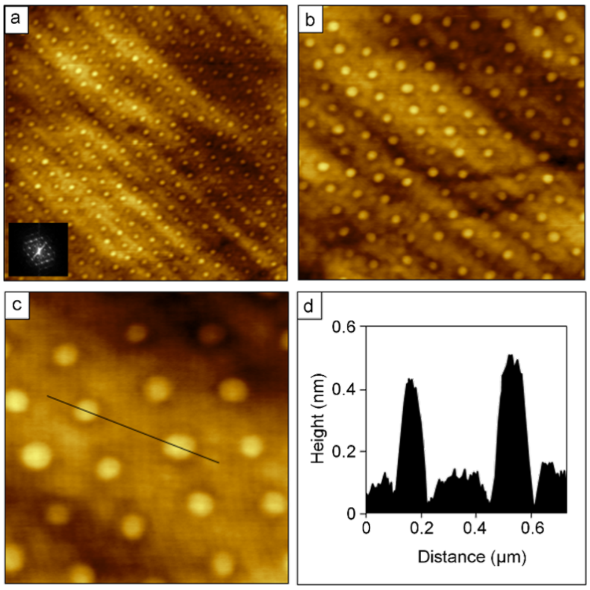

Figure 5: Nanodots of OTS produced with immersion of annealed latex masks. Contact-mode AFM images are shown for OTS nanostructures formed on Si(111) with 200 nm latex. (a) Topography image, 4.5 × 4.5 µm^2 and FFT inset; (b) zoom-in, 2.5 × 2.5 µm^2; (c) close-up view, 1 × 1 µm^2; (d) height profile of the line in (c).

Immersion of a masked substrate in a solvent is the most common approach for preparing films of OTS, and has produced the most consistent thickness of a monolayer. However, immersion in solvents causes rapid detachment of the latex masks. To enable an immersion process for particle lithography, a brief heating step was developed to solder the latex beads to the substrate (75 °C for 30 min). Latex deforms when heated, leaving less surface area available for OTS deposition [58]. After the heating step, the only remaining areas that were not masked by latex were the triple-hollow sites formed between spheres, and the geometries and periodicity of the nanodots shown in Figure 5 correspond to these sites.

Surface masks of colloidal silica mesospheres

Silica mesospheres do not deform as readily as polystyrene latex, and can sustain longer heating at higher temperatures [28]. The results for OTS nanostructures produced with silica masks are shown in Figure 6. Nanohole structures are shown in the wide-area (Figure 6a; 2.75 × 2.75 µm^2) and high-magnification images (Figure 6d; 1.5 × 1.5 µm^2).The topography frames reveal periodic patterns within a monolayer film of OTS, with exquisitely small holes at the locations where silica mesospheres (250 nm diameter) were displaced. There are 38 nanopores in the zoom-in views of Figure 6d and Figure 6e, which would scale to a surface density of 1.7 × 10^9 patterns/cm^2. The depth of the OTS film was measured to be 2.0 ± 0.2 nm (Figure 6c and Figure 6f) referring to the uncovered area of Si(111) as the baseline. This value corresponds to a nearly upright configuration of an OTS monolayer. The diameters of the nanoholes were measured to be 102 ± 11 nm. The center-to-center spacing between the holes corresponds to the diameters of the silica mesospheres (250 nm) used as a structural template to pattern the OTS. The overall coverage of the OTS film was estimated to be ~85% of the surface.

Molecular orientation of OTS within nanopatterns

For the three approaches described, the procedures are highly reproducible. Multiple samples were prepared and formed consistent shapes and thicknesses, as summarized in Table 1. A cross-linked multilayer was formed for rings of OTS, with different thicknesses within the interstitial areas of the substrates between the rings (Figure 2 and Figure 3). Using the contact-printing approach with PDMS stamps, the thickness of the OTS film corresponds to submonolayer surface coverage (Figure 4). Despite multiple tests and samples, a monolayer thickness was not achieved with latex masks and contact printing of OTS. A similar height was produced by using the immersion of annealed latex masks. The brief annealing step was effective for producing exquisitely small areas on the surface for the preparation of nanodot structures; however, the heights do not correspond to an upright orientation of OTS (Figure 5). For evaluating the molecular orientation, the thickness measurements of OTS films were obtained exclusively from AFM height profiles, rather than spatially averaged results from infrared spectroscopy. The theoretical thickness for a side-on orientation of OTS with the backbone oriented parallel to the substrate would measure 0.5 ± 0.1 nm. By changing to silica mesospheres for the immersion strategy, a taller OTS film was produced than that observed for the latex masks (Figure 6). This new result suggests that the nature of the surface of the mesosphere masks can affect the outcome of patterning with particle lithography. Polystyrene latex has been described as a “hairy” particle, with strands of polystyrene extending across the exterior surface areas of the beads. The strands provide surface sites for interaction with OTS to produce a cross-linked arrangement within the nanodot surface structures. The consistent and reproducible geometries of the different OTS nano-

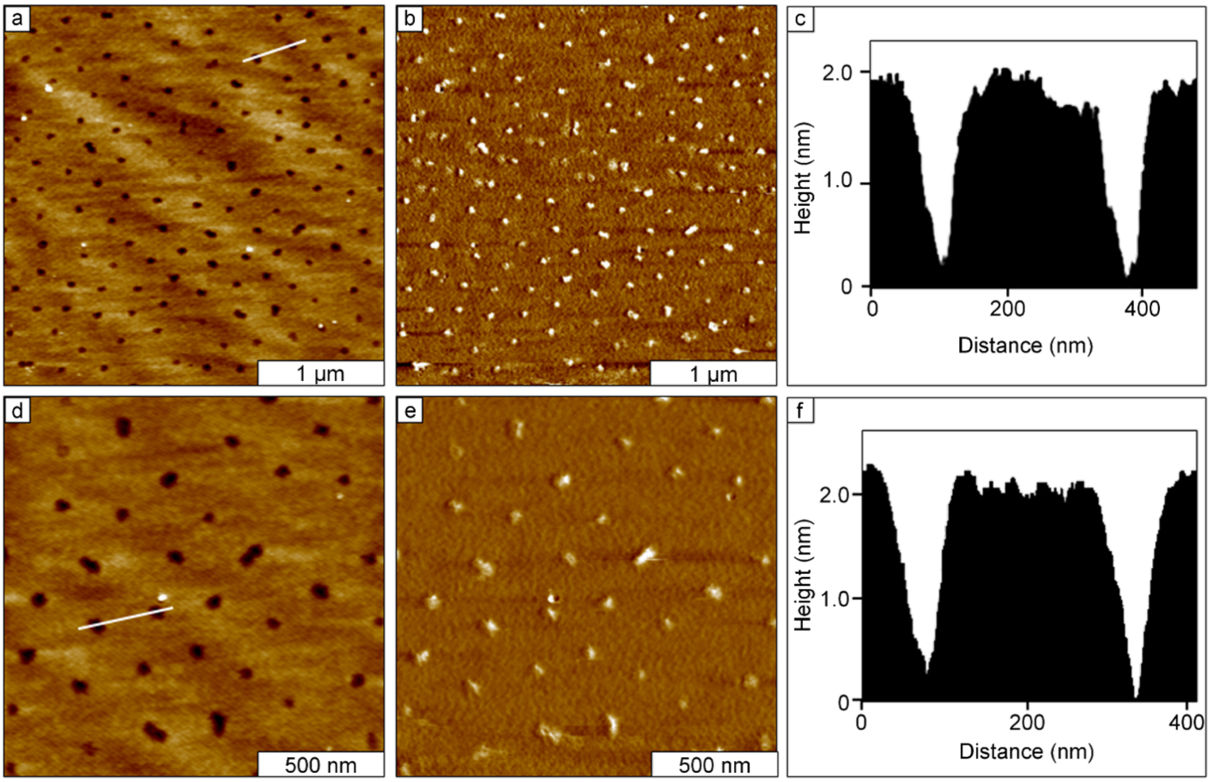

Figure 6: Nanostructured film of OTS produced by immersion of annealed silica masks in OTS solutions. Contact-mode AFM images are shown for OTS nanostructures formed on Si(111) with 250 nm silica mesospheres: (a) 2.75 × 2.75 µm^2 topograph; (b) corresponding lateral-force view; (c) height profile of the line in (a); (d) 1.5 × 1.5 µm^2 zoom-in view of (a); (e) lateral-force frame simultaneously acquired with (d); (f) cursor plot for the line in (d).

Table 1: Particle lithography with OTS based on different approaches for surface deposition.

method	mask	nanostructure shape	surface coverage (OTS)	OTS thickness
vapor deposition	200 nm latex	ring nanostructures of OTS multilayers	40%	10 ± 2 nm
contact printing	200 nm latex	nanopores of uncovered substrate within an OTS film	26%	0.6 ± 0.1 nm
immersion of annealed latex masks	200 nm latex	nanodots	10%	0.5 ± 0.3 nm
immersion of annealed silica masks	250 nm silica	nanopores of uncovered substrate within an OTS monolayer	85%	2.0 ± 0.2 nm

structures are not necessarily a “failed” approach for particle lithography, rather a range of different surface shapes and thicknesses can be generated for selected applications. Overall, the highest-quality monolayer of OTS was produced by using the immersion of annealed mesosphere masks of silica.

Conclusion

The surface self-assembly of OTS was studied by using approaches of particle lithography combined with vapor deposition, contact printing and immersion. By changing the physical approaches for applying molecules to surfaces, the molecular arrangement and surface density can be controlled. For example, submonolayer surface coverage was obtained by using protocols with contact printing. Changing the material composition of the mesoparticle masks produced entirely different surface structures for annealed masks of latex and silica spheres. The meniscus sites of water residues at the base of latex spheres furnish local containers for self-polymerization reactions to generate multilayer surface structures. Optimized structures with nearly the thickness of an ideal monolayer were achieved by using annealed masks of colloidal silica mesospheres immersed in OTS solutions. Further experiments are in progress to directly compare the surface structures formed based on immersion protocols with latex and silica masks.

Experimental

Atomic force microscopy (AFM). Organosilane thin films were characterized using models 5420 and 5500 scanning probe microscopes operated in contact or tapping-mode AFM. (Agilent Technologies, Chandler, AZ). Lateral force images were acquired for either the trace or retrace views corresponding to the scan direction of the selected topography frames. The color scales of lateral-force images indicate differences in tip–surface interactions, but were not normalized for the comparison of friction changes between different tips or experiments. The tips were silicon nitride probes. Tips used with tapping-mode AFM were rectangular shaped ultrasharp silicon tips that have an aluminium reflex coating, with a spring constant of 48 N/m (Nanoscience Instruments, Phoenix, AZ). For contact-mode images, V-shaped tips (Veeco Probes, Santa Barbara, CA) with an average force constant of 0.5 N/m were used. Data files were processed by using Gwyddion open-source software, which is freely available on the internet and supported by the Czech Metrology Institute [59]. Estimates of surface coverage were obtained for individual topography frames by manually converting images to black and white using thresholding and pixel counting with UTHSCA Image Tool [60].

Preparation of latex-particle masks. Polished silicon wafers doped with boron (Virginia Semiconductor, Fredericksburg, VA) were used as substrates. Pieces of Si(111) were cleaned by immersion in a 3:1 (v/v) piranha solution for 1 h. Piranha solution consists of sulfuric acid and hydrogen peroxide, which is highly corrosive, and should be handled carefully. After acid cleaning, the substrates were rinsed with copious amounts of deionized water and dried in air. Size-sorted, monodisperse polystyrene latex mesospheres (200 nm diameter) were used as surface masks for patterning (Thermo-Fisher Scientific, Waltman, MA). Aqueous solutions of latex were cleaned by centrifugation to remove surfactants or contaminants. Approximately 300 μL of the latex solution was placed into a microcentrifuge tube and centrifuged at 15,000 rpm for 15 min. A solid pellet was formed, and the supernatant was removed and replaced with deionized water. The latex pellet was resuspended with 300 μL of deionized water by vortex mixing to prepare a 1% w/v solution. The washing process was repeated twice. A drop (10–15 μL) of the cleaned mesospheres was deposited onto clean Si(111) substrates and dried under ambient conditions (25 °C, ~50% relative humidity) for at least one hour, in order to form surface masks for nanolithography.

Particle lithography combined with vapor deposition. The masked substrates were placed into sealed glass vessels for vapor deposition of organosilane. The samples were placed on a raised platform in a jar containing 300 μL of neat octadecyltrichlorosilane (Gelest, Morrisville, PA). A vapor was generated by heating the vessel in an oven at 70 °C. After at least 6 h, the samples were removed and rinsed with ethanol and water to remove the latex masks.

Particle lithography with contact printing. For contact printing, an inked block of polydimethylsiloxane (PDMS) (Sylgard 184, Dow Corning) was used to transfer OTS to the substrate through a physical mask of latex spheres. A drop (10–12 μL) of an OTS solution in bicyclohexyl was deposited onto a clean, dry block of PDMS (2 × 2 cm^2). A 30 μL volume of a 40% v/v solution of OTS in bicyclohexyl was deposited and spread evenly over the PDMS block, then quickly dried in a stream of ultra-high-purity argon. The PDMS block coated with OTS was placed on top of the masked substrate. The film of OTS was transferred from the PDMS block through the latex mask to the substrate by permeation. The areas of the Si(111) surface located directly underneath the latex particles were protected from silane deposition. After 1 h of physical contact, the PDMS block was removed. The sample was rinsed with copious amounts of deionized water. In the final step, the mask of latex particles was cleanly removed by sonication and rinsing with ethanol and deionized water. After removal of the mask, a nanostructured film of OTS was generated on the surface.

Particle lithography with immersion. For the immersion strategy of particle lithography, the masked substrates of latex were heated for 30 min at 75 °C in order to anneal the beads to the surface. Masked substrates of colloidal silica mesospheres were heated for 12 h at 140 °C. After heating, the samples were cooled for at least 20 min under ambient conditions. The mesosphere-coated substrates were then immersed into a 0.1% solution of OTS in bicyclohexyl or anhydrous toluene for 1 h. Next, the samples were removed and rinsed with ethanol and deionized water, and sonication was used to remove the latex masks.

Acknowledgements

This research was funded by the National Science Foundation Career program (CHE-0847291, PECASE award) and by the Dreyfus foundation, Camille Dreyfus Teacher-Scholar Award.

References

1. Jeon, N. L.; Finnie, K.; Branshaw, K.; Nuzzo, R. G. *Langmuir* **1997,** *13,* 3382–3391. doi:10.1021/la970166m
2. Maoz, R.; Frydman, E.; Cohen, S. R.; Sagiv, J. *Adv. Mater.* **2000,** *12,* 725–731. doi:10.1002/(SICI)1521-4095(200005)12:10<725::AID-ADMA725>3.0.CO;2-Z
3. Dulcey, C. S.; Georger, J. H. J.; Krauthamer, V.; Stenger, D. A.; Fare, T. L.; Calvert, J. M. *Science* **1991,** *252,* 551–554. doi:10.1126/science.2020853
4. Calvert, J. M. *J. Vac. Sci. Technol., B: Microelectron. Nanometer Struct.–Process., Meas., Phenom.* **1993,** *11,* 2155–2163. doi:10.1116/1.586449
5. Ingall, M. D. K.; Honeyman, C. H.; Mercure, J. V.; Bianconi, P. A.; Kunz, R. R. *J. Am. Chem. Soc.* **1999,** *121,* 3607–3613. doi:10.1021/ja9833927
6. Chowdhury, D. *Curr. Sci.* **2009,** *96,* 923–932.
7. Voorthuijzen, W. P.; Yilmaz, M. D.; Naber, W. J. M.; Huskens, J.; van der Wiel, W. G. *Adv. Mater.* **2011,** *23,* 1346–1350. doi:10.1002/adma.201003625
8. Wu, C.-W.; Shen, Y.-K.; Chuang, S.-Y.; Wei, C. S. *Sens. Actuators, A* **2007,** *139,* 145–151. doi:10.1016/j.sna.2006.10.017
9. Ivanisevic, A.; Mirkin, C. A. *J. Am. Chem. Soc.* **2001,** *123,* 7887–7889. doi:10.1021/ja010671c
10. Wen, K.; Maoz, R.; Cohen, H.; Sagiv, J.; Gibaud, A.; Desert, A.; Ocko, B. M. *ACS Nano* **2008,** *2,* 579–599. doi:10.1021/nn800011t
11. Sagiv, J. *J. Am. Chem. Soc.* **1980,** *102,* 92–98. doi:10.1021/ja00521a016
12. Parikh, A. N.; Allara, D. L.; Azouz, I. B.; Rondelez, F. *J. Phys. Chem.* **1994,** *98,* 7577–7590. doi:10.1021/j100082a031
13. Carson, G. A.; Granick, S. *J. Mater. Res.* **1990,** *5,* 1745–1751. doi:10.1557/JMR.1990.1745
14. Jiang, P.; McFarland, M. J. *J. Am. Chem. Soc.* **2004,** *126,* 13778–13786. doi:10.1021/ja0470923
15. Tessier, P. M.; Velev, O. D.; Kalambur, A. T.; Lenhoff, A. M.; Rabolt, J. F.; Kaler, E. W. *Adv. Mater.* **2001,** *13,* 396–400. doi:10.1002/1521-4095(200103)13:6<396::AID-ADMA396>3.0.CO;2-T
16. Chen, J. X.; Liao, W.-S.; Chen, X.; Yang, T.; Wark, S. E.; Son, D. H.; Batteas, J. D.; Cremer, P. S. *ACS Nano* **2009,** *3,* 173–180. doi:10.1021/nn800568t
17. Hulteen, J. C.; Treichel, D. A.; Smith, M. T.; Duval, M. L.; Jensen, T. R.; Van Duyne, R. P. *J. Phys. Chem. B* **1999,** *103,* 3854–3863. doi:10.1021/jp9904771
18. Lewandowski, B. R.; Kelley, A. T.; Singleton, R.; Li, J.-R.; Lowry, M.; Warner, I. M.; Garno, J. C. *J. Phys. Chem. C* **2009,** *113,* 5933–5940. doi:10.1021/jp808056x
19. Zrimsek, A. B.; Boman, F.; Van Duyne, R. P. *Abstr. Pap. - Am. Chem. Soc.* **2011,** 241.
20. Nonckreman, C. J.; Fleith, S.; Rouxhet, P. G.; Dupont-Gillain, C. C. *Colloids Surf., B* **2010,** *77,* 139–149. doi:10.1016/j.colsurfb.2010.01.014
21. Singh, G.; Gohri, V.; Pillai, S.; Arpanaei, A.; Foss, M.; Kingshott, P. *ACS Nano* **2011,** *5,* 3542–3551. doi:10.1021/nn102867z
22. Singh, G.; Griesser, H. J.; Bremmell, K.; Kingshott, P. *Adv. Funct. Mater.* **2011,** *21,* 540–546. doi:10.1002/adfm.201001340
23. Briseno, A. L.; Han, S.; Rauda, I. E.; Zhou, F.; Toh, C.-S.; Nemanick, E. J.; Lewis, N. S. *Langmuir* **2004,** *20,* 219–226. doi:10.1021/la035198q
24. Ellinas, K.; Tserepi, A.; Gogolides, E. *Langmuir* **2011,** *27,* 3960–3969. doi:10.1021/la104481p
25. Jiang, P.; Hwang, K. S.; Mittleman, D. M.; Bertone, J. F.; Colvin, V. L. *J. Am. Chem. Soc.* **1999,** *121,* 11630–11637. doi:10.1021/ja9903476
26. Singh, A.; Kulkarni, S. K.; Khan-Malek, C. *Microelectron. Eng.* **2011,** *88,* 939–944. doi:10.1016/j.mee.2010.12.026
27. Bae, C.; Kim, H.; Shin, H. *Chem. Commun.* **2011,** *47,* 5145–5147. doi:10.1039/c1cc10283d
28. Bae, C.; Shin, H.; Moon, J.; Sung, M. M. *Chem. Mater.* **2006,** *18,* 1085–1088. doi:10.1021/cm052084m
29. Geissler, M.; McLellan, J. M.; Chen, J.; Xia, Y. *Angew. Chem., Int. Ed.* **2005,** *44,* 3596–3600. doi:10.1002/anie.200500421
30. Li, J. R.; Garno, J. C. *Nano Lett.* **2008,** *8,* 1916–1922. doi:10.1021/nl0806062
31. McLellan, J. M.; Geissler, M.; Xia, Y. *J. Am. Chem. Soc.* **2004,** *126,* 10830–10831. doi:10.1021/ja0470766
32. Gun, J.; Sagiv, J. *J. Colloid Interface Sci.* **1986,** *112,* 457–472. doi:10.1016/0021-9797(86)90114-1
33. Carson, G.; Granick, S. *J. Appl. Polym. Sci.* **1989,** *37,* 2767–2772. doi:10.1002/app.1989.070370925
34. Kessel, C. R.; Granick, S. *Langmuir* **1991,** *7,* 532–538. doi:10.1021/la00051a020
35. Schwartz, D. K.; Steinberg, S.; Israelachvili, J.; Zasadzinski, J. A. N. *Phys. Rev. Lett.* **1992,** *69,* 3354–3357. doi:10.1103/PhysRevLett.69.3354
36. Brandriss, S.; Margel, S. *Langmuir* **1993,** *9,* 1232–1240. doi:10.1021/la00029a014
37. Mathauer, K.; Frank, C. W. *Langmuir* **1993,** *9,* 3002–3008. doi:10.1021/la00035a044
38. Li, J.-R.; Lusker, K. L.; Yu, J.-J.; Garno, J. C. *ACS Nano* **2009,** *3,* 2023–2035. doi:10.1021/nn9004796
39. Le Grange, J. D.; Markham, J. L.; Kurkjian, C. R. *Langmuir* **1993,** *9,* 1749–1753. doi:10.1021/la00031a023
40. Maoz, R.; Sagiv, J. *J. Colloid Interface Sci.* **1984,** *100,* 465–496. doi:10.1016/0021-9797(84)90452-1
41. Silberzan, P.; Leger, L.; Ausserre, D.; Benattar, J. J. *Langmuir* **1991,** *7,* 1647–1651. doi:10.1021/la00056a017
42. Wasserman, S. R.; Tao, Y. T.; Whitesides, G. M. *Langmuir* **1989,** *5,* 1074–1087. doi:10.1021/la00088a035
43. Finklea, H. O.; Robinson, L. R.; Blackburn, A.; Richter, B.; Allara, D.; Bright, T. *Langmuir* **1986,** *2,* 239–244. doi:10.1021/la00068a022
44. Sabatani, E.; Rubinstein, I.; Maoz, R.; Sagiv, J. *J. Electroanal. Chem.* **1987,** *219,* 365–371. doi:10.1016/0022-0728(87)85054-4
45. Yang, S.-R.; Kolbesen, B. O. *Appl. Surf. Sci.* **2008,** *255,* 1726–1735. doi:10.1016/j.apsusc.2008.06.051
46. Parikh, A. N.; Liedberg, B.; Atre, S. V.; Ho, M.; Allara, D. L. *J. Phys. Chem.* **1995,** *99,* 9996–10008. doi:10.1021/j100024a049
47. Allara, D. L.; Parikh, A. N.; Rondelez, F. *Langmuir* **1995,** *11,* 2357–2360. doi:10.1021/la00007a007
48. Brzoska, J. B.; Shahidzadeh, N.; Rondelez, F. *Nature* **1992,** *360,* 719–721. doi:10.1038/360719a0
49. McGovern, M. E.; Kallury, K. M. R.; Thompson, M. *Langmuir* **1994,** *10,* 3607–3614. doi:10.1021/la00022a038
50. Tripp, C. P.; Hair, M. L. *Langmuir* **1992,** *8,* 1120–1126. doi:10.1021/la00040a018
51. Bierbaum, K.; Grunze, M.; Baski, A. A.; Chi, L. F.; Schrepp, W.; Fuchs, H. *Langmuir* **1995,** *11,* 2143–2150. doi:10.1021/la00006a049
52. Saner, C. K.; Lusker, K. L.; LeJeune, Z. M.; Garno, J. C. In *Federation of Analytical Chemistry and Spectroscopy Societies (FACSS) National Meeting,* Raleigh, North Carolina; 2010.

53. Saner, C. K.; Lusker, K. L.; Garno, J. C. In *Federation of Analytical Chemistry and Spectroscopy Societies (FACSS) National Meeting,* Reno, Nevada; 2011.
54. Lusker, K. L.; Yu, J.-J.; Garno, J. C. *Thin Solid Films* **2011,** *519,* 5223–5229. doi:10.1016/j.tsf.2011.01.164
55. Tillman, N.; Ulman, A.; Schildkraut, J. S.; Penner, T. L. *J. Am. Chem. Soc.* **1988,** *110,* 6136–6144. doi:10.1021/ja00226a031
56. Vallant, T.; Brunner, H.; Mayer, U.; Hoffmann, H.; Leitner, T.; Resch, R.; Friedbacher, G. *J. Phys. Chem. B* **1998,** *102,* 7190–7197. doi:10.1021/jp981282g
57. Li, J.-R.; Garno, J. C. *ACS Appl. Mater. Interfaces* **2009,** *1,* 969–976. doi:10.1021/am900118x
58. Visschers, M.; Laven, J.; German, A. L. *Prog. Org. Coat.* **1997,** *30,* 39–49. doi:10.1016/S0300-9440(96)00652-2
59. Nečas, D. K. P. *Gwyddion 2.25,* Czech Metrology Institute: Brno, Czech Republic, 2009.
60. Wilcox, C. D.; Dove, S. B.; McDavid, W. D.; Greer, D. B. *ImageTool*, University of Texas Health Science Center (UTHSCSA): San Antonio, TX, 1996–2002.

License and Terms

Beilstein Journal
of Nanotechnology

Parallel- and serial-contact electrochemical metallization of monolayer nanopatterns: A versatile synthetic tool en route to bottom-up assembly of electric nanocircuits

Jonathan Berson‡, Assaf Zeira‡, Rivka Maoz* and Jacob Sagiv*

Letter

Open Access

Address:
Department of Materials and Interfaces, The Weizmann Institute of Science, Rehovot 76100, Israel

Email:
Rivka Maoz* - rivka.maoz@weizmann.ac.il; Jacob Sagiv* - jacob.sagiv@weizmann.ac.il

* Corresponding author ‡ Equal contributors

Keywords:
AFM (SFM); bipolar electrochemistry; electrochemical metal deposition; monolayer patterning; nanolithography; self-assembled organosilane monolayers

Beilstein J. Nanotechnol. **2012,** *3,* 134–143.
doi:10.3762/bjnano.3.14

Received: 18 September 2011
Accepted: 27 January 2012
Published: 16 February 2012

This article is part of the Thematic Series "Self-assembly at solid surfaces".

Associate Editor: A. Gölzhäuser

Abstract

Contact electrochemical transfer of silver from a metal-film stamp (parallel process) or a metal-coated scanning probe (serial process) is demonstrated to allow site-selective metallization of monolayer template patterns of any desired shape and size created by constructive nanolithography. The precise nanoscale control of metal delivery to predefined surface sites, achieved as a result of the selective affinity of the monolayer template for electrochemically generated metal ions, provides a versatile synthetic tool en route to the bottom-up assembly of electric nanocircuits. These findings offer direct experimental support to the view that, in electrochemical metal deposition, charge is carried across the electrode–solution interface by ion migration to the electrode rather than by electron transfer to hydrated ions in solution.

Introduction

The quest for a chemical methodology applicable to the bottom-up fabrication of planned electric nanocircuits that can be effectively addressed from the external macroscopic world continues to pose major synthetic challenges. Metal growth or deposition on or within a preformed template structure has been successfully used in the fabrication of various metallic nanoscale objects and periodic nanostructures [1-12]; however, a comprehensive chemical methodology applicable to the planned assembly of metallic nanostructures of arbitrary shape and size, spanning variable length scales, is yet to be advanced.

Our laboratory has devoted ongoing efforts to an approach centered on the use of patterned organic monolayers as stable templates on top of which guided self-assembly of other selected materials of interest, organic as well as inorganic, can take place [13-28]. To this end, a monolayer-patterning methodology, referred to as constructive lithography (CL), has been advanced, which allows nondestructive local electrooxidation of the top $-CH_3$ groups of a self-assembled OTS/Si monolayer (highly ordered monolayer assembled on silicon from *n*-octadecyltrichlorosilane precursor molecules [22,29]) to –COOH functions [14,16]. The hydrophobic and chemically inert OTS surface is thus locally converted to a hydrophilic and chemically active one. Patterns of such OTSeo (electrooxidized OTS) regions surrounded by the unmodified OTS monolayer (denoted as OTSeo@OTS/Si) were produced using either conductive SFM (scanning force microscope) probes that can serially inscribe OTSeo features on lateral length scales from nanometers to tens of micrometers (constructive nanolithography, CNL) [14,15,18,27] or conductive stamps, suitable for one-step parallel printing of OTSeo features extending over much larger surface areas, typically beyond the micrometer (constructive microlithography, CML) [16,22].

Recently, we demonstrated a two-step CL patterning and pattern metallization process, referred to as *contact electrochemical patterning and transfer* (CEP–CET), whereby OTSeo features are first printed or inscribed on a target OTS monolayer by using a stamp electrode consisting of a patterned silver film on OTS (Ag/OTS@OTS/Si) or a silver-coated SFM tip electrode, and then in-situ metallized by direct electrochemical transfer of the metal from the patterning electrode itself [30]. CEP–CET is implemented in an unconventional "contact electrochemical" configuration, similar to that employed in previously studied constructive-lithography patterning processes [14,16,18,22]. In this configuration, the patterning electrode (metal-film stamp or metal-coated scanning probe) touches the target monolayer through an interfacial water layer of molecular-to-nanoscale thickness (adsorbed on the metal grains by capillary condensation from a humid, ambient atmosphere), which fulfils the role of the electrolyte. To achieve local electrooxidation of the target monolayer (CEP step), the target is biased positively (anode) with respect to the patterning electrode, whereas for metal transfer (CET step), the polarity of the applied bias voltage is reversed so that the stamp or the SFM probe now acts as the anode and the target monolayer as the cathode [30].

Metal-on-monolayer features resulting from the serial CEP–CET process executed with a moving SFM tip were shown to correspond to the OTSeo features defined in the pattern inscription step (CEP), whereas those produced with a stamp (parallel mode) were replicas of the stamp metal features [30]. Since patterned metal-film stamps could be easily fabricated by metal evaporation through transmission electron microscopy grids used as contact masks, the parallel CEP–CET process has hitherto only been implemented on lateral length scales larger than several micrometers. Here we report proof-of-concept experimental results demonstrating the feasibility of a different and more versatile contact electrochemical strategy for the nanoscale fabrication of diverse metal/monolayer patterns, based on the finding that metal deposition by the CET process is possible only on monolayer surfaces exposing metal-ion-binding functions (e.g., –COOH, –S–S–, –SH) [31].

Results and Discussion

As shown below in Figure 1, Figure 2 and Figure 3, all OTSeo features of a serially inscribed OTSeo@OTS/Si nanopattern can be simultaneously metallized in a parallel CET operation performed with an unpatterned, thin silver-film stamp (Ag/OTS/Si), whereas precise delivery of metal to selected surface sites within selected OTSeo features of such a monolayer nanopattern can be realized in a serial mode, by moving a positively biased silver-coated SFM tip along a planned trajectory across the patterned area of the monolayer (see below in Figure 4 and Figure 5).

According to Figure 1, upon the application of a voltage bias between stamp and target, with stamp positive and target negative, silver is selectively transferred to the OTSeo lines of the target monolayer only, thus producing a pattern of metallized OTSeo lines surrounded by the unmodified OTS monolayer. As discussed in the following, the selectivity of silver deposition on the OTSeo lines follows from the fact that Ag^+ ions generated electrochemically at the metal stamp (anode) are transported through the adsorbed water film, acting as an electrolyte, to the target monolayer (cathode), where effective nucleation and growth of stable metal grains (following the reduction of Ag^+ ions to neutral atoms) can occur only at those surface sites that bind the ions, which correspond to the carboxylic acid terminated OTSeo lines of the template nanopattern. Examples of metal/monolayer nanopatterns fabricated by this parallel metallization process are given in Figure 2 and Figure 3. It should be emphasized that no metal is transferred in a dry atmosphere and in the absence of a bias voltage applied between stamp and target as shown in Figure 1, regardless of the mechanical force pressing the two surfaces together and the time of contact.

Metal-free and metal-covered OTSeo sites such as those displayed in Figure 2, Figure 3, and Figure 5 (see below) can be unambiguously identified in lateral-force (contact-mode) and semicontact-mode (tapping) topographic images, respectively [30]. This is a consequence of the large difference in the polarity of the outer exposed functions of OTSeo (–COOH) and OTS ($-CH_3$), which gives rise to a corresponding large difference in the frictional force exerted on a tip moving in contact

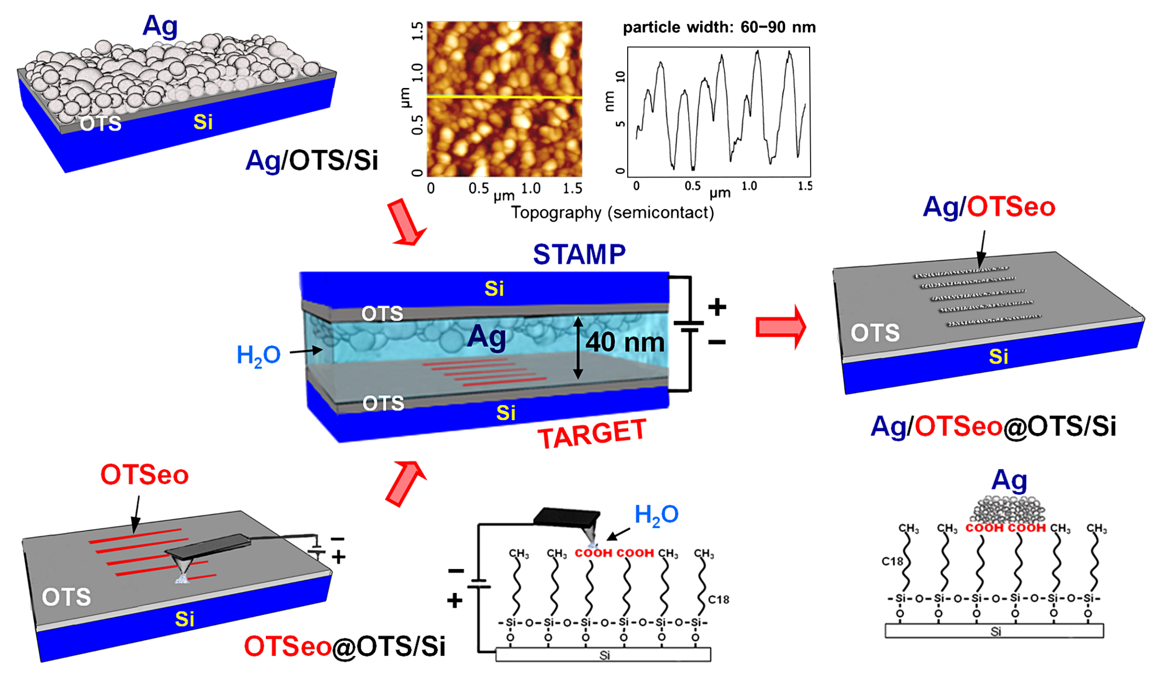

Figure 1: Scheme of parallel-contact electrochemical metallization of a OTSeo@OTS/Si template nanopattern (target, cathode) consisting of an array of parallel OTSeo lines serially inscribed with a conducting SFM tip on a self-assembled OTS monolayer on silicon (CNL process, bottom left). Selective silver deposition on the OTSeo lines of the patterned monolayer (right) is achieved by contact electrochemical transfer of the metal (center) from a stamp (anode) consisting of a thin (~40 nm), granular Ag film deposited by metal evaporation on the entire surface (2–4 cm^2) of an OTS/Si monolayer specimen (top) [30]. The granular morphology of such silver-film stamps is evident in the displayed SFM image. During the application of the bias voltage (center), the stamp–target sandwich is equilibrated with a water-saturated atmosphere (see Experimental section).

with a patterned monolayer surface of this kind. For the same reason, the corresponding contact-mode topographic images yield false height contrast, dependent on the direction of tip motion relative to the sample (see Supporting Information File 1, Figures S2 and S3). This is a characteristic feature of monolayer patterning by constructive lithography, which generates highly heterogeneous hydrophilic–hydrophobic monolayer surfaces [14,16,18,22,30]. Correct height values of the deposited silver, as displayed in Figure 2, Figure 3, and Figure 5 (see below), were thus obtained from semicontact-mode images.

An examination of the different patterns displayed in Figure 2 and Figure 3 indicates that OTSeo template features with local widths (*w*) below ca. 30 nm guide the formation of thin, platelike silver particles that span the entire width of the template and tend to grow beyond its boundaries while maintaining heights (*h*) on the order of 1–2 nm. On small dotlike template sites, this metal growth mode yields discrete Ag nanodots (Figure 2 and Figure 3, top row), whereas continuous Ag nanowires with a bamboolike structure of higher and lower metal features are formed on narrow template lines (Figure 3, middle row left). Identical deposition conditions applied to wider template features result in multiple nanoparticles with similar heights and somewhat smaller average lateral dimensions (Figure 3, middle row right and bottom row). Regions A and B in the bottom-row images in Figure 3 are representative of metal growth on both the wide regions and the narrow lines of the same template feature, respectively. Because of the high density of nanoparticles in region A, the lateral resolution of individual particles in the topographic image of this region (left) is poor, particles widths being here obtained from the simultaneously recorded phase image (right).

The size and lateral organization of metal particles formed on the different OTSeo template patterns in Figure 2 and Figure 3 are seen to differ not only from those characteristic of the granular silver film used as the stamp (see Figure 1), but also from one another. This is rather remarkable, given the fact that all these patterns are located on same target specimen and their electrochemical metallization was simultaneously performed with the same silver-film stamp. Equally remarkable is also the fact that no metal was deposited within the unmodified portions of the OTS surface and that undamaged template patterns (OTSeo@OTS/Si) could be regenerated by dissolving the electrochemically deposited metal (Figure 2). It was further observed that more metal is deposited with longer electrochemical stamping times under the same applied voltage bias, and

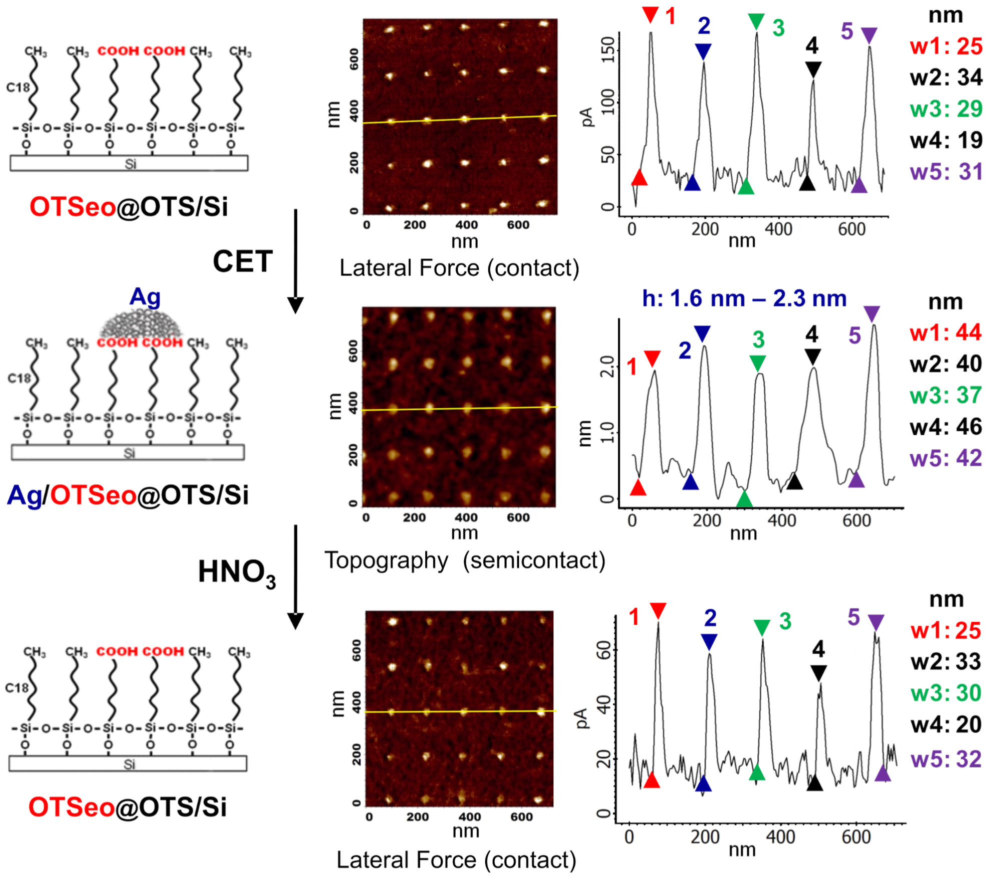

Figure 2: SFM images (and distance–height profiles along the marked lines) acquired after each step during the fabrication of an array of silver/monolayer nanodots by the contact electrochemical process depicted in Figure 1, as well as after removal of the metal by dissolution in nitric acid (see Experimental section): (Top row) the initial target array of monolayer-template nanodots (OTSeo@OTS/Si); (middle row) array of metal/monolayer template nanodots (Ag/OTSeo@OTS/Si); (bottom row) recovered array of OTSeo@OTS/Si monolayer-template nanodots, after removal of the deposited metal. Contact-mode topographic images of the metal-free dots (top and bottom rows) show a similar scan-dependent weak contrast relative to the OTS background, indicative of the structural integrity of the OTSeo monolayer template (see [30] and Supporting Information File 1, Figures S2 and S3).

metallic features were seen growing also laterally in a mushroomlike fashion (beyond the area of the underlying OTSeo template), without affecting the integrity of the surrounding OTS surface. Carrying out contact electrochemical experiments as in Figure 1 with target monolayers patterned by mask-defined local photocleavage of the OTS alkyl tails [22,27], it was finally established that no metal is deposited in bare regions present within an OTS monolayer.

In line with previously reported findings [30], these observations unequivocally demonstrate that: (i) The CET mechanism of metal transfer from stamp to target is electrochemical rather than adhesion-promoted [32-35], involving dissolution of stamp-metal grains (anode), ionic transport through an ultrathin water film adsorbed on the metal grains, and subsequent nucleation and growth of new metal grains at the target monolayer (cathode); (ii) metal grains can nucleate and grow only on monolayer-template surfaces exposing chemically active functions that bind the respective metal ions, the morphology and lateral distribution of the resulting metal features thus depending on the local dimensions and topology of the template features on which the metal grains nucleate and grow; (iii) there is no metal nucleation and growth in pinhole defects in the organic monolayer that might not be detected by the SFM imaging, so that metal deposited by the present CET process necessarily resides only on the outer surface of the monolayer template, with full preservation of its structural integrity. Recent electrical measurements indeed confirm the absence of metal–silicon conductive paths in Ag/monolayer/Si structures fabricated in this manner. The CET process thus yields metal-on-monolayer deposits with no contacts to the underlying solid substrate, in-principle different from those usually produced in conventional electrochemical deposition on thiol/gold monolayers [36-45], which may occur in the monolayer-free regions of a destructively patterned monolayer [36-42], underneath the monolayer [41,42], or on top of the monolayer with metallic

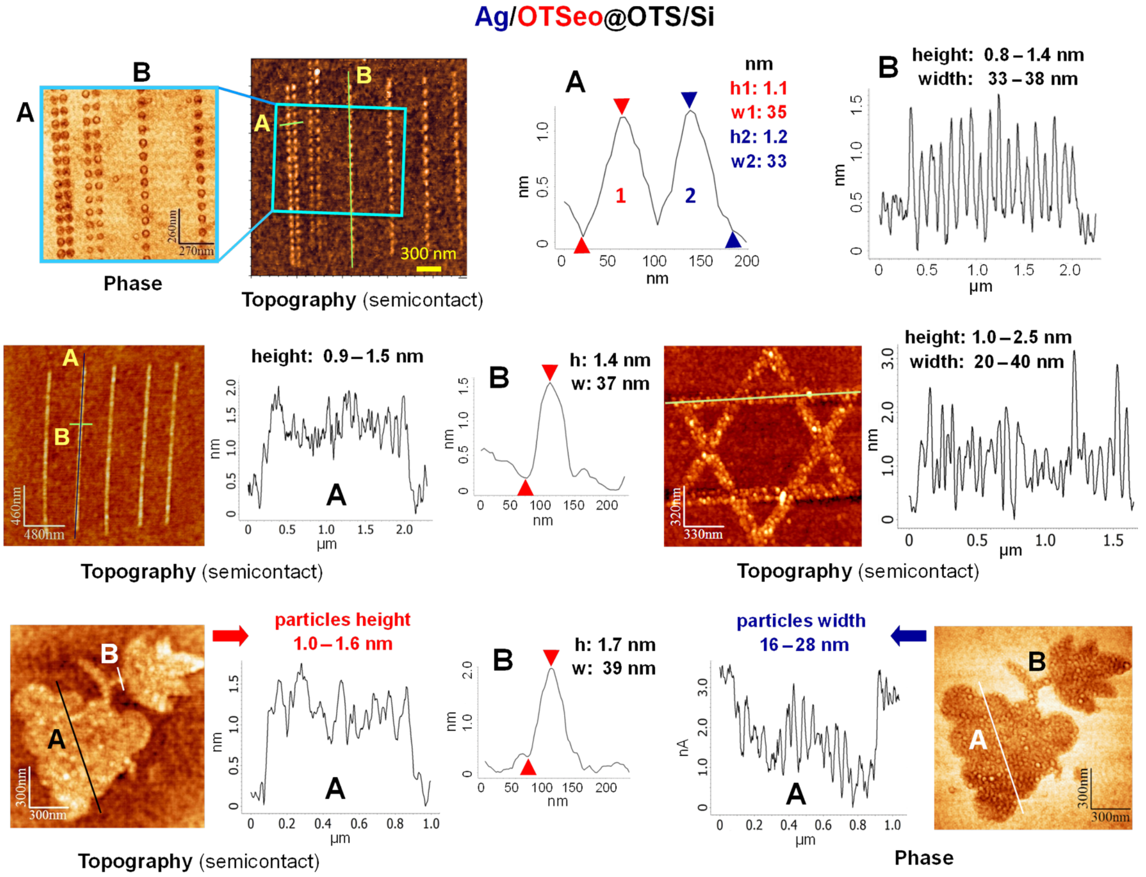

Figure 3: Semicontact SFM images (and distance–height profiles along the marked lines) of different silver/monolayer nanostructures fabricated in the same manner as the nanodots in Figure 2 (see text and Experimental section).

contacts reaching the metal substrate through defect sites in the monolayer [39-45].

In view of these experimental observations, it was anticipated that by replacing the metal stamp with a positively biased metal-loaded SFM tip that can be programmed to move across the surface according to a predefined trajectory, it should be possible to create more complex "pattern-within-pattern" structures by serial delivery of metal to selected surface sites within selected OTSeo template regions of a prepatterned OTS monolayer. For example, in the case of OTSeo lines (Figure 4), since metal is not deposited on the pristine OTS monolayer, metal transfer from tip to surface should be confined to the intersection regions of each cathodic OTSeo line with the directions of motion of the anodic tip. Experimental results confirming the feasibility of this approach are given in Figure 5 and Figure S1 (Supporting Information File 1).

In Figure 5, each on–off switching of the bias voltage, at the beginning and end of a horizontal tip excursion, respectively, is seen to be accompanied by a pair of sharp, capacitance-related current spikes of opposite sign, whereas smaller and broader positive current spikes, on the order of 30–50 pA, clearly correlate with tip-to-surface metal transfer within each tip/OTSeo crossing region. The total transferred charge (deduced from the integrated area of each current spike) is, however, significantly larger than that corresponding to the amount of deposited metal, which indicates that other bias-dependent processes, competing with the electrochemical metal transfer from tip to surface, also contribute to the total measured current [30] (see proposed model in the following). As is further evident in Figure 5, the platelike silver nanodots fabricated by this serial CET process are similar to those produced in the parallel CET mode (Figure 2 and Figure 3); however, the serial process offers the option of precise control over the generation of discrete nanoparticles at isolated sites within each OTSeo template line, in contrast to the uncontrollable fusion of adjacent nanoparticles on the narrow OTSeo lines or their random lateral distribution on the wider OTSeo regions in the parallel process (Figure 3).

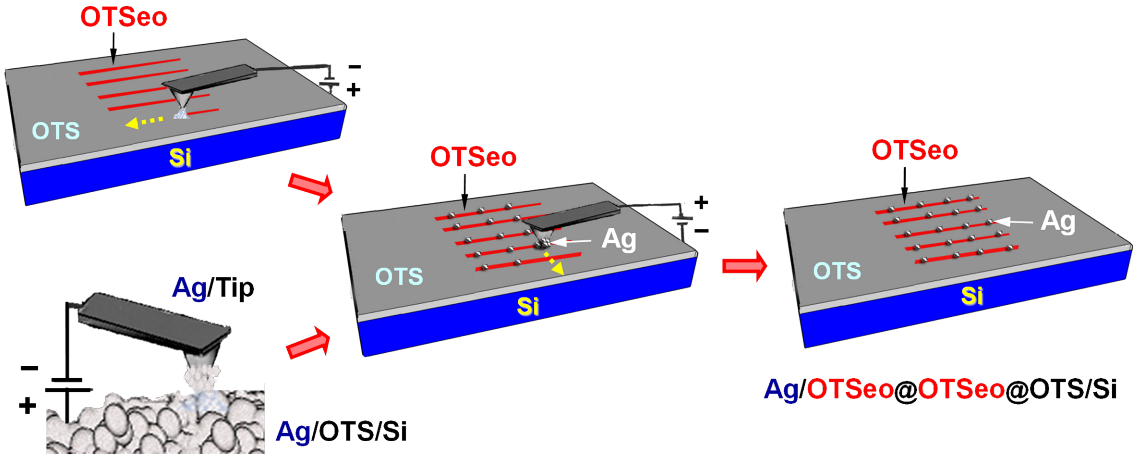

Figure 4: Scheme of serial-contact electrochemical metallization of selected sites within the OTSeo lines of a OTSeo@OTS/Si template nanopattern: (top left) inscription of OTSeo lines with a conductive SFM tip (CNL process); (bottom left) loading of silver on a conductive SFM tip by contact electrochemical transfer from a thin silver film evaporated on a OTS/Si monolayer; (center) selective-contact electrochemical transfer (CET) of silver from the silver-coated tip to selected sites along the OTSeo lines, implemented by moving the positively biased tip (mobile anode) across the OTSeo lines that play the role of cathode for metal deposition (see text); (right) resulting pattern-within-pattern array of silver/monolayer nanodots (Ag/OTSeo@OTSeo@OTS/Si denotes Ag/OTSeo sites within metal-free OTSeo regions located within the unmodified OTS/Si monolayer). As in the parallel CET process (Figure 1), no metal is transferred from tip to surface in a dry atmosphere and in the absence of an appropriate voltage bias (see Supporting Information File 1, Figure S1).

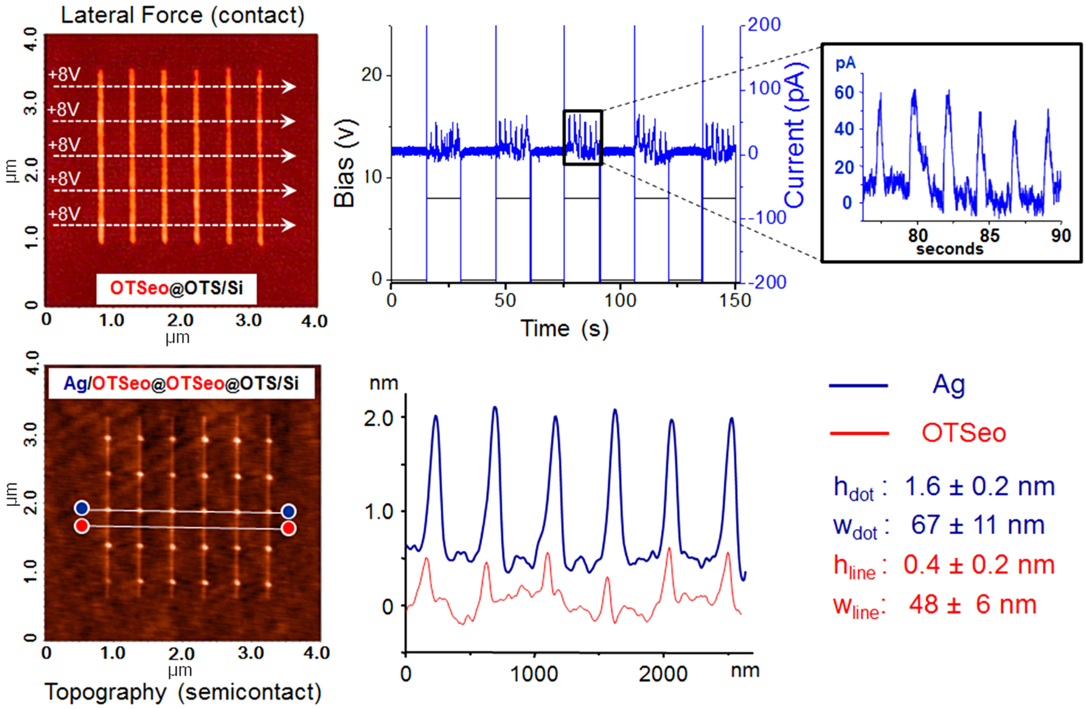

Figure 5: Fabrication of a rectangular array of 30 silver/monolayer nanodots by the serial CET process outlined in Figure 4 (see Experimental section): (Top row, left) five horizontal tip excursions across the array of six parallel OTSeo lines used in the assembly of the Ag/OTSeo nanodots (indicated by white arrows in the lateral force SFM image of the OTSeo lines); (top row, right) plots of tip bias voltage (+8 V, black curve) and corresponding current (blue curve) versus time recorded during each tip excursion (tip moving in contact with the surface at a constant speed of 250 nm/s); (bottom row) topographic semicontact-mode SFM image of the resulting dots@lines pattern (Ag/OTSeo@OTSeo@OTS/Si) and distance–height profiles along the middle row of Ag/OTSeo dots (blue curve, shifted vertically for clarity) and a closely located row of silver-free OTSeo crossing points (red curve). The average heights and widths listed on the right refer to all 30 dots and OTSeo crossing points. Contact-mode topographic images of this dots@lines pattern and a comparative analysis of the contact- and semicontact-mode topographic images (revealing the artifactual nature of the former) are provided in the Supporting Information File 1 (Figures S2 and S3).

The origin of the remarkable surface selectivity of metal deposition in these CET processes may be understood with reference to the schematic electrochemical model depicted in Figure 6, which highlights some of the salient features of the metal transfer and its high surface selectivity. As shown before [30], an ultrathin layer of water adsorbed on the metal grains of a granular Ag film stamp exposed to a humid atmosphere may convert each such grain into a tiny bipolar electrode [46-48], from which Ag^+ ions are released at its anodic side (+, facing the negative electrode) and redeposited as elemental silver at its cathodic side (−, facing the positive electrode). Since no metal ions are supplied to the cathodic side of the topmost grains in the metal film, these grains will gradually dissolve and eventually disappear. Concomitantly with their dissolution, metal is deposited on the surface of the OTSeo target monolayer through the reduction of chemisorbed Ag^+ ions (by electrons supplied by the negative silicon electrode) followed by the nucleation and growth of new metal grains. These metal grains grow at the expense of the dissolving stamp grains next to the positive electrode, thus resulting in gradual transfer of metal to the target monolayer. As emphasized before [30], in addition to the ionic current responsible for the metal transfer, the total measured current is expected to include also contributions from competing Faradaic processes, such as the electrolysis of water, as well as from direct electronic current through closely spaced metal grains in the thin silver film. The experimental data in Figure 5 support this view.

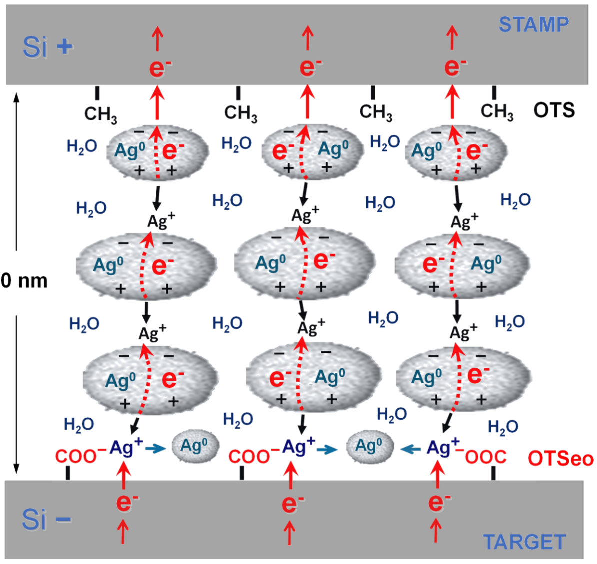

Figure 6: Proposed bipolar electrochemical mechanism of metal transfer from a thin, granular silver-film stamp (Ag/OTS/Si) to a carboxylic acid terminated target monolayer (OTSeo/Si) in a contact electrochemical configuration like that depicted in Figure 1 (see text). Key features emphasized in this schematic illustration (not to scale) are the nanoscale thickness of the granular silver film, the molecular–nanoscale thickness of the water film (electrolyte) adsorbed on the silver grains by capillary condensation from a humid atmosphere, the gradual dissolution of silver grains next to the OTS monolayer (stamp), and the nucleation of new silver grains at the OTSeo monolayer (target) upon the reduction of Ag^+ ions chemisorbed on the OTSeo surface as $–COO^-Ag^+$ species [30]. Note that several closely located Ag^+ ions need to be simultaneously discharged at the target monolayer in order to generate a stable metal cluster.

The crux of the selective electrochemical deposition of silver on the OTSeo surface has to do with the fact that single Ag^0 atoms are highly reactive and therefore short-lived [49-51]. Reaching a critical nucleus size that would allow further stable growth of a larger metal grain [52] is, thus, not possible unless a critical number of silver atoms are simultaneously generated through the reduction of an equal number of closely located silver ions. This can be accomplished at a target surface covered by a silver-binding monolayer such as OTSeo, in which the dense –COOH functionality of the organic monolayer facilitates the establishment of a sufficiently high local concentration of chemisorbed Ag^+ ions through the conversion of carboxylic acid groups to the carboxylate salt ($–COO^-Ag^+$). In contrast with OTSeo, metal deposition by this mechanism on a pristine OTS surface is not possible because of the very low probability of nucleation and growth of metal grains on such a surface devoid of ion-binding functions [53]. Since the local concentration of hydrated silver ions in solution in front of an OTS monolayer should be much lower than that of Ag^+ ions chemisorbed on the OTSeo surface, while their distance from the silicon substrate is considerably larger, isolated silver atoms that might eventually be generated as a result of the reduction of such ionic species by electrons reaching the solution through the OTS monolayer are expected to rapidly return to their ionic state (by electron transfer to surrounding water molecules [54,55]) or redeposit on preexisting stamp-metal grains, before aggregation into stable metal clusters residing on the OTS surface can occur.

Conclusion

The high selectivity achieved in the contact electrochemical deposition of silver on monolayer-template features exposing metal-ion-binding functions created by constructive nanolithography offers a versatile and reliable synthetic tool for the deliberate assembly of various metal-on-monolayer nanostructures, to be used as building blocks in the bottom-up fabrication of entire nanocircuits [56]. This is possible, as the present electrochemical methodology is compatible with low-conductivity substrates [30] and the deposited metal features reside on an extremely robust insulating layer of variable thickness (here the organic silane monolayer plus the native silicon oxide underneath it) that separates them from the substrate and provides effective electrical insulation over a range of useful applied voltages lower than those applied during the monolayer patterning and metallization processes themselves. While rapid formation of multiple circuit elements, such as arrays of metal nanodots and nanowires, may be achieved by using metal-film stamps in the parallel-metallization mode (Figure 2 and Figure 3), serial generation of metal/monolayer nanoobjects occupying only a limited portion of the total area of the respective monolayer-template features (such as the nanodots in Figure 5) should permit more complex structures to be realized through consecutive template-guided assembly steps [14,17,18,24,27]. For example, in this manner one could easily fabricate various collinear sequences of metal and semiconductor [14,17] nanodots and nanowires, confined to any desired layout of monolayer-template lines, straight, curved, parallel or intersecting. The precise deposition of metal at selected locations on the selected template lines is guaranteed here by the inherent electrochemical selectivity of the CET process, which precludes metal deposition on the unpatterned OTS surface.

For the application of this methodology to the fabrication of an entire addressable nanocircuit, the present nanoscale metallization processes need to be combined with analogous CET processes applicable on much larger length scales [30], which would enable the assembly of micro- and macroscale metal/monolayer contact electrodes. Work toward the realization of such circuits and their electrical–structural characterization is currently in progress.

As far as basic electrochemical aspects are concerned, it is of interest to note that the present findings offer direct experimental support to the recent arguments raised against the usually adopted model of electron transfer from the electrode to a metal ion in solution as the mechanism of charge transfer across the electrode–solution interface in electrochemical metal deposition [54,55]. Indeed, the exclusive deposition of silver on the Ag^+ binding (OTSeo) sites of nondestructively patterned OTS/Si monolayers demonstrates that metal ions have to shed their hydration shell and reach the electrode surface before being discharged, rather than being first reduced to neutral atoms by electron transfer to hydrated ionic species in solution [54,55].

Experimental

OTS/Si monolayer samples and Ag/OTS/Si metal film stamps were prepared following experimental procedures detailed in [22] and [30], respectively. The parallel-contact electrochemical metallization experiments (Figure 1, Figure 2 and Figure 3) were performed as described in [30], using a specially designed electrical stamping device that allows control of the bias voltage, the force pressing the stamp and the target together, and the ambient humidity. In the present experiments, a voltage bias of 3.0 V was applied for 2 min between the silver/monolayer stamp and the target monolayer while the two specimens are pressed together with a force of about 100 N in a water-saturated atmosphere (RH 100%). Deposited silver dots were removed (Figure 2) by immersion in HNO_3/H_2O (20% v/v) for ~3 h followed by rinsing with pure water.

All monolayer nanopatterning (CNL) and serial metallization (CET) operations were carried out in the contact mode (in a regime of minimal repulsive force), under controlled humidity at 55–65% RH. A SOLVER P47 SFM system (NT-MDT) was used in the fabrication of the OTSeo@OTS nanopatterns in Figure 2 and Figure 3. The patterns were written with doped-silicon contact probes (CSC-38/AlBS, MikroMasch) or metal-coated contact probes (CSC-37/Ti-Pt, MikroMasch) to which a negative bias of 7.0–8.0 V relative to the surface was applied. Contact-mode images (Figure 2) were acquired with the same probes without an applied electrical bias, and semicontact-mode (tapping) images (Figure 2 and Figure 3) with Silicon AC160TS semicontact probes (Olympus).

The serial CET experiments (Figure 4 and Figure 5) were performed on an NTEGRA Aura SFM system (NT-MDT) specially designed for electrical patterning and structural-electrical characterization of surface architectures [30]. W_2C-coated HSC20 contact probes (Team Nanotec) were used in the inscription of the OTSeo lines, (under conditions similar to those mentioned above in relation to Figure 2 and Figure 3), whereas the metal-transfer operations were executed with CSC-37/Ti-Pt contact probes (MikroMasch) on which silver was loaded by scanning the surface of an evaporated silver film on OTS for ~5 min with a tip bias of −10 V relative to the silver film. Experimental conditions for the metal delivery from tip to the OTSeo lines (Figure 5) were selected following trial experiments carried out with different applied voltages and tip speeds (Figure S1, Supporting Information File 1). Contact-mode SFM images (Figure 5 and Figures S1, S2 and S3, Supporting Information File 1) were acquired with the patterning tip without an applied bias, and semicontact-mode images (Figure 5) with Silicon AC160TS semicontact probes (Olympus).

Supporting Information

Supporting Information File 1

Serial CET trial experiments and comparison of imaging results obtained under different SFM imaging conditions.
[http://www.beilstein-journals.org/bjnano/content/supplementary/2190-4286-3-14-S1.pdf]

Acknowledgements

This research was supported by the Israel Science Foundation (grant No. 643/09), the G. M. J. Schmidt Minerva Center of Supramolecular Architectures, and Minerva Foundation with funding from the Federal German Ministry of Education and Research. We thank Stanislav Leesment of NT-MDT Company, Moscow, Russia for his support in the operation of the new SFM system used in this work.

References

1. Braun, E.; Eichen, Y.; Sivan, U.; Ben-Yoseph, G. *Nature* **1998,** *391,* 775–778. doi:10.1038/35826
2. Park, S. H.; Prior, M. W.; LaBean, T. H.; Finkelstein, G. *Appl. Phys. Lett.* **2006,** *89,* 033901. doi:10.1063/1.2234282
3. Lopes, W. A.; Jaeger, H. M. *Nature* **2001,** *414,* 735–738. doi:10.1038/414735a
4. Sauer, G.; Brehm, G.; Schneider, S.; Nielsch, K.; Wehrspohn, R. B.; Choi, J.; Hofmeister, H.; Gösele, U. *J. Appl. Phys.* **2002,** *91,* 3243–3247. doi:10.1063/1.1435830
5. Zhang, M.; Lenhert, S.; Wang, M.; Chi, L.; Lu, N.; Fuchs, H.; Ming, N. B. *Adv. Mater.* **2004,** *16,* 409–413. doi:10.1002/adma.200305577
6. Stahlmecke, B.; Meyer zu Heringdorf, F.-J.; Chelaru, L. I.; Horn-von Hoegen, M.; Dumpich, G.; Roos, K. R. *Appl. Phys. Lett.* **2006,** *88,* 053122. doi:10.1063/1.2172012
7. Wang, C.; Hu, Y.; Lieber, C. M.; Sun, S. *J. Am. Chem. Soc.* **2008,** *130,* 8902–8903. doi:10.1021/ja803408f
8. Peng, Y.; Cullis, T.; Inkson, B. *Appl. Phys. Lett.* **2008,** *93,* 183112. doi:10.1063/1.3005423
9. Huo, Z.; Tsung, C.-k.; Huang, W.; Zhang, X.; Yang, P. *Nano Lett.* **2008,** *8,* 2041–2044. doi:10.1021/nl8013549
10. Lu, X.; Yavuz, M. S.; Tuan, H.-Y.; Korgel, B. A.; Xia, Y. *J. Am. Chem. Soc.* **2008,** *130,* 8900–8901. doi:10.1021/ja803343m
11. Azulai, D.; Belenkova, T.; Gilon, H.; Barkay, Z.; Markovich, G. *Nano Lett.* **2009,** *9,* 4246–4249. doi:10.1021/nl902458j
12. Li, J.-R.; Lusker, K. L.; Yu, J.-J.; Garno, J. C. *ACS Nano* **2009,** *3,* 2023–2035. doi:10.1021/nn9004796
13. Maoz, R.; Cohen, S. R.; Sagiv, J. *Adv. Mater.* **1999,** *11,* 55–61. doi:10.1002/(SICI)1521-4095(199901)11:1<55::AID-ADMA55>3.0.CO;2-8
14. Maoz, R.; Frydman, E.; Cohen, S. R.; Sagiv, J. *Adv. Mater.* **2000,** *12,* 725–731. doi:10.1002/(SICI)1521-4095(200005)12:10<725::AID-ADMA725>3.0.CO;2-Z
15. Maoz, R.; Frydman, E.; Cohen, S. R.; Sagiv, J. *Adv. Mater.* **2000,** *12,* 424–429. doi:10.1002/(SICI)1521-4095(200003)12:6<424::AID-ADMA424>3.0.CO;2-S
16. Hoeppener, S.; Maoz, R.; Sagiv, J. *Nano Lett.* **2003,** *3,* 761–767. doi:10.1021/nl034176l
17. Hoeppener, S.; Maoz, R.; Cohen, S. R.; Chi, L. F.; Fuchs, H.; Sagiv, J. *Adv. Mater.* **2002,** *14,* 1036–1041. doi:10.1002/1521-4095(20020805)14:15<1036::AID-ADMA1036>3.0.CO;2-J
18. Liu, S.; Maoz, R.; Sagiv, J. *Nano Lett.* **2004,** *4,* 845–851. doi:10.1021/nl049755k
19. Checco, A.; Cai, Y.; Gang, O.; Ocko, B. M. *Ultramicroscopy* **2006,** *106,* 703–708. doi:10.1016/j.ultramic.2005.11.009
20. Hoeppener, S.; Susha, A. S.; Rogach, A. L.; Feldmann, J.; Schubert, U. S. *Curr. Nanosci.* **2006,** *2,* 135–141. doi:10.2174/157341306776875758
21. Andruzzi, L.; Nickel, B.; Schwake, G.; Rädler, J. O.; Sohn, K. E.; Mates, T. E.; Kramer, E. J. *Surf. Sci.* **2007,** *601,* 4984–4992. doi:10.1016/j.susc.2007.07.028
22. Zeira, A.; Chowdhury, D.; Maoz, R.; Sagiv, J. *ACS Nano* **2008,** *2,* 2554–2568. doi:10.1021/nn8005174
23. Unruh, D. A.; Mauldin, C.; Pastine, S. J.; Rolandi, M.; Fréchet, J. M. J. *J. Am. Chem. Soc.* **2010,** *132,* 6890–6891. doi:10.1021/ja101627e
24. Chowdhury, D.; Maoz, R.; Sagiv, J. *Nano Lett.* **2007,** *7,* 1770–1778. doi:10.1021/nl070842x
25. Cai, Y. *Langmuir* **2008,** *24,* 337–343. doi:10.1021/la702321d
26. Gao, P.; Cai, Y. *Ultramicroscopy* **2009,** *109,* 1023–1028. doi:10.1016/j.ultramic.2009.03.023
27. Zeira, A.; Chowdhury, D.; Hoeppener, S.; Liu, S.; Berson, J.; Cohen, S. R.; Maoz, R.; Sagiv, J. *Langmuir* **2009,** *25,* 13984–14001. doi:10.1021/la902107u
28. Xu, J.; Park, S.; Wang, S.; Russell, T. P.; Ocko, B. M.; Checco, A. *Adv. Mater.* **2010,** *22,* 2268–2272. doi:10.1002/adma.200903640
29. Wen, K.; Maoz, R.; Cohen, H.; Sagiv, J.; Gibaud, A.; Desert, A.; Ocko, B. M. *ACS Nano* **2008,** *2,* 579–599. doi:10.1021/nn800011t
30. Zeira, A.; Berson, J.; Feldman, I.; Maoz, R.; Sagiv, J. *Langmuir* **2011,** *27,* 8562–8575. doi:10.1021/la2009946
31. Zeira, A. Surface-Immobilized Hydrogel Patterns on Length Scales from Micrometer to Nanometer. Ph.D. Thesis, Weizmann Institute, Israel, 2010.
32. Loo, Y.-L.; Willett, R. L.; Baldwin, K. W.; Rogers, J. A. *J. Am. Chem. Soc.* **2002,** *124,* 7654–7655. doi:10.1021/ja026355v
33. Menard, E.; Bilhaut, L.; Zaumseil, J.; Rogers, J. A. *Langmuir* **2004,** *20,* 6871–6878. doi:10.1021/la048827k
34. Lee, B. H.; Cho, Y. H.; Lee, H.; Lee, K.-D.; Kim, S. H.; Sung, M. M. *Adv. Mater.* **2007,** *19,* 1714–1718. doi:10.1002/adma.200601884
35. Strobel, S.; Harrer, S.; Blanco, G. P.; Scarpa, G.; Abstreiter, G.; Lugli, P.; Tornow, M. *Small* **2009,** *5,* 579–582. doi:10.1002/smll.200801400
36. Sondag-Huethorst, J. A. M.; van Helleputte, H. R. J.; Fokkink, L. G. J. *Appl. Phys. Lett.* **1994,** *64,* 285–287. doi:10.1063/1.111182
37. Zamborini, F. P.; Crooks, R. M. *J. Am. Chem. Soc.* **1998,** *120,* 9700–9701. doi:10.1021/ja9821955
38. Seo, K.; Borguet, E. *Langmuir* **2006,** *22,* 1388–1391. doi:10.1021/la052489l
39. Nelson, J. B.; Schwartz, D. T. *Langmuir* **2007,** *23,* 9661–9666. doi:10.1021/la701014u
40. Mullen, T. J.; Zhang, P.; Srinivasan, C.; Horn, M. W.; Weiss, P. S. *J. Electroanal. Chem.* **2008,** *621,* 229–237. doi:10.1016/j.jelechem.2007.11.038
41. Pesika, N. S.; Fan, F.; Searson, P. C.; Stebe, K. J. *J. Am. Chem. Soc.* **2005,** *127,* 11960–11962. doi:10.1021/ja050955n
42. Pesika, N. S.; Radisic, A.; Stebe, K. J.; Searson, P. C. *Nano Lett.* **2006,** *6,* 1023–1026. doi:10.1021/nl060368f
43. Felgenhauer, T.; Yan, C.; Geyer, W.; Rong, H.-T.; Gölzhäuser, A.; Buck, M. *Appl. Phys. Lett.* **2001,** *79,* 3323–3325. doi:10.1063/1.1415771
44. Thom, I.; Hähner, G.; Buck, M. *Appl. Phys. Lett.* **2005,** *87,* 024101. doi:10.1063/1.1991992
45. Schilardi, P. L.; Dip, P.; dos Santos Claro, P. C.; Benítez, G. A.; Fonticelli, M. H.; Azzaroni, O.; Salvarezza, R. C. *Chem.–Eur. J.* **2006,** *12,* 38–49. doi:10.1002/chem.200500203
46. Plimley, R. E.; Wright, A. R. *Chem. Eng. Sci.* **1984,** *39,* 395–405. doi:10.1016/0009-2509(84)80037-8

47. Bradley, J. C.; Chen, H.-M.; Crawford, J.; Eckert, J.; Ernazarova, K.; Kurzeja, T.; Lin, M.; McGee, M.; Nadler, W.; Stephens, S. G. *Nature* **1997,** *389,* 268–271. doi:10.1038/38464
48. Bradley, J. C.; Dengra, S.; Gonzalez, G. A.; Marshall, G.; Molina, F. V. *J. Electroanal. Chem.* **1999,** *478,* 128–139. doi:10.1016/S0022-0728(99)00424-6
49. Plieth, W. J. *J. Phys. Chem.* **1982,** *86,* 3166–3170. doi:10.1021/j100213a020
50. Henglein, A.; Mulvaney, P.; Linnert, T. *Electrochim. Acta* **1991,** *36,* 1743–1745. doi:10.1016/0013-4686(91)85037-8
51. Henglein, A. *J. Phys. Chem.* **1993,** *97,* 5457–5471. doi:10.1021/j100123a004
52. Adamson, A. W.; Gast, A. P. *Physical Chemistry of Surfaces,* 6th ed.; Wiley: New York, 1997; p 328.
53. Kotov, N. A.; Darbello Zaniquelli, M. E.; Meldrum, F. C.; Fendler, J. H. *Langmuir* **1993,** *9,* 3710–3716. doi:10.1021/la00036a057 Here, an apparently related process is described, whereby electrochemical generation of particulate 2D silver films was found to occur under Langmuir monolayers spread on aqueous silver nitrate only in the presence of monolayers prepared from surfactants exposing Ag^+-binding headgroups.
54. Gileadi, E. *Chem. Phys. Lett.* **2004,** *393,* 421–424. doi:10.1016/j.cplett.2004.06.070
55. Gileadi, E. *J. Electroanal. Chem.* **2011,** *660,* 247–253. doi:10.1016/j.jelechem.2011.01.025
56. Though not yet investigated, other metals should be applicable as well.

License and Terms

The definitive version of this article is the electronic one which can be found at:
doi:10.3762/bjnano.3.14

Beilstein Journal
of Nanotechnology

Variations in the structure and reactivity of thioester functionalized self-assembled monolayers and their use for controlled surface modification

Inbal Aped, Yacov Mazuz and Chaim N. Sukenik*

Full Research Paper

Open Access

Address:
Department of Chemistry and Institute for Nanotechnology and Advanced Materials, Bar-Ilan University, Ramat-Gan, Israel 52900

Email:
Chaim N. Sukenik* - chaim.sukenik@biu.ac.il

* Corresponding author

Keywords:
siloxane-anchored self-assembled monolayers; sulfonated interfaces; surface chemistry

Beilstein J. Nanotechnol. **2012,** *3,* 213–220.
doi:10.3762/bjnano.3.24

Received: 01 December 2011
Accepted: 10 February 2012
Published: 09 March 2012

This article is part of the Thematic Series "Self-assembly at solid surfaces".

Guest Editors: S. R. Cohen and J. Sagiv

Abstract

Thioester-functionalized, siloxane-anchored, self-assembled monolayers provide a powerful tool for controlling the chemical and physical properties of surfaces. The thioester moiety is relatively stable to long-term storage and its structure can be systematically varied so as to provide a well-defined range of reactivity and wetting properties. The oxidation of thioesters with different-chain-length acyl groups allows for very hydrophobic surfaces to be transformed into very hydrophilic, sulfonic acid-bearing, surfaces. Systematic variation in the length of the polymethylene chain has also allowed us to examine how imbedding reaction sites at various depths in a densely packed monolayer changes their reactivity. π-Systems (benzene and thiophene) conjugated to the thioester carbonyl enable the facile creation of photoreactive surfaces that are able to use light of different wavelengths. These elements of structural diversity combine with the utility of the hydrophilic, strongly negatively charged sulfonate-bearing surface to constitute an important approach to systematic surface modification.

Introduction

Functionalized self-assembled monolayers (SAMs) provide powerful tools for conveniently adjusting the composition and chemistry of solid interfaces. First introduced by Jacob Sagiv and co-workers [1-3], siloxane-anchored SAMs have been used to modify the wetting and composition of variously hydroxylated surfaces. In situ chemical transformations of the SAM surfaces provide an additional dimension to the versatility and utility of the SAMs [4-7].

Our laboratory has reported in situ transformations of siloxane-anchored SAMs in which SAM surface functionality was changed from benzene rings to arylsulfonic acids [8,9], from nitrate esters to hydroxyls [10], and from carboxylate esters to carboxylic acids [11,12]. All three of these functionalized surfaces could not have been deposited directly since the requisite silanes would not have been stable. Layer-by-layer [13] and modular assembly [14] of sulfonic acid surfaces with a lower degree of order and uniformity has also been reported.

A striking example of in situ SAM transformations is based on the initial deposition of thioacetate-bearing monolayers and their in situ conversion to sulfonic acid surfaces [15]. This transformation provides the basis for surface patterning of the monolayer and for its use as a patterned template for inorganic oxide deposition [16]. The work reported herein extends this chemistry in two important directions. In one instance, thioesters with acyl components of varying chain length are shown to provide a tool for varying the initial hydrophobicity of the monolayer surface from medium hydrophobicity (water contact angles of about 70°) to very hydrophobic (water contact angles >110°). Each of these thioesters can be converted into sulfonic acids so as to provide fully wetted surfaces. The systematic variation in molecular chain length that produced the steadily changing hydrophobicity also allowed an examination of how the imbedding of reaction sites at various depths within a well-packed monolayer affects their reactivity. In another variation of monolayer structure, a set of thioesters with different aromatic rings conjugated to the carbonyl facilitate efficient photocleavage using longer wavelength light such that the photo-oxidation of the thioesters to sulfonic acid can be achieved with light of wavelength >300 nm.

We have synthesized a series of thioesters (Figure 1) that were designed to provide a range of hydrophobicities (**1a–i**) and a range of photoreactivities (**2–4**). These trichlorosilanes have been used to make siloxane-anchored monolayers on silicon wafers and quartz. The siloxane-anchored SAMs based on these materials, their tunable wetting properties and their in situ chemical transformations are the focus of this report.

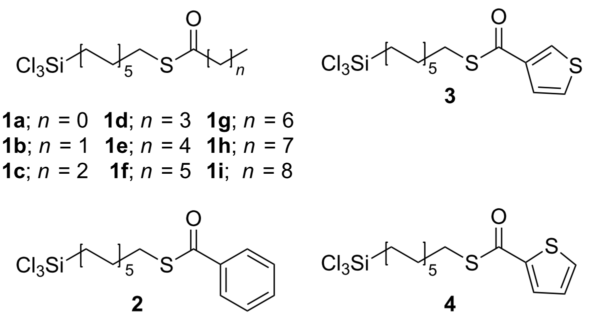

Figure 1: Trichlorosilyl thioesters.

Experimental

General methods and materials

Materials

Reagents and solvents were obtained from Sigma-Aldrich, Acros Organics, Fluka, Bio-Lab Ltd. or Merck. They were all used as received unless otherwise indicated. Water was deionized and then distilled in an all-glass apparatus. Column chromatography used silica gel 60 (230–400 mesh). Silicon wafers were obtained from Virginia Semiconductor (n-type; undoped, <100>, >1000 Ω·cm). Quartz substrates were obtained from Quarzschmelze Ilmenau.

Analytical Methods

Unless otherwise indicated, NMR spectra were obtained on a Bruker DPX 300 spectrometer (^{1}H NMR at 300 MHz; ^{13}C NMR at 75 MHz). Some were performed on a Bruker DPX 200 spectrometer (^{1}H NMR at 200 MHz; ^{13}C NMR at 50 MHz). The spectra are reported in ppm units (δ) and are referenced to TMS at 0 ppm for ^{1}H NMR and to $CDCl_3$ at 77.160 ppm for ^{13}C NMR. UV spectra (200–800 nm) were measured on a Cary Model 100 spectrometer (in double-beam transmission mode). Spectra of the as-deposited films were collected by using quartz slides. Spectra were run against a reference sample of the same quartz without the deposited films. Mass spectra were recorded on a Finnigan Model 400 mass spectrometer, by using chemical ionization (CI) with methane as the reagent gas unless otherwise indicated. Contact angle goniometry, spectroscopic ellipsometry, XPS, ATR–FTIR, were all carried out as previously described [11,12].

Syntheses

ω-Undecenylbromide was prepared as follows: In a round-bottom flask (500 mL) equipped with a magnetic stirring bar were placed CH_2Cl_2 (100 mL), commercial undecen-1-ol (12 g, 70.5 mmol) and triphenylphosphine (20.2 g, 77.0 mmol). The flask was cooled to 0 °C. While being stirred vigorously, tetrabromomethane (23.37 g, 70.5 mmol) was added slowly. After the addition, the mixture was stirred for 2 h and the CH_2Cl_2 was removed on a rotovap. The residual white paste was broken up and stirred with hexane (100 mL) and filtered into a round-bottom flask (250 mL). The hexane was removed on a rotovap. The crude product was purified by flash chromatography (hexane): Yield 15.53 g (94.5%). NMR analyses match those reported previously in the literature [6].

The preparation of (*S*)-undec-10-enyl thioacetate from ω-undecenylbromide followed the previously published procedure [17]. ω-Undecenyl thiol was prepared by acid hydrolysis of the thioacetate, as follows: In a round-bottom flask (250 mL) equipped with a magnetic stirring bar and a reflux condenser were placed methanol (135 mL) and HCl (15 mL, 37%). To this was added (*S*)-undec-10-enyl thioacetate (9 g, 39.4 mmol) and the mixture was heated under reflux overnight. The heating was stopped and the solvent was removed on a rotovap. Hexane (100 mL) was added, and the solution was extracted with water (50 mL) and brine (50 mL). The hexane was dried over $MgSO_4$ and filtered, and the solvent was removed on a rotovap. The crude ω-undecenyl thiol was purified by flash chromatography (hexane): Yield 6.02 g (82%); ^{1}H NMR δ 1.20–1.47 (m, 13H), 1.61 (m, 2H), 2.04 (m, 2H), 2.52 (q, *J* = 7.5 Hz, 2H), 4.93 (m, 2H), 5.81 (ddt, *J* = 6.6, 10.2, 17 Hz, 1H); ^{13}C NMR δ 24.80, 28.51, 29.06, 29.20, 29.24, 29.56, 29.59, 33.95, 34.19, 114.27, 139.36.

The general procedure for the conversion of ω-undecenyl thiol into the thioester–olefin precursors for compounds **1b**–**i**, **2**, **3** and **4** is as follows: In a dry, round-bottom flask equipped with a magnetic stirring bar were placed ω-undecenyl thiol (*x* mmol) and NEt_3 (6*x* mmol) in dry THF (54*x* mmol). The flask was cooled to 0 °C, and the appropriate acid chloride (1.01*x* mmol) was added slowly. After 2 h the reaction mixture was warmed to room temperature and the solvent was removed on a rotovap. Hexane (100 mL) was added and the solution was extracted with water (50 mL), 20% $NaHCO_3$ (50 mL) and brine (50 mL). The hexane was dried over $MgSO_4$, filtered and the solvent was removed on a rotovap. The aliphatic thioesters were purified by flash chromatography (5% EtOAc, 95% hexane), while vacuum distillation was used to purify the benzoyl and thiophenyl thioesters. Isolated yields, ^{1}H and ^{13}C NMR, and exact mass MS data for each of the olefin-thioesters are summarized in Supporting Information File 1.

The general procedure for the conversion of the various olefin thioesters into trichlorosilanes **1**, **2**, **3**, and **4** is as follows: The olefin thioester (1–2 mL), $HSiCl_3$ (6 mL), and a solution of $H_2PtCl_6{\cdot}6H_2O$ in iPrOH (10–20 μL, 4%; dried over 4 Å molecular sieves and distilled) were placed in a pressure tube (20 mL) containing a magnetic stirring bar. All reagents were handled in a nitrogen atmosphere. The tube was sealed and transferred to an oil bath maintained at 60–80 °C, in which it was heated for 16–40 h (the specific temperatures and times are given in Supporting Information File 1). The progress of the reaction was monitored by the disappearance of the olefinic protons in the ^{1}H NMR. After the reaction was complete, the contents of the tube were transferred to a round-bottom flask (25 mL) under a nitrogen atmosphere. Excess $HSiCl_3$ was distilled off and the product was isolated by Kugelrohr distillation. The isolated yields and NMR data for each of the trichlorosilanes is summarized in Supporting Information File 1.

Monolayer preparation

Silicon wafers (for ellipsometry and ATR–FTIR measurements) and quartz wafers (for UV and XPS measurements) were cleaned and activated as previously reported [12] and used as substrates for depositing siloxane-anchored SAMs based on compounds **1**–**4**. The SAMs were characterized by contact angle, ATR–FTIR, UV–vis, ellipsometry, and XPS. These characterization tools were applied (as previously reported [12]) both on the directly deposited SAMs and on those that had been subjected to the oxidation reactions reported herein.

General procedures for in situ oxidation of thioester SAMs

Oxidation using aqueous OXONE

A saturated solution of OXONE (potassium peroxomonosulfate, extra pure, min. 4.5% active oxygen; Acros Organics) in water was prepared. The thioester SAM-bearing substrates were immersed in the OXONE solution for times of up to 10 h (see Table 2 below), at room temperature [15]. The substrates were withdrawn from the solution, rinsed with doubly distilled water, and dried under a stream of filtered nitrogen.

UV-C irradiation in air

A UV lamp (narrow-band irradiation centered on 254 nm, 6 W lamp) was held 2 cm from the surface of the substrate for 1 h for each side (in ambient air). The oxidized surface was rinsed with doubly distilled water and dried with a stream of filtered nitrogen. In some instances, the photoreacted surfaces were rinsed with $CHCl_3$ and EtOH before the final water rinse. The consequences of these rinses with organic solvents will be discussed below.

UV-A irradiation in air

Quartz test-tubes were used as holders for silicon and quartz wafers coated with SAMs based on **1a**, **2**, **3** and **4**. The test-tubes were placed in the middle of a Luzchem model LZC4 photoreactor (8 UV-A lamps, HITACHI FL8BL-B, emission 320–400 nm, peak emission at 360 nm) such that the lamps completely surrounded the samples. Irradiation times were up to 132 h, at 24–28 °C. After irradiation, the substrates were withdrawn from the reactor, rinsed with doubly distilled water, and dried under a stream of filtered nitrogen.

Results

SAM preparation

Trichlorosilane **1a** was prepared by a method similar to that reported for its longer chain analogue [15], and compounds **1b**–**i, 2, 3** and **4** were all produced by hydrosilylation of a terminal olefin that was obtained by acylation of ω-undecenyl thiol, which had been prepared in three steps from commercial ω-undecenol. All of the trichlorosilanes were purified by distillation and deposited as siloxane-anchored SAMs.

SAM characterization

ATR–FTIR characterization of these SAMs focused on the vibrational frequencies of the carbonyl groups and of the methylene units in each of the polymethylene chains (Table 1). The carbonyl stretches of the alkyl thioesters are all in the range of 1690–1696 cm^{-1}. The conjugation in **2**, **3**, and **4** reduces the stretching frequency to 1654–1662 cm^{-1}. In all cases, the disappearance of the carbonyl stretching frequency is a straightforward diagnostic for the oxidative cleavage. The methylene stretching frequencies for all of the thioester SAMs are typical of monolayers with low crystallinity in their chain packing [18,19].

Compounds **1** represent a homologous series whose variable chain length systematically changes the film thickness and surface hydrophobicity. The thicknesses (±0.2 nm) and wetting behaviors (±3°) of the members of the series with 1–8 methylene units in the acyl chain are summarized in Figure 2 so as to highlight the steady increase in monolayer thickness (calculated based on fully extended alkyl chain and observed by ellipsometry) and hydrophobicity. The SAM based on **1a** (no methylene units) is relatively hydrophilic (contact angle 75°/67°) even when compared to the analogue containing only one methylene unit, **1b** (82°/79°). This reflects both the shorter alkyl chain and the closer proximity of its carbonyl groups to the SAM surface. The contact angles for SAMs based on compounds **2** (78°/72°), **3** (83°/75°) and **4** (80°/72°) are reasonable for such terminal aryl groups.

Table 1: FTIR data for SAMs based on compound **1–4**.

SAM	ATR–FTIR (cm^{-1})		
	CH_2 antisymmetric	CH_2 symmetric	C=O
1a	2922	2851	1695
1b	2922	2852	1696
1c	2923	2852	1693
1d	2922	2851	1691
1e	2922	2851	1691
1f	2923	2852	1691
1g	2922	2851	1690
1h	2922	2852	1691
1i	2921	2851	1690
2	2922	2851	1662
3	2922	2851	1660
4	2922	2851	1654

The UV–vis spectra of compounds **1a, 2, 3** and **4** are compared in Figure 3. The spectra of compounds **1b**–**i** are all comparable to that of **1a**. These spectral features provide the basis for their varying interactions with the different wavelengths of light used for SAM photo-oxidation.

In situ SAM oxidations

Monolayers of compounds **1**–**4** were all subjected to treatment with aqueous OXONE solutions under ambient conditions. In all cases, the starting monolayer is comprised of siloxane-anchored units with 11 methylene groups that terminate in a thioester (Si–$(CH_2)_{11}$–SCOR), and the result is always the same sulfonate-decorated SAM, tethered through a chain of

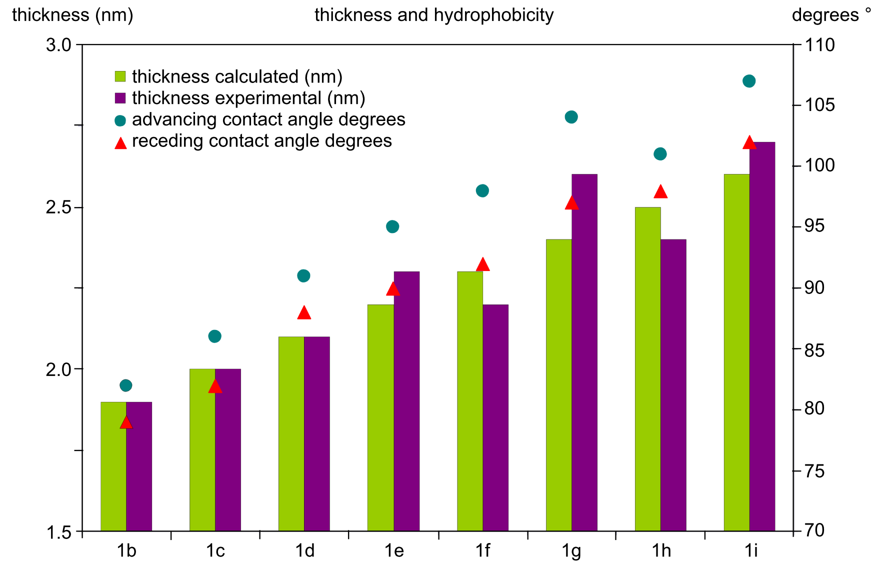

Figure 2: Thickness and contact angles (advancing/receding) for SAMs based on compounds **1b**–**i**.

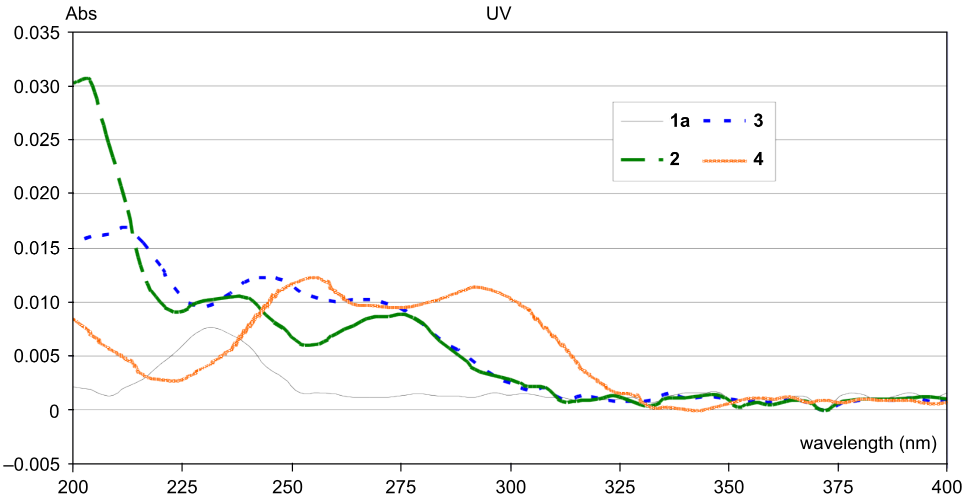

Figure 3: UV–vis spectra of SAMs of compounds **1a**, **2**, **3** and **4**.

11 methylenes (Si–$(CH_2)_{11}$–SO_3H). After reaction times of 2–10 h (Table 2), all of the surfaces became very hydrophilic, with water contact angles of <25°.

Table 2: Reaction times and methylene loss (based on ATR–FTIR integration) for OXONE oxidation of SAMs of compounds **1**–**4**; all surfaces became highly hydrophilic (water contact angles <25°).

SAM	reaction time (h)	percent of remaining methylene FTIR peak intensity	
		calculated	observed
1a	2.0	100%	92%
1b	2.0	92%	87%
1c	2.0	85%	86%
1d	2.5	79%	73%
1e	4.0	73%	78%
1f	5.0	69%	77%
1g	6.0	65%	62%
1h	7.0	61%	66%
1i	10.0	58%	51%
2	6.0	100%	98%
3	6.0	100%	94%
4	6.0	100%	108%

In SAMs based on compounds **1b**–**i** the intensity of the methylene peaks in the IR decreases after oxidation as a result of the removal of the acyl chain. We can compare the observed methylene peak intensity to that which is expected based on the number of methylenes that remain relative to the original total number of methylenes. The expected value of this ratio if only the 11-carbon polymethylene tether remained and all of the methylene units of the acyl chain were removed, as well as the observed integrated ratio of the antisymmetric methylene peaks before and after oxidation, are shown in Table 2. Since the oxidation of SAMs based on **1a**, **2**, **3** and **4** removes no methylene units, it is expected that there should be little or no change in the methylene peak intensity. The observed peak intensity matches the expected value (±10%).

The oxidation of the thioester-bearing SAMs was also followed by XPS. SAMs of compounds **1** and **2** showed peaks corresponding to the expected divalent sulfur of the thioester at 163.8 ± 0.2 eV and 164.8 ± 0.2 eV in the expected 2:1 ratio (±10%), see for example Figure 4A. The additional (thiophene) sulfur in both compounds **3** and **4** leads to a broad, merged signal (Figure 4B and Figure 4C). Deconvolution reveals the thiophene sulfurs at 164.5 ± 0.2 eV and 165.6 ± 0.2 eV. The overlap among the four peaks in the spectra, together with their inherently problematic signal-to-noise ratio, leads to a situation in which the expected 2:1 peak intensity ratio for each sulfur and the expected 1:1 ratio for the two kinds of sulfurs in a single thiophene-bearing SAM show error bars of as much as 30%. Nevertheless, the XPS result confirms the presence of the thioester and thiophene sulfurs and attests to their complete disappearance (in all cases) upon oxidation to a sulfonic acid SAM (in which the one sulfur is at 168.2 ± 0.2 eV and 169.9 ± 0.2 eV).

Finally, the photo-oxidations of the various types of thioesters were compared by using UV radiation of different wavelengths. A lamp whose output was around 254 nm was used for irradiation at shorter wavelengths. This was compared to irradiations done with a broad-spectrum, longer-wavelength UV lamp (UV-A, 320–400 nm). Since the UV–vis absorption spectra of all compounds **1** were the same, only **1a** was used in the comparisons to the photo-oxidation behavior of compounds **2**–**4** at longer wavelength.

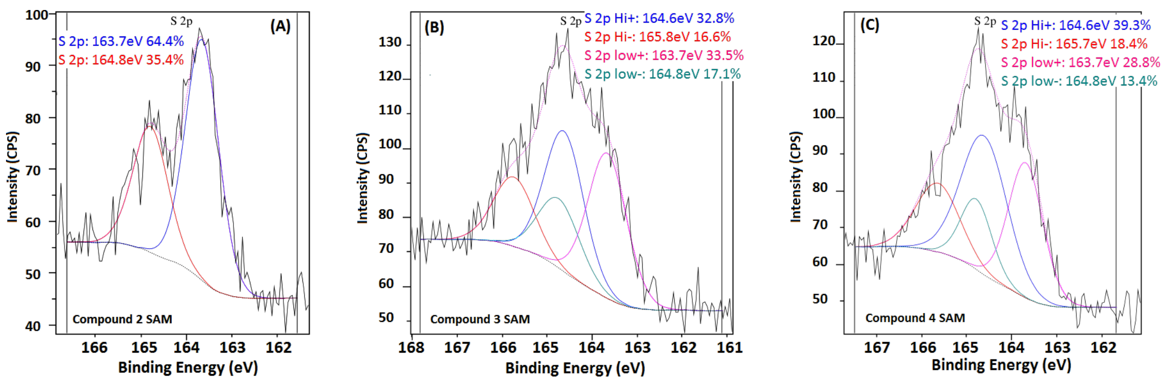

Figure 4: Representative sulfur XPS analyses of the SAMs of compounds **2** (**A**), **3** (**B**) and **4** (**C**).

The SAMs with varying alkyl chain lengths (based on compounds **1b**–**i**) were subjected to photo-oxidation at 254 nm. Table 3 shows the changes in their water contact angle upon photochemical reaction in air. The removal of the acyl methylenes (as per the above discussion of the OXONE oxidation results in Table 2) is also shown. The completeness of the photocleavage is attested to by the fact that after an oxidation time of 2 h (1 h on each side) the carbonyl and methyl peaks in the IR disappeared and the intensities of the methylene signals were reduced by the amount expected for each chain length. However, the surfaces achieved were not as hydrophilic as expected. The unexpectedly high contact angles after oxidation, and their possible relationship to solvent induced surface reorganization and/or residual long-chain contaminants, will be addressed in the Discussion section.

The irradiation with 254 nm light was also applied to monolayers based on compounds **1a, 2, 3** and **4**. Following the experience with SAMs based on compounds **1b**–**i**, and the fact that both benzoic acid and its thiophene analogues are more water soluble than the long-chain aliphatic acids, the rinsing procedure was changed so as to only use water. In this way, the complete photocleavage suggested by the disappearance of the carbonyl in the IR was accompanied by the formation of a fully wetted surface (contact angles <25°) for all of the SAMs based on compounds **1a, 2, 3** and **4**.

Table 3: Contact angles and methylene loss (based on ATR–FTIR integration ratio, calculated and observed) before and after irradiation of SAMs based on compounds **1b**–**i**.

SAM	contact-angle measurement adv[°]/rec[°]		percent of remaining methylene FTIR peak intensity	
	before irradiation	after irradiation	calculated	observed
1b	82/79	35/<20	92%	82%
1c	86/82	60/40	85%	81%
1d	91/88	48/<20	79%	72%
1e	95/90	44/37	73%	72%
1f	98/92	70/49	69%	75%
1g	104/97	62/39	65%	69%
1h	101/98	65/43	61%	67%
1i	107/102	76/65	58%	67%

Photo-oxidations of SAMs based on compounds **1a, 2, 3** and **4** were also carried out by using a UV-A (320–400 nm) light source and exposure times of up to 132 h. These experiments are summarized in Figure 5. It is clear that the acetyl group in **1a** is not cleaved by the longer wavelength light, even after 132 h. SAMs based on compounds **2** and **3** show some photocleavage under these conditions, but the process is slow and never goes to completion. Their response to the longer wavelength light is anticipated by the fact that the UV-A light only has significant intensity at wavelengths longer than 320 nm, at which **2** and **3** do not absorb. On the other hand, SAMs based on compound **4** show an intense absorption peak at 290 nm and an absorption tail that extends to slightly beyond 325 nm. They undergo effective photocleavage even at longer wavelength.

Discussion

In previous work with a longer chain analogue of **1a** (in which the thioacetyl group is connected to a 16-carbon chain instead of the 11 carbons in **1a**) [15,20], we reported the photoconversion of a thioacetate-decorated SAM to a sulfonated surface by UV irradiation in air. In that case, the initially deposited thioacetate-functionalized SAM had more closely packed alkyl chains (FTIR: methylene stretching frequencies 2919 and 2850 cm^{-1} versus the 2922–2923 cm^{-1} and 2851–2852 cm^{-1} of **1a**–**h**). Only **1i** displays some level of crystalline order (with methylene values of 2921/2851 cm^{-1}), and even that is not as ordered as the C_{16} system [15,20].

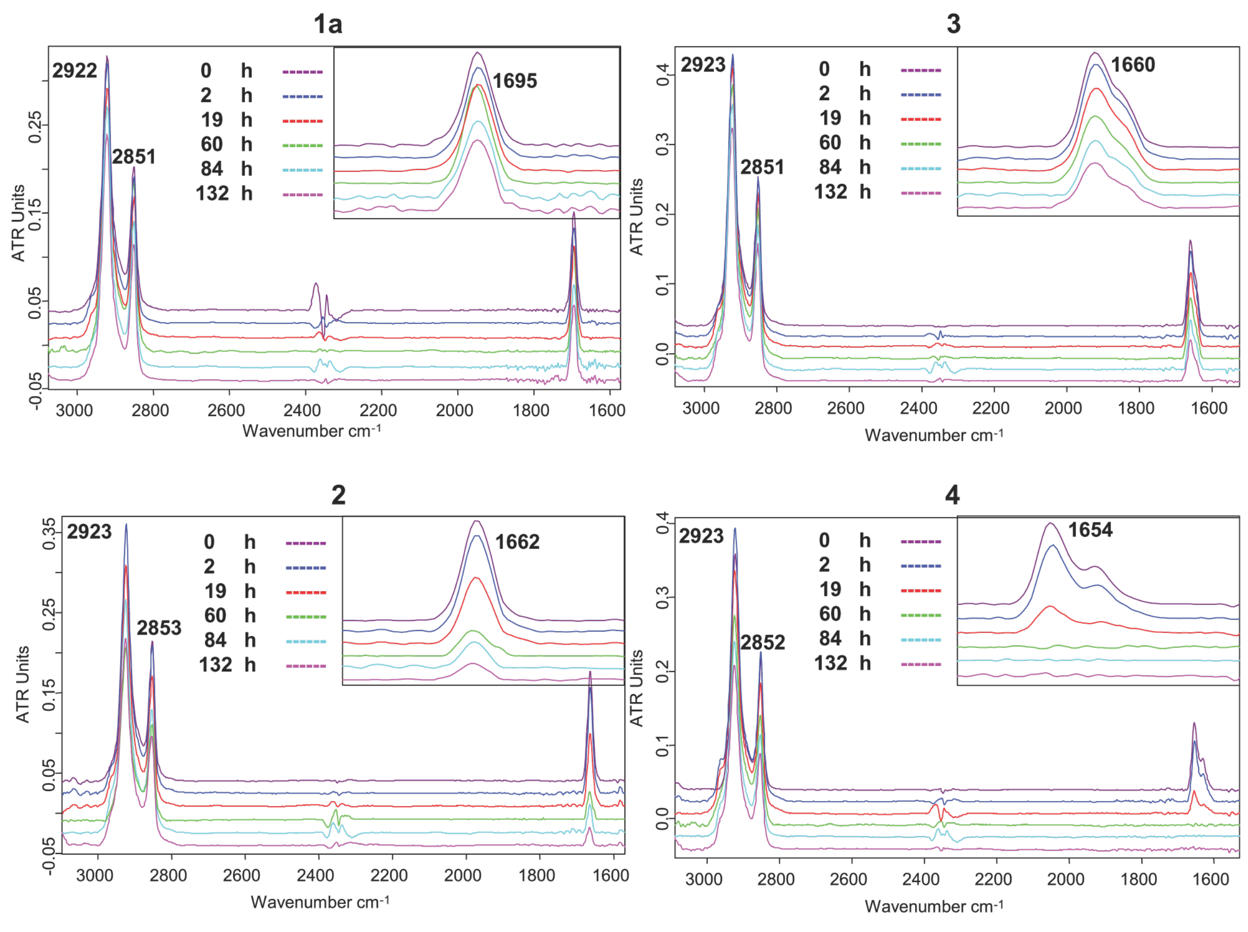

Figure 5: ATR–FTIR spectra of SAMs of compounds **1a**, **2**, **3** and **4**, as deposited, and after oxidation with UV-A in air for 2 h, 19 h, 60 h, 84 h and 132 h.

The important conclusion from the oxidation of the acetylated thiols with the two different chain lengths is that both systems provide a sulfonated surface that is fully wetted. The acetyl-derived byproduct is easily removed by rinsing with water, and the resulting surface is hydrophilic. We note that while the oxidation of the longer chain thioesters (**1b**–**i**) with OXONE takes longer (as indicated by reaction times in Table 2), as would be expected for the more hydrophobic starting SAMs, the longer chain byproducts are successfully washed away and the resulting surface is also fully wetted. The slowing of the reaction with OXONE with increasing numbers of methylene units is reminiscent of what was seen by Sagiv et al. [21-23] for permanganate oxidation in which an olefin at the monolayer surface was oxidized much faster than an olefin within the monolayer. The fact that the monolayers reported herein are somewhat less well-packed than those reported in the permanganate oxidation study may be responsible for the fact that the differences in reactivity observed herein are smaller than those reported for the permanganate oxidation.

A problem with the longer chain acyl units is seen in their photo-oxidation. In that case, there is no evidence for a slowing of the reaction based on the rate of disappearance of the carbonyl, but the high degree of hydrophilicity that is achieved with aqueous OXONE is not obtained in these longer chain systems. It seems that there is a buildup of longer chain byproducts that need organic solvents to effectively remove them. However, the exposure of the high-free-energy sulfonated surface to organic solvent leads to surface reorganization and loss of hydrophilicity. Thus, in order to take advantage of the enormous change in surface wetting achieved by the oxidation of a system such as **1g**–**i** (from a water contact angle of over 100° to a fully wetted surface), oxidation in aqueous OXONE is most effective.

Beyond the impact of changing the chain length on the chemistry described above, we have also established a clear wavelength dependence on the photo-oxidation of the thioesters. The reactions of the benzene and thiophene derivatives are notable for a number of reasons. Firstly, the aromatic ring does not interfere with the chemistry described above. The reactivity of the thioester is not undermined (despite a small retardation of the OXONE reaction), either by the bulk of the aromatic rings or by the reduced electrophilicity, which is typical of conjugated carbonyl groups.

We also note the wavelength dependence of the photochemistry reported herein. The longer wavelength absorption of the conjugated chromophore is clearly a first step towards a system that could be photoreacted with longer wavelength light. This would provide a route to photopatterned sulfonate surfaces, in which the irradiation could be performed through regular glass or Pyrex, i.e., media that are not transparent to shorter wavelength UV radiation.

Conclusion

Monolayers based on various thioacetate derivatives have been shown to provide useful control over surface wetting. The initially deposited monolayers are stable surfaces whose hydrophobicity can be systematically varied based on the length of the alkyl chain of the acyl moiety. Variously conjugated versions of the acyl moiety provide useful wavelength control over the photochemistry of the thioesters. The full exploitation of these systems in ways that take full advantage of the tunable wetting and that can extend the patterned titania deposition previously reported [16] will be the subject of future investigations.

Supporting Information

Supporting Information File 1

Isolated yields, ^{1}H and ^{13}C NMR, and exact mass MS data for the olefin-thioester precursors of compounds **1**–**4**.
[http://www.beilstein-journals.org/bjnano/content/supplementary/2190-4286-3-24-S1.pdf]

Acknowledgements

This work was supported by the Israel Science Foundation, the Bar Ilan Minerva Center for Biomaterial Interfaces, and the Edward and Judy Steinberg Chair in Nanotechnology.

References

1. Maoz, R.; Sagiv, J. *J. Colloid Interface Sci.* **1984,** *100,* 465–496. doi:10.1016/0021-9797(84)90452-1
2. Gun, J.; Iscovici, R.; Sagiv, J. *J. Colloid Interface Sci.* **1984,** *101,* 201–213. doi:10.1016/0021-9797(84)90020-1
3. Netzer, L.; Sagiv, J. *J. Am. Chem. Soc.* **1983,** *105,* 674–676. doi:10.1021/ja00341a087
4. Ulman, A. *Chem. Rev.* **1996,** *96,* 1533–1554. doi:10.1021/cr9502357
5. Wasserman, S. R.; Tao, Y. T.; Whitesides, G. M. *Langmuir* **1989,** *5,* 1074–1087. doi:10.1021/la00088a035
6. Balachander, N.; Sukenik, C. N. *Langmuir* **1990,** *6,* 1621–1627. doi:10.1021/la00101a001
7. Shyue, J.-J.; De Guire, M. R.; Nakanishi, T.; Masuda, Y.; Koumoto, K.; Sukenik, C. N. *Langmuir* **2004,** *20,* 8693–8698. doi:10.1021/la049247q
8. Katash, I.; Luo, X.; Sukenik, C. N. *Langmuir* **2008,** *24,* 10910–10919. doi:10.1021/la800746k
9. Katash, I.; Luo, X.; Sukenik, C. N. *Langmuir* **2010,** *26,* 1765–1775. doi:10.1021/la902093x
10. Collins, R. J.; Bae, I. T.; Scherson, D. A.; Sukenik, C. N. *Langmuir* **1996,** *12,* 5509–5511. doi:10.1021/la9601566
11. Gershevitz, O.; Sukenik, C. N. *J. Am. Chem. Soc.* **2004,** *126,* 482–483. doi:10.1021/ja037610u
12. Gershevitz, O.; Osnis, A.; Sukenik, C. N. *Isr. J. Chem.* **2005,** *45,* 321–336. doi:10.1560/98PR-AJY7-7JLE-63YQ
13. Lourenço, J. M. C.; Ribeiro, P. A.; Botelho do Rego, A. M.; Fernandes, F. M. B.; Moutinho, A. M. C.; Raposo, M. *Langmuir* **2004,** *20,* 8103–8109. doi:10.1021/la049872v
14. Sfez, R.; De-Zhong, L.; Turyan, I.; Mandler, D.; Yitzchaik, S. *Langmuir* **2001,** *17,* 2556–2559. doi:10.1021/la001343d
15. Collins, R. J.; Sukenik, C. N. *Langmuir* **1995,** *11,* 2322–2324. doi:10.1021/la00006a078
16. Collins, R. J.; Shin, H.; DeGuire, M. R.; Heuer, A. H.; Sukenik, C. N. *Appl. Phys. Lett.* **1996,** *69,* 860–862. doi:10.1063/1.117916
17. Meth, S.; Sukenik, C. N. *Thin Solid Films* **2003,** *425,* 49–58. doi:10.1016/S0040-6090(02)01296-8
18. Allara, D. L.; Nuzzo, R. G. *Langmuir* **1985,** *1,* 52–66. doi:10.1021/la00061a008
19. Porter, M. D.; Bright, T. B.; Allara, D. L.; Chidsey, C. E. D. *J. Am. Chem. Soc.* **1987,** *109,* 3559–3568. doi:10.1021/ja00246a011
20. Mazuz, K. M. Sc Dissertation, Bar-Ilan University, 2008.
21. Maoz, R.; Sagiv, J. *Langmuir* **1987,** *3,* 1034–1044. doi:10.1021/la00078a027
22. Maoz, R.; Sagiv, J. *Langmuir* **1987,** *3,* 1045–1051. doi:10.1021/la00078a028
23. Maoz, R.; Sagiv, J. *Thin Solid Films* **1985,** *132,* 135–151. doi:10.1016/0040-6090(85)90465-1

License and Terms

Beilstein Journal
of Nanotechnology

Colloidal lithography for fabricating patterned polymer-brush microstructures

Tao Chen*[1], Debby P. Chang[2,3], Rainer Jordan[1] and Stefan Zauscher*[2]

Full Research Paper

Address:
[1]Department of Chemie, Technische Universität Dresden, 01069 Dresden, Germany, [2]Center for Biologically Inspired Materials and Materials Systems, and Department of Mechanical Engineering and Materials Science, Duke University, Durham, NC, 27708, USA and [3]Department of Physical Chemistry, Lund University, SE-221 00 Lund, Sweden

Email:
Tao Chen* - tao.chen.small@gmail.com; Stefan Zauscher* - zauscher@duke.edu

* Corresponding author

Keywords:
atom-transfer radical polymerization; colloidal lithography; patterning; self-assembled microsphere monolayer

Beilstein J. Nanotechnol. **2012,** *3,* 397–403.
doi:10.3762/bjnano.3.46

Received: 09 February 2012
Accepted: 23 April 2012
Published: 15 May 2012

This article is part of the Thematic Series "Self-assembly at solid surfaces".

Guest Editors: S. R. Cohen and J. Sagiv

Abstract

We exploit a series of robust, but simple and convenient colloidal lithography (CL) approaches, using a microsphere array as a mask or as a guiding template, and combine this with surface-initiated atom-transfer radical polymerization (SI-ATRP) to fabricate patterned polymer-brush microstructures. The advantages of the CL technique over other lithographic approaches for the fabrication of patterned polymer brushes are (i) that it can be carried out with commercially available colloidal particles at a relatively low cost, (ii) that no complex equipment is required to create the patterned templates with micro- and nanoscale features, and (iii) that polymer brush features are controlled simply by changing the size or chemical functionality of the microspheres or the substrate.

Introduction

It is well known that monodisperse colloidal microspheres easily self-assemble into hexagonally close-packed arrays on surfaces as a result of capillary forces arising from the evaporation of solvents [1-4]. Such periodic arrays of microspheres were used already in the early 1980s by Fischer and co-workers as shadow masks in colloid lithography (CL) for the deposition of platinum nanomaterials [5]. Since then, CL has become a simple, versatile, and cost-effective fabrication technique for a large number of researchers in the field of micro/nanofabrication [2-4,6]. A variety of lithographic methods have since been developed, in which colloid microsphere arrays are used as masks for depositing nanomaterials and as scaffolds for templating 2-D or 3-D functional patterns [2-5,7-9]. When a 2-D colloidal crystal array is used as a shadow mask in metallic vapor deposition, the metal deposited by sputtering can reach the substrate only through the interstices between the spheres, and the shape of the deposits on the substrate is thus determined by the projected area of the interstices on the substrate [2,4]. Micro- and nanospheres can also be used to guide the transport of molecules so that the molecular deposition forms a ring-shaped pattern around the contact point (footprint) of the microsphere with the substrate [9]. For a self-assembled microsphere monolayer (SMM) on a substrate, the footprint between the microsphere and substrate produces a barrier array, which can be used as a template for lithography [6,10,11]. CL thus provides a straightforward way to adjust the feature size at the microscale and, by using sufficiently small spheres, the nanoscale, by changing the sphere diameter of the colloid mask. Spherical particles are commercially available with a wide range of sizes and types, or can be synthesized, e.g., by emulsion polymerization for polymer latex spheres or by controlled precipitation for inorganic oxides [12]. Patterned polymer brushes [13] are of increasing importance especially for array-based platforms because of their ability to modify surface properties and their potential applications in surface-based technologies, such as protein-resistant coatings, switchable sensors, substrates for cell-growth control, and for the separation of biological molecules [14-16]. They can be grown by surface-initiated polymerization from surface-confined initiator templates, as fabricated by various lithographic approaches. Although a range of strategies for polymer brush patterning, including photolithography [17], electron-beam lithography [18], electron-beam chemical lithography [19], microcontact printing (μCP) [20], scanning-probe lithography [21] and capillary-force lithography [22], have been exploited over the years, there is still considerable interest in the exploitation of new, simple patterning strategies that do not entail instrumental complexity. As an inexpensive alternative to conventional lithography, CL provides new possibilities to create patterned polymer brushes. So far only one of the CL strategies, using the SMM footprint as the mask, has been demonstrated for fabricating patterned pillar [23] or cavity [11,24] polymer brushes, and we recently reported how SMM could be used as μCP stamps to fabricate cone-shaped polymer brushes [25].

In this letter we report how we exploit a range of robust and simple patterning strategies offered by colloidal lithography, and combine them with surface-initiated atom-transfer radical polymerization (SI-ATRP) for patterning polymer-brush microstructures. The use of CL for patterning polymer brushes has significant advantages over the lithographic approaches mentioned above, in that it employs commercially available, relatively low cost nano- and microspheres, that it does not require complex equipment to create micro- and nanopatterned templates, and in that it allows control over polymer-brush geometry by simple changing of the diameter or chemical functionality of the nano- or microspheres. A recent paper [6] showed that colloidal particles on the order of 100 nm can be used to pattern silane features with nanometer dimensions. Due to the similarity of this and our patterning approach, we do not foresee a problem in scaling down our approach shown here, to fabricate polymeric nanostructures with lateral feature dimensions on the order of 100 nm.

Results and Discussion

Hexagonally packed arrays of self-assembled colloidal micro- and nanospheres on surfaces have been used as masks to guide deposition or etching through the interstices between the colloidal microspheres [5,6,9]. For example, arrays of triangularly shaped metal islands can be obtained by sputter deposition of the metal [2,4]. When gold is chosen as the metal, the ensuing pattern can be easily functionalized chemically with a self-assembled monolayer (SAM) of a thiol initiator, which can be subsequently amplified into polymer brushes. Figure 1 shows this strategy for the patterning of colloidal microspheres for the fabrication of polymer-brush microstructures. We first assembled a SMM of polystyrene latex (diameter ≈ 10 μm) on a silica substrate by gravity-induced sedimentation combined with solvent evaporation [26], and subsequently we deposited gold into the interstices between the microspheres (Figure 1A). After the microsphere mask was removed by sonication, an array of hexagonally arranged triangular gold islands remained (Figure 1B) on which we formed a SAM of thiol initiator ($BrC(CH_3)_2COO(CH_2)_{11}SH$) [27]. We then synthesized poly(*N*-isopropylacrylamide) (PNIPAAM) brush microstructures on the islands by SI-ATRP of NIPAAM (Figure 1C). An AFM image of the patterned gold islands reveals a feature height of about 65 nm (Figure 1D). The feature size of a triangular island (≈2.3 μm) is about one quarter of the sphere diameter, and the distance between nearest-neighbor islands (≈5.3 μm) is around half of the sphere diameter, in accordance with a previous report by Haynes et al. [7]. The resulting PNIPAAM brush height was about 350 nm, and due to polymerization also occurring at the sides of the triangles, the footprint size increased to about 2.9 μm (Figure 1E) while the distance between nearest-neighbor islands remained about 5.3 μm. The feature size of the polymer brushes can be altered by changing (i) the size of the microspheres, (ii) the assembly of the spheres on the substrate surface, or by (iii) varying the conditions of the gold vapor deposition, to yield a range of microstructures [28].

Colloidal microspheres have an inherently curved surface that can serve as a template for spreading alkanethiol molecules along the surface of the microspheres onto the gold substrate surface, creating a ring-shaped SAM feature around the footprint of the sphere–surface contact area. This so-called edge-spreading lithography (ESL) employing colloid microspheres as

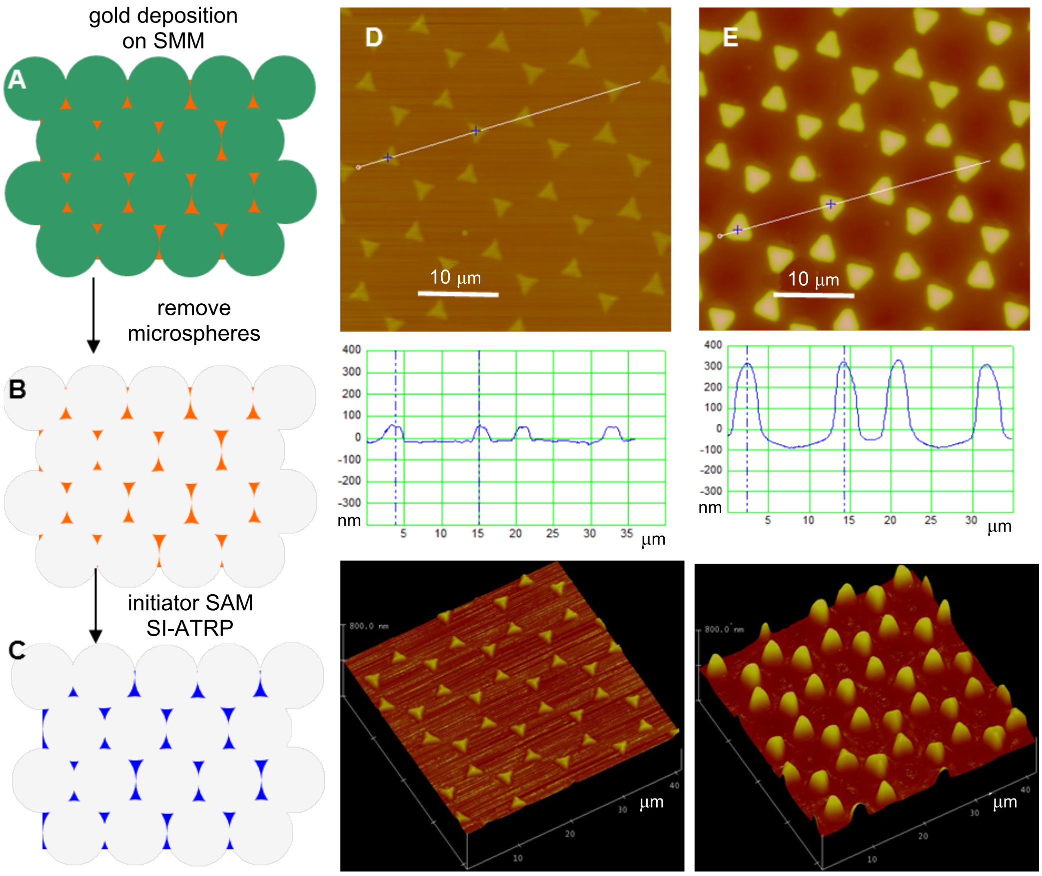

Figure 1: Schematic illustration and AFM images showing the use of CL in the fabrication of patterned polymer-brush microstructures. (A) SMM on a silica wafer serves as a template for gold deposition. (B) Removal of the microspheres by sonication. (C) Functionalization of the Au pattern with a thiol initiator SAM and subsequent amplification into polymer brushes. (D, E) Contact-mode AFM height images (40 µm × 40 µm, imaged at room temperature in air) of the patterned gold islands before and after PNIPAAM brush growth, and the corresponding height profiles and 3-D images.

templates has been previously used to fabricate ring-shaped metal patterns [9]. Here we replaced the octadecanethiol (ODT) molecules with thiol initiator ($BrC(CH_3)_2COO(CH_2)_{11}SH$), and amplified the annular thiol initiator monolayer into ring-shaped polymer brushes (Figure 2). In this patterning approach we used a SMM (sphere diameter ≈ 5 µm) to direct the transport of an alkanethiol initiator from an initiator-inked planar poly(dimethyl siloxane) (PDMS) stamp onto the gold surface (Figure 2A). Upon reaching the metal substrate, the thiol initiator molecules self-assemble into a patterned monolayer, which is confined by the footprint of each microsphere and the extent of lateral spreading of the thiols on the gold substrate (Figure 2B). Amplification of the ring-shaped initiator SAMs results in patterned, hollow cylindrical polymer brushes (Figure 2C–E). The inner diameter of the polymer-brush cylinders is about 900 nm. This diameter reflects the underlying ring-shaped initiator pattern and is on the order of 18% of the microsphere diameter, in close agreement with a previous report [9]. The outer diameter of the hollow polymer-brush cylinders is about 1.5 µm, and is largely determined by the contact time of the PDMS stamp on the microsphere template, which implies that the diffusion of the thiol initiator along the surface of each microsphere depends on the contact time with the PDMS stamp [9]. Furthermore, polymer brush microstructures may be varied by changing the concentration of the thiol initiator, or by adding inert thiol molecules [29], which affects the thiol initiator distribution and diffusion on the gold surface.

Our results show that microspheres can be used to guide the spreading of a thiol initiator to form ring-shaped thiol patterns around the footprint of microspheres on the surface. While initiator-inked stamps only provide a limited thiol reservoir, the microsphere footprint could also be used as a mask for fabricating polymer-brush pillars, by inking the microsphere array with a large amount of thiol. Such an approach was first reported by Taylor and co-workers [10], who described a simple CL technique to fabricate substrates with hexagonally patterned dots of protein surrounded by a protein-repellant layer of

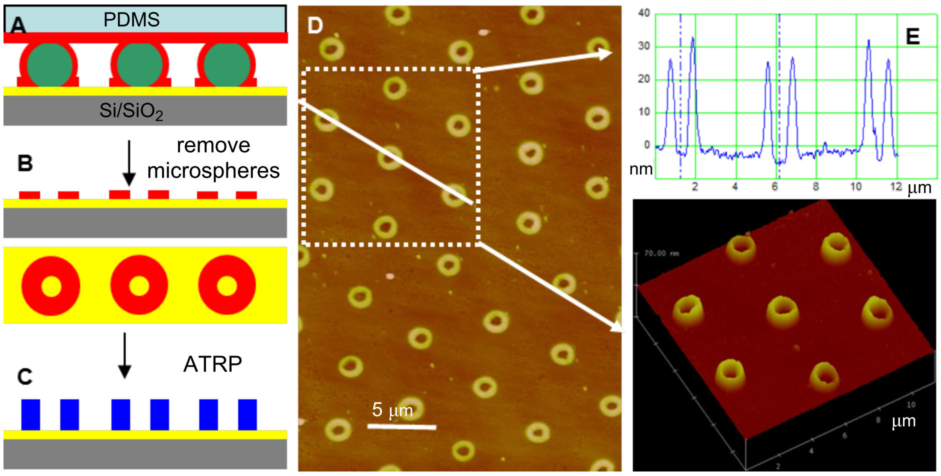

Figure 2: Schematic illustration and AFM images showing the use of ESL for the fabrication of ring-shaped polymer-brush microstructures. (A) Arrayed SMM direct the transport of alkanethiol initiator from a planar PDMS stamp onto the gold surface (printing was carried out by gently pressing the PDMS stamp onto the SMM template for 30 s). (B) Ring-shaped SAM formed after removal of the microspheres. (C) Subsequent amplification into hollow polymer-brush cylinders. (D,E) Contact-mode AFM height images of the patterned PNIPAAM brush microstructures imaged at room temperature in air, and the corresponding height profiles and 3-D image.

poly(ethylene glycol) (PEG). In that work, a self-assembled monolayer of latex spheres served as a lithographic mask to selectively graft a thin layer of PEG around the footprint of the microspheres. After removal of the spheres, a periodic pattern of holes in the protein-repellant PEG layer was exposed, and proteins could be selectively adsorbed onto the underlying surface in these holes. In a similar approach we used inert thiol to cover a SMM of polystyrene microspheres (diameter ≈ 10 µm) (Figure 3A) to form an inert thiol SAM everywhere except in the footprint of each microsphere (Figure 3B), and then backfill with a thiol initiator (Figure 3C). Amplification of this pattern, after removal of the SMM, resulted in a periodic pattern of polymer-brush pillars (about 50 nm high and about 1.5 µm in diameter, Figure 3D–F). The diameters of the

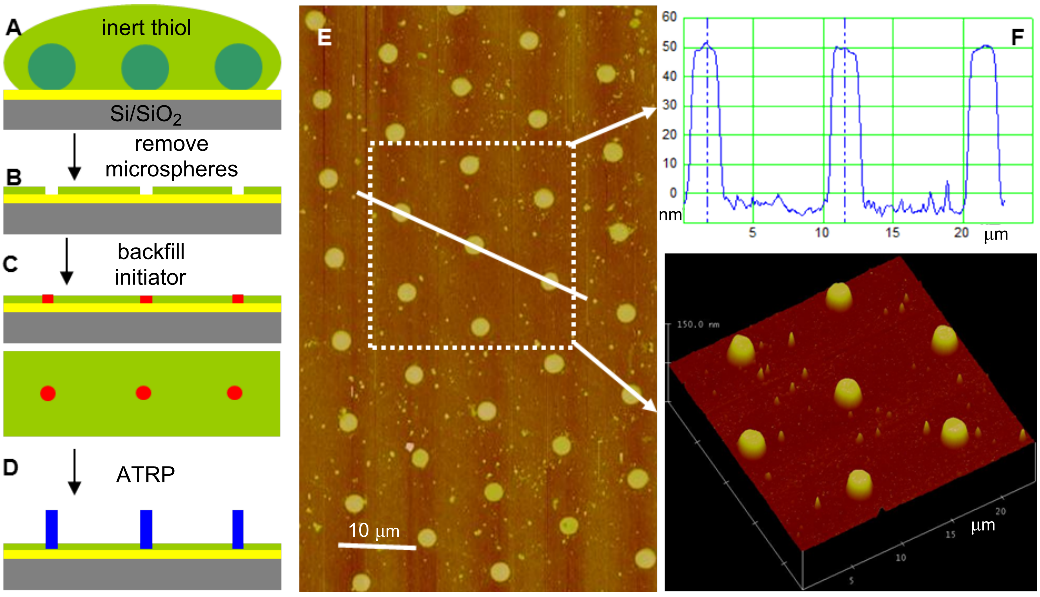

Figure 3: Schematic illustration and AFM images showing use of colloidal microsphere lithography for patterning polymer-brush pillars. (A) A SMM, assembled on a gold substrate, serves as a mask for the inert thiol SAM pattern. (B) After ink transfer and drying in nitrogen, the polystyrene microsphere mask was removed, leaving an inert thiol SAM pattern. (C) The substrate was then backfilled with thiol initiator. (D) Subsequent pattern amplification into polymer-brush microstructure by SI-ATRP of NIPAAM. (E, F) Contact-mode AFM height images of patterned PNIPAAM-brush microstructure imaged at room temperature in air and the corresponding height profiles and 3-D image.

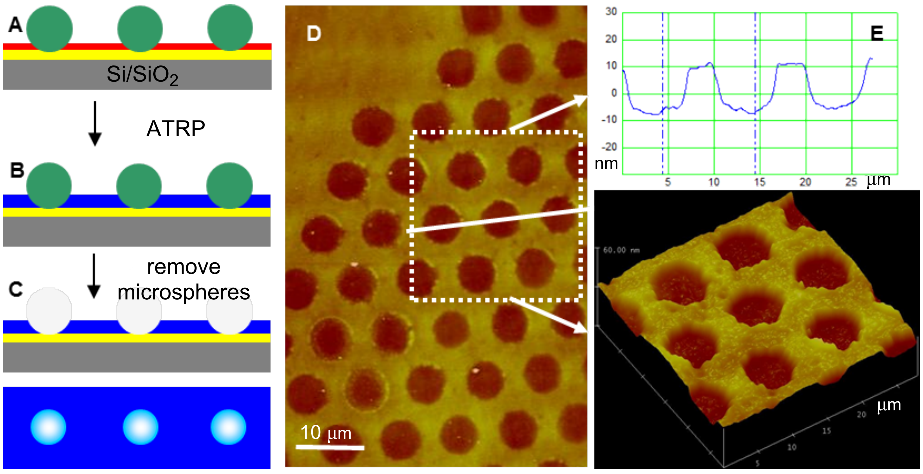

Figure 4: Schematic illustration and AFM images showing the use of colloidal microsphere lithography for patterning hole-like polymer-brush microstructures. (A) SMM on thiol initiator SAM-coated gold substrate. (B) Subsequent pattern amplification into polymer-brush microstructure by SI-ATRP of NIPAAM. (C) Removal of the polystyrene microsphere mask leaves a hole-patterned brush thin film. (D, E) Contact-mode AFM height images of hole-patterned PNIPAAM-brush thin film imaged at RT in air and the corresponding height profiles and 3-D image.

polymer cylinders were on the order of 15% of the microsphere diameter, in agreement with our result described above (ca. 18%).

Another type of polymer-brush microstructure can be designed by inking the microsphere arrays by thiol initiator first, to form an initiator SAM around the microspheres. This should result in a polymer-brush layer with a patterned hole-like microstructure after removal of the microspheres and subsequent amplification [11]. Xu et al. developed a method to pattern a surface with polymer brushes during a polymerization process in a microchannel, formed between PDMS stamps and initiator-modified substrates [30]. This so-called microchannel-confined surface-initiated polymerization technique showed that there is no polymer brush growth in the contact area of the PDMS stamp with an initiator-functionalized SAM-coated silicon wafer. This inspired us to form a SMM on thiol-initiator-coated gold substrates as a template for fabricating hole-patterned polymer brushes. We first assembled a mask of polystyrene latex particles (SMM) on a gold substrate previously covered with a SAM of thiol initiator (Figure 4A), and then amplified the exposed initiator by SI-ATRP of NIPAAM (Figure 4B). After removing the SMM, a polymer-brush thin film with a hole pattern was obtained (Figure 4C,D). The patterned polymer brush layer has a height of about 16 nm and a hole diameter of about 6 µm.

Conclusion

In summary, we have demonstrated how colloidal lithography can provide a simple approach with various strategies to fabricate a range of patterned polymer-brush microstructures. Our approaches rely on the spontaneous formation of well-ordered, colloidal microsphere arrays that provide lithographic masks, templates, and footprint-restricted geometries for creating patterns of initiator SAMs that can be used for subsequent amplification into polymer-brush patterns. Compared with other lithographic techniques to fabricate patterned polymer brushes, CL has the advantage of (i) not requiring any special instrumentation and (ii) changing feature size simply by changing the microsphere diameters used in the colloid masks, or changing the colloid deposition parameters. Patterned polymer brushes are of increasing importance for array-based platforms and applications in surface-based technologies, such as protein-resistant coatings, switchable sensors, substrates for cell-growth control, and for separation of biological molecules. We note that for convenience and proof-of-concept of our approach, we used PS microspheres to fabricate patterned polymer brushes with lateral feature dimensions on the micrometer and submicrometer length scales. A recent paper [6] shows, that colloidal particles on the order of 100 nm can be used to pattern silane features with nanometer dimensions. Due to the similarity of this and our approach, we do not foresee a problem in scaling our approach down to fabricate polymer nanostructures with lateral feature dimensions on the order of 100 nm.

Experimental

Materials: *N*-isopropylacrylamide (NIPAAM) (99%), copper(I) bromide (CuBr, 99.9%), methanol (MeOH, 99.9%) and ethanol were obtained from Sigma-Aldrich (Milwaukee, WI). Milli-Q (Millipore, Billerica, MA) water (18 MΩ·cm) and methanol were used as polymerization solvents. *N*,*N*′,*N*′,*N*″,*N*″-Pentamethyldiethylenetriamine (PMDETA) was used as received from Acros Organics (Hampton, NH). The thiol initiator ($BrC(CH_3)_2COO(CH_2)_{11}SH$) was synthesized as reported [27]. Polystyrene microspheres (5 µm and 10 µm) were donated by Dr. R. M. Erb at Duke University, who purchased them from Duke Scientific Corporation (Palo Alto, CA). To immobilize the initiators for surface-initiated polymerization, gold substrates with an average grain diameter of 60 nm were prepared by thermal evaporation under a vacuum of 4×10^{-7} Torr. For this purpose an adhesion layer of chromium (50 Å) followed by a layer of gold (600 Å) was evaporated onto silicon wafers. Before deposition, silicon wafers were cleaned in a mixture of H_2O_2/H_2SO_4 (1:3, v/v) at 80 °C ("piranha solution") for 10 min and washed thoroughly with Milli-Q-grade water. (Caution: Piranha solution reacts violently with organic matter!)

SMM on silica substrate: After the polystyrene microspheres were transferred from aqueous suspension (0.5 mL) into ethanol (1.0 mL) with subsequent shaking, they were first centrifuged and then the mixed solvent was removed. The residual was then redispersed in ethanol (0.5 mL) for subsequent pipetting onto a slightly tilted silica wafer. Upon drying at room temperature the microspheres self-assembled to form regions of hexagonally close-packed monolayers by gravity-induced sedimentation combined with solvent evaporation [1,26].

Deposition of gold on SMM-coated silica substrate: The procedure of gold coating on SMM covered silica wafers was similar to that used for the gold coating of the silicon wafers. A subsequent sonication was used to remove the polystyrene microspheres and leave an array of triangular gold dots.

ESL from a flat PDMS stamp using SMM as a mask: Inking was done by covering a stamp with a solution of 2 mM thiol-initiator/ethanol solution for 1 min, and drying the stamp in a stream of nitrogen. Printing was carried out gently by hand onto SMM-constructed gold-coated silica wafer for 30 s. Microspheres were then removed prior to polymerization by sonication in a deionized water bath for about 2 min.

Thiol-initiator monolayer preparation: Gold-coated silica wafer was put into an ethanol solution of thiol initiator (ca. 2 mM) overnight and then removed and dried with nitrogen.

SMM on initiator-monolayer-coated gold substrate: After the polystyrene microspheres were transferred from aqueous suspension (0.5 mL) into ethanol (1.0 mL) with a subsequent shake, they were first centrifuged and then the mixed solvent was removed. The residual was then redispersed in ethanol (0.5 mL) for subsequent pipetting onto a slightly tilted initiator-coated gold substrate wafer. Upon drying at room temperature the microspheres self-assembled to form regions of hexagonally close-packed monolayers by gravity-induced sedimentation combined with solvent evaporation.

SI-ATRP: The polymer brushes were prepared according to our previous procedures with some slight modifications [31]. Briefly, the polymerization solution was prepared by adding a solution of NIPAAM monomer to an organometallic catalyst. The organometallic catalyst was formed in a nitrogen atmosphere by adding CuBr (1.8 mg, 0.013 mmol) and PMDETA (14 µL, 0.064 mmol) in a 1:5 molar ratio to 1.0 mL of MeOH as solvent. The mixture was then sonicated for 1–2 min to facilitate the formation of the CuBr/PMDETA complex. Next, 1.5 g (17 mmol) of NIPAAM monomer dissolved in 5 mL of water was filtered into the catalyst-complex solution through a 0.45 µm Millipore Millex filter. The polymerization solution was then transferred into flasks containing the sample substrates with the immobilized patterned initiator. The flasks were sealed with rubber septa and kept at room temperature under nitrogen. After the desired reaction time, substrates were removed from the polymerization solution, exhaustively rinsed with deionized water to remove all traces of the polymerization solution, and dried in a stream of nitrogen.

Characterization: The patterned polymer-brush microstructure samples were rinsed with Milli-Q-grade water, dried under a stream of nitrogen, and mounted on steel sample disks prior to AFM measurements. AFM topographic images were collected in contact mode by using V-shaped silicon nitride cantilevers (Nanoprobe, Veeco, spring constant 0.12 N/m; tip radius 20–60 nm) using a MultiMode atomic force microscope (Digital Instruments, Santa Barbara, CA). The AFM topographic images performed in air, were obtained under low applied normal forces (<1 nN) to minimize compression and lateral damage of the polymer brushes. The relatively large lateral size of the polymer-brush features did not necessitate image deconvolution to account for tip-induced broadening of the feature dimensions [32].

Acknowledgements

T. C. thanks Alexander von Humboldt Foundation for support through an Alexander von Humboldt research fellowship to T. C. S. Z. thanks the National Science Foundation for support through grants NSF DMR-0502953 and NSF NIRT CBET-0609265.

References

1. Denkov, N. D.; Velev, O. D.; Kralchevsky, P. A.; Ivanov, I. B.; Yoshimura, H.; Nagayama, K. *Nature* **1993,** *361,* 26. doi:10.1038/361026a0

2. Zhang, G.; Wang, D. *Chem.–Asian J.* **2009,** *4,* 236–245. doi:10.1002/asia.200800298
3. Xia, Y. N.; Gates, B.; Yin, Y.; Lu, Y. *Adv. Mater.* **2000,** *12,* 693–713. doi:10.1002/(SICI)1521-4095(200005)12:10<693::AID-ADMA693>3.0.CO;2-J
4. Yang, S. M.; Jang, S. G.; Choi, D. G.; Kim, S.; Yu, H. K. *Small* **2006,** *2,* 458–475. doi:10.1002/smll.200500390
5. Fischer, U. C.; Zingsheim, H. P. *J. Vac. Sci. Technol.* **1981,** *19,* 881–885. doi:10.1116/1.571227
6. Saner, C. K.; Lusker, K. L.; LeJeune, Z. M.; Serem, W. K.; Garno, J. C. *Beilstein J. Nanotechnol.* **2012,** *3,* 114–122. doi:10.3762/bjnano.3.12
7. Haynes, C. L.; Van Duyne, R. P. *J. Phys. Chem. B* **2001,** *105,* 5599–5611. doi:10.1021/jp010657m
8. Veinot, J. G. C.; Veinot, H. Y.; Smith, S. M.; Cui, J.; Huang, Q.; Marks, T. J. *Nano Lett.* **2002,** *2,* 333–335. doi:10.1021/nl020293p
9. McLellan, J. M.; Geissler, M.; Xia, Y. N. *J. Am. Chem. Soc.* **2004,** *126,* 10830–10831. doi:10.1021/ja0470766
10. Taylor, Z. R.; Patel, K.; Spain, T. G.; Keay, J. C.; Jernigen, J. D.; Sanchez, E. S.; Grady, B. P.; Johnson, M. B.; Schmidtke, D. W. *Langmuir* **2009,** *25,* 10932–10938. doi:10.1021/la901512z
11. Pernites, R. B.; Foster, E. L.; Felipe, M. J. L.; Robinson, M.; Advincula, R. C. *Adv. Mater.* **2011,** *23,* 1287–1292. doi:10.1002/adma.201004003
12. Matijevic, E. *Acc. Chem. Res.* **1981,** *14,* 22–29. doi:10.1021/ar00061a004
13. Chen, T.; Amin, I.; Jordan, R. *Chem. Soc. Rev.* **2012,** *41,* 3280–3296. doi:10.1039/C2CS15225H
14. Chen, T.; Ferris, R.; Zhang, J.; Ducker, R.; Zauscher, S. *Prog. Polym. Sci.* **2010,** *35,* 94–112. doi:10.1016/j.progpolymsci.2009.11.004
15. Senaratne, W.; Andruzzi, L.; Ober, C. K. *Biomacromolecules* **2005,** *6,* 2427–2448. doi:10.1021/bm050180a
16. Zhao, B.; Brittain, W. J. *Prog. Polym. Sci.* **2000,** *25,* 677–710. doi:10.1016/S0079-6700(00)00012-5
17. Husemann, M.; Morrison, M.; Benoit, D.; Frommer, J.; Mate, C. M.; Hinsberg, W. D.; Hedrick, J. L.; Hawker, C. J. *J. Am. Chem. Soc.* **2000,** *122,* 1844–1845. doi:10.1021/ja991450y
18. Ahn, S. J.; Kaholek, M.; Lee, W. K.; LaMattina, B.; LaBean, T. H.; Zauscher, S. *Adv. Mater.* **2004,** *16,* 2141–2145. doi:10.1002/adma.200401055
19. Schmelmer, U.; Jordan, R.; Geyer, W.; Eck, W.; Golzhäuser, A.; Grunze, M.; Ulman, A. *Angew. Chem., Int. Ed.* **2003,** *42,* 559–563. doi:10.1002/anie.200390161
20. Zhou, F.; Zheng, Z.; Yu, B.; Liu, W.; Huck, W. T. S. *J. Am. Chem. Soc.* **2006,** *128,* 16253–16258. doi:10.1021/ja0654377
21. Kaholek, M.; Lee, W. K.; LaMattina, B.; Caster, K. C.; Zauscher, S. *Nano Lett.* **2004,** *4,* 373–376. doi:10.1021/nl035054w
22. Liu, Y.; Klep, V.; Luzinov, I. *J. Am. Chem. Soc.* **2006,** *128,* 8106–8107. doi:10.1021/ja061646f
23. Khanduyeva, N.; Senkovskyy, V.; Beryozkina, T.; Horecha, M.; Stamm, M.; Uhrich, C.; Riede, M.; Leo, K.; Kiriy, A. *J. Am. Chem. Soc.* **2009,** *131,* 153–161. doi:10.1021/ja8050734
24. Trujillo, N. J.; Baxamusa, S. H.; Gleason, K. K. *Chem. Mater.* **2009,** *21,* 742–750. doi:10.1021/cm803008r
25. Chen, T.; Jordan, R.; Zauscher, S. *Soft Matter* **2011,** *7,* 5532–5535. doi:10.1039/c1sm05474k
26. Erb, R. M.; Jenness, N. J.; Clark, R. L.; Yellen, B. B. *Adv. Mater.* **2009,** *21,* 4825–4829. doi:10.1002/adma.200900892
27. Jones, D. M.; Brown, A. A.; Huck, W. T. S. *Langmuir* **2002,** *18,* 1265–1269. doi:10.1021/la011365f
28. Zhang, G.; Wang, D.; Möhwald, H. *Nano Lett.* **2007,** *7,* 127–132. doi:10.1021/nl062284c
29. Geissler, M.; McLellan, J. M.; Chen, J.; Xia, Y. *Angew. Chem., Int. Ed.* **2005,** *44,* 3596–3600. doi:10.1002/anie.200500421
30. Xu, C.; Wu, T.; Drain, C. M.; Batteas, J. D.; Beers, K. L. *Macromolecules* **2005,** *38,* 6–8. doi:10.1021/ma048208i
31. Chen, T.; Zhong, J. M.; Chang, D. P.; Garcia, A.; Zauscher, S. *Adv. Mater.* **2009,** *21,* 1825–1829. doi:10.1002/adma.200802484
32. Markiewicz, P.; Goh, M. C. *Langmuir* **1994,** *10,* 5–7. doi:10.1021/la00013a002

License and Terms

Beilstein Journal
of Nanotechnology

Mapping mechanical properties of organic thin films by force-modulation microscopy in aqueous media

Jianming Zhang[1,2,§], Zehra Parlak[1,2,3,§], Carleen M. Bowers[4],
Terrence Oas[3] and Stefan Zauscher[*1,2]

Letter

Open Access

Address:
[1]Department of Mechanical Engineering and Materials Science, Duke University, Durham, North Carolina 27708, USA, [2]Center for Biologically Inspired Materials and Materials Systems, Duke University, Durham, North Carolina 27708, USA, [3]Department of Biochemistry, Box 3711, Duke University Medical Center, Durham, North Carolina 27710, USA and [4]Department of Chemistry, Duke University, Durham, North Carolina 27708, USA

Email:
Stefan Zauscher[*] - zauscher@duke.edu

* Corresponding author
§ These authors contributed equally to the paper

Keywords:
acoustic atomic force microscopy; biomolecules; elastic modulus mapping; nanomechanical characterization; self-assembled monolayers

Beilstein J. Nanotechnol. **2012,** *3,* 464–474.
doi:10.3762/bjnano.3.53

Received: 19 March 2012
Accepted: 31 May 2012
Published: 26 June 2012

This article is part of the Thematic Series "Self-assembly at solid surfaces".

Guest Editors: S. R. Cohen and J. Sagiv

Abstract

The mechanical properties of organic and biomolecular thin films on surfaces play an important role in a broad range of applications. Although force-modulation microscopy (FMM) is used to map the apparent elastic properties of such films with high lateral resolution in air, it has rarely been applied in aqueous media. In this letter we describe the use of FMM to map the apparent elastic properties of self-assembled monolayers and end-tethered protein thin films in aqueous media. Furthermore, we describe a simple analysis of the contact mechanics that enables the selection of FMM imaging parameters and thus yields a reliable interpretation of the FMM image contrast.

Introduction

Mapping the mechanical properties, such as elastic modulus, friction, and adhesion of surfaces and thin films in aqueous (or liquid) environments with nanoscale lateral resolution is important for a broad range of applications in materials science [1-10] and in the life sciences [11-20]. The atomic force microscope (AFM) [21], due to its force sensitivity and ability to image surface topography with high lateral resolution, is ideally suited to map these properties. Intermittent AFM imaging modes, such as tapping mode [22-24], and pulsed-force mode [12,25-28], have been developed for soft, often biological, samples in liquid environments. Although these imaging modes reduce the lateral forces, they often do not allow direct interpretation of the data in terms of the surface mechanical properties, due to cantilever damping in solution and the complex forces that the probe experiences when jumping in and out of contact with the surface.

Alternatively, dynamic variations of contact mode AFM, such as acoustic AFM, add a small actuation to the tip–surface contact at acoustic frequencies and are thus useful for mapping differences in the surface mechanical properties of the sample [29]. In some versions of acoustic AFM, such as ultrasonic AFM (UAFM) [30], acoustic force atomic microscopy (AFAM) [31], and contact resonance AFM (CR-AFM) [32-35], contact resonance frequencies are deliberately chosen to enhance the imaging sensitivity. However, acoustic AFM imaging in solution is challenging since the liquid phase complicates the cantilever dynamics through fluid damping. To our knowledge, only a few studies report the use of acoustic AFM on molecularly thin films or soft materials in liquid [7,36].

Here we show that force-modulation microscopy (FMM) is a powerful acoustic AFM method for mapping surface mechanical properties in fluids. In a typical FMM setup, the tip–sample contact is actuated at an off-resonance frequency, and the amplitude and phase response of the cantilever vibration are then detected at the drive frequency, by using a lock-in amplifier, and mapped concurrently with topography [37]. The narrow detection bandwidth used in FMM entails less noise, while off-resonance actuation reduces fluid-related cantilever dynamics. Consequently, FMM can map even slight differences in the sample surface stiffness (i.e., the contact stiffness). While these advantages were shown in some FMM studies performed on monolayers [38,39], the understanding of amplitude and phase contrasts and the frequency limitations of FMM in liquid, remain incomplete, which often leads to conflicting data interpretation [38,39]. Presently, these unresolved issues diminish the usefulness of FMM as a mechanical mapping tool in materials science, especially for molecular thin films and biological samples.

In this article, we describe the use of FMM for mapping subtle differences in the elastic properties of organic thin films in aqueous environments. To this end we developed a parameter selection method for FMM that helps (i) in the selection of appropriate actuation frequencies and contact forces, and (ii) in the unambiguous interpretation of the contrast in the amplitude images [38-40]. We demonstrate the capability of FMM to image mechanical properties in aqueous media on surface-tethered proteins and self-assembled EG_3-thiol (triethylene glycol mono-11-mercaptoundecyl ether) monolayers. Our studies show that subtle differences in the packing order of the self-assembled EG_3-thiols manifest as differences in the surface elastic properties that can be mapped by FMM in solution. The results presented in this paper also provide a stepping stone for the development of a quantitative viscoelastic modeling approach in liquids, in analogy to those developed for contact resonance AFM in air [32,33].

Results and Discussion

FMM working principles

Linear regime in FMM

In FMM, the cantilever tip contacts the substrate surface with a constant static force while a small force modulation is superimposed [37]. As a first approximation, this contact can be modeled by Hertzian contact theory. Though based on the assumption of a nonadhesive and elastic contact between a rigid spherical tip and the substrate surface, the model readily and adequately explains contact mechanics when the static contact force is much greater than the adhesion force [41-43]. Furthermore, the Hertzian contact model has been successfully extended to characterize the stiffness of thin, layered materials [3,44]. If necessary, tip–sample adhesion can easily be included in the contact analysis by selecting an appropriate contact mechanics model, such as the Johnson–Kendall–Roberts (JKR) or the Derjaguin–Muller–Toporov (DMT) model [41,45].

Although contact deformation and force have a nonlinear relationship in the Hertzian contact model, this model can be linearized for a small force modulation at high contact forces, and the stiffness of the contact can be determined [46,47]. Linearization is valid as long as the cantilever is in constant contact with the sample and the amplitude of the force modulation is much smaller than the contact force.

For a lossless contact and for modulation frequencies significantly below the contact resonance frequency, the cantilever and the contact can be modeled as two springs in series (see Supporting Information File 1). In summary, the deflection of the cantilever, u_c, measured by FMM is,

$$u_c = \frac{z_0 k^*}{k_c + k^*} \sin \omega t, \tag{1}$$

where z_0 is the actuation amplitude of the contact, ω is the angular frequency of the actuation, k_c is the spring constant of the AFM cantilever, and k^* is the contact stiffness,

$$k^* = \sqrt[3]{6FRE^{*2}}. \tag{2}$$

The contact stiffness is a function of the reduced Young's modulus, E^*, the tip radius, R, and the applied force, F.

Equation 1 explains how the amplitude of the AFM cantilever deflection is related to z_0, k_c and k^*. Since z_0 and k_c do not change while the surface is being scanned, u_c depends only on k^*. The cantilever vibration amplitude is thus smaller on soft regions (low k^*), and it is higher on stiff regions (high k^*). Although this simple analysis provides a convenient explanation of the contrast mechanism in FMM amplitude images, Equation 1 cannot be used to quantify FMM experiments [48], because the modulation frequency is typically not sufficiently low that the cantilever dynamics can be ignored.

Nonlinear regime in FMM

The current understanding of FMM is largely based on the amplitude and phase response of the cantilever at large static loading forces and very small modulation amplitudes. Imaging of compliant samples, however, requires overall low contact forces in combination with a high modulation amplitude for sensitive mapping. This combination precludes linearization of the contact models. For this case of soft contact, the sinusoidal force modulation at a single frequency yields a nonlinear (distorted sinusoidal) cantilever deflection response, which reflects the contact nonlinearity and gives rise to higher harmonics, as shown in Equation 3 (see also Supporting Information File 1).

The cantilever deflection with a second-order harmonic can be rewritten as,

$$u_c = \frac{k_c^2 z_0^2 \beta}{4\left(k^* + k_c\right)^3} + \frac{z_0 k^*}{k^* + k_c} \sin \omega t - \frac{k_c^2 z_0^2 \beta}{4\left(k^* + k_c\right)^3} \cos 2\omega t, \quad (3)$$

where $\beta = \dfrac{\partial^2 F}{\partial h^2} = \sqrt[3]{\dfrac{4R^2 E^{*4}}{3F}}$ is the second-harmonic factor.

The frequency-independent, zeroth-order term in Equation 3 reflects a DC deflection. The feedback loop, however, cannot differentiate this zeroth-order component from the surface-topography-induced deflection response of the cantilever, thus precluding clear signal deconvolution [29]. Both the first and second harmonics, however, do not interfere with the feedback loop and can be detected by lock-in techniques. At low forces, the second-harmonic factor (β) increases dramatically, and thus promotes the contribution from the second-harmonic amplitude.

The ratio of the second- to first-harmonic amplitudes is plotted in Figure 1 as a function of contact force for two reduced moduli. This ratio was calculated by using realistic experimental parameters, i.e., $k_c = 1$ N/m, $R = 30$ nm, and $z_0 = 2$ nm, while 0.1 GPa and 1 GPa were assigned to E^*. FMM measurements are less nonlinear at (i) high contact forces and (ii) for stiff materials, as shown by the lower amplitude ratio in these cases in Figure 1. This implies that changes in the surface elasticity can lead to nonlinear effects in FMM, making a quantitative interpretation of the amplitude and phase signals complicated, especially at low applied forces.

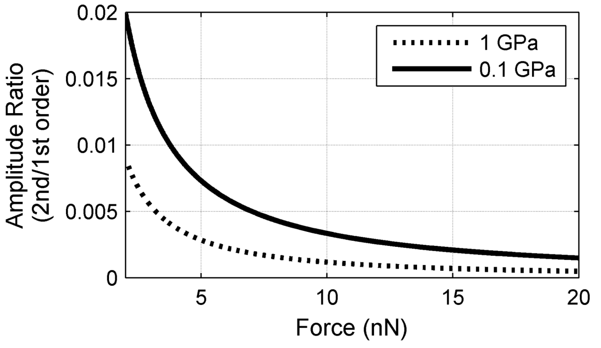

Figure 1: Amplitude ratio of the second to the first harmonic, plotted for different applied forces. The surface modulus is set to 0.1 GPa (solid) and to 1.0 GPa (dotted).

Parameter selection and contrast interpretation for hard-contact FMM in aqueous environments

The interpretation of FMM amplitude and phase images obtained on soft substrates is further complicated by viscous damping effects [49], particularly when imaging in an aqueous environment. To better interpret image contrast in that case, one needs to understand the dependence of amplitude and phase on surface stiffness, and one needs a method to select the proper contact force and actuation frequency. Here we use contact force as a variable to change the contact stiffness (Equation 2) and monitor the response of the amplitude and phase behavior of the cantilever.

In our parameter-selection process we acquire force–distance curves while the cantilever is modulated at the desired frequency. We monitor (i) the amplitude and (ii) the phase of the first harmonic, and (iii) the amplitude of the second harmonic of the cantilever oscillations, along with (iv) the cantilever deflection, as the cantilever interacts with the surface (Figure 2). The deflection of the cantilever determines the interaction force from which the contact stiffness can be calculated (Equation 2). The amplitude of the first harmonic is used to analyze the elasticity of the substrate surface in FMM and it is thus essential to relate the first harmonic with the contact stiffness experimentally. Meanwhile, the amplitude of the second harmonic, a measure of the nonlinearity in the contact, should be minimized for reliable FMM measurements. A set of representative curves for cantilever deflection, first-harmonic amplitude and phase, and second-harmonic amplitude, at 20 kHz actuation frequency in water on a gold surface, are shown in Figure 2. For these experiments, we used a cantilever with a spring constant of 0.9 N/m and a resonance frequency of 47.8 kHz in solution.

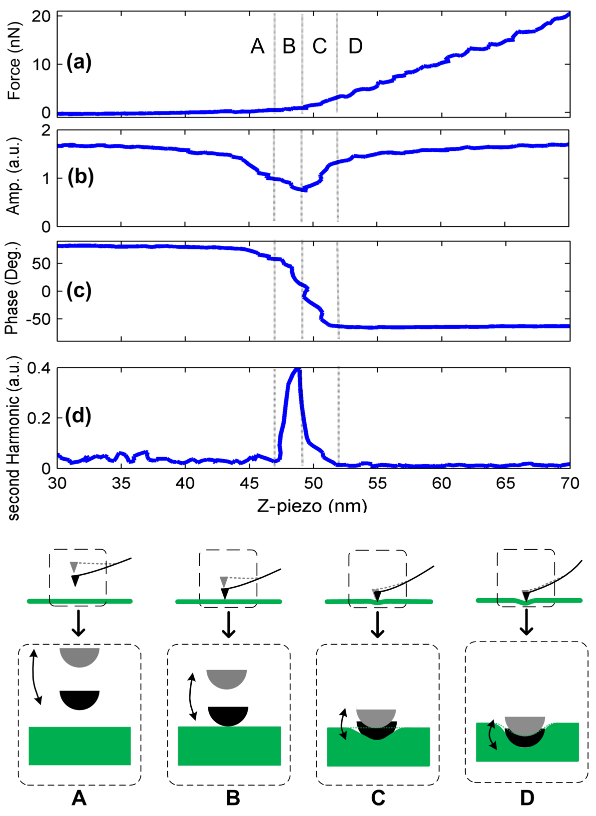

Figure 2: (a) Force, (b) first-harmonic amplitude, (c) first-harmonic phase, and (d) second-harmonic amplitude, plotted as a function of Z-piezo displacement. As the probe approaches the gold sample surface, the cantilever encounters four regimes: (A) free oscillation, (B) partial contact, (C) soft contact, and (D) hard contact. To highlight the differences in cantilever bending and the level of indentation in the four regimes, the schematic is not drawn to scale.

The different regions of the deflection (Figure 2a) and amplitude curves (Figure 2b and Figure 2d) indicate both the position of the probe and the type of the contact. In regime A the cantilever freely oscillates with a zero mean deflection; however, the amplitude decreases slightly with decreasing tip–sample distance. Because the amplitude of the second harmonic (Figure 2d) is still small [24,50], this behavior can likely be attributed to hydrodynamic lubrication forces that increase with increasing proximity of the tip to the surface [49]. In regime B, the amplitude of the first harmonic decreases, while that of the second harmonic increases, reflecting the increasing nonlinearity of the initial tip–surface interaction and the change in cantilever dynamics, when the cantilever approaches the surface. In regime C, the amplitude of the first harmonic of the cantilever vibration increases, while that of the second harmonic decreases. This behavior is consistent with the analytical expressions for the soft contact (Figure 1) [29,37]. When hard contact is reached in regime D, the contact force and the amplitude of the first harmonic are high, whereas the amplitude of the second harmonic is close to zero again. We note that both regimes, A and D, have high amplitudes for the first harmonic. This is quite different from the behavior in tapping-mode AFM, in which the amplitude in regime A is typically much larger than that in regime D [51]. In tapping-mode AFM, the cantilever is intentionally actuated at its resonance frequency to achieve a large cantilever amplitude. In FMM, however, the actuation frequency is typically well below the free resonance frequency, and the actuation amplitude is selected to yield a small cantilever amplitude in contact. Furthermore, as shown in Figure 2, AFM tip–surface interactions should be kept in regime D to obtain a linear contact response. This demand needs to be balanced by the need for low applied forces that are required to image compliant samples nondestructively. Consequently, the boundary between regimes C and D determines the minimum applicable contact force for which a sufficiently linear vibration response is obtained. To demarcate the onset of regime D, we have chosen the ratio of the first- to the second-harmonic amplitudes to be less than 0.1% (0.001). The first harmonic vibration amplitude increases with increasing contact force in regimes C and D, indicating that higher contact stiffness values (see Equation 2) cause higher amplitudes. On the other hand, increasing the contact stiffness decreases the phase response (Figure 2c). As a consequence, soft regions on the sample appear bright in the phase images. Importantly, however, the higher phase observed on softer areas reflects the convolution of the cantilever dynamics and time-dependent contact stiffness, and is thus not a result of the substrate viscoelasticity alone. The force, amplitude, and phase measurements shown in Figure 2 were carried out on thin gold surfaces whose apparent stiffness can be represented by a simple spring. Even in this simple case, a quantitative description of the cantilever dynamics in aqueous solution is complicated and not yet available. However, the measurements shown in Figure 2 can help to understand how the cantilever responds to changes in surface stiffness (for a given set of FMM imaging parameters).

To account quantitatively for the viscoelastic mechanical properties of soft polymeric and biomolecular thin films, requires the inclusion of a viscoelastic model, such as the Voigt model, to explain the tip–sample interaction. Such an approach has recently been shown for contact-resonance imaging in air [32]. However, as before, the cantilever dynamics, which depends not only on fluid loading but also on the details of the applied force (see above), needs to be captured adequately first, before a meaningful deconvolution of the contact stiffness is possible.

Another issue concerns the selection of the actuation frequency in FMM. Force–distance curves recorded at different actuation frequencies show that when actuation is above the free resonance frequency of the cantilever, higher forces are required to establish hard contact (regime D in Figure 2). This is due to the fact that the contact of the tip with the surface changes the cantilever dynamics and increase the resonance frequency. Consequently, the cantilever modulation increases and contact nonlinearity occurs. In this case, a simple correlation between contact stiffness and first-harmonic amplitude can lead to conflicting results [52]. To avoid this situation, one should select an actuation frequency far below the free resonance frequency of the cantilever.

FMM on patterned protein monolayers

Characterizing the dynamic mechanical properties of biomolecular monolayers provides insight into the dynamics of biomolecules on surfaces and aids in the design of functional biomolecular micro- and nanostructures. Here, acoustic AFM methods are promising tools since they enable sensitive mapping of the contact-mechanical properties of samples by introducing high-frequency modulation while imaging the topography [53]. Although these methods have been used in air, imaging of many polymers and biomolecules should take place in an aqueous environment or under physiological conditions. Here we show that FMM is able to provide high-contrast amplitude and phase maps of micropatterned biomolecular thin films in an aqueous environment.

The biological material of interest in our FMM experiments is the IgG-binding domain of staphylococcal protein A. Protein A is a surface protein found on the cell wall of *staphylococcus aureus* bacteria and contains five domains for IgG-binding (SpA-N). One of the domains is named the B-domain and its structure and folding behavior have been well studied [54]. Specifically, we use FMM to image and map differences in the elastic properties of micropatterned, end-tethered proteins (constructs of five repeating SpA B-domains) on gold. The topography, amplitude, and phase images were obtained in PBS buffer at 35 kHz actuation frequency with 9 Å vibration amplitude and 8 nN contact force (Figure 3), which leaves the cantilever and surface in hard contact (region D in Figure 2).

The dark regions in the amplitude image indicate that the contact stiffness (and thus largely the protein sample) is considerably softer than the gold substrate. The FMM height image (Figure 3a) shows that the protein layer is approximately 5 nm thick. The corresponding amplitude image at an excitation frequency of 35 kHz (Figure 3b) shows that protein regions have about 17% lower amplitude than the gold substrate (as shown in the cross-section). This suggests, as anticipated, that the protein patterns are significantly softer than the gold substrate. Force–distance curves on the gold and protein regions showed that the adhesion force between the AFM probe and the protein features is negligibly small. The adhesion force on gold is around 0.3 nN, which is only about 3% of the static force

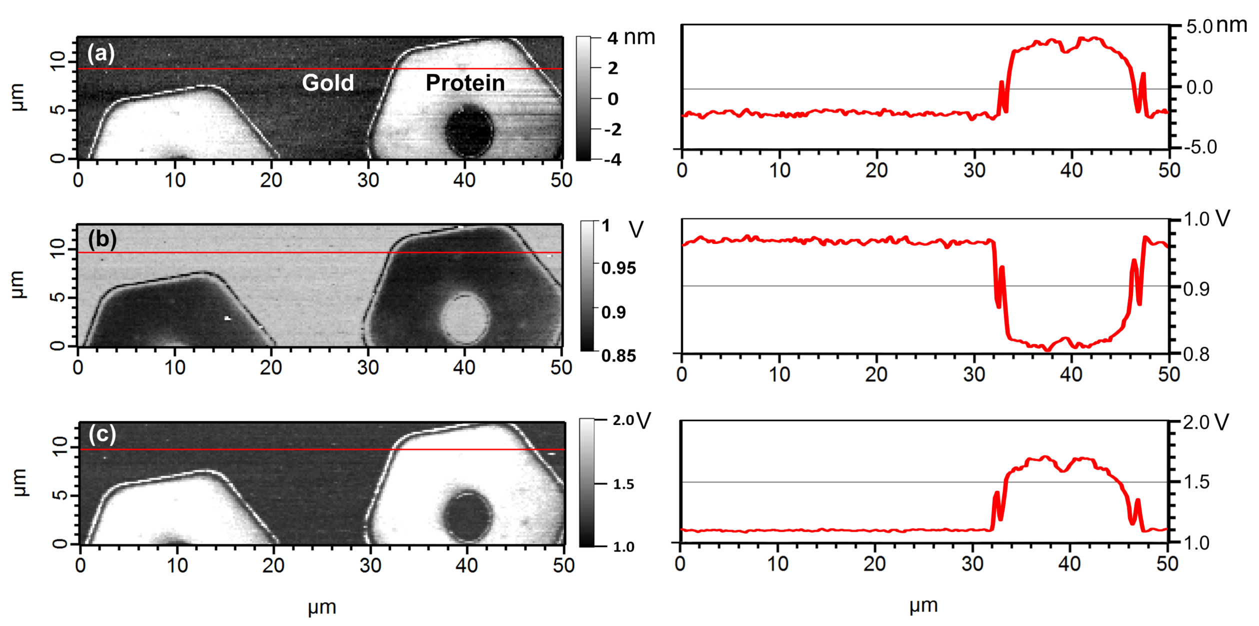

Figure 3: FMM images of SpA-N B-domain protein patterns on a gold surface, with corresponding cross-section analysis along the red line in the AFM images. (a) The height image shows a protein height of about 5 nm. (b) The amplitude and (c) phase images of the same area clearly show the elastic difference between protein and the gold substrate.

applied, while the adhesion force on the protein surface is within the noise level of the measurement. This justifies the use of a Hertzian contact mechanics model, as done here.

Our approach currently does not capture the viscoelasticity of the protein or the response of the cantilever to a viscoelastic contact in aqueous solution. Future work to quantify these properties requires additional analytical models that capture the interaction of the cantilever beam with the liquid environment.

FMM on patterned EG_3-thiol monolayers

The properties and applications of alkanethiol self-assembled monolayers (SAMs) on gold surfaces have been the subject of interface science research for many years. The self-assembly of alkane thiol molecules on gold surfaces is a two-step process. The initial physisorption step on gold substrates is typically slow and concentration-dependent [55]. Once in contact, the molecules adsorb on the gold substrate in a loosely packed configuration, with the thiol end binding to gold and the carbon chain aligning approximately parallel to the surface [56,57]. The persistence of this stage depends on the thiol concentration, and thus on the initial packing density and order of the thiol molecules on the surface. At low concentrations, this lying-down phase can persist for hours. At high concentrations, however, thiols can reorient into an upright conformation and pack tightly on the surface within seconds. The adsorption process has been studied with several surface-sensitive techniques, including surface plasmon resonance (SPR) [58], quartz-crystal microbalance (QCM) [59-61] and ellipsometry [62]. These methods, however, do not resolve differences in the grafting density and packing of the molecules with high spatial resolution (micrometer or less). Here we show that FMM in solution is able to distinguish subtle difference in the packing of self-assembled thiol monolayers on surfaces, by mapping the amplitude of the first harmonic of the cantilever vibration amplitude.

Figure 4 shows a series of FMM images of patterned EG_3-thiols (triethylene glycol mono-11-mercaptoundecyl ether, $HO(CH_2CH_2O)_3C_{11}H_{22}SH$) obtained at 20 kHz. The patterns were prepared by photolithography. Briefly, the sample was prepared by immersing the developed photoresist pattern in a 10 μM thiol solution for 60 s, followed by stripping with ethanol and washing with Milli-Q grade water (see Experimental section for details). The sample was backfilled with thiol molecules at high concentration for different lengths of time. An EG_3-thiol SAM is about 2.4 nm thick when thiols are in a close-packed $\left(\sqrt{3}\times\sqrt{3}\right)R30°$ configuration, while the thickness is only about 0.4 nm when the thiol chains lie flat on the surface [63].

The first row of FMM images in Figure 4a were obtained simultaneously on an EG_3-patterned sample. From left to right, the images are height, lateral force, and amplitude and phase of the first harmonic of the cantilever vibration, respectively. The height of the EG_3-thiol patterns is 1.7 ± 1.1 nm, which suggests that the thiol molecules are not close-packed, and have some disorder in their arrangement on the surface. The contrast in the lateral-force image shows a friction difference between the gold surface and the EG_3 patterns that can be attributed to the surface-energy difference between the ethylene glycol end groups and the gold [64]. The low amplitude and high phase of the first-harmonic signal on the thiol patterns indicate that the regions covered by EG_3 molecules are softer than the gold substrate.

The first harmonic amplitude curves obtained from force–distance measurements, reflect the apparent stiffness of the EG_3 layer (see Supporting Information File 1 for details) [65]. The apparent Young's modulus of the thiols on the surface is around 30 GPa, consistent with moduli of short alkanethiol chains obtained by using SEM and nano-indentation [66,67]. The approach to deconvolute these Young's moduli further to reflect the layered systems of thiol SAMs on gold substrates has been shown in the literature [68], but is beyond the scope of this discussion.

The second row (Figure 4b) shows images obtained on a sample first patterned by exposure to 10 μM EG_3-thiol for 1 min, followed by stripping off of the photoresist, and backfilling in 0.5 mM EG_3-thiol for 1 h. Both height and friction images do not show any pattern-related contrast, which suggests that the molecules have a similar height and the same surface chemical properties. Importantly, however, the original patterns become clearly visible in the amplitude image, and somewhat less clearly in the phase image. The contrast in the amplitude image shows that the patterned areas are "softer" than the likely more-ordered regions that are backfilled at high thiol concentrations. This result suggests that FMM detects the subtle elastic differences between the patterned and backfilled regions.

We ascribe the contrast in the FMM amplitude and phase images to differences in the packing order of the thiols on the substrate surface. The thiol SAMs assembled in the second step by backfilling with thiol solutions at high concentrations, form a standing-up phase on bare gold almost immediately [56,69]. At the same time, in areas that were previously self-assembled with thiols, the reorientation of thiols is slower than that in the backfilled areas, which would entail an overall less-ordered conformation. Our results not only illustrate the effect of grafting density and molecular packing on the apparent layer stiffness,

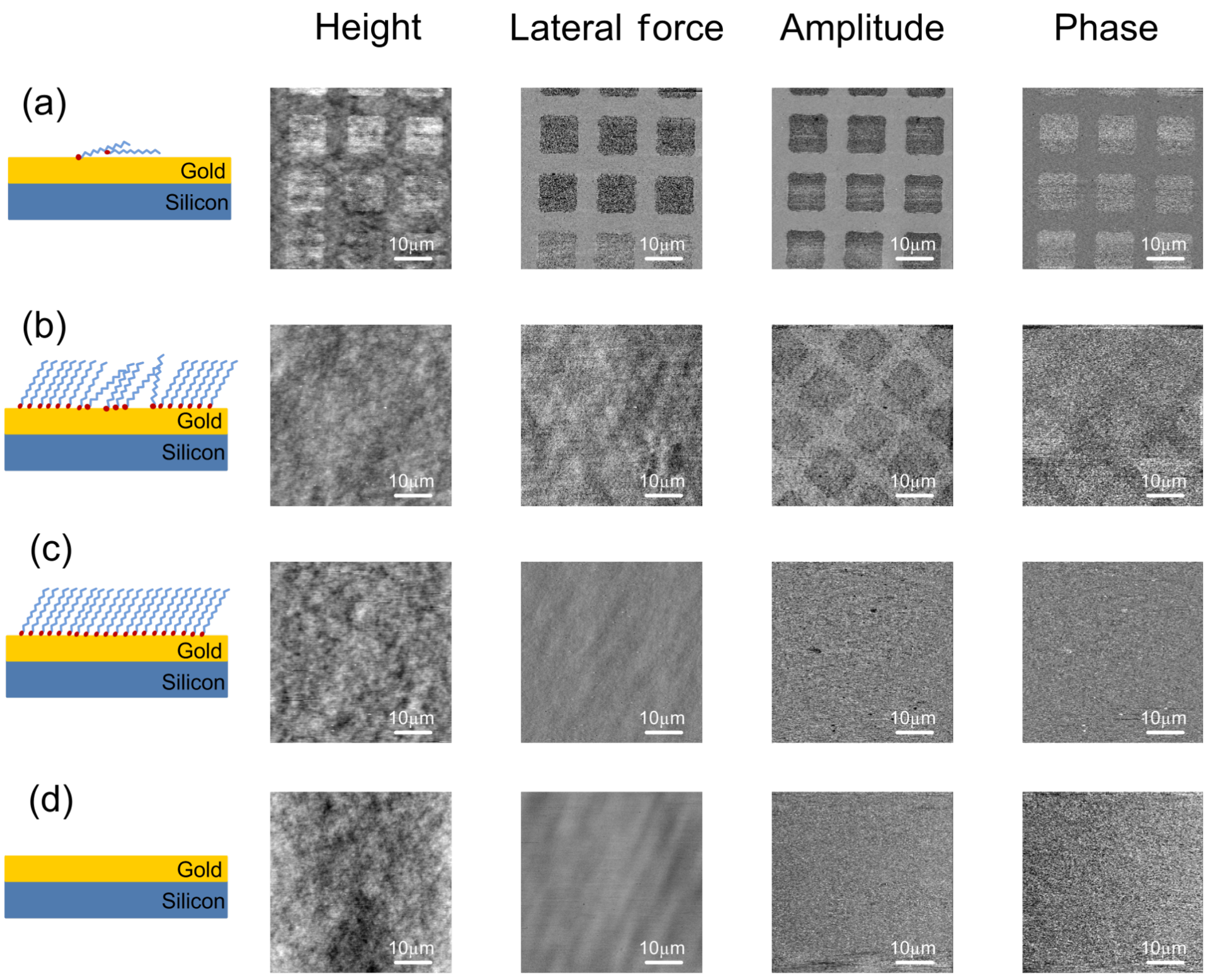

Figure 4: Schematic and FMM images of a series of EG_3 patterns on gold. Height, lateral force, amplitude, and phase images were captured simultaneously. (a) Low-EG_3-grafting-density areas patterned on a gold substrate. The height difference between EG_3 and gold is about 1 nm. The lateral-force image shows the chemical force difference between the areas. The contrast in the amplitude image demonstrates that the EG_3 areas are significantly softer than the gold background. (b) Low-EG_3-grafting-density areas (squares) and high-grafting-density background. Height and lateral-force images cannot resolve differences in the morphology and chemical force, while amplitude images differentiate between high- and low-grafting-density regions (i.e., the original patterns are visible in the amplitude image). (c) Patterned surfaces imaged after overnight exposure to a thiol solution. Height, chemical-force, and stiffness images are uniform. (d) Negative control: gold surface after photolithography and resist stripping shows no surface residues.

but also demonstrate the high sensitivity of FMM in solution for imaging self-assembled monolayers.

The third row (Figure 4c) shows images obtained on a sample first patterned by exposure in 10 µM EG_3-thiol for 1 min, followed by stripping of residue resist and overnight exposure to 0.5 mM EG_3-thiol. As shown previously, the packing of thiols on a surface equilibrates to a well-ordered layer with overnight thiol exposure [70,71]. Our data are in agreement with this notion, as we did not observe any surface morphological or mechanical differences in the AFM images. The elimination of the differences could be caused by the long-time equilibration, which leaves the surface with a uniformly ordered layer of thiol molecules. The last row (Figure 4d) shows FMM images obtained on a control sample (bare gold, after photoresist stripping), processed in parallel, but without thiol deposition. The height, lateral force, and amplitude and phase images do not show any difference in the morphology or the substrate mechanical properties, suggesting that the photoresist developing and stripping steps did not change the surface properties.

Conclusion

We showed that force-modulation microscopy (FMM) can be used to image organic thin films in aqueous environments with high spatial resolution and sensitivity to conformational details that affect the contact mechanics. FMM generated high-contrast amplitude and phase images of proteins end-grafted to gold substrates, and reflects the expected (see Equation 1) differences in contact-stiffness on the sample. Furthermore, FMM experiments on self-assembled thiol monolayers were highly sensitive to differences in the surface elastic properties arising from subtle differences in the molecular packing of the thiols on the substrate surface.

Although previous FMM studies observed the contrast in amplitude and phase images [9,37,38,72], the interpretation of the results was inconsistent because the relation between the contrast mechanism and the cantilever dynamics was not sufficiently considered [38,48], particularly in aqueous environments. We thus developed a parameter-selection procedure that allows for reliable interpretation of image data, and accounts for the effect of contact force and actuation frequency on the cantilever dynamics in FMM. More specifically, this procedure determines the minimum contact force necessary, at a certain excitation frequency, to establish a linear response in the contact regime.

Experimental

FMM setup

A commercial AFM system (Asylum MFP-3D) was modified to implement FMM [37,72] in liquid as shown in Figure 5. Like in contact-mode imaging, the feedback controller of the AFM keeps the tip–sample force constant during the surface scan. In addition, however, a piezoelectric transducer in the cantilever holder was used to excite the cantilever with a small amplitude, off-resonance frequency. A lock-in amplifier (AMETEK model 7280) was used to monitor the amplitude and phase of the resulting cantilever vibration at the actuation frequency.

All samples were imaged at a rate of 1 line/s and at a resolution of 256 pixels per line. The actuation frequency of the cantilever was kept higher than 8 kHz to avoid interference with the AFM imaging feedback control. A cantilever in contact has contact resonance modes [46] and the cantilever vibration amplitude is amplified at the contact resonance frequency, which increases with increasing surface stiffness. Contact resonances modes in air have been used to quantify the stiffness of surfaces [31]. However, the quality factor of these modes decreases significantly in solution and makes it difficult to interpret cantilever vibrations around contact resonance modes. A proper probe for FMM imaging in liquid should have a high resonance frequency to simplify data analysis and at the same time it should be soft to prevent destructive forces on compliant samples. Therefore we used ScanAsyst-Fluid cantilevers (Bruker Probes) that have 0.7 N/m nominal spring constant and 50 kHz free resonance frequency in solution. The deflection sensitivity of each cantilever was determined from a force–displacement curve taken before an FMM experiment. The spring constant of each cantilever was calculated from the power spectral density of the thermal noise fluctuations.

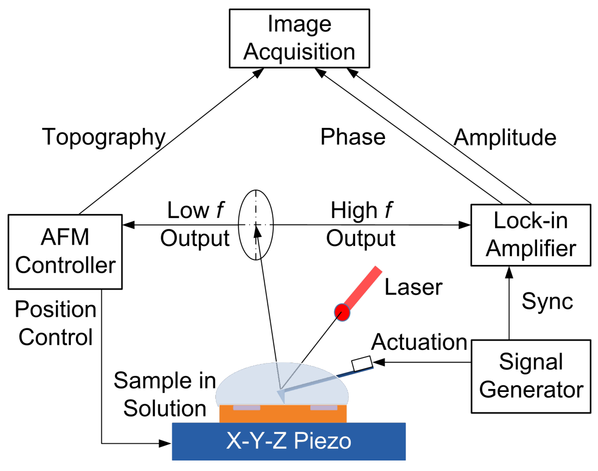

Figure 5: Schematic of the FMM setup. The AFM probe is kept at a constant static contact force when scanning the sample in solution. The signal generator actuates the cantilever probe with a single frequency signal, and the cantilever response is monitored by a lock-in amplifier.

Since FMM is a modified contact mode AFM method, frictional forces may affect the measurements. Friction leads to lateral twisting of the cantilever, which may be coupled with the actuation normal to the contact. To decrease the effect of friction on the amplitude and phase images of FMM, the slow scan direction is selected perpendicular to the cantilever axis. Meanwhile, the use of triangular cantilevers minimizes the torsional twisting of the cantilever.

Sample Preparation

Gold deposition

Silicon wafers (Virginia semiconductor, Part 325S119656) were washed in acetone, ethanol and DI water, and completely dried before use. A 45 nm gold layer with a 5 nm chromium adhesion layer was deposited on the silicon surface by using an e-beam thermal evaporator (Kurt Lesker PVD 75), and subsequently cleaned by ozone plasma ashing (Emitech K-1050X).

Protein monolayer

Five tandem B-domains of staphylococcal protein A were expressed and purified from *E. coli*. The C-terminus of the terminal protein was modified with cysteine to enable protein binding to the gold surface. Protein patterns were prepared by dry stamping of the tandem B-domains on to the gold substrate surface, by using a polyurethane (pUA) stamp (15 µm hexagon). The pUA stamp was UV cross-linked on a silicon master with hexagonal pattern features and, before each use, cleaned by UV–ozone exposure. For dry stamping, 100 µL of a 500 µM protein solution was inked on the pUA surface and incubated for 10 min, followed by drying in a stream of nitrogen. The stamp was then brought into contact with a cleaned gold surface for 30 s. The patterned surface was subsequently sonicated and rinsed in deionized (DI) water followed by nitrogen drying.

Patterned EG_3-thiol monolayers

A 3 µm thick layer of negative tone resist (NFR-016D2) was spin-coated onto a freshly deposited and cleaned gold surface at 3000 rpm (Figure 6). A photolithography mask was then used to create 8 × 8 μm^2 square patterns during UV exposure. Next, the exposed photoresist was removed (Figure 6a), and the wafer was then cut into 1 × 1 cm^2 squares, which were rinsed in 0.5% SDS solution and DI water, and dried under N_2. The substrate chips were then exposed for 60 s to a solution of 10 µM EG_3-thiol (triethylene glycol mono-11-mercaptoundecyl ether, $HO(CH_2CH_2O)_3C_{11}H_{22}SH$) in 2% ethanol (Figure 6b), followed by rinsing with copious amounts of DI water and drying in a stream of nitrogen. This treatment produced EG_3-thiol patterns with low grafting density. Next, the remaining negative photoresist was stripped by acetone sonication for 1 min and ethanol wash (Figure 6c). The whole surface was then exposed to 0.5 mM ethanolic EG_3-thiol solution for different lengths of time to generate different thiol packing densities on the substrate surface (Figure 6d). Thiol adsorption on the bare gold surfaces occurs at high solution concentrations, the thiol grafting density is high, and the molecules are in an upright conformation. With prolonged exposure to high thiol solution concentrations, the grafting density and packing of the molecules equilibrates by backfilling and exchange reactions, and becomes eventually indistinguishable from the background. By varying the reaction time and thiol concentration in the solution phase, thiol patterns with two different packing orientations were generated on the gold substrate surface.

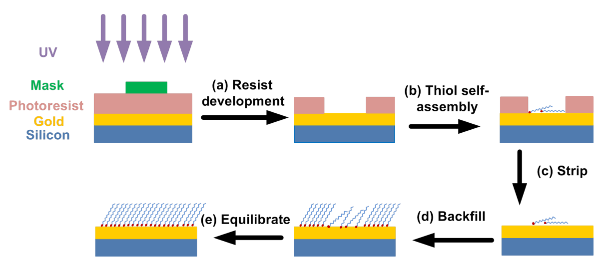

Figure 6: Schematic of the photolithography process for EG_3-thiol pattern deposition. (a) A micropatterned gold surface, covered with a negative tone resist, is patterned by exposure to UV light through a photomask. (b) Self-assembly of EG_3 thiols at low concentration generates low-grafting-density patterns. (c) Residual negative resist is stripped off by solvent washing. (d) Newly exposed gold surface is covered by high-grafting-density EG_3 thiol by backfilling. (e) Overnight exposure to EG_3 solution equilibrates the patterned-thiol SAM to a uniform surface.

Supporting Information

The cantilever response in linear and nonlinear contact regimes is derived in more detail.

Supporting Information File 1

Force modulation of the cantilever response.
[http://www.beilstein-journals.org/bjnano/content/supplementary/2190-4286-3-53-S1.pdf]

Acknowledgements

The authors thank the NIH for support through grant ARRA 3RO1GM081666-01 A2S1. Experimental help with protein expression and purification by Mr. William Franch (Duke University) is gratefully acknowledged.

References

1. Tsukruk, V. V.; Huang, Z.; Chizhik, S. A.; Gorbunov, V. V. *J. Mater. Sci.* **1998,** *33,* 4905–4909. doi:10.1023/A:1004457532183
2. Tsukruk, V. V.; Sidorenko, A.; Gorbunov, V. V.; Chizhik, S. A. *Langmuir* **2001,** *17,* 6715–6719. doi:10.1021/la010761v
3. Shulha, H.; Kovalev, A.; Myshkin, N.; Tsukruk, V. V. *Eur. Polym. J.* **2004,** *40,* 949–956. doi:10.1016/j.eurpolymj.2004.01.021
4. Tomasetti, E.; Legras, R.; Nysten, B. *Nanotechnology* **1998,** *9,* 305. doi:10.1088/0957-4484/9/4/001
5. Krotil, H.-U.; Stifter, T.; Marti, O. *Rev. Sci. Instrum.* **2001,** *72,* 150–156. doi:10.1063/1.1329898
6. Viani, M. B.; Schäffer, T. E.; Paloczi, G. T.; Pietrasanta, L. I.; Smith, B. L.; Thompson, J. B.; Richter, M.; Rief, M.; Gaub, H. E.; Plaxco, K. W.; Cleland, A. N.; Hansma, H. G.; Hansma, P. K. *Rev. Sci. Instrum.* **1999,** *70,* 4300–4303. doi:10.1063/1.1150069
7. Killgore, J. P.; Kelly, J. Y.; Stafford, C. M.; Fasolka, M. J.; Hurley, D. C. *Nanotechnology* **2011,** *22,* 175706. doi:10.1088/0957-4484/22/17/175706
8. Lahiji, R. R.; Xu, X.; Reifenberger, R.; Raman, A.; Rudie, A.; Moon, R. J. *Langmuir* **2010,** *26,* 4480–4488. doi:10.1021/la903111j
9. Bar, G.; Rubin, S.; Parikh, A. N.; Swanson, B. I.; Zawodzinski, T. A., Jr.; Whangbo, M.-H. *Langmuir* **1997,** *13,* 373–377. doi:10.1021/la960935m
10. Drake, B.; Prater, C. B.; Weisenhorn, A. L.; Gould, S. A.; Albrecht, T. R.; Quate, C. F.; Cannell, D. S.; Hansma, H. G.; Hansma, P. K. *Science* **1989,** *243,* 1586–1589. doi:10.1126/science.2928794
11. Cross, S. E.; Jin, Y.-S.; Rao, J.; Gimzewski, J. K. *Nat. Nanotechnol.* **2007,** *2,* 780–783. doi:10.1038/nnano.2007.388
12. Marti, O.; Holzwarth, M.; Beil, M. *Nanotechnology* **2008,** *19,* 384015. doi:10.1088/0957-4484/19/38/384015
13. Raman, A.; Trigueros, S.; Cartagena, A.; Stevenson, A. P. Z.; Susilo, M.; Nauman, E.; Contera, S. A. *Nat. Nanotechnol.* **2011,** *6,* 809–814. doi:10.1038/nnano.2011.186

14. Sato, M.; Nagayama, K.; Kataoka, N.; Sasaki, M.; Hane, K. *J. Biomech.* **2000,** *33,* 127–135. doi:10.1016/S0021-9290(99)00178-5
15. Vadillo-Rodríguez, V.; Busscher, H. J.; Norde, W.; de Vries, J.; Dijkstra, R. J. B.; Stokroos, I.; van der Mei, H. C. *Appl. Environ. Microbiol.* **2004,** *70,* 5441–5446. doi:10.1128/AEM.70.9.5441-5446.2004
16. Dong, M.; Husale, S.; Sahin, O. *Nat. Nanotechnol.* **2009,** *4,* 514–517. doi:10.1038/nnano.2009.156
17. Husale, S.; Persson, H. H. J.; Sahin, O. *Nature* **2009,** *462,* 1075–1078. doi:10.1038/nature08626
18. Chang, D. P.; Abu-Lail, N. I.; Coles, J. M.; Guilak, F.; Jay, G. D.; Zauscher, S. *Soft Matter* **2009,** *5,* 3438–3445. doi:10.1039/b907155e
19. Coles, J. M.; Zhang, L.; Blum, J. J.; Warman, M. L.; Jay, G. D.; Guilak, F.; Zauscher, S. *Arthritis Rheum.* **2010,** *62,* 1666–1674. doi:10.1002/art.27436
20. Ivanovska, I. L.; de Pablo, P. J.; Ibarra, B.; Sgalari, G.; MacKintosh, F. C.; Carrascosa, J. L.; Schmidt, C. F.; Wuite, G. J. L. *Proc. Natl. Acad. Sci. U. S. A.* **2004,** *101,* 7600–7605. doi:10.1073/pnas.0308198101
21. Binnig, G.; Quate, C. F.; Gerber, C. *Phys. Rev. Lett.* **1986,** *56,* 930–933. doi:10.1103/PhysRevLett.56.930
22. Tamayo, J.; García, R. *Langmuir* **1996,** *12,* 4430–4435. doi:10.1021/la960189l
23. Sahin, O.; Erina, N. *Nanotechnology* **2008,** *19,* 445717. doi:10.1088/0957-4484/19/44/445717
24. Stark, M.; Stark, R. W.; Heckl, W. M.; Guckenberger, R. *Proc. Natl. Acad. Sci. U. S. A.* **2002,** *99,* 8473–8478. doi:10.1073/pnas.122040599
25. Rosa-Zeiser, A.; Weilandt, E.; Hild, S.; Marti, O. *Meas. Sci. Technol.* **1997,** *8,* 1333–1338. doi:10.1088/0957-0233/8/11/020
26. Gigler, A.; Gnahm, C.; Marti, O.; Schimmel, T.; Walheim, S. *J. Phys.: Conf. Ser.* **2007,** *61,* 346–351. doi:10.1088/1742-6596/61/1/070
27. Degertekin, F. L.; Onaran, A. G.; Balantekin, M.; Lee, W.; Hall, N. A.; Quate, C. F. *Appl. Phys. Lett.* **2005,** *87,* 213109–213111. doi:10.1063/1.2136430
28. de Pablo, P. J.; Colchero, J.; Gómez-Herrero, J.; Baró, A. M. *Appl. Phys. Lett.* **1998,** *73,* 3300–3302. doi:10.1063/1.122751
29. Huey, B. D. *Annu. Rev. Mater. Res.* **2007,** *37,* 351–385. doi:10.1146/annurev.matsci.37.052506.084331
30. Yamanaka, K.; Noguchi, A.; Tsuji, T.; Koike, T.; Goto, T. *Surf. Interface Anal.* **1999,** *27,* 600–606. doi:10.1002/(SICI)1096-9918(199905/06)27:5/6<600::AID-SIA508>3.0.CO;2-W
31. Rabe, U.; Amelio, S.; Kester, E.; Scherer, V.; Hirsekorn, S.; Arnold, W. *Ultrasonics* **2000,** *38,* 430–437. doi:10.1016/S0041-624X(99)00207-3
32. Yuya, P. A.; Hurley, D. C.; Turner, J. A. *J. Appl. Phys.* **2008,** *104,* 074916–074922. doi:10.1063/1.2996259
33. Killgore, J. P.; Yablon, D. G.; Tsou, A. H.; Gannepalli, A.; Yuya, P. A.; Turner, J. A.; Proksch, R.; Hurley, D. C. *Langmuir* **2011,** *27,* 13983–13987. doi:10.1021/la203434w
34. Sader, J. E. *J. Appl. Phys.* **1998,** *84,* 64–76. doi:10.1063/1.368002
35. Van Eysden, C. A.; Sader, J. E. *J. Appl. Phys.* **2007,** *101,* 044908–044918. doi:10.1063/1.2654274
36. Campbell, S.; Ferguson, V.; Hurley, D. C. Linking Nano- and Micromechanical Measurements of the Bone-Cartilage Interface. In *Materials Research Society Fall Meeting,* Symposium SS: Properties and Processes at the Nanoscale—Nanomechanics of Material Behavior, Boston, MA, Nov 28–Dec 2, 2011; MRS, 2011.
37. Radmacher, M.; Tillmann, R. W.; Gaub, H. E. *Biophys. J.* **1993,** *64,* 735–742. doi:10.1016/S0006-3495(93)81433-4
38. Jourdan, J. S.; Cruchon-Dupeyrat, S. J.; Huan, Y.; Kuo, P. K.; Liu, G. Y. *Langmuir* **1999,** *15,* 6495–6504. doi:10.1021/la9902183
39. Manfred, R. *Methods Cell Biol.* **2007,** *83,* 347–372. doi:10.1016/S0091-679X(07)83015-9
40. Mazeran, P.-E.; Loubet, J.-L. *Tribol. Lett.* **1997,** *3,* 125–132. doi:10.1023/A:1019123525610
41. Grierson, D. S.; Flater, E. E.; Carpick, R. W. *J. Adhes. Sci. Technol.* **2005,** *19,* 291–311. doi:10.1163/1568561054352685
42. Johnson, K. L. *Contact Mechanics;* Cambridge University Press: Cambridge, 2003.
43. Syed Asif, S. A.; Wahl, K. J.; Colton, R. J.; Warren, O. L. *J. Appl. Phys.* **2001,** *90,* 1192–1200. doi:10.1063/1.1380218
44. Crozier, K. B.; Yaralioglu, G. G.; Degertekin, F. L.; Adams, J. D.; Minne, S. C.; Quate, C. F. *Appl. Phys. Lett.* **2000,** *76,* 1950–1952. doi:10.1063/1.126222
45. Carpick, R. W.; Ogletree, D. F.; Salmeron, M. *J. Colloid Interface Sci.* **1999,** *211,* 395–400. doi:10.1006/jcis.1998.6027
46. Rabe, U.; Janser, K.; Arnold, W. *Rev. Sci. Instrum.* **1996,** *67,* 3281–3293. doi:10.1063/1.1147409
47. Turner, J. A.; Hirsekorn, S.; Rabe, U.; Arnold, W. *J. Appl. Phys.* **1997,** *82,* 966–979. doi:10.1063/1.365935
48. Manfred, R. Studying the Mechanics of Cellular Processes by Atomic Force Microscopy. In *Methods in Cell Biology;* Li, W. Y.; Dennis, E. D., Eds.; Academic Press, 2007; pp 347–372.
49. Basak, S.; Raman, A.; Garimella, S. V. *J. Appl. Phys.* **2006,** *99,* 114906–114915. doi:10.1063/1.2202232
50. Sahin, O.; Atalar, A. *Appl. Phys. Lett.* **2001,** *79,* 4455–4457. doi:10.1063/1.1429296
51. Cleveland, J. P.; Anczykowski, B.; Schmid, A. E.; Elings, V. B. *Appl. Phys. Lett.* **1998,** *72,* 2613–2615. doi:10.1063/1.121434
52. Kiridena, W.; Jain, V.; Kuo, P. K.; Liu, G.-y. *Surf. Interface Anal.* **1997,** *25,* 383–389. doi:10.1002/(SICI)1096-9918(199706)25:6<383::AID-SIA246>3.0.CO;2-S
53. Rabe, U.; Amelio, S.; Kopycinska, M.; Hirsekorn, S.; Kempf, M.; Göken, M.; Arnold, W. *Surf. Interface Anal.* **2002,** *33,* 65–70. doi:10.1002/sia.1163
54. Myers, J. K.; Oas, T. G. *Nat. Struct. Mol. Biol.* **2001,** *8,* 552–558. doi:10.1038/88626
55. Xu, S.; Laibinis, P. E.; Liu, G.-y. *J. Am. Chem. Soc.* **1998,** *120,* 9356–9361. doi:10.1021/ja981938j
56. Poirier, G. E.; Pylant, E. D. *Science* **1996,** *272,* 1145–1148. doi:10.1126/science.272.5265.1145
57. Poirier, G. E. *Chem. Rev.* **1997,** *97,* 1117–1128. doi:10.1021/cr960074m
58. Peterlinz, K. A.; Georgiadis, R. *Langmuir* **1996,** *12,* 4731–4740. doi:10.1021/la9508452
59. Rodahl, M.; Höök, F.; Fredriksson, C.; Keller, C. A.; Krozer, A.; Brzezinski, P.; Voinova, M.; Kasemo, B. *Faraday Discuss.* **1997,** *107,* 229–246. doi:10.1039/a703137h
60. Keller, C. A.; Kasemo, B. *Biophys. J.* **1998,** *75,* 1397–1402. doi:10.1016/S0006-3495(98)74057-3
61. Karpovich, D. S.; Blanchard, G. J. *Langmuir* **1994,** *10,* 3315–3322. doi:10.1021/la00021a066
62. Porter, M. D.; Bright, T. B.; Allara, D. L.; Chidsey, C. E. D. *J. Am. Chem. Soc.* **1987,** *109,* 3559–3568. doi:10.1021/ja00246a011
63. Yu, J.-J.; Ngunjiri, J. N.; Kelley, A. T.; Garno, J. C. *Langmuir* **2008,** *24,* 11661–11668. doi:10.1021/la802235c

64. Noy, A.; Frisbie, C. D.; Rozsnyai, L. F.; Wrighton, M. S.; Lieber, C. M. *J. Am. Chem. Soc.* **1995,** *117,* 7943–7951. doi:10.1021/ja00135a012
65. Parlak, Z.; Degertekin, F. L. *Rev. Sci. Instrum.* **2011,** *82,* 013703–013706. doi:10.1063/1.3514099
66. Engelkes, V. B.; Frisbie, C. D. *J. Phys. Chem. B* **2006,** *110,* 10011–10020. doi:10.1021/jp055567m
67. Henda, R.; Grunze, M.; Pertsin, A. J. *Tribol. Lett.* **1998,** *5,* 191–195. doi:10.1023/A:1019141708230
68. DelRio, F. W.; Jaye, C.; Fischer, D. A.; Cook, R. F. *Appl. Phys. Lett.* **2009,** *94,* 131909–131911. doi:10.1063/1.3111440
69. Camillone, N., III; Leung, T. Y. B.; Schwartz, P.; Eisenberger, P.; Scoles, G. *Langmuir* **1996,** *12,* 2737–2746. doi:10.1021/la951097j
70. Kawasaki, M.; Sato, T.; Tanaka, T.; Takao, K. *Langmuir* **2000,** *16,* 1719–1728. doi:10.1021/la990310z
71. Dannenberger, O.; Buck, M.; Grunze, M. *J. Phys. Chem. B* **1999,** *103,* 2202–2213. doi:10.1021/jp983433l
72. Maivald, P.; Butt, H. J.; Gould, S. A. C.; Prater, C. B.; Drake, B.; Gurley, J. A.; Elings, V. B.; Hansma, P. K. *Nanotechnology* **1991,** *2,* 103–106. doi:10.1088/0957-4484/2/2/004

License and Terms

Beilstein Journal
of Nanotechnology

Polymer blend lithography: A versatile method to fabricate nanopatterned self-assembled monolayers

Cheng Huang[1,2,3], Markus Moosmann[1,2], Jiehong Jin[1,2], Tobias Heiler[1,2],
Stefan Walheim*[1,2] and Thomas Schimmel[1,2]

Full Research Paper

Open Access

Address:
[1]Institute of Nanotechnology (INT), Karlsruhe Institute of Technology (KIT), 76021 Karlsruhe, Germany, [2]Institute of Applied Physics and Center for Functional Nanostructures (CFN), Karlsruhe Institute of Technology (KIT), 76128 Karlsruhe, Germany and [3]Joint Research Laboratory Nanomaterials Karlsruhe Institute of Technology (KIT)/Darmstadt University of Technology, 64287 Darmstadt, Germany

Email:
Stefan Walheim* - stefan.walheim@kit.edu

* Corresponding author

Keywords:
breath figure; nanopatterned template; polymer blend lithography (PBL); self-assembled monolayer (SAM); self assembly; spin coating; vapor phase

Beilstein J. Nanotechnol. **2012,** *3,* 620–628.
doi:10.3762/bjnano.3.71

Received: 17 February 2012
Accepted: 09 August 2012
Published: 04 September 2012

This article is part of the Thematic Series "Self-assembly at solid surfaces".

Guest Editors: S. R. Cohen and J. Sagiv

Abstract

A rapid and cost-effective lithographic method, polymer blend lithography (PBL), is reported to produce patterned self-assembled monolayers (SAM) on solid substrates featuring two or three different chemical functionalities. For the pattern generation we use the phase separation of two immiscible polymers in a blend solution during a spin-coating process. By controlling the spin-coating parameters and conditions, including the ambient atmosphere (humidity), the molar mass of the polystyrene (PS) and poly(methyl methacrylate) (PMMA), and the mass ratio between the two polymers in the blend solution, the formation of a purely lateral morphology (PS islands standing on the substrate while isolated in the PMMA matrix) can be reproducibly induced. Either of the formed phases (PS or PMMA) can be selectively dissolved afterwards, and the remaining phase can be used as a lift-off mask for the formation of a nanopatterned functional silane monolayer. This "monolayer copy" of the polymer phase morphology has a topographic contrast of about 1.3 nm. A demonstration of tuning of the PS island diameter is given by changing the molar mass of PS. Moreover, polymer blend lithography can provide the possibility of fabricating a surface with three different chemical components: This is demonstrated by inducing breath figures (evaporated condensed entity) at higher humidity during the spin-coating process. Here we demonstrate the formation of a lateral pattern consisting of regions covered with 1*H*,1*H*,2*H*,2*H*-perfluorodecyltrichlorosilane (FDTS) and (3-aminopropyl)triethoxysilane (APTES), and at the same time featuring regions of bare SiO_x. The patterning process could be applied even on meter-sized substrates with various functional SAM molecules, making this process suitable for the rapid preparation of quasi two-dimensional nanopatterned functional substrates, e.g., for the template-controlled growth of ZnO nanostructures [1].

Introduction

Self-assembled monolayers (SAMs) are well-known and have been intensively studied for many years, partly because of their interesting properties and partly because of interesting perspectives for potential applications as functional, ultrathin coatings [2-5]. Due to their functionality SAMs play an important role for the construction of sensors [6,7] or, e.g., the controlling of cell adhesion [8]. Patterning of self-assembled monolayers on the nanometer scale is easily performed by sequential lithographic techniques that are well-established in the literature.

Electron beam lithography allows the desorption or destruction of molecules of a SAM layer, line by line [9,10]. Advanced scanning force microscopy (SFM) techniques allow not only the imaging of the topography of surfaces but also the spatially resolved study of surface properties, such as the electrical, elastic, tribological and wear properties [11-23]. At the same time, scanning-force-microscopy-based lithographic techniques allow the structuring and patterning of surfaces with a lateral resolution down to the nanometer scale [24-30]. The advantage of techniques such as electron beam lithography or SFM-based lithography is their high lateral resolution and their reproducibility; their major disadvantage is the fact that they rely on sequential writing processes, which are very time consuming and require expensive equipment. For patterning larger areas on the nanometer scale, e.g., for the fabrication of nanopatterned, biofunctional templates, easy-to-use, cheap and fast techniques allowing the parallel fabrication of billions of nanostructures are required.

Phase separation of binary polymer blend solutions during a spin-coating process produces nano- and micropatterns on large areas in a fast and scalable fashion. This phase separation has been intensively studied over the past two decades and allows the formation of complex layered or lateral micro- or nanoscale structures [31-38]. These structures can be used for many applications, such as antireflection coatings [39], photovoltaic devices [40,41], organic light-emitting diodes (OLED) [42-44] and more. Polymer phase separation in thin films can be obtained by methods such as spin coating [31] and Langmuir–Schaefer deposition [45]. In the case of the spin-coating technique it is possible to guide the morphogenesis by employing a prepatterned solid template in order to form layout-defined structures [46-48]. However, so far there is no direct way to use the resulting polymer blend film as a lithographic mask, because the formed structure contains both lateral and layered phase separations [49-51]. Special techniques, such as UV curing have to be combined to make the film ready for lithographic applications [52,53]. Zemla et al. [52] describe a technique where after cross-linking one polymer, the other one is removed, and a protein is adsorbed at the free surface areas. The second polymer, however, cannot be dissolved due to the cross-linking and remains on the substrate. Kawamura et al. [53] use the difference in resistance to photo-etching between the two polymers in the blend to remove the component with less stability under photo-irradiation. The remaining micropatterned polymer layer has a thickness of about 3 nm, albeit without a well-defined surface chemistry.

Here, we are aiming for a lateral polymer phase morphology that can be completely removed by a selective solvent to make the substrate available for well-defined chemical surface modification. This can be achieved by inserting a silane SAM, which then exposes a functional group. The preparation process of the SAM should not affect the remaining polymer mask, such that it can protect the substrate during the procedure and can be removed afterwards. For the spin-coating of polymer blend films, there are many parameters and conditions, such as the concentration of the polymer solution, the spin rate, and the surface property of the substrate, among others, that affect the final morphology of the polymer blend film. Some examples of both the influence of the substrate [54-56] and the solution parameters [49,54,57,58] can be found in the recent literature. We found that the formed polymer blend structures in our case are also strongly dependent upon the relative humidity during the demixing. The relative humidity influences the interaction of the two polymer phases and the affinity of the polymers to the substrate [59]. This effect has to be distinguished from the formation of so-called breath figures, which are formed at high relative humidity (over 60%) due to water condensation on the evaporatively cooled polymer solution [60,61]. The breath figure technique can be applied to generate nearly hexagonal arrays of holes [61] or for the fabrication of 3-D structures [62]. Water droplets are introduced into the polymer solution film and leave behind holes after the film has solidified. These breath figure structures can be found both in films of one-polymer systems, such as PMMA in THF, and of polymer-blend systems.

In this article we present a method to obtain a polymer-blend film with a purely lateral phase morphology, which means that the blend separates completely into two lateral phases. The introduction of a small amount of water during the spin coating process is crucial for obtaining this purely lateral morphology. Either of the two different polymers can be dissolved independently afterwards by using a selective solvent. The remaining morphology is later on applied directly as a lithographic mask to fabricate nanopatterned self-assembled-monolayer (SAM) templates. Performed at higher humidity, our technique combines polymer-blend phase separation with the breath-figure formation. A three-phase lithographic mask is formed in one process step, giving the opportunity to produce a SAM template with three different chemical functionalities.

Results and Discussion

Polymer-blend lithography

The polymer-blend lithography method is demonstrated schematically in Figure 1. The most important prerequisite is to have a polymer film consisting of two immiscible phases, which are laterally separated on the substrate. Here the polymer-blend solution is prepared with PS and PMMA dissolved in methyl ethyl ketone (MEK). As schematically shown in Figure 1, it is found that this system decays into a purely lateral phase morphology during spin-casting of the solution at a moderate humidity, which means that both phases extend from the free-air interface down to the silicon oxide substrate. This is by far not the common case. In most cases of polymer-blend solutions a mixture of lateral structures and a vertical phase morphology is formed. The result is also found for the PS + PMMA blend in MEK, if spin cast in a dry atmosphere. Immiscibility allows the possibility of selectively dissolving one component, which is on one hand important if the other component is desired to be used as a lift-off mask. The immiscibility, on the other hand, has the consequence that one component has a higher affinity to the substrate (hydrophilic) than the other one, which prefers the free-air interface (hydrophobic). The resulting morphology is a layered situation in which the hydrophilic polymer wets the substrate while the hydrophobic most likely wets the free polymer–air interface. The upper layer becomes unstable and dewets such that droplets are formed. Therefore the final morphology is usually one phase “floating” in a lake of the other one. After the selective dissolution of the “floating” phase there is still a thin film of the other polymer in every hole, which is not the desired situation for polymer-blend lithography.

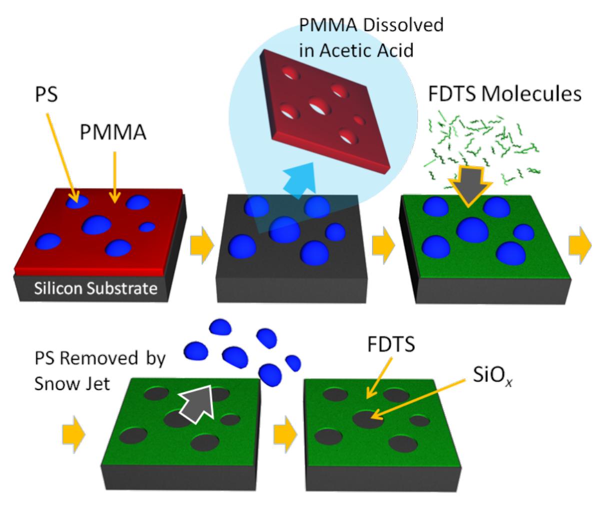

Figure 1: Schematic drawing of the polymer-blend lithography process. After spin-coating in a controlled atmosphere, a purely lateral morphology of PS droplets (blue) in a PMMA matrix (red) is formed. After the dissolution of PMMA in acetic acid, the PS droplets remain and can be used as a mask for the deposition of a fluorine-terminated SAM (FDTS/green). By a snow-jet treatment the PS droplets are selectively removed, and a patterned SAM is formed.

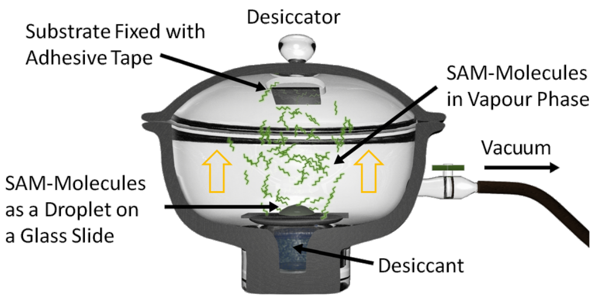

Figure 2: Preparation of a densely packed SAM, performed in the vapor phase within a desiccator.

Here we present a recipe for how to create a purely lateral morphology without this drawback. The morphogenesis of this structure will be the focus of a forthcoming publication. With the structure generated by using the given recipe it is possible to remove one component (e.g., PMMA) and to deposit a SAM on the completely freed silicon oxide substrate areas with very high reproducibility. After the silane molecules have bonded covalently, the remaining polymer phase (PS) is removed. The deposition of the SAM is performed by vapor-phase deposition [54] in a vacuum desiccator (Figure 2). During deposition, the samples are mounted face down on the lid of the desiccator. After the SAM is formed, the sample is removed from the vessel and the remaining polymer is removed by snow-jet treatment. Consequently a “monolayer copy” of the original phase morphology is left with a topographic contrast of the height of the SAM, usually in the range of 1–2 nm, depending on the type of molecules used. By the choice of the SAM molecules the desired chemical surface functionality (functional group) can be defined.

Two-phase templates

By means of a spin-coating process of a polymer-blend solution at a humidity of 45%, a purely laterally phase-separated film consisting of the two polymer components is produced (Figure 3a). In Figure 3b an SEM image of a polymer-blend mask rinsed in acetic acid is shown (the image was taken with a tilted angle of around 45°). After this treatment only the PS islands remain on the silicon substrate. The PMMA layer (marked red in Figure 3a) has been completely removed. After the deposition of the 1*H*,1*H*,2*H*,2*H*-perfluorodecyltrichlorosilane (FDTS) SAM, the polymer islands were removed by a snow-jet treatment. In Figure 3c an AFM topography image of

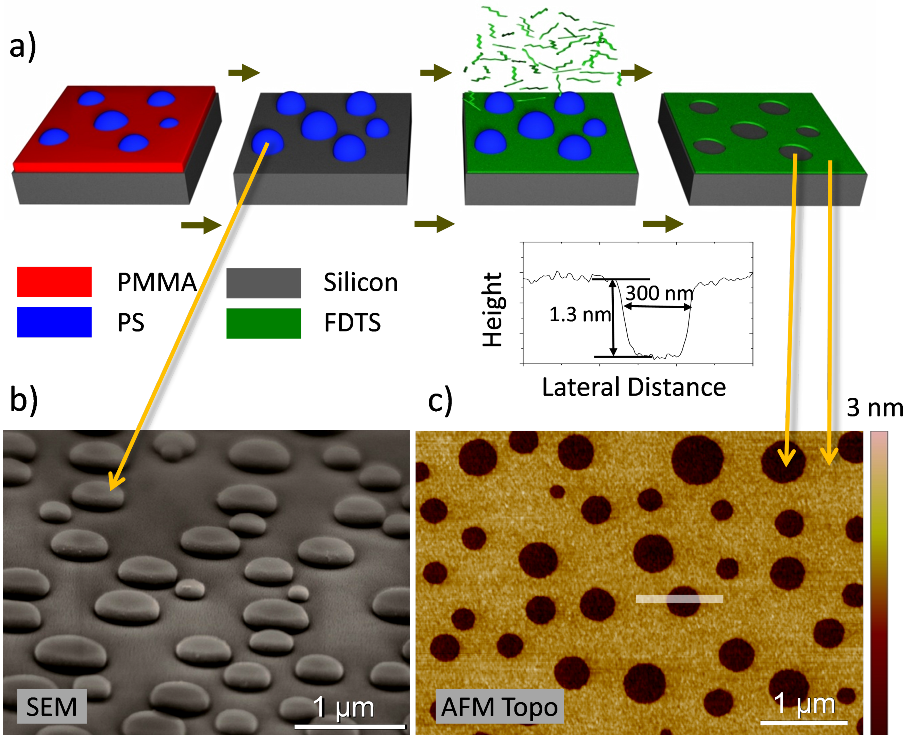

Figure 3: Fabrication of a two-phase SAM template spin-cast at a humidity of 45%. (a) Schematic drawing of the process, silicon substrate (grey), PMMA (red), PS (blue) and FDTS (green). (b) SEM image of a polymer blend mask rinsed with acetic acid. (c) AFM image (retrace image measured in contact mode in liquid) of a two-phase SAM template. The cross section demonstrated is the average of the trace and the retrace images. The depth of the holes is 1.3 nm, independent of the intensity and the duration of the snow-jet treatment.

the remaining FDTS-SAM template is shown. Each PS island leaves behind a hole in the monomolecular layer. The average diameter of these holes is about 400 nm. The film has a topographic contrast of 1.3 nm. The depth of the holes is independent of the intensity and the duration of the snow-jet treatment (see also Supporting Information File 1). This indicates that the FDTS monolayer is well bound to the substrate and that the lift-off of the PS islands is complete.

Island-size tailoring

The dependence of the PS island diameter upon the polymerization degree of PS is shown in Figure 4. It can clearly be seen that the average diameter and the width of the diameter distribution decrease with the reducing molar mass of the polymer. When PS of 9.58 kg/mol is used, the average diameter of the islands is about 90 nm, and a very narrow diameter distribution from about 50 to 150 nm is obtained. For PS of 248 kg/mol an average diameter of about 500 nm and a wider diameter distribution from about 200 to 800 nm is found. A higher molar mass of the polymer increases the viscosity of the solution and consequently increases the film thickness and at the same time the height of the PS islands. All of these islands are formed during the spin-coating process in less than two seconds. The film drying kinetics is measured by an in situ reflectometry technique performed with our laser setup as described elsewhere [41]. Increased film thickness leads to a longer drying time, a larger domain size, and a higher PS domain height, as clearly seen in Figure 4b. This result shows that the molecular weight can be used as a parameter to adjust the domain size in the polymer-blend lithography method. Besides the main structure size, which can be reliably controlled, there are always some small structures observed. In the histograms shown in Figure 4c there is a detectable tail down to 90 nm for all molecular weights. This tail is most probably a signature of a secondary phase separation during the complex structure-formation process.

Three-phase templates

For a range of relative humidity from 50 to 65%, the resulting phase morphology is different from the situation shown in Figure 3 (45% humidity). As can be seen in Figure 5b, holes in the polymer film can be observed directly after spin coating. Besides these open holes, there are smaller depressions and embedded PS droplets visible at the surface. Due to the rapid evaporation of the solvent during the spin-coating process the sample surface is cooled down. At this highly increased

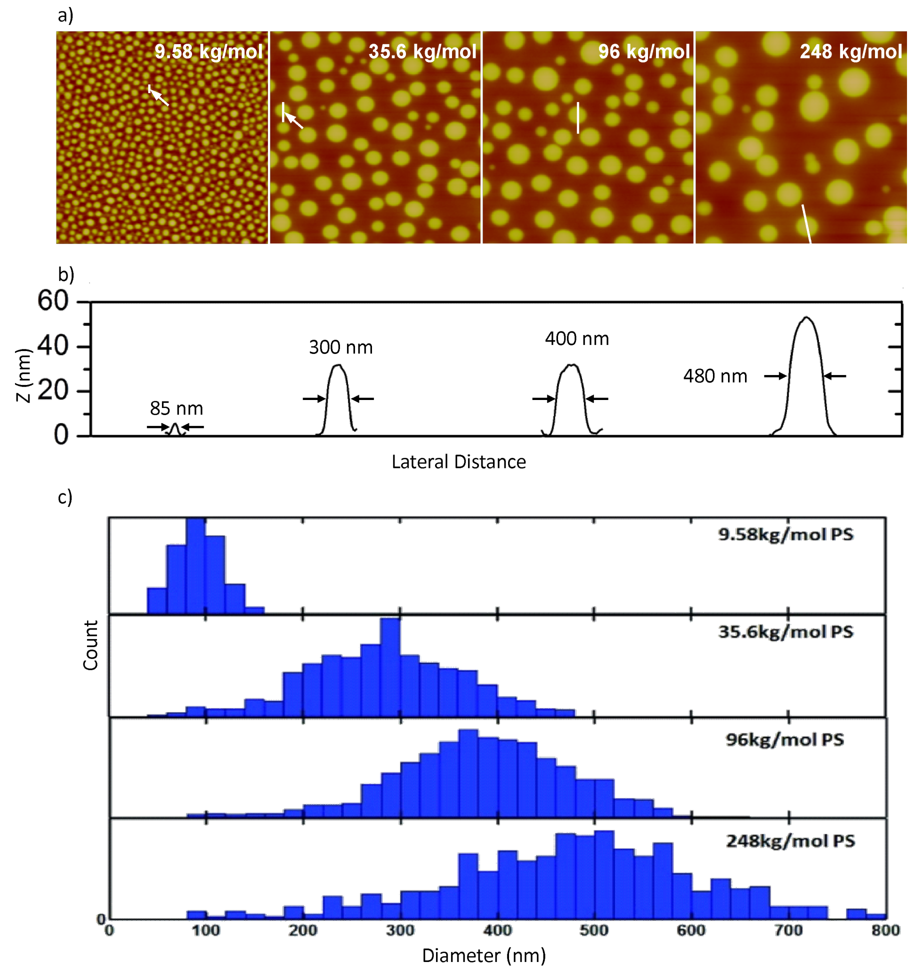

Figure 4: Dependence of the PS island diameter and height by varying the molar mass of PS. (a) AFM images of a polymer blend film formed from various PS samples with molar masses of 9.58, 35.6, 96 and 248 kg/mol. The scan areas of all AFM images are 5 × 5 µm^2. (b) Height profiles of selected PS islands of average size (height above the PMMA matrix level). (c) Distribution of the diameters of PS islands of various molar masses.

humidity the sample surface reaches the dew point. The result is that water condenses and then forms droplets, which leave holes in the polymer film after it is solidified. The small depressions are most likely relics of smaller water droplets that did not reach the silicon substrate. Hence, the result of the spin coating process is a perforated PMMA layer with embedded PS droplets. This provides the opportunity to design a three-phase pattern as described below.

The (water) holes can directly be filled with a silane monolayer. Here we used the (3-aminopropyl)triethoxysilane (APTES) molecule exposing an amino-functional group. After removal of the PMMA layer with acetic acid, the CF_3-terminated FDTS-SAM was deposited in the vapor phase. Next, we removed polystyrene by snow-jet treatment as described before. The FDTS as well as the APTES-SAMs withstand this cleaning procedure without any detectable change at their surface, as can be seen in Figure 5c. The three-phase SAM template consisting of APTES, FDTS and silicon oxide pattern elements is fabricated with a topographic contrast of approximately 1.3 nm. The roughness of 0.2 nm remaining in the SiO_x regions is in the same range as the one of the original Si wafer. The height of the APTES-SAM was found to be 0.7 nm, measured in contact-mode AFM in liquid. Thus, the APTES regions look like half-filled holes (Figure 5c).

Perspectives

These patterned two-phase or three-phase surfaces, which show a high chemical contrast and at the same time an extremely flat topography, make them an ideal template or platform for constructive lithography [1], cell adhesion studies, or the study of other template-induced phenomena. The FDTS-SAM could be replaced by other silanes, such as octadecyltrichlorosilane (OTS) or polyethylene glycol (PEG) silane, for desired applications [63,64]. The bare silicon surface at the bottom of the holes could be functionalized with another silane for certain applica-

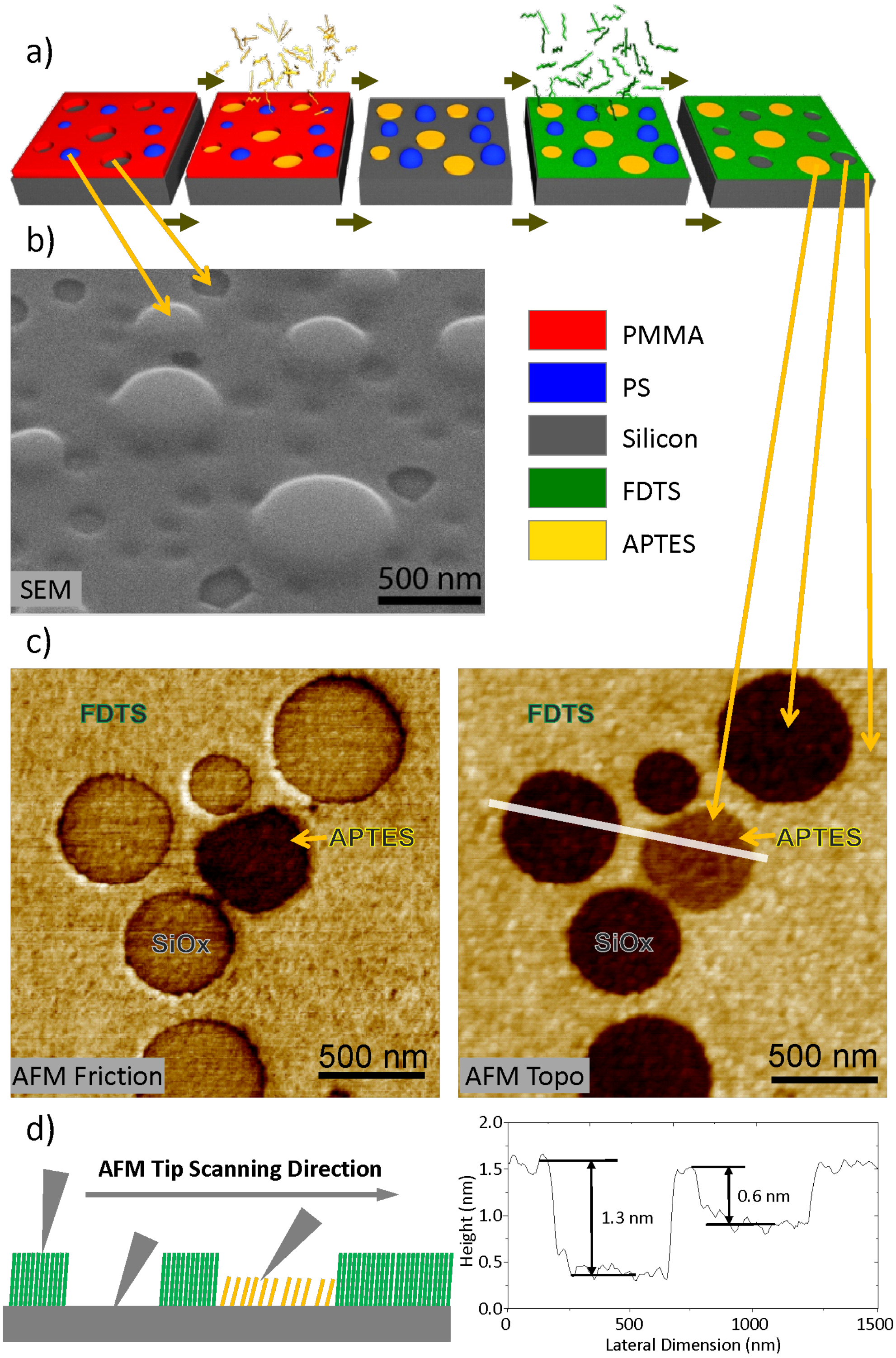

Figure 5: Fabrication of a three-phase SAM template spin cast at the humidity of 65%. (a) Schematic drawing of the process, silicon substrate (grey), PMMA (red), PS (blue), FDTS (green) and APTES (yellow). (b) SEM image of a polymer-blend mask with breath figures. (c) AFM images (both retrace images) of a three-phase SAM template. The cross section shown here is the average of the trace and the retrace images. (d) Schematic drawing of the AFM friction imaging. The first SAM that was deposited is APTES. Its height is half the height of the FDTS-SAM, which was complemented after the PMMA mask had been removed. Finally, after the removal of the PS islands the remaining holes have a depth of 1.3 nm, which is independent of the intensity and duration of the snow-jet treatment.

tions. For example, in our recent publication the holes, filled with APTES, were used for the growth of ZnO layers [1] by chemical bath deposition. Structured and nonstructured ZnO layers are used, e.g., in gas-sensor applications [65-67]. Silane-based follow-up reactions can be used to produce silane multilayers [68], which only grow in the predefined areas. This type of SAM template has also potential applications for the selective growth of titanium oxide or graphene on surfaces [69,70], or in cell-adhesion studies [64]. Here without any further treatment we have generated an amphiphilic surface, featuring at the same time both hydrophobic (FDTS) and hydrophilic (APTES or SiO_x) areas. The versatile and fast preparation technique makes this approach attractive for many applications of such ultraflat nanopatterned surfaces.

Conclusion

Polymer-blend lithography (PBL) makes use of lateral structure formation during the spin-coating process of a polymer-blend film. The structures are transformed into a patterned SAM with two or three different chemical functionalities by a lift-off process. PBL starts with spin-casting of a polymer blend (e.g., PS/PMMA in MEK) onto a substrate at a defined relative humidity. By selecting adequate conditions, a polymer blend film with a purely lateral phase morphology is formed. After the selective dissolution of one of the polymer components, the remaining second polymer component can be directly used as a lithographic mask. This lithographic mask, in turn, can be removed by snow-jet lift-off after deposition of a silane monolayer (SAM) on the unprotected areas in the vapor phase.

For the examples demonstrated, the fabricated nanopatterned template shows a chemical contrast between the functional group of the silane SAM and the bare silicon oxide. This quasi two-dimensional pattern has about 1 nm topography. The bare silicon oxide surface can be filled with another silane SAM for specific applications. The lateral structure size within the nanoscale pattern is determined by the diameter of the PS islands formed during the spin-coating process. The mean value of the statistically distributed diameters of PS islands can be varied between 90 and 500 nm by changing the molar mass of the PS moiety. Combined with breath figures, this lithographic method can even be used for the fabrication of three-component templates. Here we use it for the patterning of the CF_3-terminated FDTS monolayer and the amino-terminated APTES monolayer, and leave at the same time uncovered regions of bare silicon oxide on the substrates.

The quasi two-dimensional chemical patterns open the potential for their application as templates for the subsequent self-assembly of inorganic materials, for cell-adhesion studies, for laterally controlled dewetting, or for constructive lithography. The extreme flatness (rms roughness below 0.5 nm) allows for a highly sensitive monitoring of growth processes by AFM. Together with the chemical variability, polymer-blend lithography (PBL) can become an important tool for studying surface-initiated processes.

Experimental

Polymer solution: Poly(methyl methacrylate) (PMMA, M_w = 9.59 kg/mol, PDI = 1.05) and polystyrene (PS, M_w = 96 kg/mol, PDI = 1.04) were purchased from Polymer Standards Service GmbH and dissolved directly in methyl ethyl ketone (MEK, Aldrich). The total concentration of the two polymers was 15 mg/mL and the mass ratio between PS and PMMA was 3:7. To demonstrate the tuning of the diameter of PS islands, a set of polymer solutions were made with various PS molar masses, i.e., 9.58, 35.6, 96 and 248 kg/mol. All other parameters were kept constant.

Cleaning of Si substrates and SAM templates: Silicon substrates were used as delivered with their native oxide layer. The substrates and the SAM templates were cleaned by the snow-jet method [71]: The wafers were exposed to a jet of CO_2 ice crystals, which were produced by expanding CO_2 through a nozzle (Snow Jet model K4-05, Tectra Frankfurt/Germany). In this way, surface contaminants are removed either by mechanical impact or by dissolution in CO_2.

Preparation of a polymer-blend lithographic mask: The polymer blend films were spin-cast at a speed of ca. 1500 rpm onto silicon substrates cleaned by snow-jet treatment (at least 20 seconds for a 2 cm × 2 cm substrate). For the two-phase SAM templates, the relative humidity was set to 45% during the spin-coating process and for the three-phase templates to 65%. The humidity was controlled by venting the chamber (about 1 L volume) with a mixture of nitrogen and water-saturated nitrogen (total flow rate approximately 40 sccm). The humidity in the chamber was measured by a hygrometer (Testo 635).

Fabrication of SAM templates: For the two-phase template the PMMA was selectively dissolved by acetic acid, as shown in Figure 1a and Figure 1b. Samples were rinsed in the acid and constantly moved for 30 s. The samples were then rinsed two times with acetic acid and dried in a stream of nitrogen. The silane SAM was deposited overnight in a desiccator containing two droplets of 1*H*,1*H*,2*H*,2*H*-perfluorodecyltrichlorosilane (FDTS, Aldrich) and evacuated to a pressure of 50 mbar. The PS islands were later removed by snow-jet blasts. For sufficient impact it is important that the CO_2 gas cylinder is at room temperature and has a proper filling level. The polymer mask can be alternatively dissolved in THF, following the protocol described above for acetic acid. For the three-phase template the

(3-aminopropyl)triethoxysilane (APTES, Aldrich) SAM was deposited onto the silicon surface inside the holes of the lithographic mask in the gas phase, shown in Figure 5a and Figure 5b. The PMMA was removed by acetic acid, and the freed silicon surface was covered then by a different silane molecule, FDTS with the same deposition method as APTES. The PS islands were removed by snow-jet treatment as well. Instead of by using a snow jet, the polymer mask can also be dissolved by an organic solvent, e.g., tetrahydrofuran.

Sample characterization: The polymer blend masks were characterized by atomic force microscopy (AFM) and scanning electron microscopy (SEM). The AFM images were made with a commercial multimode system (DI Multimode IIIa) in tapping mode. The samples were scanned under ambient conditions immediately after they had been removed from the solution. SEM images were taken at 2 kV with a LEO 1530 SEM by using a secondary electron detector. All AFM images of the SAM templates were taken in contact mode in the liquid cell filled with demineralized water (Bruker Dimension Icon-PT).

Supporting Information

Supporting Information File 1

Snow-jet treatment of FDTS-SAM.
[http://www.beilstein-journals.org/bjnano/content/supplementary/2190-4286-3-71-S1.pdf]

Acknowledgements

This work was supported by the Deutsche Forschungsgemeinschaft (DFG) within the Center for Functional Nanostructures (CFN) and by the Baden-Württemberg Stiftung within the Network of Excellence “Functional Nanostructures”.

References

1. Bauermann, L. P.; Gerstel, P.; Bill, J.; Walheim, S.; Huang, C.; Pfeifer, J.; Schimmel, T. *Langmuir* **2010,** *26,* 3774–3778. doi:10.1021/la903636k
2. Sagiv, J. *J. Am. Chem. Soc.* **1980,** *102,* 92–98. doi:10.1021/ja00521a016
3. Sabatani, E.; Rubinstein, I.; Maoz, R.; Sagiv, J. *J. Electroanal. Chem. Interfacial Electrochem.* **1987,** *219,* 365–371. doi:10.1016/0022-0728(87)85054-4
4. Ulman, A. *Chem. Rev.* **1996,** *96,* 1533–1554. doi:10.1021/cr9502357
5. Zeira, A.; Berson, J.; Feldman, I.; Maoz, R.; Sagiv, J. *Langmuir* **2011,** *27,* 8562–8575. doi:10.1021/la2009946
6. Chaki, N. K.; Vijayamohanan, K. *Biosens. Bioelectron.* **2002,** *17,* 1–12. doi:10.1016/S0956-5663(01)00277-9
7. Weddeman, A.; Ennen, I.; Regtmeier, A.; Albon, C.; Wolff, A.; Eckstädt, K.; Mill, N.; Peter, M. K.-H.; Mattay, J.; Plattner, C.; Sewald, N.; Hütten, A. *Beilstein J. Nanotechnol.* **2010,** *1,* 75–93. doi:10.3762/bjnano.1.10
8. Faucheux, N.; Schweiss, R.; Luetzow, K.; Werner, C.; Groth, T. *Biomaterials* **2004,** *25,* 2721–2730. doi:10.1016/j.biomaterials.2003.09.069
9. Gölzhäuser, A.; Eck, W.; Geyer, W.; Stadler, V.; Weimann, T.; Hinze, P.; Grunze, M. *Adv. Mater.* **2001,** *13,* 803–806. doi:10.1002/1521-4095(200106)13:11%3C803::AID-ADMA806%3E3.0.CO;2-W
10. She, Z.; DiFalco, A.; Hähner, G.; Buck, M. *Beilstein J. Nanotechnol.* **2012,** *3,* 101–113. doi:10.3762/bjnano.3.11
11. García, R.; Pérez, R. *Surf. Sci. Rep.* **2002,** *47,* 197–301. doi:10.1016/S0167-5729(02)00077-8
12. Giessibl, F. J. *Rev. Mod. Phys.* **2003,** *75,* 949–983. doi:10.1103/RevModPhys.75.949
13. Merlijn van Spengen, W.; Turq, V.; Frenken, J. W. M. *Beilstein J. Nanotechnol.* **2010,** *1,* 163–171. doi:10.3762/bjnano.1.20
14. Malegori, G.; Ferrini, G. *Beilstein J. Nanotechnol.* **2010,** *1,* 172–181. doi:10.3762/bjnano.1.21
15. König, T.; Simon, G. H.; Heinke, L.; Lichtenstein, L.; Heyde, M. *Beilstein J. Nanotechnol.* **2011,** *2,* 1–14. doi:10.3762/bjnano.2.1
16. Magonov, S.; Alexander, J. *Beilstein J. Nanotechnol.* **2011,** *2,* 15–27. doi:10.3762/bjnano.2.2
17. Glatzel, T.; Zimmerli, L.; Kawai, S.; Meyer, E.; Fendt, L.-A.; Diederich, F. *Beilstein J. Nanotechnol.* **2011,** *2,* 34–39. doi:10.3762/bjnano.2.4
18. Stegemann, B.; Klemm, M.; Horn, S.; Woydt, M. *Beilstein J. Nanotechnol.* **2011,** *2,* 59–65. doi:10.3762/bjnano.2.8
19. Elias, G.; Glatzel, T.; Meyer, E.; Schwarzman, A.; Boag, A.; Rosenwaks, Y. *Beilstein J. Nanotechnol.* **2011,** *2,* 252–260. doi:10.3762/bjnano.2.29
20. Jaafar, M.; Iglesias-Freire, O.; Serrano-Ramón, L.; Ibarra, M. R.; de Teresa, J. M.; Asenjo, A. *Beilstein J. Nanotechnol.* **2011,** *2,* 552–560. doi:10.3762/bjnano.2.59
21. Stadler, J.; Schmid, T.; Opilik, L.; Kuhn, P.; Dittrich, P. S.; Zenobi, R. *Beilstein J. Nanotechnol.* **2011,** *2,* 509–515. doi:10.3762/bjnano.2.55
22. Zhang, X.; Beyer, A.; Gölzhäuser, A. *Beilstein J. Nanotechnol.* **2011,** *2,* 826–833. doi:10.3762/bjnano.2.92
23. Tirosh, E.; Benassi, E.; Pipolo, S.; Mayor, M.; Valášek, M.; Frydman, V.; Corni, S.; Cohen, S. R. *Beilstein J. Nanotechnol.* **2011,** *2,* 834–844. doi:10.3762/bjnano.2.93
24. Xu, S.; Liu, G.-y. *Langmuir* **1997,** *13,* 127–129. doi:10.1021/la962029f
25. Piner, R. D.; Zhu, J.; Xu, F.; Hong, S.; Mirkin, C. A. *Science* **1999,** *283,* 661–663. doi:10.1126/science.283.5402.661
26. Salaita, K.; Wang, Y.; Mirkin, C. A. *Nat. Nanotechnol.* **2007,** *2,* 145–155. doi:10.1038/nnano.2007.39
27. Gnecco, E. *Beilstein J. Nanotechnol.* **2010,** *1,* 158–162. doi:10.3762/bjnano.1.19
28. Garcia, R.; Martinez, R. V.; Martinez, J. *Chem. Soc. Rev.* **2006,** *35,* 29–38. doi:10.1039/b501599p
29. Darwich, S.; Mougin, K.; Rao, A.; Gnecco, E.; Jayaraman, S.; Haidara, H. *Beilstein J. Nanotechnol.* **2011,** *2,* 85–98. doi:10.3762/bjnano.2.10
30. Obermair, C.; Wagner, A.; Schimmel, T. *Beilstein J. Nanotechnol.* **2011,** *2,* 659–664. doi:10.3762/bjnano.2.70
31. Walheim, S.; Böltau, M.; Mlynek, J.; Krausch, G.; Steiner, U. *Macromolecules* **1997,** *30,* 4995–5003. doi:10.1021/ma9619288
32. Tanaka, K.; Takahara, A.; Kajiyama, T. *Macromolecules* **1996,** *29,* 3232. doi:10.1021/ma951140+
33. Genzer, J.; Kramer, E. J. *Phys. Rev. Lett.* **1997,** *78,* 4946–4949. doi:10.1103/PhysRevLett.78.4946

34. Mansky, P.; Liu, Y.; Huang, E.; Russell, T. P.; Hawker, C. *Science* **1997,** *275,* 1458–1460. doi:10.1126/science.275.5305.1458
35. Reiter, G. *Phys. Rev. Lett.* **1992,** *68,* 75–78. doi:10.1103/PhysRevLett.68.75
36. Reiter, G. *Langmuir* **1993,** *9,* 1344–1351. doi:10.1021/la00029a031
37. Kargupta, K.; Sharma, A. *Phys. Rev. Lett.* **2001,** *86,* 4536–4539. doi:10.1103/PhysRevLett.86.4536
38. Budkowski, A.; Bernasik, A.; Cyganik, P.; Raczkowska, J.; Penc, B.; Bergues, B.; Kowalski, K.; Rysz, J.; Janik, J. *Macromolecules* **2003,** *36,* 4060–4067. doi:10.1021/ma0208943
39. Walheim, S.; Schäffer, E.; Mlynek, J.; Steiner, U. *Science* **1999,** *283,* 520–522. doi:10.1126/science.283.5401.520
40. Chen, L.-M.; Xu, Z.; Hong, Z.; Yang, Y. *J. Mater. Chem.* **2010,** *20,* 2575–2598. doi:10.1039/b925382c
41. Schmidt-Hansberg, B.; Klein, M. F. G.; Peters, K.; Buss, F.; Pfeifer, J.; Walheim, S.; Colsmann, A.; Lemmer, U.; Scharfer, P.; Schabel, W. *J. Appl. Phys.* **2009,** *106,* 124501. doi:10.1063/1.3270402
42. Yim, K.-H.; Doherty, W. J.; Salaneck, W. R.; Murphy, C. E.; Friend, R. H.; Kim, J.-S. *Nano Lett.* **2010,** *10,* 385–392. doi:10.1021/nl9025105
43. Köhnen, A.; Riegel, N.; Müller, D. C.; Meerholz, K. *Adv. Mater.* **2011,** *23,* 4301–4305. doi:10.1002/adma.201102368
44. Schmidt-Hansberg, B.; Baunach, M.; Krenn, J.; Walheim, S.; Lemmer, U.; Scharfer, P.; Schabel, W. *Chem. Eng. Process.* **2011,** *50,* 509–515. doi:10.1016/j.cep.2010.12.012
45. Pohjakallio, M.; Aho, T.; Kontturi, K.; Kontturi, E. *Soft Matter* **2011,** *7,* 743–748. doi:10.1039/c0sm00360c
46. Böltau, M.; Walheim, S.; Mlynek, J.; Krausch, G.; Steiner, U. *Nature* **1998,** *391,* 877–879. doi:10.1038/36075
47. Andrew, P.; Huck, W. T. S. *Soft Matter* **2007,** *3,* 230–237. doi:10.1039/b613593e
48. Cui, L.; Zhang, Z.; Li, X.; Han, Y. *Polym. Bull.* **2005,** *55,* 131–140. doi:10.1007/s00289-005-0404-3
49. Ma, M.; He, Z.; Yang, J.; Wang, Q.; Chen, F.; Wang, K.; Zhang, Q.; Deng, H.; Fu, Q. *Langmuir* **2011,** *27,* 1056–1063. doi:10.1021/la104003p
50. Thickett, S. C.; Harris, A.; Neto, C. *Langmuir* **2010,** *26,* 15989–15999. doi:10.1021/la103078k
51. Heriot, S. Y.; Jones, R. A. L. *Nat. Mater.* **2005,** *4,* 782–786. doi:10.1038/nmat1476
52. Zemła, J.; Lekka, M.; Raczkowska, J.; Bernasik, A.; Rysz, J.; Budkowski, A. *Biomacromolecules* **2009,** *10,* 2101–2109. doi:10.1021/bm900598s
53. Kawamura, K.; Yokoi, K.; Fujita, M. *Chem. Lett.* **2010,** *39,* 254–256. doi:10.1246/cl.2010.254
54. Fang, L.; Wei, M.; Barry, C.; Mead, J. *Macromolecules* **2010,** *43,* 9747–9753. doi:10.1021/ma1017082
55. Ferrari, E.; Fabbri, P.; Pilati, F. *Langmuir* **2011,** *27,* 1874–1881. doi:10.1021/la104500j
56. Ahn, D. U.; Ding, Y. *Soft Matter* **2011,** *7,* 3794–3800. doi:10.1039/c0sm01373k
57. Dunbar, A. D. F.; Mokarian-Tabari, P.; Parnell, A. J.; Martin, S. J.; Skoda, M. W. A.; Jones, R. A. L. *Eur. Phys. J. E* **2010,** *31,* 369–375. doi:10.1140/epje/i2010-10592-4
58. Wang, X.; Azimi, H.; Mack, H.-G.; Morana, M.; Egelhaaf, H.-J.; Meixner, A. J.; Zhang, D. *Small* **2011,** *7,* 2793–2800. doi:10.1002/smll.201101000
59. Geldhauser, T.; Walheim, S.; Schimmel, T.; Leiderer, P.; Boneberg, J. *Macromolecules* **2010,** *43,* 1124–1128. doi:10.1021/ma9022058
60. Gliemann, H.; Almeida, A. T.; Petri, D. F. S.; Schimmel, T. *Surf. Interface Anal.* **2007,** *39,* 1–8. doi:10.1002/sia.2339
61. Madej, W.; Budkowski, A.; Raczkowska, J.; Rysz, J. *Langmuir* **2008,** *24,* 3517–3524. doi:10.1021/la703363a
62. Chang, C.-C.; Juang, T.-Y.; Ting, W.-H.; Lin, M.-S; Yeh, C.-M.; Dai, S. A.; Suen, S.-Y.; Liu, Y.-L.; Jeng, R.-J. *Mater. Chem. Phys.* **2011,** *128,* 157–165. doi:10.1016/j.matchemphys.2011.02.068
63. Saner, C. K.; Lusker, K. L.; LeJeune, Z. M.; Serem, W. K.; Garno, J. C. *Beilstein J. Nanotechnol.* **2012,** *3,* 114–122. doi:10.3762/bjnano.3.12
64. Choi, S.-H.; Newby, B.-m. Z. *Langmuir* **2003,** *19,* 7427–7435. doi:10.1021/la035027l
65. Wan, Q.; Li, Q. H.; Chen, Y. J.; Wang, T. H.; He, X. L.; Li, J. P.; Lin, C. L. *Appl. Phys. Lett.* **2004,** *18,* 3654–3656. doi:10.1063/1.1738932
66. Chae, K.-W.; Zhang, Q.; Kim, J. S.; Jeong, Y.-H.; Cao, G. *Beilstein J. Nanotechnol.* **2010,** *1,* 128–134. doi:10.3762/bjnano.1.15
67. Waclawik, E. R.; Chang, J.; Ponzoni, A.; Concina, I.; Zappa, D.; Comini, E.; Motta, N.; Faglia, G.; Sberveglieri, G. *Beilstein J. Nanotechnol.* **2012,** *3,* 368–377. doi:10.3762/bjnano.3.43
68. Maoz, R.; Sagiv, J. *Adv. Mater.* **1998,** *10,* 580–584. doi:10.1002/(SICI)1521-4095(199805)10:8<580::AID-ADMA580>3.0.CO;2-P
69. Paz, Y. *Beilstein J. Nanotechnol.* **2011,** *2,* 845–861. doi:10.3762/bjnano.2.94
70. Wu, C.; Cheng, Q.; Sun, S.; Han, B. *Carbon* **2012,** *50,* 1083–1089. doi:10.1016/j.carbon.2011.10.017
71. Sherman, R.; Hirt, D.; Vane, R. *J. Vac. Sci. Technol., A* **1994,** *12,* 1876–1881. doi:10.1116/1.579021

License and Terms

Beilstein Journal
of Nanotechnology

Dimer/tetramer motifs determine amphiphilic hydrazine fibril structures on graphite

Loji K. Thomas[1], Nadine Diek[2], Uwe Beginn[2] and Michael Reichling*[1]

Full Research Paper

Open Access

Address:
[1]Fachbereich Physik, Universität Osnabrück, Barbarastr. 7, 49076 Osnabrück, Germany and [2]Institut für Chemie, Universität Osnabrück, Barbarastr. 7, 49076 Osnabrück, Germany

Email:
Michael Reichling* - reichling@uos.de

* Corresponding author

Keywords:
fibrils; graphite; hydrazide; hydrazine; interface; self-assembly; STM

Beilstein J. Nanotechnol. **2012,** *3,* 658–666.
doi:10.3762/bjnano.3.75

Received: 30 April 2012
Accepted: 22 August 2012
Published: 19 September 2012

This article is part of the Thematic Series "Self-assembly at solid surfaces".

Guest Editors: S. R. Cohen and J. Sagiv

Abstract

Fibril structures are produced at a solvent–graphite interface by self-assembly of custom-designed symmetric and asymmetric amphiphilic benzamide derivatives bearing C_{10} aliphatic chains. Scanning tunnelling microscopy (STM) studies reveal geometry-dependent internal structures for the elementary fibrils of the two molecules that are distinctly different from known mesophase bulk structures. The structures are described by building-block models based on hydrogen-bonded dimer and tetramer precursors of hydrazines. The closure and growth in length of building units into fibrils takes place through van der Waals forces acting between the dangling alkyl chains. The nanoscale morphology is a consequence of the basic molecular geometry, where it follows that a closure to form a fibril is not always likely for the doubly substituted hydrazine. Therefore, we also observe crystallite formation.

Introduction

One-dimensional micro- and nanostructures of organic compounds are important for solution-processable organic electronic devices [1-3], and electron transport through organic molecules is also the basis for a large number of biological processes [4]. Organogelators have a tendency to form nanofibril structures in the bulk phase and, therefore, recently aroused much interest in the context of nanoelectronics [5]. Except for biological systems, organogel structures are the only synthetic self-organized linear entities, facilitating the construction of functional arrangements up to millimetre dimensions [6]. With suitable functional moieties, they can guide ions, electrons or even photons and can serve as interconnects when integrated into electronic or bioelectronic devices [1,5,7]. Further progress in this area is mostly limited by low charge-carrier mobility and the mostly amorphous local packing. Therefore, it is essential to synthesize optimized materials, explore supramolecular routes towards new functional structures, and understand processes of structure formation at interfaces [8,9].

The knowledge about the internal structure of the columns (fibres) in bulk columnar mesophases depends mostly on X-ray techniques, which suffice for many purposes [7,10,11]. However, information in real space, as provided by scanning tunnelling microscopy (STM), offers unparalleled advantages to the synthesis chemist who strives to functionalize fibrils that are one-dimensional structures with only a few nanometres in diameter. The control of supramolecular self-assembly to achieve functional nanostructures depends on careful design at the molecular level, and elucidation of their internal structure is important in aiding the design and to increase the sophistication of the building units.

Many low-molecular-weight, wedge-shaped amphiphilic molecules are known to form columnar mesophases [3,6]. X-ray diffraction and scattering techniques have widely been used to decipher their internal molecular arrangements, which generally suggest a stacking of mesogenic "discs" leading to column formation [7,12]. We investigate the self-assembled fibril structures of two custom-designed amphiphilic gelator molecules: *N,N′*-bis[3,4-bis(decyloxy)benzoyl]hydrazine (**2CHd-10**) and [4-(decyloxy)benzoyl]hydrazine (**1CHn-10**) on the graphite (0001) surface (Figure 1 and Experimental section). As the alkyl chain length is known to influence column formation in the bulk, the length of alkyl chains for both molecules is kept identical such that the focus of the study is solely on the geometry/symmetry aspect [6]. In Figure 1, a wedge shape is shown superimposed on the molecular structure, where the amide moieties are at the tip of the wedge and the alkoxy chains at the tail. In general, the molecular geometry of the mesogens is decisive for the generation of columnar mesophases in the bulk, i.e., the mesogens should be wedge-shaped. The wedges can form a disc with their tips all directed to the centre; for example, six such wedge pieces may lead to a hexagonal columnar mesophase. Further stacking of discs in a face-to-face configuration leads to columns [6,12,13].

To evaluate the possibilities of self-assembly of **2CHd-10** and **1CHn-10** molecules on HOPG, we note that their amide functionalities can efficiently stabilize structures through intermolecular hydrogen bonds. On the other hand, the alkyl chains are expected to promote self-assembly into extended structures through interchain van der Waals interactions as well as adsorption on HOPG due to their epitaxial match with the C–C bonds of graphite [16]. The structures produced, may, however, generally depend on a complex interplay of many weak interactions. The molecules are prototypes for symmetric and asymmetric hydrazine species, where **2CHd-10** represents two 2CHn-10 molecules linked together such that the amide functionality is not a head group but a central part, which is expected and found to have considerable influence on the self-assembly behaviour.

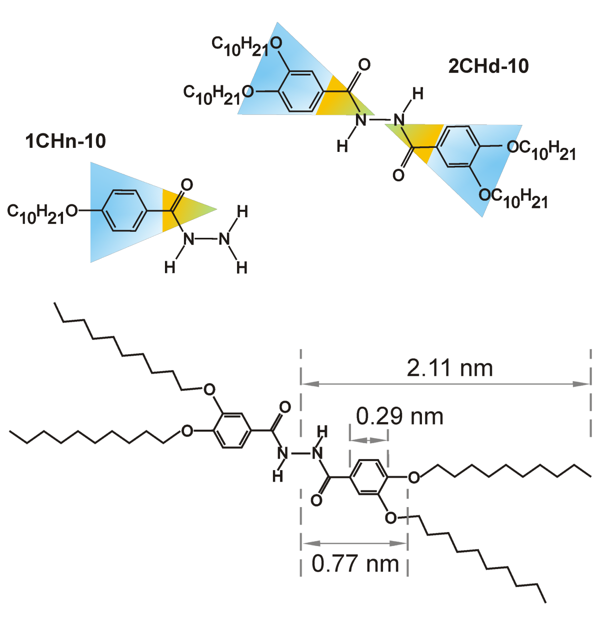

Figure 1: Structure models of **2CHd-10** (inversion symmetry) and **1CHn-10** (asymmetric). The coloured region represents the "wedge"-shaped nature of the molecules. The molecular dimensions given for **2CHd-10** are derived from [14,15].

We observe that the molecules self-assemble into one-dimensional structures at the solution/HOPG interface, which are distinctly different from those of the "disc-stacking" pattern in the bulk. The structures of elementary fibrils are explained by dimer or tetramer precursors followed by fibril formation through van der Waals interactions between alkyl chains. The molecular geometry plays a crucial role in deciding the type of oligomer precursor: self-assembly is based on dimer building blocks for **2CHd-10**, but tetramer building blocks for **1CHn-10**. It appears that the large-scale morphologies result as a direct consequence of the type of oligomer precursors they form.

As a substrate, highly oriented pyrolytic graphite (HOPG) is favoured in STM studies due to its high electrical conductivity, atomic flatness, chemical inertness and here also for its hydrophobic nature. Hydrophilic substrates could hinder the self-assembling ability of the molecules by strongly interacting with their amide functionalities and forcing them to lay flat on the surface. To study adsorbate architecture on an electrically conducting substrate in real space, scanning tunnelling microscopy (STM) is the experimental technique of choice. Although STM has been highly successful in atomic/submolecular probing of planar structures [17,18] and their dynamics [19], when it comes to one-dimensional structures, it has not shown the same level of efficacy [20]. Particularly for high-resolution imaging in an ambient/solution environment, data acquisition becomes an exhausting and time-consuming process. Difficulties arise from the requirement of having single-digit nanometre-wide isolated strands and locating them on a millimetre area substrate; thermal drift; movement/perturbation induced by tip motion and tip contamination [21]; the nonplanar nature of components within individual fibril units; and the presence of dangling alkyl chains. High-resolution STM imaging of 1-D structures has been successful in studying films of strands [22-24] and innate graphitic structures [25-27], but less so with isolated organic strands. Some reports of STM imaging to obtain high-quality images of strands include those of polypropylene [28], molecular chains of magnetic molecules [29], silicon nanowires [30], and DNA/biomolecules [31,32].

With regard to STM imaging of 1-D structures on HOPG, one should be wary of innate graphitic artefacts and 1-D fibre-like structures present on bare HOPG surface, mostly occurring as a result of cleaving [25-27]. Although, graphitic artefacts may show strikingly close resemblance to molecular fibrils, the two species can be distinguished from each other. Care has been practised at all stages during STM imaging as well as analysis to establish the adsorbate origin of the reported structures clearly. The ambiguity can be excluded due to the capability of **1CHn-10** and **2CHd-10** to produce fibrils (as evident from the AFM images), the absence of grain boundaries and single/multiple steps near the molecular wires [25] (which are the two most important causes for their appearance), and the discrepancy in periodicities between molecular structures and reported innate graphitic fibril-like objects [25-27]. Further, we note that all reported high-resolution graphitic strands exhibit a replica-type arrangement with strands appearing as a replica of each other with bright blobs aligned perfectly on a line against the long axis, while for our molecular structures such a replica pattern is not observed. We have extensively studied innate planar and fibril-like graphitic artefacts at large scales (micrometres) as well as with high-resolution (few nanometres) and found the graphitic structures to be similar to those reported previously but different from the fibril structures reported here.

Experimental

STM/AFM imaging

For sample preparation, solutions of different concentrations for each of the molecules were prepared by dissolving the respective sample in 1,2,4-trichlorobenzene ($C_6H_3Cl_3$, dielectric constant 2.2, boiling point 214 °C, 99% pure, Sigma-Aldrich Laborchemikalien GmbH, Seelze, Germany) in a dilution series in steps of 1/10. Higher concentrations often exhibit a gel-like character. The solution was usually sonicated or oven-heated to 45–50 °C for five to fifteen minutes before being applied to a freshly cleaved sample of highly oriented pyrolytic graphite (HOPG, ZYB grade, SPI supplies, West Chester, PA, USA). First, a suitably dilute concentration for STM imaging was found that leaves fibrils on HOPG without much clustering or bundling. Then, the particular concentration was repeatedly used for obtaining high-resolution STM images.

STM images were taken in the constant current mode under ambient conditions with a compact STM (Easyscan, Nanosurf AG, Liestal, Switzerland). Mechanically sharpened Pt/Ir (80/20) wires (Goodfellow Cambridge limited, Huntingdon, United Kingdom) were used as tips. Prior to measurements on molecular layers, the bare HOPG substrate was imaged to ensure the quality of the STM tip and the cleanliness of the substrate surface. By imaging the atomic structure of the bare graphite, the scanner was calibrated at regular time intervals so that the precision of measurements was solely limited by thermal drift. The entire scan area was also imaged before molecules were deposited, to check for graphite artefacts. The ambient temperature was stabilized to be within ±1.0 °C of room temperature, and the scanner was always given time to thermally equilibrate and mechanically relax, to reduce thermal drift and piezo creep to a minimum during measurements. Furthermore, images used for structural analysis were those with minimal thermal drift, and a drift correction was done whenever feasible.

For imaging of molecular structures, the tip was retracted slightly, and a drop of the solution was applied onto the basal plane of HOPG to form a meniscus between the tip and the surface. Imaging was performed at the solution–solid interface where typical operating conditions were V_t = 1.3 V tunnelling voltage and I_t = 0.60 nA tunnelling current for the molecule and 0.05 V at 1.00 nA for imaging the bare graphite substrate. Occasionally, another preparation method was used, i.e., a drop of the solution was deposited on HOPG and imaging was started after complete evaporation of the solvent. Similar results were obtained by employing either preparation method, and once formed, the structures remained stable for many hours to days.

Images represent raw data unless otherwise stated, and flattening was done only for large area images, by using the WSxM software [33]. A compact AFM (Easyscan, Nanosurf AG, Liestal, Switzerland) in contact-mode was used to characterize the nanoscale morphology. Silicon cantilevers (Nanosensors) with force constants in the range from 0.2 to 0.4 N/m were employed, and the images were taken under ambient conditions at a scanning rate of 1–3 lines/second with a typical force setpoint of 25 nN. Topographic data were recorded simultaneously in trace and retrace to check for scan artefacts. From clear solutions, imaging was done after a complete evaporation of the solvent. For concentrated solutions, solvent remained partially trapped within the gel network of fibrils during imaging.

Chemical syntheses

Materials and techniques

Methyl 4-hydroxybenzoate (99%, Sigma Aldrich), methyl 3,4-dihydroxybenzoate (97% Alfa Aesar) 1-bromodecane (98%, Alfa Aesar), potassium iodide (99.5%, Fluka), potassium carbonate (99%, Sigma Aldrich), potassium hydroxide (85–100%, Sigma Aldrich), hydrochloric acid (37%, Sigma Aldrich), thionylchloride (98%, Sigma Aldrich), hydrazine monohydrate (98%, Alfa Aesar) were used for the chemical syntheses. ^{1}H NMR (500 MHz) and ^{13}C NMR (125 MHz) were measured on a Bruker Avance DPX-250 spectrometer, tetramethylsilane (TMS) was applied as an internal standard in deuterated chloroform at 20 °C. Melting points were measured on a Netzsch DSC 204 Phoenix differential scanning calorimeter (DSC). About 10 mg of sample was used. In all cases, the heating and cooling rates were 10 °C/min. Indium and cyclohexane were used as calibration standards. IR spectra were measured on a Bruker Vertex 70 FT infrared spectrometer, equipped with a MVP Star ATR reflection device.

[4-(Decyloxy)benzoyl]hydrazine (**1CHn-10**)

Synthesis of methyl 4-(decyloxy)benzoate (1): Methyl 4-hydroxybenzoate (15.215 g; 100 mmol) was dissolved in 500 mL cyclohexanone, and 24.3 g (110 mmol) 1-bromodecane, 41.3 g (30 mmol) potassium carbonate, and 0.5 g potassium iodide were added and heated under reflux for 5 h under a nitrogen atmosphere. The reaction mixture was filtered hot and concentrated on a rotary evaporator. After recrystallization from 600 mL MeOH/EtOH (2/1), a white wax-like solid was obtained. Yield: 24.3 g (83%); mp 45 °C (lit.: 44–45 °C); ^{1}H NMR (CDCl$_3$) δ 0.916 (t, 3H, -CH$_3$), 1.337 (m, 12H, -CH$_2$-), 1.458 (m, 2H, -**CH$_2$**-CH$_2$-CH$_2$-O-), 1.812 (m, 2H, -**CH$_2$**-CH$_2$-O-), 3.896 (s, 3H,-COO-CH$_3$), 4.019 (t, 3H, -CH$_2$-O-), 6.91 (d, 2H, aromatic), 8.0 (d, 2H, aromatic).

Synthesis of [4-(decyloxy)benzoyl]hydrazine (1CHn-10)*:* Compound **1** (10 g; 34 mmol) was dissolved in 20 g pentanol, and 20 g hydrazine monohydrate was added and heated under reflux at 180 °C for 6 h; the mixture was poured into 200 mL cold MeOH and filtered. The precipitate was washed two times with 50 mL cold MeOH. Afterwards recrystallization in MeOH, 5.3 g (53%) of a white solid was obtained. IR ν: 3319, 3221, 3168, 3066, 3022, 2957, 2920, 2872, 2855, 1645, 1618, 1575, 1506, 1477, 1394, 1352, 1304, 1253, 1188, 1172, 1115, 1030, 987, 835, 652 cm^{-1}; ^{1}H NMR (CDCl$_3$) δ 0.88 (t, 3H, -CH$_3$), 1.3 (m, 12H, -CH$_2$-), 1.4 (m, 2H, -**CH$_2$**-CH$_2$-CH$_2$-O-), 1.75 (m, 6H, -**CH$_2$**-CH$_2$-O-), 2.25 (broad, 3H, -NH-NH$_2$), 3.98 (t, 2H, -CH$_2$-O-), 6.88 (d, 2H, aromatic), 7.75 (d, 2H, aromatic). **1CHn-10** has been mentioned as a synthetic intermediate in several reports [34-36].

N-*N′*-bis[3,4-bis(decyloxy)benzoyl]hydrazine (**2CHd-10**)

Synthesis of methyl 3,4-bis(decyloxy)benzoate (3): Methyl 3,4-dihydroxybenzoate (6.0 g; 32.94 mmol) was dissolved in 200 mL cyclohexanone, and 16.0284 g (72.468 mmol) 1-bromooctane, 13.658 g (98.82 mmol) potassium carbonate and 0.2 g potassium iodide were added and heated under reflux for 5 h under a nitrogen atmosphere. The reaction mixture was filtered hot and concentrated on a rotary evaporator. After recrystallization from 200 mL MeOH/EtOH (2/1), a white wax-like solid was obtained. Yield: 11.3164 g (76.6%); R_f 0.56 (CH$_2$Cl$_2$); ^{1}H NMR (CDCl$_3$) δ 0.885 (t, 6H, -CH$_3$), 1.28 (m, 24H, -CH$_2$-), 1.48 (m, 4H, -CH$_2$-CH$_2$-CH$_2$-O-), 1.83 (m, 4H, -CH$_2$-CH$_2$-O), 3.88 (s, 3H,-COO-CH$_3$), 4.04 (m, 4H, -CH$_2$-O-), 6.885 (d, 1H, aromatic.), 7.593 (d, 1H, aromatic), 7.71 (d,1H, aromatic).

Synthesis of 3,4-bis(decyloxy)benzoic acid (4): Compound **3** (8.0014 g; 17.8 mmol) was dissolved in 350 mL boiling EtOH, and a solution of 11.2 g (200 mmol) KOH in 25 mL water was added and heated under reflux for 4 h. The reaction mixture was poured into 1 L distilled water, acidified with hydrochloric acid to pH 1, and stirred for 1 h. Afterwards the precipitate was filtered and recrystallized from acetone. White crystals (7.6346 g; 98.7%) were obtained. ^{1}H NMR (CDCl$_3$) δ 0.885 (t, 6H, -CH$_3$), 1.319 (m, 24H, -CH$_2$-), 1.481 (m, 4H, -**CH$_2$**-CH$_2$-CH$_2$-O-), 1.84 (m, 4H, -**CH$_2$**-CH$_2$-O-), 4.051 (m, 4H, -CH$_2$-O-), 6.89 (d, 1H, aromatic.), 7.5935 (d, 1H, aromatic), 7.72 (d, 1H, aromatic).

Synthesis of 3,4-bis(decyloxy)benzoyl chloride (5): Compound **4** (5.0215 g; 11.55 mmol) was heated under reflux with 25 mL thionylchloride and 3 mL DMF for 2 h. The solvent was evaporated in vacuum at 60 °C. Finally 2.279 g (43.36%) of white crystals were obtained after recrystallization three times in dry acetone. ^{1}H NMR (CDCl$_3$) δ 0.878 (t, 6H, -CH$_3$), 1.282 (m, 24H, -CH$_2$-), 1.463 (m, 4H, -**CH$_2$**-CH$_2$-CH$_2$-O-), 1.833 (m, 4H, -**CH$_2$**-CH$_2$-O-), 4.045 (m, 4H, -CH$_2$-O-), 6.85 (d, 1H, aromatic.), 7.582 (d, 1H, aromatic), 7.745 (d,1H, aromatic).

Synthesis of *N*-*N′*-bis[3,4-bis(decyloxy)benzoyl]hydrazine (2CHd-10): Compound **5** (2.2644 g; 5 mmol) was dissolved in 50 mL dry dioxane, 20 mL dry THF and 2 mL benzene, then 0.25 g (5 mmol) hydrazine monohydrate was added and stirred for 24 h. The precipitate was dissolved in 400 mL CHCl$_3$ and washed two times with 400 mL concentrated NaCO$_3$ in H$_2$O and also with H$_2$O. The organic phase was concentrated on a rotary evaporator and freeze dried from benzene. Yield: 1.9715 g (91.12%) white solid; ^{1}H NMR (CDCl$_3$) δ 0.893 (m, 12H, -CH$_3$), 1.318 (m, 48H,-CH$_2$-), 1.438 (m, 8H, -**CH$_2$**-CH$_2$-CH$_2$-O-), 1.82 (m, 8H, -**CH$_2$**-CH$_2$-O-), 4.011 (m, 8H, -CH$_2$-O-

), 6.85 (d, 2H, aromatic), 7.437 (d, 4H, aromatic.), 9.464 (broad, 2H, -NH). IR ν: 3160, 2957, 2920, 2849, 1600, 1566, 1516, 1472, 1458, 1394, 1267, 1220, 1143, 1119, 1070, 1020, 990, 866, 746, 721, 63 cm^{-1}.

Results and Discussion

2CHd-10 is expected to facilitate column formation in the bulk due to its partial disc-like design (Figure 1) already bestowed upon synthesis. It is expected to self-assemble into a complete disc and thereupon to a stacked arrangement of discs. It has been reported that symmetrically substituted methyloxy-3CHd-1 and ethyloxy-3CHd-2 form crystalline compounds that melt above 177 °C, while 3CHd with longer chains as well as **2CHd-10** form a columnar, hexagonal, disordered (C_{hd}) mesophase in the bulk [6]. AFM images in Figure 2 show the morphology of **2CHd-10** and **1CHn-10** on HOPG after deposition from high-concentration solutions: around 2.4 wt % for **2CHd-10** and 2.8 wt % for **1CHn-10**. Albeit **2CHd-10** possessing a particularly favourable geometry for column formation in the bulk, its morphology on the graphite surface is that of fibrillar crystallites of varied lengths rather than pure fibrils, as shown in Figure 2a.

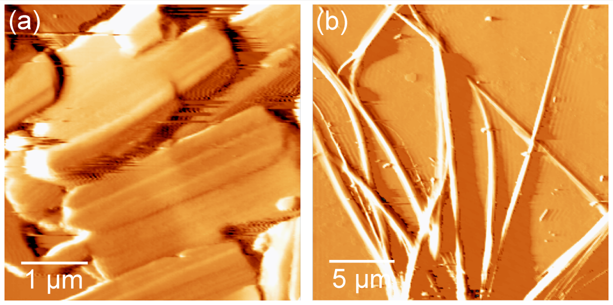

Figure 2: AFM images of randomly oriented (a) **2CHd-10** crystallites and (b) **1CHn-10** fibril bundles on HOPG obtained in high-concentration solutions.

Intrigued by the crystallite morphology of **2CHd-10**, we investigated its chain length variants, namely **2CHd-6** and **2CHd-14**, by AFM imaging, which vindicates their fibrillar-crystallite nature, with **2CHd-14** seeming to produce the longest fibres amongst the three, as demonstrated in Figure 3. On the other hand, **1CHn-10** deviates from the wedge-shape due to having only one alkoxy chain, but optical microscopy and AFM images reveal that **1CHn-10** is capable of forming fibril assemblies extending up to several tens of micrometres, as evident from Figure 2b. Note that **1CHn-10**, however, offers an additional hydrogen-bonding site (believed to enhance column ordering in the bulk). An explanation for this seemingly contrasting behaviour of **1CHn-10** and **2CHd-10** critically depends on the knowledge of the respective elementary fibril structures.

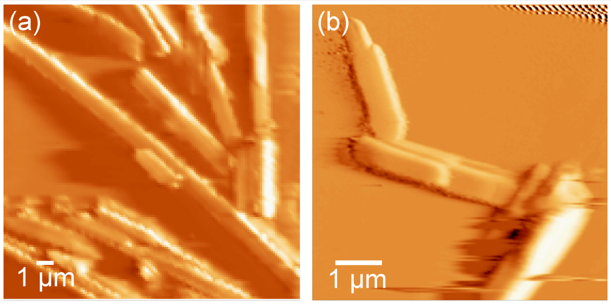

Figure 3: AFM images of (a) **2CHd-14** and (b) **2CHd-6** on HOPG taken to demonstrate the capability of the **2CHd-n** series to produce fibrillar crystallites.

To investigate the structure formation of **2CHd-10** on HOPG at a molecular scale, a drop of a dilute solution of **2CHd-10** (≈0.24 wt %) dissolved in 1,2,4-trichlorobenzene ($C_6H_3Cl_3$) was deposited on HOPG and the liquid/solid interface searched for the thinnest fibrils by STM. The use of dilute solutions for STM studies is prompted by the requisite of locating isolated elementary strands on the substrate. Fibre bundles are oriented mostly randomly but isolated elementary fibrils follow low-index graphite surface directions. Generally, the length of isolated fibrils exceeds the scan range of the STM (≈800 nm). Figure 4a is a typical STM image showing a bundle consisting of two elementary fibrils, while Figure 4d is a close-up of the left fibril taken to reveal the internal structure and its dimensions.

Having a width of 5.6 nm, the fibril consists of bright blobs arranged side-by-side in a zigzag pattern that slightly varies along the fibril. Bright blobs can sometimes be resolved into two elliptical features that are about 1.4 nm long (arrows in Figure 4d). Assuming that electron-rich delocalized π clouds of the aromatic rings dominate the image contrast [37], the bright blobs are interpreted as hydrogen-bonded dimers, as shown in Figure 4b. Note that the distance between adjacent bright blobs is 1.5 and 2.5 nm in directions perpendicular and parallel to the fibril axis, which is much larger than the interstack distance of 0.35 nm observed in mesophase columns in the bulk [10]. This means that the fibrils cannot be explained by a stacked structure stabilized by π* orbital overlap of adjacent aromatic rings. The measured heights (brightness) of individual bright blobs in a zigzag vary slightly, which could be a convolution of electronic and topographic effects implying the three-dimensional nature of the structure hidden in the topographic image.

A structural model is proposed for the **2CHd-10** fibril based on dimer precursors involving mainly hydrogen bonding along the circumference and van der Waals bonding between interdigitated dangling alkyl chains along the fibril axis, as shown in Figure 5a as a “net” of the fibril. Note that the periodicity of the

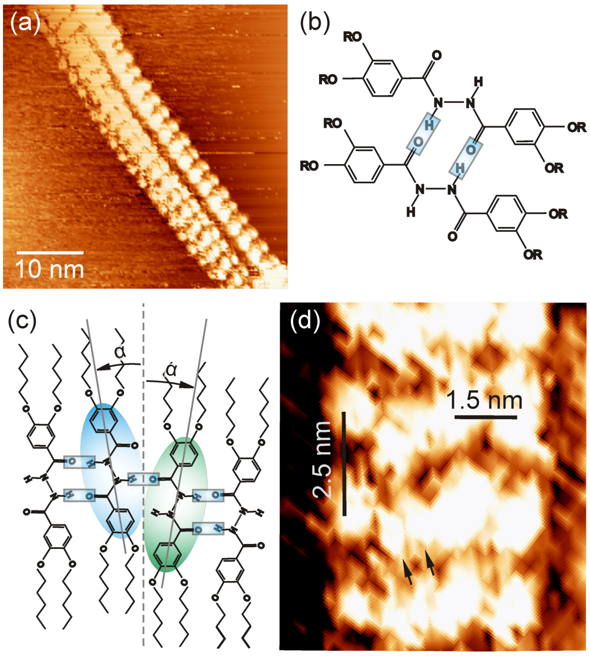

Figure 4: (a) STM image of two adjacent **2CHd-10** elementary fibrils on HOPG. Imaging parameters are V_t = 1.3 V and I_t = 0.6 nA. (b) Structure of a **2CHd-10** dimer. (c) Dimer arrangement in fibril. (d) Magnified view of the left fibril from (a) revealing details of its internal structure.

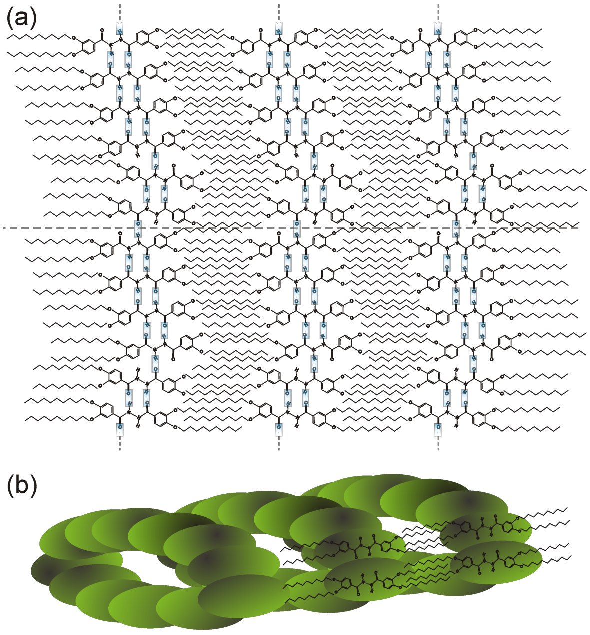

Figure 5: (a) Planar-sheet model (net) of a **2CHd-10** fibril section. The dashed line is drawn parallel to the fibrillar axis. (b) 3-D representation of a fibrillar fragment.

structure along the fibril axis, predicted by this model and the molecular dimensions given in Figure 1, is in reasonable agreement with the periodicity of 2.5 nm observed in experiments (see Figure 4d). Figure 5b is a 3-D model in which individual ellipsoids represent **2CHd-10** molecules. The ellipse representing the bright STM contrast feature defines the symmetry axis of the molecule while the fibril axis is defined by the direction of the alkyl chains, as illustrated in Figure 4c. The tilt of α = 9° between the molecular axis and the fibril axis is determined by aligning the alkyl chains while reducing their bending with respect to the aromatic rings to a minimum.

One could construct a perfectly planar molecular layer of surface-filling molecules based on the described construction principles. However, zigzag structures result from defects introduced by dimers flipped by 180° around the fibril axis (shaded blue and green in Figure 4c). As evident from Figure 4c and Figure 5a, such a flipped molecule can form only one hydrogen bond with the neighbouring dimer and is tilted in the opposite direction yielding a step in the molecular contour of the hydrogen-bonded units. The loss of one hydrogen bond at defect sites is partially compensated by additional interdimer hydrogen bonds (see Figure 5a). Due to a perfect interdigitation of alkyl chains, the fibril has only a weak interaction with the substrate. We speculate that defects introduce internal stress resulting in a small bending of the initially planar sheet. A fibril fragment may result if the specific zigzag structure facilitates a hydrogen-bond closure from open hydrogen bonds, as indicated (unbonded H atoms at the top of the net and O atoms at the bottom) in Figure 5a.

Fibril fragments can grow with different diameters depending on the number of molecules in the sheet, while the detailed zigzag structure determines whether a closure is possible or not. Once a closed fragment is formed, the fibril can easily grow along its axis by the attachment of more dimer units. Planar fragments that are unable to close may still grow axially leading to fibrillar crystallites, as the axial growth mechanism is basically the same as that for a closed net, i.e., through van der Waals interactions. It can also be conjectured that a closure is most plausible for nets with a small diameter, whereas large nets may lie flat on the surface and grow as crystallites. It is worth noting that the model described here displays striking similarities with the bulk mesophase fibrils in its basic constitution. First, from X-ray data for the bulk mesophase fibrils, the number of molecules per column (a disc) cross section is also found to be two, i.e., a dimer [6]. Second, the periphery of the fibril cross section in the columnar hexagonal disordered mesophase consists of six dimer units just as for the six-membered dimer fibril cross section shown in Figure 5b.

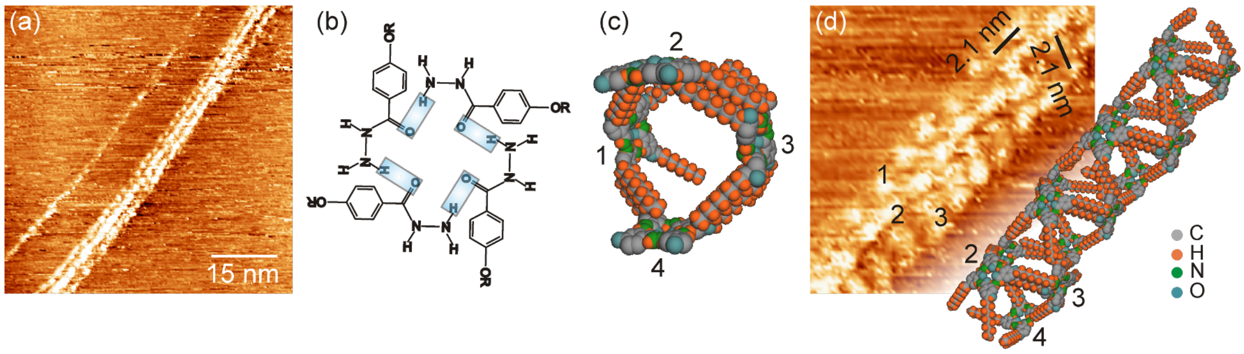

Figure 6: (a) STM image showing a single-strand and a three-strand fibril of **1CHn-10** on HOPG. Imaging parameters are V_t = 1.29 V and I_t = 0.69 nA. (b) Structure of a **1CHn-10** tetramer. (c) Model of the repeating unit of a three-strand fibril formed by four tetramers. (d) Magnified view of the three-strand fibril section from (a) and the corresponding space-filling model based on the construction principle discussed in the text.

Next, we investigated the structure formation of **1CHn-10** on HOPG at the molecular scale. Figure 6a shows an STM image taken after a drop of a dilute solution of **1CHn-10** in 1,2,4-trichlorobenzene (≈0.29 wt %) had been deposited on HOPG. Again fibrils with a length covering the entire STM scan range are observed. Unlike for **2CHd-10**, we observe single-strand and three-strand fibrils (top view) as shown in Figure 6a. As revealed by Figure 6d, the periodicity of bright blobs along the fibril bundle as well as the lateral distance between strands is 2.1 nm. The individual bright blobs of about 1.5 nm appear as rather elusive features in single-strand fibrils. We assume hydrogen-bonded tetramers, as shown in Figure 6b, to be the building blocks for the strand structure. The tiny single-strand fibrils yielding only unstable STM contrast may simply be linear arrangements of tetramers between overlapping alkyl chains.

The three-strand geometry appears as a much more rigid structure, and a plausible repeating unit for it is illustrated in Figure 6c in which four tetramer building blocks form a ring stabilized by van der Waals interactions between dangling alkyl chains. This ring is a highly symmetric unit in which the tetramer aryl cores (assuming the tetramers to be planar) appear pairwise parallel (tetramers 1‖3 and 2‖4), with 2 and 4 displaced from 1 and 3 by half the periodicity along the fibril axis. In a projection perpendicular to tetramer 2, tetramer 4 appears precisely below tetramer 2, and 1 and 3 appear symmetrically at the sides of 2 where the connecting lines 1–2 and 2–3 enclose an angle of 120°. In such a ring unit, 8 of the 16 available alkyl chains are van der Waals bonded to each other while four are dangling at one side of the ring and four at the other side (two alkyl chains each from 2 and 4 are not shown in Figure 6c).

Unlike **2CHd-10**, here no condition is to be met for the closure of **1CHn-10** tetramers to form a ring. Due to the symmetry of the ring unit, the dangling alkyl chains are at the right positions to connect to alkyl chains of a following ring in the very same manner the tetramers in a ring unit are bonded internally, i.e., through van der Waals interactions. This interaction between subsequent tetramer rings leads to their growth into a linear chain. Hence, a string of ring units yields a fibril with a well-defined diameter and a saturation of all possible van der Waals bonds between alkyl chains. Assuming the strand of tetramers numbered 4 is lying flat on the HOPG surface, the fibril structure appears in the above-mentioned projection, and tetramers 1, 2 and 3 appear as bright blobs in the STM image of Figure 6d ordered in a linear herringbone arrangement exhibiting the 120° angle. A 3-D space-filling model for the fibril is shown in Figure 6d, which is a periodic structure of the ring unit of Figure 6c at a periodicity of 2.1 nm.

To visualise the structure of the **1CHn-10** fibril more clearly, a simplified model is shown in Figure 7. The "net" in Figure 7a (fibril dimensions are not drawn to scale for the 2-D representation) shows the interdigitation of alkyl chains between neighbouring tetramers in which the tetramer building blocks are represented by squares. The structure constituted by blocks 1, 2, 3 and 4 represents a repeating unit of the fibril. The aliphatic chains of the subsequent tetramers interact through van der Waals forces between the interdigitating chains. Thus, the capability of **1CHn-10** to achieve a fibril structure is based on its tendency to form tetramers, which is a crucial step in the process. The closure of the "net" is facilitated by the coupling between tetramers 3 and 3′ and tetramers 4 and 4′ and similarly all equivalent tetramers along the fibril, naturally defining the unique diameter of the fibril.

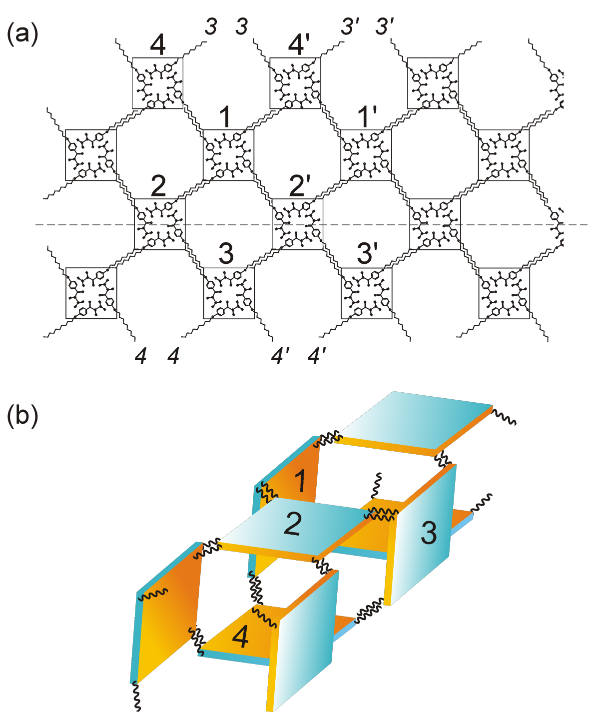

Figure 7: (a) Planar sheet (net) model (for representational purpose only) of a **1CHn-10** fibril section. The dashed line is drawn parallel to the fibril axis. (b) 3-D configuration for a three-strand fibril.

Conclusion

We describe hitherto unexplored routes for the formation of mesophase-based, one-dimensional organic structures from hydrogen-bonded dimer/tetramer motifs. Linear structures are formed from planar molecular precursors by means of ring closure aided by van der Waals interactions between alkyl chains. The elementary fibrils of amphiphilic hydrazine derivatives observed at the liquid/solid interface show a distinctly different internal structure than the "disc-stacking" arrangement observed in the bulk. The molecular geometry is decisive in determining the precursors and eventually the structure of the elementary strands: dimer precursors for **2CHd-10** and tetramers for **1CHn-10**. While the internal dimer structure of **2CHd-10** fibrils allows fibrils of different diameters to be formed, **1CHn-10** fibrils are either simple linear chains of tetramers, or tetramers interweaved to form tubes with a fixed diameter. It follows that the large-scale morphologies at the liquid/solid interface are determined at the molecular/precursor level. Despite the compounds being specially designed as symmetric and asymmetric molecules, no inference is immediately discernible on the dependence of fibril structure on the symmetry, as it can easily be seen that the asymmetry of **1CHn-10** is broken at the precursor (tetramer) level. The precursor geometry rather than molecular symmetry determines the disparate fibril structures observed for the two investigated molecules.

Supporting Information

A large-scale STM image of the area in Figure 6 and the height profile of the strands are available in the Supporting Information.

Supporting Information File 1

Large-scale STM image and height profile.
[http://www.beilstein-journals.org/bjnano/content/supplementary/2190-4286-3-75-S1.pdf]

Acknowledgements

This work has been supported by the PhD program "Synthesis and Characterization of surfaces and Interfaces assembled from Clusters and Molecules" funded by the State of Niedersachsen, Germany.

References

1. Hong, J.-P.; Um, M.-C.; Nam, S.-R.; Hong, J.-I.; Lee, S. *Chem. Commun.* **2009,** 310–312. doi:10.1039/b816030a
2. Schenning, A. P. H. J.; Meijer, E. W. *Chem. Commun.* **2005,** 3245–3258. doi:10.1039/b501804h
3. Schmidt-Mende, L.; Fechtenkötter, A.; Müllen, K.; Moons, E.; Friend, R. H.; MacKenzie, J. D. *Science* **2001,** *293,* 1119–1122. doi:10.1126/science.293.5532.1119
4. Ward, J. M.; Pei, Z.-M.; Schroeder, J. I. *Plant Cell* **1995,** *7,* 833–844. doi:10.1105/tpc.7.7.833
5. Hirst, A. R.; Escuder, B.; Miravet, J. F.; Smith, D. K. *Angew. Chem., Int. Ed.* **2008,** *47,* 8002–8018. doi:10.1002/anie.200800022
6. Beginn, U. *Prog. Polym. Sci.* **2003,** *28,* 1049–1105. doi:10.1016/S0079-6700(02)00150-8
7. Sangeetha, N. M.; Maitra, U. *Chem. Soc. Rev.* **2005,** *34,* 821–836. doi:10.1039/b417081b
8. Lei, S.; Puigmartí-Luis, J.; Minoia, A.; Van der Auweraer, M.; Rovira, C.; Lazzaroni, R.; Amabilino, D. B.; De Feyter, S. *Chem. Commun.* **2008,** *2008,* 703–705. doi:10.1039/B716533A
9. Rahe, P.; Nimmrich, M.; Greuling, A.; Schütte, J.; Stará, I. G.; Rybáček, J.; Huerta-Angeles, G.; Starý, I.; Rohlfing, M.; Kühnle, A. *J. Phys. Chem. C* **2010,** *114,* 1547–1552. doi:10.1021/jp911287p
10. Boden, N.; Bushby, R. J.; Clements, J.; Movaghar, B.; Donovan, K. J.; Kreouzis, T. *Phys. Rev. B* **1995,** *52,* 13274–13280. doi:10.1103/PhysRevB.52.13274
11. Nguyen, T.-Q.; Martel, R.; Bushey, M.; Avouris, P.; Carlsen, A.; Nuckolls, C.; Brus, L. *Phys. Chem. Chem. Phys.* **2007,** *9,* 1515–1532. doi:10.1039/b609956d
12. Chandrasekhar, S.; Ranganath, G. S. *Rep. Prog. Phys.* **1990,** *53,* 57–84. doi:10.1088/0034-4885/53/1/002
13. Percec, V.; Ahn, C.-H.; Ungar, G.; Yeardley, D. J. P.; Möller, M.; Sheiko, S. S. *Nature* **1998,** *391,* 161–164. doi:10.1038/34384
14. Lide, D. R.; Frederikse, H. P. R. *CRC Handbook of Chemistry and Physics,* 83rd ed.; CRC Press: Boca Raton, 2003.
15. Hentschke, R.; Winkler, R. G. *J. Chem. Phys.* **1993,** *99,* 5528–5534. doi:10.1063/1.465971

16. Xu, W.; Dong, M.; Gersen, H.; Rauls, E.; Vázquez-Campos, S.; Crego-Calama, M.; Reinhoudt, D. N.; Lægsgaard, E.; Stensgaard, I.; Linderoth, T. R.; Besenbacher, F. *Small* **2008,** *4,* 1620–1623. doi:10.1002/smll.200800377
17. Lackinger, M.; Griessl, S.; Heckl, W. A.; Hietschold, M.; Flynn, G. W. *Langmuir* **2005,** *21,* 4984–4988. doi:10.1021/la0467640
18. Thomas, L. K.; Kühnle, A.; Rode, S.; Beginn, U.; Reichling, M. *J. Phys. Chem. C* **2010,** *114,* 18919–18924. doi:10.1021/jp105205y
19. Lackinger, M.; Griessl, S.; Kampschulte, L.; Jamitzky, F.; Heckl, W. M. *Small* **2005,** *1,* 532–539. doi:10.1002/smll.200400078
20. del Mercato, L. L.; Pompa, P. P.; Maruccio, G.; Della Torre, A.; Sabella, S.; Tamburro, A. M.; Cingolani, R.; Rinaldi, R. *Proc. Natl. Acad. Sci. U. S. A.* **2007,** *104,* 18019–18024. doi:10.1073/pnas.0702843104
21. Rettig, C.; Bödecker, M.; Hövel, H. *J. Phys. D: Appl. Phys.* **2003,** *36,* 818–822. doi:10.1088/0022-3727/36/7/308
22. Yang, Y.; Yang, Z.-Y.; Yi, Y.-P.; Xiang, J.-F.; Chen, C.-F.; Wan, L.-J.; Shuai, Z.-G. *J. Org. Chem.* **2007,** *72,* 4936–4946. doi:10.1021/jo070525a
23. Schiffrin, A.; Riemann, A.; Auwärter, W.; Pennec, Y.; Weber-Bargioni, A.; Cvetko, D.; Cossaro, A.; Morgante, A.; Barth, J. V. *Proc. Natl. Acad. Sci. U. S. A.* **2007,** *104,* 5279–5284. doi:10.1073/pnas.0607867104
24. Yu, M.; Kalashnyk, N.; Xu, W.; Barattin, R.; Benjalal, Y.; Lægsgaard, E.; Stensgaard, I.; Hliwa, M.; Bouju, X.; Gourdon, A.; Joachim, C.; Besenbacher, F.; Linderoth, T. R. *ACS Nano* **2010,** *4,* 4097–4109. doi:10.1021/nn100450q
25. Chang, H.; Bard, A. J. *Langmuir* **1991,** *7,* 1143–1153. doi:10.1021/la00054a021
26. Heckl, W. M.; Binnig, G. *Ultramicroscopy* **1992,** *42,* 1073–1078. doi:10.1016/0304-3991(92)90404-8
27. Simonis, P.; Goffaux, C.; Thiry, P. A.; Biro, L. P.; Lambin, P.; Meunier, V. *Surf. Sci.* **2002,** *511,* 319–322. doi:10.1016/S0039-6028(02)01511-X
28. Carroll, D. L.; Czerw, R.; Tekleab, D.; Smith, D. W. *Langmuir* **2000,** *16,* 3574–3577. doi:10.1021/la991534k
29. Petukhov, K.; Alam, M. S.; Rupp, H.; Strömsdörfer, S.; Müller, P.; Scheurer, A.; Saalfrank, R. W.; Kortus, J.; Postnikov, A.; Ruben, M.; Thompson, L. K.; Lehn, J.-M. *Coord. Chem. Rev.* **2009,** *253,* 2387–2398. doi:10.1016/j.ccr.2009.01.024
30. Ma, D. D. D.; Lee, C. S.; Au, F. C. K.; Tong, S. Y.; Lee, S. T. *Science* **2003,** *299,* 1874–1877. doi:10.1126/science.1080313
31. Clemmer, C. R.; Beebe, T. P., Jr. *Science* **1991,** *251,* 640–642. doi:10.1126/science.1992517
32. Riemann, A.; Nelson, B. *Langmuir* **2009,** *25,* 4522–4525. doi:10.1021/la803867w
33. Horcas, I.; Fernández, R.; Gómez-Rodríguez, J. M.; Colchero, J.; Gómez-Herrero, J.; Baro, A. M. *Rev. Sci. Instrum.* **2007,** *78,* 013705. doi:10.1063/1.2432410
34. Zaschke, H.; Nitsche, K.; Schubert, H. *J. Prakt. Chem.* **1977,** *319,* 475–484. doi:10.1002/prac.19773190317
35. Parra, M.; Belmar, J.; Zunza, H.; Zúñiga, C.; Villouta, S.; Martínez, R. *Bol. Soc. Chil. Quim.* **1993,** *38,* 325–330.
36. Khairuddean, M.; Twieg, R. J. *Mol. Cryst. Liq. Cryst.* **2009,** *503,* 3–31. doi:10.1080/15421400902841478
37. Gawronski, H.; Henzi, J.; Simic-Milosevic, V.; Morgenstern, K. *Appl. Surf. Sci.* **2007,** *253,* 9047–9053. doi:10.1016/j.apsusc.2007.04.038

License and Terms